Search for direct production of charginos and neutralinos using final states with highly boosted hadronically decaying bosons in pp collisions at $\sqrt{s}$ = 13 TeV with the ATLAS detector

Yuta Okazaki

Abstract

The Standard Model (SM) in particle physics describes the interaction among elementary particles and successfully explains most of the experimental results. However, some problems still remain, for instance, missing dark matter candidates and the quadratic divergence of Higgs boson mass. Supersymmetry (SUSY) is based on a space-time symmetry of quantum field theory, which transforms bosons into fermions and vice versa. The SUSY introduces superpartners of the SM particles, is one of the most promising new physics scenarios beyond the SM. In this scenario, if the masses of the SUSY particles are typically $O(100\ \text{GeV}) \sim O(\text{TeV})$, it is known that the lightest neutralino can be a good candidate for the dark matter and that the problem is solved by canceling the correction of the Higgs boson mass by the SM particle and its superpartners. Besides, SUSY can explain the recent experimental result on the muon magnetic moment (g-2). Large Hadron Collider (LHC) provides TeV-scale elementary process in proton-proton (pp) collisions. Therefore, it is the only place where the SUSY particles can be directly searched for.

In this thesis, a search for electroweakinos (charginos and neutralinos), which are the superpartners of the SM electroweak bosons, is reported by using 139 fb^{-1} of $\sqrt{s}$ = 13 TeV pp-collision data at the LHC collected by the ATLAS detector. The signals are pair-produced charginos and neutralinos, which decay into light electroweakinos and the SM electroweak bosons ($W/Z/h$). With the mass difference between heavy electroweakinos and the light ones being large, the SM electroweak bosons have high momenta in the target models.

The production cross-section of electroweakinos is smaller than one of the strong SUSY particles, such as squark or gluino. In order to overcome the small production cross-section of electroweakinos, a fully hadronic final state is focused on in this thesis. Then, the SM electroweak bosons decay hadronically, and the quarks decayed from the bosons are collimated. Consequently, while each quark is not reconstructed as a jet separately, and two quarks can be reconstructed as a single large-radius jet.

There are three advantages of the fully hadronic final state. The first one is a statistical benefit by large branching ratios of the SM electroweak bosons. The second one is using characteristic signatures of jets to identify as the SM electroweak bosons. The last one is a small dependency on the signal model by targeting all the SM electroweak bosons because they are reconstructed as large-radius jets. Thanks to them, the search for electroweakinos with only light quarks ($u,\ d,\ s,\ c$) in the final state is for the first time performed in this thesis, and the sensitivity on the heavy electroweakinos is significantly improved compared to the previous analyses using other final states. A new boosted $W/Z/h$ jet identification using the mass and substructures of the large-radius jets significantly improves the sensitivity.

The number of observed events in the data was consistent with the SM prediction, and there was no significant excess derived from electroweakinos in the data with respect to the SM prediction. Exclusion limits at the 95% confidence level on the heavy electroweakino mass parameter are set as a function of the light electroweakino mass parameter. They are set on wino or higgsino production models with various assumptions, such as the branching ratio of their decaying and the type of lightest SUSY particle. In the wino (higgsino) production models, a wino (higgsino) mass up to 1060 (900) GeV is excluded when the lightest SUSY particle mass is below 400 (240) GeV and the mass difference is larger than 400 (450) GeV.

Thus, this analysis provides the most stringent limits on the wino or higgsino pair production modes with various branching ratio and the type of the LSP. Besides, the most stringent constraints on various SUSY scenarios motivated by the dark matter, the muon g-2 anomaly, and the naturalness are set by interpreting the results.

Acknowlegements

This thesis could not have been completed without the support of many people.

I would like to thank Prof. Tsuyoshi Nakaya for all his comments and suggestions of this paper. This thesis had been stalled for about two months, but his comments accelerated its completion. I also deeply appreciate Prof. Kunihiro Nagano for discussing the structure of this thesis with me in detail and helping me to complete it more readable. I also express Dr. Toshi Sumida for the suggestions for papers and presentations in both English and Japanese and discussion during about five years.

My special thanks go to Dr. Takuya Nobe and Dr. Shion Chen, who have been good advisors for jets (especially boson tagging technique) and the ATLAS SUSY analysis, roommates. I greatly thank Dr. Takuya's advice for boson tagging, large-R jet energy and mass calibration in my another works to search for di-boson resonance. Besides, Dr. Takuya used to cook biryani, stewed diced pork in Japanese "kakuni", Tiramisù, and diet food "Numa", then, my diet has been enhanced. Additionally, I would express my great appreciation to Dr. Shion for his advice on helping me to interpret my results. I also thank Dr. Shion for running with me.

I would like to thank Mr. Yoshiaki Tsujikawa. I would not have been able to submit this thesis without him.

I would express my appreciation to Prof. Koji Terashi and Dr. Tomoyuki Saito for their advice on the analysis. Besides, Prof. Koji gave me many advice for boson tagging, large-R jet energy and mass calibration. Additionally, I thank Dr. Tomoyuki for working together to upgarde the ATLAS muon level-1 trigger system.

I express my gratitude to Prof. Osamu Sasaki, Prof. Yasuyuki Okumura, Prof. Masaya Ishino, Prof. Hisaya Kurashige, Prof. Makoto Tomoto, Dr. Junpei Maeda, Dr. Masato Aoki, Dr. Tatsuya Masubuchi, Dr. Kentaro Kawade, Dr. Yasuyuki Horii to working together to operate ATLAS endcap muon level-1 trigger system.

I would like to thank Dr. Shunichi Akatsuka and Dr. Yohei Noguchi for their supports on the life in Kyoto and French and sharing time of research and eating. I am grateful to Dr. Takuya Tashiro and Dr. Takuto Kunigo for their advice on the life at CERN and how to brew coffee. I appreciate Dr. Kenta Uno, Mr. Kenta Uchida, Mr. Atsushi Mizukami for letting me ride with them in their cars and sharing time to relax my life at CERN by playing tennis and cycling. I express my gratitude to Dr. Kosuke Takeda and Dr. Tomomi Kawaguchi for sharing time of research.

I appreciate Dr. Yuji Enari and his wife for supporting to solve some trouble in French.

I would like to thank Mr. Yuya Mino for the discussion of SUSY analysis. I express Mr. Koichiro Kuniyoshi, Mr. Masayuki Hatano, Mr. Yoshiaki Tsujikawa, Mr. Ren Kobayashi, Mr. Nobuyuki Yoshimura, Mr. Takane Sano, Mr. Chihiro Kawamoto for interesting presentations and discussions on the trigger at the meetings.

I thank to the members of the Kyoto University HEP group, especially Dr. Masamitsu Mori, Mr. Masashi Yoshida, Mr. Kazuhiro Nakamura, Mr. Wataru Uno for sharing time. I appreciate Prof. Roger A. Wendell, Prof. Osamu Tajima, Prof. Atsuko Ichikawa, Dr. Junya Suzuki, Dr. Tatsuya Kikawa, Dr. Shunsuke Adachi for interesting stories.

I express all the other members for their supports. I am grateful Ms. Eriko Hayashi, Ms. Harumi Sekiguchi, Ms. Mana Sasaki for all the support.

I would like to thank supports from my family, Masatoshi, Miyuki, and Kana.

Finally, I thank my wife, Hanayo for support at any time. She taught me that interacting with my family, Maron and Chiaki, can refresh me. Without her love and supports, I would not have completed this thesis.

Contents

List of Figures

List of Tables

1 Introduction

The Standard Model (SM) of the particle physics describes the interaction among elementary particles and successfully explains most experimental results. With Higgs boson discovery [1, 2] by the ATLAS [3] and CMS [4] experiments, all predicted particles in the SM have been observed. Since its discovery, the ATLAS and CMS experiments have been measuring the nature of the Higgs boson, such as the Yukawa coupling, using the Large Hadron Collider (LHC), the world's highest energy proton-proton collision (pp-collision). There is no deviation of the Yukawa couplings to SM fermions in the third generation (b, t, τ) and gauge bosons from the expected values [5]. However, there are still several remaining problems in the SM. One is that the SM does not explain naturally why the observed Higgs mass is $O(100\ \text{GeV})$, regardless of the large quantum correction ($> O(10^{36}\ \text{GeV}^2)$) by the SM particles. Another is the existence of the dark matter, which accounts for $\sim 85\%$ of the matter in the universe. However, it cannot be explained by the SM [6–9]. Thus, the existence of a new physics beyond the Standard Model (BSM) is implied.

One of the promising theoretical frameworks to resolve these problems is Supersymmetry (SUSY), which introduces an additional symmetry between fermions and bosons. SUSY also adds supersymmetric partners (superpartners) of the SM particles, with the same quantum numbers except for their spins. In the supersymmetry framework, the quantum correction for the Higgs mass is canceled between the SM particles and their superpartners ("naturalness"). Besides, the lightest SUSY particle can be a good candidate of the dark matter. The masses of the superpartners of the SM particles are predicted to be less than $O(\text{TeV})$ to explain these problems. Additionally, light SUSY particles can provide an explanation of the muon g-2 anomaly. LHC is the first and only accelerator that explores $O(\text{TeV})$ scale physics. Therefore, only the possible place where SUSY particles ($< O(\text{TeV})$) can be searched for directly.

The superpartners of quarks and gluons, called strong SUSY particles, have already been explored up to approximately 2 TeV on their mass. However, since the cross-sections of the superpartners of the SM electroweak bosons (electroweakinos) are smaller than strong SUSY particles, the electroweakinos have not yet been explored up to high mass. For example, the exclusion limit in the mass of a wino, which is the superpartner of the SU(2) gauge field, is up to 700 GeV. Then, in this thesis, we search for electroweakinos using the full amount of available data, corresponding to 139 fb^{-1}, collected by the ATLAS detector in 2015-2018. Our target is the pair production of electroweakinos ($\tilde{\chi}_{\text{heavy}}$), which decay into light electroweakinos ($\tilde{\chi}_{\text{light}}$) and either of W boson, Z boson, or Higgs boson ($W/Z/h$). In the previous searches, leptonically decaying W/Z bosons or b-tagged jets of $Z/h \to bb$ have been used in these searches for $\tilde{\chi}_{\text{heavy}} \to \tilde{\chi}_{\text{light}} + W/Z/h$. This is to suppress a huge amount of backgrounds caused by jets originating from quarks and gluons. However, the previous searches suffer from a low branching ratio of leptonically decaying bosons. Here, on the contrary, we challenge the fully hadronic final states ($W/Z/h \to qq/bb$ where q denotes light flavor quark, u, d, s, c), as shown in Figure 1.1 to profit its large branching fraction. The search for electroweakinos in the $qqqq$ final state with two W/Z bosons decaying into two light-flavor quarks is the first time at the LHC.

In the previous analyses, the number of leptons is required explicitly, i.e., the target bosons decayed from $\tilde{\chi}_{\text{heavy}}$ are determined for each analysis, for example, 1-lepton for $W \to l\nu$ and 2-leptons for $Z \to ll$. On

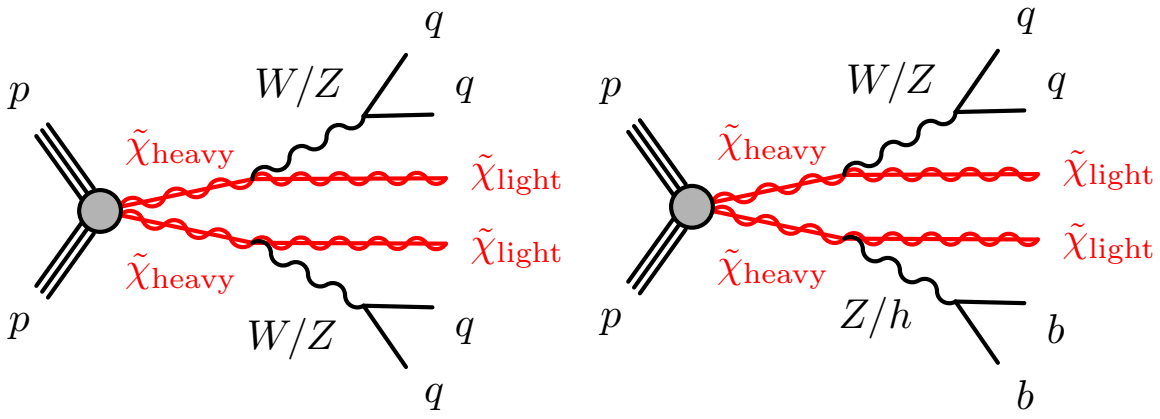

(a) $qqqq$ final state

(b) $qqbb$ final state

Figure 1.1: Diagram of the electroweakino decay in fully hadronic final states.

the contrary, $W/Z/h$ are all reconstructed as jets in the fully hadronic final states. Therefore, this analysis enables to search for electroweakinos comprehensively regardless of the decay process since the difference between $\tilde{\chi}^{\pm}_{\text{heavy}} \to W^{\pm} + \tilde{\chi}^{0}_{\text{light}}$ and $\tilde{\chi}^{\pm}_{\text{heavy}} \to Z/h + \tilde{\chi}^{\pm}_{\text{light}}$ is not deliberately identified.

The advantages of the search for electroweakinos in fully hadronic final states are:

- Statistical benefit due to a large branching ratio of hadronically decaying $W/Z/h$ bosons
- Characteristic signatures of boosted $W/Z/h$ for the case of a large mass splitting between $\tilde{\chi}_{\text{heavy}}$ and $\tilde{\chi}_{\text{light}}$, i.e., the two quarks from hadronically decaying bosons are collimated
- Less dependency to theoretical models (flavor independency)

We make use of the following two characteristic signatures for the search. One is the large missing transverse energy, $E_{\text{T}}^{\text{miss}}$, due to $\tilde{\chi}_{\text{light}}$ does not interact with the detector. The other is a large radius jet to reconstruct collimated daughter quarks decayed from boosted $W/Z/h$ as a single jet. Especially for this analysis, we introduced a novel experimental method of tagging boosted $W/Z/h$ bosons using large-radius jets ("boson tagging"). In the boson tagging, we use the jet substructure variables to distinguish $W/Z/h$ bosons from the quark- or gluon-initiated jets, as shown in Figure 1.2. The boson tagging was optimized to retain approximately 50% efficiency to $W/Z/h$ while to makes quark- or gluon-initiated jets down to 1-10%. The dominant backgrounds are $Z(\to \nu\nu)$ + jets, W + jets, and VV (V denotes $W/Z/h$), where $E_{\text{T}}^{\text{miss}}$ is due to leptonically decaying W/Z and quark- or gluon-initiated jets are mis-identified as boosted $W/Z/h$. Most of these backgrounds are not well described by a simulation. However, in this analysis, we estimated these backgrounds in a data-driven way.

After target theoretical models of this thesis are described in Chapter 2, experimental setup is discussed in Chapter 3 and 4. Then, how physics objects are experimentally reconstructed is explained in Chapter 5, additionally in Chapter 6, for the boson tagging, which is one of the keys of this thesis. How the candidates are selected and how backgrounds are evaluated as written in Chapter 7 and 8. Systematic uncertainties considered in this thesis are described in Chapter 9, and the results and theoretical interpretations are discussed in Chapter 10 and 11. The SUSY scenarios motivated by the dark matter, the naturalness, and the muon g-2 anomaly are discussed in the same chapter. The final conclusion is given in Chapter 12.

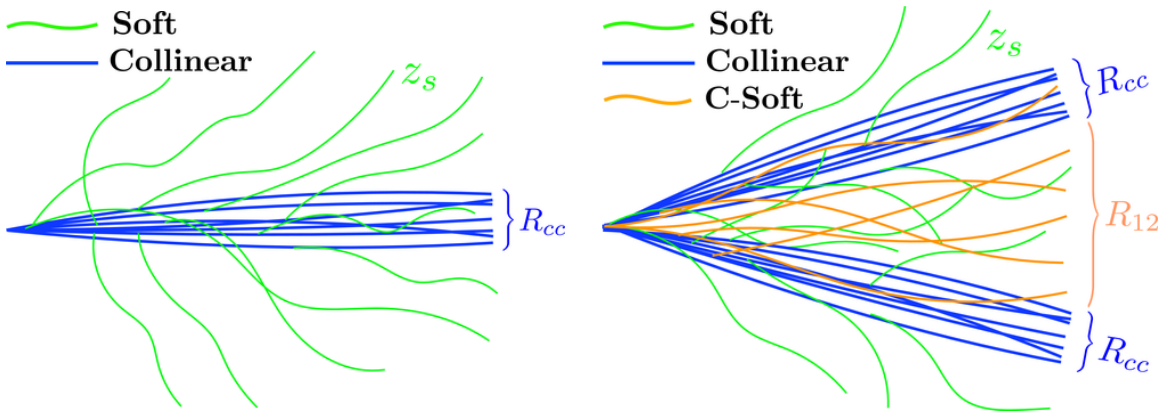

(a) 1-prong jets such as quark- or gluon-initiated jet

(b) 2-prong jets such as the hadronic decays of W/Z bosons

Figure 1.2: Schematic views of 1-prong jets (a) and 2-prong jets (b). Collinear (blue) and soft (green) radiations are illustrated. The angular size of the collinear radiation is R_{cc} and the p_{T} fraction of the soft radiation is z_s. For 2-prong jets, collinear-soft radiation emitted from the dipole formed by the two subjets represents the orange line. R_{12} represents the angle between these two subjets [10].

2 Theoretical Background

In this chapter, the theoretical backgrounds of the Standard Model (SM) and Supersymmetry (SUSY) are described. In the latter part, the target SUSY scenarios in this thesis and the search strategies for them are discussed in Sections 2.3 and 2.4.

2.1 The Standard Model

The Standard Model (SM) in particle physics provides the knowledge of interactions between elementary particles, and explains the most of experimental results. The outline of the SM and the problems are described in this section. More detail is discussed in Ref.[11].

In the SM, three types of particles are contained. One is fermions, which have the spin of 1/2 and compose matters. There are two groups in fermions: quarks and leptons. Both of the groups have up- and down-type, and three generations, as shown in Table 2.1. Each fermion has the charge conjugated partner referred to as anti-fermions, which have the same mass and spin. The second is gauge bosons, which have the spin of 1 and mediate the interaction between particles. There are three types of gauge bosons; gluon (g) characterizes strong interaction, and weak bosons (W, Z) and photon (γ) describe weak and electromagnetic interactions, respectively. The last one is the Higgs boson (h), which has the spin of 0 and provides the mass of particles through the Brout-Englert-Higgs (BEH) mechanism [12, 13].

Quarks and gluons carry color charges in the strong interaction, and three color charges and three anti-color charges are defined. The Quantum Chromodynamics (QCD) allows only particles with colorless states to exist as free particles, such as baryons or mesons composed of multiple quarks and gluons. Thus, when quarks and gluons are accelerated in scattering, bremsstrahlung cascades of gluons and quark-antiquark pairs are developed in the vicinity. The cascade is called "jet."

In the SM, there is a problem: the masses of the SM weak bosons (W, Z) are massive, while the electroweak Lagrangian prohibits the mass terms not to violate the gauge invariance. In order to solve this problem, the BEH mechanism [12, 13] is introduced to add an SU(2) doublet with a scalar field and potential to the SM Lagrangian. The vacuum expectation value in the potential is not 0, which is called "electroweak spontaneous symmetry breaking." In this mechanism, a new particle, the Higgs boson, is predicted. The Higgs boson was discovered by the ATLAS/CMS [1, 2], and the measured value of the spin was 0, i.e., it is consistent with the predicted particle. Therefore, all the particles in the SM were found.

Although the SM explains the most of experimental results, there are still some problems to be solved, for example, the quadratic divergence of the Higgs mass. In order to solve these problems, new particles yet to be discovered are introduced. One of the promising frameworks is Supersymmetry (SUSY). The outlines and possible solutions in the SUSY models are described in Section 2.3.4.

Table 2.1: Fermions in the Standard Model.

		1st generation	2nd generation	3rd generation
Quarks	up-type	u	c	t
	down-type	d	s	b
Leptons	charged	e	μ	τ
	neutral	ν_e	ν_μ	ν_τ

2.2 Supersymmetry

Supersymmetry (SUSY) [14–19] is a framework that extends the SM by adding the space-time symmetry in quantum field theory that transforms fermions into bosons and vice versa, i.e. a new operator Q carries itself a half-integer spin angular momentum and transforms bosonic states to fermionic states and vice versa. Consequently, the fermionic (bosonic) partner of SM particles, called "superpartner," are introduced. They have the same mass and quantum numbers as the SM particles, except for spins (described in Appendix A.1). In the supersymmetric theory, the SM particles and the superpartners are described as irreducible representations of SUSY algebra, called "supermultiplet."

2.2.1 *R*-parity

In the SUSY Lagrangian, which is the SM extends minimally, terms that violate either baryon number (B) or lepton number (L) are contained in the superpotential (W) term, which represents a function of supersymmetric quantum mechanics. The terms are described as follows;

$$W_{\Delta L=1} = \frac{1}{2}\lambda^{ijk} L_i L_j \bar{e}_k + \lambda'^{ijk} L_i Q_j \bar{d}_k + \mu'^i L_i H_u \,, \tag{2.1}$$

$$W_{\Delta B=1} = \frac{1}{2}\lambda''^{ijk} \bar{u}_i \bar{d}_j \bar{d}_k \,, \tag{2.2}$$

where B and L are not fundamental symmetries in the SM while there are no observed results violating either B or L. Similarly, B and L are not treated as symmetries in the SUSY framework. In order to allow the SM particles and their superpartners to have different quantum numbers, a new symmetry that has no effect of the possibility of these B and L violating terms are introduced. The new symmetry is called "R-parity", and defined as:

$$P_R = (-1)^{3(B-L)+2s} \,, \tag{2.3}$$

where s is the spin of particles. Thus, the the SM particles have $P_R = +1$, and their superpartners have $P_R = -1$.

2.2.2 SUSY Breaking

SUSY represents a generalization of the space-time symmetries in quantum field theory. If SUSY was not broken and the superpartners of the SM particles existed, the mass of the superpartner particles would be required to be as same as the SM particles. However, as superpartners of the SM particles have not

been observed yet, the supersymmetry must be broken in a certain way. If the supersymmetry is softly broken, an effective Lagrangian of SUSY is composed of a supersymmetry invariant part ($\mathcal{L}_{\rm SUSY}$) and a soft supersymmetry violating term ($\mathcal{L}_{\rm soft}$), as follows [20] :

$$\mathcal{L} \quad = \quad \mathcal{L}_{\rm SUSY} + \mathcal{L}_{\rm soft} \ . \tag{2.4}$$

$\mathcal{L}_{\rm SUSY}$ contains kinetic terms, the gauge and Yukawa interactions, and terms with prescriptions using super-space or superpotential [20]. To ensure the cancelation of fermions and sfermions (discussed in Section 2.3.4.1), $\mathcal{L}_{\rm soft}$ contains only mass terms and coupling parameters of positive mass dimension and does not contain dimensionless couplings.

2.3 Minimal Supersymmetric Standard Model

One of the simple models in SUSY is called Minimal Supersymmetric Standard Model (MSSM), which extends the SM to add only the minimal number of supersymmetric particles. In this thesis, we assume that the R-parity is conserved in the MSSM. Then, there can be no mixing between the SM particles and sparticles because all SM particles have even R-parity, and sparticles have odd R-parity. From these assumptions, two phenomenological consequences are obtained:

- The lightest sparticle is absolutely stable (called "lightest supersymmetric particle", "LSP").
- Only even numbers of sparticles can be produced in collider experiments.

2.3.1 Particle Contents in MSSM

In the MSSM, the number of supersymmetries is assumed to be 1. Thus, only one superpartner corresponding to one SM particle is considered. There are two types of supermultiplets. One is the "chiral supermultiplet," which consists of doublets containing spin-0 particles and their spin-1/2 superpartners (vice versa), as summarized in Table 2.2. The superpartners of the spin-1/2 SM fermions are referred to as "sfermions" and have a spin of 1. Sfermions are divided into two types; "squarks" and "sleptons," which are the superpartners of the SM quarks and leptons, respectively. They are $SU(2)_L$ doublets in left-handed parts and singlets in right-handed. These left-handed and right-handed sfermions are denoted as $\tilde{f}_{\rm L}$ and $\tilde{f}_{\rm R}$ as same as the SM particles.

The Higgs boson is also included in the chiral supermultiplets since it has spin-0. Since supersymmetry requires at least two $SU(2)$ doublets [21], the MSSM contains two Higgs doubles. One denoted as H_u gives mass to up-type quarks and the other denoted as H_d provides mass to down-type quarks. They are weak isospin doublets with weak hypercharge $Y = \pm 1/2$. Here, H_u is denoted (H_u^+,H_u^0) and H_d is denoted (H_d^0, H_d^-). Higgsinos, which are the superpartners of Higgs bosons, are denoted as $\tilde{H}_u$, $\tilde{H}_d$ for the $SU(2)_L$ doublets in left-handed Weyl spinor fields. Their isospin components are denoted $\tilde{H_u^+}$, $\tilde{H_u^0}$, $\tilde{H_d^0}$, and $\tilde{H_d^-}$.

The other type of supermultiplet is the "gauge supermultiplets," which compose of gauge bosons and their superpartners, "gaugino," as summarized in Table 2.3. Gauginos have spin-1/2 and are associated with SM bosons as Weyl fermions. The name of gauginos is expressed by adding an "-ino" suffix to the end to one of the SM bosons. "Gluino" is the superpartner of the gluon. "Wino" and "Bino," which are denoted by $\tilde{W^\pm}$, $\tilde{W^0}$, and $\tilde{B^0}$, are the superpartners of the electroweak bosons denoted as $W^\pm$, W^0, and B^0.

In this thesis, Wino ($\tilde{W}$), Bino ($\tilde{B}$), and Higgsino ($\tilde{H}$) are collectively called "electroweakinos."

Table 2.2: Chiral supermultiplets in the Minimal Supersymmetric Standard Model. The spin-0 fields are complex scalars, and the spin-1/2 fields are left-handed two-component Weyl fermions [20]. Q denotes quarks and including up-type quark u_L, $\tilde{u_L}$ and down-type quark $d_L, \tilde{d}_L$. i represents a family index. The parentheses in the spin 0, 1/2 columns represent $SU(2)_L$ doublets. The bar on $\bar{u}$, $\bar{d}$, $\bar{e}$ fields is part of the name and does not denote any kind of conjugation. They are categorized into the SM gauge group $SU(3)_C \times SU(2)_L \times U(1)_Y$.

Names		spin 0	spin 1/2	$SU(3)_C,\ SU(2)_L,\ U(1)_Y$
squarks, quarks (×3 families)	Q_i	$(\tilde{u}_L\ \tilde{d}_L)$	$(u_L\ d_L)$	$(\mathbf{3}, \mathbf{2}, \frac{1}{6})$
	$\bar{u}_i$	$\tilde{u}^*_R$	$u^\dagger_R$	$(\bar{\mathbf{3}}, \mathbf{1}, -\frac{2}{3})$
	$\bar{d}_i$	$\tilde{d}^*_R$	$d^\dagger_R$	$(\bar{\mathbf{3}}, \mathbf{1}, \frac{1}{3})$
sleptons, leptons (×3 families)	L_i	$(\tilde{\nu}\ \tilde{e}_L)$	$(\nu\ e_L)$	$(\mathbf{1}, \mathbf{2}, -\frac{1}{2})$
	$\bar{e}_i$	$\tilde{e}^*_R$	$e^\dagger_R$	$(\mathbf{1}, \mathbf{1}, 1)$
Higgs, Higgsinos	H_u	$(H_u^+\ H_u^0)$	$(\tilde{H}_u^+\ \tilde{H}_u^0)$	$(\mathbf{1}, \mathbf{2}, +\frac{1}{2})$
	H_d	$(H_d^0\ H_d^-)$	$(\tilde{H}_d^0\ \tilde{H}_d^-)$	$(\mathbf{1}, \mathbf{2}, -\frac{1}{2})$

Table 2.3: Gauge supermultiplets in the Minimal Supersymmetric Standard Model [20]. They are categorized into the SM gauge group $SU(3)_C \times SU(2)_L \times U(1)_Y$.

Names	spin 1/2	spin 0	$SU(3)_C,\ SU(2)_L,\ U(1)_Y$
gluino, gluon	$\tilde{g}$	g	$(\mathbf{8}, \mathbf{1}, 0)$
Wino, W bosons	$\tilde{W}^\pm, \tilde{W}^0$	$W^\pm, W^0$	$(\mathbf{1}, \mathbf{3}, 0)$
Bino, B boson	$\tilde{B}^0$	B^0	$(\mathbf{1}, \mathbf{1}, 0)$

2.3.2 Soft Breaking and the Soft Term in the MSSM Lagrangian

Most terms of $\mathcal{L}_{\text{soft}}$ in Equation 2.4 are described in general theory, as follows [20]:

$$\begin{aligned}\mathcal{L}^{\text{MSSM}}_{\text{soft}} = &-\frac{1}{2}\left(M_3\tilde{g}\tilde{g} + M_2\tilde{W}\tilde{W} + M_1\tilde{B}\tilde{B} + c.c.\right)\\ &-\left(\tilde{u}\mathbf{a_u}\tilde{Q}H_u - \tilde{d}\mathbf{a_d}\tilde{Q}H_d - \tilde{e}\mathbf{a_e}\tilde{L}H_d + c.c.\right)\\ &-\tilde{Q}^\dagger\mathbf{m}^2_{\tilde{\boldsymbol{Q}}}\tilde{Q} - \tilde{L}^\dagger\mathbf{m}^2_{\tilde{\boldsymbol{L}}}\tilde{L} - \tilde{u}\mathbf{m}^2_{\tilde{\boldsymbol{u}}}\tilde{u}^\dagger - \tilde{d}\mathbf{m}^2_{\tilde{\boldsymbol{d}}}\tilde{d}^\dagger - \tilde{e}\mathbf{m}^2_{\tilde{\boldsymbol{e}}}\tilde{e}^\dagger\\ &-m^2_{H_u}H^*_uH_u - m^2_{H_d}H^*_dH_d - (bH_uH_d + c.c.),\end{aligned} \tag{2.5}$$

where M_1, M_2, and M_3 are the mass terms of bino ($\tilde{B}$), wino ($\tilde{W}$), and gluino ($\tilde{g}$). $\mathbf{a_i}$ ($i = u, d, e$) represents a complex 3×3 matrix in family space and has dimensions of mass. $\mathbf{m^2_{\tilde{i}}}$ ($i = Q, L, \bar{u}, \bar{d}, \bar{e}$) is a 3×3 matrix and $\mathbf{m^2_{\tilde{i}}}$ and b have dimensions of squared-mass. The terms containing $\mathbf{a_i}$ and b represent soft trilinear and bilinear scalar interactions, respectively. The MSSM Lagrangian obtains arbitrariness by introducing additional 105 parameters of mass, phases, and mixing angles not contained in the SM [22].

Equation 2.5 allows flavor-mixing (CP-violating) effects because squarks and sleptons have the same electroweak quantum numbers. However, they are disfavored by experiments. In order to avoid these effects, supersymmetry breaking is assumed to be universal. In an idealized limit where $\mathbf{m^2_{\tilde{i}}}$ are flavor-blind,

$\mathbf{m}_{\tilde{i}}^2$ are described as follows:

$$\mathbf{m}_{\tilde{i}}^2 = \mathrm{m}_{\tilde{i}}^2 \mathbf{1},\ i = Q, L, \bar{u}, \bar{d}, \bar{e}. \tag{2.6}$$

Additionally, the (scaler)^3 couplings, including CP-violating effects, are assumed to be proportional to the corresponding Yukawa coupling matrices;

$$\mathbf{a}_i = A_{i0}\mathbf{y}_i,\ i = u, d, e. \tag{2.7}$$

Finally, to avoid CP-violating effects by new complex phases from the soft parameters, M_1, M_2, M_3, A_{u0}, A_{d0}, and A_{e0} are all required to be real numbers.

2.3.3 Gaugino Mass

In this thesis, we mainly focus on the electroweakinos. Only the mass spectra of electroweakinos are discussed.

Due to the effects of the electroweak symmetry breaking, electroweak gauginos mix with higgsinos. Neutral higgsinos ($\tilde{H}_u^0$ and $\tilde{H}_d^0$) constitute mass eigenstates called "neutralinos" with neutral gauginos ($\tilde{B}$ and $\tilde{W}^0$). The neutralino mass eigenstates are composed of four eigenstates and are denoted by $\tilde{N}_i$ ($i = 1, 2, 3, 4$). Charged higgsinos ($\tilde{H}_u^+$ and $\tilde{H}_d^-$) and winos ($\tilde{W}^+$ and $\tilde{W}^-$) mix with each other and combine to form two mass eigenstates. They are called "charginos." Neutralinos and charginos are labeled in ascending order, such as $\tilde{\chi}_{1\sim4}^0 = \tilde{N}_{1\sim4}$ and $\tilde{\chi}_{1\sim2}^\pm = \tilde{C}_{1\sim2}^\pm$. The neutralino mass terms of the Lagrangian with the gauge-eigenstates $\psi^0 = (\tilde{B}, \tilde{W}^0, \tilde{H}_d^0, \tilde{H}_u^0)$ are described as:

$$\mathcal{L}_{\text{neutralino mass}} = -\frac{1}{2}(\psi^0)^{\mathrm{T}} \boldsymbol{M}_{\tilde{N}} \psi^0 + c.c.\,, \tag{2.8}$$

where

$$\boldsymbol{M}_{\tilde{N}} = \begin{pmatrix} M_1 & 0 & -c_\beta s_W m_Z & s_\beta s_W m_Z \\ 0 & M_2 & c_\beta c_W m_Z & -s_\beta c_W m_Z \\ -c_\beta s_W m_Z & c_\beta c_W m_Z & 0 & -\mu \\ s_\beta s_W m_Z & -s_\beta c_W m_Z & -\mu & 0 \end{pmatrix}, \tag{2.9}$$

with new abbreviations: $s_\beta = \sin\beta$, $c_\beta = \cos\beta$, $s_W = \sin\theta_W$, and $c_W = \cos\theta_W$. θ_W is the Weinberg angle, and the definition of β is from the ratio of the two vacuum expectation values of the two higgs doublets;

$$\tan\beta \equiv \left\langle H_u^0 \right\rangle / \left\langle H_d^0 \right\rangle. \tag{2.10}$$

M_1 and M_2 are introduced in Eq.2.5 and can have arbitrary complex phases in general. However, we can redefine the phases of $\tilde{B}$ and $\tilde{W}$ that M_1 and M_2 are real and positive. The higgsino mass parameter μ is usually assumed to be real while the sign is not determined.

Similarly, the chargino mass terms of the Lagrangian with the gauge-eigenstates basis $\psi^\pm = (\tilde{W}^+, \tilde{H}_u^+, \tilde{W}^-, \tilde{H}_d^-)$ are described as:

$$\mathcal{L}_{\text{chargino mass}} = -\frac{1}{2}(\psi^\pm)^{\mathrm{T}} \boldsymbol{M}_{\tilde{C}} \psi^\pm + c.c.\,, \tag{2.11}$$

where

$$\boldsymbol{M}_{\tilde{C}} = \begin{pmatrix} 0 & \boldsymbol{X}^{\mathrm{T}} \\ \boldsymbol{X} & 0 \end{pmatrix}, \text{with } \boldsymbol{X} = \begin{pmatrix} M_2 & \sqrt{2} s_\beta m_W \\ \sqrt{2} c_\beta m_W & \mu \end{pmatrix}. \tag{2.12}$$

More details are described in Appendix A.2.

2.3.4 SUSY Solutions of the SM Problems in the MSSM

SUSY provides explanations for some problems in the SM; for example, the quadratic divergence of the Higgs mass, the dark matter, the muon g-2 anomaly. In this sub-section, the solutions for them by introducing SUSY are described. The coupling constant in the Grand Unified Theory (GUT) scale is discussed in Appendix A.3.

2.3.4.1 Quadratic Divergence of the Higgs Mass

The Higgs boson mass (m_H) receives quantum corrections through virtual effects by particles that Higgs boson couples. For example, the contribution to the Higgs squared mass parameter from a Dirac fermion f with a term of $-\lambda_f H \bar{f} f$ in the Lagrangian, as shown in Figure 2.1 is described:

$$\Delta m_H^2 = -\frac{|\lambda_f|^2}{8\pi^2}\Lambda_{\rm UV}^2 + O(\log \Lambda_{\rm UV}), \tag{2.13}$$

where $\Lambda_{\rm UV}$ is an ultraviolet momentum cutoff interpreted as the energy scale where the contribution of new physics changes the behavior of the theory. If the SM is an effective theory to be extended to the Planck scale ($M_{\rm P} \sim 10^{18}$), $\Lambda_{\rm UV} = M_{\rm P}$. The problem is that this quantum correction to Δm_H^2 is larger than $O(10^{36}\ {\rm GeV}^2)$ [20], even though the observed Higgs mass is $O(100\ {\rm GeV})$. This requires the parameters to reproduce the electroweak scale mass for all orders of the perturbation and all particles that couple to the Higgs boson. This problem is called "fine-tuning problem" or "hierarchy problem." The contribution to the Higgs squared mass parameter from a scalar particle with mass with a term of $-\lambda_S |H|^2 |S|^2$ in the Lagrangian, as shown in Figure 2.1, is described:

$$\Delta m_H^2 = \frac{\lambda_S}{16\pi^2}\Lambda_{\rm UV}^2 + O(\log \Lambda_{\rm UV}). \tag{2.14}$$

In the MSSM, two scalar partners (denoted as $\tilde{f}_L$ and $\tilde{f}_R$) corresponding to one two-component Weyl SM fermion are introduced and the $\Lambda_{\rm UV}^2$ contributions in Equation 2.13 and 2.14 are canceled by $|\lambda_f|^2 = \lambda_S$, then, terms with $O(\log \Lambda_{\rm UV})$ remain. If the mass difference between particles in the same supermultiplets is reasonably small, it will be a solution for the hierarchy problem and the fine-tuning problem. This notion is called the "natural SUSY" scenario. Since all the superpartners do not necessarily have the same relevance for the Higgs mass corrections, some superpartners are required to be light, and other superpartners can be extremely heavy. We consider a total correction to produce the Higgs mass of 125 GeV since the bare mass is limited to $m_{h^0} < m_Z |\cos 2\beta|$ [20]. Considering the one-loop level correction, Higgs mass with a dominant contribution of top and stop is described [23] :

$$m_h^2 \approx m_Z^2 \cos^2 2\beta + \frac{3}{(4\pi)^2}\frac{m_t^4}{v^2}\left[\ln\frac{m_{\tilde{t}}^2}{m_t^2} + \frac{X_t^2}{m_{\tilde{t}}^2}\left(1 - \frac{X_t^2}{12 m_{\tilde{t}^2}}\right)\right], \tag{2.15}$$

where X_t is a stop mixing parameter defined in Ref. [23]. X_t represents the magnitude of the mixed of eigenstates ($\tilde{t}_L, \tilde{t}_R$) to the mass eigenstates ($\tilde{t}_1, \tilde{t}_2$). $m_{\tilde{t}}^2 = m_{\tilde{t}_1} m_{\tilde{t}_2}$ is the geometric mean of the stop mass. v is the vacuum expectation value (174 GeV). From Equation 2.15, higgsino mass depends on the mixing parameter and stop mass. These correlations are shown in Figure 2.2. In this case, we also consider the contribution from gluinos which give a one-loop correction to the stop mass. Thus, the minimal requirements to satisfy a "natural" SUSY mass spectrum. [24], as shown in Figure 2.3 are as follows:

Figure 2.1: One-loop quantum corrections to the Higgs squared mass parameter m_H^2, from Dirac fermion f (left) and scalar S (right) [20].

- All two stops and one (left-handed) sbottom are lighter than 500 - 700 GeV.
- One chargino and two neutralinos are lighter than 200 - 350 GeV, and the spectrums of other chargino and neutralinos are quasi-degenerate.
- Gluino is not too heavy, lighter than 900 - 1500 GeV.

The ATLAS experiment [29] set stringent exclusion limits for the stop and gluino mass, as shown in Figure 2.4. Similar constraints are provided by the CMS experiment [30]. The gluino and stop mass limits are excluded up to 2 TeV and 1.2 TeV, respectively, if the lightest neutralino mass $m(\tilde{\chi}_1^0)$ is less than 1 TeV and 400 GeV. However, these results are extracted with "simplified" models [31–33] where all the SUSY particles except for stop, gluino, and the decayed particles from them are decoupled by their heavy mass larger than a few TeV, and the branching ratio of their decay process is assumed to be 100%. Considering general cases, called "not simplified" models, the limits are smaller, as shown in Figure 2.5.

Another "natural" SUSY model [34] can explain the Higgs mass of 125 GeV with large stop or gluino mass keeping the reasonable level of fine-tuning. In this study, a likelihood approach considering the effect of all parameters in the MSSM and the correlations among them is employed. The upper bound of the higgsino mass parameter is about 700 GeV, and stop and gluino mass is allowed to be larger than the recent ATLAS limits if we allow $O(1\%)$ of a fine-tuning. Some other $\tilde{H}$-LSP scenarios [24, 35–37] suggest that the higgsino mass parameter is near the electroweak scale.

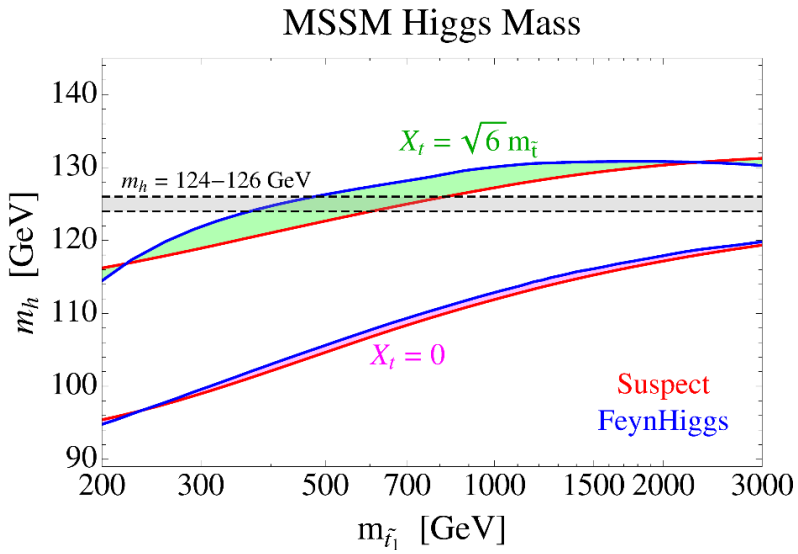

Figure 2.2: The Higgs mass in the MSSM as a function of the lightest top squark mass ($m_{\tilde{t}_1}$) [23]. The red solid line shows the computed values using the library ("Suspect" [25]), and the blue one with the library ("FeynHiggs" [26–28]). The two upper lines represent the correlation if the stop mixing parameter is maximized assuming degenerate stop soft masses with $\tan\beta = 20$, and lower lines if the mixing parameter is zero.

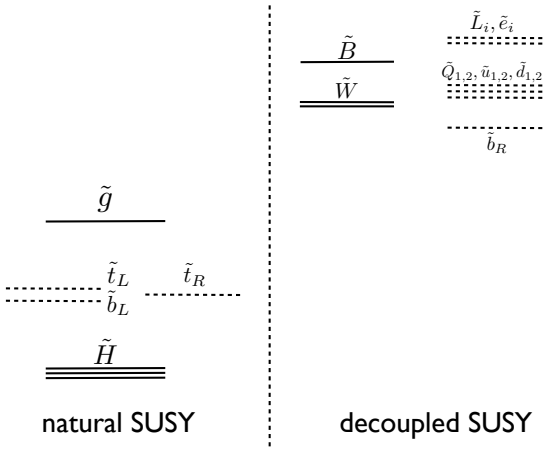

Figure 2.3: The mass spectra in the natural SUSY scenario. Electroweak symmetry breaking constrains the superpartners on the left to be light. Other superpartners on the right can be heavy ($M \gg 1$ TeV) [24].

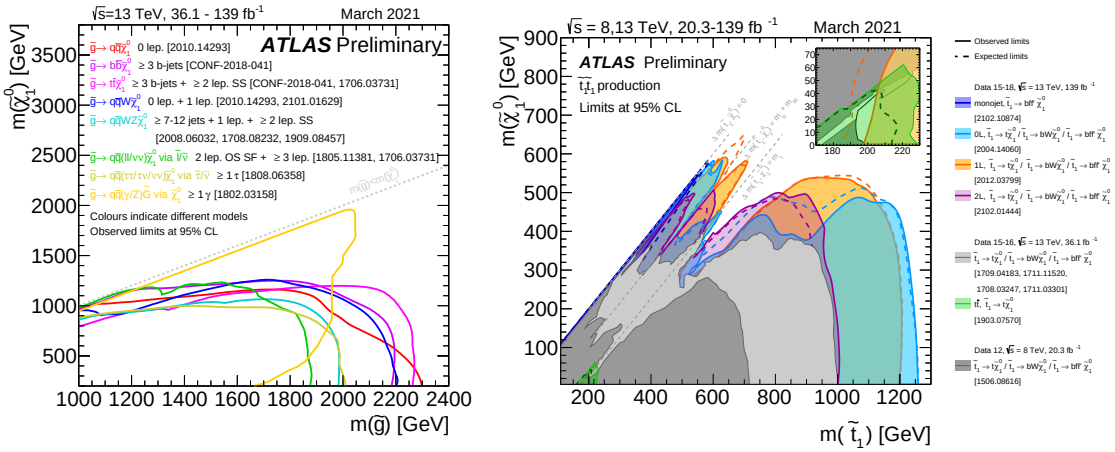

(a) $\tilde{g} \to X\tilde{\chi}_1^0$ (b) $\tilde{t} \to X\tilde{\chi}_1^0$

Figure 2.4: The exclusion limits at 95% C.L. for gluino ($\tilde{g}$) production (a) and stop ($\tilde{t}$) production (b), obtained in the simplified model using 36.1-139 fb^{-1} of pp-collision in Run-2 with ATLAS detector [29]. The horizontal axis represents $\tilde{g}$ or $\tilde{t}$ mass, and the vertical axis represents the lightest neutralino mass ($m(\tilde{\chi}_1^0)$). The regions inside (lower left side of) the contours are excluded (a), and the colored region is excluded (b).

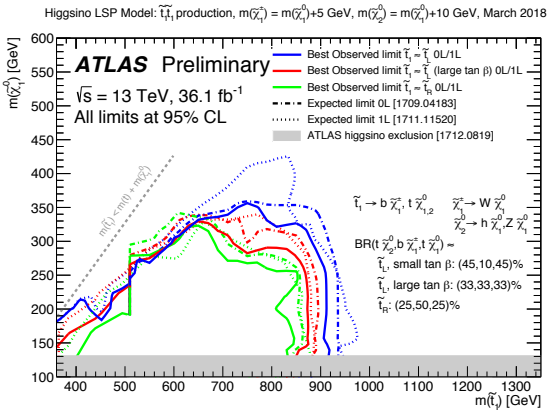

Figure 2.5: The exclusion limits at 95% C.L. for stop ($\tilde{t}$) production and higgsino ($\tilde{H}$) LSP model, obtained using 36.1 fb^{-1} of pp-collision in Run-2 with ATLAS detector [29]. The horizontal axis represents $\tilde{t}$ mass, and the vertical axis represents the lightest neutral higgsino mass ($m(\tilde{\chi}_1^0)$). The regions inside (lower left side of) the contours are excluded. Only higgsino mass splitting among the higgsino mass eigenstates ($\tilde{\chi}_1^0$, $\tilde{\chi}_2^0$ $\tilde{\chi}_1^\pm$) is fixed. The stop can decay to the LSP($\tilde{\chi}_1^0$) with top quark or in two steps via chargino($\tilde{\chi}_1^\pm$) or not the lightest neutralino($\tilde{\chi}_2^0$). This corresponding branching fraction depends on parameters, such as the stop left-right mixing and $\tan\beta$. Three results in different scenarios are described as different color lines.

2.3.4.2 Dark Matter

The galaxy rotation curve measurements [6, 7] imply the existence of the dark matter, which interacts very weakly with the neutral matter. The cosmic microwave background measurements from the WMAP and Planck collaborations [8, 9] imply that the baryonic matters described by the SM account for only 5% of the energy density in the universe.

Under the situation, the Λ-CDM model, which is the most commonly considered framework for the dark matter is considered. The Λ-CDM model introduces the dark matter whose velocity is far less than the speed of light ("non-relativistic"). The dark matter is assumed to be electrically neutral as it is invisible through electromagnetic interaction and should be interacting with the SM particles weakly through weak interaction or gravity. In the early universe, the dark matter was generated by thermal equilibrium. When the universe expands and the temperature is less than the dark matter mass, the production of the dark matter becomes kinematically suppressed. After the time when the cosmic expansion rate is large and an annihilation rate of the dark matter is small, this equilibrium is switched off and the density of dark matter does not increase any longer. This mechanism is called a "freeze-out."

However, there is no dark matter candidate in the SM. The LSP particle in the MSSM, the lightest neutralino $\tilde{\chi}_1^0$ in the general cases, can be a good dark matter candidate in the MSSM if the R-parity is conserved.

The predicted neutralino mass to explain the dark matter depends on the component by $\tilde{B}$, $\tilde{W}$, and $\tilde{H}$. Some of the free parameters in the MSSM are constrained to give a reasonable phenomenological assumption called a phenomenological MSSM (pMSSM) [38]. A result of the neutralino mass scan, where only neutralinos are dark matter candidates and no contribution from other particles, is shown in Figure 2.6. Here, $m(\tilde{\chi}_1^0)$ represents the lightest neutralino mass as the dark matter candidate with remaining various parameters by pMSSM constraints, and $\Omega_{\tilde{\chi}_1^0} h^2$ represents the dark matter density. The colors of the points indicate the composition of the lightest neutralino with dominant electroweakinos. In the $\tilde{W}$-($\tilde{H}$-)like dark matter case, m_χ of 1 TeV (3 TeV) is favored because the annihilation cross-section depends on the inverse square of $m(\tilde{\chi}_1^0)$. However, light $\tilde{W}$ ($\tilde{H}$) cases are not excluded if $\tilde{W}$ ($\tilde{H}$) is a part of the dark matter components.

In the $\tilde{B}$-like dark matter case (red points in Figure 2.6), the wide m_χ range from 40 GeV to 3 TeV is favored. In the light $\tilde{B}$-LSP case, the dark matter density is larger than the observed value because of small annihilation cross-sections of the $\tilde{B}$ pairs to the SM particles. If other SUSY particles have a slightly larger mass than $\tilde{B}$, annihilation cross-sections can be large and consistent with the observed value. However, these models with the small mass differences are not considered in this thesis. The SUSY scenario motivated by the dark matter where $m_\chi \sim m_Z/2$ or $m_h/2$ is considered. The $\tilde{B}$-like neutralino dark matter can satisfy the observed dark matter density via the Z- and Higgs-resonant annihilations [41]. More details of possible explanations are discussed in Appendix A.4.

2.3.4.3 Muon g-2 Anomaly

One of the experimental results the SM can not currently explain is the "muon g-2 anomaly." An anomalous magnetic dipole moment of the muon denoted as a_μ:

$$a_\mu = \frac{g-2}{2}, \tag{2.16}$$

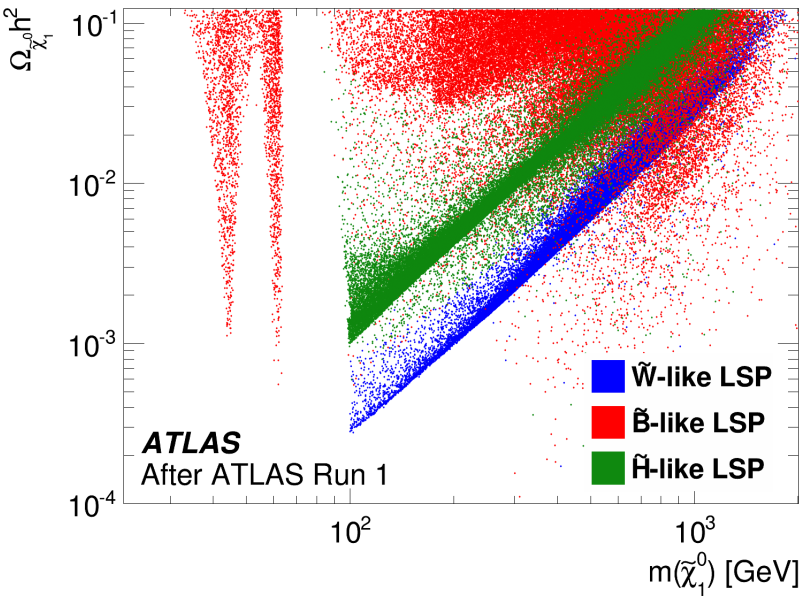

Figure 2.6: Observed dark matter density corresponding to the LSP as a function of the LSP mass [39]. The observed $\Omega_{\tilde{\chi}_1^0}h^2$ is about 0.12. The points represent the model of the pMSSM parameter scan. In Bino-like dark matter case, in order to explain the observed dark matter density, other SUSY particles, such as slepton, wino, higgsino, stop, and gluon, are required to have slightly heavier mass than bino However, these cases with $m < 100$ GeV have been already excluded by LEP searches [40].

where g is a dimensionless coefficient derived from the spin. The theoretically calculated value of a_μ in the SM is $(11659181.08 \pm 3.78) \times 10^{-10}$ [42] or $(11659183.0 \pm 4.8) \times 10^{-10}$ [43]. However, the Fermilab group reported that the measured value [44] is $116592040\ (54) \times 10^{-11}$. The combined result [45] with previous measurements of the BNL group is

$$a_\mu(\text{Exp.}) = 116592061\ (41) \times 10^{-11}. \tag{2.17}$$

The discrepancy between the theoretical and experimental values corresponds to be 4.2 standard deviations. This discrepancy implies that new physics beyond the SM exists in the electroweak scale.

Here, SUSY potentially explains the discrepancy. The dominant contribution to the muon g-2 is the chargino-sneutrino and the neutralino-smuon loop diagrams, for example, the $\tilde{W}$-$\tilde{H}$-$\tilde{\mu}$ loop, as shown in Figure 2.7. We can also consider the similar loops of $\tilde{W}$, $\tilde{B}$, $\tilde{H}$, $\tilde{\mu}$, and $\tilde{\nu}_\mu$. Thier contributions are summarized in Appendix A.5, and further detail is described in Ref. [47], The contributions can be $O(10^{-9})$ with $m_{\text{soft}} = O(100)$ GeV and $\tan\beta = O(10)$ in Ref.[47] and explain the anomaly with a strong dependence on $m_{\tilde{\mu}}$ and $\tan\beta$.

2.3.5 Target Scenarios and Signal Models

In this thesis, the target models are represented as $(\tilde{\chi}_{\text{heavy}}, \tilde{\chi}_{\text{light}})$, where $\tilde{\chi}_{\text{heavy}}$ is the gaugino produced directly in the pp-collision and $\tilde{\chi}_{\text{light}}$ is decayed from $\tilde{\chi}_{\text{heavy}}$. Only R-parity conservation scenarios with a large mass difference between $\tilde{\chi}_{\text{heavy}}$ and $\tilde{\chi}_{\text{light}}$ are discussed. Due to the small cross-section of heavy $\tilde{\chi}_{\text{heavy}}$, it is difficult to search for electroweakinos in many backgrounds. However, hard kinematic selections

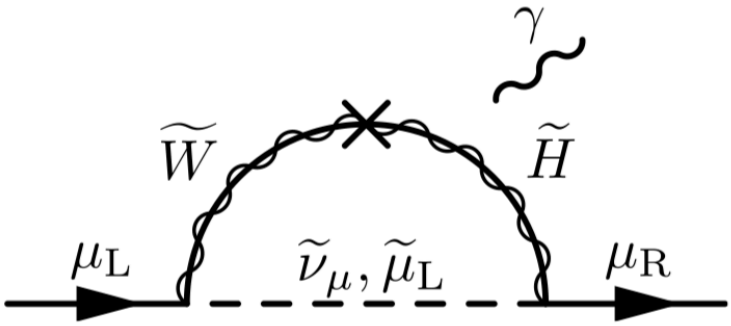

Figure 2.7: The loop of wino-higgsino-smuon [46].

corresponding to the mass difference are required to enhance the purity of SUSY signals. Additionally, the SM electroweak boson with a high momentum, which is decayed from $\tilde{\chi}_{\text{heavy}}$, is used. Due to focusing on the hadronically decaying bosons, there are boosted jets from the bosons and the jet substructures to identify the boson can be used, as described in Chapter 6. Additionally, the branching ratio of the hadronic decay of the SM electroweak bosons is larger than the leptonic decay of bosons. Since all the $W/Z/h$ bosons are reconstructed as jets and targeted, the search for electroweakinos without requiring the type of the SM electroweak bosons explicitly can be performed.

2.3.6 Signal Topology

In this thesis, SUSY particles, except for electroweakinos, are assumed to be heavy and decoupled. Thus, it is not necessary to consider all production and decay modes, such as the process including sleptons.

Production Modes The target of this analysis is the direct production of electroweakinos, such as charginos and neutralinos, via electroweak interactions. Considering $\tilde{B}$ production in the LHC, $\tilde{B}$ pairs can only be produced via a t-channel exchange of sfermions. However, since sfermions are assumed to be decoupled, $\tilde{B}$ production cross-section is small. Thus, $\tilde{\chi}_{\text{heavy}}$ is assumed to be $\tilde{W}$ or $\tilde{H}$. Their production cross-sections with a function of $m(\tilde{\chi}_{\text{heavy}})$ are shown in Figure 2.8.

Decay Modes Ony the decay process where $\tilde{\chi}_{\text{heavy}}$ decays into $\tilde{\chi}_{\text{light}}$ with the SM electroweak boson ($W/Z/h$), and there is a large mass difference between $\tilde{\chi}_{\text{heavy}}$ and $\tilde{\chi}_{\text{light}}$ (> 400 GeV) is considered. The decay modes are summarized as follows;

$$\tilde{\chi}_i^0 \rightarrow W\tilde{\chi}_j^{\pm}\,,\; Z\tilde{\chi}_j^0\,,\; h\tilde{\chi}_j^0\,, \tag{2.18}$$

$$\tilde{\chi}_i^{\pm} \rightarrow W\tilde{\chi}_j^0\,,\; Z\tilde{\chi}_j^{\pm}\,,\; h\tilde{\chi}_j^{\pm}\,. \tag{2.19}$$

In this case, the SM electroweak bosons generated from $\tilde{\chi}_{\text{heavy}}$ are on-shell. The hadronic decay processes of $W/Z/h$, such as $W \rightarrow qq$, $Z \rightarrow qq/bb$, and $h \rightarrow bb$ where q represents u, d, s, or c are considered. In the fully hadronic final state, there are many QCD jets in pp-collision. However, the branching ratio of the hadronic decay is large, and the characterized signatures of the hadronically decaying bosons with high momenta can be used to reject QCD jets.

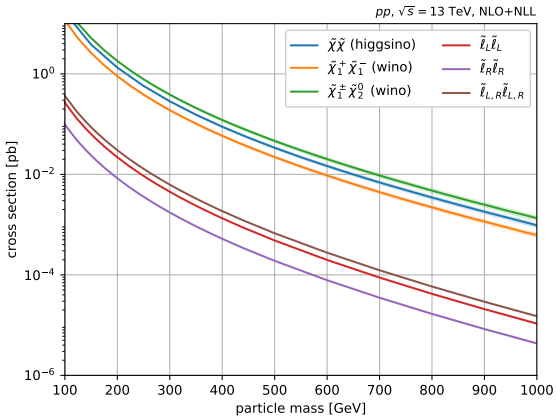

Figure 2.8: The production cross-section as a function of the mass of $\tilde{W}$, $\tilde{H}$, or $\tilde{\ell}$ [48]. Charginos and neutralinos are degenerate assuming pure $\tilde{W}$ and $\tilde{H}$,

Setups of Signal Models To consider a simple case, the effect of kinetic mixing between $\tilde{B}$, $\tilde{W}$, and $\tilde{H}$, is assumed to be small. In other words, the components of $\tilde{\chi}_{\text{heavy}}$ and $\tilde{\chi}_{\text{light}}$ are dominated by one supersymmetry field for each. From this assumption, other than two supersymmetry particles do not affect the production cross-section and the decay branching ratio of $\tilde{\chi}_{\text{heavy}}$. As discussed above, $\tilde{\chi}_{\text{heavy}}$ is $\tilde{W}$ or $\tilde{H}$. $\tilde{\chi}_{\text{light}}$ is one of $\tilde{B}$, $\tilde{W}$, or $\tilde{H}$. Thus, four models, $(\tilde{W}, \tilde{B})$, $(\tilde{W}, \tilde{H})$, $(\tilde{H}, \tilde{B})$, and $(\tilde{H}, \tilde{W})$, are considered in this thesis. They are summarized in Table 2.4.

In the $(\tilde{W}, \tilde{B})$ model, $m(\tilde{\chi}_2^0)$ and $m(\tilde{\chi}_1^\pm)$ degenerates, and $|\mu| \gg M_2 > M_1$. The mass spectrum is shown in Figure 2.9(a). In this case, two production modes: chargino pair production $(\tilde{\chi}_1^\pm \tilde{\chi}_1^\mp)$ and chargino-neutralino production $(\tilde{\chi}_1^\pm \tilde{\chi}_2^0)$ and three decay processes: $\tilde{\chi}_1^\pm \to W + \tilde{\chi}_1^0$ and $\tilde{\chi}_2^0 \to Z/h + \tilde{\chi}_1^0$ are considered, as shown in Figure 2.10(a), Figure 2.10(b), and Figure 2.10(c). The branching ratio of $\tilde{\chi}_2^0$ is a free parameter under a constraint where $\mathcal{B}(\tilde{\chi}_2^0 \to Z\tilde{\chi}_1^0) = 1 - \mathcal{B}(\tilde{\chi}_2^0 \to h\tilde{\chi}_1^0)$.

The simple $(\tilde{W}, \tilde{B})$ model ("simplified models") [31–33] is also considered. The simplified model in $(\tilde{W}, \tilde{B})$ is abbreviated as $(\tilde{W}, \tilde{B})$-SIM. In the $(\tilde{W}, \tilde{B})$-SIM, the branching ratio of only one of three processes to be 100% is set. Thus, $\mathcal{B}(\tilde{\chi}_1^\pm \to W\tilde{\chi}_1^0) = 100\%$ is always assumed, however, $\mathcal{B}(\tilde{\chi}_2^0 \to Z\tilde{\chi}_1^0) = 100\%$ or $\mathcal{B}(\tilde{\chi}_2^0 \to h\tilde{\chi}_1^0) = 100\%$ is selected corresponding to target models. In this thesis, the $\tilde{\chi}_1^\pm \tilde{\chi}_1^\mp \to WW\tilde{\chi}_1^0\tilde{\chi}_1^0$ process of the simplified model is abbreviated as "C1C1-WW." Similarly, $\tilde{\chi}_1^\pm \tilde{\chi}_2^0 \to WZ\tilde{\chi}_1^0\tilde{\chi}_1^0$ and $\tilde{\chi}_1^\pm \tilde{\chi}_2^0 \to Wh\tilde{\chi}_1^0\tilde{\chi}_1^0$ processes of simplified models are abbreviated as "C1N2-WZ" and "C1N2-Wh," respectively.

The $(\tilde{H}, \tilde{B})$, $(\tilde{W}, \tilde{H})$, and $(\tilde{H}, \tilde{W})$ models are also considered. The mass spectra are shown in Figure 2.9. The $(\tilde{H}, \tilde{B})$ model is similar to the $(\tilde{W}, \tilde{B})$ model where the branching ratio of $\tilde{\chi}_2^0 \to Z/h + \tilde{\chi}_1^0$ is a free parameter and $m(\tilde{\chi}_2^0) \sim m(\tilde{\chi}_3^0) \sim m(\tilde{\chi}_1^\pm)$. The differences between $(\tilde{H}, \tilde{B})$ and $(\tilde{W}, \tilde{B})$ are the mass hierarchy and additional production mode $(pp \to \tilde{\chi}_2^0\tilde{\chi}_3^0)$ in the $(\tilde{H}, \tilde{B})$ model. The branching ratio of $\tilde{\chi}_3^0$ is constrained by the condition where $\mathcal{B}(\tilde{\chi}_3^0 \to Z\tilde{\chi}_1^0) = 1 - \mathcal{B}(\tilde{\chi}_3^0 \to h\tilde{\chi}_1^0) = 1 - \mathcal{B}(\tilde{\chi}_2^0 \to Z\tilde{\chi}_1^0) = \mathcal{B}(\tilde{\chi}_2^0 \to h\tilde{\chi}_1^0)$. In the $(\tilde{W}, \tilde{H})$ and $(\tilde{H}, \tilde{W})$ models, $\tilde{B}$ is assumed to be decoupled, i.e., M_1 is larger than M_2 and $|\mu|$. In these models, each mass difference between $\tilde{\chi}^0$ and $\tilde{\chi}^\pm$ of $\tilde{W}/\tilde{H}$ is assumed to be very small, and the decay processes are not considered since quarks and leptons generated from their decay are soft. Since only the hard jets from the hadronically decaying bosons are focused in this thesis, the search for electroweakinos

Table 2.4: Summary of target models and scenarios.

$\tilde{\chi}_{\text{heavy}}$	$\tilde{\chi}_{\text{light}}$	Main target scenarios
$\tilde{W}$	$\tilde{B}$	Dark matter, muon g-2
$\tilde{H}$	$\tilde{B}$	Naturalness, Dark matter, muon g-2
$\tilde{W}$	$\tilde{H}$	Naturalness, Dark matter, muon g-2
$\tilde{H}$	$\tilde{W}$	Naturalness, Dark matter, muon g-2

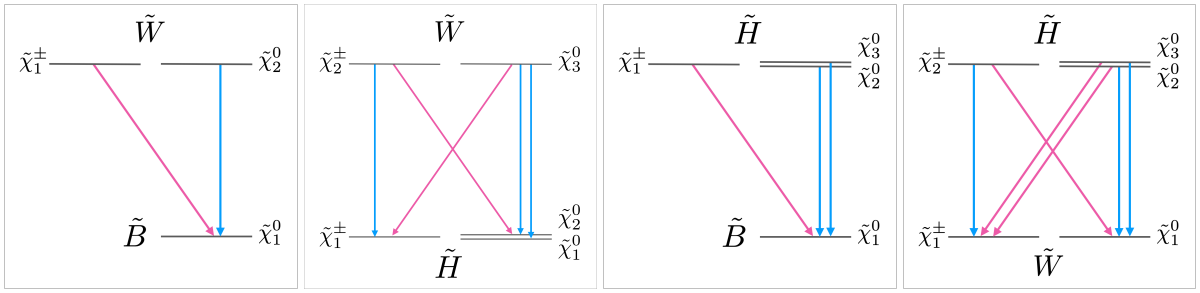

(a) $(\tilde{W}, \tilde{B})$ (b) $(\tilde{W}, \tilde{H})$ (c) $(\tilde{H}, \tilde{B})$ (d) $(\tilde{H}, \tilde{W})$

Figure 2.9: The electroweakino mass spectra and the corresponding mass eigen-states in each mass hierarchy in the bino/wino/higgsino LSP scenarios [49]. The pink (blue) arrows represent the decay mode emitting a W (a Z or a h): A W-boson is generated when a chargino decays into a neutralino or a neutralino decays into a chargino; and a Z- or h-boson is emitted when a chargino decays into a chargino or a neutralino decays into a neutralino. The other decays are not considered in the thesis.

can be performed regardless of the LSP type. The decay processes of $\tilde{W} \to \tilde{H}$ and $\tilde{H} \to \tilde{W}$, as shown in Figure 2.9(b) and 2.9(d), depend on the free parameters, M_2, μ and $\tan\beta$.

The summary of targeted models in this thesis is summarized in Table 2.5.

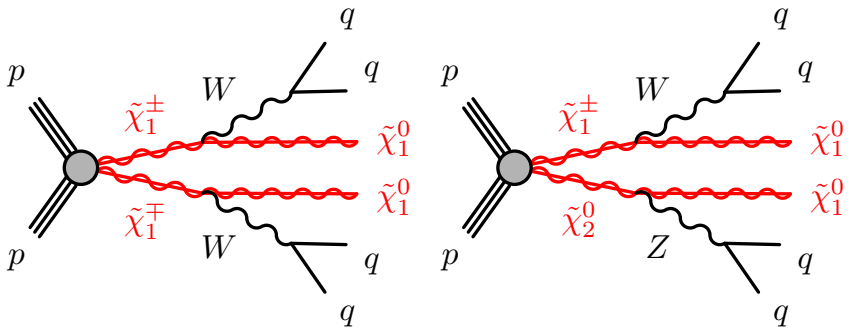

(a) $(\tilde{W}, \tilde{B})$-SIM, C1C1-WW

(b) $(\tilde{W}, \tilde{B})$-SIM, C1N2-WZ

(c) $(\tilde{W}, \tilde{B})$-SIM, C1N2-Wh

Figure 2.10: Main diagrams of signatures in the baseline MSSM scenarios; (a)–(c) $\tilde{\chi}_1^{\pm}$ $\tilde{\chi}_2^0/\tilde{\chi}_1^{\pm}$ $\tilde{\chi}_1^{\pm}$ pair productions in the $(\tilde{W}, \tilde{B})$ simplified model [49].

Table 2.5: Summary of the production modes, final states, and the branching ratio assumptions for the signal models targeted in the search. The $(\tilde{W}, \tilde{B})$ model is used as benchmark signals for optimizing the definitions of selections for the search, as described in Section 7.5. The rest is used only for interpretation, not for optimization. For the $(\tilde{W}, \tilde{H})$ and $(\tilde{H}, \tilde{W})$ models, M_2, μ and $\tan\beta$ are scanned. The cases with 0 TeV $< M_2 <$ 1.2 TeV, -1.2 TeV $< \mu <$ 1.2 TeV, and $\tan\beta = 2, 5, 10, 30$ are considered.

Model	**Production**	**Final states**	**Branching ratio**
$(\tilde{W},\tilde{B})$	$\tilde{\chi}_1^\pm\tilde{\chi}_1^\mp$, $\tilde{\chi}_1^\pm\tilde{\chi}_2^0$	WW, WZ, Wh	$\mathcal{B}(\tilde{\chi}_1^\pm \to W\tilde{\chi}_1^0) = 1$, $\mathcal{B}(\tilde{\chi}_2^0 \to Z\tilde{\chi}_1^0)$ scanned.
$(\tilde{H},\tilde{B})$	$\tilde{\chi}_1^\pm\tilde{\chi}_1^\mp$, $\tilde{\chi}_1^\pm\tilde{\chi}_2^0$, $\tilde{\chi}_1^\pm\tilde{\chi}_3^0$, $\tilde{\chi}_2^0\tilde{\chi}_3^0$	$WW, WZ, Wh,$ ZZ, Zh, hh	$\mathcal{B}(\tilde{\chi}_1^\pm \to W\tilde{\chi}_1^0) = 1$, $\mathcal{B}(\tilde{\chi}_2^0 \to Z\tilde{\chi}_1^0)$ scanned, $\mathcal{B}(\tilde{\chi}_3^0 \to h\tilde{\chi}_1^0) = 1 - \mathcal{B}(\tilde{\chi}_2^0 \to Z\tilde{\chi}_1^0)$
$(\tilde{W},\tilde{H})$	$\tilde{\chi}_2^\pm\tilde{\chi}_2^\mp$, $\tilde{\chi}_2^\pm\tilde{\chi}_3^0$	$WW, WZ, Wh,$ ZZ, Zh, hh	Determined from $(M_2, \mu, \tan\beta)$.
$(\tilde{H},\tilde{W})$	$\tilde{\chi}_2^\pm\tilde{\chi}_2^\mp$, $\tilde{\chi}_2^\pm\tilde{\chi}_2^0$, $\tilde{\chi}_2^\pm\tilde{\chi}_3^0$, $\tilde{\chi}_2^0\tilde{\chi}_3^0$	$WW, WZ, Wh,$ ZZ, Zh, hh	Determined from $(M_2, \mu, \tan\beta)$.
$(\tilde{W}, \tilde{B})$ simplified models: $(\tilde{W}, \tilde{B})$-SIM			
C1C1-WW	$\tilde{\chi}_1^\pm\tilde{\chi}_1^\mp$	WW	$\mathcal{B}(\tilde{\chi}_1^\pm \to W\tilde{\chi}_1^0) = 1$.
C1N2-WZ	$\tilde{\chi}_1^\pm\tilde{\chi}_2^0$	WZ	$\mathcal{B}(\tilde{\chi}_1^\pm \to W\tilde{\chi}_1^0) = \mathcal{B}(\tilde{\chi}_2^0 \to Z\tilde{\chi}_1^0) = 1$.
C1N2-Wh	$\tilde{\chi}_1^\pm\tilde{\chi}_2^0$	Wh	$\mathcal{B}(\tilde{\chi}_1^\pm \to W\tilde{\chi}_1^0) = \mathcal{B}(\tilde{\chi}_2^0 \to h\tilde{\chi}_1^0) = 1$.

2.3.7 Current Limits by Collider Experiments

The current ATLAS limits for the $(\tilde{W}, \tilde{B})$-SIM are shown in Figure 2.11. CMS provides similar results [50, 51]. The horizontal axis represents the $\tilde{\chi}_{\text{heavy}}$ mass, $\tilde{\chi}_1^{\pm}$ and $\tilde{\chi}_2^0$ in the $(\tilde{W}, \tilde{B})$ model. The previous searches by ATLAS use 20.3-139 fb^{-1} of data, and the exclusion limit at the 95% confidence level extends to $m(\tilde{W}) = 700$ GeV with $m(\tilde{B}) = 200$ GeV in the $(\tilde{W}, \tilde{B})$-SIM.

The other searches, which target the models where $\tilde{W}$ or $\tilde{H}$ is the LSP and $\tilde{\chi}_{\text{heavy}}$ is decoupled, also provide exclusion limits in ATLAS and CMS experiments [52–57]. The summary of results in the ATLAS experiment (including preliminary results) is shown in Figure 2.12. The CMS experiment provides similar results [57]. If the LSP is $\tilde{W}$ $(\tilde{H})$, $m(\tilde{\chi}_1^{\pm}) < 650$ (210) GeV is excluded.

2.3.8 Current Limits by Other Experiments

Considering the MSSM, some direct/indirect searches for the dark matter provide limits on the LSP mass and the cross-section of the dark matter scattering or annihilation. Some results are introduced.

Direct Dark Matter Searches XENON-1T [59] provides the upper limits on the dark matter-nucleon spin-independent elastic scatter cross-section ($\sigma_{\chi n}^{SI} < 4.1 \times 10^{-47}$ cm^2 with $m(\tilde{\chi}_1^0) \sim 30$ GeV) [60] and the dark matter-nucleon spin dependent cross-section ($\sigma_{\chi n}^{SD} < 6.3 \times 10^{-42}$ cm^2 with $m(\tilde{\chi}_1^0) \sim 30$ GeV) [61]. The PICO-60 experiment provides the upper limits on the dark matter-proton spin dependent cross-section ($\sigma_{\chi p}^{SD} < 2.5 \times 10^{-41}$ cm^2 with $m(\tilde{\chi}_1^0) \sim 30$ GeV) [62].

As discussed in Section 2.3.5, in the $\tilde{B}$-like dark matter case, the scattering cross-section of $\tilde{B}$ strongly depends on μ and $\tan\beta$. For the $\tilde{H}$-like dark matter case in the $(\tilde{W}, \tilde{H})$ model and $\tilde{W}$-like dark matter case in $(\tilde{H}, \tilde{W})$, the cross-section is typically $\sigma_{\chi n}^{SI} < O(10^{-45})$ cm^2 and $\sigma_{\chi n}^{SD}$, $\sigma_{\chi p}^{SD} < O(10^{-38})$ cm^2. The dark matter direct searches provide the limits with the observed dark matter density, in other words, the dark matter is assumed to be consist of one component. However, the predicted dark matter density of $\tilde{W}$- or $\tilde{H}$-like dark matter is smaller than the observed dark matter density. In order to apply the limits of the direct dark matter search to $\tilde{W}$- or $\tilde{H}$-like dark matter scenarios, the limits need to be scaled to the expected dark matter density corresponding to their mass and types.

Indirect Dark Matter Searches Indirect dark matter searches, such as Fermi-LAT and AMS-02, measure the anti-proton and gamma-ray energy spectra in the universe. In the SUSY framework, the anti-proton and gamma-ray are generated through the neutralino pair annihilation in the universe. The dominant processes are $s-$ and $t-$channel involving charginos or Z boson, for example, $\tilde{\chi}_1^0 \tilde{\chi}_1^0 \to WW$ with chargino exchange. Fermi-LAT [63] and AMS-02 [64] provide the upper limits on thermally averaged cross-section: $\langle \sigma v \rangle_{WW} < O(10^{-25})$ cm$^3 s^{-1}$.

In the $\tilde{W}$- $(\tilde{H}$-)like dark matter case, the thermally avergaed cross-section is $O(10^{-24})$ cm$^3 s^{-1}$ $(O(10^{-25})$ cm$^3 s^{-1})$ with $m(\tilde{\chi}_1^0) < 1$ TeV. Like the direct dark matter searches, the limits are set, assuming that the dark matter consists of one component. If the limits are scaled to the predicted density of $\tilde{W}$-like dark matter, $m(\tilde{\chi}_1^0) > 1600$ GeV is excluded by the AMS-02 experiment [64]. In the $\tilde{H}$-like dark matter case, no exclusion limit is set.

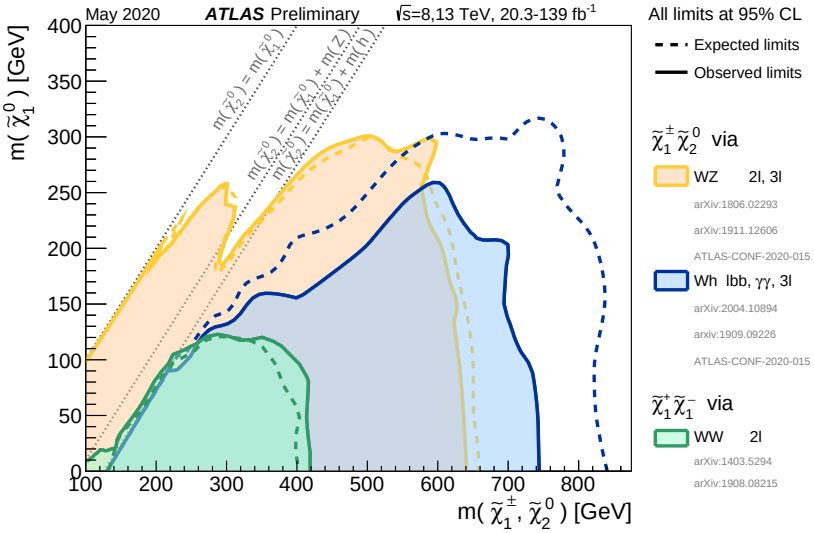

Figure 2.11: The 95% CL exclusion limits on $\tilde{\chi}_1^+\ \tilde{\chi}_1^-$ or $\tilde{\chi}_1^\pm\ \tilde{\chi}_2^0$ production in the $(\tilde{W}, \tilde{B})$-SIM with a function of $\tilde{W}$ $(\tilde{\chi}_1^\pm, \tilde{\chi}_2^0)$ mass [29]. The vertical axis represents the LSP $(\tilde{B})$ mass $(=m(\tilde{\chi}_1^0))$. The dashed (solid) line represents the expected (observed) limits. The orange (blue) regions are excluded by the $\tilde{\chi}_1^\pm\ \tilde{\chi}_2^0$ production and the decay with $WZ(Wh)$. The green regions are excluded by the C1C1-WW model.

In the $\tilde{B}$-like dark matter case, the dominant process is $\tilde{\chi}_1^0\tilde{\chi}_1^0 \to Z/h \to f\bar{f}$. As discussed in Ref.[41], the annihilation cross-section is at most $O(10^{-28})$ cm$^3 s^{-1}$. Thus, this case still remains.

2.4 Other SUSY Models

Additional two target models in this thesis, the $(\tilde{H}, \tilde{G})$ model and the $(\tilde{H}, \tilde{a})$ model, are introduced in this section. In the $(\tilde{H}, \tilde{G})$ model, the superpartner of the spin-2 graviton (gravitino, $\tilde{G}$) is the LSP. In the $(\tilde{H}, \tilde{a})$ model, the superpartner of the axion (axino, $\tilde{a}$) is the LSP. The details of the models are discussed below. The details of the models are described in Sections 2.4.2 and 2.4.3.

2.4.1 Soft Breaking Mechanism

The target in this thesis is not only a general search without assuming a SUSY breaking model but also a model with a SUSY breaking mechanism. There are some models of SUSY braking, such as supergravity (SUGRA) [65], gauge-mediated supersymmetry breaking (GMSB) models, and anomaly-mediated supersymmetry breaking (AMSB) models [66, 67]. In the GMSB models, gravitino ($\tilde{G}$), which is the superpartner of the graviton, is the LSP. Supersymmetry-breaking occurs in a hidden sector and couples to the visible sector through the mediator. The detail is discussed in Appendix A.6. In this thesis, GMSB is one of the target models.

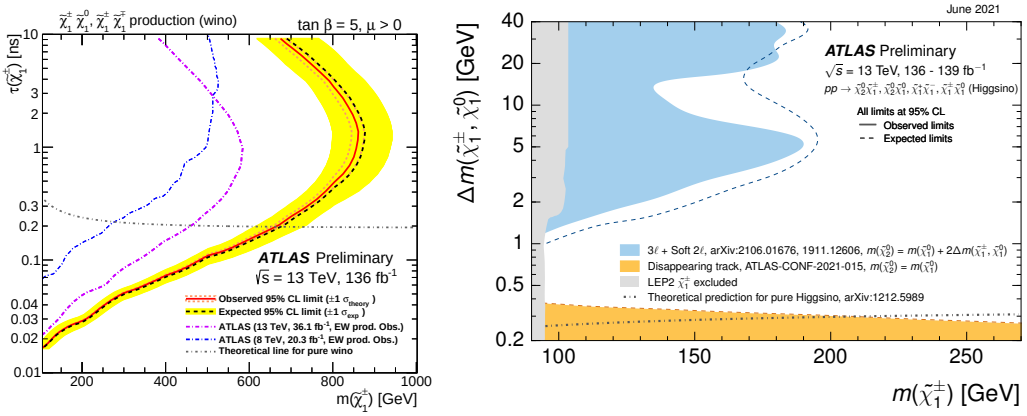

(a) $\tilde{W}$-LSP (ATLAS)

(b) $\tilde{H}$-LSP (ATLAS)

Figure 2.12: The 95% CL exclusion limits for $\tilde{W}$- and $\tilde{H}$-LSP in the ATLAS experiments. $\tilde{W}$ or $\tilde{H}$ is produced directly by pp-collision. (a) $\tilde{W}$ is the LSP and $\tilde{\chi}_1^\pm$, and $\tilde{\chi}_1^0$ degenerate [52]. x-axis and y-axis represent the mass and lifetime of $\tilde{\chi}_1^\pm$, respectively. The smaller the mass difference between $\tilde{\chi}_1^\pm$ and $\tilde{\chi}_1^0$ is, the longer the lifetime of $\tilde{\chi}_1^\pm$ is. (b) The LSP is higgsino [58]. The x-axis represents the mass of $\tilde{\chi}_1^\pm$, and the y-axis represents the mass difference between $\tilde{\chi}_1^0$ and $\tilde{\chi}_1^\pm$. The small mass difference region (long lifetime of $\tilde{\chi}_1^\pm$ region) is excluded by the disappearing track analysis. If the mass difference is larger than 1 GeV, the compressed analysis excludes soft (low p_T) lepton.

2.4.2 General Gauge Mediation Scenario

For the naturalness, the $(\tilde{H}, \tilde{G})$ model is considered. In this scenario, $\tilde{G}$ is the superpartner of the graviton with the spin of 2 and nearly massless, i.e., the LSP. $\tilde{H}$ is the next to lightest supersymmetric particle (NLSP). By the assumptions similar to the baseline MSSM scenarios, other SUSY particles are assumed to be heavy and decoupled. Therefore, only $\tilde{H}$ pair production mode is considered. In the $(\tilde{H}, \tilde{G})$ model, the coupling between $\tilde{H}$ and $\tilde{G}$ is assumed to be small. Thus, we consider the decay $\tilde{\chi}_1^0 \to Z/h + \tilde{G}$, as shown in Figure 2.13. The total branching ratio is assumed to be 100% while each branching ratio depends on the lightest neutralino mass and $\tan\beta$ [68]. In this thesis, the branching ratio of $\tilde{\chi}_1^0 \to Z\tilde{G}$ is scanned instead of the lightest neutralino mass and $\tan\beta$.

The ATLAS experiment provides the exclusion limit, as shown in Figure 2.14. The CMS experiment provides a similar limit [69]. The exclusion limit for $m(\tilde{H})$ extends up to 600 GeV at the branching ratio of $\mathcal{B}(\tilde{\chi}_1^0 \to h\tilde{G}) = 50\%$.

If $\tilde{G}$ was the dark matter, there would be some cosmological problems [70–76], such as overclosing the universe. To avoid these problems, the gravitino mass $m_{3/2}$ is required to be less than $\sim$ 1 keV if gravitino is produced thermally in the early universe. Then, a reheating temperature of inflation is required to be low in order to reduce the gravitino abundance. A low reheating temperature of inflation leads to difficulty in explaining the observed baryon asymmetry. Therefore, the $(\tilde{H}, \tilde{G})$ model motivated by the dark matter is not discussed in this thesis.

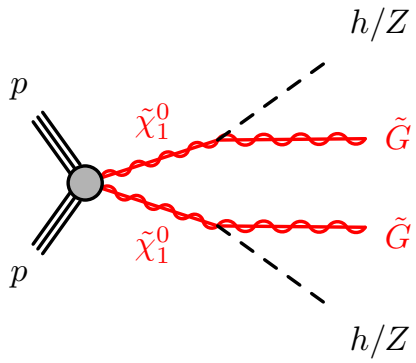

Figure 2.13: The diagram of $(\tilde{H}, \tilde{G})$ [49].

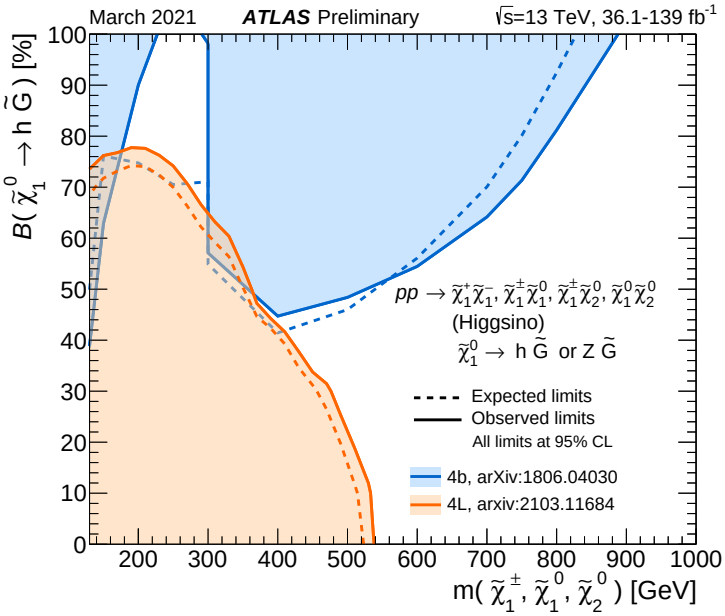

Figure 2.14: The 95% CL exclusion limits on $(\tilde{H}, \tilde{G})$ model, as a function of $\tilde{H}$ $(\tilde{\chi}_1^\pm, \tilde{\chi}_2^0, \tilde{\chi}_1^0)$ mass and the branching ratio of lightest higgsino to Higgs gravitino [29]. Blue (orange) regions are excluded by the analyses for $\tilde{\chi}_1^0\ \tilde{\chi}_1^0 \rightarrow \tilde{G}\ \tilde{G}$ with hh (ZZ) bosons.

2.4.3 Naturalness Driven Axino LSP Scenario

In the SM, there is another problem that a CP-violating angle in the QCD Lagrangian is quite small. The angle of the CP-violation term is constrained to be less than 10^{-10} rad by the measurement [77] of the electric dipole moment of neutrons while there is no reason why the angle is so small in the SM. This problem is known as the "strong-CP problem." To resolve the strong-CP problem, the SM is extended by introducing a new U(1) symmetry called "Peccei-Quinn (PQ) symmetry." If the PQ symmetry is spontaneously broken, a pseudo-Nambu-Goldstone boson called "axion" is added to the SM. Consequently, the saxion (s) and the axino $(\tilde{a})$, which are a scalar partner and the fermion superpartner of the axion, appeared in the MSSM. The axino mass is expected to be the soft supersymmetry breaking scale while it depends on the models [78–80].

In this thesis, the supersymmetric DFSZ axion model [81] where axino is the LSP is considered. No interaction with the SM electroweak bosons or the leptons is considered. Axinos directly couple to the gluons and gluinos via the anomaly coupling and are produced in the primordial plasma by scatterings of the colored particles that are in thermal equilibrium. The axino number density is proportional to the reheating temperature after inflation [82]. Axino is also generated by the non-thermal production via out of equilibrium decays from the heavier superpartners.

Since there is axino-neutralino mixing in this model, axino can be a dark matter candidate. To explain the WMAP result about the dark matter, $m_{\tilde{a}} \sim O(100\ \text{GeV})$ is favored when the reheating temperature is less than 400 GeV [83]. In this thesis, constraints on the axino dark matter models are not discussed due to the dependencies on the reheating temperature of a production mechanism after inflation and the PQ scale.

In this thesis, $\tilde{H}$ is assumed to be the NLSP. If $m(\tilde{H}) - m(\tilde{a}) > 300$ GeV, $\tilde{H}$ decays to $\tilde{a}$ promptly. In the $(\tilde{H}, \tilde{a})$ case, $\tilde{H}$-$\tilde{a}$ coupling is assumed to be small. Thus, we consider that $\tilde{\chi}_1^0 \to Z/h + \tilde{a}$, as shown in Figure 2.15. In this scenario, the branching ratio is treated as a free parameter. The scenario can explain the naturalness and the dark matter.

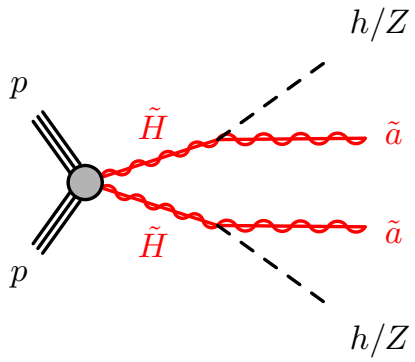

Figure 2.15: The diagram of $(\tilde{H}, \tilde{a})$ [49].

3 Experimental Apparatus

3.1 Large Hadron Collider

Large Hadron Collider (LHC) is a circular accelerator 27 km long and a collider of protons. Before being injected into the LHC, protons are accelerated by several pre-accelerators [84]: LINAC2, the Proton Synchrotron Booster (PSB), the Proton Synchrotron (PS), and the Super Proton Synchrotron (SPS), as shown in Figure 3.1. There are four collision points at the LHC. At the diametrically opposite points, ATLAS [85] and CMS [4] detectors are located. Additionally, LHCb [86] targeting B-hadron physics and ALICE [87] for heavy-ion collisions to study QCD phenomena are located at the other points.

In 2015-2018 (called LHC Run-2), the LHC accelerated the proton beams up to 6.5 TeV, providing pp-collisions at the center of mass energy ($\sqrt{s}$ = 13 TeV). In the LHC, there are 2500 or more bunches with 25 ns spacing, and 10^{11} or more protons are contained per bunch. Thus, the number of inelastic pp-collisions per bunch crossing called "pile-up", is typically 10-70. The peak luminosity reached beyond $2.0 \times 10^{34}\,\mathrm{cm}^{-2}\mathrm{s}^{-1}$ at the ATLAS and CMS in 2017 and delivers 156 fb^{-1} to ATLAS from 2015 to 2018. The 156 fb^{-1} dataset (139 fb^{-1} for physics analyses) of ATLAS is used in this thesis.

3.2 ATLAS Detector

The ATLAS detector is designed as a general-purpose detector to search for the Beyond Standard Model (BSM) physics and to measure the Standard Model properties in the high luminosity environment. A benchmark considered in the design is the SM Higgs boson that decays into, for instance, $b\bar{b}$ and $ZZ^* \to llll$. Thus, the ATLAS detector performance is optimized to identify the flavor of quarks/leptons and photons. From these requirements, the ATLAS detector consists of Inner Detector, Calorimeter, and Muon Spectrometer sub-systems as shown in Figure 3.2(a). Each sub-system is introduced in Section 3.2.3, 3.2.4, and 3.2.5, respectively. To operate the experiment and record the physics events with numerous channels of the ATLAS detector in high event rates, an online event selection called "trigger" is employed. The trigger system is presented in Section 3.2.6.

The outline is introduced in this section. The detail is presented in Ref.[85].

3.2.1 Coordinate Systems in ATLAS

In the ATLAS experiment, two coordinate systems are employed. One is the Cartesian coordinate system as the right-handed system and is shown in Figure 3.2(b). The transverse plane with respect to the beamline is defined as the $x-y$ plane. The x-axis and y-axis point to the center of the LHC ring and vertical upward, respectively. The z-axis is defined along with the beam axis, and the direction is counterclockwise. The other is the cylindrical coordinate system, and the position is represented (r, z, ϕ).

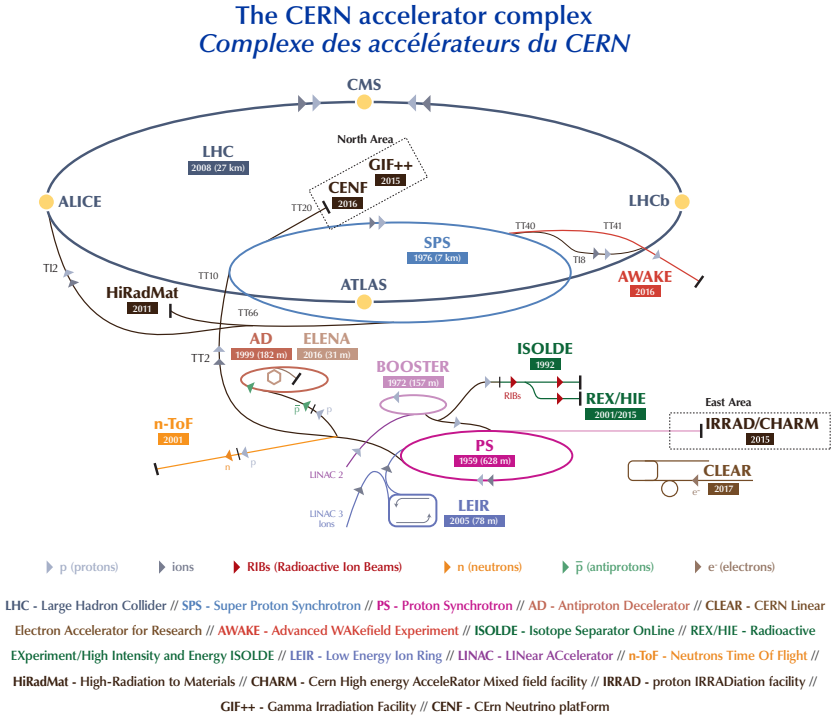

Figure 3.1: Schematic layout of a complex chain of the CERN accelerator [88]. The LINAC2 is the first accelerator of protons (violet) and the protons are injected into the LHC (large dark blue ring) finally.

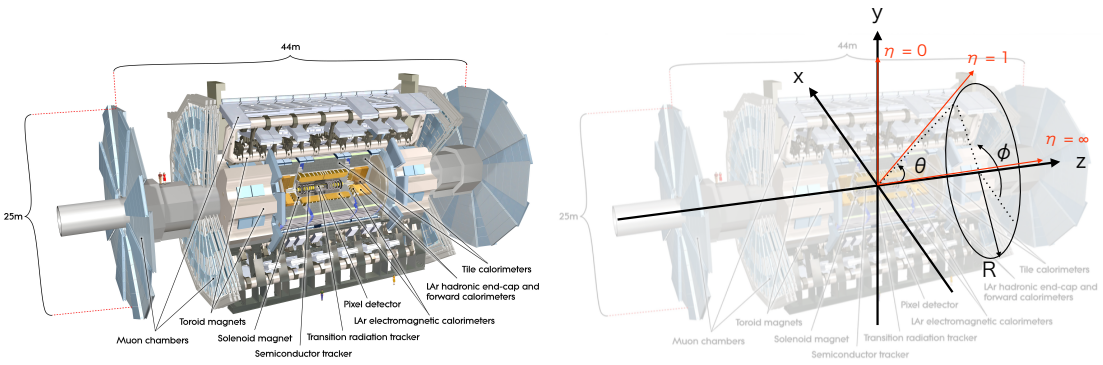

(a) Cross-sectional view

(b) Coordinate systems

Figure 3.2: Cross-sectional view and coordinate systems of the ATLAS detector [85].

The pseudorapidity η is defined as the rapidity y with the high energy limit ($m \ll E$), $-\frac{1}{2}\ln\tan(\theta/2)$. The differences of η and ϕ are Lorentz invariant under a boost along with the z-direction. Thus, $\Delta R_{12} = \sqrt{(\eta_1 - \eta_2)^2 + (\phi_1 - \phi_2)^2}$ is Lorentz invariant.

The ATLAS detector is a form of a cylinder and can be divided into the side of a cylinder called "barrel" and bottom parts referred to as "end-caps." In particular, the region, $|\eta| \gtrsim 2.5$, is called "forward."

In the pp-collision, the constitutes of protons, quarks and gluons, interact as elementary particles. Since the

initial momenta of the quarks and gluons cannot be known, we cannot impose conservation rules. However, we can impose conservation rules in a transverse plane approximately since the transverse momentum of partons, the quarks and gluons, is small in the initial states. Thus, the transverse momentum (p_{T}) and the transverse energy (E_{T}) are used in this thesis.

3.2.2 Magnet System

Three types of superconducting magnets are used to bend the trajectories of charged particles measure their transverse momenta. The layout of magnets is shown in Figure 3.3. One is the solenoid magnet placed on the outside of the Inner Detectors. The trajectories of charged particles are bent in the ϕ direction inside the solenoid magnet. The others are the toroidal magnets in the barrel region and the end-cap regions. They consist of eight coils and provide the toroidal magnetic fields inside the coils. They are placed between the innermost and the outermost of the Muon Spectrometers. The trajectories of muons are bent in the η direction.

3.2.3 Inner Detector

The Inner Detector (ID) is placed at the innermost in the ATLAS detector. The layout is shown in Figure 3.4. The ID plays an important role in reconstructing the primary vertex and measuring the momentum of charged particles using the 2T solenoid magnetic field. The ID consists of Insertable B-Layer (IBL) [89], Pixel, Silicon Microstrip Tracker (SCT), and Transition Radiation Tracker (TRT) from inside to outside. They are placed inside the solenoid magnet. They are installed in $0 < R < 1150\,\mathrm{mm}$, $0 < |z| < 3512\,\mathrm{mm}$ ($|\eta| < 2.5$), where R is a radial distance from the beam axis.

The design momentum resolution of the ID is $\sigma_{p_{\mathrm{T}}}/p_{\mathrm{T}} = 0.05\%\ p_{\mathrm{T}}[\mathrm{GeV}] \bigoplus 1\%$.

3.2.3.1 Pixel detector and Insertable B-Layer

The pixel detectors are placed at the innermost part of the ID and have high granularity. n-type wafers are used, and n^{+}-side of the detector has the readout. The innermost layer is called IBL and was introduced before Run 2.

IBL is installed at $R = 33.3$ mm in the barrel region and has a pixel with the size of $\Delta\phi \times \Delta z = 50 \times 250\,\mu\mathrm{m}^2$. On the outer side, three pixel layers in the barrel region are installed at $R = 50.5,\ 88.5,\ 122.5$ mm and cover the range ($|z| < 400.5$ mm). Their pixel size is $\Delta\phi \times \Delta z = 50 \times 400\,\mu\mathrm{m}^2$. In the end-cap regions, 3 disks are installed in $495 < |z| < 650\,\mathrm{mm}$ and cover $88.8 < R < 149.6\,\mathrm{mm}$ at each side.

3.2.3.2 Silicon Microstrip Tracker

The SCT has sensors based on a single-sided p-in-n technology with AC-coupled strips for the readout. The SCT consists of two layers with an average pitch of strips $80\,\mu\mathrm{m}$. They are equipped with only 40 mrad tilted. Thus, the two-dimensional position at the detector location can be reconstructed from the information in two layers.

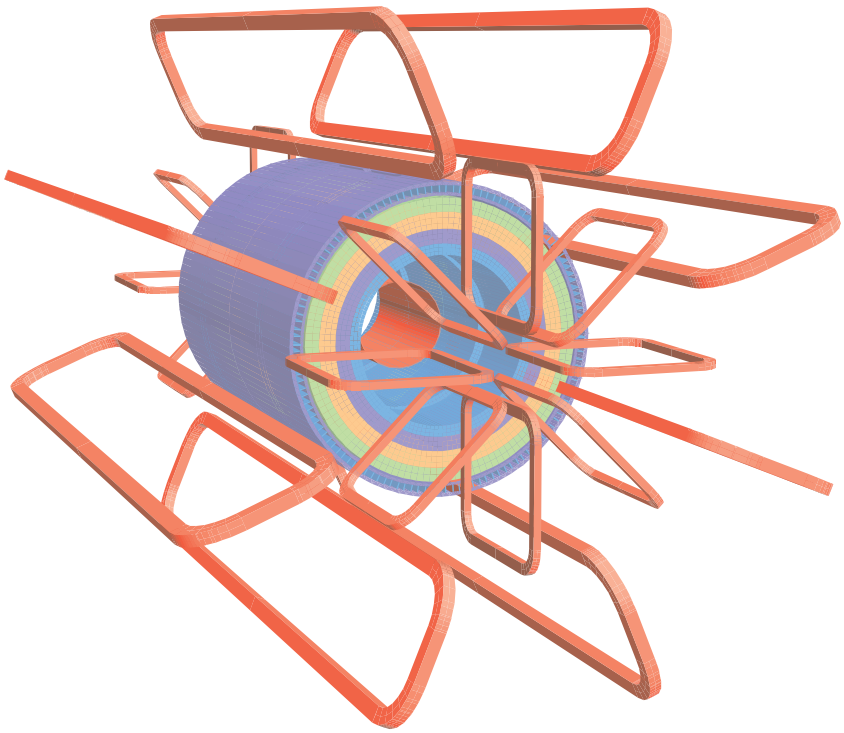

Figure 3.3: Overview of the magnet system [85].

In the barrel region, 4 layers are installed in $299 < R < 514$ mm and cover $0 < |z| < 749$ mm. They measure the position of z and ϕ. In the end-cap region, 9 disks on each side are installed in $839 < |z| < 2735$ mm and cover $275 < R < 560$ mm. They measure the position of R and ϕ.

3.2.3.3 Transition Radiation Tracker

The TRT consists of polyimide straw tubes with a 4 mm diameter and detects transition radiation photons. In the barrel region, 73 straw planes are installed parallel to the beam axis in $563 < R < 1066$ mm and cover $0 < |z| < 712$ mm. They are read out from each end. Thus, the $R - \phi$ position is obtained in the barrel region. In the end-cap region, 160 straw planes are installed along the radial direction in $848 < |z| < 2710$ mm and cover $644 < R < 1004$ mm. $z - \phi$ position is obtained.

Due to the large coverage and many hits (typically 36 per track) with 130 μm accuracy per tube, the TRT plays an important role to measure the momentum. Additionally, the combination of the trackers at small radii with the TRT at a larger radius can provide high-precision measurements and enables the identification of particles with high-quality using robust pattern recognition, such as electrons and $\pi^{\pm}$.

3.2.4 Calorimeters

The ATLAS calorimeter system locates outside of the ID, as shown in Figure 3.5. The electromagnetic (EM) calorimeter and hadronic calorimeter are categorized into sampling calorimeters and arranged in this order from the inside. In $3.1 < |\eta| < 4.9$ (forward region), the calorimeter plays a different role in each

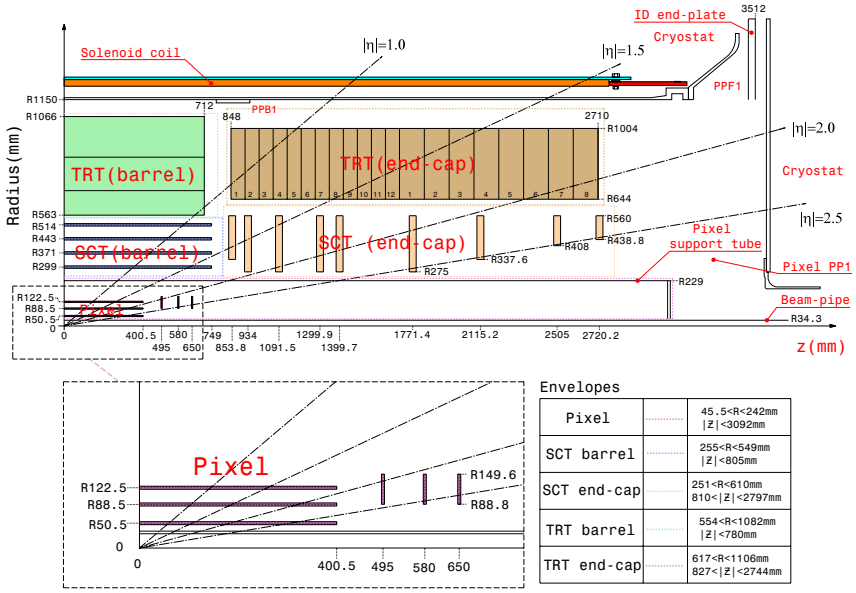

Figure 3.4: Overview of the Inner Detector [85].

layer, i.e., the inner layer works as an EM calorimeter, and the outer layer works as a hadronic calorimeter. The EM calorimeters measure the positions and energy of electrons and photons by the electromagnetic shower. Jet is one of the most basic processes in the pp-collision and represents a characteristic feature of short-distance interactions between partons. Since hadrons mainly lose the energy in the hadronic calorimeter, the hadronic calorimeter measures the energy and positions of jets. The amount of materials in the EM and hadronic calorimeter is greater than 9.7 interaction length (λ) in the barrel and 10 λ in the end-cap.

The calorimeters are installed outside of the Inner Detector as shown in Figure 3.5. The thickness of the calorimeters is designed to contain EM and hadronic shows fully and is 11 interaction length (λ) at $\eta = 0$ including the outer support. The active material has ~ 9.7 λ in the barrel and ~ 10 λ in the end-cap

The EM and hadronic calorimeters are categorized into sampling calorimeters. The main advantage of the sampling calorimeters is the easiness of segment laterally and longitudinally, while the sampling calorimeter has worse energy resolution than homogenous calorimeters. The advantage leads to the good performance of position measurements and particle identification using shapes of electromagnetic and hadronic showers.

3.2.4.1 Electromagnetic Calorimeter

The EM calorimeter consists of liquid-argon as the active material and lead plates as the absorber and has a presampler and 3-layers. The main parameters of the EM calorimeter are summarized in Table 3.1. Due to the high granularity in the first and second layers ($|\eta| < 2.5$), their information is useful to determine the photon position. The presampler ($|\eta| < 1.8$) corrects the energy lost inside the EM calorimeter.

The design energy resolution of the EM calorimeter is $\sigma_E/E = 10\%/\sqrt{E\ [\mathrm{GeV}]} \bigoplus 0.7\%$.

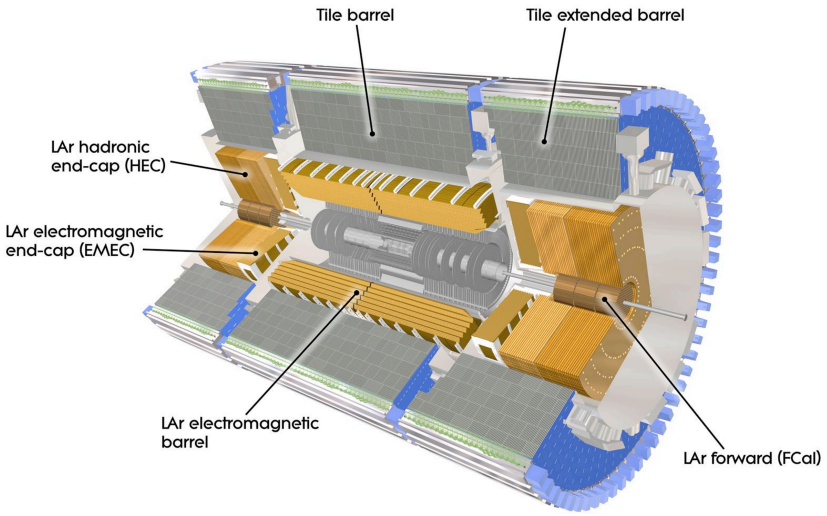

Figure 3.5: Overview of the ATLAS calorimeter system [85]. Corresponding to each arrangement position, EM (hadronic) calorimeters are housed in "barrel cryostat" and "end-cap cryostats." In the forward region, the calorimeters are called "forward calorimeters."

Table 3.1: Main parameters of the EM calorimeter [85].

Granularity $\Delta\eta \times \Delta\phi$ versus $\lvert\eta\rvert$				
Presampler	0.025×0.1	$\lvert\eta\rvert < 1.52$	0.025×0.1	$1.5 < \lvert\eta\rvert < 1.8$
Calorimeter 1st layer	$0.025/8 \times 0.1$	$\lvert\eta\rvert < 1.40$	0.050×0.1	$1.375 < \lvert\eta\rvert < 1.425$
	0.025×0.025	$1.40 < \lvert\eta\rvert < 1.475$	0.025×0.1	$1.425 < \lvert\eta\rvert < 1.5$
			$0.025/8 \times 0.1$	$1.5 < \lvert\eta\rvert < 1.8$
			$0.025/6 \times 0.1$	$1.8 < \lvert\eta\rvert < 2.0$
			$0.025/4 \times 0.1$	$2.0 < \lvert\eta\rvert < 2.4$
			0.025×0.1	$2.4 < \lvert\eta\rvert < 2.5$
			0.1×0.1	$2.5 < \lvert\eta\rvert < 3.2$
Calorimeter 2nd layer	0.025×0.025	$\lvert\eta\rvert < 1.40$	0.050×0.025	$1.375 < \lvert\eta\rvert < 1.425$
	0.075×0.025	$1.40 < \lvert\eta\rvert < 1.475$	0.025×0.025	$1.425 < \lvert\eta\rvert < 2.5$
			0.1×0.1	$2.5 < \lvert\eta\rvert < 3.2$
Calorimeter 3rd layer	0.050×0.025	$\lvert\eta\rvert < 1.35$	0.050×0.025	$1.5 < \lvert\eta\rvert < 2.5$

3.2.4.2 Hadronic Calorimeter

The tile calorimeter, the liquid-argon hadronic end-cap calorimeter (HEC), and the liquid-argon forward calorimeter (FCal) are installed in the barrel, end-cap, and forward region, respectively. The parameters of each calorimeter are summarized in Table 3.2, 3.3.

The design energy resolution of the hadron calorimeter is $\sigma_E/E = 50\%/\sqrt{E\ [\mathrm{GeV}]} \bigoplus 3\%$ in the barrel and end-cap ($|\eta| < 3.2$), $\sigma_E/E = 100\%/\sqrt{E\ [\mathrm{GeV}]} \bigoplus 10\%$ in the forward ($3.1 < |\eta| < 4.9$).

Table 3.2: Main parameters of the tile calorimeter [85].

Tile calorimeter		
	Barrel	Extended barrel
$\|\eta\|$ coverage	$\|\eta\| < 1.0$	$0.8 < \|\eta\| < 1.7$
Number of layers	3	3
Granularity $\Delta\eta \times \Delta\phi$	0.1×0.1	0.1×0.1
Last layer	0.2×0.1	0.2×0.1

Table 3.3: Main parameters of the LAr hadronic calorimeter and forward calorimeter [85].

LAr hadronic calorimeter (HEC)		
$\|\eta\|$ coverage	$1.5 < \|\eta\| < 3.2$	
Number of layers	4	
Granularity $\Delta\eta \times \Delta\phi$	0.1×0.1	$1.5 < \|\eta\| < 2.5$
	0.2×0.2	$2.5 < \|\eta\| < 3.2$
LAr forward calorimeter (FCal)		
$\|\eta\|$ coverage	$3.1 < \|\eta\| < 4.9$	
Number of layers	3	
Granularity $\Delta x \times \Delta y$ (cm)	FCal1: 3.0×2.6	$3.15 < \|\eta\| < 4.30$
	FCal1: ~ four times finer	$3.10 < \|\eta\| < 3.15$
		$4.30 < \|\eta\| < 4.83$
	FCal2: 3.3×4.2	$3.24 < \|\eta\| < 4.50$
	FCal2: ~ four times finer	$3.20 < \|\eta\| < 3.24$
		$4.50 < \|\eta\| < 4.81$
	FCal3: 5.4×4.7	$3.32 < \|\eta\| < 4.60$
	FCal3: ~ four times finer	$3.29 < \|\eta\| < 3.32$
		$4.60 < \|\eta\| < 4.75$

Tile Calorimeter The tile calorimeter is a sampling calorimeter composed of steel as the absorber and scintillator as the active material. They are divided into three parts, one is located in $|\eta| < 1.0$ (barrel) and two parts in each side are called extended barrels ($0.8 < |\eta| < 1.7$). The unit divided azimuthally into 64 parts in full ϕ range is referred to as a module and equivalent to the unit of the readout. The structure of the tile calorimeter is divided in the direction of R.

The thickness of the first layer is equivalent to 1.5 λ in the barrel and 3.3 λ in the extended barrel. The thickness of the second (third) layer is equivalent to 4.1 (1.8) λ in the barrel and 2.6 (3.3) λ in the extended barrel, respectively.

LAr Hadronic End-cap Calorimeter The HEC is a sampling calorimeter composed of copper as the absorber and liquid-argon as the active material. The HEC consists of two wheels in each end-cap cryostat, and each wheel contains two longitudinal sections. The HEC is located outside the end-cap EM calorimeter and covers $1.5 < |\eta| < 3.2$.

Forward Calorimeter The FCal, which covers $3.1 < |\eta| < 4.9$, is composed of three modules. The innermost module is called "FCal1" and works as an electromagnetic calorimeter. The outer modules are "FCal2" and "FCal3," and they work as hadronic calorimeters. FCal1 is constructed with copper tubes and copper rods with LAr gaps, and the rods work as the absorber. FCal2 and FCal3 use tungsten as the absorber and consist of copper tubes and tungsten rods. A copper-shielding plug is installed on the outside of the FCal3 to reduce the background in the muon system.

3.2.5 Muon Spectrometer

The Muon Spectrometer (MS) is placed at the outermost since muons punch through the calorimeters due to the long lifetime and the small energy loss. As shown in Figure 3.6, the MS consists of 2 detectors for trigger and of 2 detectors for the precise measurement. Resistive Plate Chamber (RPC) and Thin Gap Chamber (TGC) are used for triggers. Monitored Drift Tube (MDT) and Cathode Strip Chamber (CSC) are used for the precise measurement.

RPC is placed at the barrel region ($|\eta| < 1.05$) and TGC is placed at the end-cap region ($1.05 < |\eta| < 2.7$). MDT is placed in the barrel and end-cap regions, and CSC is placed in a high $|\eta|$ of the end-cap region ($2.0 < |\eta| < 2.7$).

In the barrel region, three stations, which consist of multiple types of muon detectors, are installed at $R \sim 5\,\text{m}$, $7.5\,\text{m}$, $10\,\text{m}$. On the other hand, three stations are installed at $|z| \sim 7.4\,\text{m}$, $14\,\text{m}$, $21.5\,\text{m}$ in the end-cap region. The trajectories of muons are bent by the barrel/end-cap toroidal magnet between the inner and middle stations.

The resolution of the momentum in the MS is $\sigma_{p_\text{T}}/p_\text{T} = 10\%$ at $p_\text{T} = 1$ TeV.

3.2.5.1 Resistive Plate Chamber

Each strip of RPC for the readout is arranged orthogonally. Thus, $z - \phi$ information is obtained from the RPC, and the trajectory of a muon is reconstructed from the positions in each layer. The RPC consists of 3 layers, two inner layers (RPC1 and RPC2) are located on the middle station and the outer layer (RPC3) is on the outer station. Thanks to the toroidal magnetic field in the barrel region, the transverse momentum of a muon is estimated by the trajectory.

3.2.5.2 Thin Gap Chamber

The TGC is a multi-wire chamber (MWPC) with a 2.8 mm gas gap and a 1.8 mm interval of the wire. Anode wires and pick-up strips are arranged orthogonally for each other, and the wires (strips) provide the r (ϕ) position. Due to the short drift length, the response time of the TGC is fast. Thus, the TGC can reconstruct the trajectory of muons quickly, and the trajectory is used for triggers. For the trigger, the seeds of muon trajectories are reconstructed from the information of the third and fourth layers. $|\eta| < 2.4$ is used for the trigger.

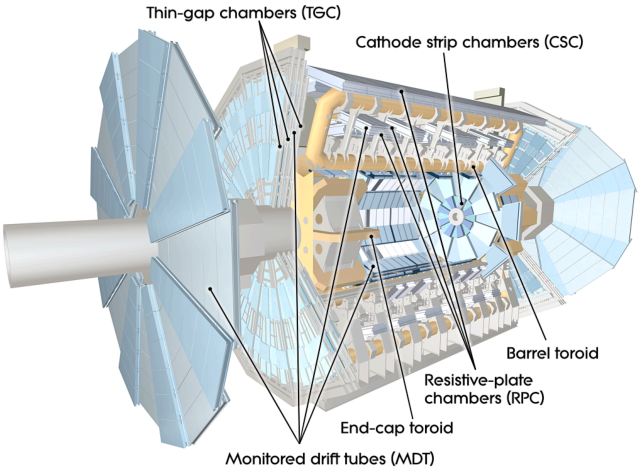

Figure 3.6: Overview of the muon spectrometer [85].

3.2.5.3 Monitored Drift Tube

The structure of MDT is multi-layers of the drift tubes. The diameter of the drift tubes is 29.97 mm. The MDT has 3-8 layers in each station. The tubes are installed along with ϕ in the barrel and end-cap regions, providing information about η. Since the resolution of the MDT is better than that of RPC and TGC, the MDT plays an important role in the muon momentum measurement.

3.2.5.4 Cathode Strip Chamber

CSC is an MWPC for precise measurements and is placed in the forward region ($2.0 < |\eta| < 2.7$) of the inner station. In this region, the rate of particles such as neutrons, γ-rays, and charged particles is greater than the limit of the MDT to operate with high precision ($150\,\mathrm{Hz/cm^2}$). Thus, CSC is used instead of MDT. The strips are arranged orthogonally for each other and are used for the readout. Therefore, the $R-\phi$ position is obtained.

3.2.6 Trigger and Data Acquisition

The ATLAS experiment employs an online event selection system, called "trigger," to reduce the data recording rate from 40 MHz to a recordable rate (in Run-2, it was $\sim$ 1 kHz on average). The trigger system consists of hardware-based "Level-1 Trigger (L1)" and CPU-based "High Level Trigger (HLT)," as shown in Figure 3.7.

Theoretical predicted and measured cross-sections of various SM processes are shown in Figure 3.8. The total cross-section of the pp inelastic scattering is about 70 mb. However, the production cross-sections of weak bosons, Higgs bosons, top quarks are small, such as $< 10^{-7}$ of the cross-section of the pp inelastic scattering. The cross-sections of BSM physics are even smaller. Therefore, the trigger performance is important to select BSM physics events from many not interesting events, such as the pp inelastic scattering, and record them.

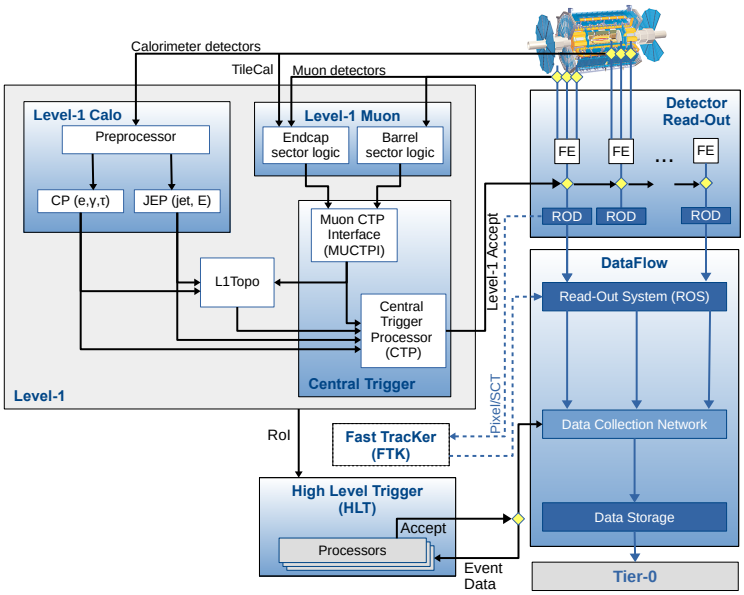

Figure 3.7: The schematic view of the ATLAS trigger and data acquisition system [90].

At the trigger level, particular physics signatures such as leptons (e, μ), photons, jets, missing transverse momentum, and the presence of B-meson candidates are reconstructed. The trigger selection is based on these objects, which threshold applied.

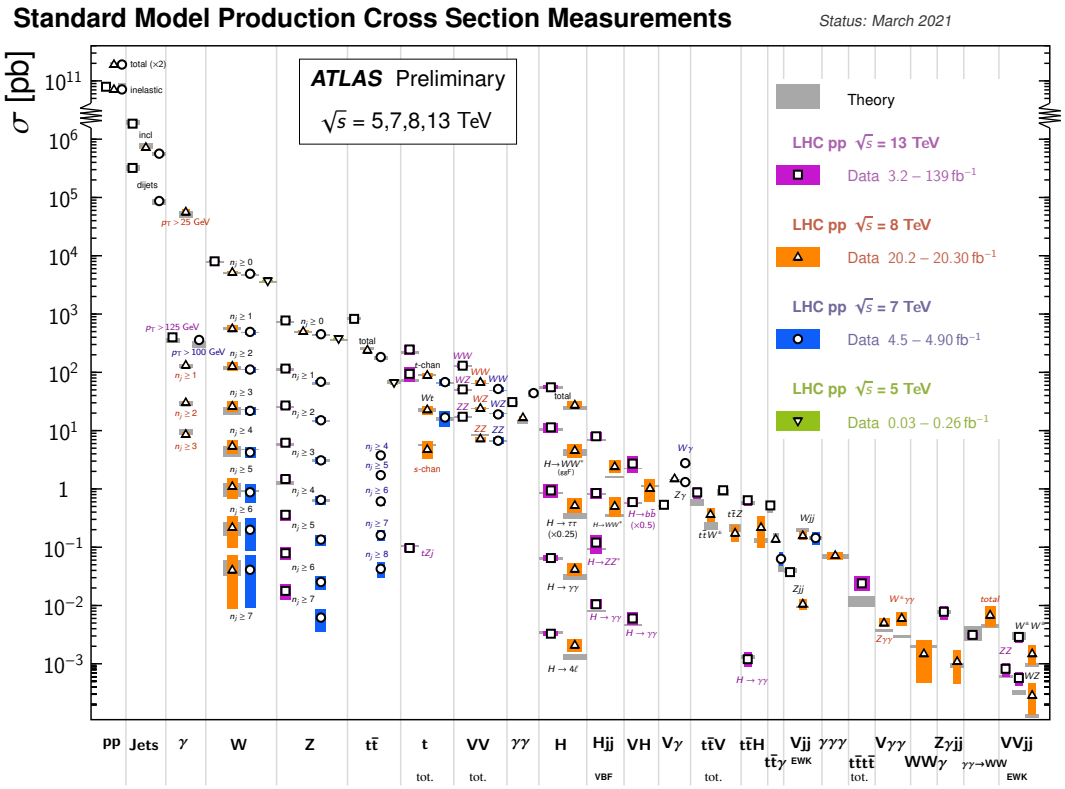

Figure 3.8: Summary of several SM total and fiducial production cross section measurements, corrected for branching fractions, compared to the corresponding theoretical expectations [91].

4 Data and Monte Carlo Simulations

In this thesis, the data of pp-collisions delivered from the LHC are used. As well as, signal and some of the SM background simulated samples are used to understand SM background processes. These data sets are described in this chapter.

4.1 Recorded Data by the ATLAS Detector

The data of the pp-collisions at $\sqrt{s}$ = 13 TeV collected by the ATLAS detector in 2015-2018 are used. The amount of the data corresponds to 139 fb^{-1} with 1.7% uncertainty on the integrated luminosity [92]. The total integrated luminosity as a function of time is shown in Figure 4.1. The amounts of the data are 3.2 fb^{-1} in 2015, 33.0 fb^{-1} in 2016, 44.3 fb^{-1} in 2017, and 58.5 fb^{-1} in 2018. The luminosity is determined with the LUCID2 Cherenkov detector [93], which is calibrated using the van der Meer method, as presented in Ref.[92]

The mean number of interactions per bunch-crossing depends on the parameter of the beam, and the distributions vary greatly depending on the data-taking periods, as shown in Figure 4.2. Monte Carlo simulations are reweighted to have the same mean number of interactions per bunch-crossing distribution as the data samples,

4.2 Monte Carlo Simulation

Monte Carlo simulation samples are used to estimate the yields of the signal and the SM backgrounds. The first phase of the event simulation is the hard scattering process. In the pp-collisions, multiple proton-proton collisions are occurring in the same and neighboring bunch crossings; other particles from collisions other than a collision of interest contribute to the mis-reconstruction and mis-measurement. These contributions are called "pile-up effect." To simulate this pile-up effect, we use the samples simulated with Pythia 8.186 [95], the NNPDF2.3$_{\mathrm{LO}}$ PDF set [96], and A3 set of tuned parameters [97] to overlay to other hard scatter simulation samples. The response of the ATLAS detector is simulated with the ATLAS simulation software [98] based on the Geant 4 [99].

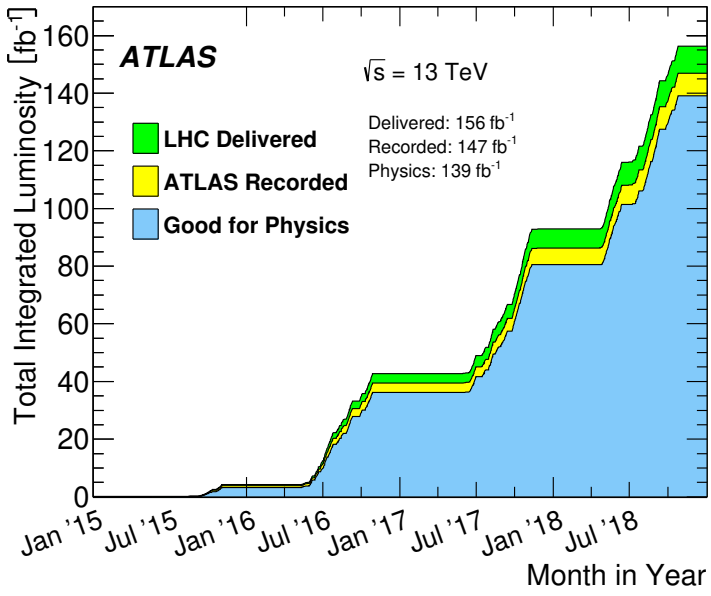

Figure 4.1: Total integrated luminosity with a function of time delivered from the LHC (green) and recorded by ATLAS (yellow) during stable beams for the pp-collisions at $\sqrt{s}$ = 13 TeV in 2015-2018 [94]. Good quality data for the analyses represent a blue histogram.

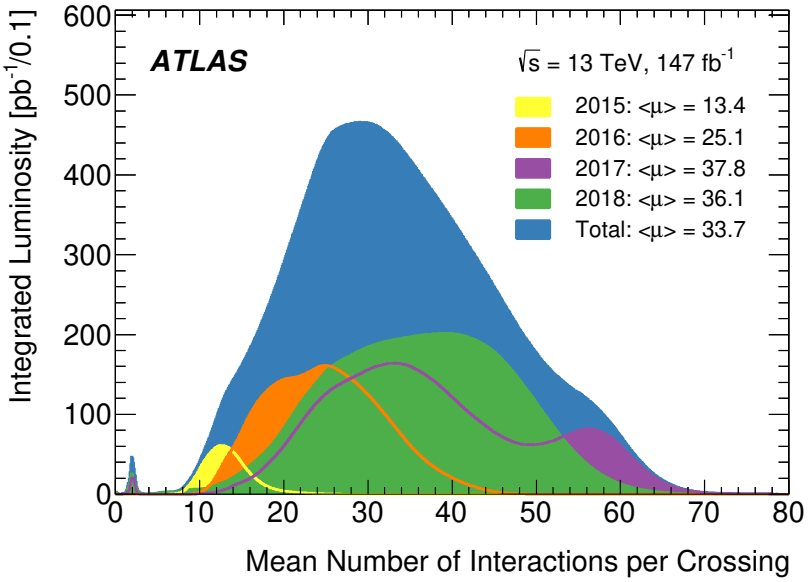

Figure 4.2: Luminosity-weighted distribution of the mean number of interactions per bunch crossing [94]. The distribution in 2015-2018 represents the blue histogram.

4.2.1 Hard-scatter Event Generation

In the Monte Carlo event generations, the hadron interactions are described with sub-divided calculation, such as the hard short-distance physics, the nonperturbative transition from partons ("hadronization"), and hadron decays. The differential cross-section with an initial state (a, b) and a final state (F) in the hard-scattering process for an observable O is written by Ref.[100],

$$\frac{d\sigma}{dO} = \sum_{a,b} \int_0^1 dx_a dx_b \sum_F \int d\Phi_F f_a^{h1}(x_a, \mu_F) f_b^{h2}(x_b, \mu_F) \frac{d\hat{\sigma}_{ab\to F}}{d\hat{O}} D_F(\hat{O} \to O, \mu_F), \tag{4.1}$$

where $h_{1,2}$ represent the colliding hadrons in the initial state a, b, respectively, and $d\Phi_F$ is the standard final-state phase-space differential. $f_{a,b}$ is the parton distribution function (PDF), $d\hat{\sigma}$ is the perturbatively calculable short-distance cross-section and D_F is a fragmentation function (FF). μ_F is an arbitrary energy scale to separate between long and short distance physics, i.e. emissions with energy scales above μ_F are included in the short-distance calculation (term relating $d\hat{\sigma}$) and emissions with energy scales below μ_F are included in the long-distance calculation (terms relating $f_{a,b}$ and D_F). Therefore, μ_F is referred to as a "factorization scale."

The PDF ($f_i^h(x_i, \mu_F)$) represents the probability where a parton i carry a fraction x_i of the parton's momentum at a hard interaction of the energy scale μ_F. The PDFs are obtained from the calculations using the results of collider physics experiments, deep-inelastic scattering measurements, and fixed-target Drell-Yan experiments as inputs. Several groups provide the sets of PDFs with different calculations and inputs. To estimate the uncertainty of PDF, we consider that it relates to the choice of PDF sets, as described in Section 9.4.

The partonic scattering cross-section $d\hat{\sigma}_{ab\to F}$ is calculable in perturbative QCD with fixed-order and written as,

$$d\hat{\sigma}_{ab\to F} = \frac{1}{2\hat{s}_{ab}} |\mathcal{M}_{ab\to F}|^2(\Phi; \mu_F, \mu_R), \tag{4.2}$$

where $|\mathcal{M}|^2$ represents the matrix element squared for the process and $\frac{1}{2\hat{s}_{ab}}$ is the parton flux factor. The matrix element (ME) is the sum of the transition amplitude with an initial state and a final state, regardless of intermediate states. μ_R is referred to as a "renormalization scale" and an unphysical term to get rid of UV divergence. The parton shower approximation, which corrects higher-order real-emission in the hard scattering, is applied. The fragmentation function is a universal function that describes the hadronic observable in the final state at the partonic level. They are used in the non-perturbative calculation and parameterized with the μ_F in the event generation.

4.2.2 SM Background Simulation

As introduced in Chapter 1, two particular experimental signatures in this thesis, large missing transverse energy ($E_{\mathrm{T}}^{\mathrm{miss}}$) and large-radius jets, are used. The background sources are vector bosons associated with jets, for example, V + jets, Tops, Multi-bosons production, and Higgs production. Since large $E_{\mathrm{T}}^{\mathrm{miss}}$ is required, the contribution of multi-jet events is negligible in this analysis. More detail is described in Appendix J.

The detail (including the generator setup) of the SM background samples is described in Appendix B.1.

V + jets $Z(\to \nu\nu)$ + jets process can have large $E_{\mathrm{T}}^{\mathrm{miss}}$ and jets from initial state radiation or final state radiation. $W \to e\nu$ ($\mu\nu$)+jets processes can be backgrounds when e or μ is not reconstructed. In $W \to \tau\nu$+jets process, leptonically decaying τ process is similar to $W \to e\nu(\mu\nu)$+jets processes. Hadronically decaying τ process remains since the hadronically decaying τ is reconstructed as a jet. γ + jets process is also considered because γ + jets events can be backgrounds when $E_{\mathrm{T}}^{\mathrm{miss}}$ is mis-measured.

Tops Leptonically decaying top quarks ($t \to bl\nu$) remain if lepton is not reconstructed, as same as W + jets. $t\bar{t}$, $t + W/Z$, tWZ, and $t\bar{t} + X$ ($X = t,\ t\bar{t},\ WW\cdots$) samples are considered.

Multi-bosons Diboson processes denoted as VV ($V = W,\ Z$), such as WW, WZ, ZZ, and triboson processes denoted as VVV, such as WWW, WWZ, WZZ, and ZZZ, are considered. Since one of the bosons decays leptonically, these processes remain. $V\gamma$ process is also considered.

Higgs Due to the large branching ratio of $h \to b\bar{b}$, Vh samples with leptonic decaying W/Z can remain.

4.2.3 Signal Simulation Samples

As introduced in Section 2.3.5, the $(\tilde{W}, \tilde{B})$, $(\tilde{H}, \tilde{B})$, $(\tilde{W}, \tilde{H})$, $(\tilde{H}, \tilde{W})$, $(\tilde{H}, \tilde{G})$, and $(\tilde{H}, \tilde{a})$ models are considered. However, it is difficult to create signal samples with all production, decay processes, and SUSY parameters to scan. Thus, benchmark signal samples are created and interpreted using normalized them, as summarized in Table 4.1.

4.2.3.1 SUSY signal generation

Seven benchmark signal samples, C1C1-WW, C1N2-WZ, C1N2-Wh, N2N3-ZZ, N2N3-Zh, N2N3-hh, and the $(\tilde{H}, \tilde{G})$ model with $\mathcal{B}(\tilde{\chi}_1^0 \to Z\tilde{G}) = 50\%$, are created. C1C1-WW, C1N2-WZ, and C1N2-Wh are assumed to be the $(\tilde{W}, \tilde{B})$-SIM. N2N3-ZZ, N2N3-Zh, and N2N3-hh are assumed to be $\tilde{H}$ pair production and only one decay process with ZZ, Zh, hh, respectively. These samples are called the "$(\tilde{H}, \tilde{B})$-SIM." Since $\tilde{G}$ has spin-3/2, unlike $\tilde{B}/\tilde{W}/\tilde{H}$, the $(\tilde{H}, \tilde{G})$ samples are generated separately.

The setup of MC samples is summarized in Appendix B.2. For the chargino-neutralino production mode, the cross-section of $\tilde{W}$ ($\tilde{H}$) is 4.76 (1.12) fb, assuming their masses are 800 GeV.

4.2.3.2 SUSY Signal Interpretation

For the simulations of general models, re-weighted samples of simplified models by the theoretical prediction values of the production cross-sections of $\tilde{\chi}_{\mathrm{heavy}}$ and the branching ratios are used. It is confirmed that the event kinematics do not depend on $\tilde{\chi}_{\mathrm{heavy}}$ and $\tilde{\chi}_{\mathrm{light}}$ in the phase space of this analysis using the generator-level samples.

Table 4.1: Summary of the production modes, final states, and the interpretations for the signal models targeted in the search.

Model	Production	Final states	MC samples used for interpretation
$(\tilde{W},\tilde{B})$	$\tilde{\chi}_1^\pm\tilde{\chi}_1^\mp$, $\tilde{\chi}_1^\pm\tilde{\chi}_2^0$	WW, WZ, Wh	C1C1-WW, C1N2-WZ, and C1N2-Wh
$(\tilde{H},\tilde{B})$	$\tilde{\chi}_1^\pm\tilde{\chi}_1^\mp$, $\tilde{\chi}_1^\pm\tilde{\chi}_2^0$, $\tilde{\chi}_1^\pm\tilde{\chi}_3^0$, $\tilde{\chi}_2^0\tilde{\chi}_3^0$	WW, WZ, Wh, ZZ, Zh, hh	C1C1-WW, C1N2-WZ, C1N2-Wh, N2N3-ZZ, N2N3-Zh, and N2N3-hh
$(\tilde{W},\tilde{H})$	$\tilde{\chi}_2^\pm\tilde{\chi}_2^\mp$, $\tilde{\chi}_2^\pm\tilde{\chi}_3^0$	WW, WZ, Wh, ZZ, Zh, hh	C1C1-WW, C1N2-WZ, C1N2-Wh, N2N3-ZZ, N2N3-Zh, and N2N3-hh
$(\tilde{H},\tilde{W})$	$\tilde{\chi}_2^\pm\tilde{\chi}_2^\mp$, $\tilde{\chi}_2^\pm\tilde{\chi}_2^0$, $\tilde{\chi}_2^\pm\tilde{\chi}_3^0$, $\tilde{\chi}_2^0\tilde{\chi}_3^0$	WW, WZ, Wh, ZZ, Zh, hh	C1C1-WW, C1N2-WZ, C1N2-Wh, N2N3-ZZ, N2N3-Zh, and N2N3-hh
$(\tilde{H},\tilde{G})$	$\tilde{\chi}_1^\pm\tilde{\chi}_1^\mp$, $\tilde{\chi}_1^\pm\tilde{\chi}_1^0$, $\tilde{\chi}_1^\pm\tilde{\chi}_2^0$, $\tilde{\chi}_1^0\tilde{\chi}_2^0$	ZZ, Zh, hh	$(\tilde{H},\tilde{G})$ with $\mathcal{B}(\tilde{\chi}_1^0 \to Z\tilde{G}) = 50\%$
$(\tilde{H},\tilde{a})$	$\tilde{\chi}_1^\pm\tilde{\chi}_1^\mp$, $\tilde{\chi}_1^\pm\tilde{\chi}_1^0$, $\tilde{\chi}_1^\pm\tilde{\chi}_2^0$, $\tilde{\chi}_1^0\tilde{\chi}_2^0$	ZZ, Zh, hh	N2N3-ZZ, N2N3-Zh, and N2N3-hh
$(\tilde{W},\tilde{B})$ simplified models: $(\tilde{W},\tilde{B})$-SIM			
C1C1-WW	$\tilde{\chi}_1^\pm\tilde{\chi}_1^\mp$	WW	C1C1-WW
C1N2-WZ	$\tilde{\chi}_1^\pm\tilde{\chi}_2^0$	WZ	C1N2-WZ
C1N2-Wh	$\tilde{\chi}_1^\pm\tilde{\chi}_2^0$	Wh	C1N2-Wh

$(\tilde{W},\tilde{B})$-SIM In the $(\tilde{W},\tilde{B})$-SIM model, the branching ratios are assumed to be 100%, and only one production mode is considered. Thus, the benchmark signal simulation samples are used directly, without re-weighting.

$(\tilde{W},\tilde{B})$ Considering the chargino pair production mode, C1C1-WW samples are used directly since only one decay process, $\tilde{\chi}_1^\pm\tilde{\chi}_1^\mp \to WW\tilde{\chi}_1^0\tilde{\chi}_1^0$, is allowed in this setup. On the other hand, in the chargino-neutralino production case, two decay processes via WZ or Wh boson pairs can be taken into account. Since the branching ratios of two decay processes are variable, the re-weighted samples of C1N2-WZ and C1N2-Wh to correspond to the assumed branching ratio with the constraint, $\mathcal{B}(\tilde{\chi}_2^0 \to Z\tilde{\chi}_1^0) = 1 - \mathcal{B}(\tilde{\chi}_2^0 \to h\tilde{\chi}_1^0)$, are used.

$(\tilde{H},\tilde{B})$ Four production modes ($\tilde{\chi}_1^\pm\,\tilde{\chi}_1^\mp$, $\tilde{\chi}_1^\pm\,\tilde{\chi}_2^0$, $\tilde{\chi}_1^\pm\,\tilde{\chi}_3^0$, $\tilde{\chi}_2^0\,\tilde{\chi}_3^0$) and corresponding decay process, i.e., six final states, as summarized in Table 4.1, are considered. Re-weighting C1C1-WW, C1N2-WZ, and C1N2-Wh samples to the production cross-section of higgsino are used as $\tilde{\chi}_1^\pm\,\tilde{\chi}_1^\mp$, $\tilde{\chi}_1^\pm\,\tilde{\chi}_2^0$, and $\tilde{\chi}_1^\pm\,\tilde{\chi}_3^0$ production samples. N2N3-ZZ, N2N3-Zh, and N2N3-hh samples are used without re-reweighting. However, the branching ratios are variable. In this analysis, it is assumed that $\mathcal{B}(\tilde{\chi}_2^0 \to Z\tilde{\chi}_1^0) = 1 - \mathcal{B}(\tilde{\chi}_2^0 \to h\tilde{\chi}_1^0) = 1 - \mathcal{B}(\tilde{\chi}_3^0 \to Z\tilde{\chi}_1^0) = \mathcal{B}(\tilde{\chi}_3^0 \to h\tilde{\chi}_1^0)$, and these re-weighted samples corresponding to the branching ratio are used.

$(\tilde{W},\tilde{H})$ and $(\tilde{H},\tilde{W})$ Like the $(\tilde{H},\tilde{B})$ model, signal samples of the simplified models are re-weighted to proper cross-sections. However, the branching ratio of $\tilde{\chi}_{\text{heavy}}$ depends on MSSM parameters, such as $M_2,\ \mu,\ \tan\beta$. Thus, the $(M_2,\ \mu,\ \tan\beta)$ is scanned over and is used the re-weighted samples corresponding

to the branching ratios. The branching ratios of $(\tilde{W}, \tilde{H})$ and $(\tilde{H}, \tilde{W})$ with different $(M_2,\ \mu,\ \tan\beta)$ are shown in Appendix C.

$(\tilde{H}, \tilde{G})$ In the $(\tilde{H}, \tilde{G})$ model, the higgsino-gravitino coupling is assumed to be small, and only two decay modes, $\tilde{\chi}_1^0 \to Z/h + \tilde{G}$, are considered. Since $\mathcal{B}(\tilde{\chi}_1^0 \to Z + \tilde{G})$ is variable, re-weighted $(\tilde{H}, \tilde{G})$ simulation samples corresponding to the assumed branching ratio are used.

$(\tilde{H}, \tilde{a})$ Like the $(\tilde{H}, \tilde{G})$ model, the higgsino-axino coupling is assumed to be small. Therefore, $\tilde{\chi}_1^\pm$ and $\tilde{\chi}_2^0$ decay into $\tilde{\chi}_1^0$, and then $\tilde{\chi}_1^0$ decays into $\tilde{a}$ with Z/h bosons. $(\tilde{H}, \tilde{B})$-SIM simulation samples are re-weighted to the total cross-section (= the sum of $\tilde{\chi}_1^\pm\ \tilde{\chi}_1^\mp$, $\tilde{\chi}_1^\pm\ \tilde{\chi}_1^0$, $\tilde{\chi}_1^\pm\ \tilde{\chi}_2^0$, $\tilde{\chi}_1^0\ \tilde{\chi}_2^0$) and the assumed branching ratio of $\mathcal{B}(\tilde{\chi}_1^0 \to Z + \tilde{a})$.

5 Physics Object Reconstruction

5.1 Overview

In order to reconstruct physics objects in the pp-collision events, tracks, vertices, and topo-clusters are reconstructed from raw detector information. They are mainly used as inputs of the reconstruction for electrons, photons, muons, jets, and missing transverse energy ($E_{\mathrm{T}}^{\mathrm{miss}}$). Additionally, tracks are used to improve the resolution of the jet mass and in the boson tagging technique described in Chapter 6.

In this thesis, the jets and $E_{\mathrm{T}}^{\mathrm{miss}}$ are used for the event selection to search for electroweakinos. Jets are primary objects and are categorized into three types; small-radius (small-R) jets, large-radius (large-R) jets, and track jets. Small-R jets and track jets are used for the definition of event selections to search for electroweakinos, described in Section 7.5. Large-R jets are used to tag the SM electroweak bosons, which are decayed from $\tilde{\chi}_{\mathrm{heavy}}$. Since $\tilde{\chi}_{\mathrm{light}}$ does not interact with the detector, $E_{\mathrm{T}}^{\mathrm{miss}}$ is an important signal to search for electroweakinos. Electrons, photons, muons, and small-R jets are used for the calculation of $E_{\mathrm{T}}^{\mathrm{miss}}$ and the validation of the background estimation (described in Chapter 8).

5.2 Tracks, Vertices, and Topo-clusters

In the pp-collision, inner detector tracks (or just "tracks" in the rest of the literature) are reconstructed to identify the passage of charged particles by connecting the ionization deposit in the inner detector. The outline of the track reconstruction algorithm is introduced. More detail is described in Ref.[101]. When charged particles pass through the Pixel and the silicon microstrip detector (SCT), “clusters” are formed from multiple adjacent Pixels. These clusters are combined to reconstruct “track candidates”. Then, “track score” with “holes” (inefficiency layer) in the detector, the χ^2 of track fit, and kinematic cuts are also used to solve the overlap and reduce the low-quality tracks. In order to solve the overlap furthermore and measure the momentum with a high resolution, the reconstructed track candidates are extrapolated to the transition radiation tracker (TRT). The momentum is calculated by fitting the helical trajectory bent by a magnetic field using hits in the TRT.

In the pp-collision, multiple interactions occur in the same, and neighboring bunch crossings are referred to as “pile-up.” Then, the vertex reconstruction is important to determine at which vertex particles are generated. Consequently, the track momentum resolution is improved by using the vertex position in the track fitting. Additionally, to suppress the impact by the pile-up, particles are required to be associated with vertices. Vertex is reconstructed using two finding algorithms described in Ref.[102]. The first one is to find vertex candidates using the high quality tracks selected by kinematic selections. The vertices are required to be associated with at least two tracks. The other one is to fit the reconstructed vertex position. Additionally, a primary vertex defined as the vertex of the event is selected by the largest $\sum p_{\mathrm{T}}^2$ of associated tracks.

Energy deposit in the calorimeter cells is clustered to reconstruct the original electromagnetic or hadronic showers, referred to as "clusters." The generic type of clusters ("topo-clusters") is reconstructed using the energy measurement information and the spatial profile [103], and the energy is in the electromagnetic scale. Topo-clusters are used to reject non-prompt leptons. The detail of the reconstruction algorithm is presented in Appendix D.1.

5.3 Jets

As described in Section 2.1, quarks and gluons are reconstructed as jets. The reconstruction of jets is based on the anti-k_t algorithm [104] to merge clusters or tracks using a specific choice of the radius parameter (R) defining the radial size of the jet, as described in Appendix D.2. The reconstruction algorithm is implemented in the FastJet package [105]. In this analysis, three types of jets differed by choice of R are employed, serving for own different purposes; namely large-R jets (denoted as J), small-R jets (denoted as j), and track jets as summarized in Table 5.1. In the reconstruction algorithms of large-R jets and small-R jets, "Local hadronic cell weighting (LCW)" (described in Appendix D.3) corrects the energy in the hadronic scale at the cluster level.

"Truth jets" in the MC samples are used and are denoted with the superscript "true." Truth jets are composed of stable particles from hard scatter with a lifetime greater than 10 ps, except for muons and neutrinos.

In this thesis, the targets are fully hadronic final states where SM electroweak bosons decay hadronically and are reconstructed as jets. Since there are many jets from QCD interactions in the pp-collisions, it is important to distinguish between the boson jets and the QCD jets (background jets) and reject pile-up jets.

5.3.1 Large-R Jet

When an SM electroweak boson with high p_{T} decays hadronically, the opening angle between the daughter quarks becomes small. This is characterized by the angular distance defined by $\Delta R = \sqrt{\Delta\eta^2 + \Delta\phi^2}$ where $\Delta\eta$ ($\Delta\phi$) is spatial distance in pseudo-rapidity (azmuthal angle). The distance between quarks is typically 0.4 for a W boson with $p_{\mathrm{T}} = 400$ GeV. While the most commonly used $R = 0.4$ jets, referred to as "small-R jets" (described in Section 5.3.2) in the document, have difficulty in reconstructing hadronically decaying SM electroweak bosons as a single jet or two separate jets with all decay products, large-radius jets have the advantage to reconstruct the two quarks as a single jet. $R = 1.0$ is chosen for this analysis referred to as "large-R jets." The large-R jet reconstruction method, including a pile-up mitigation technique, is described in this sub-section. The boson tagging technique to identify the SM electroweak bosons using large-R jets is introduced in Chapter 6. In this analysis, to search for electroweakinos, kinematic selections are applied to select the large-R jets originating from the SM electroweak bosons with high p_{T}. The selections are described in Section 5.6.

5.3.1.1 Trimming and Mass

The large-R jets after the anti-k_T algorithm clustering with $R = 1.0$ are referred to as "ungroomed jets." In order to remove the contribution from the underlying event and pile-up, "trimming" [106] is applied to the

Table 5.1: Overview of the three types of jets used in the analysis.

Object name	R parameter of the anti-k_T algorithm	Input	Usage
Small-R jets	0.4	tracks, topo-clusters	To derive $E_{\mathrm{T}}^{\mathrm{miss}}$ and an angular variable min $\Delta\phi(j, E_{\mathrm{T}}^{\mathrm{miss}})$ used in the event selection described in Section 7.3.
Large-R jets	1.0	topo-clusters	To identify boosted W/Z decaying into qq and to reconstruct the kinematics.
Track jets	Variable radius (0.02-0.4)	tracks	To count the b-hadron jet multiplicity inside a large-R jet.

ungroomed jets. Any sub-jets clustered by the k_t algorithm with $R = 0.2$ [104] are removed if the p_{T} is less than the 5% of that of the ungroomed large-R jet.

The performance of the trimming algorithm against the pile-up is discussed below using the jet mass as an observable. As discussed later in Chapter 6, the jet mass is one of the key variables to distinguish between the boson jets and background jets originating from quarks or gluons effectively. The calorimeter-based jet mass (m^{calo}) of a large-R jet is calculated from the topo-cluster energy and defined as:

$$m^{\mathrm{calo}} = \sqrt{\left(\sum_{i\in J} E_i\right)^2 - \left(\sum_{i\in J} \boldsymbol{p_i}\right)^2}, \tag{5.1}$$

where E_i ($\boldsymbol{p_i}$) is the energy (momentum) of i-th cluster. For sufficiently high Lorentz-boosted massive particles, the angular spread in the decay products is comparable with the granularity of the calorimeter cell segmentation. The mean uncalibrated jet mass value $\langle m^{\mathrm{jet}} \rangle = \langle m^{\mathrm{calo}} \rangle$ is shown in Figure 5.1. Good stability of large-R jets against the reconstructed primary vertex multiplicity (N_{PV}) is seen after the trimming, while ungroomed jet mass is strongly dependent.

From here on, how to improve the resolution of the jet mass is discussed. In order to avoid the limitation on the granularity of the calorimeter cell, information from the associated tracks are additionally employed. Track-assisted mass, m^{TA}, is defined as:

$$m^{\mathrm{TA}} = \frac{p_{\mathrm{T}}^{\mathrm{calo}}}{p_{\mathrm{T}}^{\mathrm{track}}} \times m^{\mathrm{track}}, \tag{5.2}$$

where $p_{\mathrm{T}}^{\mathrm{calo}}$ is a transverse momentum of a large-R jet calculated by calorimeter-cell cluster constituents, $p_{\mathrm{T}}^{\mathrm{track}}$ is a transverse momentum of the four-vector sum of tracks associated with the large-R jet, and m^{track} is an invariant mass of the four-vector sum of tracks, which the pion mass is assigned for each track. Since $p_{\mathrm{T}}^{\mathrm{track}}$ is calculated using only charged particles and $p_{\mathrm{T}}^{\mathrm{calo}}$ is calculated by charged and neutral particles, the ratio of $p_{\mathrm{T}}^{\mathrm{calo}}$ to $p_{\mathrm{T}}^{\mathrm{track}}$ is used to correct charged-to-neutral fluctuations and improve the jet mass resolution with respect to a track-only jet mass definition (m^{track}) as shown in Figure 5.2.

Figure 5.3 shows the resolution of jet mass response defined as the ratio of the reconstructed jet mass to the truth jet mass as a function of truth jet from W/Z bosons. Half of the 68% interquartile range (IQnR)[1] divided by the median are used to represent the resolution. Thanks to the spatial resolution of the constituents using the track information, the resolution of m^{TA} is better than m^{calo} in the high p_{T} region ($p_{\mathrm{T}} > 1$ TeV). However, since $p_{\mathrm{T}}^{\mathrm{track}}$ is only based on charged particles and m^{calo}, $p_{\mathrm{T}}^{\mathrm{calo}}$ are calculated by charged and neutral particles, the resolution of m^{calo} is better in the low p_{T} region.

[1] This is defined as the difference between the 16$^{\mathrm{th}}$ and 84$^{\mathrm{th}}$ percentiles of a given distribution.

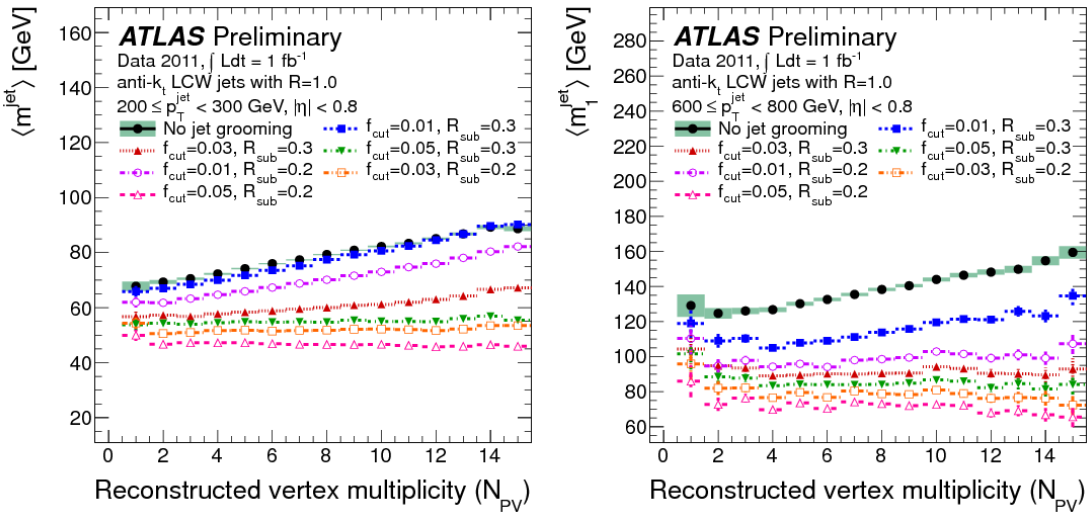

(a) 200 GeV < $p_{\mathrm{T}}^{\mathrm{jet}}$ < 300 GeV

(b) 600 GeV < $p_{\mathrm{T}}^{\mathrm{jet}}$ < 800 GeV

Figure 5.1: Performance of the jet grooming. The distribution of mean uncalibrated jet mass with a function of the reconstructed vertex multiplicity (N_{PV}) [107] in $t\bar{t}$ MC sample is shown. The black line represents the mean mass of large-R jets without trimming. The red line represents the default ATLAS option for the trimming parameters.

To exploit the merit of both m^{calo} and m^{TA}, a statistical combination of the masses are considered, referred to as "combined mass" (m^{comb}):

$$m^{\mathrm{comb}} = a \times m^{\mathrm{calo}} + b \times m^{\mathrm{TA}}, \tag{5.3}$$

$$a = \frac{\sigma_{\mathrm{calo}}^{-2}}{\sigma_{\mathrm{calo}}^{-2} + \sigma_{\mathrm{TA}}^{-2}}, \tag{5.4}$$

$$b = \frac{\sigma_{\mathrm{TA}}^{-2}}{\sigma_{\mathrm{calo}}^{-2} + \sigma_{\mathrm{TA}}^{-2}}, \tag{5.5}$$

where σ_{calo} (σ_{TA}) is the parametrized m^{calo} (m^{TA}) resolution obtained from the jet mass response distribution, using the central 68% inter-quantile range of the jet mass response distribution. As shown in Figure 5.3, m^{comb} outperfoms both m^{calo} and m^{TA} in the resolution across the p_{T} regions.

In this thesis, large-R jet mass refers to m^{comb}.

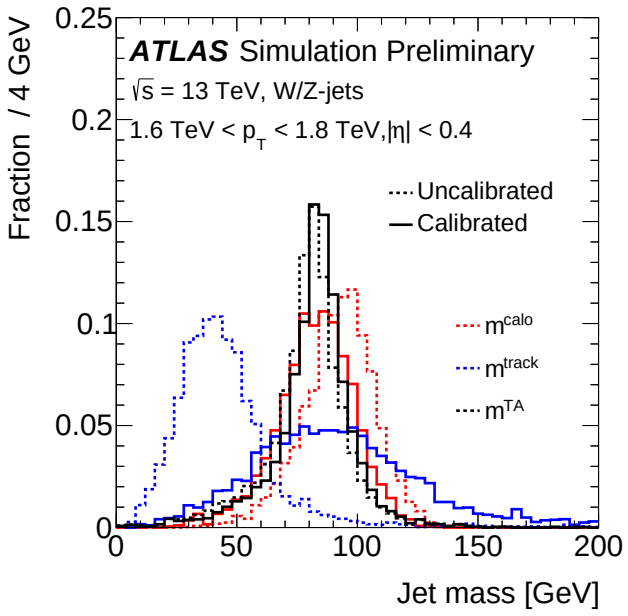

Figure 5.2: Mass distribution of uncalibrated (before jet mass calibration, represented as dashed line) and calibrated (after jet mass calibration, represented as solid line) jets originating from W/Z bosons [108]. The red line represents calorimeter-based jet mass (m^{calo}), the blue one represents track-assisted jet mass (m^{TA}) and the green represents the invariant mass of the four-vector sum of tracks associated with the large-R jet m^{track}.

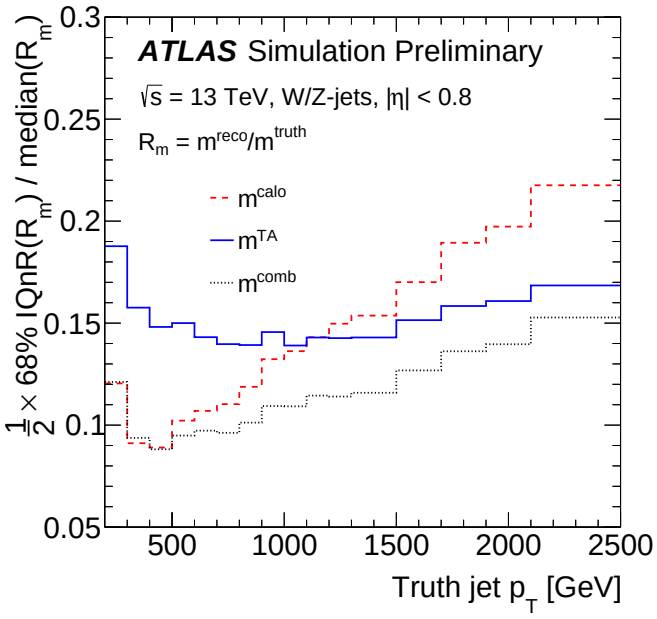

Figure 5.3: The resolution of the jet mass response as a function of truth jet p_{T} originating from W/Z bosons for calorimeter-based jet mass (red dashed line), track-assisted jet mass (blue solid line), and the combined jet mass (black dotted line) [109].

5.3.1.2 Energy and Mass Calibration

Since the calorimeter in the ATLAS detector is categorized into sampling calorimeters, only some of the energy is measured. Thus, the measured energy of jets needs to be scaled. The scale factor is called "jet energy scale" (JES), and the method to obtain the scale factor is called "scale calibration." The calibration is composed of two steps; one is an MC-based calibration to obtain the JES, and the other is "in-situ calibration" to correct the difference between the data and MC samples using a data-driven method. The jet mass needs to be corrected for residual bias between the data and MC samples to be applied while the jet is calibrated. Like the jet energy, the scale factor for the jet mass (JMS) is obtained by the MC-based calibration and in-situ calibration. In the in-situ calibration, the jet energy resolution (JER) and the jet mass resolution (JMR) are measured, and their differences between the data and MC samples are evaluated as the correction for the MC samples.

The workflow of large-R jet calibration, together with the reconstruction, is summarized in Figure 5.4.

MC-based Calibration At the MC-based calibration step, the JES for large-R jets is evaluated as a ratio of their energy to the truth jets. The average jet energy response of reconstructed jets to truth jets ($E_{\text{reco}}/E_{\text{truth}}$) is parametrized as the function of truth jet energy and η. After the JES correction based on MC simulation, a similar procedure applies to the JMS calibration using the jet mass response of reconstructed jets to the truth. The JMS is derived using the MC samples with the p_{T} fixed to the post-JES calibration values. The JMS is computed for m^{calo} and m^{TA} independently and depends on the jet p_{T}, mass, and η. The m^{comb} is derived using the same coefficients.

In-situ Calibration After the MC-based calibration, the difference in the jet energy between the data (reconstructed jets) and MC samples (truth jets) still remains. In order to reduce the residual difference, data-driven measurements are performed using samples of jets balanced with well-calibrated objects such as photons, leptons, and small-R jets [109]. Three processes, Z + jets, γ + jets, and multi-jets, are used depending on the p_{T} of target jets. In these processes, each p_{T} balance of jets with respect to well-calibrated reference objects or systems of the data and MC samples, such as Z bosons reconstructed by lepton decays, γ, and low-p_{T} jets system is measured. The reference in multi-jets events is $p_{\text{T}}^{\text{recoil}}$ obtained as the four-vector sum of calibrated small-R jets. To apply the calibration for the forward jets ($0.8 < |\eta| < 2.5$), we also measure the ratio of two jets using di-jet topology. In this measurement, one each jet in the central region ($|\eta| < 0.8$) and in the forward region ($0.8 \leq |\eta| \leq 2.5$) is required. We measure the momentum asymmetry:

$$\mathcal{A} = \frac{p_{\text{T}}^{\text{left}} - p_{\text{T}}^{\text{right}}}{p_{\text{T}}^{\text{avg}}}, \tag{5.6}$$

where "left" and "right" are denoted for simplicity; $p_{\text{T}}^{\text{avg}} = (p_{\text{T}}^{\text{left}} + p_{\text{T}}^{\text{right}})/2$. The calibration factor c for each jet is described as,

$$\mathcal{R} = \frac{c^{\text{left}}}{c^{\text{right}}} = \frac{2 + \langle \mathcal{A} \rangle}{2 - \langle \mathcal{A} \rangle} = \frac{p_{\text{T}}^{\text{left}}}{p_{\text{T}}^{\text{right}}}. \tag{5.7}$$

The final result of these measurements is shown in Figure 5.5. The difference between the data and MC samples is smaller than 3%, and the statistical uncertainty is dominant in $p_{\text{T}} \geq 1.5$ TeV.

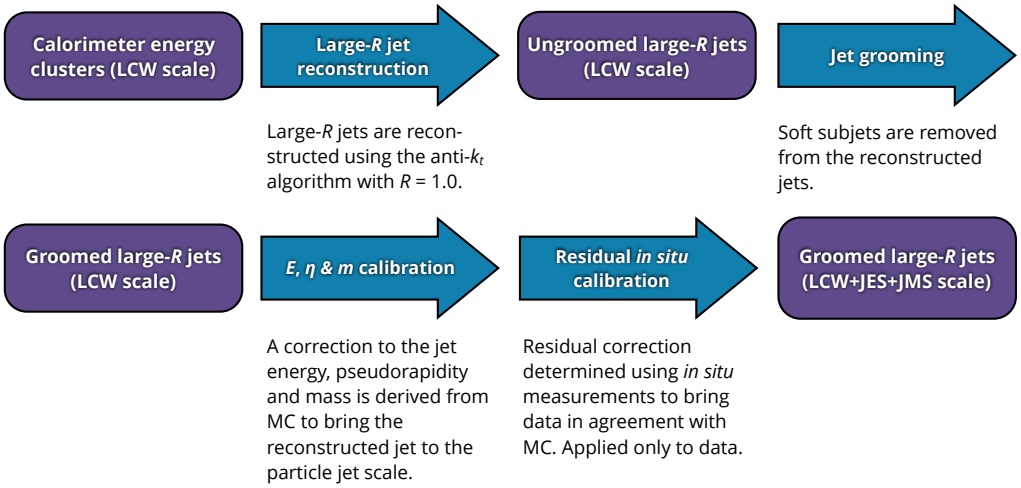

Figure 5.4: Summary of large-R jet reconstruction and calibration procedure [109].

m^{calo} and m^{track} are corrected by in-situ calibration after the MC-based calibration. The detailed procedure is described in Ref.[109]. For calibrating the jet mass scale, we measure the average calorimeter-to-tracker response defined as:

$$R^{m}_{\text{trk}} = \left\langle \frac{m^{\text{calo}}}{m^{\text{track}}} \right\rangle, \tag{5.8}$$

where m^{calo} is measured mass using topo-clusters of calorimeter cells and m^{track} is a track jet mass that matches the same jet. This method is called "R_{trk} method," done by di-jet events. The results are shown in Figure 5.6. In this study, three different generators and three different tracking variations for the default generator Pythia 8 are used to estimate systematic uncertainties. These systematic uncertainties are discussed in Section 9.1.

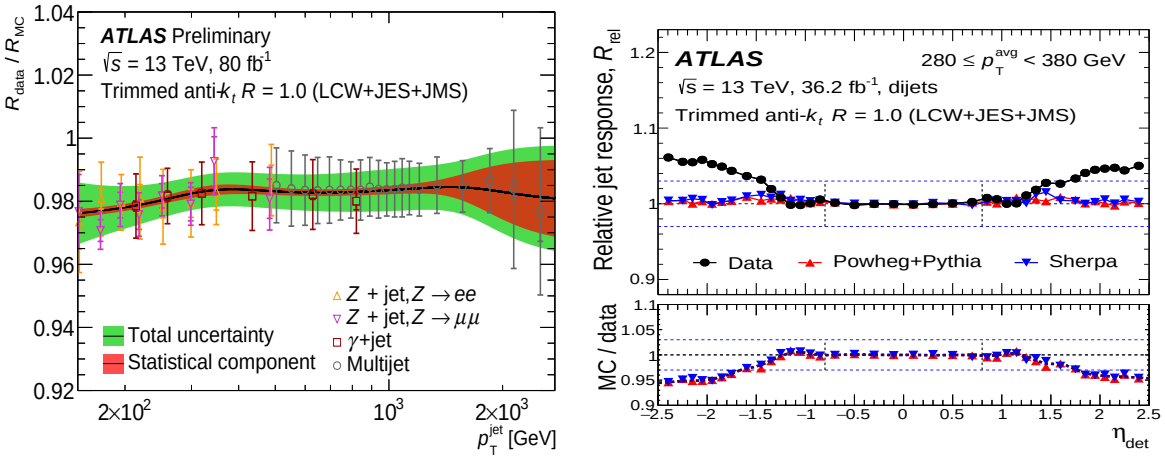

(a) in situ method for the central jets

(b) η inter-calibration

Figure 5.5: Large-R jets response by in-situ calibration. (a) The result is combined with three measurements using Z + jets (dielectron channel, upward-pointing triangles; and dimuon channel, downward-pointing triangles), γ + jets ((open squares), and multi-jets (open circles) events. The response defined as $R = \left\langle p_{\mathrm{T}}^{\mathrm{jet}} / p_{\mathrm{T}}^{\mathrm{reference}} \right\rangle$, where the bracket represents the average. The ratio of the response in the data to that in MC samples as a function of the jet p_{T} is shown. The correction factor shown in the black curve is derived by smoothing the measurements and is applied on the jet p_{T} in the data [110]. (b) Relative response of jets in the data (black circles) and MC samples (red and blue triangles with difference generators) as a function of η in the detector. The response of large-R jets with 280 GeV $\leq p_{\mathrm{T}} \leq$ 380 GeV is shown as an example. This figure shows the result with the data in 2015 and 2016. The lower panel shows the ratio of MC samples to the data. The dashed lines provide reference points for the viewer [109].

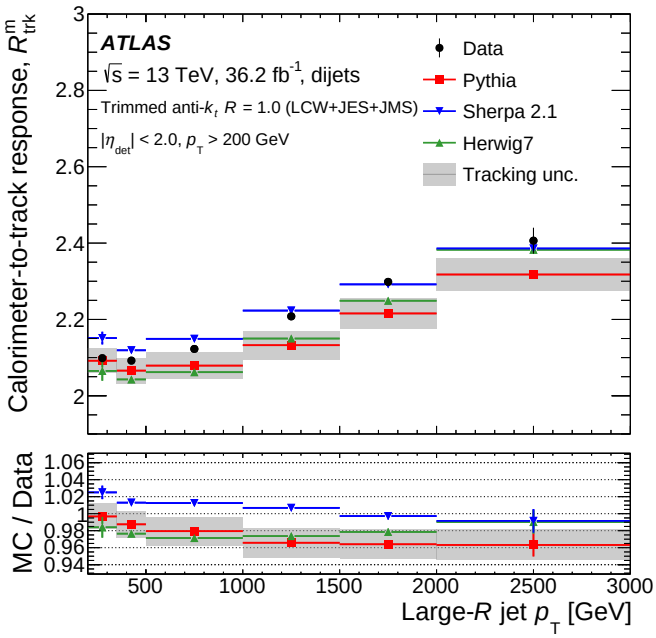

Figure 5.6: JMS in the $R_{textrmtrk}$ method as a function of the large-R jet p_{T}. Measurement of R^{m}_{trk} as a function of the large-R jet p_{T} with large-R jet $m/p_{\mathrm{T}} = 0.2$. Results using three different generators are shown. Tracking uncertainty for the default generator Pythia 8 is shown in a the gray band [109].

5.3.2 Small-*R* Jet

Small-*R* jets reconstructed by the topo-clusters using anti-k_t algorithm with R of 0.4 are used as the seed to construct the $E_{\mathrm{T}}^{\mathrm{miss}}$ (Section 5.7) and to construct a kinematic variable $\min \Delta\phi(j, E_{\mathrm{T}}^{\mathrm{miss}})$ used for background rejection in the event selection (Section 7.3). To improve the performance of the hadronic jet measurement, the particle flow algorithm, which represents individual particles as clusters ideally using tracks and determines the jet energy, is employed. The detail of the particle flow algorithm is described in Appendix D.4.

5.3.2.1 Small-*R* Jet Reconstruction

In the pp-collision, small-R jets can originate from the hard-scattering process as well as from pile-up. The small-R jets with $p_{\mathrm{T}} > 30$ GeV, $|\eta| < 2.8$ are used in this analysis. Due to the low p_{T} threshold, jet multiplicity depends on the pile-up effect. To reject jets containing contaminations from pile-up interactions, a multi-variable algorithm called "Jet Vertex Tagger (JVT)" using tracks originating in the hard-scatter primary vertex is employed for the jets with $p_{\mathrm{T}} < 60$ GeV, $|\eta| < 2.5$. The upper thresholds are determined by the followings:

- Most jets from pile-up have typically low p_{T} (< 60 GeV).
- There is no track in $|\eta| > 2.5$ because the Inner Detector is not placed.

The detail is described in Appendix D.5 and in Ref.[111, 112].

5.3.2.2 Energy Calibration for Small-*R* Jet

The energy calibration of small-R jets consists of largely similar steps as the large-R jets as described in Section 5.3.1.2: MC simulation-based calibration and the in-situ calibration. In the MC-based calibration, JES is obtained as the function of the average number of pile-up ($\langle\mu\rangle$) and the number of reconstructed PVs (N_{PV}) in addition to the p_{T} and η of the corresponding truth jet as done in the large-R jet case. This is due to subtracting the effect by the relatively severe contamination by pile-up jets. In order to reduce the difference of the flavor of jets, multiple correction factors are defined by the jet energy, the tracks in the Inner Detector, and the muon track in the Muon Spectrometer. The correction factors are obtained as the function of truth jet p_{T} and η. Finally, an in-situ calibration based on the measured kinematic balance of well-calibrated objects is applied. In this calibration, we use Z + jets, γ + jets, and multi-jets control samples. The detail of the calibration is presented in Ref.[113].

5.3.3 Track Jet

Track-based jets, referred to as track jets, are reconstructed from the inner detector tracks using the anti-k_T algorithm and used to count the number of b-quarks in large-R jets. It is important to identify b-tagged track jets for tagging large-R jets of $Z/h \to bb$. However, two b-quarks decayed from Z/h bosons with high p_{T} are collimated, and it is difficult to identify them separately. Then, the anti-k_T algorithm with a variable radius R parameter is employed. In this algorithm, R parameter for high p_{T} track jets is small. The reconstructed track jets are referred to as "Variable Radius (VR) track jets" [114].

5.3.3.1 Track Jet Reconstruction

The variable radius parameter is defined:

$$R = \frac{\rho}{p_{\mathrm{T}}}, \tag{5.9}$$

where ρ is set to be 30 GeV in this analysis. The minimum radius parameter is 0.02 and the maximum is 0.4 while p_{T} is smaller than 75 GeV or larger than 1500 GeV. The track jets with $p_{\mathrm{T}} \geq 20$ GeV and $|\eta| < 2.5$ are used in this analysis.

5.3.3.2 *b*-tagging

b-tagging is used to identify track jets from *b*-quarks. The *b*-tagging is based on the MV2 algorithm [115], which calculates a boosted decision tree (BDT) discriminant using *b*-jet likelihoods. The *b*-jet likelihoods are calculated by four algorithms individually; two complementary impact parameter-based algorithms, a secondary vertex tagging algorithm related to the lifetime of *b*-hadrons, and a topological multi-vertex algorithm related with the kinematics of *b*-hadron decaying. More details are presented in Appendix D.6. The algorithm is optimized for 85% *b*-tagging efficiency using training samples containing 10%(90%) *c*-(light-) flavor jets as background samples.

***b*-tagging Efficiency Measurement** The *b*-tagging efficiency is measured in $t\bar{t}$ control samples using the $t \to Wb \to lvb$ topology [116]. Additionally, the tagging performances on charm jets and light-flavor jets are measured [117, 118]. The difference between the data and MC samples on the tagging efficiency is calculated to obtain scale factors to correct the MC modeling.

5.4 Electrons and Photons

Electrons and photons are used to calculate $E_{\mathrm{T}}^{\mathrm{miss}}$ and validate a background estimation in this analysis, as described later in Chapter 8. In this section, the summary of the reconstruction, the identification, the isolation, and the calibration method is introduced. More details are described in Appendix D.7 and Ref.[119].

Electrons and photons are reconstructed using similar algorithms with topo-clusters in the EM calorimeter, tracks, and conversion vertices. "Superclusters" are reconstructed by combining them, and they are categorized into electrons and photons.

In order to identify electrons, hits in the Inner Detector, track p_{T}, and measured energy in the calorimeter are used. Additionally, shapes of the electromagnetic shower in the calorimeter, hadronic leakage, and spatial matching between the tracks and the clusters are used to distinguish promptly isolated electrons from hadronic jets, converted photons, and true electrons from heavy-flavor hadrons decay. In the identification algorithm, the likelihood is calculated by them. "Tight" and "Loose" [119] selections based on the likelihood discriminants are used in this analysis. In order to ensure a high selection purity, the significance for the transverse impact parameter, tracks associated with the primary vertex, the energy in the calorimeter, and p_{T} of tracks near electrons are used. In this analysis, "Tight" [119] selection is required as an isolation criteria. The energy calibration of electrons is performed in $Z \to ee$ control samples using a data-driven method with the m_{ee} distribution.

Similarly, to distinguish prompt isolated photons from hadronic jets, the variables of hadronic leakage, shower shape variables, and the energy measured in the first layer at the EM calorimeter are used. "Tight" [119] selection based on the likelihood discriminants is used in this analysis. In order to ensure a high selection purity, the significance for the transverse impact parameter, the energy in the calorimeter, and p_{T} of tracks near photons are used. In this analysis, "Tight" [119] selection is required as an isolation criteria. The correction factor for the photon energy is based on the factor of electrons, and an additional factor, which corrects the residual energy scale derived from the difference between electrons and photons, is extracted from the $m_{ll\gamma}$ distribution.

5.5 Muons

Muons are used to calculate $E_{\mathrm{T}}^{\mathrm{miss}}$ and validate a background estimation in this analysis, as described later in Chapter 8. In this section, the summary of the reconstruction, the identification, the isolation, and the calibration method is introduced. More details are described in Appendix D.8 and Ref.[120].

Muons are reconstructed from the Muon Spectrometer (MS) and the Inner Detector (ID) information using combined fit procedures for each track. In order to identify muons, "Medium" [120] criteria based on hits, measured charge and momenta in the ID and MS is used in this analysis. In order to distinguish between muons from the reconstructed primary vertex and ones from other sources, such as pile-up interactions, cosmic rays, and hadron decays, two selections are imposed: one is the spatial matching between muons and the reconstructed primary vertex, and the other is the isolation based on track p_{T} in the ID and the transverse energy in the calorimeter. In this analysis, "Tight" [120] isolation criteria is required in this analysis. The momentum calibration of muons is performed in $J/\psi \to \mu\mu$ and $Z \to \mu\mu$ control samples using a data-driven method with the $m_{\mu\mu}$ distributions. The correction factors of reconstructed muons by the ID and MS are estimated individually. n order to correct the energy loss in the calorimeter located between the ID and the MS, a p_{T} imbalance variable between the ID and MS is applied to the muons in the MS.

5.6 Object Selection

In this analysis, to search for electroweakinos, two sets of selection criteria, the "baseline" criteria and the "signal" criteria, for jets, electrons, photons, and muons are used. They are summarized in Table 5.2. The baseline criteria are composed of looser selections than the signal criteria. The baseline objects are used for $E_{\mathrm{T}}^{\mathrm{miss}}$ calculation and event cleaning, described in Appendix H. The overlap removal to resolve the ambiguity of duplicated objects in the reconstruction algorithm is also done with the baseline objects, as discussed below. The signal objects are used to ensure the high purity of selections. For example, signal criteria of electrons and muons, which are referred to as leptons, and photons are used for validation of the background estimation.

In the reconstruction procedure, these objects are reconstructed individually. Thus, a single particle may be reconstructed in two or more objects. The ambiguity of the duplicated objects needs to be resolved by the overlap removal. The algorithm of the overlap removal procedure is designed to find two different objects sharing tracks and clusters using spatial matching and discard one of them based on the desired priority. The detailed selections are described in Appendix D.9.

Table 5.2: Summary of definitions for electrons, muons, photons, and jets in the search for electroweakinos. d_0 is referred to as the transverse impact parameter and represents the shortest distance between a track and the measured beamline position in the transverse plane, and $\sigma(d_0)$ is the total uncertainty of track fit. $|z_0 \sin\theta|$ represents the shortest distance between the muon track and the primary vertex in a longitudinal projection. Objects with the baseline selections are used for the calculation of $E_{\mathrm{T}}^{\mathrm{miss}}$ in this thesis.

Property	Signal	Baseline
Large-*R* jets		
Radius parameter	$R = 1.0$	
Kinematic	$p_{\mathrm{T}} > 200$ GeV, $\lvert\eta\rvert < 2.0, m^{\mathrm{comb}} > 40$ GeV	
Small-*R* jets		
Radius parameter	$R = 0.4$	
Kinematic	$p_{\mathrm{T}} > 30$ GeV, $\lvert\eta\rvert < 2.8$	$p_{\mathrm{T}} > 30$ GeV, $\lvert\eta\rvert < 4.5$
Track *R* jets		
Radius parameter	Variable ($R = 0.02 - 0.4$)	
Kinematic	$p_{\mathrm{T}} > 20$ GeV, $\lvert\eta\rvert < 2.5$	
Electrons		
Kinematic	$p_{\mathrm{T}} > 6$ GeV, $\lvert\eta\rvert < 2.47$	$p_{\mathrm{T}} > 4.5$ GeV, $\lvert\eta\rvert < 2.47$
Identification	Tight [119]	Loose [119]
Isolation	Tight/HighPtCaloOnly (for $p_{\mathrm{T}} > /< 200$ GeV) [119]	not apply
Impact parameter	$\lvert d_0/\sigma(d_0)\rvert < 5, \lvert z_0 \sin\theta\rvert < 0.5$ mm	$\lvert z_0 \sin\theta\rvert < 0.5$ mm
Photons		
Kinematic	$p_{\mathrm{T}} > 150$ GeV, $\lvert\eta\rvert < 2.4$	$p_{\mathrm{T}} > 50$ GeV, $\lvert\eta\rvert < 2.4$
Identification	Tight [119]	
Isolation	FixedCutTight [119]	not apply
Muons		
Kinematic	$p_{\mathrm{T}} > 5$ GeV, $\lvert\eta\rvert < 2.7$	$p_{\mathrm{T}} > 3$ GeV, $\lvert\eta\rvert < 2.7$
Identification	Medium [120]	
Isolation	Tight [120]	not apply
Impact parameter	$\lvert d_0/\sigma(d_0)\rvert < 3, \lvert z_0 \sin\theta\rvert < 0.5$ mm	$\lvert z_0 \sin\theta\rvert < 0.5$ mm

5.7 Missing Transverse Energy

Particles that do not interact with the detector ("invisible"), such as neutrinos, cause a momentum imbalance, particularly in the transverse direction with respect to the beam axis due to the conservation of the transverse momentum of the system. Thus, a large imbalance of transverse momentum can be used as the proxy to the presence and the momentum of the invisible particles. The transverse momentum imbalance is referred to as "missing transverse momentum" ($\boldsymbol{p}_{\mathrm{T}}^{\mathrm{miss}}$), with its magnitude being known as "missing transverse energy" ($E_{\mathrm{T}}^{\mathrm{miss}}$). Since the LSP does not interact with the detector, the target signal has a large $E_{\mathrm{T}}^{\mathrm{miss}}$.

Missing transverse momentum is reconstructed as the negative vector sum of the transverse momentum of all the visible particles through a "hard term" and a "soft term." The hard term is calculated from the selected muons, electrons, photons, and small-R jets in the baseline criteria, as discussed in Section 5.6. The soft term is calculated based on the tracks that do not match muons, electrons, photons, and small-R

jets, and pass a set of quality criteria to ensure being well-reconstructed and being oriented from the hard-collision primary vertex.

Another type of $E_{\mathrm{T}}^{\mathrm{miss}}$ in this analysis calculated from the transverse momentum imbalance from the sum of tracks, referred to as track MET ("$E_{T,\mathrm{track}}^{\mathrm{miss}}$"). $E_{T,\mathrm{track}}^{\mathrm{miss}}$is calculated in a similar way of $E_{\mathrm{T}}^{\mathrm{miss}}$ calculation, except that it does not include the photon contribution.

6 Boson Tagging

"Boson tagging" technique [121, 122] has been developed to identify two-body hadronic decays of the SM electroweak boson, such as $W \to qq$, $Z \to qq/bb$, and $h \to bb$ where q denotes u, d, s, c. When highly boosted bosons decay into two quarks, these quarks are collimated and the distance between them is approximated as $dR(q,q) \sim 2m_V/p_{\mathrm{T}V}$ using the boson mass (m_V) and transverse momentum ($p_{\mathrm{T}V}$), as shown in Figure 6.1. The fraction that the distance between the daughter quarks of W (Z) in the (η, ϕ) plane is less than 1.0 is 90% (84%) with $p_{\mathrm{T}}(W/Z) = 200$ GeV. With $p_{\mathrm{T}}(W/Z) \geq 300$ GeV, both fraction is larger than 99%. The difference between W and Z boson mass causes a slight difference in their fraction.

This section introduces the boson tagging technique for $W/Z \to qq$ signals and $Z/h \to bb$ signals. First, boson tagging for $W/Z \to qq$ signals is introduced. The optimization of the boson tagging is described in Section 6.1.2. The efficiency of the optimized boson tagging is measured in the data using $t\bar{t}$, multi-jets, and γ + jets control samples, and the difference from the simulation is studied in Sections 6.1.3, and 6.1.4. Finally, the other boson tagging for $Z/h \to bb$ signals is introduced in Section 6.2.

6.1 Boosted W/Z Tagging

6.1.1 Overview

As shown in Figure 1.2, the W/Z boson jets have 2-prongness, and the quark- or gluon-initiated jets have 1-prongness. Then, an important difference in substructure within jets originating from W/Z bosons and quarks/gluons is the prongness of jets. To describe the prongness, the energy correlation ratios [10, 123, 124], the splitting scale [125], and the subjettiness [126, 127] which represent the relative positions and momenta of jet constituents, the clustering history, the substructure templates of the constituents by fit, respectively, are studied [128]. In this thesis, the energy correlation ratio is used for the boson tagging. The other variables representing the jet mass and the number of charged particles are also found to be important because the W/Z boson jets have a peak in the jet mass distribution, and W/Z bosons are color-singlet.

The three variables described below are used to identify jets originating from hadronic decaying bosons. One is the combined mass of large-R jets introduced in Section 5.3.1.1. As shown in Figure 6.2(a), there is a peak near the W boson mass in the jet mass distribution originating from W bosons (light gray and light blue). Other jets are distributed like the tail from the low mass region. Their labeling represents the flavor of jets requiring spatial matching between truth particles and reconstructed jets (called "jet truth labeling " as described in Appendix E). In this chapter, the jets originating from W/Z bosons and labeled as W/Z are called "signal jets." The other jets are called "background jets."

The second is D_2^{β}, which is a key of a jet substructure variable to separate the hadronic decays of W/Z bosons from massive QCD jets. To describe the prongness of jets, one-, two- and three-point energy

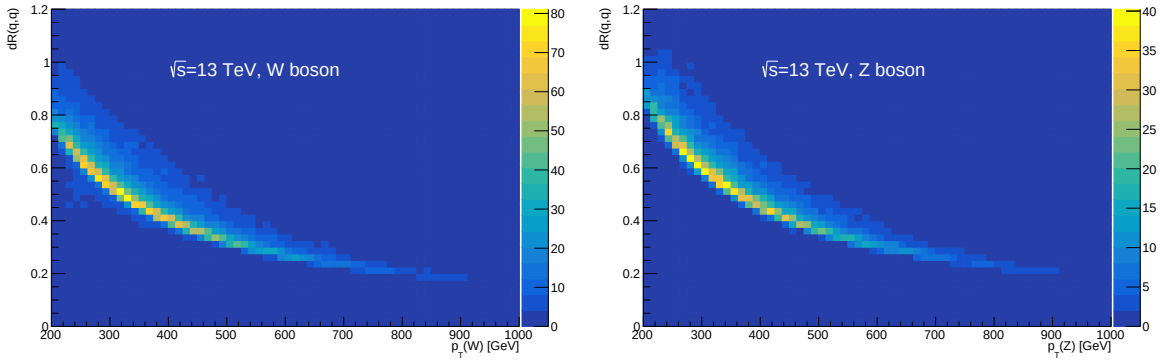

(a) W boson (b) Z boson

Figure 6.1: The correlation of distance between daughter quarks from W/Z boson and transverse momentum of W/Z boson ($p_{\mathrm{T}}(W/Z)$). The distance is approximated as a function of p_{T}, $dR(q,q) \sim \frac{2m_V}{p_{\mathrm{T}}(V)}$.

correlation functions (N-point correlation functions denoted as ECF(N, β)) are used. Their definitions are,

$$\mathrm{ECF}(1,\beta) = \sum_{i\in J} p_{\mathrm{T}i}, \tag{6.1}$$

$$\mathrm{ECF}(2,\beta) = \sum_{i<j\in J} p_{\mathrm{T}i}p_{\mathrm{T}j}\left(\Delta R_{ij}\right)^{\beta}, \tag{6.2}$$

$$\mathrm{ECF}(3,\beta) = \sum_{i<j<k\in J} p_{\mathrm{T}i}p_{\mathrm{T}j}p_{\mathrm{T}k}\left(\Delta R_{ij}\Delta R_{ik}\Delta R_{jk}\right)^{\beta}, \tag{6.3}$$

where $p_{\mathrm{T}i}$ is the transverse momentum of the cluster i, J is the large-R jet, and ΔR_{ij} is the Euclidean distance between i and j in the rapidity-azimuth angle plane, $R_{ij}^2 = (y_i - y_j)^2 + (\phi_i - \phi_j)^2$. For infrared and collinear (IRC) safety, all $\beta > 0$. D_2^{β} is defined using ECF(N, β),

$$D_2^{\beta} = \frac{\mathrm{ECF}(3,\beta)\left(\mathrm{ECF}(1,\beta)\right)^3}{\left(\mathrm{ECF}(2,\beta)\right)^2}. \tag{6.4}$$

In this analysis, $\beta = 1$ is employed and D_2 represents $D_2^{(\beta=1)}$. As shown in Figure 6.2(b), jets originating from W/Z bosons have a small D_2 value, while quark- or gluon-initiated jets have large D_2.

The last one is the multiplicity of tracks inside the jet (n_{trk}). The tracks that ghost-associate [129] with an ungroomed jet and have larger p_{T} than 500 MeV are used. The distribution of n_{trk} is shown in Figure 6.2(c). As shown in Figure 6.3, W/Z bosons are color-singlet and the particle multiplicity is nearly independent of p_{T}. In contrast to W/Z bosons, the multiplicity of quark- or gluon-initiated jets increases to the jet p_{T}. Thus, the upper cut is effective for high p_{T} jets.

However, n_{trk} value depends on the kinematics of charged particles alone (for example $\pi^{\pm}$), not including neutral particles (for example π^0). Therefore, n_{trk} is not an IRC safe variable, and the n_{trk} distribution in simulation is greatly influenced by hadronization effects such as soft emissions and arbitrary collinear parton splittings. The data/MC discrepancy in Figure 6.2(c) is caused by mis-modeling of low energy scale QCD dynamics. The discrepancies of jet substructure variables can cause an efficiency difference between

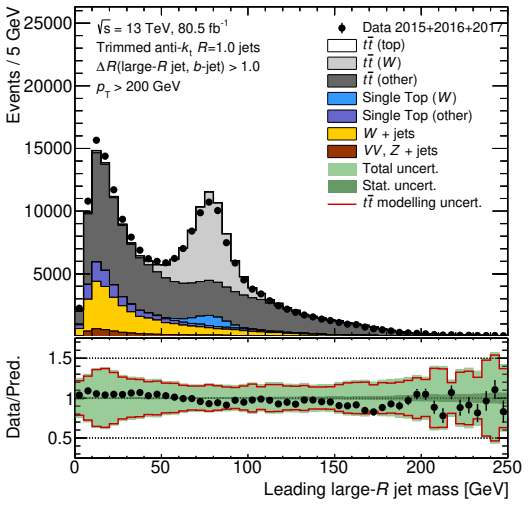

(a) m^{comb}

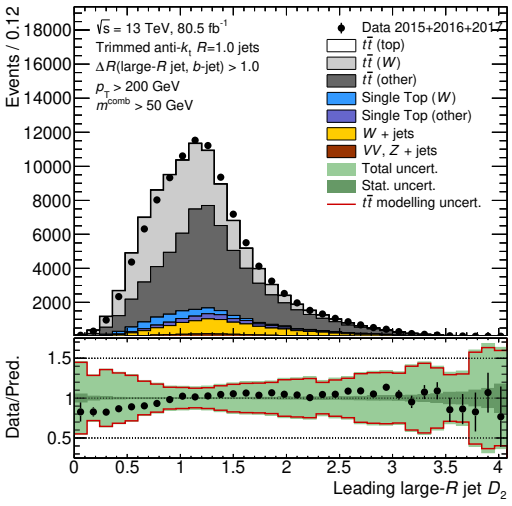

(b) D_2

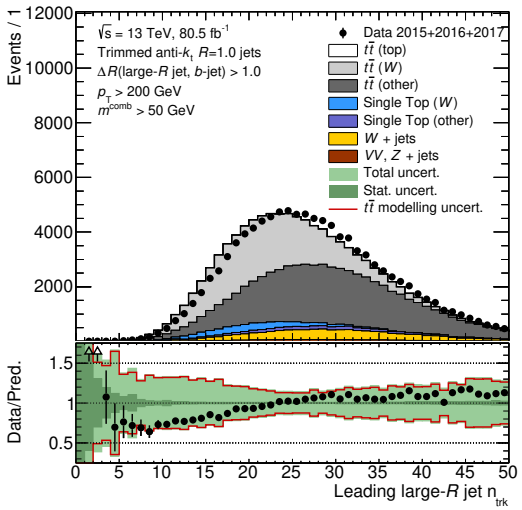

(c) n_{trk}

Figure 6.2: Distributions of jet substructure variables in the W-enhanced regions (described in Section 6.1.3.1). Light gray and light blue represent jets labeled as W bosons. (a) The combined mass distribution of large-R jets from W boson has a peak near about the W boson mass. The discrepancies of D_2 (b) and n_{trk} (c) are seen after a mass selection (> 50 GeV).

the data and MC. We correct the efficiency difference separately for each flavor of jets. How the correction is obtained is discussed in Sections 6.1.3, and 6.1.4.

6.1.2 Optimization

It is important to maintain high efficiency for the signal jets and achieve a high rejection against the background jets by the boson tagging. The selections of $W/Z \to qq$ jets are composed of the selections on

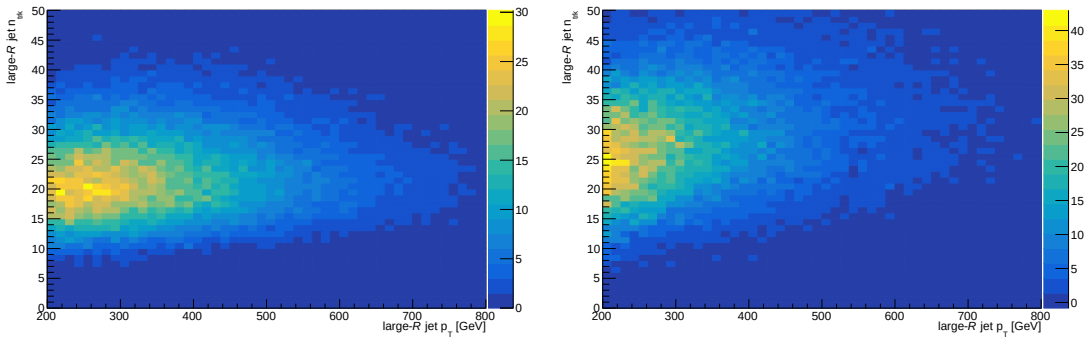

(a) W boson jets

(b) quark- or gluon-initiated jets

Figure 6.3: n_{trk} dependency on the jet p_{T} originating from W bosons decayed from electroweakinos (a) and quarks/gluons in $Z(\rightarrow \nu\nu)$ + jets MC samples (b).

the three variables as described in the following functions:

- $f_{m,\text{low}} < m < f_{m,\text{high}}$,
- $D_2 < f_{D2}$,
- $n_{\text{trk}} \leq f_{n_{\text{trk}}}$,

where the cut thresholds for the jet mass, f_m, for D_2, f_{D2}, are parameterized as a function of jet p_{T} as:

- $f_m(p_{\text{T}}) = \sqrt{\left(\frac{a_m^0}{p_{\text{T}}} + a_m^1\right)^2 + (a_m^2 p_{\text{T}} + a_m^3)^2}$,
- $f_{D2}(p_{\text{T}}) = b_{D2}^0 + b_{D2}^1 p_{\text{T}} + b_{D2}^2 p_{\text{T}}^2 + b_{D2}^3 p_{\text{T}}^3$.

The n_{trk} selections are kept constant to the jet p_{T}. A "working point" is defined as a combination of these functions with the parameters, a_m^i, b_{D2}^j, and $f_{n_{\text{trk}}}$. To optimize the boson tagging working point for this analysis, these parameters are determined in the following procedures:

- prepare some working points each of which should satisfy
  - efficiency for $W/Z \rightarrow qq$ is 45, 50, 55, 60, 65, 70, 75%, respectively and is flat with respect to jet p_{T}.
  - the largest $S/\sqrt{B}$ of candidate solutions that satisfy the above efficiency requirements, where S is the number of jets originating from W/Z bosons of the benchmark SUSY signals, and B is the number of jets in $Z(\rightarrow \nu\nu)$ + jets events (the dominant backgrounds in this analysis, discussed in Section 7.5) applying the preselection (defined in Table 7.1), the boson tagging requirements, and a scalar sum of $E_{\text{T}}^{\text{miss}}$, p_{T} of leading and sub-leading large-R jets is larger than 1000 GeV, which are similar selections with the main analysis signal regions to search for electroweakinos.
- select one of the working points that minimize p-value, defined as:

$$B\left(\frac{1}{b\sigma^2};\ s+b,\ 1+\sigma^{-2}\right) = \frac{\int_0^{\frac{1}{b\sigma^2}} u^{s+b-1}(1-u)^{\sigma^{-2}}}{B(s+b,\ 1+\sigma^{-2})},$$

where s, b, and σ represent the expected signal yields of $\tilde{\chi}_1^{\pm}\tilde{\chi}_2^0 \rightarrow WZ\tilde{\chi}_1^0\tilde{\chi}_1^0 \rightarrow qqqq\tilde{\chi}_1^0\tilde{\chi}_1^0$ with $m(\tilde{W}) = 900$ GeV, $m(\tilde{B}) = 100$ GeV, the expected background yields, and 30% background uncertainty, respectively, $B(x;\ a,\ b)$ is the normalized incomplete beta function, and $B(a,\ b)$ is the beta function. In this step, kinematic selections to search for electroweakinos are optimized simultaneously. This is because that some backgrounds which pass the boson tagging selections can be rejected by requiring hard kinematic selections using $E_{\mathrm{T}}^{\mathrm{miss}}$ and the jet p_{T}. Thus, it is more important to include kinematic selections of this search in optimization than to optimize only the background rejection and signal efficiency of the boson tagging. Thus, the background rejection

The most optimized working point for this analysis has a 50% signal boson tagging efficiency, and the final kinematic selection is described in Section 7.5. The W and Z tagging are optimized to use different parameters due to the difference in the boson masses. The obtained parameters are summarized in Table 6.1 and the selection functions are illustrated in Figure 6.4.

The performance of the optimized boson tagging working point is shown in Figure 6.5. A signal efficiency is defined as a fraction of large-R jets matching with W/Z bosons that pass the boson tagging to all the matched jets. It can be seen that the signal efficiency is about 50%. The background rejection is defined as the inverse of the efficiency measured by large-R jets in $Z(\rightarrow \nu\nu)$ + jets MC samples. In the high p_{T} region, n_{trk} selections are effective, resulting in a more significant background rejection.

6.1.3 Efficiency for Signal Jets

The signal efficiency is measured using hadronic decaying W bosons in semi-leptonic $t\bar{t}$ events. This measurement is independent of the SUSY analysis because the measurement region and the analysis region of the search for electroweakinos are not overlapped. The data sample in 2015-2017, not including 2018, is used. The difference between the data periods is small enough with respect to the statistical uncertainty of the data in this analysis[1].

For the signal efficiency measurement in the data, the large-R jet mass distribution is used as a template, and the template in the data is fitted with the MC template to minimize the χ^2. In this fit, shape variations are not included. The observed difference between the data and MC samples is used for correcting the boson tagging efficiency. However, this method is limited to the jet p_{T} range. To extend to a higher p_{T} range, the other MC-based study to measure the efficiency in the high p_{T} region is conducted using $W(\rightarrow qq)$+jets samples. It is difficult to define a Z boson enriched region because no phase space includes the $Z \rightarrow qq$ process with high purity. Since it can be well expected that there will be no significant difference in jet substructure variables between W and Z bosons except for jet mass, the study to extrapolate from the W tagging efficiency correction to the Z tagging is conducted using MC samples.

6.1.3.1 Event Selection for the Measurement Region

"W boson enriched region" is defined by requiring a single-muon trigger [130], an event cleaning (details are described in Appendix H.1), one muon, electron veto, and kinematic selections. These selections are illustarted in Figure 6.6. In this topology, $E_{\mathrm{T}}^{\mathrm{miss}}$ is due to neutrino from leptonic decaying top quark. Additionally, at least one large-R jet from hadronic decaying W boson, one b-tagged track jet from hadronic

[1] The difference in the efficiency for signal jets between 2015-2016 and 2017 is typically less than 5% in both the data and MC samples. The ratio as data/MC is consistent within the statistical error.

Table 6.1: Summary of coefficients of the smooth W and Z tagging threshold functions, as well as the upper cut limit of n_{trk} ($f_{n_{\text{trk}}}$).

	$a^0_{m,\text{low}}$	$a^1_{m,\text{low}}$	$a^2_{m,\text{low}}$	$a^3_{m,\text{low}}$
W_{qq}-tagging	-11.7489	63.4351	-23.9185	69.2862
Z_{qq}-tagging	-14.4222	72.5877	-27.5481	78.7757
	$a^0_{m,\text{high}}$	$a^1_{m,\text{high}}$	$a^2_{m,\text{high}}$	$a^3_{m,\text{high}}$
W_{qq}-tagging	15.9377	-29.087	4.92512	89.4082
Z_{qq}-tagging	6.22596	8.27925	7.5106	97.6893
	b^0_{D2}	b^1_{D2}	b^2_{D2}	b^3_{D2}
W_{qq}-tagging	0.824747	1.55628	-0.770576	0.177142
Z_{qq}-tagging	0.730715	1.75931	-1.01457	0.246442
	$f_{n_{\text{trk}}}$			
W_{qq}-tagging	32			
Z_{qq}-tagging	34			

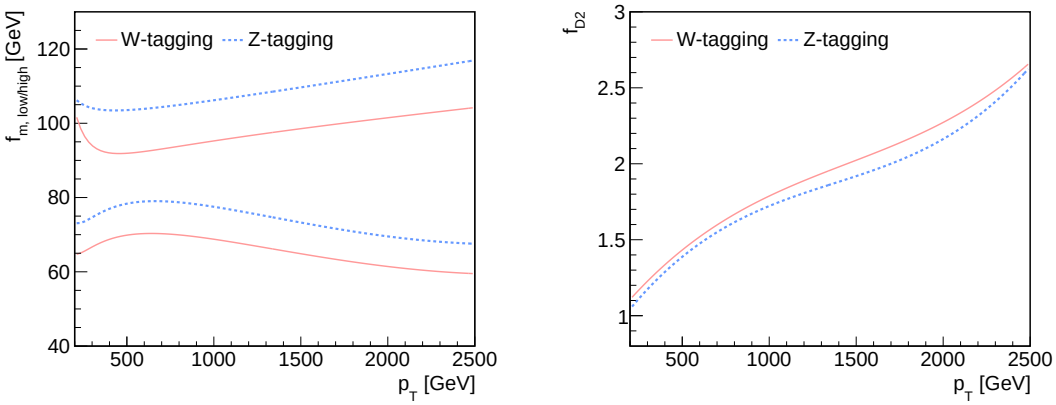

(a) $f_{m,\text{low/high}}$ (b) f_{D2}

Figure 6.4: The illustration of the mass and D_2 cut values for the W/Z-tagging as a function of p_{T}.

decaying top quark, and one small-R jet from leptonic decaying top quark are required. The requirement of the distance between large-R jet and b-tagged track jet ($\Delta R(J, b\text{-tagged track jet}) > 1.0$) is used to reject large-R jets containing b quark. Mass, D_2 and n_{trk} distributions of selected jets in the W boson enriched region are shown in Figure 6.2. $t\bar{t}$ events account for 75% in the W boson enriched region, and the jets labeled as $W \to qq$ account for 28% of $t\bar{t}$ events in the MC. With simple jet mass requirements $\in$ [50 GeV, 110 GeV], the jets labeled as $W \to qq$ in $t\bar{t}$ and single-top events account for 50%.

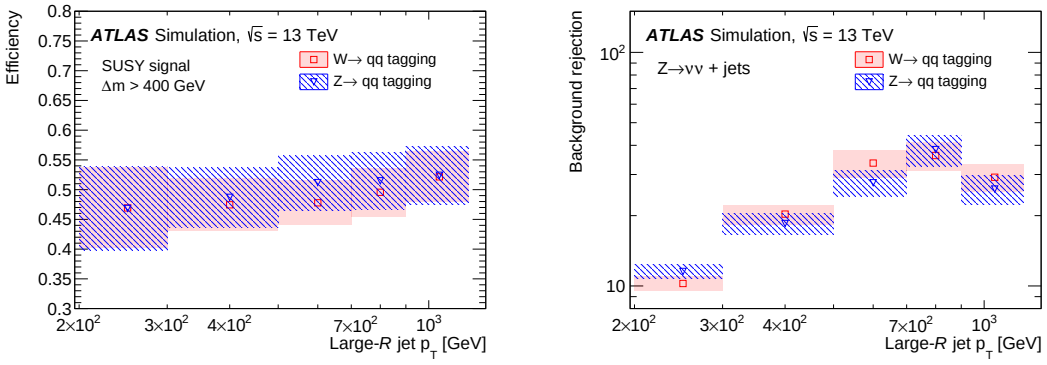

(a) signal efficiency (b) background rejection

Figure 6.5: Performance of the W/Z tagging. (a) Signal efficiency and (b) background rejection factor of the W (red) and Z tagging (blue) [49]. A sample of large-R jets labeled as W/Z bosons in the $(\tilde{W}, \tilde{B})$ signal events is used for the efficiency calculation. For the rejection, a sample of large-R jets in the $Z(\rightarrow \nu\nu)$ + jets MC sample is used for the estimation. The uncertainty is represented by the hashed bands, which include the MC statistical uncertainty and the systematic uncertainties discussed in Section 9.2.

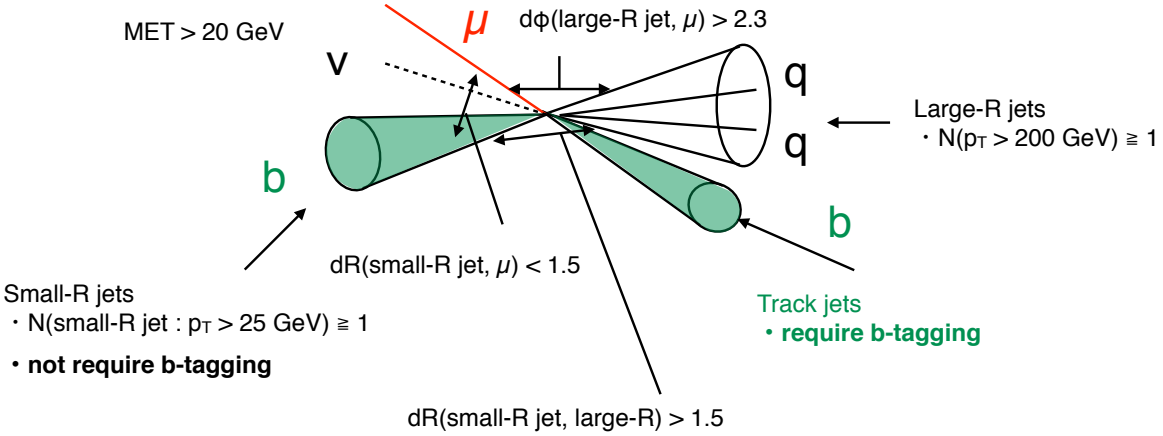

Figure 6.6: Selections to define the W boson enriched region in semi-leptonic $t\bar{t}$ topology. ν is measured as $E_{\mathrm{T}}^{\mathrm{miss}}$. W bosons are reconstructed by combining μ and ν. The small-R jet near the reconstructed W boson is not required b-tagging because W bosons are used in tW events. To identify large-R jets originating from W bosons, a b-tagged track jet is required to be outside large-R jets.

6.1.3.2 Efficiency measurement

The signal efficiency in MC samples is calculated as :

$$\epsilon_{\mathrm{MC}}(p_{\mathrm{T}}) = \frac{N_{\mathrm{signal}}^{\mathrm{tagged}}}{N_{\mathrm{signal}}^{\mathrm{tagged}} + N_{\mathrm{signal}}^{\mathrm{not\ tagged}}}, \tag{6.5}$$

where $N_{\mathrm{signal}}^{\mathrm{tagged}}$ and $N_{\mathrm{signal}}^{\mathrm{not\ tagged}}$ are the numbers of events containing "signal jets", which pass ("tagged") or fail ("not tagged") the tagger requirements, respectively. The signal efficiency is calculated in each p_{T}

bin of large-R jets, [200, 250, 300, 350, 600] GeV . The efficiency in the region where p_{T} is greater than 600 GeV no longer derived using the method due to the insufficient data statistics.

The signal efficiency for the data sample is measured as :

$$\epsilon_{\mathrm{data}}(p_{\mathrm{T}}) \quad = \quad \frac{N^{\mathrm{tagged}}_{\mathrm{fitted\ signal}}}{N^{\mathrm{tagged}}_{\mathrm{fitted\ signal}} + N^{\mathrm{not\ tagged}}_{\mathrm{fitted\ signal}}}, \tag{6.6}$$

where $N^{\mathrm{tagged}}_{\mathrm{fitted\ signal}}$ and $N^{\mathrm{not\ tagged}}_{\mathrm{fitted\ signal}}$ are the estimated numbers of signal jets which pass (tagged) or fail (not tagged) the tagging, respectively. The estimation method is described below.

The large-R jet mass distributions (templates) are made separately for

- $t\bar{t}$ signal : jets of $t\bar{t}$ and single-top samples labeled as W,
- background : jets of $t\bar{t}$ and single-top samples not labeled as W or other background samples.

These templates are fitted simultaneously to minimize χ^2 in each p_{T} bin and the normalization factors for tagged and not tagged signals, and backgrounds. Consequently, $N^{\mathrm{tagged}}_{\mathrm{fitted\ signal}}$ and $N^{\mathrm{not\ tagged}}_{\mathrm{fitted\ signal}}$ are obtained. Figure 6.7 shows examples of the jet mass distribution before/after fitting. Other distributions are shown in Appendix F.

6.1.3.3 Results of Efficiency Measurement and Systematic uncertainties

The results of the signal efficiency measurement are shown in Figure 6.8. The signal efficiency of the MC sample is almost constant. However, it turns out that the data/MC is weakly dependent on jet p_{T}.

As shown in Figure 6.8, the difference in the efficiency between the data and MC sample is large. To correct the difference, a signal efficiency scale factor (SF) is defined as;

$$\mathrm{SF}(p_{\mathrm{T}}) \quad = \quad \frac{\epsilon_{\mathrm{data}}(p_{\mathrm{T}})}{\epsilon_{\mathrm{MC}}(p_{\mathrm{T}})}. \tag{6.7}$$

In this thesis, the jets failing the boson tagging are used for a background estimation discussed in Chapter 8. To conserve the sum of the efficiency and inefficiency to 1, an inefficiency SF is defined as;

$$\mathrm{SF}_{\mathrm{ineff}}(p_{\mathrm{T}}) \quad = \quad \frac{1 - \epsilon_{\mathrm{MC}}(p_{\mathrm{T}}) \times \mathrm{SF}(p_{\mathrm{T}})}{1 - \epsilon_{\mathrm{MC}}(p_{\mathrm{T}})}. \tag{6.8}$$

The systematic uncertainties in the efficiency measurement are evaluated for the following systematic sources;

- $t\bar{t}$ modeling: Uncertainties calculated as the difference between nominal (Powheg+Pythia 8 [95, 131–134]) and alternative samples. The uncertainty from the choice of parton shower algorithm is estimated by the difference between nominal and Powheg +Herwig [135, 136] samples. To estimate the matching of next-to-leading-order (NLO) matrix-elements and parton shower, nominal, and MadGraph5_aMC@NLO [137] generated samples with shower modeling of Pythia 8 used. For QCD radiation uncertainty estimation, a different parameter to control the p_{T} of the first additional emission beyond the leading-order Feynman diagram in the parton shower and regulate the high-p_{T} emission against which the $t\bar{t}$ system recoils [134].

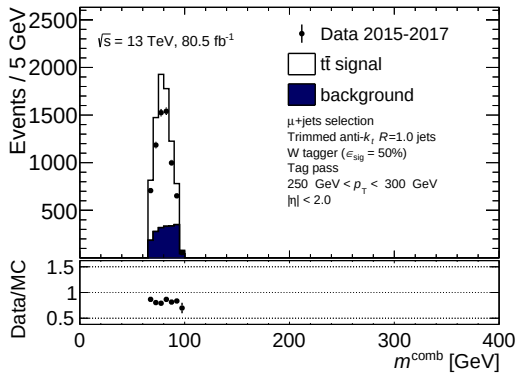

(a) m^{comb} in W-tag pass region before fitting

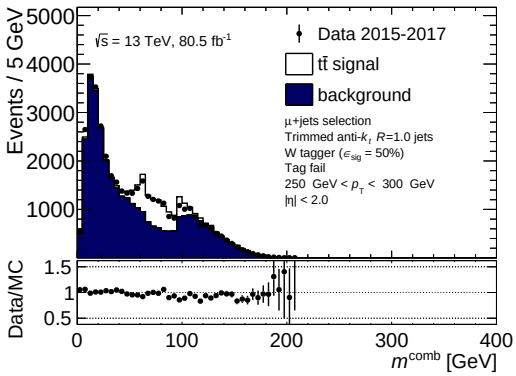

(b) m^{comb} in W-tag fail region before fitting

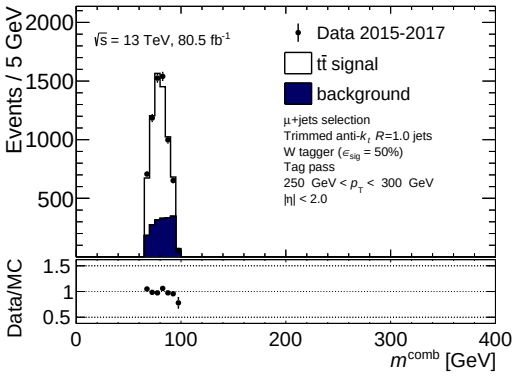

(c) m^{comb} in W-tag pass region after fitting

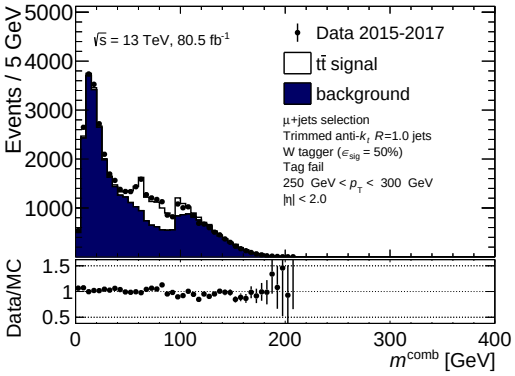

(d) m^{comb} in W-tag fail region after fitting

Figure 6.7: (a)(b) Pre-fit or (c)(d) post-fit distribution of m^{comb} in the (250 GeV $< p_{\text{T}} <$ 300 GeV) bin. The regions passing ((a)(c)) or failing ((b)(d)) are shown.

- Theory: Uncertainties on $t\bar{t}$, single-top and W+jets cross-sections.
- Large-R jet: Uncertainties on the large-R jet energy scale (JES) and resolution (JER).
- b-tagging: Uncertainties of the b-tagging efficiency measurement.
- Other experimental sources: A relative luminosity measurement uncertainty, detector response to muons, $E_{\text{T}}^{\text{miss}}$, and small-$R$ jets are considered.

Each systematic uncertainty is evaluated as a difference in the SF using each template of nominal and alternative MC samples. Large-R jet uncertainties correlate with uncertainties of final results in the statistical analysis to search for electroweakinos. The η dependencies for large-R jets are corrected by the calibration described in Section 5.3.1.2, and the uncertainties are included in the large-R jet uncertainties. b-tagging uncertainties and other experimental uncertainties do not correlate since their effect is small, and these uncertainties are assigned conservatively. The dependency between 10 and 40 in the average number of interactions per bunch crossing is smaller than 4% in the MC and data efficiency measurements. The ratios of the data to MC are consistent within the statistical uncertainty. Since the pile-up dependencies are small enough to be ignored to the statistical uncertainty of the analysis, no additional uncertainty is assigned.

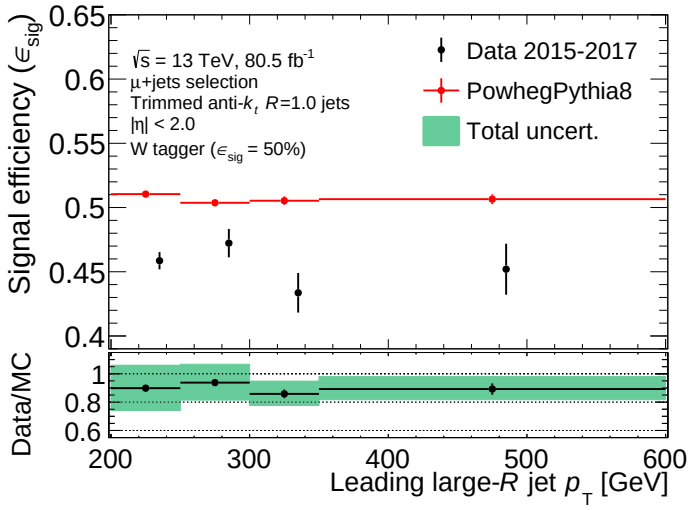

Figure 6.8: Measured efficiency of W_{qq}-tagging. $\epsilon_{\mathrm{MC}}(p_{\mathrm{T}})$ (red) and $\epsilon_{\mathrm{data}}(p_{\mathrm{T}})$ (black) in each p_{T} bin. The values are almost constant within statistical errors.

The systematic uncertainties are summarized in Table 6.2. The statistical uncertainty due to the limited data sample size is substantially small compared with the total uncertainty. The total systematic uncertainty is dominated by $t\bar{t}$ modeling uncertainties that arise from parton shower modeling. As shown in Figure 6.9(a), there is a small difference in the mass distribution of jets labeled as W bosons in $t\bar{t}$ samples, between different MC for jets with 250 GeV $\leq p_{\mathrm{T}} \leq$ 300 GeV (other distributions in different p_{T} range are shown in Appendix G). However, D_2 and n_{trk} have a large difference among different MCs, as shown in Figure 6.9(b), and Figure 6.9(c). These differences between MC samples lead to large $t\bar{t}$ modeling uncertainty, parton shower variation sample has a large contribution. In contrast, it has good agreement with the data distributions as shown in Figure 6.10. For the QCD radiation sample, the data/MC value is small. Since the efficiency is measured, the agreement of the distribution is important, not the normalization. Thus, the modeling uncertainty derived from the QCD radiation is small. Since jet substructure variables are not modeled well, the differences in the efficiency SF are symmetrized and assigned as uncertainties.

In order to estimate the uncertainty on the SF derived from the choice of the p_{T} binning in the measurement, the uncertainty is evaluated as the difference between the original and alternative binning, [200, 275, 350, 425, 600] GeV . A linear function is used to fit the SF to reduce the effect of the difference at the binning boundary. As shown in Figure 6.11, the difference in SF (ΔSF) between the two binnings is less than 1% and small enough to be compared to the statistical uncertainty ($\sim$ 10%). The smoothed signal efficiency SF estimated from the original p_{T} binning is applied to large-R jets, and the absolute value of ΔSF is assigned as the systematic uncertainty.

Table 6.2: Summary of systematic uncertainties of signal efficiency SF. Each uncertainty group shows the uncertainty by adding in quadrature.

Systematics Group	W tagger p_{T} bins [GeV]			
	[200,250]	[250,300]	[300,350]	[350,600]
$t\bar{t}$ modelling	0.16	0.13	0.10	0.04
Theory	< 0.01	< 0.01	< 0.01	< 0.01
Large-R jet	< 0.01	< 0.01	< 0.01	< 0.01
b-tagging	< 0.01	< 0.01	< 0.01	< 0.01
Other Experiment	< 0.01	< 0.01	< 0.01	< 0.01
Statistical	0.01	0.02	0.03	0.04

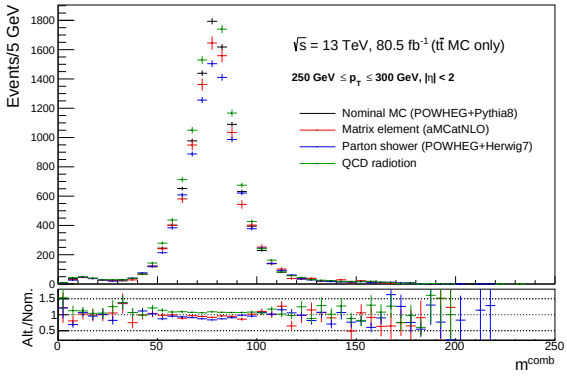

(a) m^{comb}

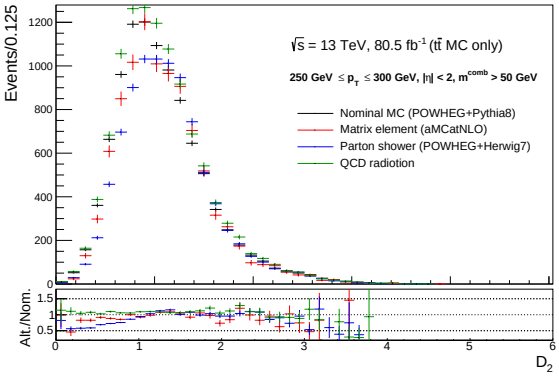

(b) D_2

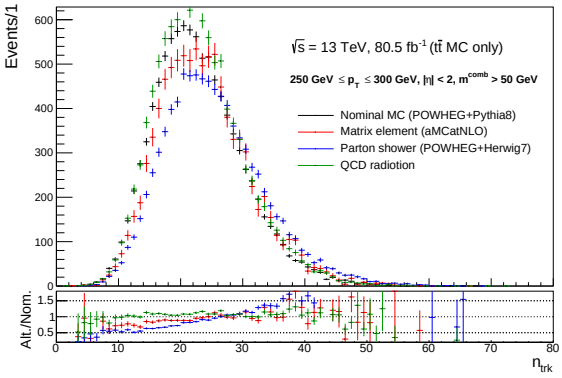

(c) n_{trk}

Figure 6.9: Distributions of m^{comb} (a), D_2 (b) and n_{trk} (c) in $t\bar{t}$ MC samples (250 GeV < p_{T} < 300 GeV). Nominal MC represents black line. Alternative MCs for the variation of matrix elements (red), parton shower (blue), and QCD radiation (green) are shown.

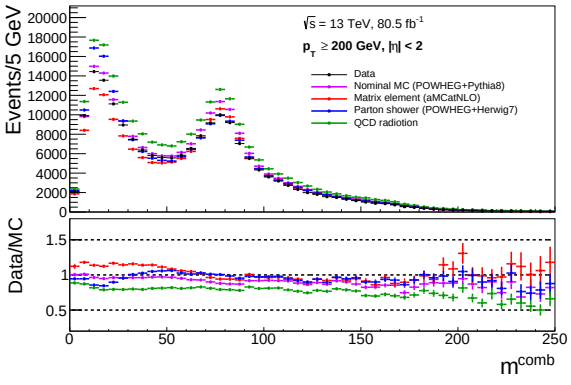

(a) m^{comb}

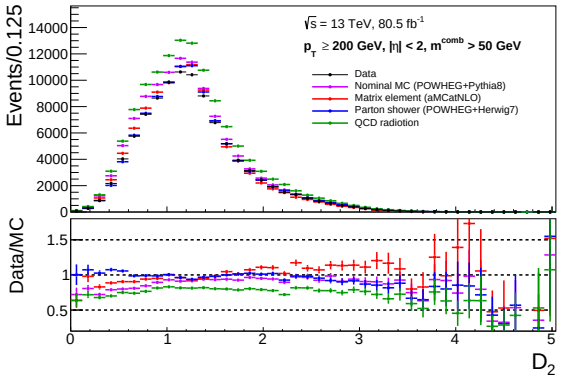

(b) D_2

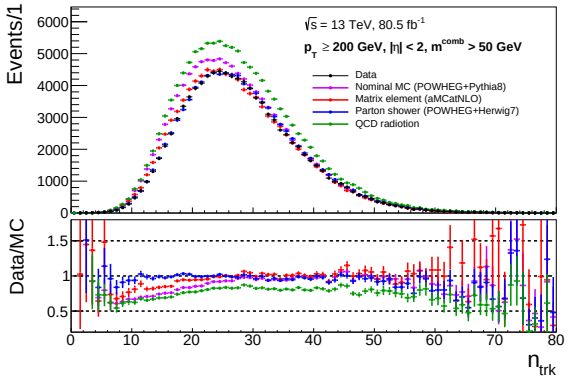

(c) n_{trk}

Figure 6.10: Distributions of m^{comb} (a), D_2 (b), and n_{trk} (c) in data and MC samples. The black line represents data samples. Except for the black line, each color represents MC expected distributions with different $t\bar{t}$ MC samples (other samples are common). Each line represents nominal MC sample (violet), alternative MCs for the variation of matrix elements (red), parton shower (blue), and QCD radiation (green) are shown.

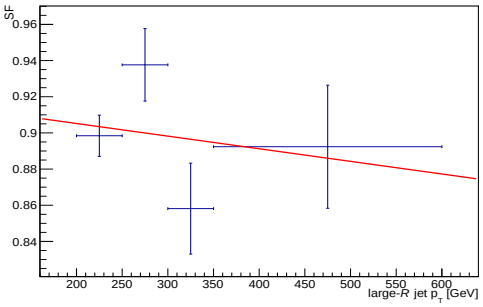

(a) SFs with original p_{T} binning

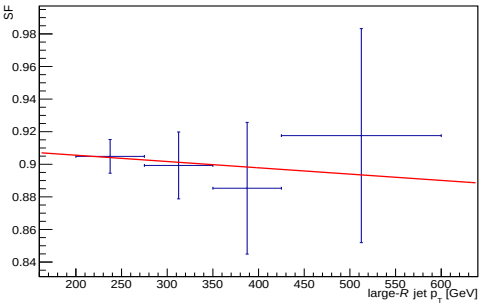

(b) SFs with alternative p_{T} binning

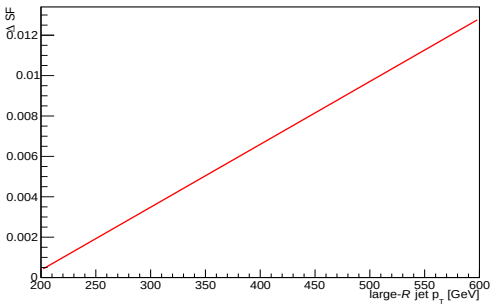

(c) Absolute value of ΔSF

Figure 6.11: The efficiency SFs are estimated in the original binning (a) and the alternative binning (b). The error bar represents the statistical error. The difference between the two options (c) is assigned as a systematic uncertainty.

6.1.3.4 High p_{T} Extrapolation

As discussed in Section 6.1.3.2, a p_{T} range where the signal efficiency SF can be used is up to 600 GeV due to requiring the separation between b-quark and W boson, such as $dR(b\text{-jet},\ J) > 1.0$. However, large-$R$ jets with higher p_{T} than 600 GeV are used in the main analysis, for example, such high p_{T} jet account for 30% in the $(\tilde{W}, \tilde{B})$-SIM with $m(\tilde{\chi}_{\mathrm{heavy}}) = 900$ GeV, $m(\tilde{\chi}_{\mathrm{light}}) = 100$ GeV.

If there are sufficient statistics in the data at high p_{T}, the SF can be defined as:

$$\mathrm{SF}(p_{\mathrm{T}}) = R(p_{\mathrm{T}}) \times \mathrm{SF}(p_{\mathrm{T}}^{\mathrm{ref}}), \tag{6.9}$$

$$R(p_{\mathrm{T}}) = \frac{\epsilon^{\mathrm{Data}}(p_{\mathrm{T}})/\epsilon^{\mathrm{Data}}(p_{\mathrm{T}}^{\mathrm{ref}})}{\epsilon^{\mathrm{MC}}(p_{\mathrm{T}})/\epsilon^{\mathrm{MC}}(p_{\mathrm{T}}^{\mathrm{ref}})}, \tag{6.10}$$

where $p_{\mathrm{T}}^{\mathrm{ref}}$ is the highest p_{T} (= 600 GeV) of the measurement in the semi-leptonic $t\bar{t}$ topology. However, the high purity region of W bosons in high p_{T} region cannot be defined. Therefore, an approximation where the SF value in $p_{\mathrm{T}} > 600$ GeV is the same as the one at $p_{\mathrm{T}} = 600$ GeV, i.e. $R(p_{\mathrm{T}}) = 1$, is introduced, and then, an additional uncertainty on this assumption for the $W \to qq$ tagging is assigned. This uncertainty is evaluated as the deviation of $R(p_{\mathrm{T}})$ from unity using different hadronic shower schemes and ATLAS detector geometry in the GEANT 4 simulation. This study measures the double ratio of $R(p_{\mathrm{T}})$ with nominal MC and alternative MC samples. In order to evaluate the systematic uncertainty, W + jets MC samples containing $W \to qq$ are used, and the calculation is performed in each jet p_{T} bin, [600, 700, 1000, 3000] GeV . The double ratio is evaluated as $a\log(p_{\mathrm{T}})^b$ where a and b are free parameters. The function parameters of systematic uncertainties are summarized in Table 6.3. The impact of each systematic variation is not large. The total uncertainty of high p_{T} extrapolation is assigned as a quadruple sum of all systematic variations and approximately 5%. The uncertainty has a small effect on the main analysis because the statistical error is sufficiently larger than high p_{T} extrapolation uncertainty, described in Section 9.5.

Table 6.3: The fitted paramters of systemtic uncertainty for high p_{T} extrapolation uncertainty. Systematic variations are assigned as the difference between nominal MC and alternative MC.

	Systematic variations	parameters of $a\log(p_{\mathrm{T}})^b$ a	b
Hadronic shower scheme	Hadron-nucleus diffraction model	8.56×10^{-10}	8.39
	Quark gluon string model	$1.08 \times 10^{+1}$	−3.31
	Re-scattering model of the final state	7.76×10^{-6}	3.95
	Inelastic hadron-nucleus cross-sections	4.22×10^{-3}	0.67
	Transportation of neutrons more accurately	5.96×10^{-2}	−0.82
Distorted ATLAS geometry	Additional material between LAr and Tile	$2.17 \times 10^{+6}$	−9.62
	Pre-LAr distorted geometry	$5.99 \times 10^{+5}$	−9.31
	Additional material in the ID specific regions	$9.01 \times 10^{+7}$	−11.96
	5% more material in the ID	2.09×10^{-2}	−0.09

6.1.3.5 W-to-Z Extrapolation

The correction for the Z tagging can not be estimated because it is difficult to define a Z boson enriched region. Then, it is assumed that there is no significant difference in the efficiency SF between the W and Z tagging. Thus, the signal efficiency SF of the Z tagging is assumed to be equal to the W tagging. However, the uncertainty derived from the assumption is needed. It is called "W-to-Z extrapolation uncertainty."

W-to-Z extrapolation uncertainty is estimated in a similar way to evaluate high p_{T} extrapolation uncertainty. The systematic uncertainty is defined as the double ratio with the generator and process differences between $W(\rightarrow qq)$+jets and $Z(\rightarrow qq)$+jets. The double ratio definition is :

$$R^{\mathrm{model}}(p_{\mathrm{T}}) = \frac{\epsilon^{Herwig++}_{Z+\mathrm{jets}}(p_{\mathrm{T}})/\epsilon^{\mathrm{SHERPA}}_{Z+\mathrm{jets}}(p_{\mathrm{T}})}{\epsilon^{Herwig++}_{W+\mathrm{jets}}(p_{\mathrm{T}})/\epsilon^{\mathrm{SHERPA}}_{W+\mathrm{jets}}(p_{\mathrm{T}})}, \tag{6.11}$$

$$\Delta R^{\mathrm{model}}(p_{\mathrm{T}}) = R^{\mathrm{model}}(p_{\mathrm{T}}) - 1. \tag{6.12}$$

$\Delta R^{\mathrm{model}}(p_{\mathrm{T}})$ has a small dependency on p_{T} because the cut values for each boson tagging are optimized to reduce the dependency of performance on p_{T}. The $\Delta R^{\mathrm{model}}(p_{\mathrm{T}})$ is $\sim 4.4\%$, and it is assigned as the uncertainty without the dependency on p_{T}.

6.1.4 Efficiency for Background Jets

6.1.4.1 Event Selection for the Measurement Regions

Like the signal efficiency measurement, the background jet efficiency is measured in γ + jets and multi-jets samples. The γ + jets sample is used in the low p_{T} region ($p_{\mathrm{T}} \leq 500$ GeV) and multi-jets sample is used in the high p_{T} region (500 GeV $\leq p_{\mathrm{T}} \leq$ 3000 GeV). To define "γ + jets enhanced region," the events collected by a single-photon trigger [138] are used, and at least one photon and one large-R jet are required. For "multi-jets enhanced region," the events collected by a single-jet trigger are used, and at least two large-R jets and a lepton veto are required. One of the large-R jets is required to have $p_{\mathrm{T}} > 500$ GeV.

The distributions of jet substructure variables in each region are shown in Figures 6.12, and Figure 6.13 in the γ + jets and multi-jets enhanced regions, respectively. In the multi-jet enhanced region, multi-jet events account for more than 99%. In the γ + jets enhanced region, γ + jets events also account for more than 98%. m^{comb} and D_2 distributions of Pythia 8 [95] and Sherpa [139] samples are good agreements with data in the multi-jet and γ + jets enhanced regions. However, n_{trk} distributions of Pythia 8 are different from Sherpa samples and data. n_{trk} distributions of Sherpa samples have similar mis-modeling in both the multi-jet and γ + jets enhanced regions. A similar trend can be seen in the $W \rightarrow qq$ signal efficiency measurement as shown in Figure 6.2(c), and n_{trk} is mis-modeled because it is not an IRC safe variable.

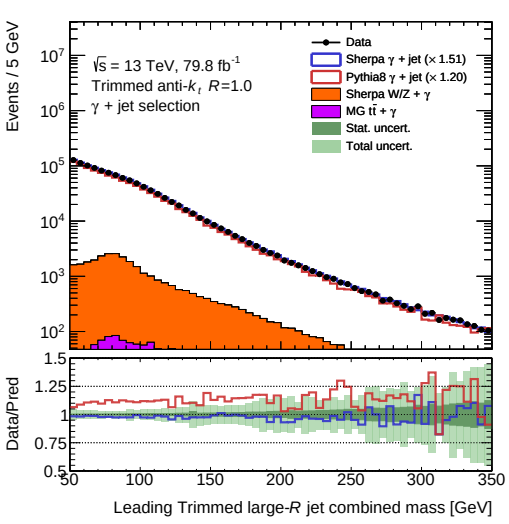

(a) m^{comb}

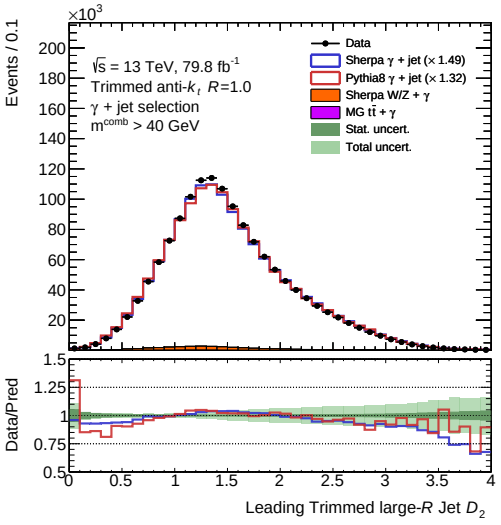

(b) D_2

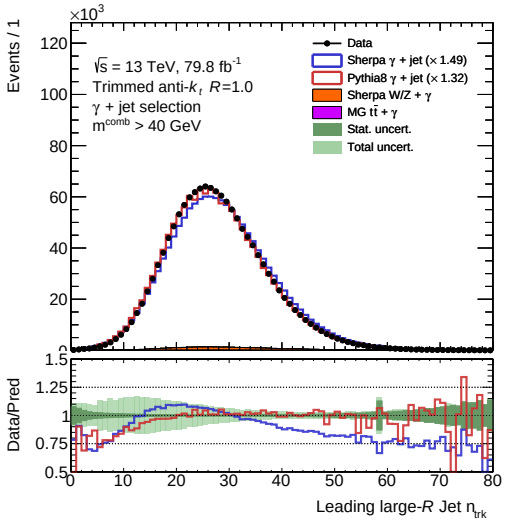

(c) n_{trk}

Figure 6.12: Distributions of m^{comb} (a), D_2 (b) and n_{trk} (c) in γ + jets enhanced region. SHERPA samples are nominal MC and the difference between PYTHIA 8 and SHERPA samples is assigned as a systematic uncertainty from generator difference.

6.1.4.2 Efficiency Measurement and Systematic Uncertainties

The efficiency of the data and MC is measured as,

$$\epsilon_{\text{data}}(p_{\text{T}}, \log(m/p_{\text{T}})) = \frac{N^{\text{tagged}}_{\text{data}} - N^{\text{tagged}}_{\text{MC background}}}{N^{\text{total}}_{\text{data}} - N^{\text{total}}_{\text{MC background}}}, \tag{6.13}$$

$$\epsilon_{\text{MC}}(p_{\text{T}}, \log(m/p_{\text{T}})) = \frac{N^{\text{tagged}}_{\text{MC}\gamma\text{+jets/multi-jets}}}{N^{\text{tagged}}_{\text{MC}\gamma\text{+jets/multi-jets}} + N^{\text{not tagged}}_{\text{MC}\gamma\text{+jets/multi-jets}}}, \tag{6.14}$$

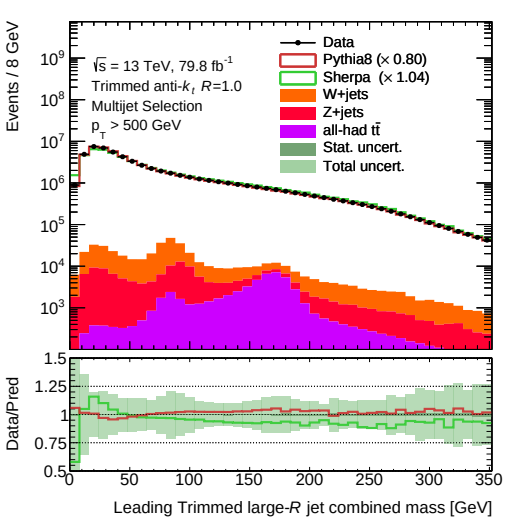

(a) m^{comb}

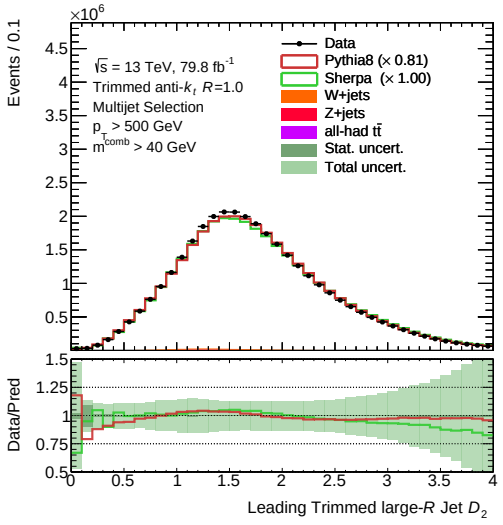

(b) D_2

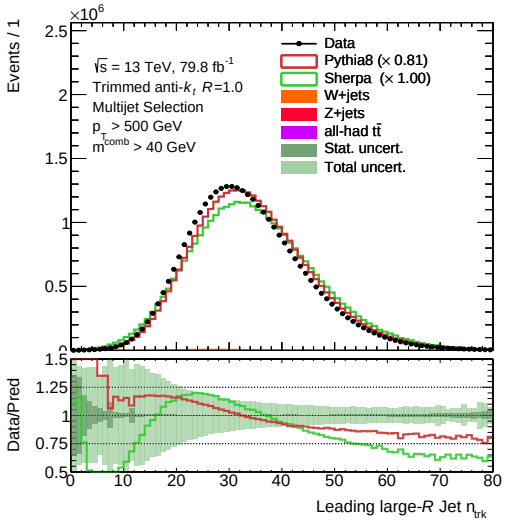

(c) n_{trk}

Figure 6.13: Distributions of m^{comb} (a), D_2 (b) and n_{trk} (c) in multi-jet enhanced region. PYTHIA 8 samples are nominal MC and the difference between PYTHIA 8 and SHERPA samples is assigned as a systematic uncertainty from generator difference.

where $N_{\text{MC}}^{\text{tagged,not tagged}}$ represents the number of events estimated with jets which pass or fail the boson tagging of γ + jets or multi-jets MC samples, $N_{\text{data}}^{\text{total,tagged}}$ represents the number of events of the data in total or with jets which pass boson tagging requiremnets, and $N_{\text{MC background}}^{\text{total,tagged}}$ represents the number of the other background events, such as W/Z + jets, $t\bar{t}$, $W/Z + \gamma$, $t\bar{t} + \gamma$, as estimated with MC samples. Unlike the signal efficiency measurement, fits need not be performed thanks to the high purity of quark- or gluon-initiated jets.

PYTHIA 8 samples are treated as nominal MC in the multi-jet enhanced region and alternative MC in γ + jets enhanced region. In contrast, SHERPA samples are treated as the opposite of PYTHIA 8 samples.

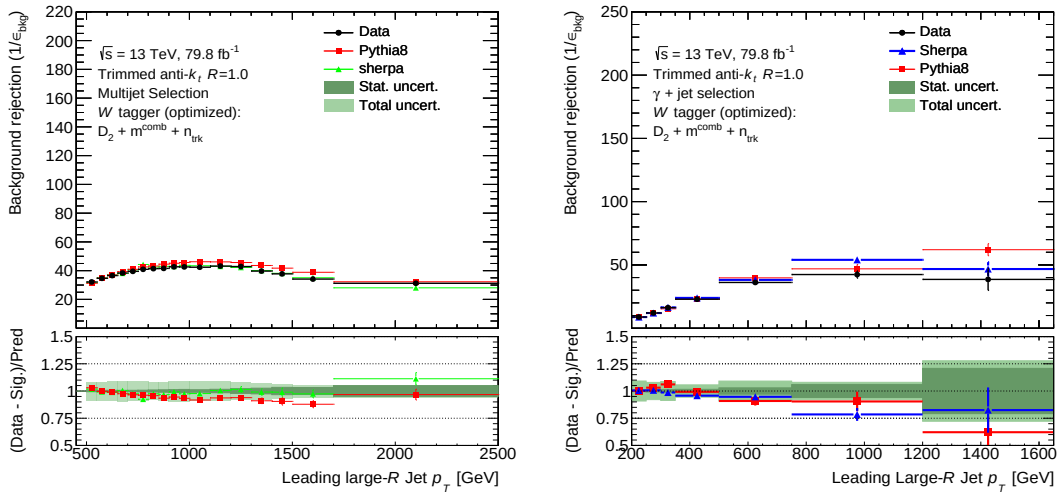

(a) multijet (b) γ+jets

Figure 6.14: Measured background rejections for the W-tagging on the top panel, and the inverse of the $\log(m/p_{\mathrm{T}})$-inclusive SFs on the bottom panel. The results from (a) the multi-jet measurement and (b) the γ + jets are shown respectively.

The background rejection (defined as the inverse of the efficiency) is shown in Figure 6.14. The low background rejection at the low p_{T} region is caused by loose cut values of jet mass and n_{trk}. Similarly, in the high p_{T} region ($p_{\mathrm{T}} > 1300$ GeV), loose cut values of the mass window and D_2 lead to the low background rejection.

In order to correct the difference in the measured efficiency between the data and MC, the SF for background jets is defined as the ratio of the data to MC. The difference between the signal and background efficiency SF is that background SF is evaluated as a function of a jet p_{T} and mass because the statistics of data samples are sufficient.

To check the difference of quark- and gluon-initiated jets, the background rejections in the multi-jet and γ + jets enhanced regions are compared. In the γ + jets enhanced regions, quark-initiated jets account for much. The difference in the rejection factor (500 GeV $\leq p_{\mathrm{T}} \leq$ 600 GeV) between the multi-jets and γ + jets enhanced regions is about 10% and smaller than the statistical uncertainty. The difference between the two measurements is larger in the higher p_{T} region, while the statistical uncertainty is also larger, so they agree within the statistical uncertainty. Furthermore, the difference in terms of the SF is canceled by the data and MC samples and reduced to 2%. Therefore, the two measurements are consistent, and thus, the difference in the SF derived from the two measurements is ignored.

Total systematic uncertainty is discussed in Section 9.2. In the background efficiency measurements, systematic uncertainties derived from the jet energy scale and resolution of large-R jets and these generator differences are considered. The generator difference between Pythia 8 and Sherpa is assigned as a modeling uncertainty, and it is a dominant source of uncertainty.

6.1.4.3 Background efficiency SF for Z boson tagging

Unlike the signal efficiency SF, the background SF depends on the jet mass. Thus, the Z tagging SF is defined by shifting the W tagging,

$$\mathrm{SF}_Z(p_\mathrm{T}, \log(m/p_\mathrm{T})) \quad = \quad \mathrm{SF}_W(p_\mathrm{T}, \log((m - 10.803)/p_\mathrm{T})). \tag{6.15}$$

The difference in the SF values between the measurement using the Z boson tagging and evaluation with shifted mass method from the W boson tagging is typically 1%, at maximum 4%. It is small enough compared with total uncertainty (10-12%).

6.1.5 Physics Process Dependency

In order to compare the efficiency between the efficiency measurement regions and the main analysis regions to search for electroweakinos (described in Section 7.5), the signal and background efficiency using MC samples of the SUSY signals and $Z(\rightarrow \nu\nu)$ + jets backgrounds are evaluated and compared with $t\bar{t}$, γ + jets, and multi-jets, respectively. The comparisons are shown in Figure 6.15.

Figure 6.15(a) shows that the difference in the efficiency of the signal jets is about 10%. The difference can be explained as due to the polarization of W bosons, i.e., the fraction of W bosons originating from top quarks with longitudinal polarization is $\sim$ 69% [140], and W bosons from SUSY particles have $\sim$ 100% longitudinal polarization. Since MC modeling of top quarks agrees with the data, the difference in the data/MC between the parents of W bosons is assumed to be negligible. Thus, the measured signal efficiency in the W boson enhanced region is used without additional uncertainties in the analysis. However, since the inefficiency SF depends on the efficiency and efficiency SF, the inefficiency SF may be incorrectly estimated due to the difference. Therefore, additional uncertainty (10%) on the inefficiency SF derived from the difference in the efficiency is applied.

For the backgrounds, the difference in the background rejection derived from the jet origin can be seen in Figure 6.15(b). As discussed in Section 6.1.4, while there is the difference in the background rejection factor, the difference in the data/MC is canceled, i.e., the difference of the SF is small. Thus, no additional uncertainty for the background efficiency SF is applied. However, additional uncertainty on the background inefficiency SF derived from the difference in the measured efficiency is assigned.

6.2 $V \rightarrow bb$ Tagging Techinique

For $Z/h \rightarrow bb$ tagging, two b-tagged track jets inside a large-R jet ($\Delta R(J, b\text{-jet}) < 1.0$) and the large-$R$ jet mass to be consistent with the mass of Z/h are required correspondingly [122]. The mass resolution of 2b-tagged large-R jets (J_{bb}) is relatively poor compared to the two light flavor jets ($V \rightarrow qq$) due to muons generating from semi-leptonic decaying b/c hadrons. Muons pass through the calorimeters giving only a few GeV and taking away the rest of the energy from the reconstructed $V \rightarrow bb$ candidates. To correct jet mass and improve the resolution, the four-momentum of a spatially matched muon ($\Delta R(J, \mu) < 0.8$) is added, and the jet mass is calculated by including the matched muons, denoted as $m(J_{bb})$. If multiple muons pass the spatial requirement, only the highest p_T muon is used for the correction. The corrected mass distribution has a narrow peak near the Higgs boson mass, as shown in Figure 6.16(a). 2.5% improves the σ value of the Gaussian distribution from 13.9 to 13.6, and the mean value is changed from 117 GeV

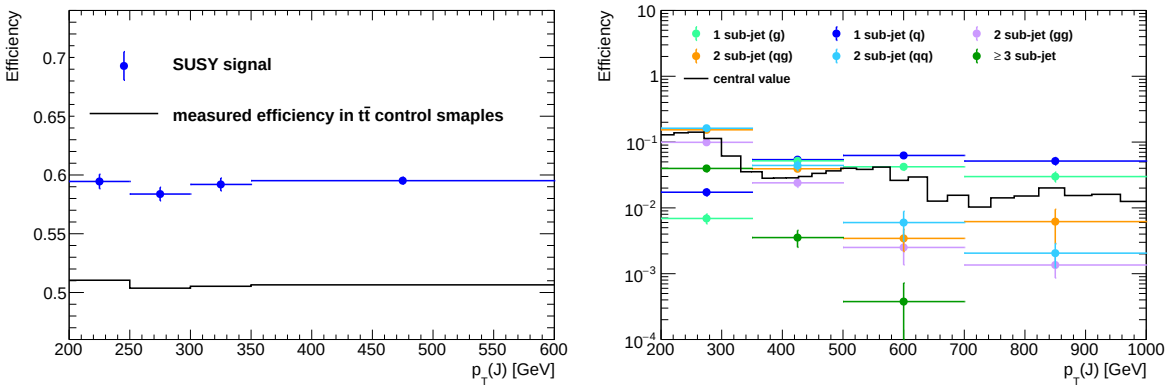

(a) Signal efficiency

(b) Background efficiency

Figure 6.15: (a) The boson tagging signal efficiency of $t\bar{t}$ control samples in the measured region and SUSY signals in the analysis regions. (b) The boson tagging background rejection of γ + jets and multi-jets control samples in the measured region and $Z(\rightarrow \nu\nu)$ + jets backgrounds in the analysis regions. The signal efficiency is measured using large-R jets labeled as W bosons, and the polarization causes the difference derived from the origins of W bosons. In the background efficiency, the number of sub-jet (spatially matched small-R jets to large-R jets with dR(small-R jet, large-R jet) < 1.0) is sensitive to jet substructure variables because it correlates D_2 value. Background jets are categorized with the hardest associated truth particle of spatially matched small-R jets.

to 118 GeV. As shown in Figure 6.16(b), the $m(J_{bb})$ distribution originating from $Z \rightarrow bb$ has a peak near Z boson mass. A broad peak is seen in $t\bar{t}$ MC samples because one of $t \rightarrow qqb$ decay products is outside the large-R jet. To summarize, the requirements for the large-R jet mass are:

- $m_J \in [70, 100]$ GeV for $Z \rightarrow bb$ tagging,
- $m_J \in [100, 135]$ GeV for $h \rightarrow bb$ tagging.

The performance of $Z/h \rightarrow bb$ tagging is shown in Figure 6.17. At the low p_{T} bin, the efficiency is slightly low because the b quarks are not contained in one large-R jet, for example, $\frac{2m_h}{p_{\mathrm{T}h}} \sim 1.25$ where $p_{\mathrm{T}h} = 200$ GeV [2]. In the high jet p_{T} region, the low efficiency is caused by overlapping the two track jets originating from b-quarks. The rejection factor for the large-R jets with c-quark initiated sub-jets included is smaller than those with the included light flavor initiated sub-jets. It is because that the inability of falsely tagged as b-jet (mis-b-tag) is large for c-quark initiated sub-jets. The background estimation, as described later in Chapter 8, is designed to be not sensitive to the $Z/h \rightarrow bb$ tagging efficiency. Hence its efficiency in the simulation is not corrected in this main analysis.

The outline of the impact on systematic uncertainties is introduced below, while more detail is discussed in Section 9.1. The dominant systematic sources are the jet mass scale (JMS), jet mass resolution (JMR), and b-tagging uncertainties. As shown in Figure 6.18, the largest difference in the acceptance between nominal and systematic MC samples is about 10% and derived from the smearing scheme for the truth jet mass. The differences in the acceptance with systematic variations are assigned as systematic uncertainties for the $Z/h \rightarrow bb$ tagging.

[2] $dR(b, b)$ of Higgs is about 40% larger than one of Z because Higgs mass is about 40% larger than the Z mass.

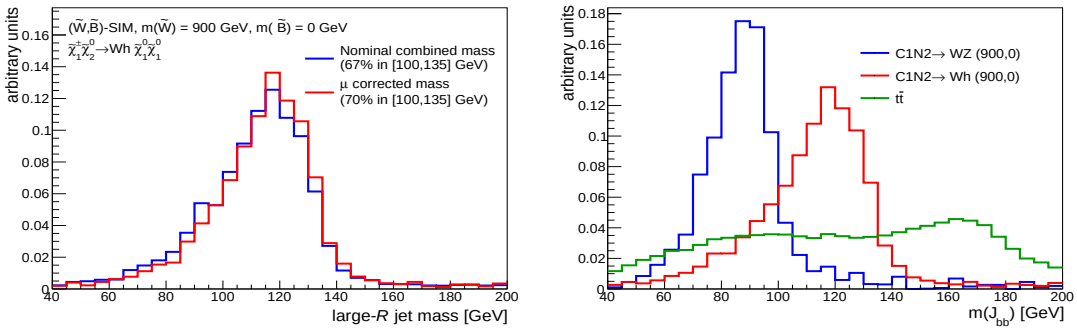

(a) Comparison of large-R jet mass distribution

(b) $m(J_{bb})$ distribution

Figure 6.16: (a) Large-R jet mass distribution containg $2b$-tagged track jets in $\tilde{\chi}_1^{\pm}\tilde{\chi}_2^0(m(\tilde{\chi}_1^{\pm}/\tilde{\chi}_2^0) = 900$ GeV, $m(\tilde{\chi}_1^0) = 0$ GeV$) \rightarrow Wh\tilde{\chi}_1^0\tilde{\chi}_1^0 \rightarrow qqbb\tilde{\chi}_1^0\tilde{\chi}_1^0$ events. The blue line represents the default mass distribution, and the red line represents the corrected distribution by a muon. (b) Distribution of $m(J_{bb})$ in signal and $t\bar{t}$ (green) events. Signal samples are $\tilde{\chi}_1^{\pm}\tilde{\chi}_2^0(m(\tilde{\chi}_1^{\pm}/\tilde{\chi}_2^0) = 900$ GeV, $m(\tilde{\chi}_1^0) = 0$ GeV) with $Z \rightarrow bb$ (blue) and $h \rightarrow bb$ (red).

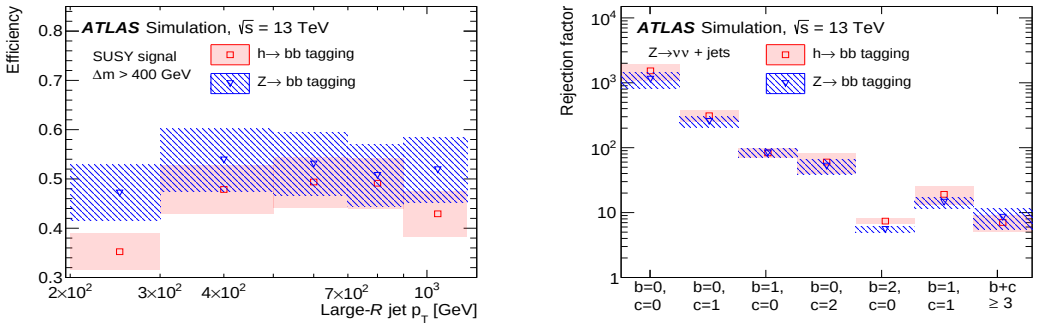

(a) Efficiency

(b) Rejection factor

Figure 6.17: (a) Efficiency of $h \rightarrow bb$ (red) and $Z \rightarrow bb$ (blue) tagging efficiency by $\tilde{\chi}_1^{\pm}\tilde{\chi}_2^0$ signals [49]. (b) Rejection factor (defined as the inverse of efficiency). The x-axis represents the number of b- or c-quark initiated sub-jets. The hashed bands represent the uncertainty, including the MC statistical uncertainty and the systematic uncertainties, such as the jet mass scale, the jet mass resolution, and the b-tagging uncertainties.

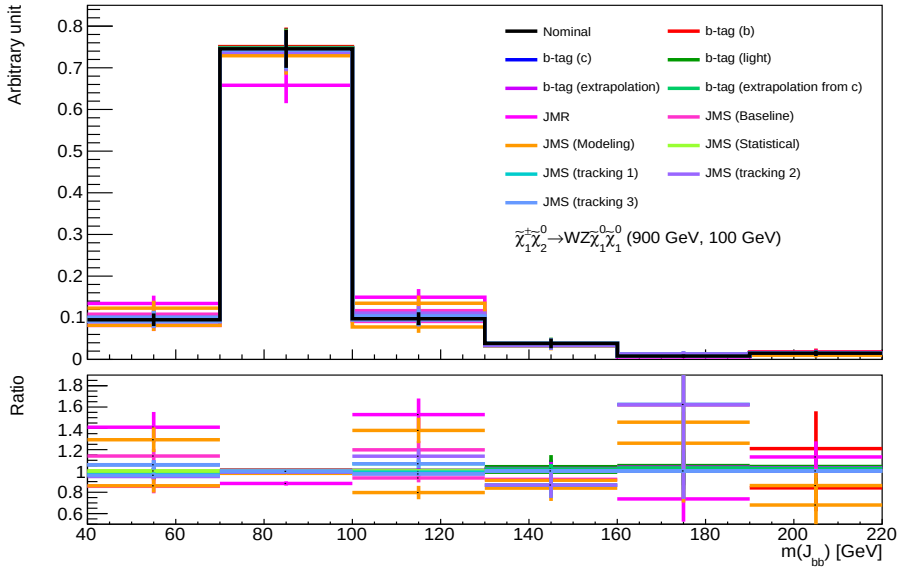

(a) C1N2-WZ

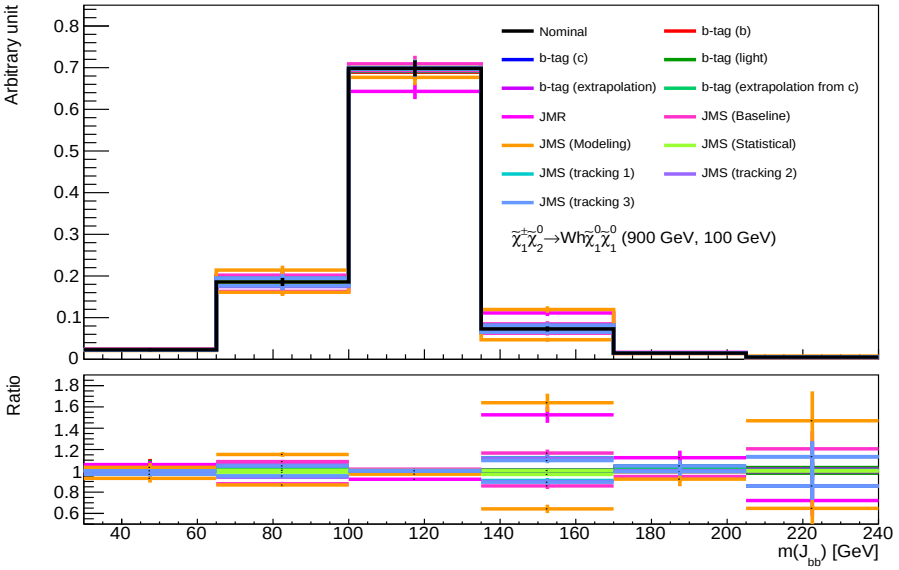

(b) C1N2-Wh

Figure 6.18: $m(J_{bb})$ distributions of C1N2-WZ (a) and C1N2-Wh (b) with systematic variations. The jet mass scale (JMS), jet mass resolution (JMR), and b-tagging uncertainties are shown. The details are described in Section 9.1.

7 Event Selection

In this section, event selections of the search for electroweakinos are discussed. First, the analysis strategy is introduced in Section 7.1. Then, trigger and discriminating variables are introduced in Sections 7.2 and 7.3, respectively. Finally, the preselection and final selection for signal (called "signal region") is discussed in Sections 7.4 and 7.5, respectively.

7.1 Selection Strategy

As discussed in Section 2.3.5, the target models of electroweakinos have a large mass difference $\Delta m = m(\tilde{\chi}_{\text{heavy}}) - m(\tilde{\chi}_{\text{light}})$. Then, two large-$R$ jets tagged as the SM electroweak bosons using the boson tagging techniques and large $E_{\text{T}}^{\text{miss}}$ generated from the $\tilde{\chi}_{\text{light}}$ are required. Since there is no lepton in the final states, the number of leptons is required to be 0 ("0L"), explicitly.

Two categories are used in this analysis: one is "4Q" category, and the other is "2B2Q" category. In the 4Q category, the target is the events where both bosons decay into light quarks (q). Thus, both large-R jets are required to pass $W/Z \to qq$ tagging requirements. In the 2B2Q category, one of the large-R jets is required to satisfy $W/Z \to qq$ tagging requirements, and the other is required to satisfy the $Z/h \to bb$ tagging. In each category, subdivided regions depending on target bosons are defined:

- 4Q category : WW, WZ, ZZ for $\tilde{\chi}_{\text{heavy}}\tilde{\chi}_{\text{heavy}} \to (W/Z)(W/Z)\tilde{\chi}_{\text{light}}\tilde{\chi}_{\text{light}} \to qqqq\tilde{\chi}_{\text{light}}\tilde{\chi}_{\text{light}}$,
- 2B2Q category : WZ, Wh, ZZ, Zh for $\tilde{\chi}_{\text{heavy}}\tilde{\chi}_{\text{heavy}} \to (W/Z)(Z/h)\tilde{\chi}_{\text{light}}\tilde{\chi}_{\text{light}} \to qqbb\tilde{\chi}_{\text{light}}\tilde{\chi}_{\text{light}}$.

7.2 Trigger Selection and Event Cleaning

Events collected by $E_{\text{T}}^{\text{miss}}$ trigger are used for this analysis. The thresholds of $E_{\text{T}}^{\text{miss}}$ triggers and the algorithm of $E_{\text{T}}^{\text{miss}}$ reconstruction at the trigger level were optimized to the operation parameter of the LHC, i.e., they depend on the data period since the pile-up conditions were different. More detail is presented in Ref.[141].

The efficiencies of the $E_{\text{T}}^{\text{miss}}$ trigger in each year are shown in Figure 7.1. The events were selected by $Z \to \mu\mu$ candidates because muons do not contribute to the calculation of $E_{\text{T}}^{\text{miss}}$ at the trigger level, which is based only on the calorimeter information. Thus, the transverse momentum of the di-muon system, $p_{\text{T}}(\mu\mu)$, can be a good proxy for $E_{\text{T}}^{\text{miss}}$. As described in Section 7.4, we apply $E_{\text{T}}^{\text{miss}} > 200$ GeV cut at the offline level. The trigger efficiency at $E_{\text{T}}^{\text{miss}} > 200$ GeV is kept high ($> 95\%$) in all years, and the differences are small.

At the offline level, we apply four event cleaning cuts; noise cut in the LAr calorimeters, dead tile module veto to reject fake $E_{\text{T}}^{\text{miss}}$ events, non-collision background veto to reject fake jets caused by beam-induced

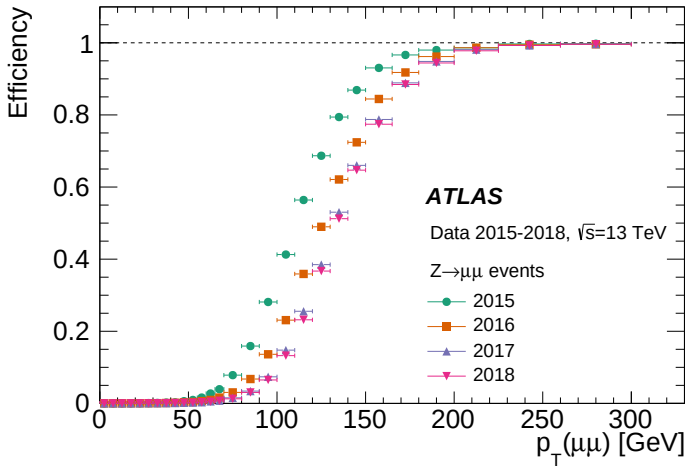

Figure 7.1: The lowest $E_{\mathrm{T}}^{\mathrm{miss}}$ trigger efficiency combined L1 and HLT for the years 2015 to 2018 is shown as a function of the Z boson transverse momentum (Ref. [142]). The events are taken from data with a $Z \to \mu\mu$ selection. Muons are treated as invisible particles, and the transverse momentum of the di-muon system ($p_{\mathrm{T}}(\mu\mu)$) is a proxy for $E_{\mathrm{T}}^{\mathrm{miss}}$. In all years, high efficiency is maintained at the high $E_{\mathrm{T}}^{\mathrm{miss}}$ region ($E_{\mathrm{T}}^{\mathrm{miss}} \geq 200$ GeV).

particles knocking the detector materials, track jets cleaning to avoid overestimating the number of b-quarks by overlapped track jets. More details are described in Appendix H.

7.3 Discriminating Variables

In this section, the definition of the discriminating variables which are used to optimize and define the main analysis selections to search for electroweakinos is summarized. These variables can be categorized into three groups according to purpose:

1. The number of reconstructed objects to define the regions
2. The jet substructure variables to use the boson tagging
3. The kinematic variables to enhance the purity of signal samples.

For these variables, two types of jets are used: the small-R jet denoted as j, and the large-R jet denoted as J.

1. Number of Objects

- $n_{\mathrm{lepton}}, n_{\mathrm{lepton}}^{\mathrm{sig}}$: Numbers of leptons identified as electrons or muons with $p_{\mathrm{T}} > 30$ GeV. Hadronic decaying τ is not included. n_{lepton} is the number of leptons with the baseline selections, as described in Table 5.2. The definition of the variable with the superscript "sig" is the number of leptons with the signal selections, as described in Table 5.2.
- n_{photon}: Number of photons identified as photons with $p_{\mathrm{T}} > 200$ GeV with the signal selections, as described in Table 5.2.

- $n_{\text{Large}-R\text{ jets}}$: Number of large-$R$ jets with the selection, as described in Table 5.2.
- J_{bb} (J_{qq}): J_{bb} is a large-R jet targeted as $Z/h \to bb$; it is required to have two b-tagged track jets satisfying spatially matching to b-tagged track jets, i.e. $\Delta R(J, b\text{-tagged track jets}) < 1.0$. J_{qq} is a large-R jet targeted as $W/Z \to qq$. By considering the possibility that track jets from light-flavor quarks can be mis-tagged as b-tagged track jets, we require the number of b-tagged track jets matching to J_{qq} is less than or equal to 1. $n(J_{bb})$ and $n(J_{qq})$ represents the numbers of J_{bb} and J_{qq}, respectively.
- $n^{\text{trk}}_{b-\text{jet (outside J)}}$: A total number of b-tagged track jets which are not spatially matched with any of the two leading large-R jets in the event. This variable is used as b-veto to reject background events, such as top backgrounds.
- $n^{\text{trk}}_{b-\text{jet (inside J)}}$: A total number of b-tagged track jets spatially matched with the two leading large-R jets in the event. This variable is useful to reject $t\bar{t}$ backgrounds.

2. Jet Substructure Variables

- $m(J)$, $D_2(J)$, $n_{\text{trk}}(J)$: The jet mass, substructure variables representing the 2-prongness and number of ghost-associated tracks of large-R jets, as defined in Sections 5.3.1 and 6.1.1. They are mainly used for the boson tagging. The subscript of J, such as J_1, J_2, represents the descending order of the large-R jet p_{T}.
- $m(J_{bb})$: The jet mass of J_{bb} is corrected by the muon-in-jet, as discussed in Section 6.2.

3. Kinematic Variables

- $E_{\text{T}}^{\text{miss}}$, $E_{T,\text{track}}^{\text{miss}}$: $E_{T,\text{track}}^{\text{miss}}$is $E_{\text{T}}^{\text{miss}}$ calculated by using tracks. $E_{\text{T}}^{\text{miss}}$ distributions of background and $\tilde{\chi}_1^{\pm}\tilde{\chi}_2^0 \to WZ\tilde{\chi}_1^0\tilde{\chi}_1^0$ signal with $m(\tilde{W}) = 900$ GeV, $m(\tilde{B}) = 100$ GeV are shown in Figure 7.2(a). For the background, the distribution gradually decreases because $E_{\text{T}}^{\text{miss}}$ is generated from neutrinos originating from leptonic decaying bosons, such as $W \to l\nu$ or $Z \to \nu\nu$. On the contrary, in the signal process, $E_{\text{T}}^{\text{miss}}$ is generated from $\tilde{\chi}_{\text{light}}$. Thus, $E_{\text{T}}^{\text{miss}}$ depends on the $\tilde{\chi}_{\text{light}}$ mass and the transverse momenta of the $\tilde{\chi}_{\text{light}}$, i.e., $\Delta m = m(\tilde{\chi}_{\text{heavy}}) - m(\tilde{\chi}_{\text{light}})$. Since the targets are large Δm cases, large $E_{\text{T}}^{\text{miss}}$ is required. As shown in Figure 7.2(b), $E_{\text{T}}^{\text{miss}}$ is sensitive to Δm and the $\tilde{\chi}_{\text{light}}$ mass ($= m(\tilde{\chi}_1^0)$ in the $(\tilde{W}, \tilde{B})$-SIM).
- $\Delta\phi(E_{T,\text{track}}^{\text{miss}}, E_{\text{T}}^{\text{miss}})$: Azimuthal angle between the direction of $E_{\text{T}}^{\text{miss}}$ and $E_{T,\text{track}}^{\text{miss}}$. This variable is used to reject the events with jet-like signatures by beam-induced particles. More details are presented in Appendix H.
- $\min\Delta\phi(j, E_{\text{T}}^{\text{miss}})$: Minimum azimuthal angle between the $E_{\text{T}}^{\text{miss}}$ vector and small-R jets with $p_{\text{T}} \geq 30$ GeV. Signal events have large $\min\Delta\phi(j, E_{\text{T}}^{\text{miss}})$ because the directions of $\tilde{\chi}_{\text{light}}$ and bosons are emitted in opposite directions in the center-of-mass frame of $\tilde{\chi}_{\text{heavy}}$. For the background with top quarks, $E_{\text{T}}^{\text{miss}}$ is generated from top semi-leptonic decay, such as $t \to bW \to bl\nu$. Small-R jets originating from b quarks are close by neutrino, and there is a tendency that $\min\Delta\phi(j, E_{\text{T}}^{\text{miss}})$ is small. The distributions of background and $\tilde{\chi}_1^{\pm}\tilde{\chi}_2^0 \to WZ\tilde{\chi}_1^0\tilde{\chi}_1^0$ signal with $m(\tilde{W}) = 900$ GeV, $m(\tilde{B}) = 100$ GeV are shown in Figure 7.3(a). The distributions of the signals do not depend on Δm and decay processes, as shown in Figure 7.3(b).

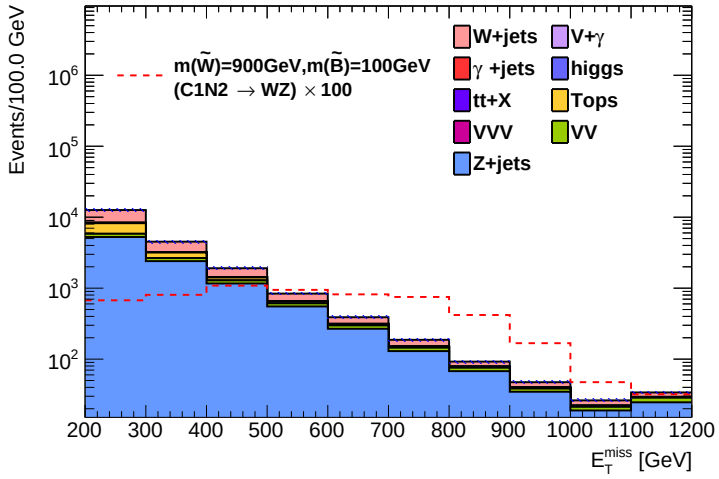

(a) Background and signal

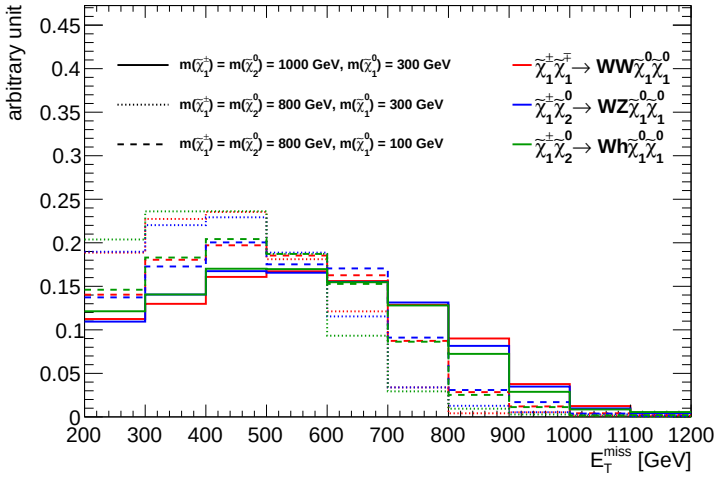

(b) Normalized $E_{\mathrm{T}}^{\mathrm{miss}}$ distribution of $(\tilde{W}, \tilde{B})$ samples

Figure 7.2: $E_{\mathrm{T}}^{\mathrm{miss}}$ distributions after applying preselection (see Section 7.4). For backgrounds (a), the distribution gradually decreases. The peak corresponding to the mass difference and the $\tilde{\chi}_1^0$ mass is seen for $(\tilde{W}, \tilde{B})$ samples (b).

- $m_{\mathrm{eff}}(J)$: Effective mass, which is defined as the scalar sums for $E_{\mathrm{T}}^{\mathrm{miss}}$ and p_{T} of two leading large-R jets:

$$m_{\mathrm{eff}}(J) = p_{\mathrm{T}}(J_1) + p_{\mathrm{T}}(J_2) + E_{\mathrm{T}}^{\mathrm{miss}}. \tag{7.1}$$

  The $m_{\mathrm{eff}}(J)$ distribution of signal and backgrounds are shown in Figure 7.4(a). In the background process, large-R jets are generated from the initial state radiation or final state radiation. Therefore, p_{T} distribution gradually decreases. However, after $\min \Delta\phi(j, E_{\mathrm{T}}^{\mathrm{miss}}) > 1.0$, $E_{\mathrm{T}}^{\mathrm{miss}} > 200$ GeV and $p_{\mathrm{T}}(J) > 200$ GeV are required, a peak of the $m_{\mathrm{eff}}(J)$ distribution in the background samples is seen at $m_{\mathrm{eff}}(J) \sim 800$ GeV. On the other hand, for the signal processes, p_{T} of large-R jets depends on Δm. Thus, $m_{\mathrm{eff}}(J)$ of the signal samples strongly depends on Δm, as shown in Figure 7.4(b).

- $m_{\mathrm{T2}}(J_1, J_2; E_{\mathrm{T}}^{\mathrm{miss}})$: To reconstruct particles that decay into visible and invisible particles, the

transverse mass variable m_{T} is often used, which is defined as the following:

$$m_{\mathrm{T}} = \sqrt{2 p_{\mathrm{T}} E_{\mathrm{T}}^{\mathrm{miss}} (1 - \cos \Delta\phi(\boldsymbol{p}_{\mathrm{T}}^{\mathrm{visible}}, \boldsymbol{p}_{\mathrm{T}}^{\mathrm{miss}}))}. \tag{7.2}$$

For example, a leptonic decaying W boson is reconstructed by a charged lepton and $E_{\mathrm{T}}^{\mathrm{miss}}$, where $E_{\mathrm{T}}^{\mathrm{miss}} = |\boldsymbol{p}_{\mathrm{T}}^{\mathrm{miss}}|$. However, if two invisible particles are generated, $\boldsymbol{p}_{\mathrm{T}}^{\mathrm{miss}}$ represents a vector sum of their momenta. For the SUSY signals, since there are two $\tilde{\chi}_{\mathrm{light}}$ and two SM electroweak bosons in the final state, visible particles are bosons reconstructed as large-R jets (J) and invisible particles are $\tilde{\chi}_{\mathrm{light}}$. Then, we can obtain the following relationship using the transverse momentum of one $\tilde{\chi}_{\mathrm{light}}$, $\boldsymbol{q}_{\mathrm{T}}^{\mathrm{miss}}$,

$$m_{\tilde{\chi}_{\mathrm{heavy}}}^2 \geq \max\left(m_{\mathrm{T}}\left(\boldsymbol{p}_{\mathrm{T}}^{J,1}, \boldsymbol{q}_{\mathrm{T}}\right), m_{\mathrm{T}}\left(\boldsymbol{p}_{\mathrm{T}}^{J,2}, \boldsymbol{p}_{\mathrm{T}}^{\mathrm{miss}} - \boldsymbol{q}_{\mathrm{T}}\right)\right). \tag{7.3}$$

Then, $m_{\mathrm{T2}}(J_1, J_2; E_{\mathrm{T}}^{\mathrm{miss}})$ is defined as the above right function with the minimization over all $\boldsymbol{q}_{\mathrm{T}}^{\mathrm{miss}}$, with the test $\tilde{\chi}_{\mathrm{light}}$ mass (= 100 GeV) subtracted:

$$m_{\mathrm{T2}}(J_1, J_2; E_{\mathrm{T}}^{\mathrm{miss}}) = \min_{q_{\mathrm{T}}}\left[\max\left(m_{\mathrm{T}}\left(\boldsymbol{p}_{\mathrm{T}}^{J,1}, \boldsymbol{q}_{\mathrm{T}}\right), m_{\mathrm{T}}\left(\boldsymbol{p}_{\mathrm{T}}^{J,2}, E_{\mathrm{T}}^{\mathrm{miss}} - \boldsymbol{q}_{\mathrm{T}}\right)\right)\right] - 100(\text{ GeV}). \tag{7.4}$$

For top backgrounds, $m_{\mathrm{T2}}(J_1, J_2; E_{\mathrm{T}}^{\mathrm{miss}})$ is generally small due to $W \to l\nu$. For the SUSY signals, $m_{\mathrm{T2}}(J_1, J_2; E_{\mathrm{T}}^{\mathrm{miss}})$ depends on the $\tilde{\chi}_{\mathrm{heavy}}$ and $\tilde{\chi}_{\mathrm{light}}$ mass. The upper limit depends on $m(\tilde{\chi}_{\mathrm{heavy}})$ due to the definition. If the $\tilde{\chi}_{\mathrm{light}}$ mass is larger than the test value (100 GeV), the upper limit is shifted due to the real and assumed $m(\tilde{\chi}_{\mathrm{light}})$ difference. As shown in Figure 7.5, $m_{\mathrm{T2}}(J_1, J_2; E_{\mathrm{T}}^{\mathrm{miss}})$ values in signal samples are larger than the backgrounds. The maximum value of $m_{\mathrm{T2}}(J_1, J_2; E_{\mathrm{T}}^{\mathrm{miss}})$ depends on the $\tilde{\chi}_{\mathrm{heavy}}$ and $\tilde{\chi}_{\mathrm{light}}$ mass.

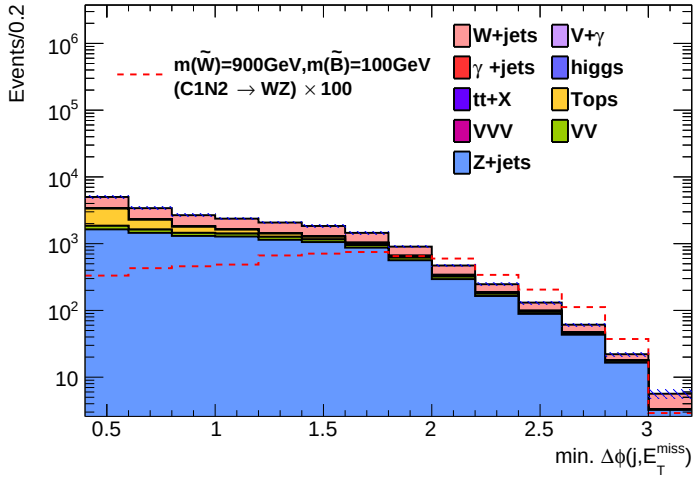

(a) Backgrounds and signal

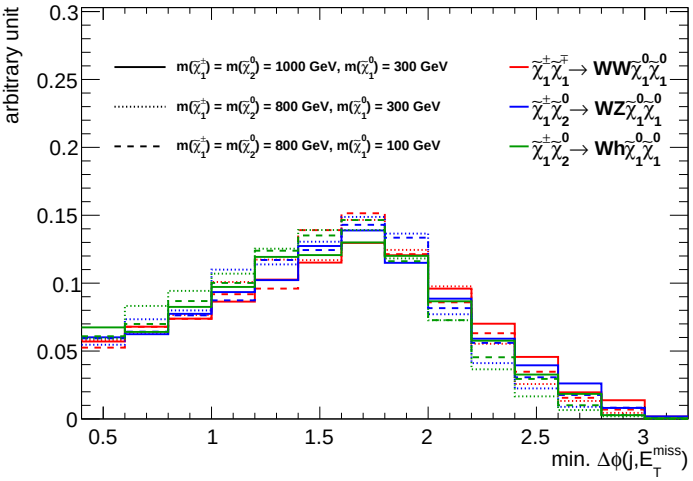

(b) Normalized min $\Delta\phi(j, E_{\mathrm{T}}^{\mathrm{miss}})$ distribution of $(\tilde{W}, \tilde{B})$ samples

Figure 7.3: min $\Delta\phi(j, E_{\mathrm{T}}^{\mathrm{miss}})$ distributions after applying preselection (see Section 7.4) except for min $\Delta\phi(j, E_{\mathrm{T}}^{\mathrm{miss}})$ cut. For backgrounds (a), the distribution gradually decreases. $E_{\mathrm{T}}^{\mathrm{miss}}$ is generated from neutrinos produced by leptonic decay of bosons, such as $W \to l\nu$ and $Z \to \nu\nu$, in $Z(\to \nu\nu)$ + jets, W + jets, and diboson events. However, small min $\Delta\phi(j, E_{\mathrm{T}}^{\mathrm{miss}})$ values are measured in events with top quarks because neutrino ($E_{\mathrm{T}}^{\mathrm{miss}}$) can be measured near jets by $t \to bl\nu$. $(\tilde{W}, \tilde{B})$ samples have large min $\Delta\phi(j, E_{\mathrm{T}}^{\mathrm{miss}})$ values and the peak that does not depend on the mass difference and the $\tilde{\chi}_1^0$ mass (b). There is a peak in the signal distributions at min $\Delta\phi(j, E_{\mathrm{T}}^{\mathrm{miss}}) \sim 1.7$. Thus, min $\Delta\phi(j, E_{\mathrm{T}}^{\mathrm{miss}})$ is effective in reducing the backgrounds.

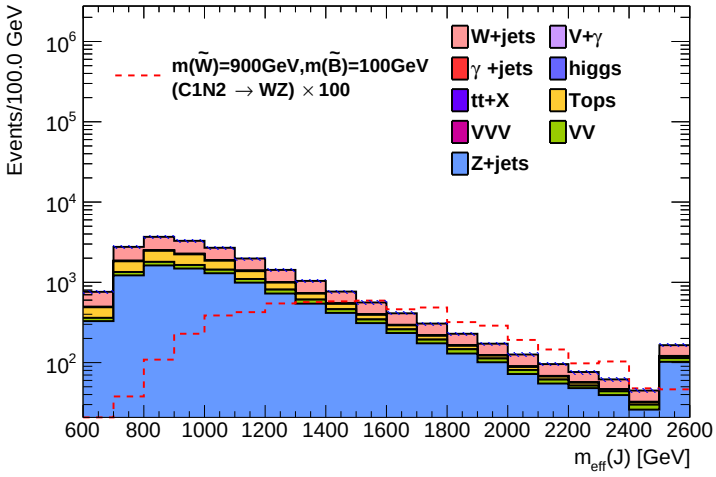

(a) $m_{\text{eff}}(J)$ distribution

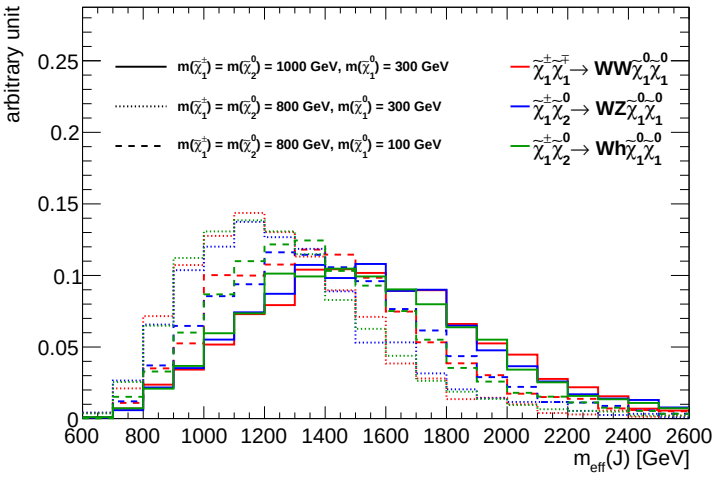

(b) Normalized $m_{\text{eff}}(J)$ distribution of $(\tilde{W}, \tilde{B})$ samples

Figure 7.4: $m_{\text{eff}}(J)$ distributions after applying preselection (see Section 7.4). For backgrounds (a), the peak about 800 GeV is seen and the distribution gradually decreases because $E_{\text{T}}^{\text{miss}}$ ($>$ 200 GeV), $n_{\text{Large}-R\text{ jets}}$ ($\geq$ 2 with $p_{\text{T}} \geq$ 200 GeV) and $\min \Delta\phi(j, E_{\text{T}}^{\text{miss}})$ ($>$ 1.0) cuts are applied. The peaks of $(\tilde{W}, \tilde{B})$ samples depend on the mass difference.

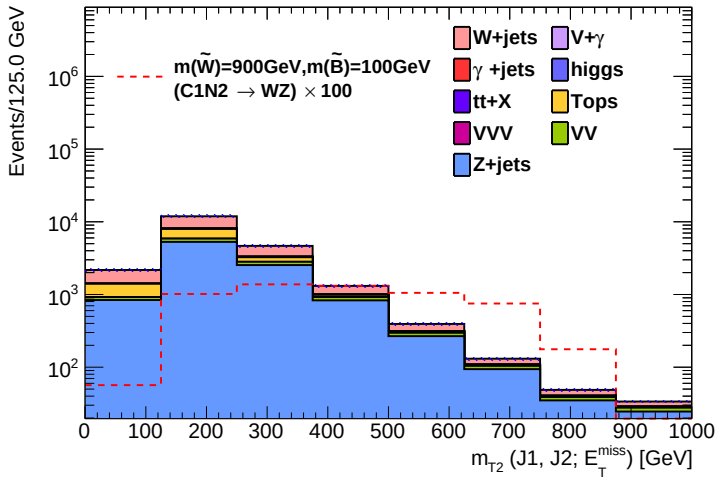

(a) Distribution of $m_{\mathrm{T2}}(J_1, J_2; E_{\mathrm{T}}^{\mathrm{miss}})$ with signal distribution (×100)

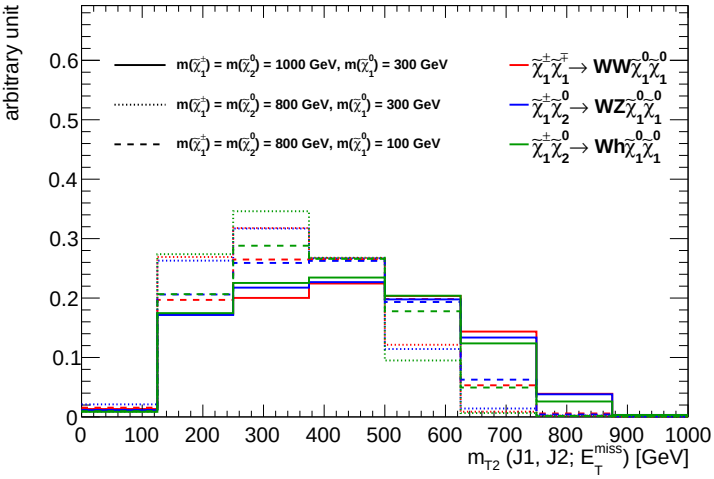

(b) Normalized $m_{\mathrm{T2}}(J_1, J_2; E_{\mathrm{T}}^{\mathrm{miss}})$ distribution of $(\tilde{W}, \tilde{B})$ samples for various decay processes and mass points

Figure 7.5: $m_{\mathrm{T2}}(J_1, J_2; E_{\mathrm{T}}^{\mathrm{miss}})$ distributions after applying preselection (see Section 7.4). For the backgrounds (a), the peak about 200 GeV is seen and the distribution gradually decreases because $E_{\mathrm{T}}^{\mathrm{miss}}$ (> 200 GeV), $n_{\mathrm{Large}-R\ \mathrm{jets}}$ (≥ 2 with $p_{\mathrm{T}} \geq 200$ GeV) and min $\Delta\phi(j, E_{\mathrm{T}}^{\mathrm{miss}})$ (> 1.0) cuts are applied. Small values are seen in events with top quarks due to decay process, $t \to bl\nu$. The peaks of $(\tilde{W}, \tilde{B})$ samples are larger than backgrounds and depend on the mass points weakly (b).

7.4 Preselection

As a baseline cut selection before applying final selections, the preselection is defined as follows. First, events are selected by the fully hadronic final state:

- $n_{\text{Large}-R\text{ jets}} \geq 2$,
- $E_{\text{T}}^{\text{miss}} > 200$ GeV,
- $n_{\text{lepton}} = 0$,

given that those are main characteristic signatures of signal events. Then, further selections are required:

- $n^{\text{trk}}_{b-\text{jet (outside J)}} = 0$,
- $\min \Delta\phi(j, E_{\text{T}}^{\text{miss}}) > 1.0$,

to suppress backgrounds. As described in Section 7.3, these two quantities are effective to reduce top backgrounds. We call this selection "Precut0L."

This preselection is further divided into two; "Precut0L4Q" and "Precut0L2B2Q", corresponding to target categories of 4Q signals $\tilde{\chi}_{\text{heavy}}\tilde{\chi}_{\text{heavy}} \rightarrow qqqq\tilde{\chi}_{\text{light}}\tilde{\chi}_{\text{light}}$ and 2B2Q signals $\tilde{\chi}_{\text{heavy}}\tilde{\chi}_{\text{heavy}} \rightarrow qqbb\tilde{\chi}_{\text{light}}\tilde{\chi}_{\text{light}}$. In order to divide two categories, the number of J_{bb} is used. In the 2B2Q category, $n(J_{bb}) = 1$ is required. In the 4Q category, $n(J_{bb}) = 0$ is required. Since at most one b-tagged track jets in a large-R jet is allowed from the definition of J_{qq}, $t\bar{t}$ backgrounds remain in the 4Q category. Thus, a further selection, $n^{\text{trk}}_{b-\text{jet (inside J)}} \leq 1$, is required to reduce the contribution of $t\bar{t}$ only for the 4Q category. These cuts are summarized in Table 7.1.

The distributions of a few typical kinematic variables of the events selected with Precut0L4Q and Precut0L2B2Q are shown in Figure 7.6. Many other kinematic distributions are shown in Appendix I. No significant difference between the data and background MC samples is observed except for $m(J_{bb})$; as shown in Figure 7.6(d), a data excess is observed in low $m(J_{bb})$ region. It is caused by the mis-modeling of b-tagged track jets when two track jets are collimated. This tendency is also observed in similar phase spaces of independent measurements, such as $Z \rightarrow ll + b-$jets and $ZH \rightarrow \nu\nu bb$ [143]. The data excess has no significant impact on the analysis because the low $m(J_{bb})$ region is not used for the signal searches nor background estimations.

A difference in the data/MC between Precut0L4Q and Precut0L2B2Q is observed. It is caused by the MC under-prediction of $2b$-tagged fraction (such as a gluon splitting into a bb pair). The detail is discussed in Section 8.3.

7.5 Signal Region Selection

As described in Section 7.1, three signal regions (SRs) for 4Q (WW, WZ, ZZ) and four SRs for 2B2Q (WZ, Wh, ZZ, Zh) are defined by explicitly identifying boson spices (either $W/Z/h$). Thus, it is done using the boson tagging as summarized in Table 7.2. In addition to these exclusive boson identified SRs, one inclusive SR for 4Q (VV) and two SRs for 2B2Q (VZ and Vh) where V is inclusive to W/Z are also defined. The definitions of these SRs are also shown in Table 7.2. An illustration of these SRs is given in Figure 7.7.

Table 7.1: Definition of the preselection.

Region groups	Precut0L	
Trigger	MET	
Event cleaning (Sec.7.2)	yes	
$n_{\text{Large}-R\text{ jets}}$	≥ 2	
$n^{\text{trk}}_{b-\text{jet (outside J)}}$	$= 0$	
$E_{\text{T}}^{\text{miss}}$ [GeV]	> 200	
n_{lepton}	$= 0$	
$\min \Delta\phi(j, E_{\text{T}}^{\text{miss}})$	> 1.0	
Additional cuts to divide into 4Q regions and 2B2Q regions		
Region groups	Precut0L4Q	Precut0L2B2Q
$n(J_{bb})$	$= 0$	$= 1$
$n^{\text{trk}}_{b-\text{jet (inside J)}}$	≤ 1	not apply

Table 7.2: SR structure in the 4Q and 2B2Q categories. $n_{W\to qq}$, $n_{Z\to qq}$, $n_{Z\to bb}$, and n_h are the number of reconstructed $W \to qq$, $Z \to qq$, $Z \to bb$, $h \to bb$. The overlap of excluded SRs is illustrated in Fig 7.7. 3 inclusive SRs are mutually orthogonal.

SR category	**SR type**	**SR name**	**Definition**				
			$n_{W\to qq}$	$n_{Z\to qq}$	$n_{W\text{or}Z\to qq}$	$n_{Z\to bb}$	n_h
4Q	exclusive	WW	$= 2$	-	$= 2$	$= 0$	$= 0$
		WZ	≥ 1	≥ 1	$= 2$	$= 0$	$= 0$
		ZZ	-	$= 2$	$= 2$	$= 0$	$= 0$
	inclusive	VV	-	-	$= 2$	$= 0$	$= 0$
2B2Q	exclusive	WZ	$= 1$	-	$= 1$	$= 1$	$= 0$
		ZZ	-	$= 1$	$= 1$	$= 1$	$= 0$
		Wh	$= 1$	-	$= 1$	$= 0$	$= 1$
		Zh	-	$= 1$	$= 1$	$= 0$	$= 1$
	inclusive	VZ	-	-	$= 1$	$= 1$	$= 0$
		Vh	-	-	$= 1$	$= 0$	$= 1$

7.5.1 SR-4Q

As well as classifying into the respective SRs (WW, WZ, ZZ) using numbers of boson tagging, the followings are applied as the final selection:

- $E_{\text{T}}^{\text{miss}} > 300$ GeV,
- $m_{\text{eff}}(J) > 1300$ GeV,

in addition to the Precut0L4Q as a preselection.

These selections on $E_{\text{T}}^{\text{miss}}$ and $m_{\text{eff}}(J)$ are optimized to maximize Z_N value (significance)[1] [144] with the $(\tilde{W}, \tilde{B})$-SIM of $(m(\tilde{\chi}_{\text{heavy}}) = 900$ GeV, $m(\tilde{\chi}_{\text{light}}) = 100$ GeV) and 30% background uncertainty in the

[1] Z_N represents the significance based on he normalized incomplete beta function $B\left(\frac{1}{b\sigma^2};\ s+b,\ 1+\sigma^{-2}\right)$ =

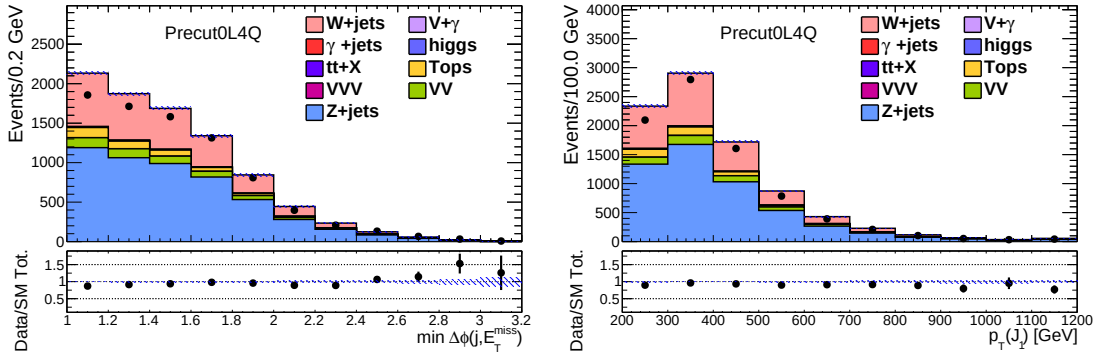

(a) $\min \Delta\phi(j, E_{\mathrm{T}}^{\mathrm{miss}})$ in Precut0L4Q

(b) leading large-R jet p_{T} in Precut0L4Q

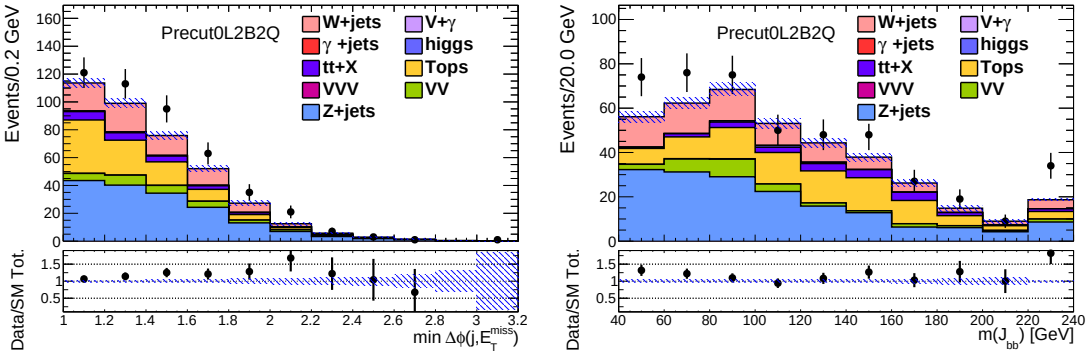

(c) $\min \Delta\phi(j, E_{\mathrm{T}}^{\mathrm{miss}})$ in Precut0L2B2Q

(d) $m(J_{bb})$ in Precut0L2B2Q

Figure 7.6: Kinematic distributions of $\min \Delta\phi(j, E_{\mathrm{T}}^{\mathrm{miss}})$ in Precut0L4Q (a) and Precut0L2B2Q (c). Leading large-R jet p_{T} in Precut0L4Q (b) and J_{bb} mass in Precut0L2B2Q (d) are shown.

4Q-VV region. The kinematic distributions are shown in Figure 7.8. A large step at $m_{\mathrm{eff}}(J) \sim 1.2$ TeV in Figure 7.8(a) is seen, however, it is caused by one MC event has a large event weight. In order to avoid fine tunings of selections, kinematic selections are optimized by checking the distributions with different bin sizes and that the total expected background yield in the SR is not less than 2.

7.5.2 SR-2B2Q

Similarly to SR-4Q, as well as classifying into the respective SRs using numbers of boson tagging, the followings are applied as the final selection:

- $m_{\mathrm{T2}}(J_1, J_2; E_{\mathrm{T}}^{\mathrm{miss}}) > 250$ GeV,
- $m_{\mathrm{eff}}(J) > 1000$ GeV,

in addition to the Precut0L2B2Q as a preselection.

$\frac{\int_0^{\frac{1}{b\sigma^2}} u^{s+b-1}(1-u)^{\sigma^{-2}}}{B(s+b,\ 1+\sigma^{-2})}$, where $B(a,\ b)$ is the beta function, s, b, and σ represent the expected signal yields, the expected background yields, and the background uncertainty, respectively.

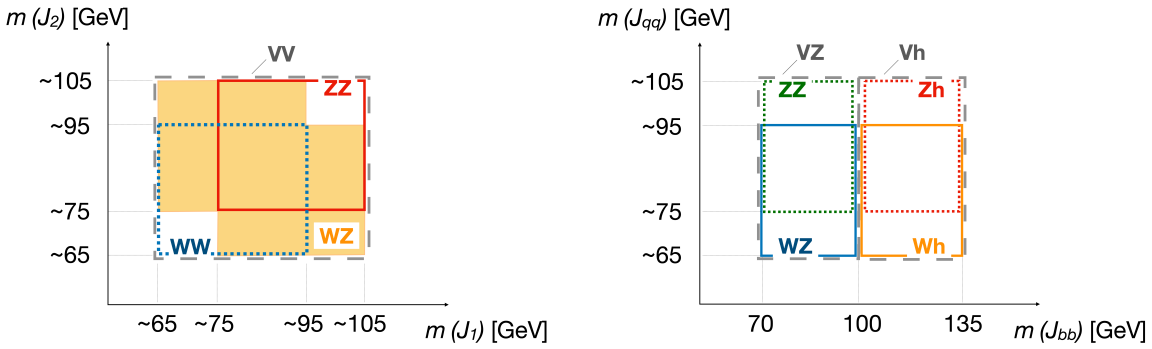

(a) SR-4Q (b) SR-2B2Q

Figure 7.7: Illustration of segments and overlap between the exclusive SRs in (a) 4Q and (b) 2B2Q category as a function of the reconstructed boson mass (corrected by muons for $Z/h \to bb$ candidates) [49]. Overlap arises in the borders between SR bins involving $W \to qq$ and $Z \to qq$. All the other borders maintain the orthogonality between the regions.

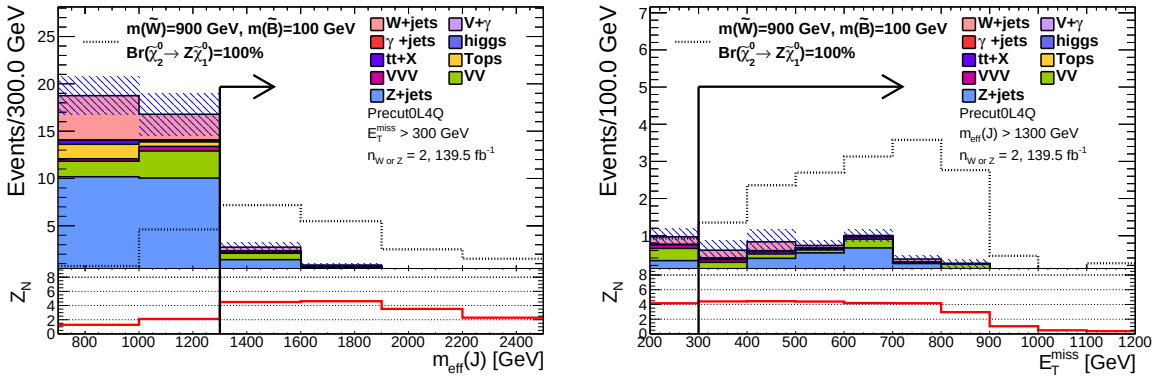

(a) $m_{\text{eff}}(J)$ in SR-4Q-VV (b) $E_{\text{T}}^{\text{miss}}$ in SR-4Q-VV

Figure 7.8: $m_{\text{eff}}(J)$ (a) and $E_{\text{T}}^{\text{miss}}$ (b) distributions applying selections without itself in SR-4Q-VV. Grid line represents rhe distributions of the $(\tilde{W}, \tilde{B})$ signals ($m(\tilde{W}) = 900$ GeV, $m(\tilde{B}) = 100$ GeV and $\text{Br}(\tilde{\chi}_2^0 \to Z\tilde{\chi}_1^0) = 100\%$). The bottom panels show the Z_N values (significance) with each selection value.

These selection values on $m_{\text{T2}}(J_1, J_2; E_{\text{T}}^{\text{miss}})$ and $m_{\text{eff}}(J)$ are optimized to maximize Z_N value using with the $(\tilde{W}, \tilde{B})$-SIM of ($m(\tilde{\chi}_{\text{heavy}}) = 900$ GeV, $m(\tilde{\chi}_{\text{light}}) = 100$ GeV) and 30% background uncertainty in the selected region with $W \to qq$ and $h \to bb$ candidates (SR-2B2Q-Wh). The kinematic distributions are shown in Figure 7.9. $m_{\text{T2}}(J_1, J_2; E_{\text{T}}^{\text{miss}})$ selection reduces the top backgrounds effectively.

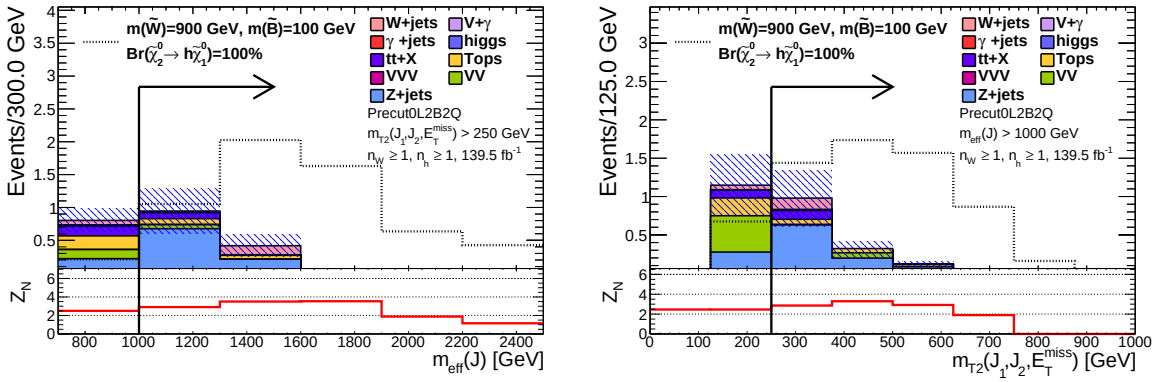

(a) $m_{\text{eff}}(J)$ in SR-2B2Q-Wh

(b) $m_{\text{T2}}(J_1, J_2; E_{\text{T}}^{\text{miss}})$ in SR-2B2Q-Wh

Figure 7.9: $m_{\text{eff}}(J)$ (a) and $m_{\text{T2}}(J_1, J_2; E_{\text{T}}^{\text{miss}})$ (b) distributions applying selections without itself in SR-2B2Q-Wh. Grid line represents rhe distributions of the $(\tilde{W}, \tilde{B})$ signals ($m(\tilde{W})$ = 900 GeV, $m(\tilde{B})$ = 100 GeV and $\text{Br}(\tilde{\chi}_2^0 \to h\tilde{\chi}_1^0)$ = 100%). The bottom panels show the Z_N values (significance) with each selection value.

8 Background estimation

In this chapter, a method to estimate backgrounds is described. The background composition in each SR as estimated with MC samples is shown in Figure 8.1 as an illustration. The dominant background is V+jets in all the SRs and accounts for $> 60\%$ where V stands for the SM electroweak boson. VV, $t + X$, and $t\bar{t}$ are the sub-dominant backgrounds. These are classified as reducible backgrounds, as explained in Section 8.1. VVV and $t\bar{t} + X$ are minor backgrounds and account for $\sim 10\%$. These are classified as irreducible backgrounds. The overview of the strategy how to estimate the background is explained in Section 8.1. Then, how the reducible backgrounds are estimated and validated are described in Sections 8.2 and 8.3, respectively. The irreducible background estimation is discussed in Section 8.5. Multi-jet backgrounds are negligible in the SRs since high $E_{\mathrm{T}}^{\mathrm{miss}}$ is required. More detail is described in Appendix J.

8.1 Strategy

Due to requiring large $E_{\mathrm{T}}^{\mathrm{miss}}$ ($E_{\mathrm{T}}^{\mathrm{miss}} > 200$ GeV or 300 GeV), SM processes containing leptonically decaying bosons, such as $W \to l\nu$ and $Z \to \nu\nu$, can remain as backgrounds by $E_{\mathrm{T}}^{\mathrm{miss}}$ originating from ν. For the case of $W \to l\nu$, l must be τ decaying hadronically or e/μ experimentally not identified as lepton, since $n_{\mathrm{lepton}} = 0$ is required. These backgrounds can be classified into two categories, "reducible backgrounds" and "irreducible backgrounds."

Reducible backgrounds : At most one of two leading large-R jets originate from the real SM electroweak bosons, and the others are not from $W/Z/h$ bosons. V + jets (including γ + jets), VV (including $V\gamma$), $t + X$, $t\bar{t}$ and Vh processes are categorized. Figure 8.2 and Figure 8.3 show, the true origins of the large-R jets as estimated from MC samples for the case of $Z(\to \nu\nu)$ + jets, VV in SR-4Q-VV, and $t\bar{t}$ in SR-2B2Q-Vzh (the logical union of SR-2B2Q-VZ and SR-2B2Q-Vh). It is seen that they contain at least one large-R jet that originates from quarks or gluons of initial or final state radiations, as illustrated in Figure 8.4. This holds for all the reducible backgrounds (the origin of the large-R jets for the other processes are in Appendix K). The reducible backgrounds account for at least 85% of SRs. $Z(\to \nu\nu)$ + jets background is the dominant background in all the SRs, and the sub-dominant backgrounds are W + jets and VV (mainly $ZV \to \nu\nu qq$).

Irreducible backgrounds : Both two leading large-R jets originate from the real SM electroweak bosons, which decay hadronically. In the SM, processes producing at least three SM electroweak bosons can create large $E_{\mathrm{T}}^{\mathrm{miss}}$ (from one boson decaying leptonically) as well as two large-R jets; therefore, they can become these irreducible backgrounds. $t\bar{t} + X$ (mainly $tt(\to bqqbqq) + Z(\to \nu\nu)$) and VVV (mainly $VV(\to qqqq) + Z(\to \nu\nu)$) are the main of this category.

The irreducible backgrounds are estimated with MC samples directly. The reducible backgrounds are estimated in a data-driven way as follows. "Control regions" (CRs) with high purity of the reducible

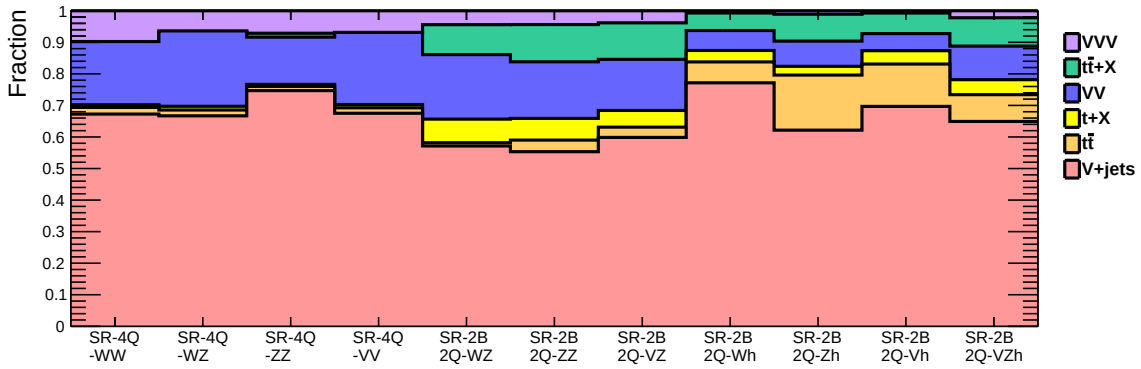

Figure 8.1: Background composition of physics processes estimated from the MC samples in SRs, directly. SR-2B2Q-VZh is the logical union of SR-2B2Q-VZ and SR-2B2Q-Vh. V denotes $W/Z/h/\gamma$ in this figure.

backgrounds are defined. The reducible backgrounds are normalized in the CRs using the following normalization factor (NF):

$$\mathrm{NF} = \frac{N_{\mathrm{data}} - N_{\mathrm{irreducible\ BG}}}{N_{\mathrm{reducible\ BG}}}, \tag{8.1}$$

where $N_{\mathrm{irreducible\ BG}}$ and $N_{\mathrm{reducible\ BG}}$ represent the number of events estimated by irreducible and reducible background MC samples directly. This normalization factor is almost solely due to the $W/Z \to qq$ tagging for quark- and gluon-initiated jets, i.e., correcting for the data and MC difference in such mis-tagging efficiency. Then, to estimate the reducible backgrounds in the SRs, this normalization factor is applied to those in the SRs estimated with MC samples. This corresponds to the extrapolation of the $W/Z \to qq$ (mis-)tagging against quark- or gluon-initiated jets from the CR to SR. The normalization factors separately for the 4Q and 2B2Q categories are estimated. More detail is introduced in Section 8.2.

In this analysis, the statistical error on the data is 40-100% in the SRs (discussed in Section 10.1, and uncertainties are shown in Figure 10.6). Thus, a robust background estimation is important, even if the uncertainty derived from the background estimation is a bit large.

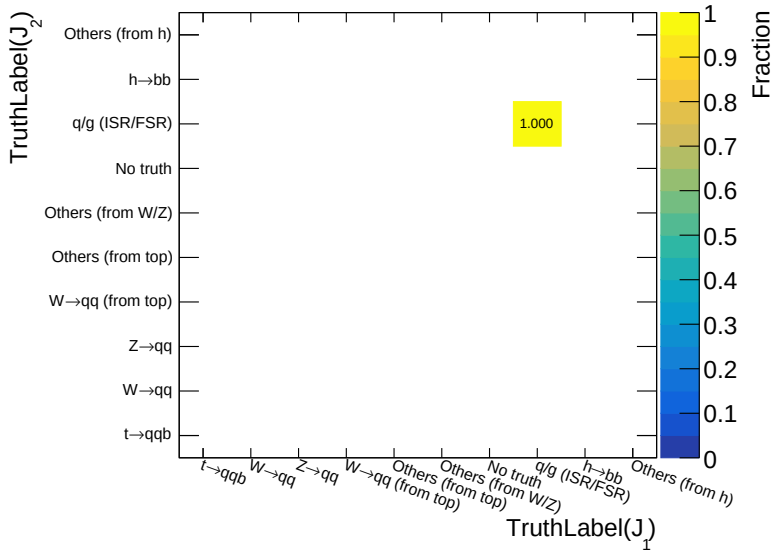

(a) $Z(\to \nu\nu)$ + jets in SR-4Q-VV

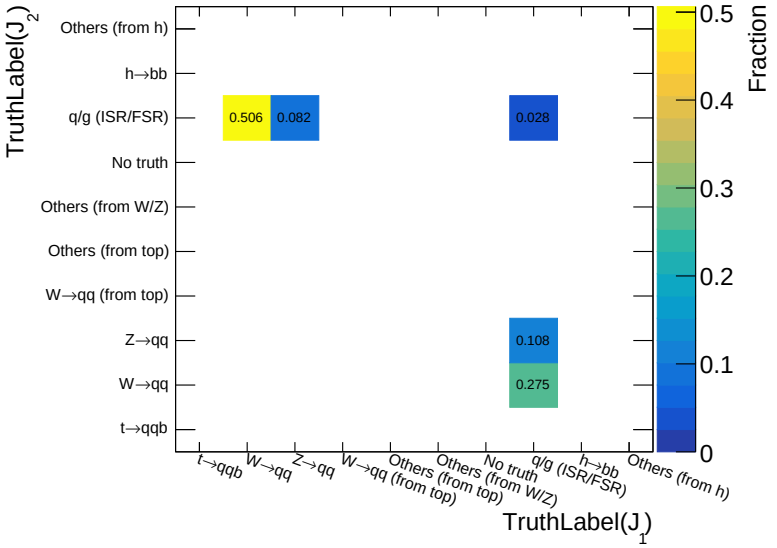

(b) VV in SR-4Q-VV

Figure 8.2: The fractions of the jet origin of $Z(\to \nu\nu)$ + jets (a) and VV (b) in SR-4Q-VV are shown. The x-axis represents the origin of a leading large-R jet, and the y-axis represents a sub-leading large-R jet. At least one jet is originated from quark or gluon, denoted as q/g (ISR/FSR).

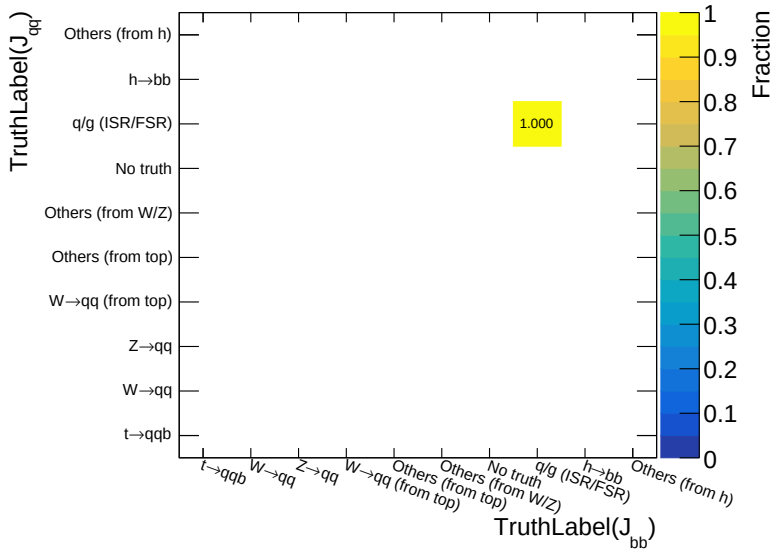

(a) $Z(\rightarrow \nu\nu)$ + jets in SR-2B2Q-VZh

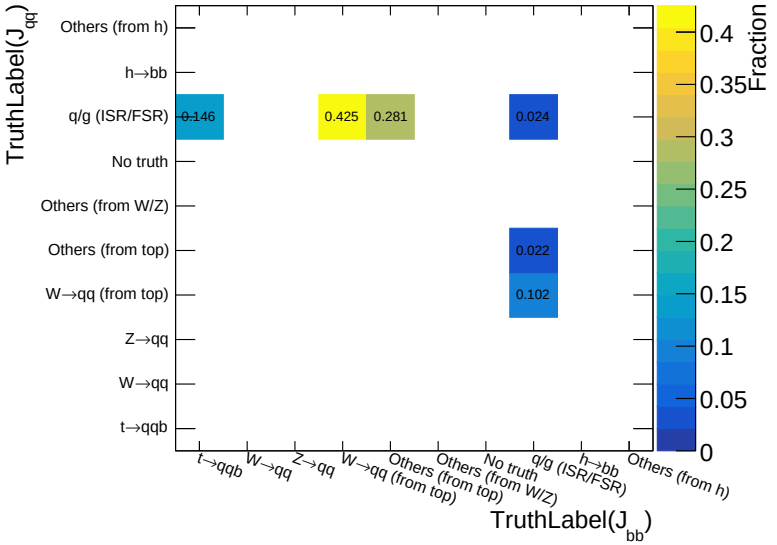

(b) $t\bar{t}$ in SR-2B2Q-VZh

Figure 8.3: The fractions of the origin of J_{qq} and J_{bb} in $Z(\rightarrow \nu\nu)$ + jets (a) and $t\bar{t}$ (b) control samples with SR-2B2Q-VZh selections are shown. The x-axis represents the origin of J_{bb}, and the y-axis represents J_{qq}. At least one jet is originated from quark or gluon, denoted as q/g (ISR/FSR).

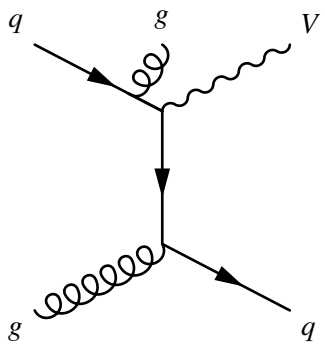

Figure 8.4: Feynman diagrams for the single boson production (V + jets) with ISR/FSR jets.

8.2 Reducible Backgrounds Estimation

8.2.1 Overview

To estimate the reducible background using the data-driven method, CRs are defined. Reducible backgrounds are constrained in the CRs using data and MC samples, and the numbers of events are estimated using extrapolation from the CRs to SRs. For reducible backgrounds, the CRs are better to base the followings:

- Sufficient statistics,
- Low contribution from signals and other backgrounds (irreducible backgrounds),
- Similar phase spaces with SRs.

To meet them, the CRs are defined by inverting the $W/Z \to qq$ tagging requirement on one of the non $2b$-tagged large-R jets (J_{qq}) to the SRs, as illustrated in Figure 8.5. This estimation method has some advantages:

- Given that $W/Z \to qq$ tagging has a large rejection, i.e., the stats in the CRs are sufficient.
- Uncertainties on the extrapolation mainly depend on the $W/Z \to qq$ tagging, which is reasonably well modeled by the efficiency measurement (15-20%), as described in Section 6.1.3.3.
- The jet composition of the reducible backgrounds is similar in both the CRs and SRs, while the reducible backgrounds contain different physics processes (W/Z + jets, VV, $t\bar{t}$...). Thus, all reducible backgrounds are treated as one component, and additional control or validation regions for backgrounds containing one hadronically decaying SM electroweak boson, such as VV, need not be defined.

Thus, the normalization factors in the CRs as defined by Equation 8.1 are estimated and are applied to evaluate the reducible backgrounds in the SRs.

To validate the extrapolation, the two kinematically equivalent regions are defined: one is "1-lepton category" (denoted as "1L") defined by requiring $n^{\text{sig}}_{\text{lepton}} = 1$, and the other is "1-photon category" (denoted as "1Y") defined by requiring $n_{\text{photon}} = 1$ and $E_{\text{T}}^{\text{miss}} < 200$ GeV.

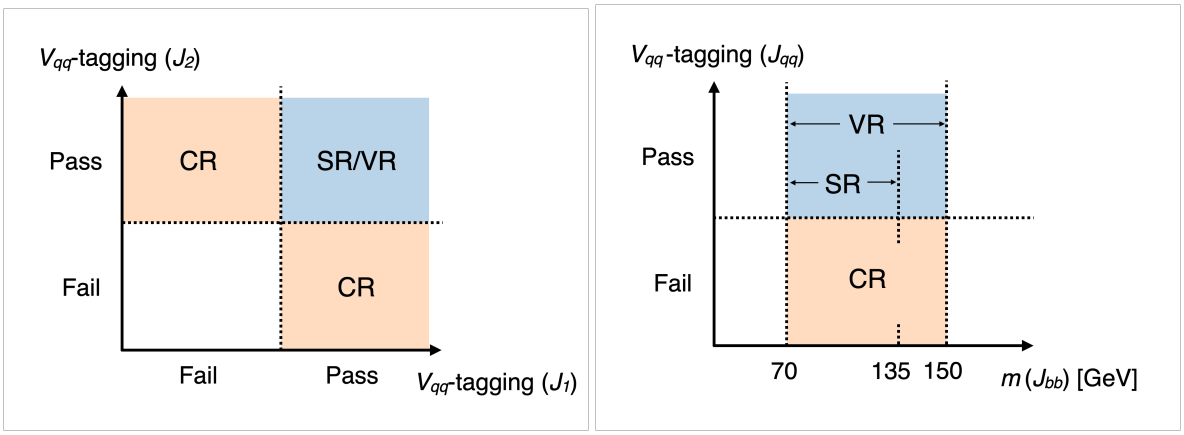

(a) 4Q (b) 2B2Q

Figure 8.5: Schematics illustrating the relation between the SRs (VRs) and CRs in the (a) 4Q and (b) 2B2Q categories. SRs (VRs) are required to pass boson tagging requirements for both two leading large-R jets, and the CRs are constructed by inverting the W_{qq}/Z_{qq}-tagging requirement for one of them. In the 2B2Q category, the J_{bb} mass window cuts in the CRs and VRs are loosened to increase data statistics and suppress signal contaminations.

In this section, a method to estimate the reducible backgrounds in the SRs is introduced, and the validation method for this estimation is discussed in the next section. Only statistical uncertainty is considered in this section.

8.2.2 Control Regions

As same as the selection for the SRs, except for the result of the boson tagging, CR0L-4Q and CR0L-2B2Q are defined as the corresponding CRs with respect to the SRs in the 4Q and 2B2Q categories, respectively. The selections in CR0L-4Q and CR0L-2B2Q are summarized in Table 8.1. $m(J_{bb})$ and $m_{\mathrm{T2}}(J_1, J_2; E_{\mathrm{T}}^{\mathrm{miss}})$ selections are loosened to decrease the contribution from SUSY signals and increase the data statistics in the CR0L-2B2Q. Signal contaminations after applying selections for CR0L-4Q or CR0L-2B2Q are shown in Figure 8.6 and Figure 8.7. Other signal contaminations of the different models are shown in Appendix L. Relative $10-15\%$ contamination to total backgrounds remains in each CR, except for the excluded region by previous analyses, at most 23% contamination of the $(\tilde{H}, \tilde{G})$ model in CR0L-2B2Q. Since the signal contributions in the CRs are treated the same as the irreducible backgrounds in the calculation of the normalization factors (Equation 8.1), it leads to underestimating the normalization factors. However, these contributions are smaller than systematic uncertainties of the background (discussed in Section 9.5 and shown in Figure 9.6). Thus, the impact is small enough. For example, the significance value is $< 10\%$ worse than the case without signal contamination of $m(\tilde{H}) = 700$ GeV, $\mathrm{Br}(\tilde{\chi}_1^0 \to h\tilde{G}) = 40\%$, and upper limits is worse than the case without signal contamination.

In the CRs, most large-R jets which fail both W_{qq} and Z_{qq} tagging ($J^{\text{fail V-tag}}$) originates from ISR/FSR jet, as shown in Figure 8.8 and Figure 8.9. Other samples are shown in Appendix K. There is no significant difference between physics processes. The extrapolation from the CRs to the SRs is equivalent to the extrapolation from failed ISR/FSR jets to pass. Thus, reducible backgrounds are treated as one component. In other words, common normalization factors are assigned for whole reducible backgrounds.

Table 8.1: Definition of control regions in the 4Q and 2B2Q categories. The most inclusive signal regions (SR-4Q-VV,SR-2B2Q-VZ,SR-2B2Q-Vh) are list for comparison.

	SR-4Q-VV	CR0L-4Q	SR-2B2Q-VZ (SR-2B2Q-Vh)	CR0L-2B2Q
Pre-selection				
	Precut0L4Q		Precut0L2B2Q	
Large-R jet selections				
$n^{\text{pass V-tag}}_{\text{Large}-R\text{ jets}}$	$= 2$	$= 1$	$= 1$	$= 0$
$n^{\text{fail V-tag}}_{\text{Large}-R\text{ jets}}$	$= 0$	$= 1$	$= 0$	$= 1$
$n(J_{bb})$	$= 0$	$= 0$	$= 1$	$= 1$
$m(J_{bb})$ [GeV]	not apply	not apply	$\in [70, 100]$ ($\in [100, 135]$)	$\in [70, 150]$
Kinematic cuts				
$\min \Delta\phi(j, E_{\text{T}}^{\text{miss}})$	> 1.0		> 1.0	
$E_{\text{T}}^{\text{miss}}$ [GeV]	> 300		> 200 GeV	
$p_{\text{T}}(V) + p_{\text{T}}(J_1) + p_{\text{T}}(J_2)$ [GeV]	> 1300		> 1000	> 900
$m_{\text{T2}}(J_1, J_2; E_{\text{T}}^{\text{miss}})$ [GeV]	not apply		> 250	

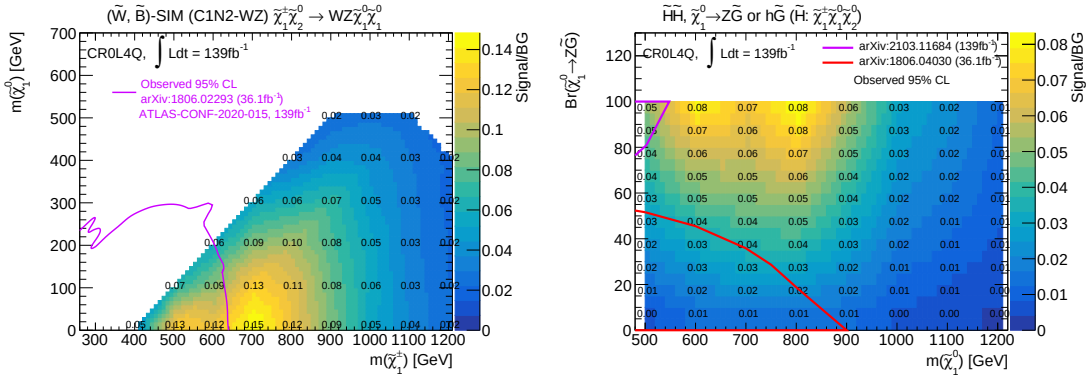

(a) The C1N2-WZ

(b) The $(\tilde{H}, \tilde{G})$ model

Figure 8.6: Signal contaminations of the C1N2-WZ and $(\tilde{H}, \tilde{G})$ signals relative to the total backgrounds in CR0L-4Q. Previous searches exclude regions surrounded by lines.

As discussed in Section 7.4, the data/MC values in the 4Q and 2B2Q categories have a large difference. The difference is caused by the MC underprediction of $2b$-tagged fraction, and the mis-modeling is the same between the SRs and CRs. The difference is canceled by the ratio of the CRs to the SRs. Thus, each normalization factor is estimated in corresponding CRs. For example, the normalization factor evaluated in CR0L-4Q applies to SR-4Q bins, and CR0L-2B2Q for SR-2B2Q bins, respectively.

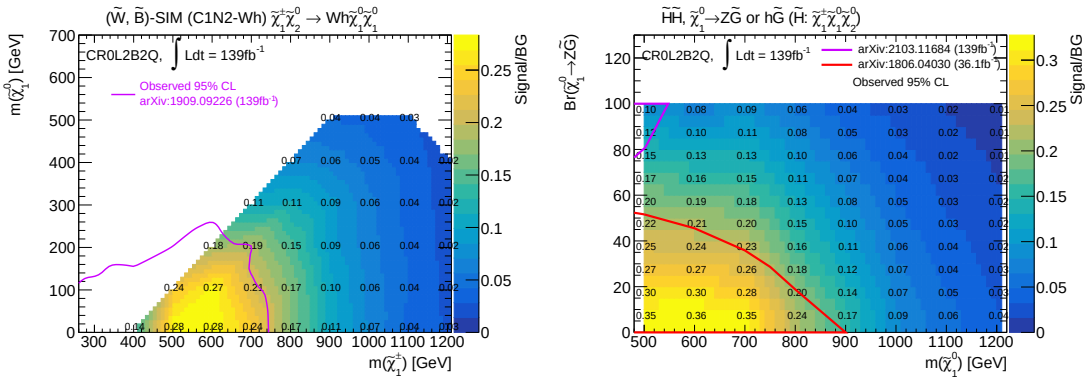

(a) The C1N2-Wh

(b) The $(\tilde{H}, \tilde{G})$ model

Figure 8.7: Signal contaminations of the C1N2-Wh and $(\tilde{H}, \tilde{G})$ signals relative to the total backgrounds in CR0L-2B2Q. Previous searches exclude regions surrounded by lines.

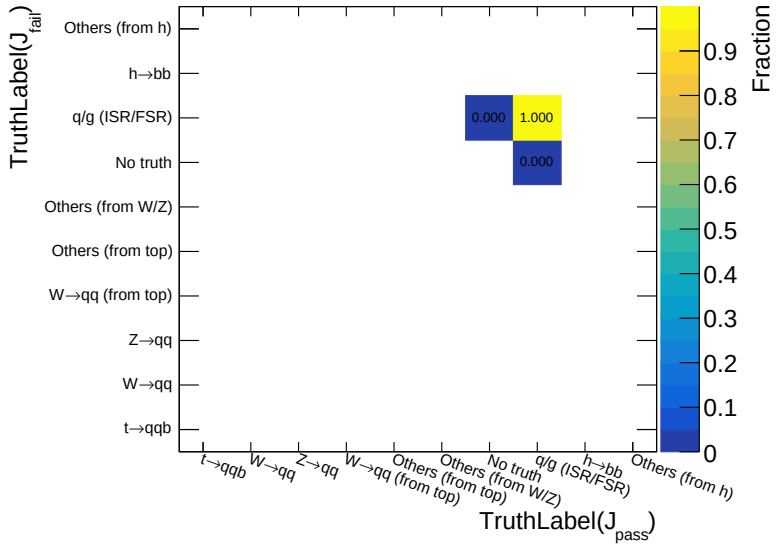

(a) $Z(\to \nu\nu)$ + jets

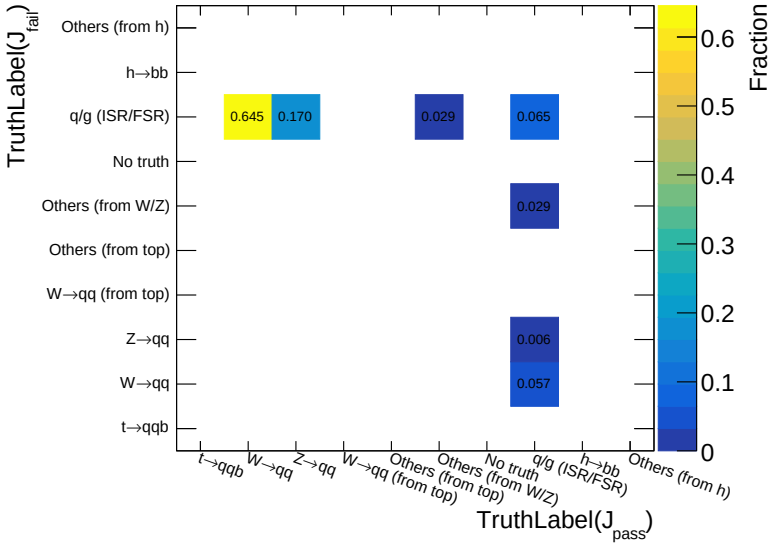

(b) VV

Figure 8.8: The fraction of the large-R jets of the reducible background events in CR0L-4Q. The x-axis represents the origin of large-R jets which pass either W_{qq}-tagging or Z_{qq}-tagging ($J^{\text{pass V-tag}}$) and the y-axis represents the origin of large-R jets which fail both W_{qq}-tagging and Z_{qq}-tagging ($J^{\text{fail V-tag}}$).

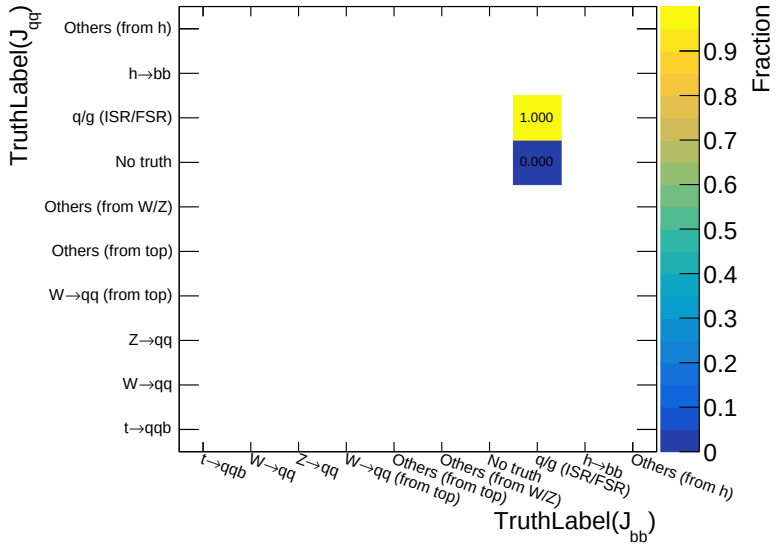

(a) $Z(\rightarrow \nu\nu)$ + jets

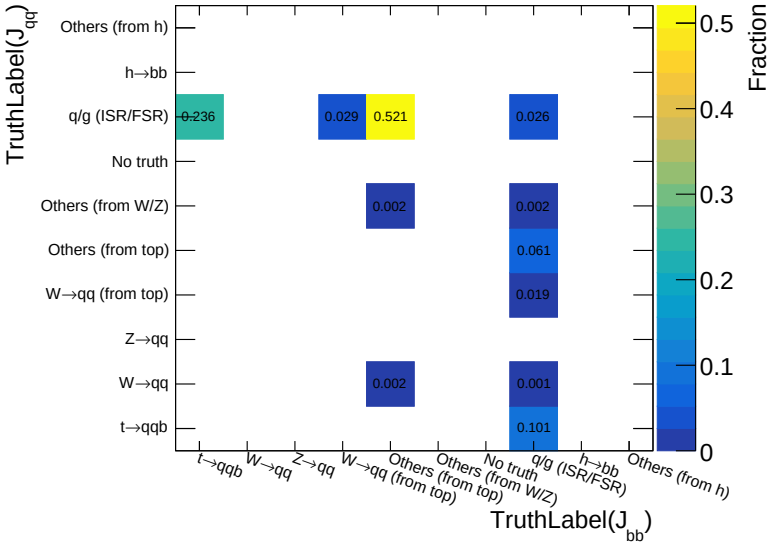

(b) $t\bar{t}$

Figure 8.9: The fraction of J_{qq} and J_{bb} of the reducible background events in CR0L-2B2Q. The x-axis represents the origin of J_{bb} and the y-axis represents the origin of J_{qq}.

8.3 Validation for the Reducible Background Estimation

Since the extrapolation from the CRs to the SRs relies on MC simulation, the modeling of MC simulation is important. $W(\rightarrow l\nu)$ + jets and γ + jets have larger cross-sections and similar diagrams with Z + jets, which is the dominant background process in the SRs. Then, $W(\rightarrow l\nu)$ + jets and γ + jets are used to validate the background estimation.

In the $Z(\rightarrow \nu\nu)$ + jets process, $E_{\mathrm{T}}^{\mathrm{miss}}$ represents p_{T} of a Z boson. As discussed later in Section 8.3.3, the p_{T} of W boson for W + jets in the 1L category and photon for γ+jets in the 1Y category can be used as good proxies of Z bosons. Additional CRs and validation regions (denoted as "VRs") like the SRs for W + jets/γ + jets in the 1L/1Y categories are defined. Similarly, the normalization factors are defined in the CRs and are applied in the VRs.

Like the 0L category, multi-jet backgrounds are also negligible in the 1L and 1Y categories since an isolated lepton or a high p_{T} photon in validation regions is required. More detail is described in Appendix J.

8.3.1 Preselection in 1L/1Y Categories

Selections to define CRs and VRs in the 1L and 1Y categories are introduced. The definitions are similar to the CRs and SRs in the 0L category. The difference between target backgrounds in each category is the species of bosons. In the 0L category, $Z(\rightarrow \nu\nu)$ + jets backgrounds are targeted, and $E_{\mathrm{T}}^{\mathrm{miss}}$ is used to define the SRs. In $Z(\rightarrow \nu\nu)$ + jets events, $E_{\mathrm{T}}^{\mathrm{miss}}$ represents p_{T} of Z bosons. Thus, we need to use variables that are a substitute for $E_{\mathrm{T}}^{\mathrm{miss}}$. In the 1Y category, γ + jets backgrounds are targeted, and p_{T} of photons ($p_{\mathrm{T}}(\gamma)$) is a good proxy of $E_{\mathrm{T}}^{\mathrm{miss}}$. Then, we can use $p_{\mathrm{T}}(\gamma)$ instead of $E_{\mathrm{T}}^{\mathrm{miss}}$ to calculate substitute variables of $m_{\mathrm{eff}}(J)$, $\min\Delta\phi(j, E_{\mathrm{T}}^{\mathrm{miss}})$, and $m_{\mathrm{T2}}(J_1, J_2; E_{\mathrm{T}}^{\mathrm{miss}})$. Considering W + jets in the 1L category, we can use p_{T} of reconstructed W ($p_{\mathrm{T}}(W)$) as a vector sum of transverse momentum of a lepton and $\boldsymbol{p}_{\mathrm{T}}^{\mathrm{miss}}$. We define $p_{\mathrm{T}}(V) + p_{\mathrm{T}}(J_1) + p_{\mathrm{T}}(J_2)$, $\min\Delta\phi(j, V)$, and $m_{\mathrm{T2}}(J_1, J_2; V)$ as common variables in the 0L, 1L, and 1Y categories. They are extended variables for $m_{\mathrm{eff}}(J)$, $\min\Delta\phi(j, E_{\mathrm{T}}^{\mathrm{miss}})$, and $m_{\mathrm{T2}}(J_1, J_2; E_{\mathrm{T}}^{\mathrm{miss}})$ in the 1L/1Y categories where $p_{\mathrm{T}}(W)$ and $p_{\mathrm{T}}(\gamma)$ are used instead of $E_{\mathrm{T}}^{\mathrm{miss}}$.

In the 1L category, a new preselection is defined. Two types of single-lepton triggers are required: a single-electron trigger and a single-muon trigger. The thresholds of these triggers are selected to correspond to the data period [130, 138]. As described above, kinematic selections are also defined using $p_{\mathrm{T}}(W)$ instead of $E_{\mathrm{T}}^{\mathrm{miss}}$. Similarly, a new preselection is also defined in the 1Y category, such as single-photon triggers, $p_{\mathrm{T}}(\gamma)$, and $\min\Delta\phi(j, V)$. The preselections are summarized in Table 8.2.

The data and MC distributions in preselected regions of 1L/1Y categories are shown in Figure 8.10, 8.11 The normalization of the 1Y4Q region is caused by the overestimated cross-section of γ + jets in Sherpa samples. The cross-section is calculated at the NLO, and a similar tendency is also observed in the SM γ + jets measurement [145]. However, the disagreement is not significant because it is constrained by using the normalization factor.

The general trends of 2B2Q/4Q are seen in each 0L, 1L, 1Y category. Each double ratio of the data/MC in 2B2Q/4Q is 1.27 ± 0.05 in 0L, 1.17 ± 0.05 in 1L, and 1.23 ± 0.06 in 1Y. The double ratios have good agreement between the 0L, 1L, and 1Y categories. Then, they imply that the $2b$-tagged fraction (such as a gluon splitting into a bb pair) is underpredicted by MC samples. Since the difference in the normalization between the regions is large, the normalization factor in each region is evaluated individually. Consequently, the difference is not sensitive to the background estimation strategy in the analysis because

Table 8.2: Definition of preselected regions. $E_{\mathrm{T}}^{\mathrm{miss}}$ as V in 0L regions is used for the $\min \Delta\phi(j, V)$ calculations. Reconstructed W boson and photon are used in 1L/1Y regions.

Region groups	Precut0L		Precut1L		Precut1Y	
Trigger	MET		Single-lepton		Single-photon	
Event cleaning	yes		yes		yes	
Dead tile module jets veto	yes		yes		yes	
Non-collision veto	yes		not apply		not apply	
$n_{\text{Large}-R \text{ jets}}$	≥ 2		≥ 2		≥ 2	
$n^{\text{trk}}_{b-\text{jet (outside J)}}$	$= 0$		$= 0$		$= 0$	
$n_{\text{lepton}}(n^{\text{sig}}_{\text{lepton}})$	$= 0(= 0)$		$= 1(= 1)$		$= 0(= 0)$	
n_{photon}	not apply		not apply		$= 1$	
$E_{\mathrm{T}}^{\mathrm{miss}}$ [GeV]	> 200		> 50		< 200	
$p_{\mathrm{T}}(W)$ [GeV]	not apply		> 200		not apply	
$p_{\mathrm{T}}(l)$ [GeV]	not apply		> 30		not apply	
$p_{\mathrm{T}}(\gamma)$ [GeV]	not apply		not apply		> 200	
$\min \Delta\phi(j, V)$	> 1.0		> 1.0		> 1.0	
Additional cuts to divide into 4Q regions and 2B2Q regions						
Region groups	Precut0L4Q	Precut0L2B2Q	Precut1L4Q	Precut1L2B2Q	Precut1Y4Q	Precut1Y2B2Q
$n(J_{bb})$	$= 0$	$= 1$	$= 0$	$= 1$	$= 0$	$= 1$
$n^{\text{trk}}_{b-\text{jet (inside J)}}$	≤ 1	not apply	≤ 1	not apply	≤ 1	not apply

the data/MC value is canceled by the ratio of VRs/CRs or SRs/CRs. What is more important in the background estimation is the shape similarity of backgrounds between 0L/1L/1Y categories, as discussed below.

8.3.2 Definition of CRs and VRs in the 1L/1Y Categories

New CRs in 1L/1Y categories are defined and denoted as CR1L-4Q, CR1L-2B2Q, CR1Y-4Q, and CR1Y-2B2Q, respectively. Additionally, new VRs are defined and denoted as VR1L-4Q, VR1L-2B2Q, VR1Y-4Q, and VR1Y-2B2Q, respectively. The selections of the CRs and VRs are summarized in Table 8.3 and Table 8.4. However, looser kinematic selections are applied to maintain sufficient data statistics than similar ones in the 0L category. For the 2B2Q regions in the 1L/1Y categories, $m(J_{bb})$ selections in CR1L-2B2Q and CR1Y-2B2Q are consistent with CR0L-2B2Q, and inclusive $m(J_{bb})$ selections in VR1L-2B2Q and VR1Y-2B2Q are applied.

Background compositions in each region are shown in Figure 8.12. The composition of minor backgrounds in the 1L and 1Y categories are similar to the 0L category, and it is similar between SRs and VRs and corresponding CRs.

In order to guarantee that W + jets and γ + jets can be used for validation, the kinematic distributions of W + jets and γ + jets need to be confirmed to have similar shapes of Z + jets and whether reconstructed W bosons in the 1L category and photons in the 1Y category are good proxies as Z bosons in the 0L category, or not. The jet origins of Z + jets, W + jets, and γ + jets are similar in each CR, SR, and VR since W, Z, and γ are not the origin of jets. More details of jet origins are shown in Appendix K. In the 1L/1Y VRs, signal contaminations (shown in Appendix L) are negligible since signals are required to decay semi-leptonically and need a hard initial state radiation jet ($p_{\mathrm{T}} > 200$ GeV, $m > 40$ GeV) to pass $n_{\text{Large}-R \text{ jets}} \geq 2$ requirement in the 1L category, or emit a hard initial state radiation photon in the 1Y category.

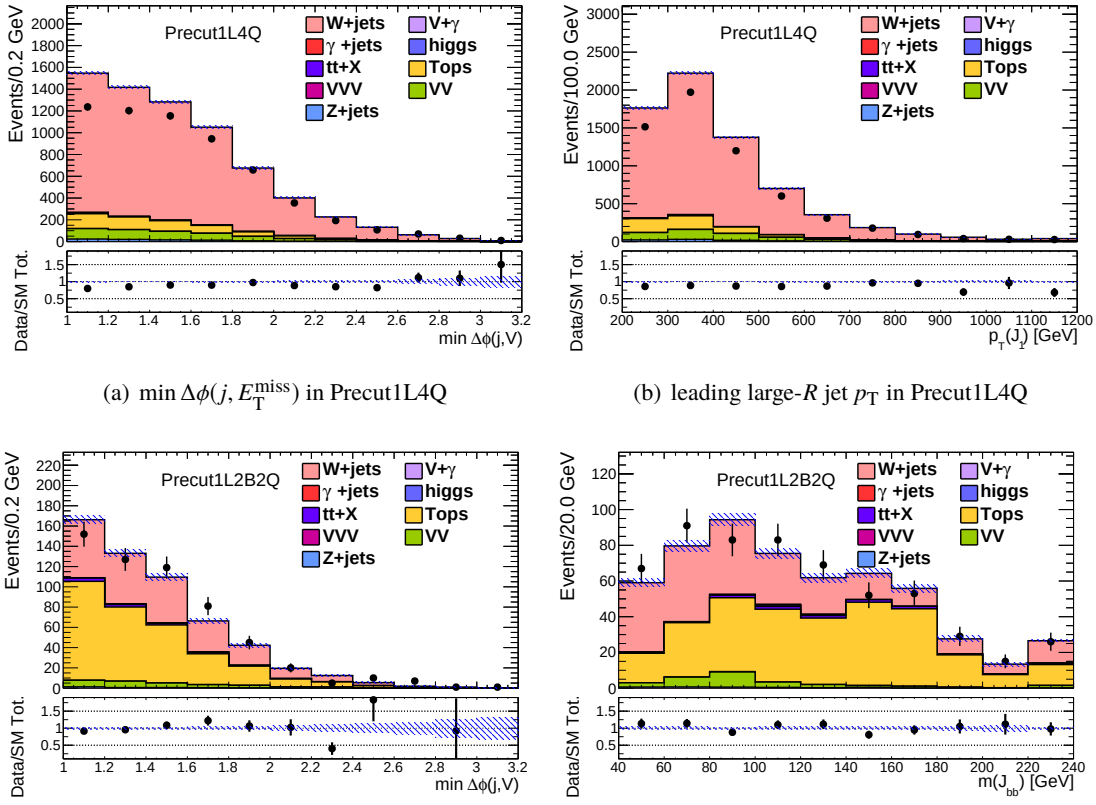

(a) $\min \Delta\phi(j, E_{\mathrm{T}}^{\mathrm{miss}})$ in Precut1L4Q

(b) leading large-R jet p_{T} in Precut1L4Q

(c) $\min \Delta\phi(j, E_{\mathrm{T}}^{\mathrm{miss}})$ in Precut1L2B2Q

(d) $m(J_{bb})$ in Precut1L2B2Q

Figure 8.10: Kinematic distributions of $\min \Delta\phi(j, E_{\mathrm{T}}^{\mathrm{miss}})$ in Precut1L4Q (a) and Precut1L2B2Q (c). Leading large-R jet p_{T} in Precut1L4Q (b) and $m(J_{bb})$ in Precut1L2B2Q (d) are shown.

MC modeling in each region should be compared to verify the reducible background estimation strategy. A transfer factor (TF) as a ratio of the event yields from region A to region B, i.e. $r(A \to B) := y(B)/y(A)$, is defined. The MC modelings as the TFs between $r(\mathrm{CR0L} \to \mathrm{SR})$ and $r(\mathrm{CR1L/1Y} \to \mathrm{VR1L/1Y})$ need to be checked and confirmed that they are similar. Two following assumptions will be checked,

- The extrapolations from CRs to SRs/VRs depend on the $W/Z \to qq$ tagging when kinematic selections are matched in all regions
- The difference between the data and MC samples in actual CRs/SRs/VRs is small enough

For checking the first item, the distributions of jet substructure variables and the TFs between 0L, 1L, and 1Y categories are compared in Section 8.3.4. Additionally, the TF trends in the data and MC samples are compared by the level of the agreement for the second item in Section 8.3.5.

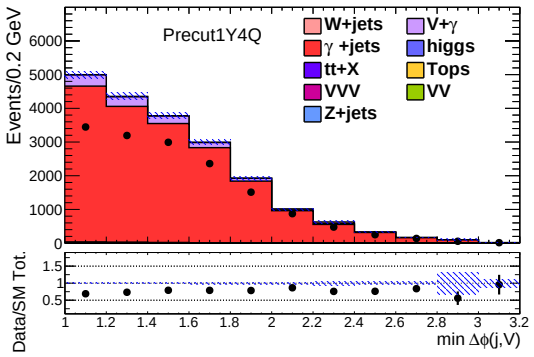

(a) $\min \Delta\phi(j, E_{\mathrm{T}}^{\mathrm{miss}})$ in Precut1Y4Q

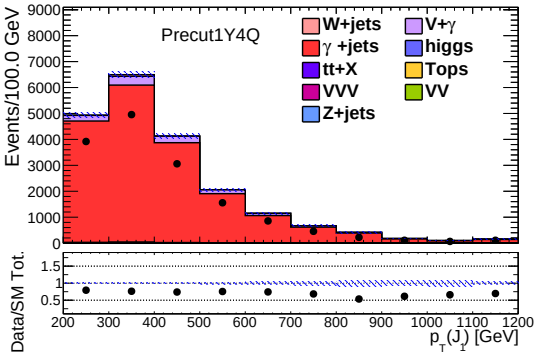

(b) leading large-R jet p_{T} in Precut1Y4Q

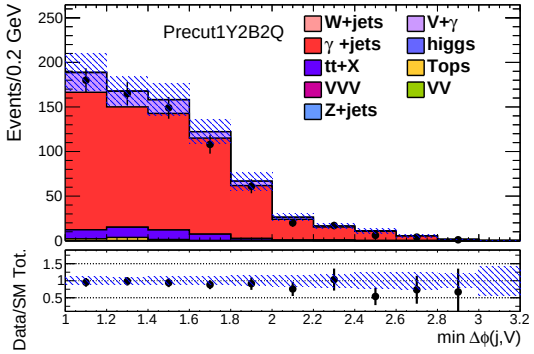

(c) $\min \Delta\phi(j, E_{\mathrm{T}}^{\mathrm{miss}})$ in Precut1Y2B2Q

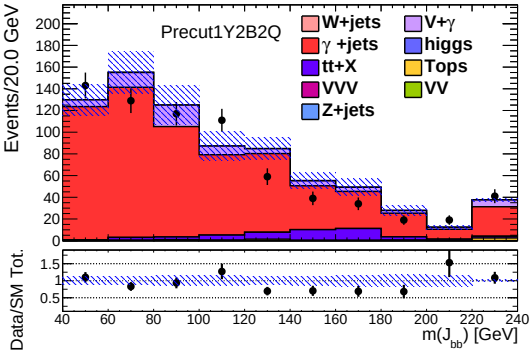

(d) $m(J_{bb})$ in Precut1Y2B2Q

Figure 8.11: Kinematic distributions of $\min \Delta\phi(j, E_{\mathrm{T}}^{\mathrm{miss}})$ in Precut1Y4Q (a) and Precut1Y2B2Q (c). Leading large-R jet p_{T} in Precut1Y4Q (b) and $m(J_{bb})$ in Precut1Y2B2Q (d) are shown.

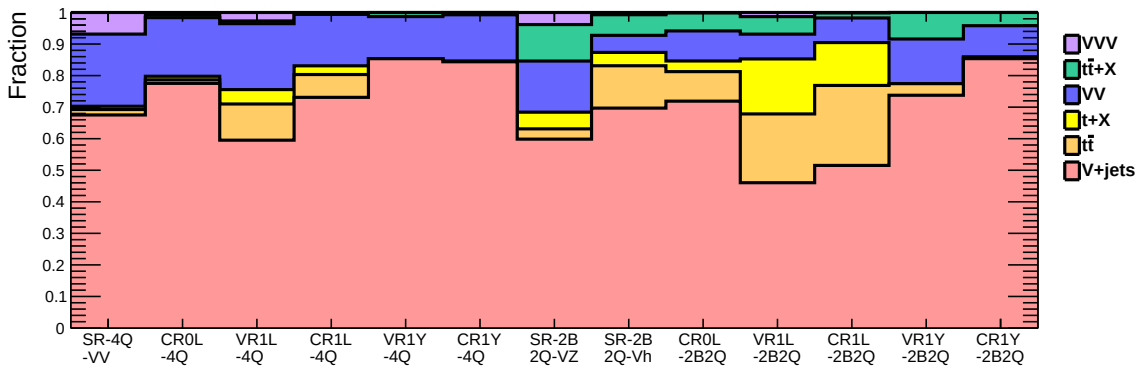

Figure 8.12: Background composition of physics processes in CRs, VRs, and SRs.

Table 8.3: Definition of control regions and validation regions in the 1L category. $p_{\mathrm{T}}(V) + p_{\mathrm{T}}(J_1) + p_{\mathrm{T}}(J_2)$ and $p_{\mathrm{T}}(W)$ cuts are looser than $m_{\mathrm{eff}}(J)$ and $E_{\mathrm{T}}^{\mathrm{miss}}$ cuts in the 0L category due to sufficient data statistics.

	CR1L-4Q	VR1L-4Q	CR1L-2B2Q	VR1L-2B2Q
Pre-selection				
Trigger	Single-lepton			
Event Cleaning	yes			
$n_{\mathrm{lepton}}^{\mathrm{sig}}$	$= 1$			
$n_{\mathrm{Large-}R\text{ jets}}$	≥ 2			
$n_{b\mathrm{-jet\ (outside\ J)}}^{\mathrm{trk}}$	$= 0$			
$p_{\mathrm{T}}(W)$ [GeV]	> 200			
$p_{\mathrm{T}}(l)$ [GeV]	> 30			
$\min \Delta\phi(j, V)$	> 1.0			
$n_{b\mathrm{-jet\ (inside\ J)}}^{\mathrm{trk}}$	≤ 1		not apply	
$n(J_{bb})$	$= 0$		$= 1$	
Large-R selections				
$n_{\mathrm{Large-}R\text{ jets}}^{\text{pass V-tag}}$	$= 1$	$= 2$	$= 0$	$= 1$
$n_{\mathrm{Large-}R\text{ jets}}^{\text{fail V-tag}}$	$= 1$	$= 0$	$= 1$	$= 0$
$n(J_{bb})$	$= 0$	$= 0$	$= 1$	$= 1$
$m(J_{bb})$ [GeV]	not apply		$\in [70, 150]$	$\in [70, 135]$
Kinematic cuts				
$p_{\mathrm{T}}(V) + p_{\mathrm{T}}(J_1) + p_{\mathrm{T}}(J_2)$ [GeV]	> 1000		> 900	
$m_{\mathrm{T2}}(J_1, J_2; V)$ [GeV]	not apply		> 250	

Table 8.4: Definition of control regions and validation regions in the 1Y category. $p_{\mathrm{T}}(V) + p_{\mathrm{T}}(J_1) + p_{\mathrm{T}}(J_2)$ and $p_{\mathrm{T}}(\gamma)$ cuts are looser than $m_{\mathrm{eff}}(J)$ and $E_{\mathrm{T}}^{\mathrm{miss}}$ cuts in the 0L category due to sufficient data statistics.

	CR1Y-4Q	VR1Y-4Q	CR1Y-2B2Q	VR1Y-2B2Q
Pre-selection				
Trigger	Single-photon			
Event Cleaning	yes			
n_{photon}	$= 1$			
$n_{\mathrm{Large-}R\text{ jets}}$	≥ 2			
$n^{\mathrm{trk}}_{b-\text{jet (outside J)}}$	$= 0$			
$E_{\mathrm{T}}^{\mathrm{miss}}$ [GeV]	< 200			
$p_{\mathrm{T}}(\gamma)$ [GeV]	> 200			
$\min \Delta\phi(j, V)$	> 1.0			
$n^{\mathrm{trk}}_{b-\text{jet (inside J)}}$	≤ 1		not apply	
$n(J_{bb})$	$= 0$		$= 1$	
Large-R selections				
$n^{\text{pass V-tag}}_{\text{Large-}R\text{ jets}}$	$= 1$	$= 2$	$= 0$	$= 1$
$n^{\text{fail V-tag}}_{\text{Large-}R\text{ jets}}$	$= 1$	$= 0$	$= 1$	$= 0$
$n(J_{bb})$	$= 0$	$= 0$	$= 1$	$= 1$
$m(J_{bb})$ [GeV]	not apply		$\in [70, 150]$	$\in [70, 135]$
Kinematic cuts				
$p_{\mathrm{T}}(V) + p_{\mathrm{T}}(J_1) + p_{\mathrm{T}}(J_2)$ [GeV]	> 1000		> 900	
$m_{\mathrm{T2}}(J_1, J_2; V)$ [GeV]	not apply		> 250	

8.3.3 Comparison between 0L/1L/1Y for V+jets MC

In this sub-section, we discuss whether W + jets/γ + jets in the 1L/1Y category can be nearly equivalent to the validation of $Z(\rightarrow \nu\nu)$ + jets in the 0L category. The kinematic distributions are checked in each category with loose selections summarized in Table 8.5, and shown in Figure 8.13.

The distributions of jet variables are similar and $W/Z \rightarrow qq$ tagging performances of W + jets and γ + jets samples are consistent within the statistical errors due to the similar diagrams. Thus, the extrapolation from fail criteria to pass criteria of $W/Z \rightarrow qq$ tagging in the 0L category can be validated by W + jets and γ + jets samples. In addition, kinematic variables of $W/Z/\gamma$, such as $p_{\mathrm{T}}(V)$, min $\Delta\phi(j, V)$, $p_{\mathrm{T}}(V) + p_{\mathrm{T}}(J_1) + p_{\mathrm{T}}(J_2)$ and $m_{\mathrm{T2}}(J_1, J_2; V)$, are also similar.

8.3.4 Jet variable comparison in the CRs and SRs/VRs

The MC-to-MC distributions of $J^{\text{fail V-tag}}$ variables in CR0L-4Q, CR1L-4Q, and CR1Y-4Q are shown in Figure 8.14. This figure shows the sum of the reducible backgrounds, containing other than V + jets MC samples too. Selections in CR0L-4Q are loosened so that they are consistent with the same as selections of CR1L-4Q/CR1Y-4Q, i.e., $p_{\mathrm{T}}(V) + p_{\mathrm{T}}(J_1) + p_{\mathrm{T}}(J_2)$ ($p_{\mathrm{T}}(V)$) cut is loosened from 1300 (300) GeV to 1000 (200) GeV. Reasonable agreements of jet variables between the three regions are found in MC samples. Figure 8.15 shows a similar MC-to-MC comparison for 2B2Q regions. Like the 4Q categories, reasonable consistencies within the limited MC statistics are seen in all samples. The data-to-data distributions in the data are shown in Appendix N.

Similarly, MC-to-MC comparisons are checked in the SR-like regions where both jets are satisfied with boson tagging requirements, as shown in Figure 8.16. Other variables are shown in Appendix N. To maintain MC statistics, $p_{\mathrm{T}}(V) + p_{\mathrm{T}}(J_1) + p_{\mathrm{T}}(J_2)$ and $p_{\mathrm{T}}(V)$ cuts are loosened to 800 GeV and 200 GeV. For the 2B2Q categories, $m(J_{bb})$ cut in SR-2B2Q is changed to the logical union of $Z \rightarrow bb$ and $h \rightarrow bb$ cuts to align with VR1L-2B2Q and VR1Y-2B2Q. Like the CRs, reasonable consistencies within the limited MC statistical uncertainty are seen in all regions.

Table 8.5: Cuts for the comparison of kinematic distributions between V+jets MC samples.

Samples	$Z(\rightarrow \nu\nu)$ + jets (0L)	W + jets (1L)	γ+jets (1γ)
Trigger	MET	Single-lepton	Single-photon
Dead tile module jets veto	yes	yes	yes
Non-collision veto	yes	not apply	not apply
n_{lepton}	= 0	= 1	= 0
n_{photon}	not apply	not apply	= 1
$n_{\text{Large}-R\text{ jets}}$		≥ 2	
$E_{\text{T}}^{\text{miss}}$ [GeV]	> 200	not apply	< 200
$p_{\text{T}}(W)$ [GeV]	not apply	> 200	not apply
$p_{\text{T}})l)$ [GeV]	not apply	> 30	not apply
$p_{\text{T}}(\gamma)$ [GeV]	not apply	not apply	> 200
$\min \Delta\phi(j, V)$		> 1.0	

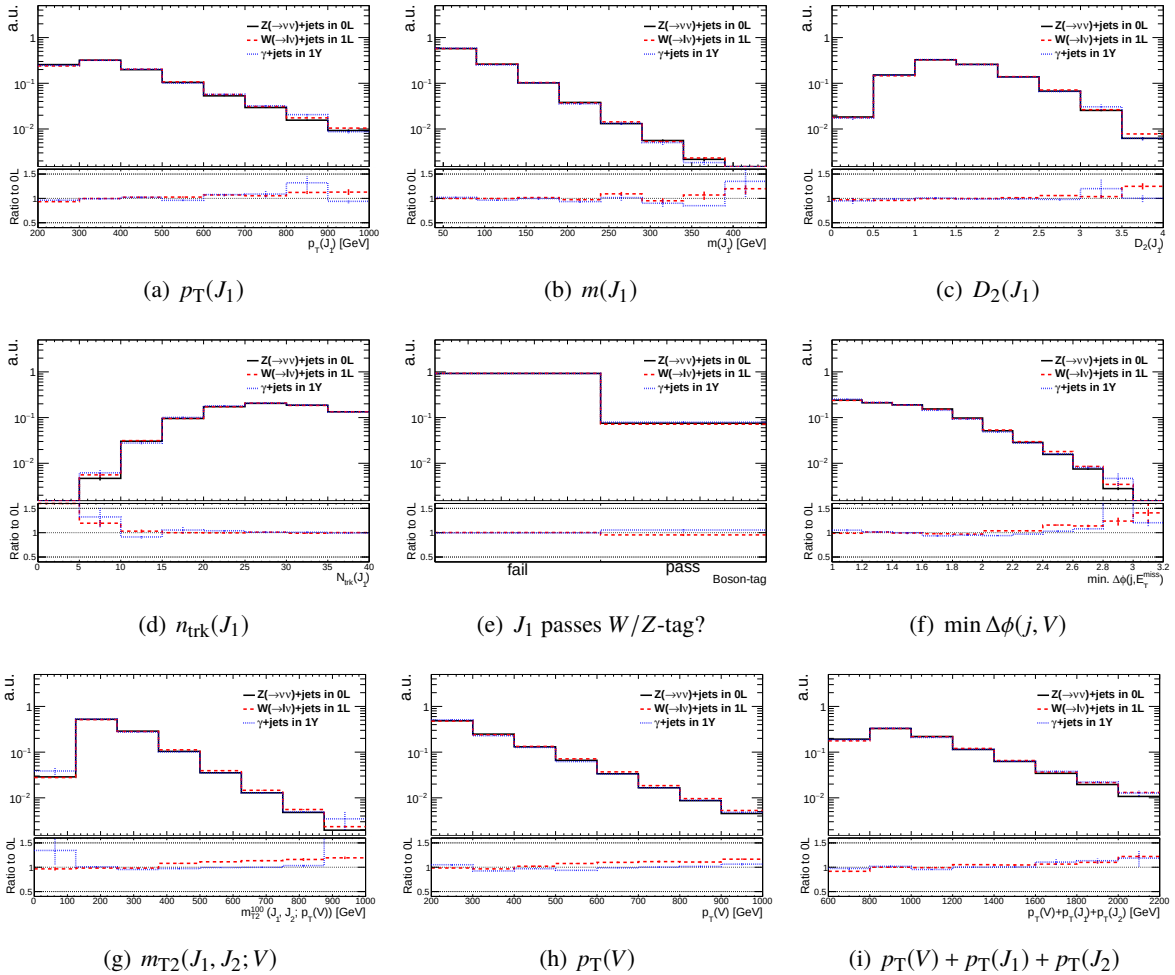

(a) $p_{\text{T}}(J_1)$ (b) $m(J_1)$ (c) $D_2(J_1)$

(d) $n_{\text{trk}}(J_1)$ (e) J_1 passes W/Z-tag? (f) $\min \Delta\phi(j, V)$

(g) $m_{\text{T2}}(J_1, J_2; V)$ (h) $p_{\text{T}}(V)$ (i) $p_{\text{T}}(V) + p_{\text{T}}(J_1) + p_{\text{T}}(J_2)$

Figure 8.13: Shape comparison between $Z(\rightarrow \nu\nu)$ + jets with the 0L, $W(\rightarrow \ell\nu)$ + jets with the 1L, and γ + jets with the 1Y preselections summarized in Table 8.5. To mimic the variables used in the 0L category, $E_{\text{T}}^{\text{miss}}$ is replaced into $p_{\text{T}}(W) = p_{\text{T}}(\ell) + E_{\text{T}}^{\text{miss}}$ or $p_{\text{T}}(\gamma)$.

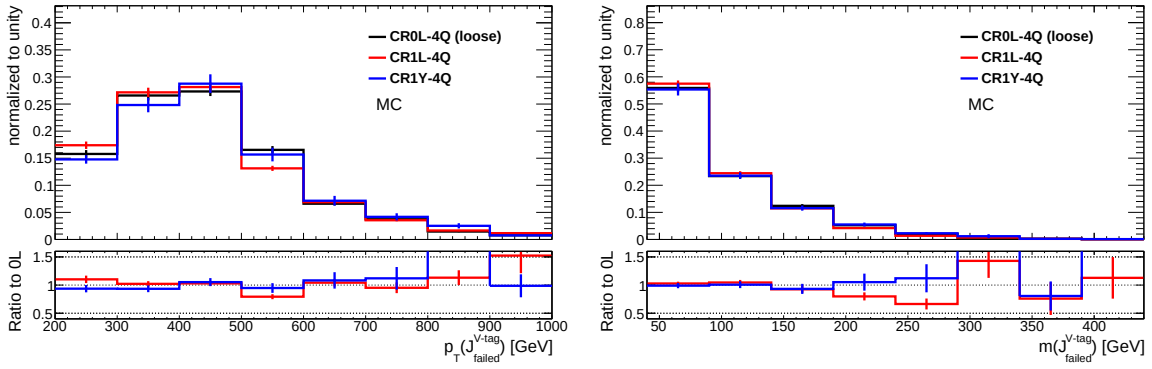

(a) p_{T}

(b) mass

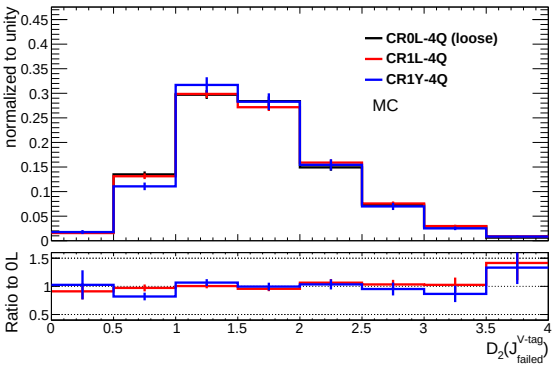

(c) D_2

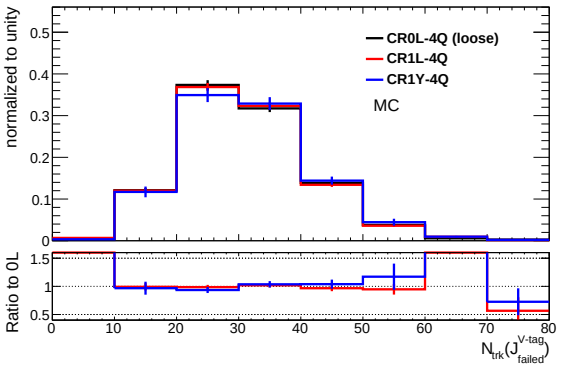

(d) n_{trk}

Figure 8.14: MC-to-MC comparison of et substructure variables of the failed jet for boson tagging requirements in CR0L-4Q, CR1L-4Q, and CR1Y-4Q. CR0L-4Q selections are loosened to $p_{\mathrm{T}}(V) + p_{\mathrm{T}}(J_1) + p_{\mathrm{T}}(J_2) > 1000$ GeV, $p_{\mathrm{T}}(V) > 200$ GeV, respectively, to align with CR1L-4Q and CR1Y-4Q.

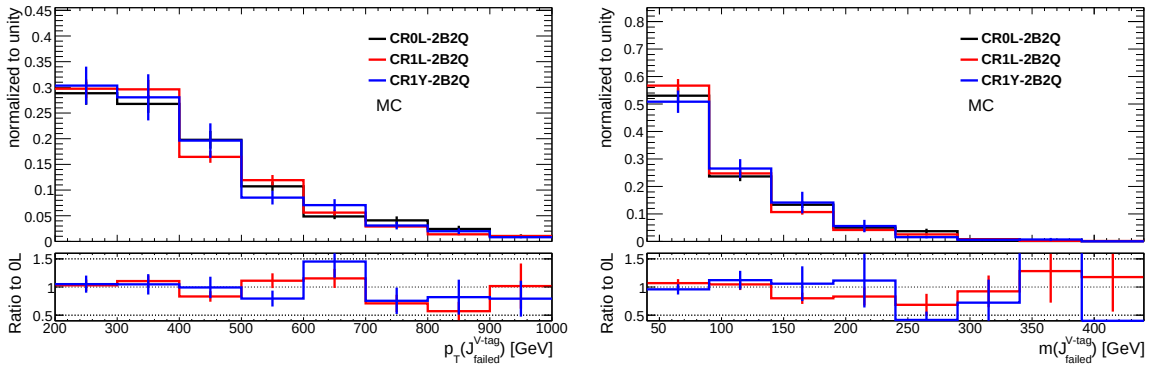

(a) p_{T}

(b) mass

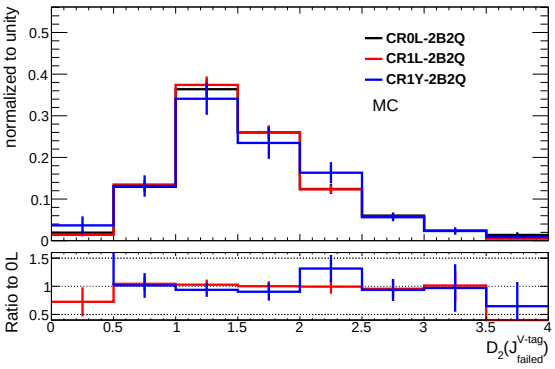

(c) D_2

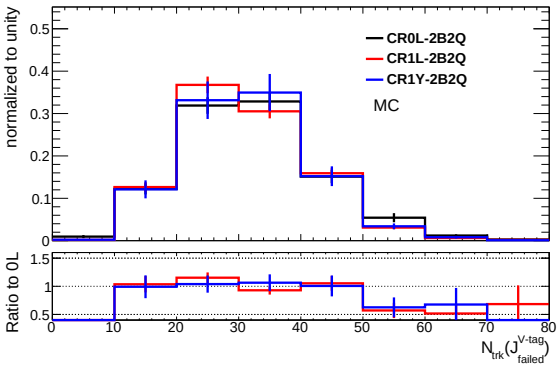

(d) n_{trk}

Figure 8.15: MC-to-MC comparison of jet substructure variables of the fail jet for boson tagging requirements in CR0L-2B2Q, CR1L-2B2Q, and CR1Y-2B2Q.

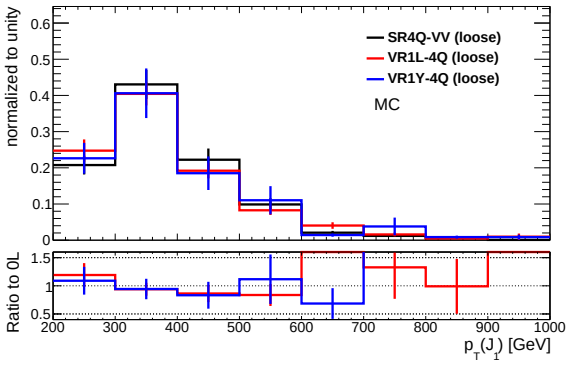

(a) leading large-R jet p_{T} in SR-4Q and VR-4Q bins

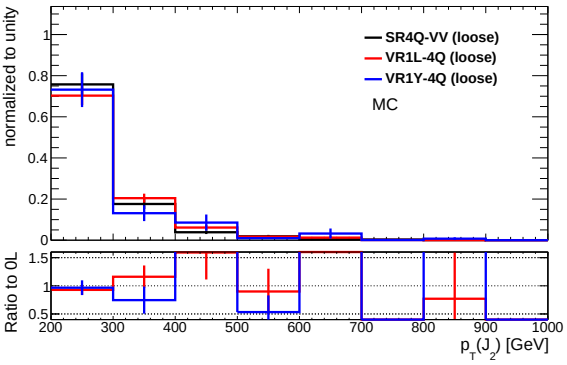

(b) sub-leading large-R jet p_{T} in SR-4Q and VR-4Q bins

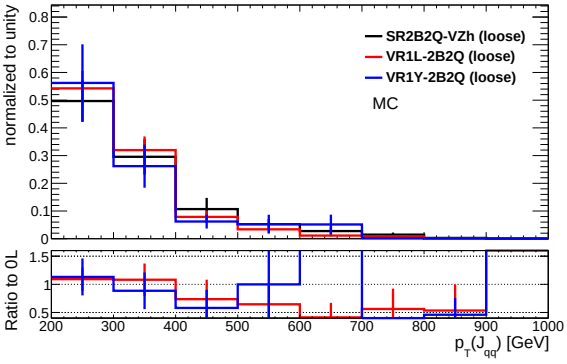

(c) J_{qq} p_{T} in SR-2B2Q and VR-2B2Q bins

Figure 8.16: MC-to-MC comparison of leading large-R jet p_{T} distributions (a) and sub-leading large-R jet p_{T} distributions (b) in SR-4Q-VV, VR1L-4Q, and VR1Y-4Q with loose kinematic selections, $p_{\mathrm{T}}(V) + p_{\mathrm{T}}(J_1) + p_{\mathrm{T}}(J_2) >$ 800 GeV, $p_{\mathrm{T}}(V) > 200$ GeV in all regions to maintain MC statistics. MC-to-MC comparison of $p_{\mathrm{T}}(J_{qq})$ distributions (c) in SR-2B2Q-VZh, VR1L-2B2Q, and VR1Y-2B2Q with loose kinematic selections, $p_{\mathrm{T}}(V) + p_{\mathrm{T}}(J_1) + p_{\mathrm{T}}(J_2) >$ 800 GeV.

8.3.5 Transfer factor comparison

To avoid the fluctuation of the data and MC samples, the transfer factor (TF) comparisons with loose kinematic selections ($p_{\mathrm{T}}(V) > 200$ GeV, $m_{\mathrm{eff}}(J, V) > 0.8$ TeV in the 4Q and 2B2Q categories, additionally $m_{\mathrm{T2}}(J_1, J_2; V) > 200$ GeV for the 2B2Q categories) are shown in Figure 8.17(a). The largest disagreement between the data and MC samples is observed in the 1Y-2B2Q region, but the difference is consistent within the statistical uncertainty. The transfer factors of the data and MC samples in the 0L-2B2Q region are in good agreement with the 1L-2B2Q and 1Y-2B2Q regions. Additionally, the transfer factors are good agreements in the 4Q regions of the 0L, 1L, and 1Y categories. The difference in the TFs between the 4Q and 2B2Q categories is a factor of 2 and this value is reasonable because

- The ratios in the 4Q categories are defined as (J_1 and J_2 pass)/((J_1 pass and J_2 fail) || (J_1 fail and J_2 pass)) $\sim 1/2\times$(pass/fail).
- In 2B2Q categories, the ratios defined as (J_{qq} pass)/(J_{qq} fail) $\sim$ (pass/fail).

A similar check is also performed using kinematic selections aligned to SRs and shown in Figure 8.17(b). In the 2B2Q categories, the TFs of MC samples are good agreements between the 0L, 1L, and 1Y categories. However, the TF in VR1L-4Q is larger than SR-4Q bins and VR1Y-4Q. The difference is mainly caused by the limitation of the MC statistics.

The TFs with various kinematic selections are considered to check trends of TFs in the 4Q categories. Figure 8.18 shows the TFs as a function of varying $p_{\mathrm{T}}(V) + p_{\mathrm{T}}(J_1) + p_{\mathrm{T}}(J_2)$ thresholds with constant $p_{\mathrm{T}}(V)$ selection ($p_{\mathrm{T}}(V) > 200$ GeV). There is no significant difference between the 0L and 1Y categories. However, some up-trends with respect to the 0L above 1.3 TeV in $p_{\mathrm{T}}(V) + p_{\mathrm{T}}(J_1) + p_{\mathrm{T}}(J_2)$ threshold are seen in the 1L category. This trend is caused by the MC stat fluctuation. The TFs between the data and MC samples in the 1Y category are consistent within the statistical error. However, some down-trend of data/MC above 0.9 TeV $p_{\mathrm{T}}(V) + p_{\mathrm{T}}(J_1) + p_{\mathrm{T}}(J_2)$ threshold is seen in the 1L category. As shown in Figure 8.19, the difference is caused by the data down fluctuation because a good agreement is found in $p_{\mathrm{T}}(V) + p_{\mathrm{T}}(J_1) + p_{\mathrm{T}}(J_2) < 1$ TeV.

Additionally, Figure 8.20 shows the trend of the 4Q TFs as a function of $p_{\mathrm{T}}(V)$ with loose $p_{\mathrm{T}}(V) + p_{\mathrm{T}}(J_1) + p_{\mathrm{T}}(J_2)$ cut ($p_{\mathrm{T}}(V) + p_{\mathrm{T}}(J_1) + p_{\mathrm{T}}(J_2) > 1$ TeV). For the MC TFs, there is no significant trend of $p_{\mathrm{T}}(V)$ cut values in the 0L/1L/1Y regions and good agreement between the 0L and 1L regions. There is no significant difference in the MC TFs between the 0L and 1Y because the MC fluctuation causes the 1Y/0L ratio deviation from unity.

For the data/MC of the TFs in the 1Y region, there is no dependency on $p_{\mathrm{T}}(V)$ cut values and a good agreement between the data and MC samples. In the 1L region, due to the data down fluctuation at $p_{\mathrm{T}}(V) + p_{\mathrm{T}}(J_1) + p_{\mathrm{T}}(J_2) \sim 1$ TeV, there is no trend for the $p_{\mathrm{T}}(V)$ cut values while the ratio is ~ 0.7

In conclusion, no significant trend in TF disagreement between the 0L, 1L, and 1Y categories is seen. As well as between the data and the MC samples, no disagreement is seen in the 1L/1Y categories. The results in VRs with full systematics are discussed in Section 10.1.

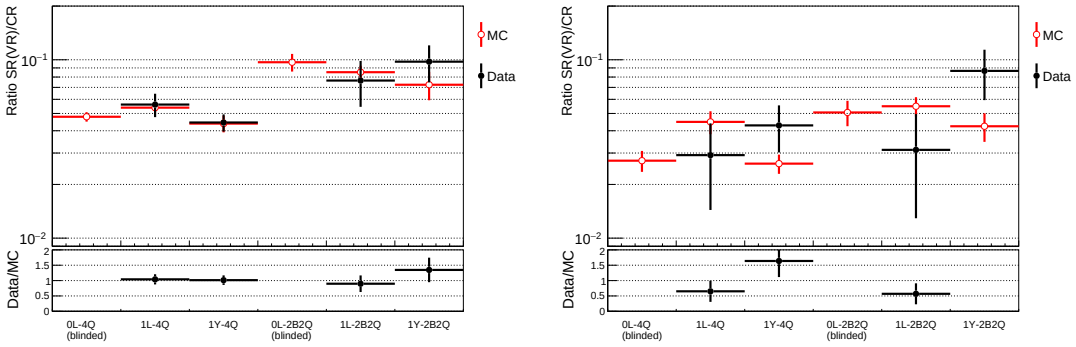

(a) loose selected region

(b) original SR/VR selection

Figure 8.17: Data/MC comparison of the transfer factors (the ratios in the yields) from CR-like regions to the SR-like regions with the kinematics matched between the 0L, 1L and the 1Y categories. (a) All the regions are loosened commonly to $p_{\mathrm{T}}(V) > 200$ GeV, $m_{\mathrm{eff}}(J,V) > 0.8$ TeV for the 4Q category, or $p_{\mathrm{T}}(V) > 200$ GeV, $m_{\mathrm{T2}}(J_1, J_2; V) > 200$ GeV, $m_{\mathrm{eff}}(J,V) > 0.8$ TeV for the 2B2Q category. (b) The kinematic selections in $m_{\mathrm{eff}}(J,V)(:= p_{\mathrm{T}}(V) + p_{\mathrm{T}}(J_1) + p_{\mathrm{T}}(J_2))$, $p_{\mathrm{T}}(V)$ and $m_{\mathrm{T2}}(J_1, J_2; V)$ in the 1L and 1Y categories are changed to match with that in the SRs: $p_{\mathrm{T}}(V) > 300$ GeV, $m_{\mathrm{eff}}(J,V) > 1.3$ TeV for the 4Q category and $p_{\mathrm{T}}(V) > 200$ GeV, $m_{\mathrm{T2}}(J_1, J_2; V) > 250$ GeV, $m_{\mathrm{eff}}(J,V) > 1$ TeV for the 2B2Q category.

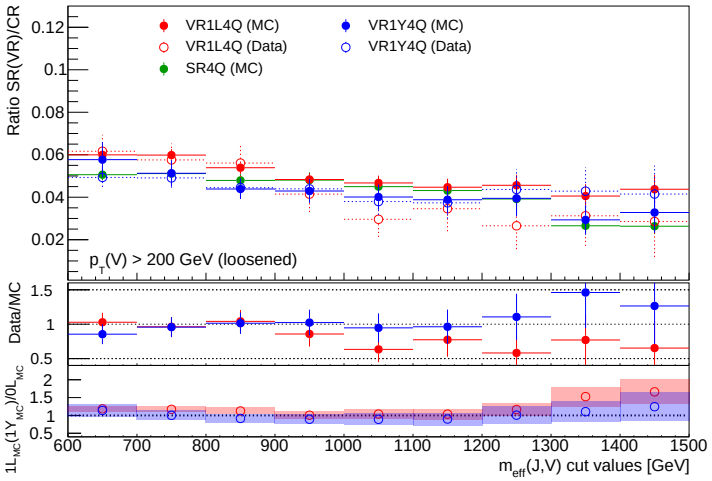

Figure 8.18: Top panel: TF (CR-like → SR/VR-like) for the 0L-4Q, 1L-4Q, and 1Y-4Q regions, as a function of the $p_{\mathrm{T}}(V) + p_{\mathrm{T}}(J_1) + p_{\mathrm{T}}(J_2)$ cut value. The MC TFs are shown in dashed lines and the data TFs (only for the 1L-4Q and 1Y-4Q) are illustrated in the solid ones. Middle panel: Data/MC of the TFs from the top panel. Bottom panel: MC-to-MC ratio of 1L/1Y MC TF to the 0L MC TF, with the $p_{\mathrm{T}}(V)$ cut aligned with the VR1L(1Y)-4Q ($p_{\mathrm{T}}(V) > 200$ GeV).

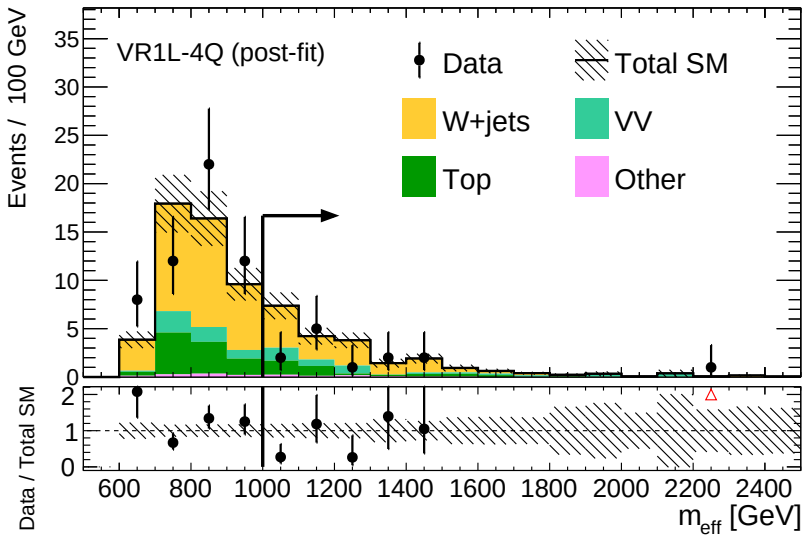

Figure 8.19: $p_{\mathrm{T}}(V) + p_{\mathrm{T}}(J_1) + p_{\mathrm{T}}(J_2)$ distribution in VR1L-4Q region (after fit).

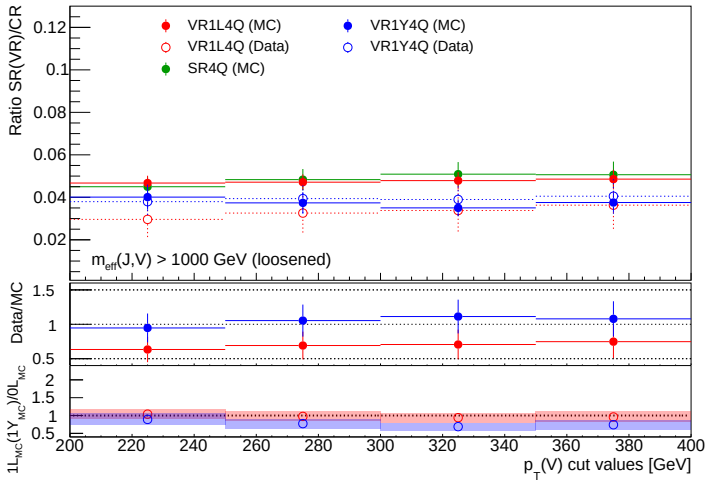

Figure 8.20: Top panel: TF (CR-like → SR/VR-like) for the 0L-4Q, 1L-4Q, and 1Y-4Q regions, as a function of the $p_{\mathrm{T}}(V)$ cut value. The MC TFs are shown in dashed lines and the data TFs (only for the 1L-4Q and 1Y-4Q) are illustrated in the solid ones. Middle panel: Data/MC of the TFs from the top panel. Bottom panel: MC-to-MC ratio of 1L/1Y MC TF to the 0L MC TF, with the $m_{\mathrm{eff}}(J,V)$ cut aligned with the VR1L(1Y)-4Q ($m_{\mathrm{eff}}(J,V) > 1.0$ TeV).

8.4 Physics Process Dependency in the Reducible Background Estimation and the Impact of the Composition Uncertainty

The extrapolation of quark- or gluon-initiated jets depends mainly on the boson tagging efficiency. Thus, it is necessary to check the differences of the jet variables between the different physics processes in each region.

Figures 8.21 and Figure 8.22 show a comparison of the physics processes of the quark- or gluon-initiated jet distribution with the only 0L-4Q/1Y-4Q preselections. Other distributions in each preselected region are shown in Appendix O. Generally, the V + jets, VV, and $t + X$ have similar distributions of the jet substructure. However, in $t\bar{t}$ events, there is a little difference in p_{T}, D_2, and n_{trk}. These differences are due to the origin of the jets: $t\bar{t}$ has much more jets from gluons than the other; in the low p_{T} region, the gluon-initiated jets have larger track multiplicity and higher boson tagging rejection than the quark-initiated jets. Additionally, a difference of n_{trk} between γ + jets and $V + \gamma$ is large in Precut1Y4Q. Since n_{trk} increases to the jet p_{T}, the difference is derived from the p_{T}. Thus, there is no significant difference in jet substructure variables derived from the physics processes. These results in the differences in the transfer factor (TF) (defined by the yield ratio y(SR/VR)/y(CR)), as shown in Figure 8.23. The TF is consistent across physics processes, while the error in the MC statistics is large.

If the process breakdowns are modeled incorrectly in the MC simulation, the remaining TFs can affect the final estimation. To check the impact of this potential breakdown uncertainty, we shift the normalization of one process up or down by a factor of two and evaluate the response in the TF of the total reducible background. The results are shown in Figure 8.24. For the $t + X$ process (mainly $t + W$), a factor of 10 is used as the down-variation to account for the interference between $t\bar{t}$ and $t + W$ production [146]. This factor is finally determined by considering the difference between diagram removal and diagram subtraction methods [146]. The maximum difference in CR0L-4Q is ~ 9.17 except in the low MC statistical regions. A factor of 10 is assigned as the conservative evaluation for $t + X$ process because it is a minor background in all regions and is not significantly affected. The envelope of the transfer factor variation shown in Figure 8.24 is quoted as the transfer factor uncertainty for the reducible backgrounds. For example, the largest deviation, 6% from the $Z(\rightarrow \nu\nu)$ + jets variation, is quoted for all SR-4Q bins.

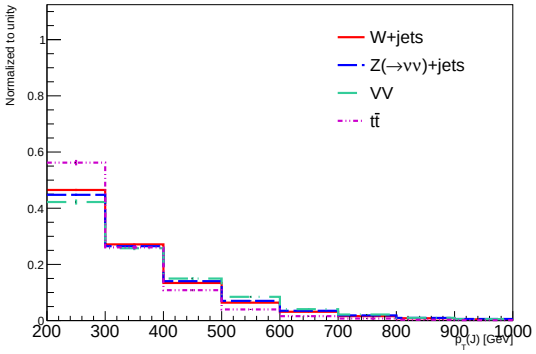

(a) p_{T}

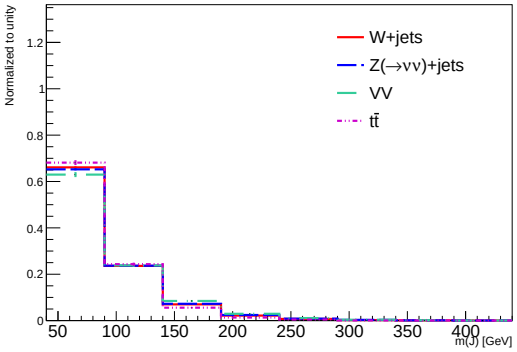

(b) Mass

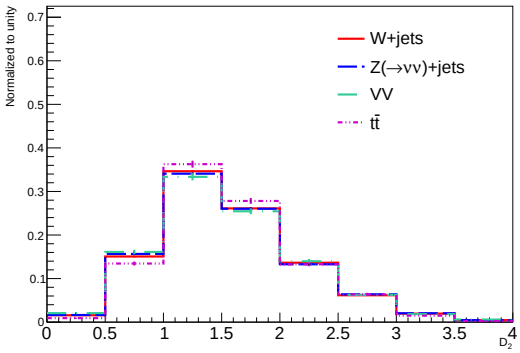

(c) D_2

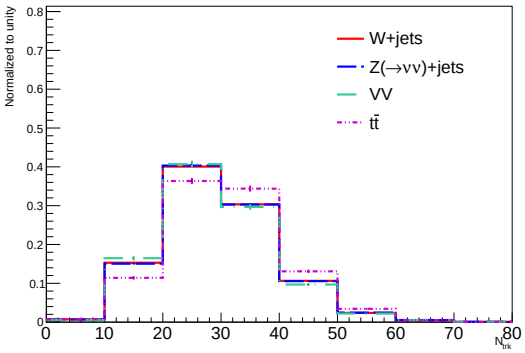

(d) n_{trk}

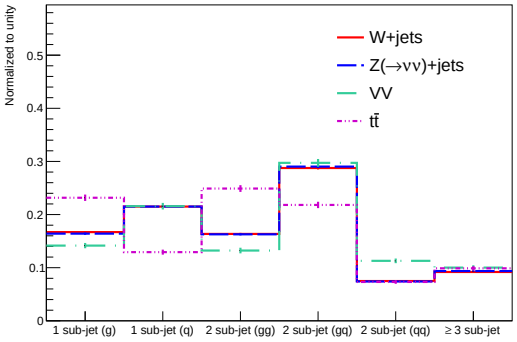

(e) The hardest associated truth particle of spatially matched small-R jets

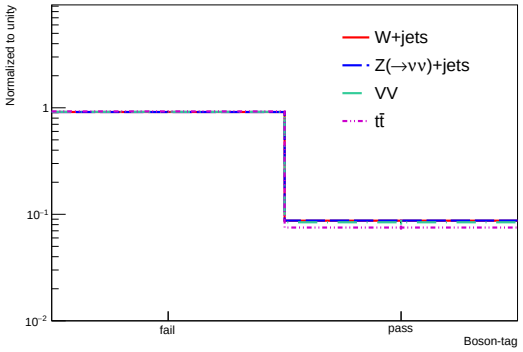

(f) Passes W/Z-tag?

Figure 8.21: The kinematic distributions of large-R jets which originate from quarks or gluons with Precut0L4Q in various physics processes. All distributions are normalized to unity. Only the main backgrounds of these regions are shown. The large-R jets are selected by the truth information, as described in Appendix E. A single event fills multiple entries if more than one such jet is found.

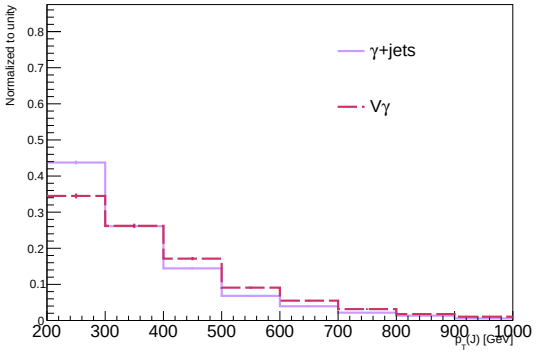

(a) p_{T}

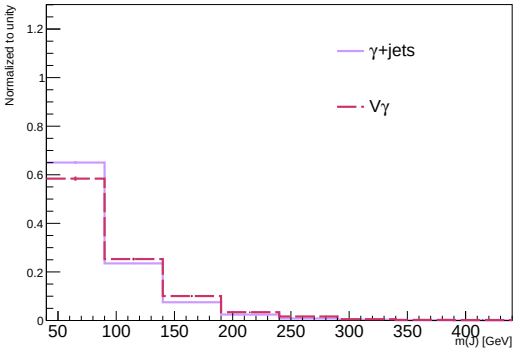

(b) Mass

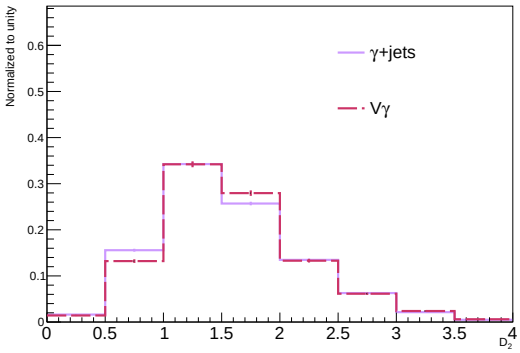

(c) D_2

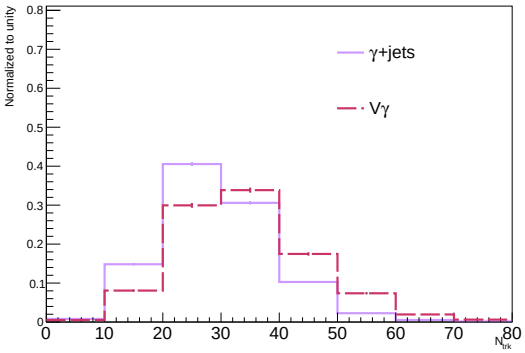

(d) n_{trk}

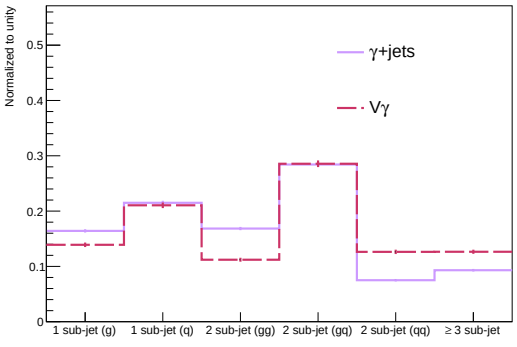

(e) The hardest associated truth particle of spatially matched small-R jets

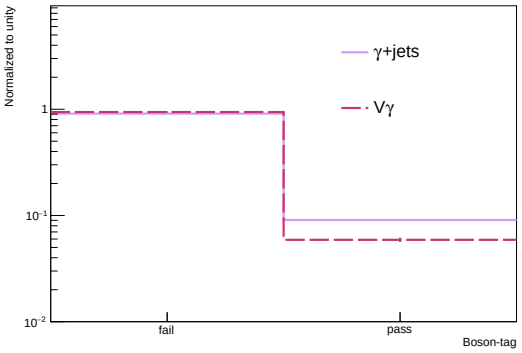

(f) Passes W/Z-tag?

Figure 8.22: The kinematic distributions of large-R jets which originate from quarks or gluons with Precut1Y4Q in various physics processes. The same descriptions as Figure 8.21 are applied.

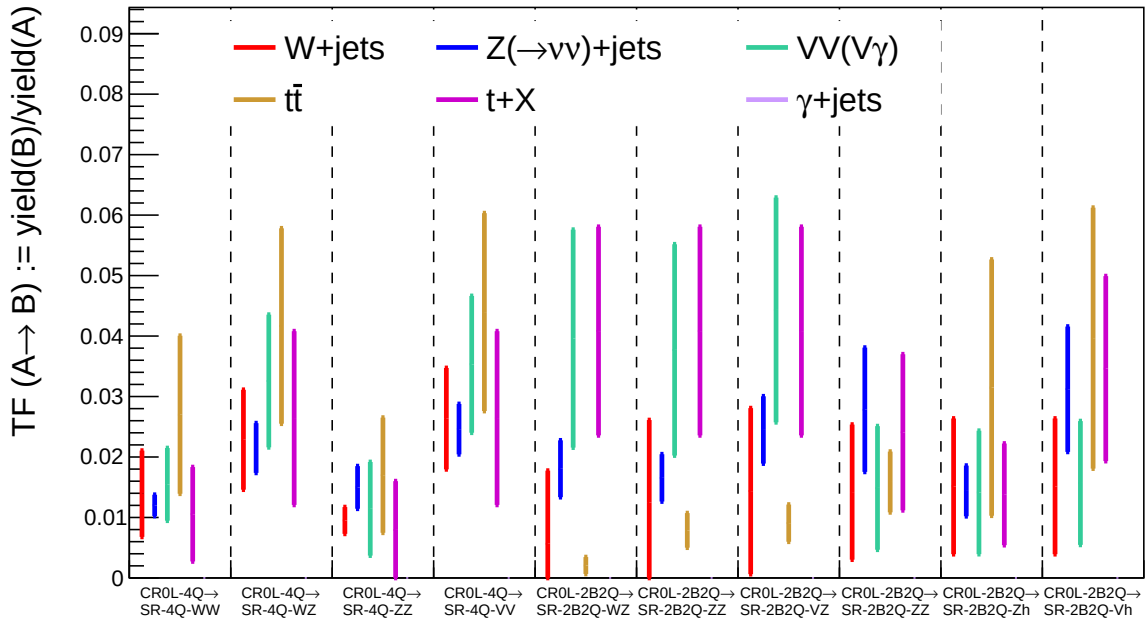

(a) SRs

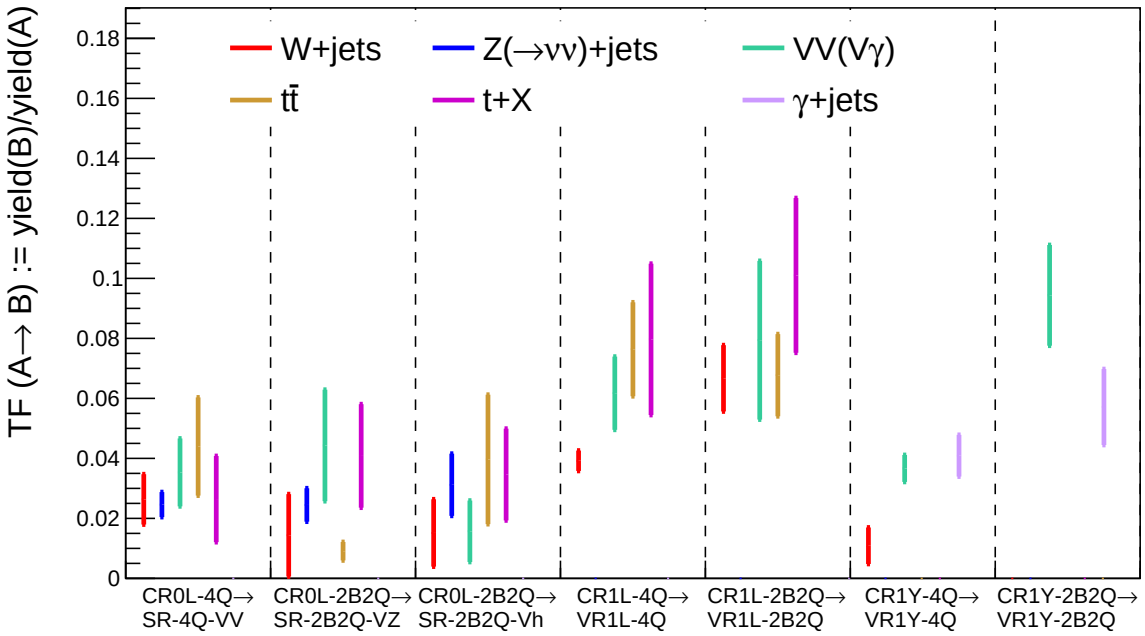

(b) VRs (vs SRs)

Figure 8.23: The TFs of the individual physics component are calculated using the MC samples. The TF is defined by the yield ratio of an SR (VR) to the corresponding CR. The error bars represent the MC stat errors. Note that some SRs are mutually overlapping.

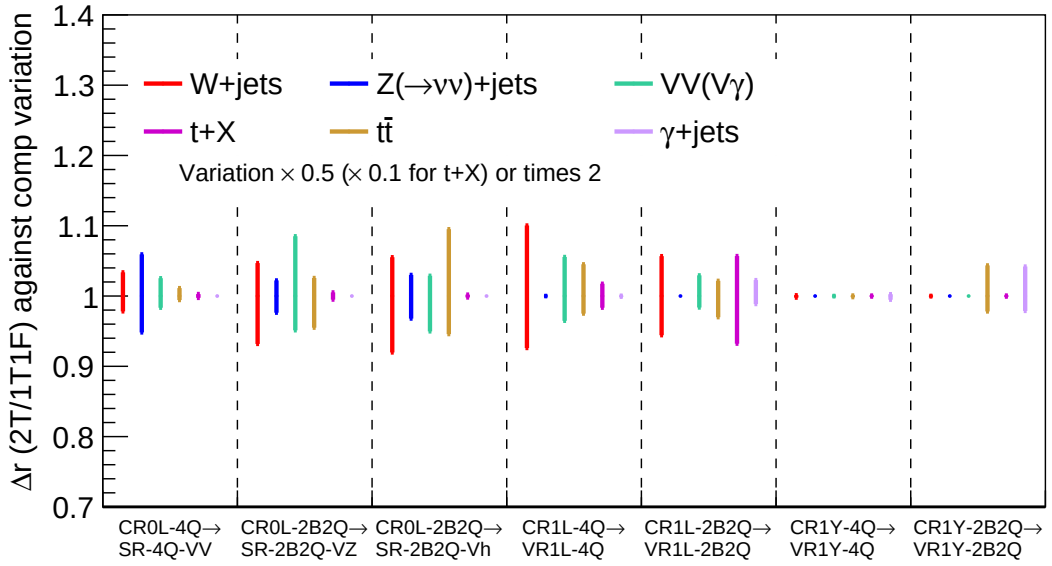

Figure 8.24: The change in the transfer factors (SR/CR or VR/CR ratio) for the sum of the reducible BGs, caused by shifting the MC normalization of each process up and down by a factor of 2 (factor of 10 for single-top down-variation). The maximum value is assigned as a modeling uncertainty for reducible backgrounds.

8.5 Irreducible Backgrounds Estimation

The irreducible backgrounds, such as $t\bar{t} + X$ and VVV, have a small contribution to the SRs and are estimated from MC samples directly. For VVV process, the dominant process is $VV(\rightarrow qqqq) + Z(\rightarrow \nu\nu)$. In ATLAS and CMS experiments, VVV has been observed [147, 148] by multi-lepton analyses. However, the data size is insufficient to define the control and validation regions. Additionally, the purity of VVV will be poor by loosening selections for sufficient data statistics. For the modeling validation of $t\bar{t} + X$, a validation region with three leptons called "VRTTX" is defined.

$t\bar{t}+X$ contributions are negligible in SR-4Q bins due to $n^{\text{trk}}_{b-\text{jet (inside J)}} \leq 1$. However, they account for $\sim 10\%$ in the SR-2B2Q bins. The dominant process of $t\bar{t} + X$ in SR-2B2Q bins is $tt(\rightarrow bqqbqq) + Z(\rightarrow \nu\nu)$. For validation of kinematic distributions and the normalization of $t\bar{t} + X$, we define VRTTX with the selections summarized in Table 8.6. VRTTX is designed as a VR for $tt + Z$, such as $tt\ (\rightarrow bqqblv) + Z(\rightarrow ll)$. One of the top quarks is required to semi-leptonically decay to suppress the contributions from the other background, and Z boson is required to decay into a charged lepton pair. At least one large-R jet from the top quark is required, and the jet contains two b-tagged track jets inside.

To maintain sufficient statistics, looser kinematic selections apply to VRTTX, without corresponding Precut0L to $E_{\text{T}}^{\text{miss}} > 200$ GeV, $p_{\text{T}}(J_{qq}) > 200$ GeV, and $\min \Delta\phi(j, E_{\text{T}}^{\text{miss}}) > 1.0$. Alternative variables in VRTTX are used to verify the distribution. $E_{\text{T}}^{\text{miss}}$ in the 0L category represents the p_{T} of Z boson because most $t\bar{t} + X$ processes are $tt(\rightarrow bqqbqq) + Z(\rightarrow \nu\nu)$. Thus, the p_{T} of di-lepton system reconstructed as Z candidate from the opposite sign same flavor leptons is a good proxy. Additionally, $\min \Delta\phi(j, Z)$ is used instead of $\min \Delta\phi(j, E_{\text{T}}^{\text{miss}})$. Since $p_{\text{T}}(J_{qq})$ represents the p_{T} of W boson from top quark in the

Table 8.6: Definition of VRTTX to validate $t\bar{t} + X$ modelling. ℓ_3 represents third highest p_{T} lepton.

	VRTTX
Trigger	Single-e/μ
Track jet cleaning	yes
n_{lepton}	$= 3$
$p_{\mathrm{T}}(\ell_1)$ [GeV]	> 30
$p_{\mathrm{T}}(\ell_3)$ [GeV]	> 10
$n_{\mathrm{Large-}R\ \mathrm{jets}}$	≥ 1
$n(J_{bb})$	$= 1$

0L category, $p_{\mathrm{T}}(W)$ can be used as an alternative variable. For the reconstruction of W boson, the rest lepton, which is not used for the di-lepton system, and $E_{\mathrm{T}}^{\mathrm{miss}}$ treated as a neutrino is used. The physics sub-process in VRTTX and the 0L-2B2Q regions are similar between the 0L-2B2Q ($tt + Z(\rightarrow \nu\nu)$) and VRTTX ($tt + Z(\rightarrow ll)$), as shown in Figure 8.25.

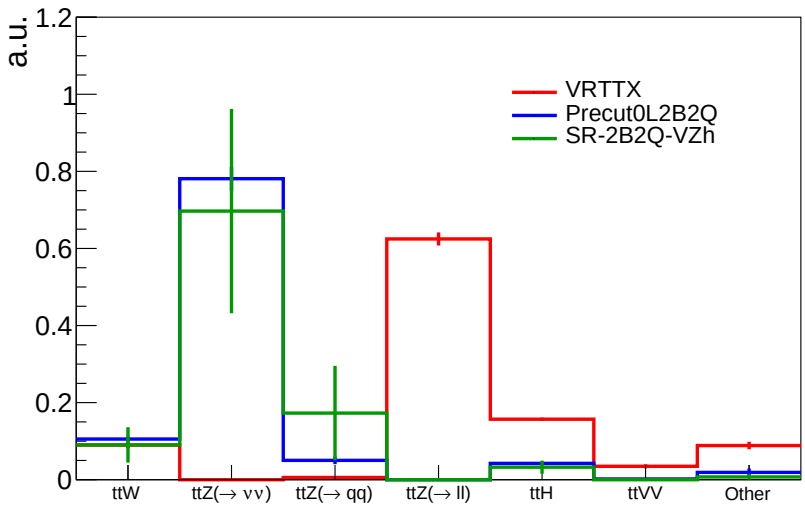

Figure 8.25: Fraction of $t\bar{t} + X$ processes in VRTTX, Precut0L and inclusive SR-2B2Q.

The best-fit normalization factor for $t\bar{t} + X$ is 1.68 ± 0.32 if it allows floating. The distributions in VRTTX after fit are shown in Figure 8.26. While there was a large deviation of MC normalization from data in this region, the distributions between the data and MC samples are in good agreement. The large normalization factor for $t\bar{t} + X$ is caused by the mis-modeling of $2b$-tagged large-R jets. Thus, the yields of $t\bar{t} + X$ samples are estimated using MC samples directly, and 68% flat uncertainty is assigned as the modeling uncertainty on the $2b$-atgged large-R jets.

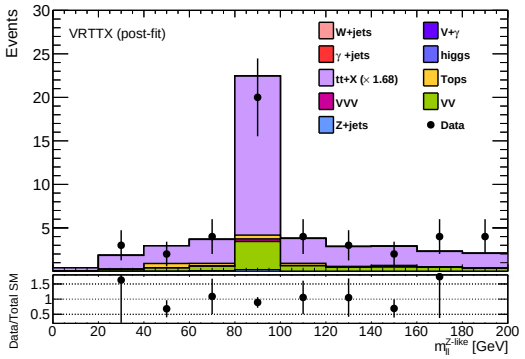

(a) $m(Z)$

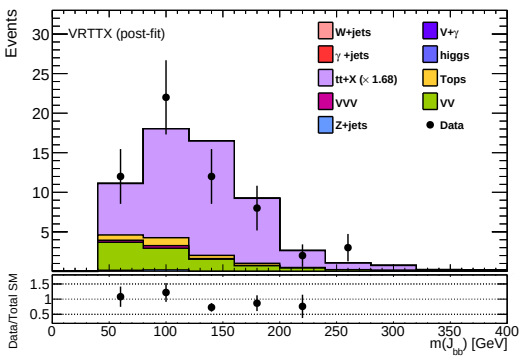

(b) $m(J_{bb})$

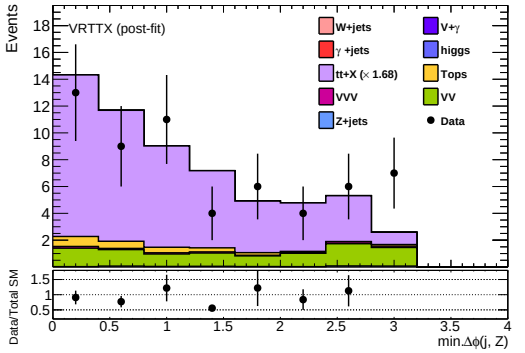

(c) $\min \Delta\phi(j, Z)$

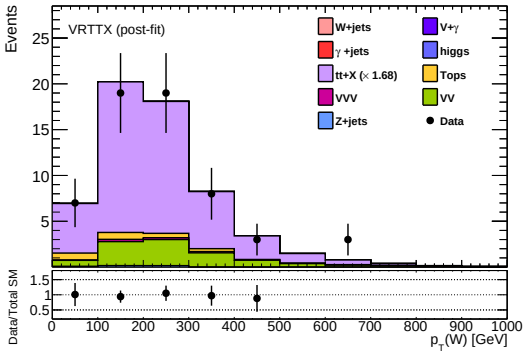

(d) $p_{\mathrm{T}}(W)$

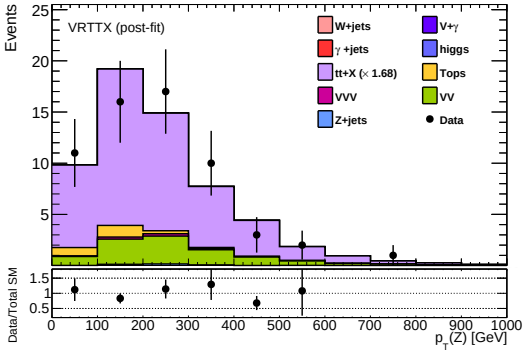

(e) $p_{\mathrm{T}}(Z)$

Figure 8.26: Kinematic distributions after fit in VRTTX. Only $t\bar{t} + X$ is scaled by the normalization factor (= 1.68). There is no trend between data and MC samples.

9 Systematic Uncertainties

Systematic uncertainty is categorized into experimental and theoretical uncertainties. The experimental uncertainties derive from experimental techniques such as the modeling of particle reconstruction in the detector simulation, the measurement of the luminosity, and pile-up. The difference between the data and MC samples is corrected by "scale factors," which could also cause systematic uncertainties. The boson tagging uncertainties are also included in the experimental uncertainties. The theoretical uncertainties are due to differences among the simulation method.

In this thesis, output variables of the $W/Z \to qq$ tagging are employed to estimate the reducible backgrounds, as explained in the previous chapter. The normalization factor and the extrapolation from the CRs to SRs are used. Then, the systematic uncertainties for reducible backgrounds are evaluated as originating from the normalization factor. For the irreducible background and the SUSY signals, the systematic uncertainties affect the yield in each region.

9.1 Large-R Jets

The uncertainties for large-R jets from jet energy scale (JES), jet energy resolution (JER), jet mass scale (JMS), and jet mass resolution (JMR) uncertainties are considered. The estimation of the uncertainties is described in Ref.[109].

Jet Energy Scale (JES) We use "in-situ" methods to correct residual difference between the data and MC samples, as described in Section 5.3.1.2. In this method, three control samples, Z + jets, γ + jets, and multi-jet, are used to estimate the JES uncertainty depending on the p_{T} of the jet; Z + jets and γ + jets events are used for calibrating large-R jets, which have $p_{\mathrm{T}} \geq 200$ GeV and $|\eta| < 0.8$, and multi-jets events are used to calibrate higher p_{T} large-R jets ($p_{\mathrm{T}} \geq 300$ GeV and $|\eta| < 0.8$). The uncertainties in the in-situ calibration are shown in Figure 5.5. The differences of the calibration factors between MC samples using different generators and a combination of three measurements are assigned as systematic uncertainties.

An additional uncertainty depending on the flavor of large-R jets is also considered. This additional uncertainty is zero for gluon- and quark-initiated jets and non-zero for large-R jets originating from W/Z boson and top quarks. The total uncertainties for the large-R jets are shown in Figure 9.1.

Jet Energy Resolution (JER) The jet energy resolution is measured in two η regions; one in the central region ($|\eta| < 0.8$) and the other in the forward region ($0.8 < |\eta| < 2.0$). An absolute 2% uncertainty for jet energy resolution estimated by the differences of the width in the truth and reconstructed jet energy distributions is assigned.

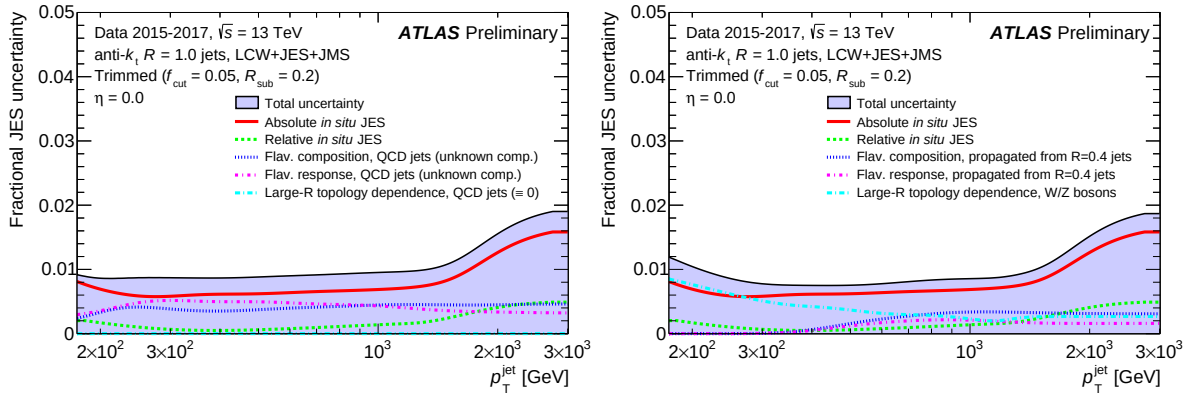

(a) Gluon- and quark-initiated jets

(b) Jets resulting from hadronically decaying W/Z boson

Figure 9.1: The uncertainty as a function of jet p_{T} of gluon- and quark-initiated jets (a) and jets resulting from hadronically decaying W/Z boson (b). Flavor uncertainties are propagated from small-R jets. "Relative *in situ* JES" are uncertainties from the η inter-calibration, and "Absolute *in situ* JES" includes all uncertainties of in-situ measurement in the central region. Total uncertainties are determined as the quadruple sum of each component [110].

Jet Mass Scale (JMS) and Jet Mass Resolution (JMR) For the jet mass resolution uncertainty, the jet mass response, defined as the ratio of the reconstructed mass to the true jet mass ($\mathcal{R} = m^{\mathrm{reco}}/m^{\mathrm{true}}$) is measured in the MC based study. The measurement method is described in Ref.[149]. A relative 20% uncertainty extracted from the jet mass distribution using a Gaussian width is assigned.

The jet mass scale is estimated in the R_{trk} method, as described in Section 5.3.1.2. In this method, three generators are used to estimate the theoretical uncertainties, and three types of mis-modeling for tracking (efficiency, fake rates, and q/p_{T} bias) as sources of uncertainties are considered. The systematic uncertainty evaluated in the R_{trk} method is shown in Figure 9.2. In the higher p_{T} region, the double ratio of MC samples (Pythia 8) to data in R^{m}_{trk} is ~ 0.96. The deviation from unity is assigned as a systematic uncertainty and is shown as a red line. This uncertainty from the R_{trk} method is a dominant source of the JMS uncertainty.

The JMS/JMR uncertainties for $Z/h \to bb$ tagging need to be estimated, and the differences between the data and MC samples are corrected. For the irreducible backgrounds, they are evaluated on the relative yields, such as the ratio of the yields with the JMS/JMR systematic variations to the nominal MC samples. The uncertainties for the reducible backgrounds are evaluated as systematic uncertainties on the transfer factor, such as the double ratio in the CRs and SRs with the JMS/JMR systematic variations to the nominal. For the SUSY signals, the JMS/JMR systematic uncertainties on the acceptance of $m(J_{bb})$ selections are estimated. The relative yields of each signal process in each SR are calculated with systematic uncertainties. There is no significant dependency on the signal mass. Thus, all signal samples are summed up for the estimation. The relative yields of the JMS uncertainty are shown in Figure 9.3. For the JMR uncertainty, the relative yields are shown in Figure 9.4. There is no problem while these uncertainties are large in not proper SRs for the SUSY signals due to the MC statistics. The systematic uncertainties of the $Z/h \to bb$ tagging are fully correlated with them on the normalization factors of kinematic extrapolations.

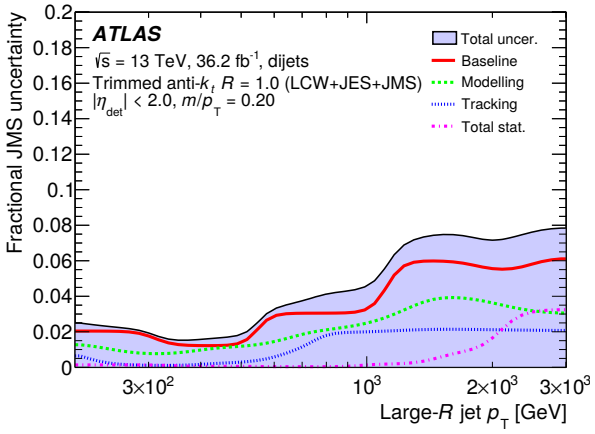

Figure 9.2: The uncertainty in the relative jet mass scale as a function of the large-R jet p_{T} with large-R jet $m/p_{\mathrm{T}} = 0.2$. The baseline uncertainty represents the deviation of the double ratio from unity for Pythia 8. The modeling uncertainty represents the largest deviation from the unity of alternative MC generators. The tracking uncertainty represents the quadratic sum of the effect of three tracking variations [109].

9.2 Boson Tagging Efficiency Uncertainty

As measurements of the scale factor of $W/Z \to qq$ tagging efficiency are in Sections 6.1.3 and 6.1.4, a short summary is presented in this section.

The uncertainties derived from the physics objects are estimated as the impact on the $W/Z \to qq$ tagging efficiency. Additionally, theoretical and modeling uncertainties are also estimated with different generators considering the cross-section uncertainty. As discussed in Section 6.1.3, the uncertainty on smoothing the SF, the high p_{T} extrapolation, and the W-to-Z extrapolation in the signal SF measurement are also considered. The total uncertainties for the tagged jets are shown in Figure 9.5. The dominant uncertainty sources are derived from the modeling and extrapolations.

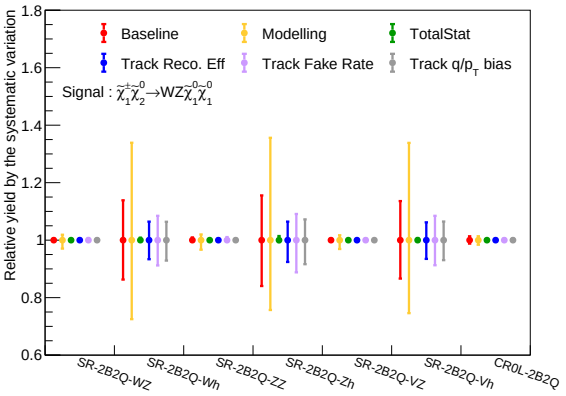

(a) $\tilde{\chi}_1^{\pm}\ \tilde{\chi}_2^0 \to WZ\tilde{\chi}_1^0\ \tilde{\chi}_1^0$ signal

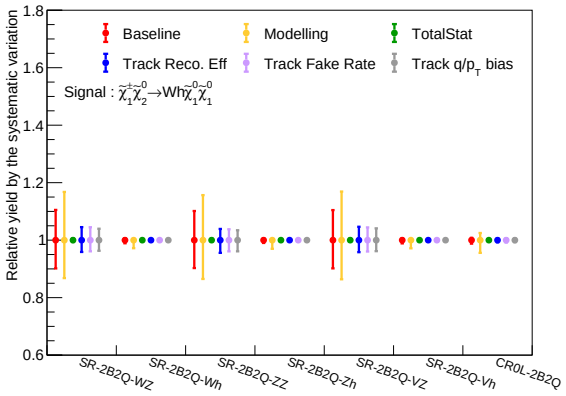

(b) $\tilde{\chi}_1^{\pm}\ \tilde{\chi}_2^0 \to Wh\tilde{\chi}_1^0\ \tilde{\chi}_1^0$ signal

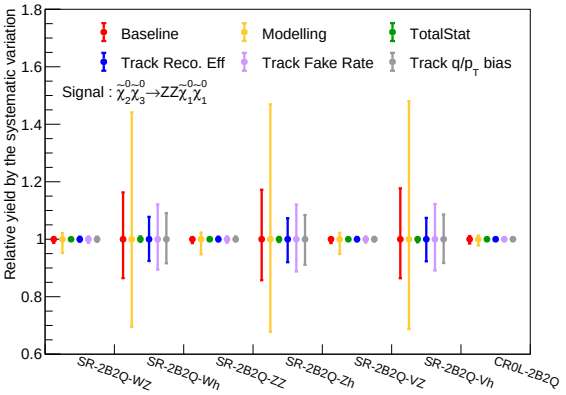

(c) $\tilde{\chi}_2^0\ \tilde{\chi}_3^0 \to ZZ\tilde{\chi}_1^0\ \tilde{\chi}_1^0$ signal

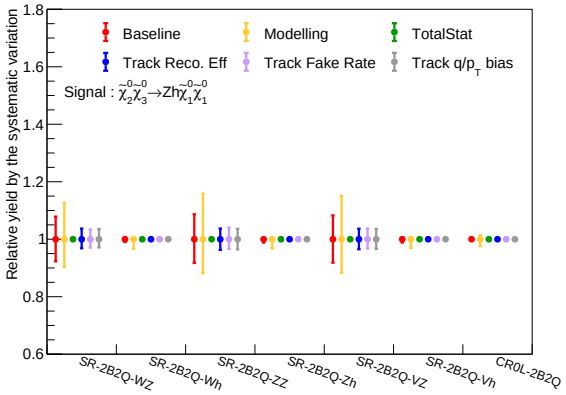

(d) $\tilde{\chi}_2^0\ \tilde{\chi}_3^0 \to Zh\tilde{\chi}_1^0\ \tilde{\chi}_1^0$ signal

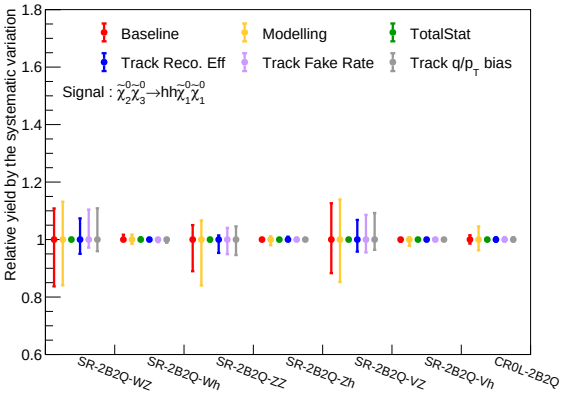

(e) $\tilde{\chi}_2^0\ \tilde{\chi}_3^0 \to hh\tilde{\chi}_1^0\ \tilde{\chi}_1^0$ signal

Figure 9.3: The relative acceptance change in each signal and control region of the 0L-2B2Q category. The differences are due to the JMS variations in Figure 9.2. All the statistics from each signal combined as no statistically significant mass dependence on the acceptance is found. "Track Reco. Eff" represents the track reconstruction efficiency and related uncertainty.

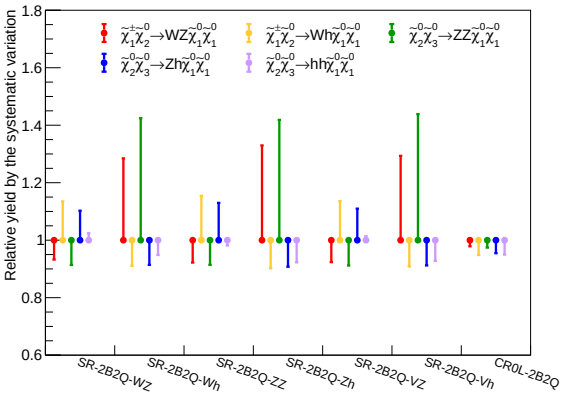

Figure 9.4: The relative acceptance change in each signal and control region of the 0L-2B2Q category. The differences are due to the JMR variation.

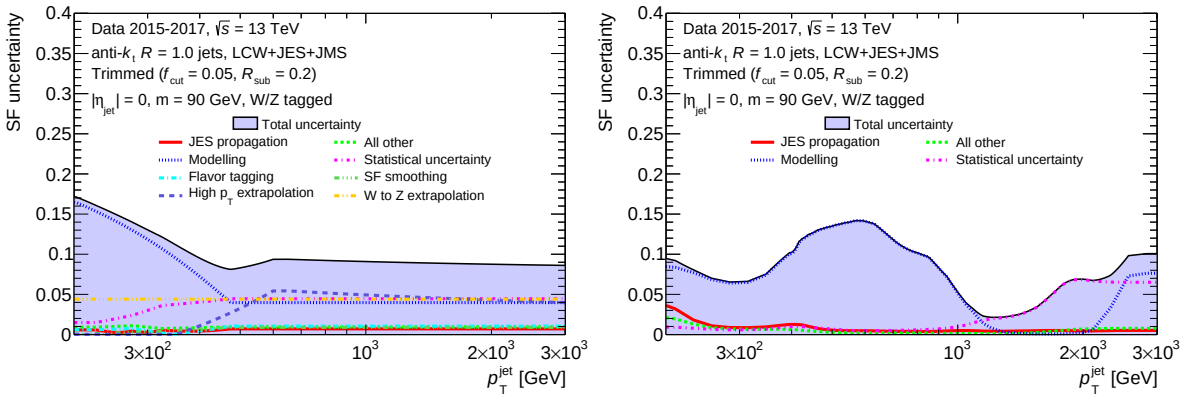

(a) Signal efficiency SF uncertainty

(b) Background efficiency SF uncertainty

Figure 9.5: Uncertainties for signal jets (a) and background jets (b) passing the $W/Z \to qq$ tagging. The red line represents jet energy scale uncertainties. "Modeling uncertainty" is derived from generator differences. "Flavor tagging" is the uncertainty of the event selection for the signal efficiency measurement. "SF smoothing" uncertainty is derived from the choice of binnings in the signal efficiency measurement. "High p_{T} extrapolation" and "W to Z extrapolation" uncertainties are derived from extrapolating the W boson tagging efficiency measurement to high p_{T} region and Z boson tagging, respectively. "All other" (the light green line) includes other sources of uncertainties than the ones described above.

9.3 Other Experimental Uncertainties

The uncertainties on electrons, muons, small-R jets, and $E_{\mathrm{T}}^{\mathrm{miss}}$, which are smaller than ones of large-R jets, are summarized in Table 9.1. Energy scales and resolutions of small-R jets, electrons, and muons, are considered because they are used to calculate $E_{\mathrm{T}}^{\mathrm{miss}}$. Additionally, the efficiency of reconstructed objects is considered. The pile-up correction and the luminosity measurement are taken into account. More detail is described in Appendix P.

Table 9.1: Minor uncertainties of the objects except for large-R jets.

Objects	Systematic sources	Impact
Small-R jets	Jet energy scale, Jet energy resolution, Jet Vertex Tagger	$< 5\%$
Track jets	b-tagging	$< 5\%$
Electrons	Energy scale, Energy resolution Efficiency measurement (reconstruction, identification, isolation, trigger)	$< 1\%$
Photons	Efficiency measurement (reconstruction, identification, isolation, trigger)	$< 1\%$
Muons	Momentum resolution (in ID, MS), Momentum scale Efficiency measurement (reconstruction, identification, isolation, trigger)	$< 1\%$
$E_{\mathrm{T}}^{\mathrm{miss}}$	Scale and resolution of soft term	$< 2\%$
Pile-up	Correction of the difference between the data and MC	$< 2\%$
Luminosity	Luminosity measurement	1.7%

9.4 Theoretical Uncertainty

Some physics parameters derived from the MC samples generations for the signal and backgrounds are considered. Thus, the choice of parameters is assigned as theoretical uncertainties. For example, the uncertainties come from Parton Distribution Function (PDF) and the strong coupling constant (α_s) are evaluated as the difference in the yield in each region using different PDFs and α_s values. The variations on PDF and α_s are based on the nominal choice (NNPDF [96, 150]) and on alternative PDF (MMHT2014 [151] and CT14 [152]).

Other uncertainties from parameters in the MC sample generation are considered. For example, the factorization scale (μ_F) and the renormalization scale (μ_R), which is introduced in Section 4.2.1, is considered. This uncertainty is evaluated as the difference in the yield with varying the parameters by a factor of 2 and 0.5. Additional uncertainty for W/Z+jets modeling is the matrix element matching uncertainty. This uncertainty is evaluated as a difference in the yields with different scales using the nominal value 20 GeV and the up/down variation value (30/15 GeV). The other uncertainty is related to the scale for the resummation of soft gluon emission. This uncertainty is evaluated as the difference in the yield by varying the parameters by a factor of 4 and 0.25.

The factorization and renormalization scale uncertainties for the SUSY signals are also considered. This uncertainty is evaluated as the difference in the yield with varying the parameters of the matrix-element to parton-shower matching parameter (nominal value: $m_{\tilde{\chi}_{\mathrm{heavy}}}/4$) by a factor of 2 and 0.5, parton shower tuning and radiation. Relative 10% uncertainty is assigned as the total signal theoretical uncertainty,

conservatively. Additionally, the signal cross-section uncertainty is considered. This uncertainty is mainly driven by the PDF uncertainty [153] and typically 6-20%.

9.5 Summary of Systematic Uncertainties

In addition to the uncertainties discussed above, statistical errors in control regions (CRs) are considered. The statistical errors in CRs affect the normalization factors of the reducible backgrounds.

Figure 9.6 shows the total uncertainty and the breakdown in the signal regions (SRs) and the validation regions (VRs) by the fit without signal contribution. The "Reducible BG composition" represents the composition of reducible backgrounds is discussed in Section 8.4. The dominant uncertainty in the SRs is the statistics of MC samples, mainly from $Z \rightarrow \nu\nu$+jets, which is smaller than the statistical errors in data, as discussed later in Section 10.2. The systematic uncertainties in all the SRs of the 4Q and 2B2Q categories are similar.

Major systematic sources in each SR are shown in Table 9.2 and Table 9.3. The dominant sources of uncertainty are the data and MC statistical uncertainties. The sub-dominant sources are uncertainty originating from the background components in the CRs, W/Z-tagging uncertainties for quark-/gluon-initiated jets, and theoretical uncertainties of backgrounds.

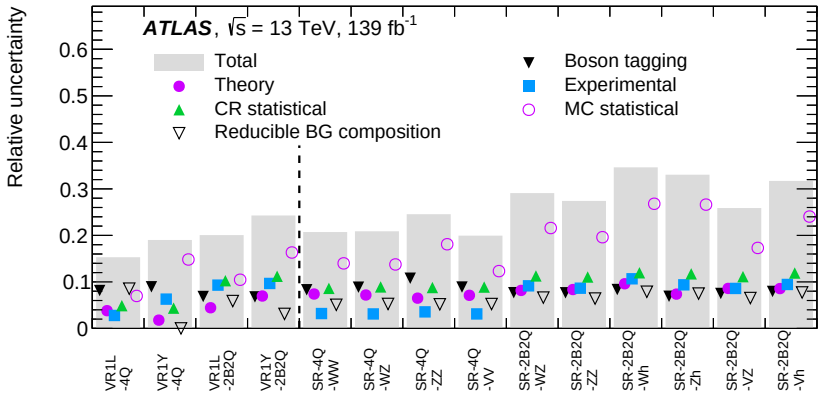

Figure 9.6: The total uncertainty and its breakdown obtained from the background-only fit (described in Section 10.1) in all SRs and VRs [49]. "Boson tagging" represents the uncertainty on the boson tagging (W_{qq}/Z_{qq}) efficiency. "Theory" indicates the theoretical uncertainty of the backgrounds. "Experimental" shows the contribution from the rest of the experimental uncertainties. "CR statistical" and "MC statistical" represent the statistical uncertainty in CR and SR/VR, respectively. "Reducible BG composition" is the uncertainty assigned to the transfer factor, as shown in Figure 8.24.

Table 9.2: Major sources of uncertainties in SR-4Q bins. Statistical error in data (40 ∼ 100%) is not included in this table. W/Z-tagging uncertainties for quark-/gluon-initiated jets are sub-dominant sources. Due to requiring high m_{eff}, i.e. high p_{T} jet, the impact from di-jet modeling uncertainty is larger than gamma-jet modeling. The uncertainty originating from the background estimation method is also a sub-dominant source.

Systematic group	Dominant component	SR-4Q-WW	SR-4Q-WZ	SR-4Q-ZZ	SR-4Q-VV
CR statistical error		8.6%	8.9%	8.8%	8.9%
Reducible BG composition		5.1%	5.3%	5.2%	5.2%
Boson tagging	Di-jet modeling	6.6%	7.6%	10.0%	7.7%
Boson tagging	γ + jets modeling	4.6%	4.3%	3.8%	4.3%
SR statistical error		14.0%	13.8%	18.1%	12.3%

Table 9.3: Major sources of uncertianites in SR-2B2Q bins. Statistical error in data (40 ∼ 100%) is not included in this table. The uncertainty originating from the background estimation method is found to be larger than W/Z-tagging uncertainties in this table. The impact on the W/Z-tagging uncertainties in SR-2B2Q bins is smaller than SR-4Q bins because one of two leading large-R jets is required. Z + jets and $t\bar{t}$ + X theoretical uncertainties are also dominant sources.

Systematic group	Dominant component	SR-2B2Q-WZ	SR-2B2Q-ZZ	SR-2B2Q-VZ
CR statistical error		11.3%	11.1%	11.1%
Reducible BG composition		6.3%	6.1%	6.2%
Boson tagging	Di-jet modeling	5.9%	5.9%	5.9%
Boson tagging	γ + jets modeling	4.2%	4.0%	4.0%
Theory	Z + jets PDF	4.7%	4.0%	4.5%
Theory	$t\bar{t}$ + X normalization	4.5%	5.8%	5.6%
SR statistical error		21.6%	19.6%	17.3%

Systematic group	Dominant component	SR-2B2Q-Wh	SR-2B2Q-Zh	SR-2B2Q-Vh
CR statistical error		12.0%	11.7%	11.9%
Reducible BG composition		7.5%	7.3%	7.4%
Boson tagging	Di-jet modeling	1.5%	4.1%	3.2%
Boson tagging	γ + jets modeling	8.1%	5.3%	7.1%
Theory	Z + jets PDF	7.5%	4.8%	6.5%
Theory	$t\bar{t}$ + X normalization	2.5%	3.7%	2.9%
SR statistical error		26.8%	26.6%	24.1%

10 Results

Results of the search for electroweakinos are presented in this chapter. The significance for the beyond SM (BSM) signals is examined by comparing the yields of the data and SM backgrounds in the defined signal regions (SRs). Thus, the background estimation needs to be confirmed that it is a reliable method, as discussed in Section 8.3. The backgrounds are determined in the control regions (CRs) and evaluated in the validation regions (VRs) to confirm correct estimation. Once confirmed, the backgrounds in the SRs are evaluated and compared with the data yields to search for signal excess.

Practically, this is done with a likelihood fitting with normalization factors for reducible backgrounds in each CR as free parameters to be determined, as well as systematic and statistical uncertainties as nuisance parameters. The fit is performed simultaneously for all the CRs without assuming the contribution of the BSM signals. This method is called "background-only fit." The results of the background estimation method, such as the normalization factors, the yields, and kinematic distributions in the CRs and VRs, are described in Sections 10.1. The results of the search are discussed after Section 10.2.

10.1 Background Determination

In order to obtain the normalization factors, we use the following likelihood function:

$$L(x;(\mu_B,\boldsymbol{\theta})) = \prod_j^N \frac{(E_j(\mu_B,\boldsymbol{\theta}))^{x_j}}{x_j!} e^{-E_j(\mu_B,\boldsymbol{\theta})}, \tag{10.1}$$

where μ_B is the normalization factor of reducible backgrounds, $\boldsymbol{\theta}$ is the nuisance parameters derived from the systematic and statistical uncertainties, x_j and $E_j(\mu_B,\boldsymbol{\theta})$ represent the observed events and probability density function of reducible and irreducible backgrounds in j-th region. The maximum likelihood approach to fit MC samples to the observed data in the CRs is performed, and the normalization factors are obtained. More details are described in Appendix Q.1.

A simultaneous fit computes the normalization factors for the reducible backgrounds in all the CRs (CR0L-4Q, CR0L-2B2Q, CR1L-4Q, CR1L-2B2Q, CR1Y-4Q, and CR1Y-2B2Q). The normalization factors in CRs (defined in Table 8.1, Table 8.3, and Table 8.4) are used to estimate the backgrounds in the SRs, and estimate the background in the VRs. The obtained normalization factors are summarized in Table 10.1. As discussed in Section 8.3, the deviation from unity in the NFs is not problematic. The post-fit numbers for the backgrounds in the CRs are summarized in Table 10.2.

In the VRs for the 1L and 1Y categories, the CR $\rightarrow$ VR extrapolation is validated using W + jets and γ + jets control samples, which have similar diagrams of the dominant background in the 0L category, $Z(\rightarrow \nu\nu)$ + jets. The post-fit breakdown of backgrounds is summarized in Table 10.3, which is visualy illustrated in Figure 10.1.

Table 10.1: Normalization factors for the reducible backgrounds by the background-only fit in each CR.

Region	Normalization Factor
0L-4Q	0.90 ± 0.08
1L-4Q	0.87 ± 0.04
1Y-4Q	0.71 ± 0.03
0L-2B2Q	1.31 ± 0.16
1L-2B2Q	0.99 ± 0.11
1Y-2B2Q	0.79 ± 0.10

Table 10.2: Observed data events and the post-fit SM background prediction in the CRs [49]. "-" indicates negligible contribution.

Region	CR0L-4Q	CR1L-4Q	CR1Y-4Q	CR0L-2B2Q	CR1L-2B2Q	CR1Y-2B2Q
Observed	129	439	1001	83	96	127
Post-fit	129 ± 11	439 ± 21	1001 ± 32	83 ± 9	96 ± 10	127 ± 11
W + jets	24.2 ± 2.2	325 ± 16	2.59 ± 0.08	16.6 ± 2.0	48 ± 5	< 0.1
Z + jets	78 ± 7	4.45 ± 0.21	< 1	44 ± 5	0.58 ± 0.06	< 0.01
γ + jets	-	< 1	856 ± 28	-	0.57 ± 0.06	107 ± 11
VV	21.5 ± 1.9	65.4 ± 3.1	< 1	7.1 ± 0.9	6.9 ± 0.7	-
$V\gamma$	-	< 1	131 ± 4	< 0.01	< 0.1	12.6 ± 1.3
VVV	0.9 ± 0.4	1.3 ± 0.6	< 0.1	0.10 ± 0.05	0.14 ± 0.08	-
$t\bar{t}$	1.38 ± 0.12	30.4 ± 1.5	1.28 ± 0.04	7.8 ± 0.9	24.0 ± 2.5	0.57 ± 0.06
$t + X$	1.32 ± 0.12	11.0 ± 0.5	< 1	2.87 ± 0.34	13.2 ± 1.4	< 0.1
$t\bar{t} + X$	1.3 ± 0.9	1.5 ± 1.2	9 ± 6	3.7 ± 2.6	1.5 ± 1.1	7 ± 5
Vh	< 0.1	< 0.1	< 0.001	0.95 ± 0.11	0.69 ± 0.07	< 0.01

The post-fit distributions in VRs are shown in Figure 10.2 and Figure 10.3 for the key kinematic variables. Other distributions are shown in Appendix R. The most significant disagreement between the data and the estimated backgrounds are observed in VR1L-4Q, corresponding to a statistical significance of 1.8σ. In order to confirm that the discrepancy is caused by data fluctuation and the background estimation is reliable, an additional check is performed as discussed below. As discussed in Section 8.3.5, seemingly discontinuous data deficits observed around $m_{\text{eff}} = 1$ TeV and $m_{\text{eff}} = 1.3$ TeV, which are most likely due to statistical fluctuation in the data given that the m_{eff} spectra should follow according to a steep-falling probability distribution. With loosening the $p_{\text{T}}(V) + p_{\text{T}}(J_1) + p_{\text{T}}(J_2)$ cut from 1 TeV to 0.9 TeV, the deficit becomes smaller since the normalization factor becomes smaller in the CR1L-4Q, as shown in Figure 10.4, and the discrepancy in the total becomes smaller than 0.9σ in the region. Thus, these disagreements are due to statistical fluctuations.

Therefore, it is concluded that the kinematic distributions and the data/MC agreement in the VRs are very well; hence the background estimation is well validated. Thus, systematic uncertainties originating from the background estimation method are not assigned.

Table 10.3: Observed data events and the post-fit SM background prediction in the VR1L (1Y) bins [49]. The corresponding CR1L (1Y) bins are shown in Table 10.2. "-" indicates negligible contribution.

Region	VR1L-4Q	VR1Y-4Q	VR1L-2B2Q	VR1Y-2B2Q
Observed	13	38	5	14
Post-fit	22.0 ± 3.4	43 ± 8	7.8 ± 1.5	8.6 ± 2.0
W + jets	13.4 ± 2.2	< 0.1	3.4 ± 0.7	-
Z + jets	0.198 ± 0.035	-	0.044 ± 0.012	-
γ + jets	-	37 ± 7	0.22 ± 0.10	6.4 ± 1.6
VV	4.1 ± 0.8	-	0.55 ± 0.15	-
$V\gamma$	-	5.0 ± 0.9	-	1.13 ± 0.27
VVV	0.52 ± 0.28	< 0.01	0.09 ± 0.05	-
$t\bar{t}$	2.7 ± 0.4	-	1.8 ± 0.4	0.28 ± 0.18
$t + X$	0.91 ± 0.21	-	1.27 ± 0.34	-
$t\bar{t} + X$	0.16 ± 0.12	0.6 ± 0.5	0.4 ± 0.4	0.8 ± 0.6
Vh	< 0.001	-	0.046 ± 0.009	-

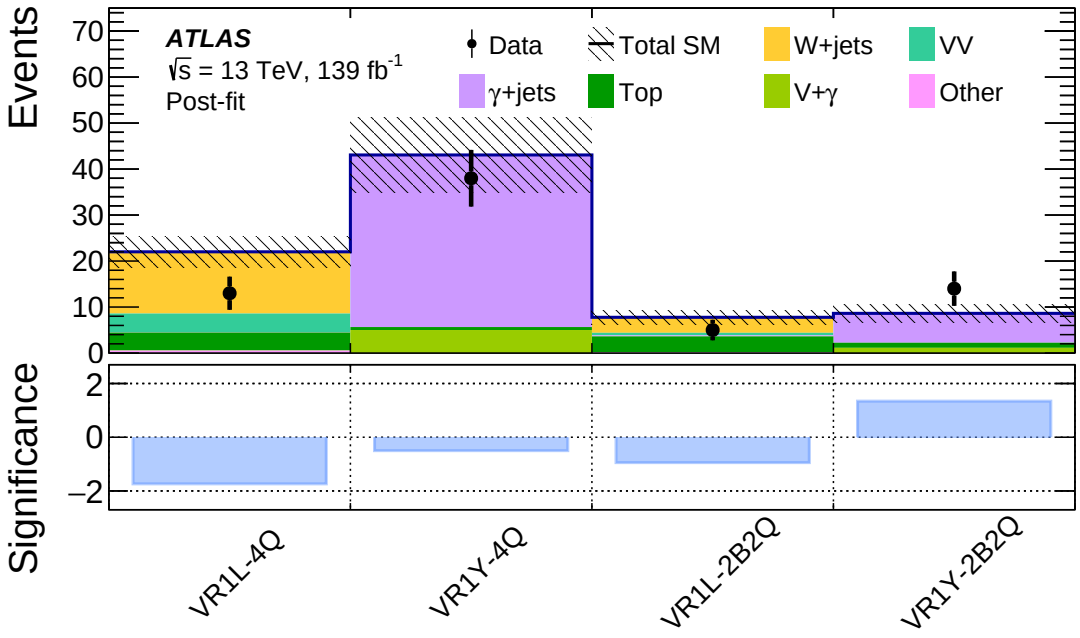

Figure 10.1: Comparison between the observed data and the post-fit SM background prediction in the VRs [49]. "Tops" includes $t\bar{t}$, $t + X$, and $t\bar{t} + X$. "Other" includes Z + jets, VVV, and Vh. The bottom panel shows the statistical significance for the discrepancy between the observed numbers of events and the expected SM backgrounds.

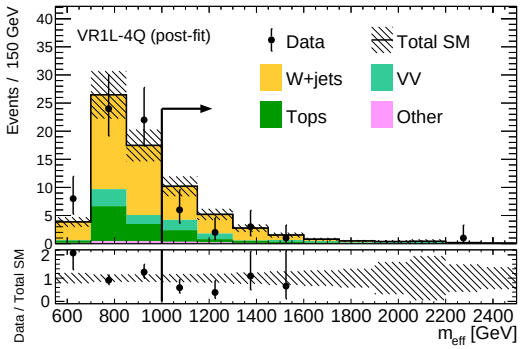

(a) $p_{\mathrm{T}}(V) + p_{\mathrm{T}}(J_1) + p_{\mathrm{T}}(J_2)$ in VR1L-4Q

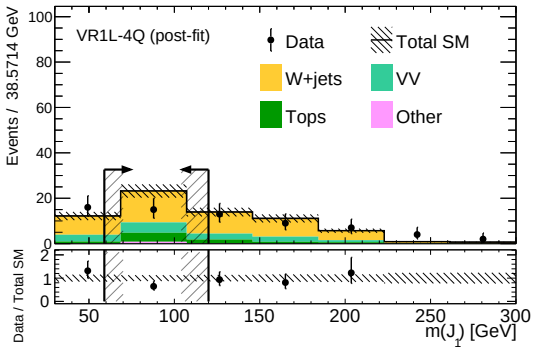

(b) $m(J_1)$ in VR1L-4Q

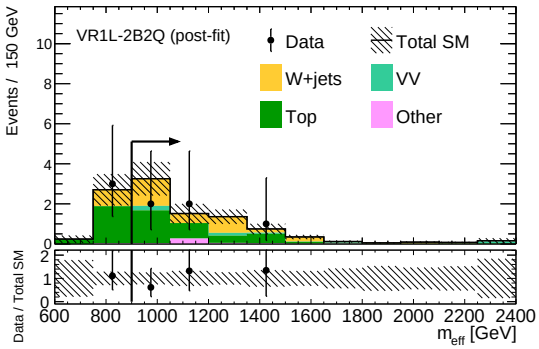

(c) $p_{\mathrm{T}}(V) + p_{\mathrm{T}}(J_1) + p_{\mathrm{T}}(J_2)$ in VR1L-2B2Q

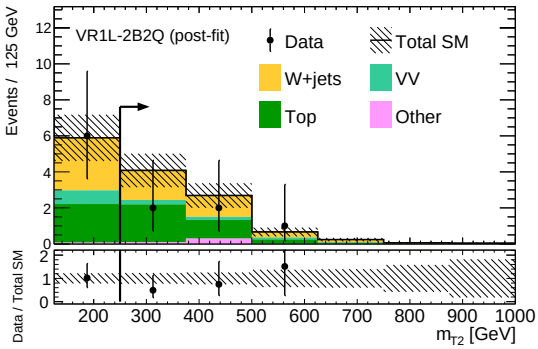

(d) $m_{\mathrm{T2}}(J_1, J_2; V)$ in VR1L-2B2Q

Figure 10.2: Distributions of $p_{\mathrm{T}}(V) + p_{\mathrm{T}}(J_1) + p_{\mathrm{T}}(J_2)$ (a), leading large-R jet mass (b) in VR1L-4Q, $p_{\mathrm{T}}(V) + p_{\mathrm{T}}(J_1) + p_{\mathrm{T}}(J_2)$ (c), $m_{\mathrm{T2}}(J_1, J_2; V)$ (d) in VR1L-2B2Q. "Tops" includes $t\bar{t}$, $t + X$, and $t\bar{t} + X$. "Other" includes Z + jets, VVV, Vh, γ + jets, and $V\gamma$.

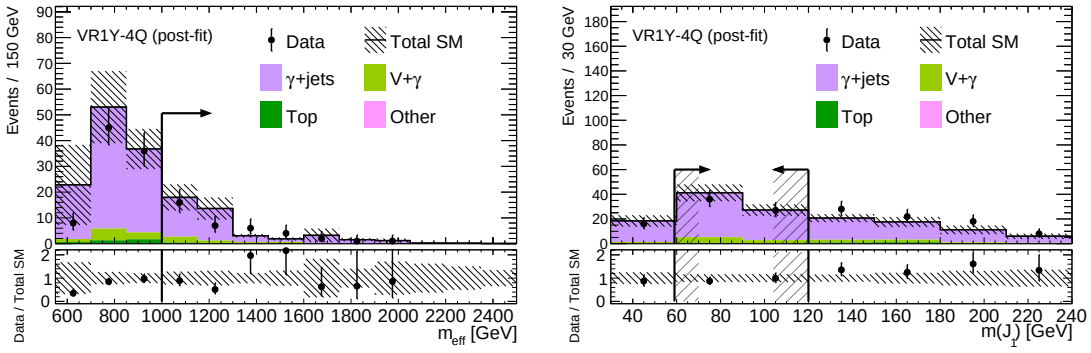

(a) $p_{\mathrm{T}}(V) + p_{\mathrm{T}}(J_1) + p_{\mathrm{T}}(J_2)$ in VR1Y-4Q

(b) $m(J_1)$ in VR1Y-4Q

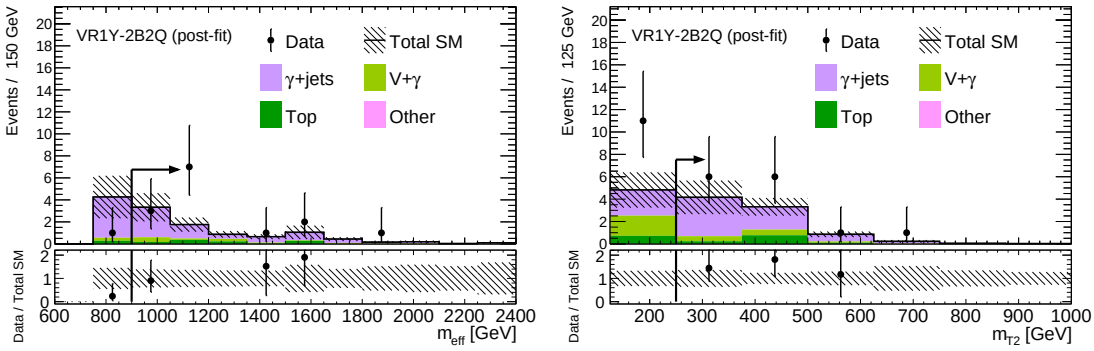

(c) $p_{\mathrm{T}}(V) + p_{\mathrm{T}}(J_1) + p_{\mathrm{T}}(J_2)$ in VR1Y-2B2Q

(d) $m_{\mathrm{T2}}(J_1, J_2; V)$ in VR1Y-2B2Q

Figure 10.3: Distributions of $p_{\mathrm{T}}(V) + p_{\mathrm{T}}(J_1) + p_{\mathrm{T}}(J_2)$ (a) and leading large-R jet mass (b) in VR1Y-4Q. Distributions of $p_{\mathrm{T}}(V) + p_{\mathrm{T}}(J_1) + p_{\mathrm{T}}(J_2)$ (c) and $m_{\mathrm{T2}}(J_1, J_2; V)$ (d) in VR1Y-2B2Q. "Tops" includes $t\bar{t}$, $t + X$, and $t\bar{t} + X$. "Other" includes Z + jets, VVV, Vh, W + jets, and VV.

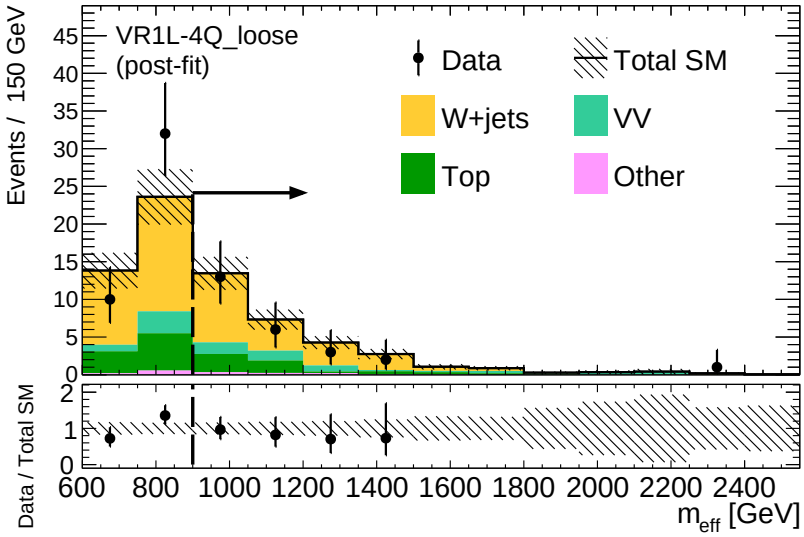

Figure 10.4: $p_{\mathrm{T}}(V) + p_{\mathrm{T}}(J_1) + p_{\mathrm{T}}(J_2)$ distribution in loose VR1L-4Q-like region with the $p_{\mathrm{T}}(V) + p_{\mathrm{T}}(J_1) + p_{\mathrm{T}}(J_2)$ selection loosened from 1 TeV to 0.9 TeV. The normalization factor of 1L-4Q region is evaluated from CR1L-4Q-like region with the same kinematic selections as CR1L-4Q except for $p_{\mathrm{T}}(V) + p_{\mathrm{T}}(J_1) + p_{\mathrm{T}}(J_2)$ selection. "Tops" includes $t\bar{t}$, $t + X$, and $t\bar{t} + X$. "Other" includes Z + jets, VVV, Vh, γ + jets, and $V\gamma$.

10.2 Results on the Signal Regions

Given that the background estimation method is validated, the yields of the data events in the signal regions (SRs) are finally measured and compared with the SM backgrounds. In addition to the evaluation of the statistical deviation between the data and the SM prediction, upper limits of a generic beyond-the-SM (BSM) signal are set in each SR under the background-only hypothesis. Statistical analysis with a fixed number of signal events without considering specific models is performed. The method is referred to as "model-independent fit." In this model-independent fit, we use the likelihood by adding the number of signal events to Equation 10.1:

$$L(x; (\boldsymbol{s}, \mu_B, \boldsymbol{\theta})) = \prod_j^N \frac{(E_j(\boldsymbol{s}, \mu_B, \boldsymbol{\theta}))^{x_j}}{x_j!} e^{-E_j(\boldsymbol{s}, \mu_B, \boldsymbol{\theta})}, \tag{10.2}$$

where $\boldsymbol{s} = (s_0, ..., s_N)$ and s_j is the assumed number of BSM signal events in j-th region, $E_j(\boldsymbol{s}, \mu_B, \boldsymbol{\theta})$ is a sum of s_j and the number of background events. In this method, BSM signals are assumed not to remain in the CRs, $s_{\mathrm{CR}} = 0$.

Next, the profile likelihood ratio with various assumptions of signal events in the SRs (s) is calculated:

$$\lambda(s) = \frac{L(s, \hat{\hat{\mu}}_B, \hat{\hat{\boldsymbol{\theta}}})}{L(\hat{s}, \hat{\mu}_B, \hat{\boldsymbol{\theta}})}, \tag{10.3}$$

where $\hat{s}, \hat{\mu}_B, \hat{\boldsymbol{\theta}}$ are a set of $s, \mu_B, \boldsymbol{\theta}$ that plausibly explains the measurement under the condition of maximizing the likelihood when s is a free parameter, and $\hat{\hat{\mu}}_B, \hat{\hat{\boldsymbol{\theta}}}$ are the similar to $\hat{\mu}_B, \hat{\boldsymbol{\theta}}$ while additional constraint

where s is fixed is added. The profile likelihood ratio is used for the calculation of p-value:

$$p_s = \int_{q_s,\mathrm{obs}}^{\infty} f(q_s|s)\, dq_s, \tag{10.4}$$

where $q_s = -2\ln\lambda(s)$ is called "test statistics," $f(q_s|s)$ is the probability density function of q_s with the assumption of the fixed signal strength s. Figure 10.5 illustrates the relation between the p-value and $f(q_s|s)$ distribution, and the significance Z. The $f(q_s|s)$ function can be obtained by the pseudo experiments called "toy experiments." The data of pseudo experiments are generated with fixed nuisance parameters to the maximum likelihood estimation, and the test statistic function is sampled using the data.

To set upper limits, $\mathrm{CL_s}$ value [155] is defined:

$$\mathrm{CL_s} = \frac{\mathrm{CL_{s+b}}}{\mathrm{CL_b}} = \frac{p_s}{p_{s=0}}, \tag{10.5}$$

where $\mathrm{CL_{s+b}}$ ($\mathrm{CL_b}$) and p_s ($p_{s=0}$) are the confidence level (CL) and the p-value of signal-plus-background (background-only) hypothesis [155]. The upper limit on the number of BSM signal events is set at 95% CL ($\mathrm{CL_s} = 0.05$).

The upper limits are summarized in Table 10.4. The upper limits on expected and observed signal events are denoted as S^{95}_{exp} and S^{95}_{obs}, respectively. The expected confidence level (CL_B), the one-side p-value (p_0), and the significance (Z) for the background-only hypothesis are also summarized. The upper limits on the visible cross-section (efficiency times cross-section: $\langle\epsilon\sigma\rangle^{95}_{obs}$) is defined:

$$\langle\epsilon\sigma\rangle^{95}_{obs} = S^{95}_{obs}/(\text{Integrated luminosity} = 139\ \mathrm{fb}^{-1}). \tag{10.6}$$

As shown in Table 10.4, no significant data excess is observed in each SR, and good agreement between the data and the expected SM backgrounds is observed. The upper limit on the efficiency times the cross-section of generic BSM signals in each SR allows for easy interpretation of other BSM signals such as heavy triplet leptons [156]. In this thesis, since the search for electroweakinos is focused, there is no discussion about other BSM models.

The upper limits in additional signal regions are also set. 10 SRs are already defined in Section 7.5, and 2 inclusive signal regions are added. One is Disc-SR-2B2Q, defined as the logical union of SR-2B2Q-VZ and SR-2B2Q-Vh. The other is Disc-SR-Incl, defined as the logical union of SR-4Q-VV and Disc-SR-2B2Q. In SR-2B2Q-Wh and SR-2B2Q-Vh, more stringent observed upper limits than expected are set due to the large deficit.

The yields of the observed data and expected SM backgrounds in all the SRs are shown in Figure 10.6. The expected signal from the benchmark SUSY model is also illustrated in the figure. The breakdowns of the backgrounds in the SRs are shown in Table 10.5 and Table 10.6. Some small data deficits with the data are observed in SR-2B2Q-Wh and SR-2B2Q-Vh, corresponding to statistical significances 1.0σ.

The post-fit distributions of the kinematic variables in SR-4Q-VV, SR-2B2Q-VZ, and SR-2B2Q-Vh are shown in Figure 10.7-10.9. Other distributions are shown in Appendix R. A reasonable agreement is generally found between the data and the expected SM backgrounds across the spectra as well.

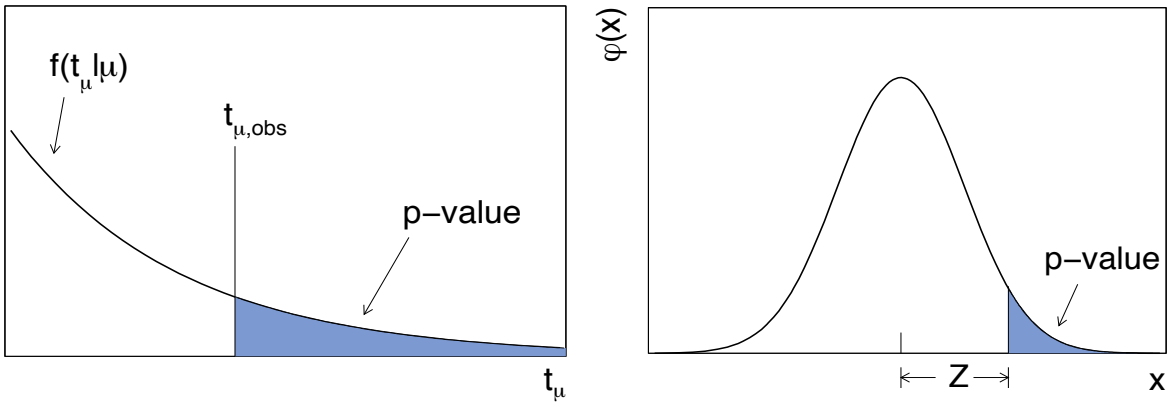

(a) $f(t_\mu|\mu)$ and p-value

(b) Significance Z and p-value

Figure 10.5: (a) Illustration of the relation between the p-value obtained from an observed value of the test statistic t_μ, instead of s in Equation 10.4. (b) The standard normal distribution $\varphi(x) = (1/\sqrt{2\pi})\exp(-x^2/2$ showing the relation between the significance Z and the p-value [154].

Table 10.4: 95% CL upper limits on the visible cross-section, defined as efficiency times cross-section ($\langle\epsilon\sigma\rangle^{95}_{exp}$) [49]. S^{95}_{obs} (S^{95}_{exp}) shows the 95% CL upper limit on the number of signal events, given the observed number (expected number and $\pm1\sigma$ excursions) of background events. CL_B is the confidence level expected for the background-only hypothesis. The last column is the discovery p-value ($p(s = 0)$) with the corresponding Gaussian significance (Z). This value indicates a compatibility of the observed data with the background-only hypothesis relative to fluctuations of the background, and is not calculated in the region where the deficit of the data is observed.

Signal region	$\langle\epsilon\sigma\rangle^{95}_{obs}$[fb]	S^{95}_{obs}	S^{95}_{exp}	CL_B	$p(s = 0)$ (Z)
SR-4Q-WW	0.032	4.5	$4.2^{+1.8}_{-1.0}$	0.55	0.44 (0.15)
SR-4Q-WZ	0.036	5.0	$5.1^{+2.1}_{-1.3}$	0.46	–
SR-4Q-ZZ	0.025	3.6	$4.1^{+1.8}_{-1.0}$	0.30	–
SR-4Q-VV	0.034	4.7	$5.3^{+2.3}_{-1.5}$	0.38	–
SR-2B2Q-WZ	0.033	4.7	$4.0^{+1.7}_{-0.7}$	0.66	0.33 (0.44)
SR-2B2Q-Wh	0.022	3.1	$3.9^{+1.3}_{-0.7}$	0.28	–
SR-2B2Q-ZZ	0.033	4.5	$4.1^{+1.7}_{-0.9}$	0.63	0.37 (0.32)
SR-2B2Q-Zh	0.026	3.6	$3.9^{+1.4}_{-0.7}$	0.38	–
SR-2B2Q-VZ	0.032	4.4	$4.4^{+1.8}_{-1.0}$	0.50	–
SR-2B2Q-Vh	0.026	3.6	$4.4^{+1.7}_{-1.0}$	0.24	–
Disc-SR-2B2Q	0.034	4.8	$5.6^{+2.4}_{-1.6}$	0.30	–
Disc-SR-Incl	0.042	5.9	$7.2^{+2.2}_{-2.0}$	0.27	–

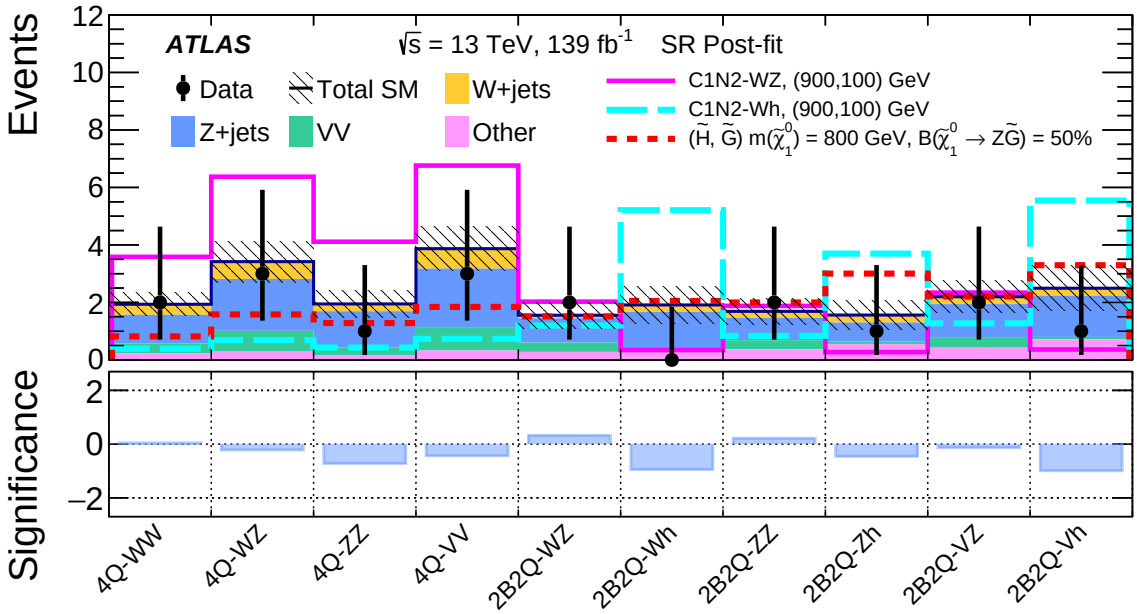

Figure 10.6: Comparison between the observed data and the post-fit SM background prediction in the SRs [49]. For the C1N2-WZ and C1N2-Wh models, the label (900, 100) GeV represents ($m(\tilde{\chi}_2^0) = 900$ GeV, $m(\tilde{\chi}_1^0) = 100$ GeV). "Other" includes VVV, $t\bar{t}$, $t + X$, $t\bar{t} + X$, Vh, γ + jets, and $V\gamma$.The bottom panel shows the statistical significance of the discrepancy between the observed events and the expected SM backgrounds.

Table 10.5: Observed data events and the post-fit SM background prediction in the SR-4Q bins [49]. The corresponding CR0L bins are shown in Table 10.2. "-" indicates a negligible contribution. "Other" includes Vh, γ + jets, $V\gamma$, and $t\bar{t} + X$.

Region	SR-4Q-WW	SR-4Q-WZ	SR-4Q-ZZ	SR-4Q-VV
Observed	2	3	1	3
Post-fit	1.9 ± 0.4	3.4 ± 0.7	1.9 ± 0.5	3.9 ± 0.8
W+jets	0.37 ± 0.08	0.60 ± 0.13	0.26 ± 0.07	0.69 ± 0.15
Z+jets	1.0 ± 0.21	1.8 ± 0.4	1.26 ± 0.32	2.1 ± 0.4
VV	0.35 ± 0.11	0.73 ± 0.24	0.26 ± 0.09	0.79 ± 0.25
VVV	0.17 ± 0.09	0.19 ± 0.10	0.11 ± 0.07	0.23 ± 0.12
$t\bar{t}$	0.039 ± 0.009	0.060 ± 0.018	0.025 ± 0.010	0.063 ± 0.018
$t + X$	0.015 ± 0.006	0.039 ± 0.016	0.012 ± 0.005	0.039 ± 0.016
Other	< 0.001	< 0.001	< 0.001	< 0.001

Table 10.6: Observed data events and the post-fit SM background prediction in the SR-2B2Q bins [49]. The corresponding CR0L bins are shown in Table 10.2. "-" indicates a negligible contribution. "Other" includes Vh, γ + jets and $V\gamma$.

Region	SR-2B2Q-WZ	SR-2B2Q-Wh	SR-2B2Q-ZZ	SR-2B2Q-Zh	SR-2B2Q-VZ	SR-2B2Q-Vh
Observed	2	0	2	1	2	1
Post-fit	1.6 ± 0.4	1.9 ± 0.7	1.7 ± 0.5	1.6 ± 0.5	2.2 ± 0.6	2.5 ± 0.8
W+jets	0.11 ± 0.06	0.24 ± 0.09	0.23 ± 0.08	0.26 ± 0.10	0.26 ± 0.09	0.26 ± 0.09
Z+jets	0.84 ± 0.27	1.3 ± 0.5	0.78 ± 0.23	0.66 ± 0.24	1.15 ± 0.33	1.4 ± 0.5
VV	0.33 ± 0.11	0.09 ± 0.03	0.32 ± 0.10	0.085 ± 0.032	0.37 ± 0.11	0.085 ± 0.030
VVV	0.047 ± 0.027	< 0.01	0.051 ± 0.032	0.011 ± 0.007	0.06 ± 0.04	0.011 ± 0.007
$t\bar{t}$	0.016 ± 0.006	0.13 ± 0.04	0.064 ± 0.019	0.40 ± 0.16	0.072 ± 0.021	0.46 ± 0.18
$t + X$	0.11 ± 0.05	0.07 ± 0.04	0.11 ± 0.05	0.041 ± 0.022	0.11 ± 0.05	0.10 ± 0.05
$t\bar{t} + X$	0.10 ± 0.08	$0.07^{+0.10}_{-0.07}$	0.14 ± 0.12	$0.08^{+0.09}_{-0.08}$	0.18 ± 0.14	$0.10^{+0.11}_{-0.10}$
Other	< 0.01	0.03 ± 0.01	< 0.01	0.024 ± 0.008	< 0.01	0.037 ± 0.011

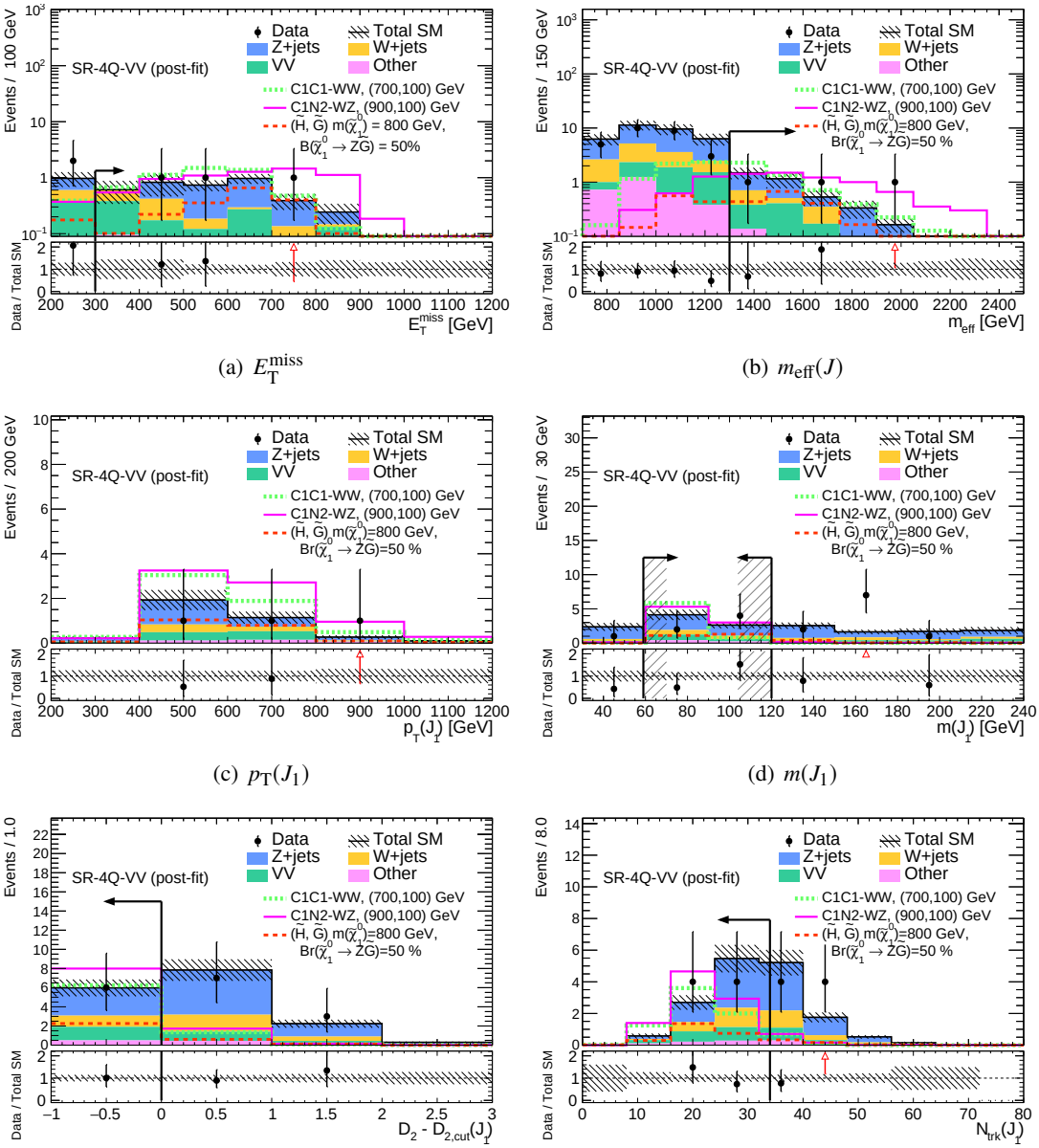

(a) $E_{\mathrm{T}}^{\mathrm{miss}}$ (b) $m_{\mathrm{eff}}(J)$

(c) $p_{\mathrm{T}}(J_1)$ (d) $m(J_1)$

(e) $D_2(J_1)$ (f) n_{trk} (J_1)

Figure 10.7: Distributions of $p_{\mathrm{T}}(V)$ (a), $p_{\mathrm{T}}(V) + p_{\mathrm{T}}(J_1) + p_{\mathrm{T}}(J_2)$ (b), leading large-R jet p_{T} (c), mass (d), D_2 (e), and n_{trk} (f) in SR-4Q-VV. "Other" includes VVV, $t\bar{t}$, $t + X$, $t\bar{t} + X$, Vh, γ + jets, and $V\gamma$. In the D_2 and n_{trk} plots, kinematic cuts except for $W/Z \to qq$ tagging cuts and mass cuts for the targeting jets are applied.

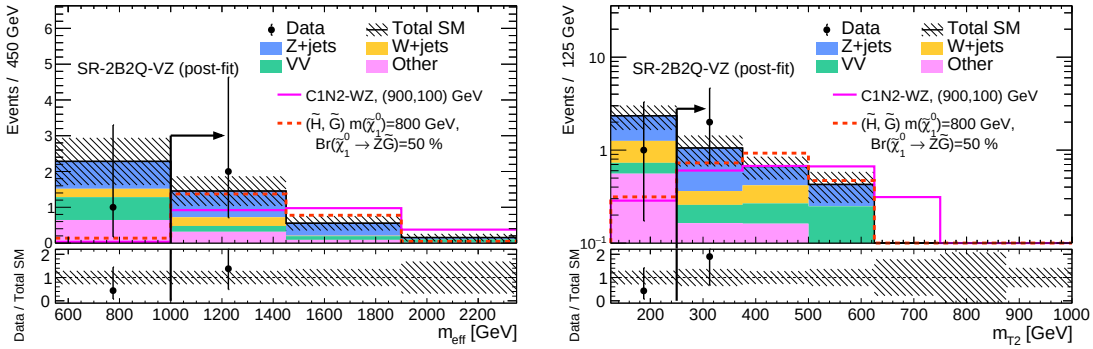

(a) $p_{\mathrm{T}}(V) + p_{\mathrm{T}}(J_1) + p_{\mathrm{T}}(J_2)$

(b) $m_{\mathrm{T2}}(J_1, J_2; V)$

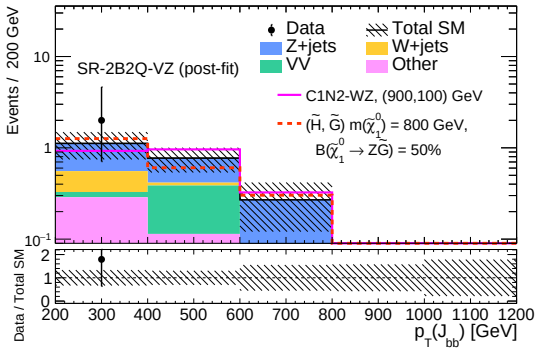

(c) $p_{\mathrm{T}}(J_{bb})$

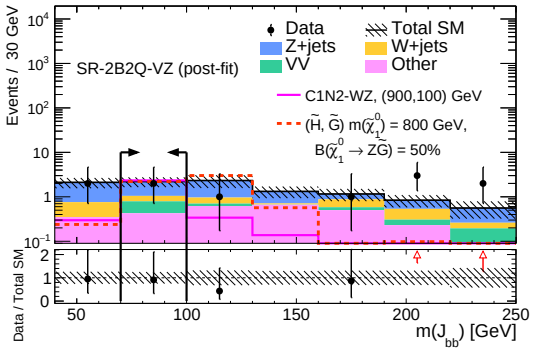

(d) $m(J_{bb})$

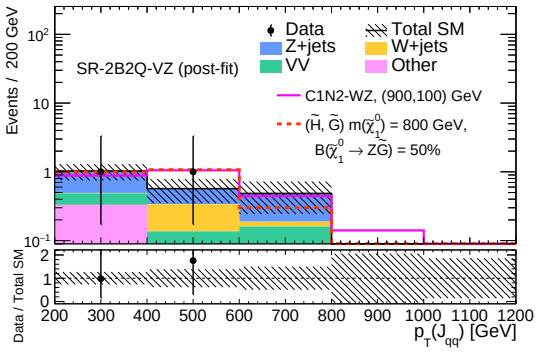

(e) $p_{\mathrm{T}}(J_{qq})$

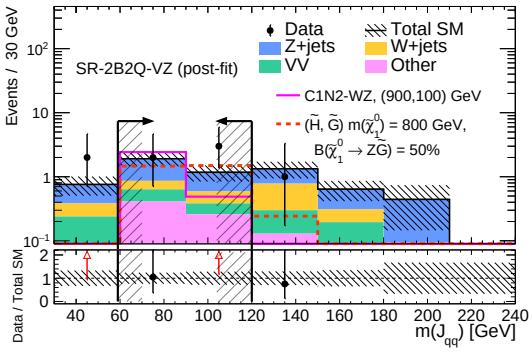

(f) $m(J_{qq})$

Figure 10.8: Distributions of $p_{\mathrm{T}}(V) + p_{\mathrm{T}}(J_1) + p_{\mathrm{T}}(J_2)$ (a), $m_{\mathrm{T2}}(J_1, J_2; V)$ (b), $p_{\mathrm{T}}(J_{bb})$ (c), $m(J_{bb})$ (d), $p_{\mathrm{T}}(J_{qq})$ (e), and $m(J_{qq})$ (f) in SR-2B2Q-VZ. "Other" includes VVV, $t\bar{t}$, $t + X$, $t\bar{t} + X$, Vh, γ + jets, and $V\gamma$.

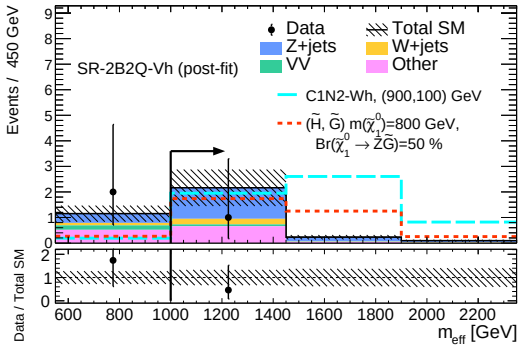

(a) $p_{\mathrm{T}}(V) + p_{\mathrm{T}}(J_1) + p_{\mathrm{T}}(J_2)$

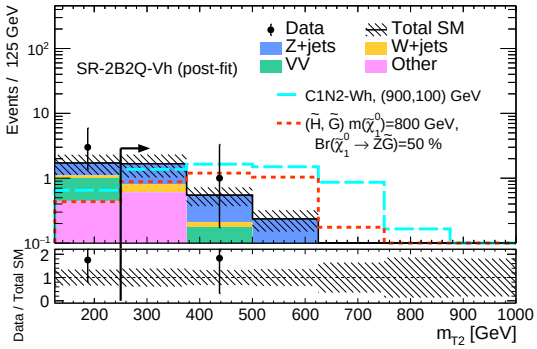

(b) $m_{\mathrm{T2}}(J_1, J_2; V)$

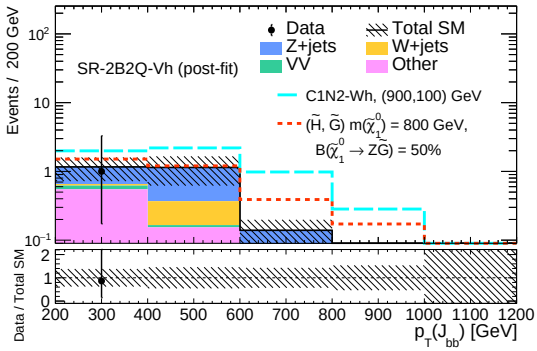

(c) $p_{\mathrm{T}}(J_{bb})$

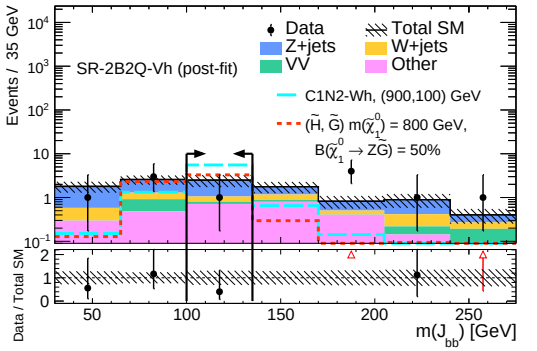

(d) $m(J_{bb})$

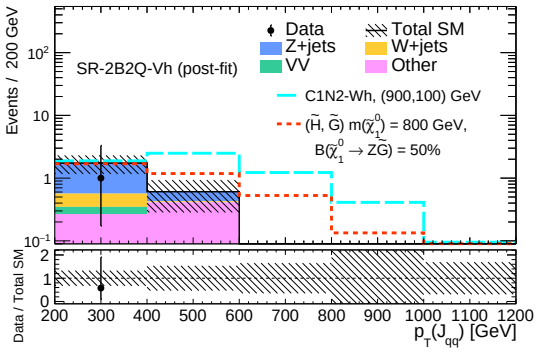

(e) $p_{\mathrm{T}}(J_{qq})$

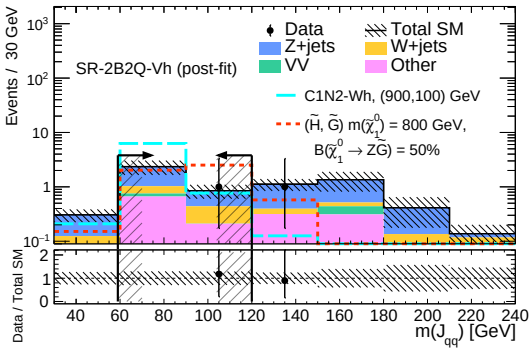

(f) $m(J_{qq})$

Figure 10.9: Distributions of $p_{\mathrm{T}}(V) + p_{\mathrm{T}}(J_1) + p_{\mathrm{T}}(J_2)$ (a), $m_{\mathrm{T2}}(J_1, J_2; V)$ (b), $p_{\mathrm{T}}(J_{bb})$ (c), $m(J_{bb})$ (d), $p_{\mathrm{T}}(J_{qq})$ (e), and $m(J_{qq})$ (f) in SR-2B2Q-Vh. "Other" includes VVV, $t\bar{t}$, $t + X$, $t\bar{t} + X$, Vh, γ + jets, and $V\gamma$.

10.3 Model-specific Exclusion Limits

In this section, the impact of this analysis in specific models (summarized in Table 10.7) is discussed. We calculate the CL_s in a similar way as described in Section 10.2. However, the only difference of $\boldsymbol{s}$ in Equation 10.2 is the numbers of the expected yields of signal MC samples, and the signal contribution to the CRs are properly taken into account ($s_{CR} > 0$). Thus, the normalization factors for reducible backgrounds are different from ones in the background-only fit. Additionally, the systematic uncertainties for signals are considered, and they correlate with the same systematic uncertainties for backgrounds. This method is called "model-dependent fit."

In the model-dependent fit, the CL_s value, which is defined in Equation 10.5, are calculated for each signal point defined in the model space, and the exclusion limits are typically presented in a 2D plane of $(m(\tilde{\chi}_{\text{heavy}}), m(\tilde{\chi}_{\text{light}}))$ by interpolating the CL_s values from the descrete signal points. Some benchmark combination points of the SUSY parameters are set and the CL_s values are interpolated from these points to points at the 95% CL ($CL_s = 0.05$). The contours corresponding to $CL_s = 0.05$ is referred to as the "exclusion limits", and the region where the $CL_s < 0.05$ is called the " excluded region." In this fit, some SRs according to the signal models are used, as summarized in Table 10.7.

10.3.1 $(\tilde{W}, \tilde{B})$-SIM

The $(\tilde{W}, \tilde{B})$-SIM model is often used as the benchmark SUSY model in the ATLAS/CMS analyses, and therefore, useful for comparing with the previous analyses [157]. As described in Section 2.3.5, the branching fraction of $\tilde{\chi}_2^0$ into $\tilde{\chi}_1^0$ with Z or h is assumed to be 100%. The exclusion limits for the three simplified models are shown in Figure 10.10 and Figure 10.11. For the C1C1-WW model, as shown in Figure 10.10, the mass of the lightest chargino $m(\tilde{\chi}_1^\pm)$ between 630 GeV and 760 GeV is excluded for the mass of the lightest neutralino $m(\tilde{\chi}_1^0) < 80$ GeV by this analysis while the previous analysis excluded up to 420 GeV for $m(\tilde{\chi}_1^\pm)$, corresponding to exclusion of signals with a 15 times smaller production cross-section.

For the C1N2-WZ and C1N2-Wh models, as shown in Figure 10.11, more stringent limits can be obtained compared to the C1C1-WW model, owing to the large production cross-section. In the C1N2-WZ model, as shown in Figure 10.11(a), $m(\tilde{\chi}_1^\pm/\tilde{\chi}_2^0)$ between 440 GeV and 960 GeV is excluded for $m(\tilde{\chi}_1^0) < 300$ GeV in this analysis while the previous analysis [158, 159] excluded up to 640 GeV for $m(\tilde{\chi}_1^\pm/\tilde{\chi}_2^0)$, corresponding to exclusion of signals with a 7.5 times smaller production cross-section. In the C1N2-Wh model, as shown in Figure 10.11(b), $m(\tilde{\chi}_1^\pm/\tilde{\chi}_2^0)$ between 400 GeV and 1060 GeV is excluded for $m(\tilde{\chi}_1^0) < 420$ GeV in this analysis while the previous analysis [160] excluded up to 740 GeV for $m(\tilde{\chi}_1^\pm/\tilde{\chi}_2^0)$, corresponding to exclusion of signals with a 3.9 times smaller production cross-section.

Table 10.7: Summary of the signal models targeted in the search, including the production modes, final states, signal regions (SRs) used for the hypothetical tests [49]. For the $(\tilde{W},\tilde{H})$ and $(\tilde{H},\tilde{W})$ models, M_2, μ and $\tan\beta$ are scanned. We consider cases with 0 TeV $< M_2 <$ 1.2 TeV, -1.2 TeV $< \mu <$ 1.2 TeV, and $\tan\beta = 2, 5, 10, 30$.

Model	Production	Final states	SRs simultaneously fitted	Branching ratio
$(\tilde{W},\tilde{B})$	$\tilde{\chi}_1^\pm\tilde{\chi}_1^\mp$, $\tilde{\chi}_1^\pm\tilde{\chi}_2^0$	WW, WZ, Wh	4Q-VV, 2B2Q-WZ, 2B2Q-Wh	$\mathcal{B}(\tilde{\chi}_1^\pm \to W\tilde{\chi}_1^0) = 1$, $\mathcal{B}(\tilde{\chi}_2^0 \to Z\tilde{\chi}_1^0)$ scanned.
$(\tilde{H},\tilde{B})$	$\tilde{\chi}_1^\pm\tilde{\chi}_1^\mp$, $\tilde{\chi}_1^\pm\tilde{\chi}_2^0$, $\tilde{\chi}_1^\pm\tilde{\chi}_3^0$, $\tilde{\chi}_2^0\tilde{\chi}_3^0$	WW, WZ, Wh, ZZ, Zh, hh	4Q-VV, 2B2Q-VZ, 2B2Q-Vh	$\mathcal{B}(\tilde{\chi}_1^\pm \to W\tilde{\chi}_1^0) = 1$, $\mathcal{B}(\tilde{\chi}_2^0 \to Z\tilde{\chi}_1^0)$ scanned, $\mathcal{B}(\tilde{\chi}_3^0 \to h\tilde{\chi}_1^0) = 1 - \mathcal{B}(\tilde{\chi}_2^0 \to Z\tilde{\chi}_1^0)$
$(\tilde{W},\tilde{H})$	$\tilde{\chi}_2^\pm\tilde{\chi}_2^\mp$, $\tilde{\chi}_2^\pm\tilde{\chi}_3^0$	WW, WZ, Wh, ZZ, Zh, hh	4Q-VV, 2B2Q-VZ, 2B2Q-Vh	Determined from $(M_2, \mu, \tan\beta)$.
$(\tilde{H},\tilde{W})$	$\tilde{\chi}_2^\pm\tilde{\chi}_2^\mp$, $\tilde{\chi}_2^\pm\tilde{\chi}_2^0$, $\tilde{\chi}_2^\pm\tilde{\chi}_3^0$, $\tilde{\chi}_2^0\tilde{\chi}_3^0$	WW, WZ, Wh, ZZ, Zh, hh	4Q-VV, 2B2Q-VZ, 2B2Q-Vh	Determined from $(M_2, \mu, \tan\beta)$.
$(\tilde{H},\tilde{G})$	$\tilde{\chi}_1^\pm\tilde{\chi}_1^\mp$, $\tilde{\chi}_1^\pm\tilde{\chi}_1^0$, $\tilde{\chi}_1^\pm\tilde{\chi}_2^0$, $\tilde{\chi}_1^0\tilde{\chi}_2^0$	ZZ, Zh, hh	4Q-ZZ, 2B2Q-ZZ, 2B2Q-Zh	$\mathcal{B}(\tilde{\chi}_1^0 \to Z\tilde{G})$ scanned.
$(\tilde{H},\tilde{a})$	$\tilde{\chi}_1^\pm\tilde{\chi}_1^\mp$, $\tilde{\chi}_1^\pm\tilde{\chi}_1^0$, $\tilde{\chi}_1^\pm\tilde{\chi}_2^0$, $\tilde{\chi}_1^0\tilde{\chi}_2^0$	ZZ, Zh, hh	4Q-ZZ, 2B2Q-ZZ, 2B2Q-Zh	$\mathcal{B}(\tilde{\chi}_1^0 \to Z\tilde{a})$ scanned.
$(\tilde{W},\tilde{B})$ simplified models: $(\tilde{W},\tilde{B})$-SIM				
C1C1-WW	$\tilde{\chi}_1^\pm\tilde{\chi}_1^\mp$	WW	4Q-WW	$\mathcal{B}(\tilde{\chi}_1^\pm \to W\tilde{\chi}_1^0) = 1$.
C1N2-WZ	$\tilde{\chi}_1^\pm\tilde{\chi}_2^0$	WZ	4Q-WZ, 2B2Q-WZ	$\mathcal{B}(\tilde{\chi}_1^\pm \to W\tilde{\chi}_1^0) = \mathcal{B}(\tilde{\chi}_2^0 \to Z\tilde{\chi}_1^0) = 1$.
C1N2-Wh	$\tilde{\chi}_1^\pm\tilde{\chi}_2^0$	Wh	2B2Q-Wh	$\mathcal{B}(\tilde{\chi}_1^\pm \to W\tilde{\chi}_1^0) = \mathcal{B}(\tilde{\chi}_2^0 \to h\tilde{\chi}_1^0) = 1$.

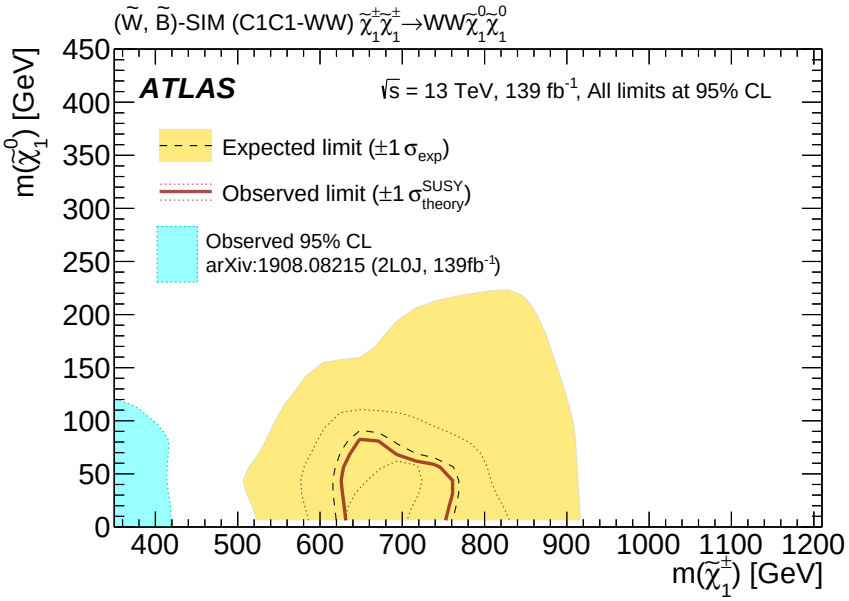

Figure 10.10: The expected and observed limits for the C1C1-WW model at the 95% CL [49]. The x-axis represents the lightest chargino mass $m(\tilde{\chi}_1^\pm)$ and the y-axis represents the lightest neutralino mass $m(\tilde{\chi}_1^0)$. The surrounding regions by black dashed and soild brown lines represent the expected and observed excluded regions, respectively. The light blue regions are already excluded by previous searches [157].

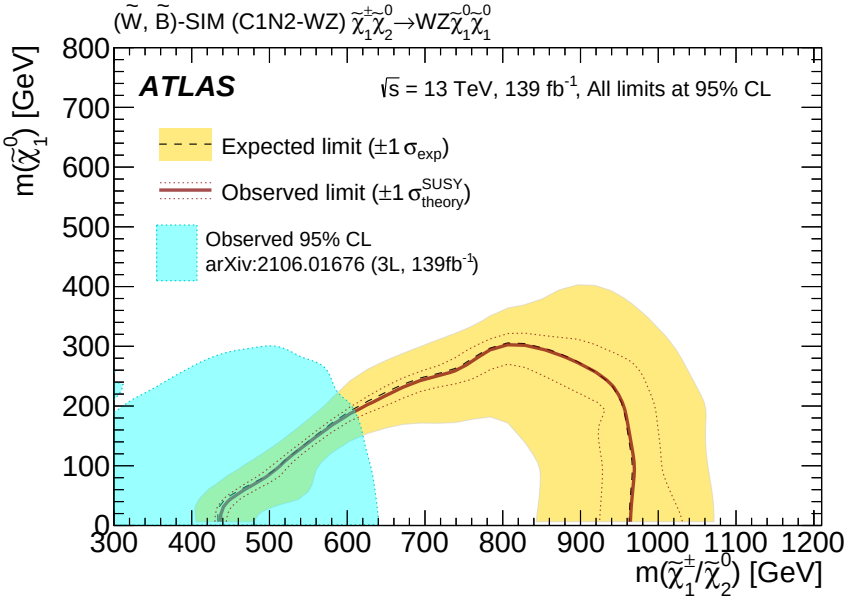

(a) $\tilde{\chi}_1^{\pm}\ \tilde{\chi}_2^0 \to WZ\tilde{\chi}_1^0\ \tilde{\chi}_1^0$

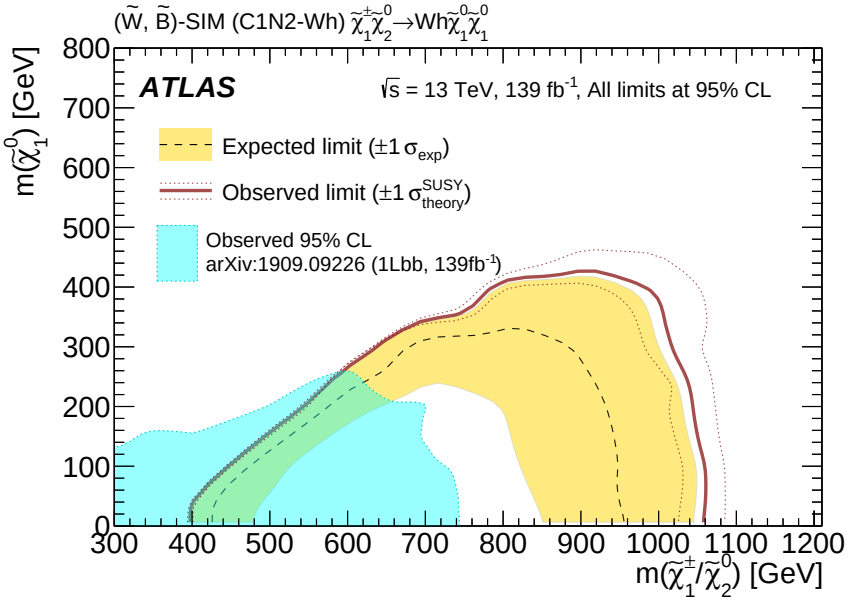

(b) $\tilde{\chi}_1^{\pm}\ \tilde{\chi}_2^0 \to Wh\tilde{\chi}_1^0\ \tilde{\chi}_1^0$

Figure 10.11: The expected and observed limits for the C1N2-WZ and C1N2-Wh models at the 95% CL [49]. $\tilde{\chi}_1^{\pm}\ \tilde{\chi}_2^0 \to WZ\tilde{\chi}_1^0\ \tilde{\chi}_1^0$ process (a) and $\tilde{\chi}_1^{\pm}\ \tilde{\chi}_2^0 \to Wh\tilde{\chi}_1^0\ \tilde{\chi}_1^0$ process (b) are shown. The x-axis represents the lightest chargino mass $m(\tilde{\chi}_1^{\pm})$ and the y-axis represents the lightest neutralino mass $m(\tilde{\chi}_1^0)$. The surrounding regions by black dashed and soild brown lines represent the expected and observed excluded regions, respectively. The light blue regions are already excluded by previous searches [158–160].

10.3.2 $(\tilde{W}, \tilde{B})$, $(\tilde{H}, \tilde{B})$, $(\tilde{W}, \tilde{H})$ and $(\tilde{H}, \tilde{W})$ models

In order to search for the $(\tilde{W}, \tilde{B})$, $(\tilde{H}, \tilde{B})$, $(\tilde{W}, \tilde{H})$, and $(\tilde{H}, \tilde{W})$ models, inclusive signal regions, such as SR-4Q-VV, SR-2B2Q-VZ, and SR-2B2Q-Vh are used to target all of the $W/Z/h$. The exclusion limits on the $(\tilde{W}, \tilde{B})$ and $(\tilde{H}, \tilde{B})$ models with various assumptions on the branching ratio, $\mathcal{B}(\tilde{\chi}_2^0 \to Z\tilde{\chi}_1^0)$, are shown in Figure 10.12. A small dependency of the limits on the branching ratio in the $(\tilde{W}, \tilde{B})$ model is found. The statistical combination of SR-4Q and SR-2B2Q bins leads to very stable sensitivity against varying branching ratio hypotheses. For example, $\mathcal{B}(\tilde{\chi}_2^0 \to Z\tilde{\chi}_1^0)$ is a free parameter in the $(\tilde{W}, \tilde{B})$ model. Comparing the case of $\mathcal{B}(\tilde{\chi}_2^0 \to Z\tilde{\chi}_1^0) = 100\%$ and 50%, the amount of $\tilde{\chi}_1^\pm\tilde{\chi}_2^0 \to WZ\tilde{\chi}_1^0\tilde{\chi}_1^0$ will be a half. However, $\tilde{\chi}_1^\pm\tilde{\chi}_2^0 \to Wh\tilde{\chi}_1^0\tilde{\chi}_1^0$ increases by the same amount that $\tilde{\chi}_1^\pm\tilde{\chi}_2^0 \to WZ\tilde{\chi}_1^0\tilde{\chi}_1^0$ decreases. Consequently, the events of $\tilde{\chi}_1^\pm\tilde{\chi}_2^0 \to Wh\tilde{\chi}_1^0\tilde{\chi}_1^0$ in SR-2B2Q-Wh increase while the events of $\tilde{\chi}_1^\pm\tilde{\chi}_2^0 \to WZ\tilde{\chi}_1^0\tilde{\chi}_1^0$ in SR-4Q-WZ and SR-2B2Q-WZ decreases. Thus, the total number of signal events does not change significantly. This is opposed to what has been commonly done in the result presentation in the ATLAS/CMS publication, which quotes the CL_s value from the most sensitive SR bin, effectively discarding the signals in one of the SRs.

For the $(\tilde{W}, \tilde{B})$ model, $m(\tilde{\chi}_1^\pm/\tilde{\chi}_2^0)$ between 400 GeV and 1080 GeV is excluded for $m(\tilde{\chi}_1^0) < 400$ GeV. As described in Section 2.3.5, since signal productions of $\tilde{\chi}_1^\pm\,\tilde{\chi}_1^\mp$ and $\tilde{\chi}_1^\pm\,\tilde{\chi}_2^0$ are considered simultaneously, the limits of the $(\tilde{W}, \tilde{B})$ model are more stringent than the $(\tilde{W}, \tilde{B})$-SIM. For the $(\tilde{H}, \tilde{B})$ model, $m(\tilde{\chi}_2^0)$ between 450 GeV and 900 GeV for $m(\tilde{\chi}_1^0) < 240$ GeV is excluded.

Since various decay processes can be considered in the $(\tilde{W}, \tilde{H})$ and $(\tilde{H}, \tilde{W})$ model, as shown in Figure 2.9(b) and Figure 2.9(d), the limit are first evaluated based on the 3D parameter space of $(\mu, M_2, \tan\beta)$ where $\mu, M_2, \tan\beta$ are the bilinear Higgs mass parameter, $\tilde{W}$ mass, the ratio of the Higgs vacuum expectation values. In these models, other SUSY particles than $\tilde{W}$ and $\tilde{H}$ are assumed to be decoupled; then, all the decay branching ratios can be determined at signal points of $(\mu, M_2, \tan\beta)$. Consequently, the expected signal yields in the SRs can be calculated, and CL_s values and exclusion limits can be obtained. Additionally, if $(\tan\beta, \mathrm{sign}(\mu))$ is fixed, a pair of (M_2, μ) can be uniquely projected to the corresponding pair of $(m(\tilde{\chi}_2^\pm), m(\tilde{\chi}_1^0))$. The results are shown in Figure 10.13. Small dependency on $\tan\beta$ and the sign of μ is found in the statistical combination of SR-4Q and SR-2B2Q bins. For the $(\tilde{W}, \tilde{H})$ model, $m(\tilde{\chi}_2^\pm/\tilde{\chi}_3^0)$ between 400 GeV and 1060 GeV is excluded for $m(\tilde{\chi}_1^0) < 400$ GeV. For the $(\tilde{H}, \tilde{W})$ model, $m(\tilde{\chi}_2^0)$ between 440 GeV and 910 GeV is excluded for $m(\tilde{\chi}_1^0) < 250$ GeV.

As shown in Figure 10.12 and Figure 10.13, the dependencies on the branching fraction and the LSP types are found to be small. This is because all the $W/Z/h$ are targeted inclusively without requiring leptons in the final states, and the multiple decay processes are combined statistically.

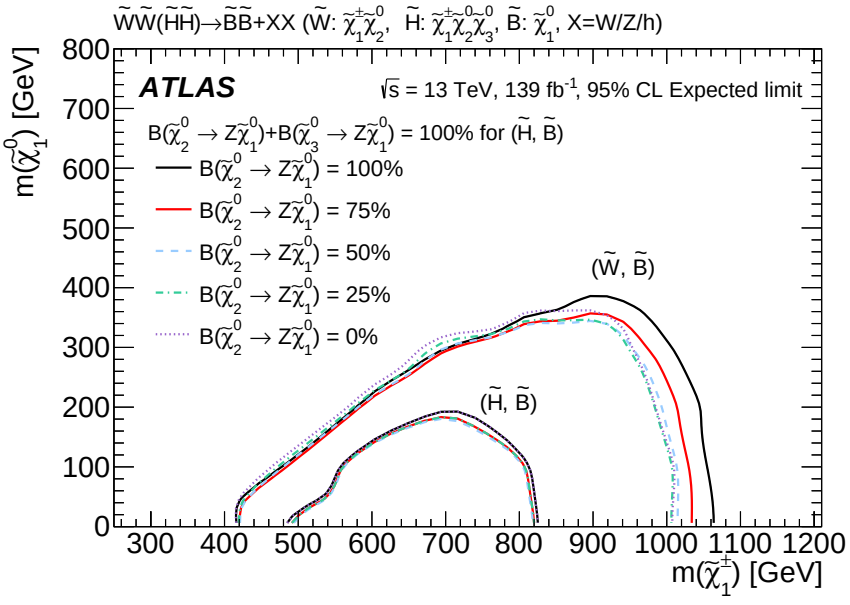

(a) Expected limits with various $\mathcal{B}(\tilde{\chi}_2^0 \to Z\tilde{\chi}_1^0)$

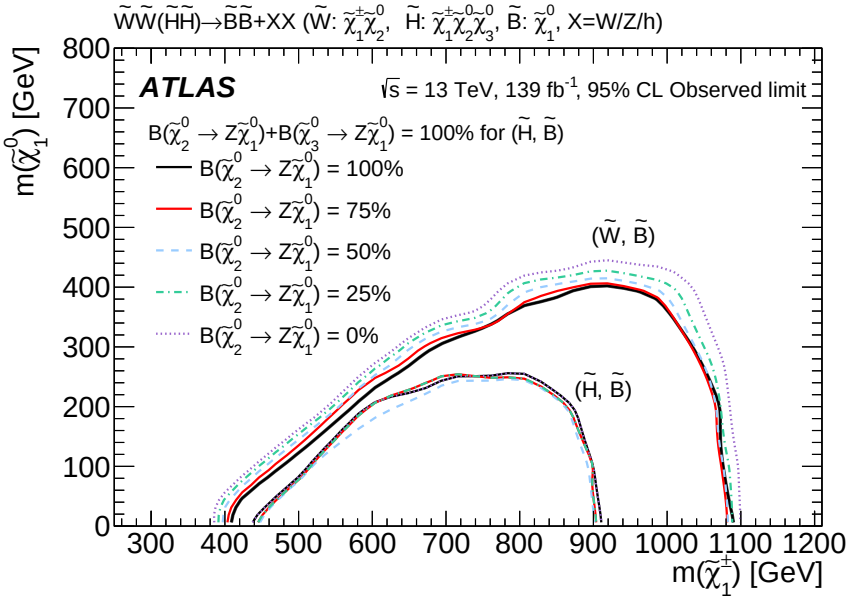

(b) Observed limits with various $\mathcal{B}(\tilde{\chi}_2^0 \to Z\tilde{\chi}_1^0)$

Figure 10.12: Exclusion limits for the $(\tilde{W}, \tilde{B})$ and $(\tilde{H}, \tilde{B})$ models at the 95% CL shown as a function of the lightest chargino mass $m(\tilde{\chi}_1^{\pm})$ (the x-axis) and the lightest neutralino mass $m(\tilde{\chi}_1^0)$ (the y-axis) [49]. Expected (a) and observed (b) limits for various $\mathcal{B}(\tilde{\chi}_2^0 \to Z\tilde{\chi}_1^0)$ hypotheses overlaid. The outer and inner lines correspond to the limits for the $(\tilde{W}, \tilde{B})$ and $(\tilde{H}, \tilde{B})$ models, respectively.

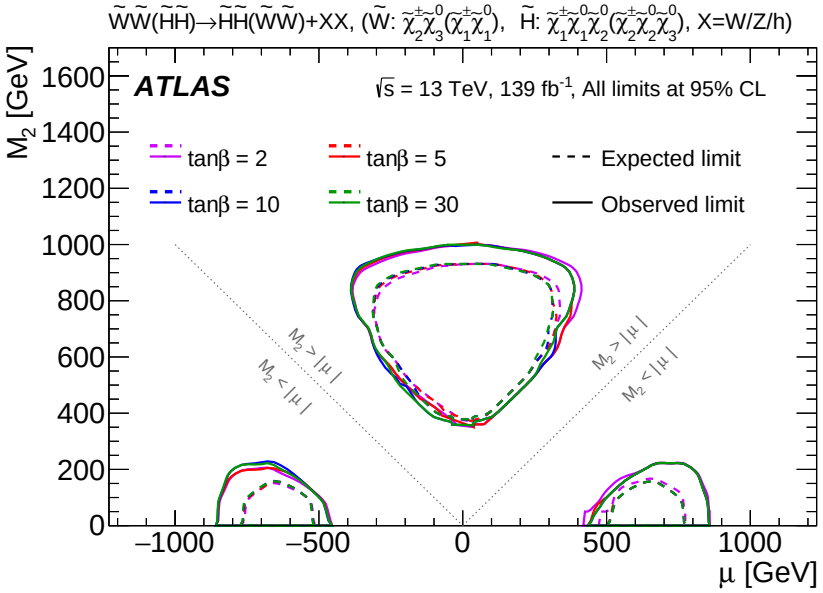

(a) Limits in the (μ, M_2) plane with various $\tan\beta$

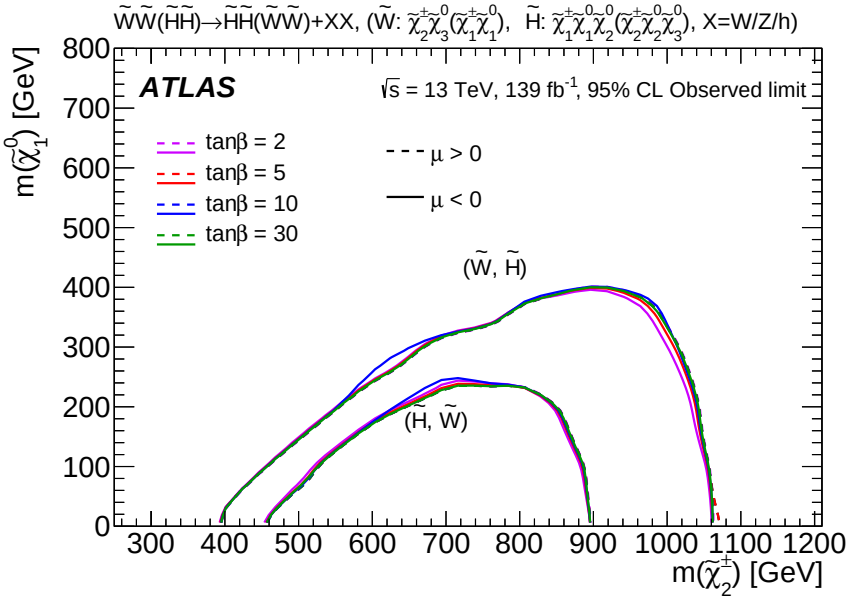

(b) Limits in the $(m(\tilde{\chi}_2^{\pm}),\ m(\tilde{\chi}_1^0))$ plane with various $\tan\beta$

Figure 10.13: Exclusion limits for the $(\tilde{W}, \tilde{H})$ and $(\tilde{H}, \tilde{W})$ models at the 95% CL shown [49]. The limits are projected to the higgsino mass and wino mass parameters plane (μ, M_2) (a). Additionally, the limits are projected to the gaugino mass eigenstates plane (b). The limits are shown as a function of the heavy chargino mass $m(\tilde{\chi}_2^{\pm})$ (the x-axis) and the lightest neutralino mass $m(\tilde{\chi}_1^0)$ (the y-axis).

10.3.3 $(\tilde{H}, \tilde{G})$ model

Figure 10.14 shows the exclusion limit for the $(\tilde{H}, \tilde{G})$ model as a function of the mass of the lightest neutralino $m(\tilde{\chi}_1^0)$ and the branching ratio $\mathcal{B}(\tilde{\chi}_1^0 \to Z\tilde{G})$. The region with $m(\tilde{\chi}_1^0)$ between 450 GeV and 940 GeV is excluded for $\mathcal{B}(\tilde{\chi}_1^0 \to Z\tilde{G}) = 100\%$ in this analysis while the previous analysis [161] excluded up to 540 GeV by the multi-lepton analysis. The improvement in the sensitivity corresponds to 17 times on the production cross-section of $\tilde{H}$. The region with $m(\tilde{\chi}_1^0)$ between 500 GeV and 850 GeV is excluded for $\mathcal{B}(\tilde{\chi}_1^0 \to Z\tilde{G}) = 50\%$ in this analysis while the previous analysis [162] excluded up to 580 GeV by the multi-b analysis. The sensitivity with $\mathcal{B}(\tilde{\chi}_1^0 \to Z\tilde{G}) = 50\%$ in the previous analyses is worse because their targets are only $\tilde{\chi}_1^0\tilde{\chi}_1^0 \to ZZ\tilde{G}\tilde{G}$ or $\tilde{\chi}_1^0\tilde{\chi}_1^0 \to hh\tilde{G}\tilde{G}$ process. The sensitivity at $\mathcal{B}(\tilde{\chi}_1^0 \to Z\tilde{G}) = 50\%$ is improved by targeting the $\tilde{\chi}_1^0\tilde{\chi}_1^0 \to Zh\tilde{G}\tilde{G}$ process for the first time.

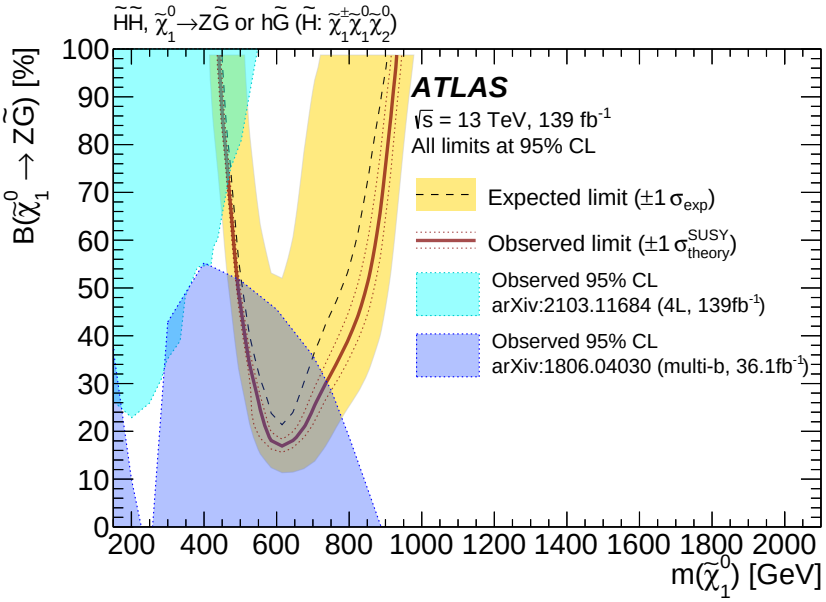

Figure 10.14: Expected (dashed black) and observed (solid red) exclusion limits for the $(\tilde{H}, \tilde{G})$ model at the 95% CL, as a function of the lightest neutralino mass $m(\tilde{\chi}_1^0)$ and the branching ratio $\mathcal{B}(\tilde{\chi}_1^0 \to Z\tilde{G}) = 1 - \mathcal{B}(\tilde{\chi}_1^0 \to h\tilde{G})$ [49]. The exclusion limits from the previous ATLAS search using multi-lepton analysis [161] (cyan) and final states with multi-b analysis [162] (blue) are shown by the shades.

10.3.4 $(\tilde{H}, \tilde{a})$ model

Figure 10.15 shows the exclusion limit for the $(\tilde{H}, \tilde{a})$ model as a function of the mass of the lightest neutralino $m(\tilde{\chi}_1^0)$ and the axino mass $m(\tilde{a})$. As in the $(\tilde{H}, \tilde{G})$ model, the excluded lightest neutralino mass range strongly depends on the branching ratio. The region with $m(\tilde{\chi}_1^0)$ between 450 (500) GeV and 940 (850) GeV is excluded for the massless-like axino and $\mathcal{B}(\tilde{\chi}_1^0 \to Z\tilde{a}) = 100\ (50)\%$.

In the $(\tilde{H}, \tilde{a})$ model, this analysis provides the exclusion limit for the first time since the previous study [163]. The sensitivity is significantly improved by about 600 GeV on $m(\tilde{\chi}_1^0)$.

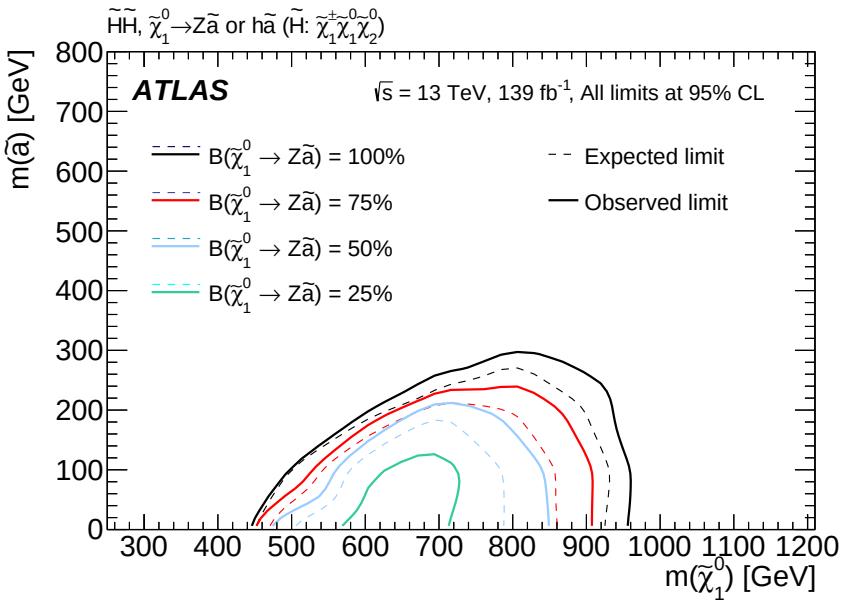

Figure 10.15: Expected (dashed lines) and observed (solid lines) limits with various $\mathcal{B}(\tilde{\chi}_1^0 \to Z\tilde{a})$ (= $1-\mathcal{B}(\tilde{\chi}_1^0 \to h\tilde{a})$) hypothesis as a function of the lightest neutralino mass $m(\tilde{\chi}_1^0)$ and the axino mass $m(\tilde{a})$ at the 95% CL [49]. There is no expected limit with $\mathcal{B}(\tilde{\chi}_1^0 \to Z\tilde{a}) = 25\%$ because the CLs values of all the benchmark signal points in the $(m(\tilde{\chi}_1^0),\ m(\tilde{a}))$ plane is less than 0.05.

11 Discussions

The future prospects in this analysis and the comparisons between the results in this analysis and the prospects in other final states are discussed in Section 11.1. How the results of this analysis have changed the direction of the search for electroweakinos with a large mass difference between $\tilde{\chi}_{\text{heavy}}$ and $\tilde{\chi}_{\text{light}}$ in the future ATLAS experiment is discussed.

As discussed in Section 2.3.4, the MSSM provides the solutions for the problems in the SM. The lightest neutralino is the LSP and can be a good dark matter candidate. Thus, the impact on the SUSY scenarios motivated by the dark matter with the $\tilde{B}/\tilde{W}/\tilde{H}$-LSP by the results in this thesis is discussed using the pMSSM framework in Section 11.2. The MSSM can also explain the muon g-2 anomaly by introducing the loops between sleptons and electroweakinos. In this thesis, sleptons are assumed to be heavy and not generated in the production or decay processes of target topologies. The impact of this analysis on the scenarios motivated by the muon g-2 anomaly is checked using the pMSSM framework in Section 11.3. The naturalness in the light higgsino case is also discussed in Section 11.4.

11.1 Future Prospects

The LHC Run-3 is planned to start in 2022, and an additional 160 fb^{-1} of data is expected to be recorded in 3 years. The High-Luminosity LHC (HL-LHC) [164] is planned after the LHC Run-3. In the HL-LHC, a center-of-mass energy will be 14 TeV and a luminosity of $5.0 \sim 7.5 \times 10^{34}\,\text{cm}^{-2}\text{s}^{-1}$ is expected by the upgrade of the accelerator. Thus, 3000 $\sim$ 4000 fb^{-1} of data is expected to be recorded in $\sim$ 10 years. The exclusion limits of this analysis and the future limit projections of multi-lepton and multi-b analyses are compared, and the sensitivity of this analysis is extrapolated to the LHC Run-3 and HL-LHC.

11.1.1 Future Prospects of the Multi-Lepton and Multi-b-and-1-Lepton Analyses

Figure 11.1 shows the future limit projection of the multi-lepton analysis and the exclusion limit for the C1N2-WZ model in this analysis. The multi-lepton analysis will exclude $m(\tilde{\chi}_1^\pm/\tilde{\chi}_2^0) < 840$ GeV at 300 fb^{-1} [165]. In this analysis, the exclusion has been improved to 960 GeV for $m(\tilde{\chi}_1^\pm/\tilde{\chi}_2^0)$, which outperforms the multi-lepton analysis at 300 fb^{-1}.

Figure 11.2 shows the future limit projection of the multi-b-and-1-lepton analysis and the exclusion limit in this analysis. The multi-b-and-1-lepton analysis will exclude $m(\tilde{\chi}_1^\pm/\tilde{\chi}_2^0) < 920$ GeV at 300 fb^{-1}. In this analysis, the exclusion has been improved to 1060 GeV for $m(\tilde{\chi}_1^\pm/\tilde{\chi}_2^0)$, which outperforms the multi-b-and-1-lepton analysis at 300 fb^{-1}. The multi-lepton analysis for $\tilde{\chi}_1^\pm\tilde{\chi}_2^0 \rightarrow Wh\tilde{\chi}_1^0\tilde{\chi}_1^0 \rightarrow l\nu ll\ (l\nu\tau\tau) + \tilde{\chi}_1^0\tilde{\chi}_1^0$ also provides the future limit projection [165]. The multi-lepton analysis will exclude $m(\tilde{\chi}_1^\pm/\tilde{\chi}_2^0) < 940$ GeV at 3000 fb^{-1} collected in the HL-LHC, which the exclusion limit achieved in this analysis already surpasses for scenarios with $\Delta m > 500$ GeV in the multi-lepton analyses using 21 times or more data statistics.

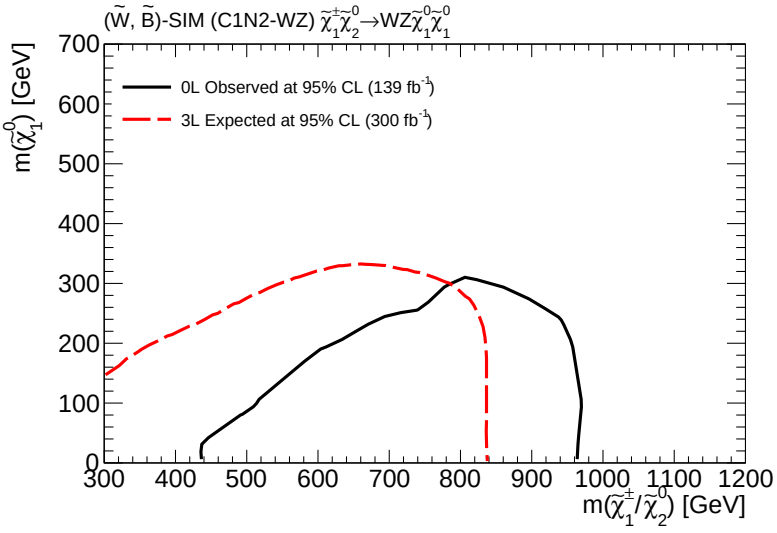

Figure 11.1: Comparison of exclusion limits in the C1N2-WZ model at the 95% CL and the future projection of the multi-lepton analysis, as a function of the bino mass $m(\tilde{\chi}_1^0)$ and the wino mass $m(\tilde{\chi}_1^\pm/\tilde{\chi}_2^0)$. The solid black line is the exclusion limit at the 95% CL in this analysis using the fully hadronic final state. The dashed red line is the expected exclusion limit at the 95% CL of the future multi-lepton analysis at 300 fb^{-1} taken by ATLAS in the future [165].

Figure 11.3 shows the future limit projection of the multi-lepton and multi-b analyses at 300 fb^{-1}. The combined results will exclude $m(\tilde{\chi}_1^\pm) < 600$ GeV at 300 fb^{-1}. In this analysis, the exclusion has been improved to 900 GeV for $m(\tilde{\chi}_1^\pm)$, which outperforms the combined analyses at 300 fb^{-1}.

In the $(\tilde{W}, \tilde{H})$ model, Ref.[168] provides the future limit projection of the same sign multi-lepton analysis. The same sign multi-lepton analysis will exclude $m(\tilde{W}) < 800$ GeV at 1000 fb^{-1}. In this analysis, the exclusion has been improved to 1000 GeV for $m(\tilde{W})$, which outperforms the same sign multi-lepton analyses at 1000 fb^{-1}.

In the $(\tilde{H}, \tilde{a})$ model, Ref.[169] reports the exclusion limits up to 300 GeV for $m(\tilde{\chi}_2^0)$. In this analysis, the exclusion has been improved to 960 GeV if $\mathcal{B}(\tilde{\chi}_1^0 \rightarrow Z\tilde{a}) = 100\%$, and the sensitivity is significantly improved.

As discussed above, the sensitivities in this analysis to search for heavy electroweakinos outperform the future limit projections of the other analyses without any significant improvements. However, the other analyses have better sensitivity with a small difference ($\tilde{\chi}_{\text{heavy}} - \tilde{\chi}_{\text{light}} < 300$ GeV) since this analysis focus on the heavy electroweakino scenarios with the large mass difference. Therefore, by optimizing the other analyses for a small mass difference, efficient SUSY searches can be performed in ATLAS as a whole.

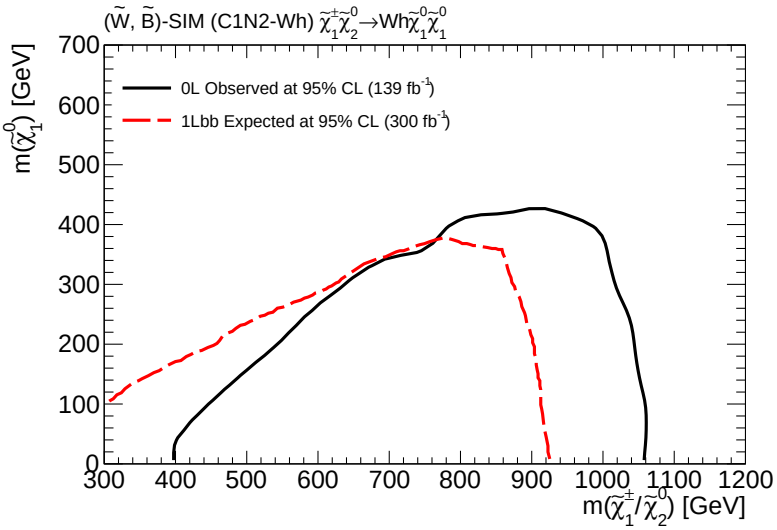

Figure 11.2: Comparison of exclusion limits in the C1N2-Wh model at the 95% CL and the future projection of the multi-b-and-1-lepton analysis, as a function of the bino mass $m(\tilde{\chi}_1^0)$ and the wino mass $m(\tilde{\chi}_1^\pm/\tilde{\chi}_2^0)$. The solid black line is the exclusion limit at the 95% CL in this analysis using the fully hadronic final state. The dashed red line is the expected exclusion limit at the 95% CL of the future multi-lepton analysis at 300 fb^{-1} taken by ATLAS in the future [166].

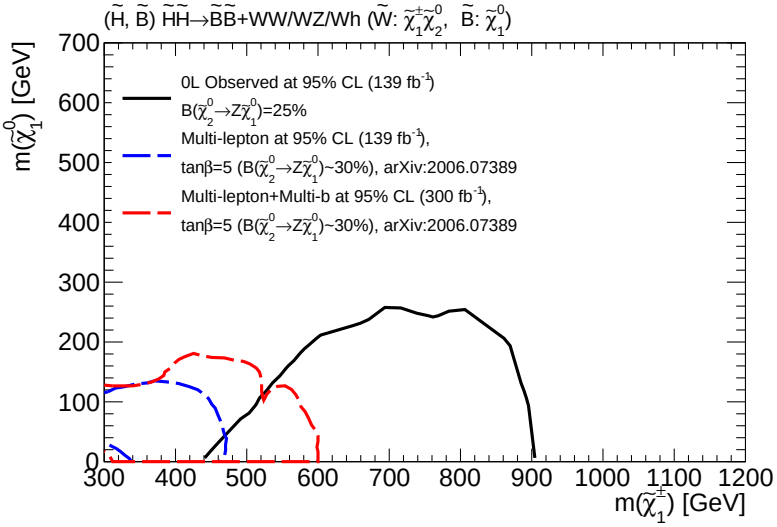

Figure 11.3: Exclusion limits in the $(\tilde{H}, \tilde{B})$ model at the 95% CL, as a function of the bino mass $m(\tilde{\chi}_1^0)$ and the charged higgsino mass $m(\tilde{\chi}_1^\pm)$. The solid black line is the exclusion limit with $\mathcal{B}(\tilde{\chi}_2^0 \to Z\tilde{\chi}_1^0) = 50\%$ at the 95% CL in this analysis using the fully hadronic final state. The dashed blue (red) line is the obtained (expected) limit by interpreting the results in the previous analyses at the 95% CL at 139 fb^{-1} (300 fb^{-1}) taken by ATLAS in the future [167].

11.1.2 Future Prospects of the Full-Hadronic Analysis

This analysis can impose much tighter event selections to search heavier electroweakinos with larger mass splittings and large data statistics in the HL-LHC. The event selections are summarized in Table 11.1.

The limit projections of some benchmark signals are shown in Figure 11.4. Considering the $(\tilde{W}, \tilde{B})$-SIM, the sensitivity can be extended up to 1.3-1.5 TeV in $m(\tilde{\chi}_1^{\pm}/\tilde{\chi}_2^0)$ with $\mathcal{L} = 3000$ fb^{-1}. In $(\tilde{H}, \tilde{G})$, the sensitivity can be extended up to 1.3 TeV in $m(\tilde{\chi}_1^0)$ with $\mathcal{L} = 3000$ fb^{-1}.

Table 11.1: Event selections for the future limit projection. Preselction (Precut0L4Q and Precut0L2B2Q) and the boson tagging requirements are not changed and omitted while they are required.

Category	Integrated luminosity	Selections		
SR-4Q	139 fb^{-1} (Run-2)	$E_{\mathrm{T}}^{\mathrm{miss}} > 300$ GeV	$\min \Delta\phi(j, E_{\mathrm{T}}^{\mathrm{miss}}) > 1.0$	$m_{\mathrm{eff}} > 1300$ GeV
	300 fb^{-1} (Run-3)	$E_{\mathrm{T}}^{\mathrm{miss}} > 400$ GeV	$\min \Delta\phi(j, E_{\mathrm{T}}^{\mathrm{miss}}) > 1.0$	$m_{\mathrm{eff}} > 1500$ GeV
	3000 fb^{-1} (HL-LHC)	$E_{\mathrm{T}}^{\mathrm{miss}} > 400$ GeV	$\min \Delta\phi(j, E_{\mathrm{T}}^{\mathrm{miss}}) > 1.6$	$m_{\mathrm{eff}} > 1900$ GeV
SR-2B2Q	139 fb^{-1} (Run-2)	$E_{\mathrm{T}}^{\mathrm{miss}} > 200$ GeV	$m_{\mathrm{T2}} > 250$ GeV	$m_{\mathrm{eff}} > 1000$ GeV
	300 fb^{-1} (Run-3)	$E_{\mathrm{T}}^{\mathrm{miss}} > 200$ GeV	$m_{\mathrm{T2}} > 250$ GeV	$m_{\mathrm{eff}} > 1100$ GeV
	3000 fb^{-1} (HL-LHC)	$E_{\mathrm{T}}^{\mathrm{miss}} > 400$ GeV	$m_{\mathrm{T2}} > 250$ GeV	$m_{\mathrm{eff}} > 1600$ GeV

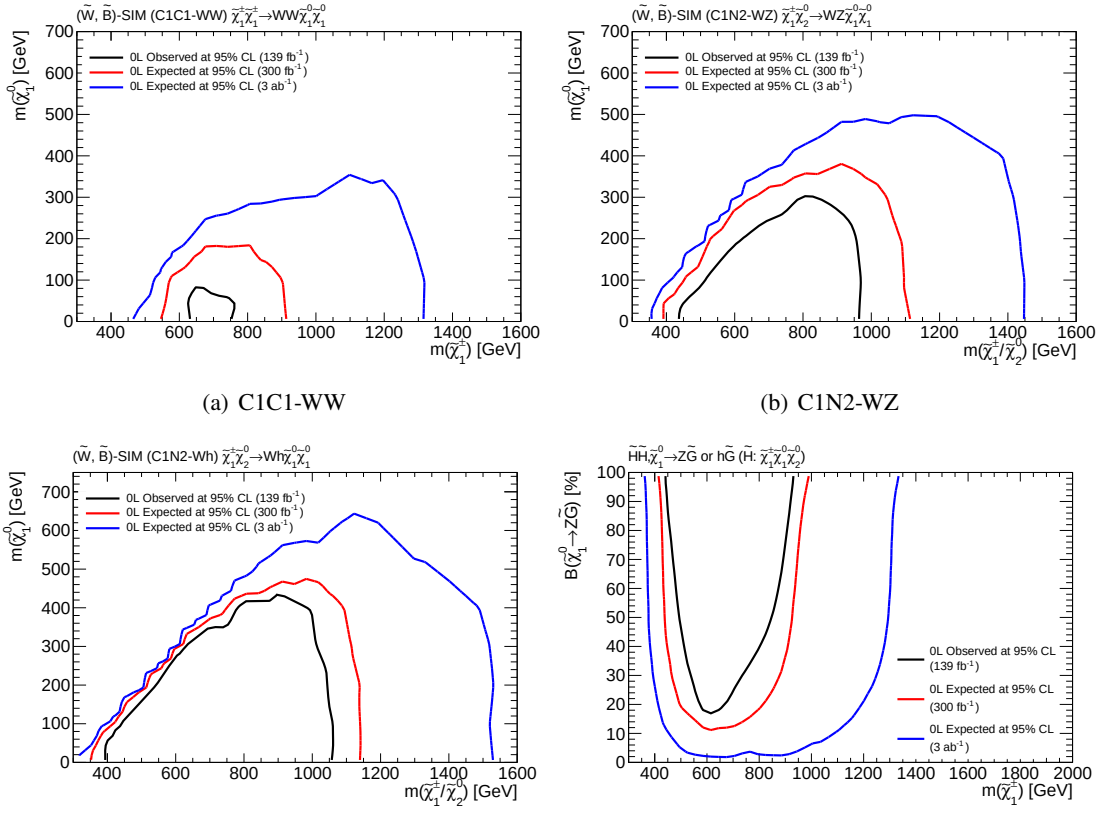

(a) C1C1-WW

(b) C1N2-WZ

(c) C1N2-Wh

(d) $(\tilde{H}, \tilde{G})$

Figure 11.4: The prospects for the $(\tilde{W}, \tilde{B})$-SIM and $(\tilde{H}, \tilde{G})$ models. The exclusion limits at the 95% CL in the C1C1-WW (a), C1N2-WZ (b), and C1N2-Wh models as functions of $m(\tilde{\chi}_1^{\pm}/\tilde{\chi}_2^0)$ and $m(\tilde{\chi}_1^0)$. The exclusion limits at the 95% CL in the $(\tilde{H}, \tilde{G})$ model as functions of $m(\tilde{\chi}_1^0)$ and the branching ratio of $\tilde{\chi}_1^0 \to Z\tilde{G}$. The black lines represent the observed limits of this analysis using 139 fb^{-1} with 30% systematic uncertainty of backgrounds. Red (blue) lines correspond to the expected limits with 300 (3000) fb^{-1} and 30% systematic uncertainty of backgrounds.

11.2 Implication to Dark Matter

As discussed in Section 2.3.4.2, the lightest neutralino can be a good candidate for the dark matter. Figure 2.6 shows the dark matter density with $\tilde{B}/\tilde{W}/\tilde{H}$-like dark matter as a function of $m(\tilde{\chi}_1^0)$. If other particles can also be dark matter components, the expected dark matter density of $\tilde{B}/\tilde{W}/\tilde{H}$ will be small.

11.2.1 $\tilde{B}$-like Dark Matter

In this thesis, the SUSY models with a large mass difference between $\tilde{\chi}_{\text{heavy}}$ and $\tilde{\chi}_{\text{light}}$ are targeted, and the other SUSY particles, such as sleptons and BSM Higgs bosons, are decoupled. Thus, only the Z-/h-funnel models [41] as the $\tilde{B}$-dominant dark matter scenario can explain the dark matter density ($\Omega_{\tilde{\chi}_1^0}h^2 = 0.12$). In these models, $m(\tilde{\chi}_1^0) \sim m(Z)/2,\ m(h)/2$. For the Z-/h-funnel models, the density of $\tilde{B}$ is determined by the coupling between the dark matter (LSP) and Z/h bosons. The coupling depends on the higgsino mass parameter μ and the ratio of the Higgs vacuum expectation values $\tan\beta$ (more details described in Appendix A.4). Therefore, the upper limit for μ can be set if the density of $\tilde{B}$ is allowed to be smaller than the observed dark matter density.

Then, the $(\tilde{H}, \tilde{B})$ model[1] is considered. Figure 11.5 shows the constraint from this analysis. From the results in this analysis, the $m(\tilde{\chi}_2^0)$ between 500 GeV and 900 GeV are excluded regardless of $\tan\beta$ and the sign of μ. Thus, in the $(\tilde{H}, \tilde{B})$ scenario motivated by the dark matter, $5.5 < \tan\beta < 7$ is excluded in the h-funnel case with $\mu < 0$ and $\tan\beta > 8.5$ is excluded in the h-funnel case with $\mu > 0$. In these regions, the XENON-1T experiment is insensitive (more detail is described in Appendix A.4). While the indirect dark matter searches, such as Fermi-LAT [63] and AMS-02 [64], provide the limits on the dark matter annihilation cross-sections times the velocity for $\tilde{\chi}_1^0\tilde{\chi}_1^0 \to b\bar{b}$ or $\tau\bar{\tau}$, they do not provide the significant constraint for the Z-/h-funnel models since the upper limit is at most $O(10^{-28})$ cm^{3}s^{-1} and enough smaller than the expected cross-sections times the velocity of $\tilde{B}$ [41]. Other constraints discussed in Ref.[41] do not provide effective exclusion limits. Therefore, this analysis provides the most stringent limit on the $(\tilde{H}, \tilde{B})$ scenario motivated by the dark matter.

11.2.2 $\tilde{W}$-/$\tilde{H}$-like Dark Matter

In the light $\tilde{W}$-LSP or $\tilde{H}$-LSP cases, the lightest chargino degenerates. Such case with $m(\tilde{\chi}_1^\pm) < 103$ GeV is already excluded by LEP [40]. Considering the heavy $\tilde{W}$-LSP or $\tilde{H}$-LSP cases, the lightest neutralino mass $m(\tilde{\chi}_1^0)$ is favored to be 3 (1) TeV, as shown in Figure 2.6. However, these heavy LSPs are not considered in this analysis, but the models where $\tilde{W}$ or $\tilde{H}$ is the LSP and one of the dark matter components. To study these dark matter models, the phenomelogical MSSM parameters are scanned over using libraries, such as SOFTSUSY [170], SPheno [171], FeynHiggs [172], GM2Calc [173] and micrOMEGAs [174]. The ranges for scan of the parameters are summarized in Table 11.2. In this thesis, the $(\tilde{W}, \tilde{H})$ and $(\tilde{H}, \tilde{W})$ models are considered. Then, the ranges of scan for these models are considered, and the results are shown in the $\tilde{H}$ and $\tilde{W}$ mass parameters plane (μ, M_2). In this study, the positive $\tilde{W}$ mass ($M_2 > 0$) and the positive/negative $\tilde{H}$ mass case is only considered. The reason why the negative M_2 case is not considered is

[1] In the $(\tilde{W}, \tilde{B})$ model, we need to introduce an inconsistent assumption for this analysis. To explain the observed dark matter density, the higgsino mass parameter μ is required to be not very large, even though higgsino is assumed to be decoupled. Thus, the $(\tilde{W}, \tilde{B})$ model motivated by the dark matter is not considered here.

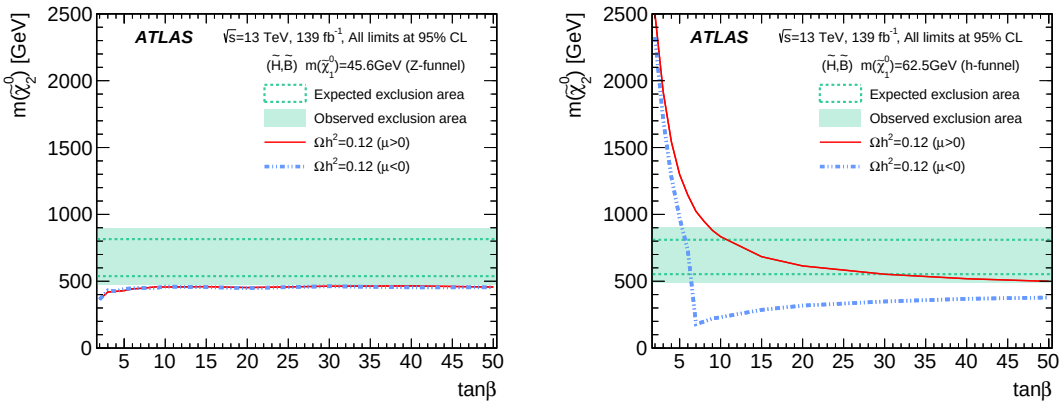

(a) Z funnel

(b) h funnel

Figure 11.5: Expected (dashed green band) and observed (hashed green band) limits at the 95% CL on the $(\tilde{H}, \tilde{B})$ model as a function of $\tan\beta$ and $m(\tilde{\chi}_2^0)$, when the mass of $\tilde{B}$-like LSP ($\tilde{\chi}_1^0$) being (a) half of the Z-mass (42.6 GeV), or (b) half of the h-mass (62.5 GeV) so that the LSP dark matter can annihilate via Z/h resonance [49]. The areas surrounded by the bands represent the excluded range of $\tilde{\chi}_2^0$. The limits are assumed to be constant along $\tan\beta$ given the small dependency on $\mathcal{B}(\tilde{\chi}_2^0 \to Z\tilde{\chi}_1^0)$ seen in Figure 10.12. The overlaid red solid (blue dashed) line indicates $\tilde{\chi}_2^0$ that reproduces the observed dark matter relic density, $\Omega h^2 = 0.12$, with $\mu > 0$ ($\mu < 0$) [41].

that the transformation that $M_2 \to -M_2$ corresponds to the conversion of $\mu \to -\mu$, i.e., the sign of $M_2 \times \mu$ is important.

Some MSSM parameters, such as the mass parameters for superpartners, are constrained by the ATLAS and CMS analyses. However, these constraints depend on the LSP type; in most cases, $\tilde{B}$-LSP is considered. Thus, the exclusion limits can not apply to this study for the $\tilde{W}$-LSP or $\tilde{H}$-LSP cases. For example, the searches for stop, as shown in Figure 2.4(b) target the decay process of $\tilde{t} \to X\tilde{\chi}_1^0$, however, in the $\tilde{W}$-LSP or $\tilde{H}$-LSP cases, $\tilde{t} \to X\tilde{\chi}_1^\pm$ process is allowed. Then, the exclusion limits become smaller.

Thus, the following selections for the dark matter motivated scenario in the $(\tilde{W}, \tilde{H})$ or $(\tilde{H}, \tilde{W})$ case are imposed:

- Selections for the $(\tilde{W}, \tilde{H})$ and $(\tilde{H}, \tilde{W})$ models:
  - $|M_2|, |\mu| < |M_1|$ ($\tilde{B}$ is decoupled)
  - $\mathcal{B}(\tilde{W} \to W/Z/h + \tilde{H}) \sim 100\%$ or $\mathcal{B}(\tilde{H} \to W/Z/h + \tilde{W}) \sim 100\%$
- Passing the loose constraint on the observed dark matter density: $\Omega_M h^2 < 0.14$
- Passing the constraint on the Higgs mass: 124 GeV $< m_h <$ 128 GeV
- Passing the constraints from other analyses
  - XENON-1T [60, 61] (direct dark matter search)
  - Fermi-LAT [175] and AMS-02 [64] (indirect dark matter search)
  - The searches for electroweakinos with a small mass difference between $\tilde{\chi}_1^\pm$ ($\tilde{\chi}_2^0$) and $\tilde{\chi}_1^0$ [53, 55, 176]

Table 11.2: The ranges of the pMSSM parameters scan in the dark matter motivated scenarios for the $\tilde{W}$-LSP and $\tilde{H}$-LSP cases.

Parameter	**Min value**	**Max value**	**Note**
$m_{\tilde{L}_1}(= m_{\tilde{L}_2})$	90 GeV	4 TeV	Left-handed slepton (first two gens.) mass
$m_{\tilde{e}_1}(= m_{\tilde{e}_2})$	90 GeV	4 TeV	Right-handed slepton (first two gens.) mass
$m_{\tilde{L}_3}$	90 GeV	4 TeV	Left-handed stau doublet mass
$m_{\tilde{e}_3}$	90 GeV	4 TeV	Right-handed stau mass
$m_{\tilde{Q}_1}(= m_{\tilde{Q}_2})$	1 TeV	10 TeV	Left-handed squark (first two gens.) mass
$m_{\tilde{u}_1}(= m_{\tilde{u}_2})$	1 TeV	10 TeV	Right-handed up-type squark (first two gens.) mass
$m_{\tilde{d}_1}(= m_{\tilde{d}_2})$	1 TeV	10 TeV	Right-handed down-type squark (first two gens.) mass
$m_{\tilde{Q}_3}$	1 TeV	10 TeV	Left-handed squark (third gen.) mass
$m_{\tilde{u}_3}$	1 TeV	10 TeV	Right-handed top squark mass
$m_{\tilde{d}_3}$	1 TeV	10 TeV	Right-handed bottom squark mass
$\lvert M_1 \rvert$	400 GeV	13 TeV	Bino mass parameter
M_2	70 GeV	1.2 TeV	Wino mass parameter
$\lvert \mu \rvert$	80 GeV	1.0 TeV	Bilinear Higgs mass parameter
M_3	1.5 TeV	4 TeV	Gluino mass parameter
$\lvert A_t \rvert$	0 GeV	16 TeV	Trilinear top coupling
$\lvert A_b \rvert$	0 GeV	4 TeV	Trilinear bottom coupling
$\lvert A_\tau \rvert$	0 GeV	4 TeV	Trilinear τ lepton coupling
m_A	100 GeV	4 TeV	Pseudoscalar Higgs boson mass
$\tan\beta$	1	70	Ratio of the Higgs vacuum expectation values

- The combined LEP search [40] ($m(\tilde{\chi}_1^\pm) > 103$ GeV)
- $2.69\times10^{-4} < \mathcal{B}(b \to s\gamma) < 3.87\times10^{-4}$ ($\pm2\sigma$ of theoretical prediction [177] and experimental measurements [178])
- $1.6\times10^{-9} < \mathcal{B}(B_s \to \mu^+\mu^-) < 4.2\times10^{-9}$ ($\pm2\sigma$ of LHCb [179] and CMS [180] measurements)
- $6.6\times10^{-5} < \mathcal{B}(B^+ \to \tau^+\nu_\tau) < 16.1\times10^{-5}$ ($\pm2\sigma$ of experimental results [181] and theoretical prediction [182])

The result of the scan is shown in Figure 11.6. $|M_2 - \mu| < 90$ GeV is not considered in this thesis. In large $(\mu - M_2)$ region, i.e., the target phase space in this analysis, $\tilde{W}$-like $\tilde{\chi}_1^\pm$ and $\tilde{\chi}_1^0$ degenerate. Thus, the search for a small mass difference between $\tilde{\chi}_1^\pm$ and $\tilde{\chi}_1^0$ in ATLAS [55] provides a stringent limit. However, if $\tilde{H}$ is the LSP, this analysis provides the most powerful sensitivity than other experiments. That is because the direct and indirect searches have low sensitivities and provide the constraints of interactions of whole the dark matter, not one component, such as $\tilde{\chi}_1^0$. ATLAS and CMS have poor sensitivities in a mass difference between $\tilde{\chi}_1^\pm$ and $\tilde{\chi}_1^0$ (> 2 GeV). The asymmetry on the sign of μ is caused by a difference in the dark matter annihilation cross-sections. This analysis provides the most stringent limits for the scenario motivated by the dark matter with $\tilde{H}$-like LSP ($\mu > 150$ GeV).

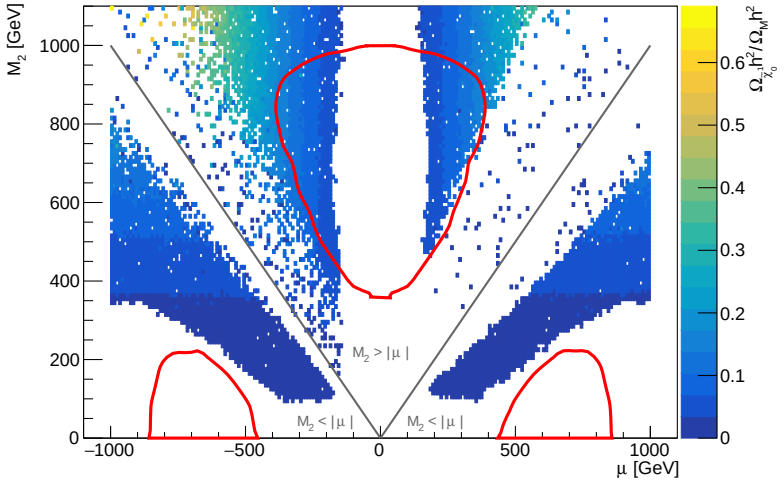

Figure 11.6: Reults of pMSSM scan in the $(\tilde{W}, \tilde{H})$ and $(\tilde{H}, \tilde{W})$ model motivated by the dark matter in $(\mu,\ M_2)$. The z-axis represents the fraction of relic density. The red lines represent the observed exclusion limits of this analysis ($\tan\beta = 30$) at the 95% CL. The gray lines represent $M_2 = |\mu|$.

11.3 Implication to Muon g-2 anomaly

As discussed in Section 2.3.4.3, the discrepancy can be explained using the loop of electroweakinos and sleptons. Discrepancy of the muon g-2 at 4.2σ level is reported by the Fermilab group [45]:

$$\Delta a_\mu = a_\mu^{\mathrm{expm}} - a_\mu^{\mathrm{SM}} = (25.1 \pm 5.9) \times 10^{-10}. \tag{11.1}$$

A contribution of Δa_μ by the SUSY particles ($\Delta a_\mu^{\mathrm{SUSY}}$) is proportional to $\tan\beta$. Thus, if $\tan\beta$ is small, electroweakinos are required to be light to explain the muon g-2 anomaly. The light electroweakino cases have already been excluded by the previous analyses with multi-lepton final states. Thus, the heavy electroweakino cases, i.e., with large $\tan\beta$ are considered in this thesis.

In order to evaluate the contribution by the SUSY particles in the target models of this thesis, $\Delta a_\mu^{\mathrm{SUSY}}$ is calculated with various $\tilde{B}/\tilde{W}/\tilde{H}$ mass parameter ($M_1,\ M_2,\ \mu$), and the fixed smuon mass, $\tan\beta$. The settings of calculations are,

- $\tan\beta = 60$
- $m_{\tilde{\mu}_L} = 700$ GeV
- $m_{\tilde{\mu}_R} = \begin{cases} 701 \text{ GeV} & \text{(light } \tilde{\mu}_R \text{ model)} \\ 3000 \text{ GeV} & \text{(heavy } \tilde{\mu}_R \text{ model)} \end{cases}$
- The heaviest of ($M_1,\ M_2,\ \mu$) is assumed to be 3000 GeV.

The settings are determined by the typical upper limit of $\tan\beta$ and passing the constraints on the smuon search [157].

The results with the light or heavy $\tilde{\mu}_R$ models are shown in Figure 11.8 and Figure 11.9. Figure 11.8 shows the results in the heavy $\tilde{\mu}_R$ model, where the contributions of right-handed smuons are assumed to be negligible. Figure 11.9 shows the results in the light $\tilde{\mu}_R$ model. The red lines represent the observed exclusion limits of this analysis.

In the $(\tilde{W}, \tilde{B})$ and $(\tilde{H}, \tilde{B})$ models, $\Delta a_\mu^{\mathrm{SUSY}}$ is typically smaller than 1.5×10^{-9} with $\tan\beta = 60$ and $m_{\tilde{\mu}} \sim 700$ GeV. However, $\Delta a_\mu^{\mathrm{SUSY}}$ with large $\tan\beta$ (for example, $\tan\beta = 100$) is consistent with the anomaly since $\Delta a_\mu^{\mathrm{SUSY}}$ strongly depends on $\tan\beta$ and $m_{\tilde{\mu}}$. Since the results in this analysis only depend on the mass, constraints on the scenarios motivated by the muon g-2 anomaly can be set if very large $\tan\beta$ is assumed. On the other hand, the $(\tilde{W}, \tilde{H})$ and $(\tilde{H}, \tilde{W})$ models are favored by the muon g-2 anomaly. XENON-1T provides stringent limits on the dark matter mass in the $(\tilde{W}, \tilde{H})$ model, as discussed in Ref.[46]. The search for electroweakinos with a small mass difference between $\tilde{\chi}_1^\pm$ and $\tilde{\chi}_1^0$ in the ATLAS experiment [55] provides stringent limits for the $(\tilde{H}, \tilde{W})$ model, as discussed in Section 11.2. The $(\tilde{W}, \tilde{H})$ and $(\tilde{H}, \tilde{W})$ models motivated by the muon g-2 anomaly are constrained by this analysis as well.

11.3.1 Light Electroweakino Scenarios motivated by Muon g-2 Anomaly

In this sub-section, specific parameter space, which passes the constraints by the other analyses and has a similar topology of target models in this thesis, is considered. The target models in this thesis are required to have a large mass difference (> 400 GeV) and light $\tilde{W}$ and $\tilde{H}$ cases, such as the $(\tilde{W}, \tilde{H})$ or $(\tilde{H}, \tilde{W})$ model is favored by the muon g-2 anomaly, as discussed above. However, these models have already been excluded by the other analyses [46, 55]. Then, light $\tilde{B}$ is also introduced in these models. If $\tilde{H}$ is the lightest or

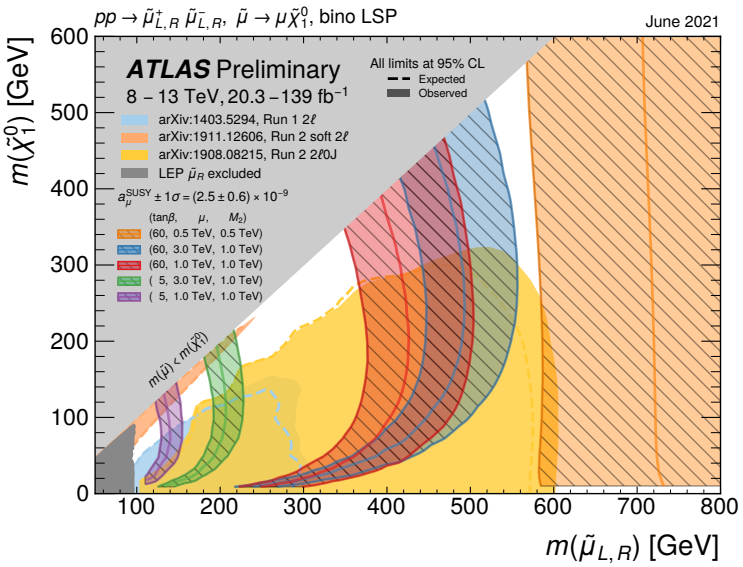

Figure 11.7: Exclusion limits of smuon at the 95% CL [58]. The hatched bands correspond to the observed muon g-2 anomaly [45]. The muon g-2 bands are calculated using the GM2Calc [173] and SPheno [171] packages.

second lightest of ($\tilde{B}$, $\tilde{W}$, $\tilde{H}$), the case is excluded by XENON-1T. Thus, the heaviest $\tilde{H}$ case is considered. If $\tilde{W}$ and $\tilde{B}$ do not degenerated, the multi-decay process with different Δm, such as $\tilde{H} \to V\tilde{W}$ and $\tilde{H} \to V\tilde{B}$, can be observed and they are not targeted in this thesis. On the contrary, if $\tilde{W}$ and $\tilde{B}$ degenerate (typically < 5 GeV), the results in this thesis can be interpreted since the difference in observed mass difference between two processes is small, and decay products of $\tilde{W}$ ($\tilde{B}$) decaying into $\tilde{B}$ ($\tilde{W}$) have low momenta and cannot be reconstructed by kinematic selections in this thesis. Since $\tilde{W}$-like dark matter case is excluded by XENON-1T, the case where $m(\tilde{B}) < m(\tilde{W}) < m(\tilde{H})$ and $m(\tilde{W}) - m(\tilde{B})$ is typically less than 5 GeV is considerd. The mass hierarchies of this case and a similar case such as ($\tilde{H}$, $\tilde{W}$) are shown in Figure 11.10. In this case, the mass difference between $\tilde{\chi}^{\pm}_{1}$ and $\tilde{\chi}^{0}_{1}$ is larger than the $\tilde{W}$-like LSP case. The target decay processes in this thesis are illustrated as red lines. The orange lines represent the decay process with a small mass difference, such as $\tilde{\chi}^{\pm}_{1}$ and $\tilde{\chi}^{0}_{1}$, and the decay products have low momenta. Thus, they are not observed in this thesis due to kinematic selections.

As the mass differences between $\tilde{\chi}^{\pm}_{1}$ ($\tilde{\chi}^{0}_{2}$) and $\tilde{\chi}^{0}_{1}$ are small, similar exclusion limits to the ($\tilde{H}$, $\tilde{W}$) model in this thesis because low p_{T} leptons and jets, as illustrated in an orange arrow in Figure 11.10, do not pass the lepton and jet selections and the exclusion limits for the ($\tilde{H}$, $\tilde{W}$) model in this thesis have a small dependency on MSSM parameters.

The phenomenological MSSM parameters are scanned over using libraries, such as SOFTSUSY [170], SPheno [171], FeynHiggs [172], GM2Calc [173] and micrOMEGAs [174]. The scan ranges of the parameters are summarized in Table 11.3. M_2 and μ are assumed to be positive because Δa_μ is low due to small $\tan\beta$ if $M_2 < 0$, and the dominant contribution of the $\tilde{W}$-$\tilde{H}$-$\tilde{\nu}_\mu$ is negative value if $M_2 > 0$ and $\mu < 0$.

The following selections are applied:

- Selections for the this target the ($\tilde{W}$, $\tilde{H}$) and ($\tilde{H}$, $\tilde{W}$) models:
  - $|M_2|, |M_1| < |\mu|$

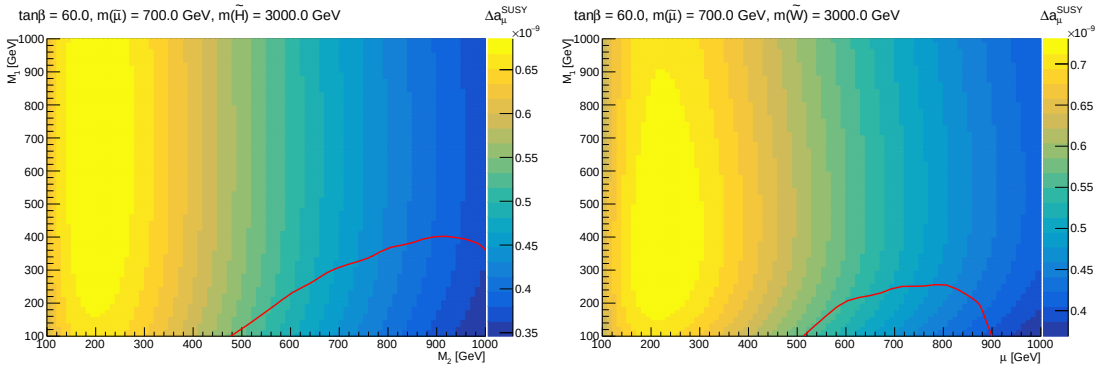

(a) $(\tilde{W}, \tilde{B})$ (b) $(\tilde{H}, \tilde{B})$

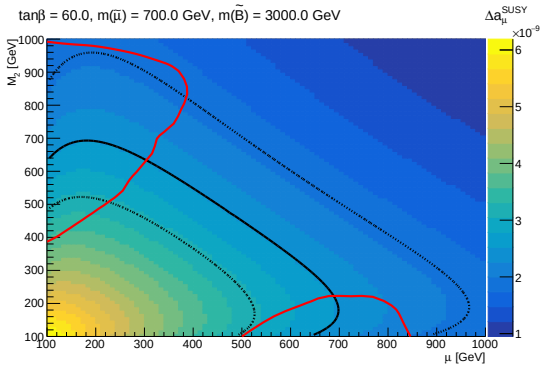

(c) $(\tilde{W}, \tilde{H})$, $(\tilde{H}, \tilde{W})$

Figure 11.8: $\Delta a_\mu^{\mathrm{SUSY}}$ with heavy right-handed smuon in the $(\tilde{W}, \tilde{B})$ (a), $(\tilde{H}, \tilde{B})$ (b), $(\tilde{W}, \tilde{H})$ and $(\tilde{H}, \tilde{W})$ (c) models. The black solid line represents $\Delta a_\mu^{\mathrm{SUSY}} = 2.5 \times 10^{-9}$, and the dashed lines represent 1σ band. The red lines are the observed exclusion limits of the $(\tilde{W}, \tilde{B})$ model with $\mathcal{B}(\tilde{\chi}_2^0 \to Z\tilde{\chi}_1^0) = 100\%$ (a), the $(\tilde{H}, \tilde{B})$ model with $\mathcal{B}(\tilde{\chi}_2^0 \to Z\tilde{\chi}_1^0) = \mathcal{B}(\tilde{\chi}_3^0 \to h\tilde{\chi}_1^0) = 100\%$ (b), and the $(\tilde{W}, \tilde{H})$ and $(\tilde{H}, \tilde{W})$ models with $\tan\beta = 30$ and $\mu > 0$ (c) at the 95% CL in this analysis.

  - $\mathcal{B}(\tilde{H} \to W/Z/h + \tilde{W}/\tilde{B}) \sim 100\%$
  - $m(\tilde{\chi}_1^\pm) - m(\tilde{\chi}_1^0) < 5$ GeV, $m(\tilde{\chi}_2^0) - m(\tilde{\chi}_1^0) < 5$ GeV
- Passing the constraint on the observed dark matter density: $\Omega_M h^2 < 0.12$ [8, 9]
- Passing the constraint on the Higgs mass: 124 GeV $< m_h <$ 128 GeV
- Passing the constraints from other analyses
  - XENON-1T [60, 61] (direct dark matter search)
  - Fermi-LAT [175] and AMS-02 [64] (indirect dark matter search)
  - The searches for electroweakinos with a small mass difference between $\tilde{\chi}_1^\pm$ ($\tilde{\chi}_2^0$) and $\tilde{\chi}_1^0$ [53, 55, 176]
  - The combined LEP search [40] ($m(\tilde{\chi}_1^\pm) > 103$ GeV)

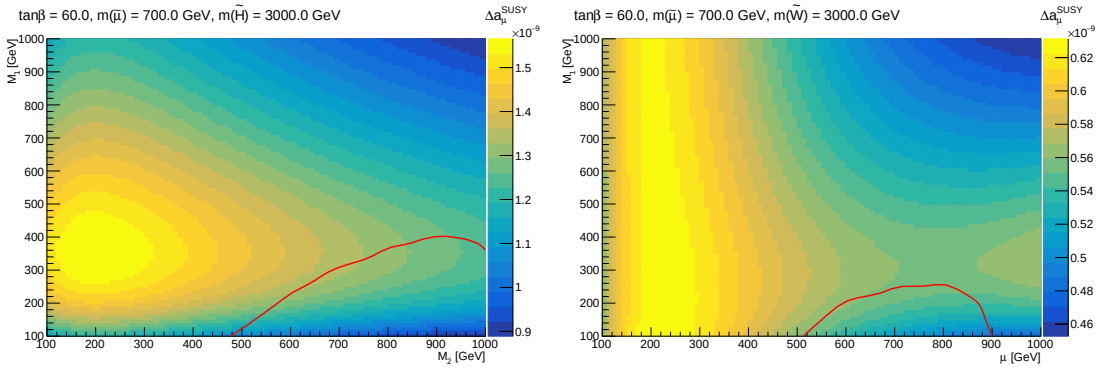

(a) $(\tilde{W}, \tilde{B})$ (b) $(\tilde{H}, \tilde{B})$

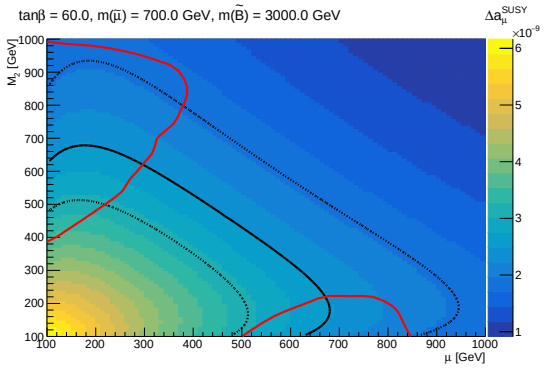

(c) $(\tilde{W}, \tilde{H})$, $(\tilde{H}, \tilde{W})$

Figure 11.9: $\Delta a_\mu^{\mathrm{SUSY}}$ with $m_{\tilde{\mu}_L} \sim m_{\tilde{\mu}_R}$ in the $(\tilde{W}, \tilde{B})$ (a), $(\tilde{H}, \tilde{B})$ (b), $(\tilde{W}, \tilde{H})$ and $(\tilde{H}, \tilde{W})$ (c) models. The black solid line represents $\Delta a_\mu^{\mathrm{SUSY}} = 2.5\times10^{-9}$, and the dashed lines represent 1σ band. The red lines are the observed exclusion limits of the $(\tilde{W}, \tilde{B})$ model with $\mathcal{B}(\tilde{\chi}_2^0 \to Z\tilde{\chi}_1^0) = 100\%$ (a), the $(\tilde{H}, \tilde{B})$ model with $\mathcal{B}(\tilde{\chi}_2^0 \to Z\tilde{\chi}_1^0) = \mathcal{B}(\tilde{\chi}_3^0 \to h\tilde{\chi}_1^0) = 100\%$ (b), and the $(\tilde{W}, \tilde{H})$ and $(\tilde{H}, \tilde{W})$ models with $\tan\beta = 30$ and $\mu > 0$ (c) at the 95% CL in this analysis.

- $2.69\times10^{-4} < \mathcal{B}(b \to s\gamma) < 3.87\times10^{-4}$ ($\pm2\sigma$ of theoretical prediction [177] and experimental measurement [178])
- $1.6\times10^{-9} < \mathcal{B}(B_s \to \mu^+\mu^-) < 4.2\times10^{-9}$ ($\pm2\sigma$ of LHCb [179] and CMS [180] measurements)
- $6.6\times10^{-5} < \mathcal{B}(B^+ \to \tau^+\nu_\tau) < 16.1\times10^{-5}$ ($\pm2\sigma$ of experimental results [181] and theoretical prediction [182])

The result of the parameter scan is shown in Figure 11.11. The blue points represent the remaining models after the selections described above. This analysis provides the exclusion limits on this SUSY scenario motivated by the muon g-2 anomaly.

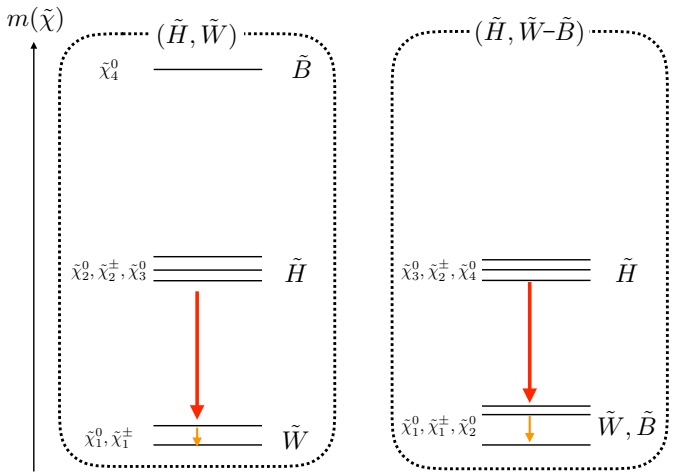

Figure 11.10: Mass hierarchies of the $(\tilde{H}, \tilde{W})$ (left) and $(\tilde{H},\ \tilde{W}$-$\tilde{B})$ (right) models. The decay processes shown with the orange arrowsare not considered if Δm between $\tilde{\chi}_1^\pm/\tilde{\chi}_2^0$ and $\tilde{\chi}_1^0$ is small enough.

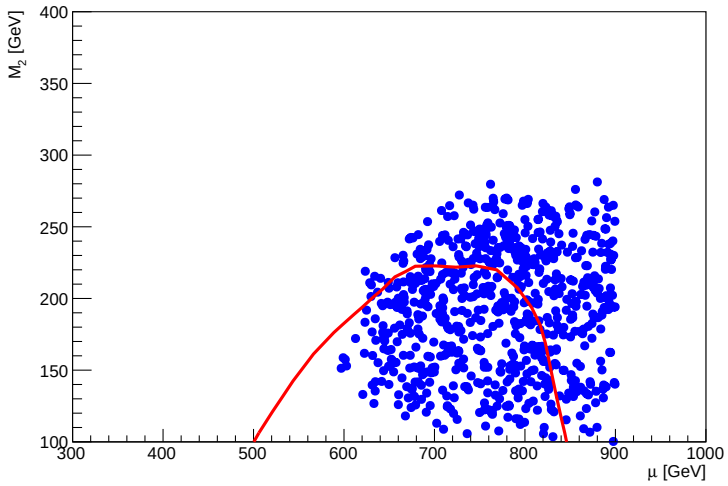

Figure 11.11: Results of pMSSM scan in the $(\tilde{H},\ \tilde{W}$-$\tilde{B})$ model motivated by the muon g-2 anomaly. The red lines represent the observed exclusion limit in this analysis ($\tan\beta = 30$) at the 95% CL for the $(\tilde{H}, \tilde{W})$ model.

Table 11.3: The ranges of the pMSSM parameters scan in the scenarios motivated by the muon g-2 anomaly for the ($\tilde{H}$, $\tilde{W}$-$\tilde{B}$) model.

Parameter	**Min value**	**Max value**	**Note**
$m_{\tilde{L}_1}(= m_{\tilde{L}_2})$	90 GeV	4 TeV	Left-handed slepton (first two gens.) mass
$m_{\tilde{e}_1}(= m_{\tilde{e}_2})$	90 GeV	4 TeV	Right-handed slepton (first two gens.) mass
$m_{\tilde{L}_3}$	90 GeV	4 TeV	Left-handed stau doublet mass
$m_{\tilde{e}_3}$	90 GeV	4 TeV	Right-handed stau mass
$m_{\tilde{Q}_1}(= m_{\tilde{Q}_2})$	1 TeV	10 TeV	Left-handed squark (first two gens.) mass
$m_{\tilde{u}_1}(= m_{\tilde{u}_2})$	1 TeV	10 TeV	Right-handed up-type squark (first two gens.) mass
$m_{\tilde{d}_1}(= m_{\tilde{d}_2})$	1 TeV	10 TeV	Right-handed down-type squark (first two gens.) mass
$m_{\tilde{Q}_3}$	1 TeV	10 TeV	Left-handed squark (third gen.) mass
$m_{\tilde{u}_3}$	1 TeV	10 TeV	Right-handed top squark mass
$m_{\tilde{d}_3}$	1 TeV	10 TeV	Right-handed bottom squark mass
M_1	100 GeV	300 GeV	Bino mass parameter
M_2	100 GeV	300 GeV	Wino mass parameter
μ	400 GeV	900 GeV	Bilinear Higgs mass parameter
M_3	1.5 TeV	4 TeV	Gluino mass parameter
$\lvert A_t \rvert$	0 GeV	16 TeV	Trilinear top coupling
$\lvert A_b \rvert$	0 GeV	4 TeV	Trilinear bottom coupling
$\lvert A_\tau \rvert$	0 GeV	4 TeV	Trilinear τ lepton coupling
m_A	100 GeV	4 TeV	Pseudoscalar Higgs boson mass
$\tan\beta$	1	70	Ratio of the Higgs vacuum expectation values

11.4 Implication to Naturalness

From the viewpoint of naturalness, light higgsino is favored. As discussed in Sec.2.3.5, $\mu < 700$ GeV is allowed with 1% fine-tuning. In this thesis, we consider the $(\tilde{W}, \tilde{H})$ model as the $\tilde{H}$-LSP model. In this model, XENON-1T [60, 61] and the previous analyses in ATLAS/CMS [53, 55, 176] provide limits on the higgsino mass and exclude $m(\tilde{\chi}_1^0) < 200$ GeV. On the other hand, we provide the limit up to 400 GeV with $m(\tilde{W}) < 1$ TeV. For the $\tilde{H}$-NLSP case, the $(\tilde{H}, \tilde{B})$, $(\tilde{H}, \tilde{W})$, $(\tilde{H}, \tilde{G})$, and $(\tilde{H}, \tilde{a})$ models are considered. For the $(\tilde{H}, \tilde{G})$ model, only the gravitino LSP case has been explored, and the limits on higgsino mass reach ~ 890 GeV in the ATLAS and CMS, as shown in Figure 2.14. In this case, we explore the heavy higgsino mass ($m(\tilde{\chi}_1^0) > 900$ GeV) for the first time. For the $(\tilde{H}, \tilde{B})$, $(\tilde{H}, \tilde{W})$, $(\tilde{H}, \tilde{a})$ models, we set stringent limits on the higgsino mass at the first time.

Therefore, this analysis provides the stringent limits on $m(\tilde{H})$ up to 960 GeV in the SUSY scenarios motivated by the naturalness such as allowing 1% fine-tuning.

12 Conclusions

The search for supersymmetric electroweakinos using 139 fb^{-1} of $\sqrt{s}$ = 13 TeV pp-collision data collected by the ATLAS detector was reported. Particularly targeted in this thesis are those in which $\tilde{\chi}_{\text{heavy}}$ decays into $\tilde{\chi}_{\text{light}}$ and $W/Z/h$ bosons, with a large mass difference between $\tilde{\chi}_{\text{heavy}}$ and $\tilde{\chi}_{\text{light}}$ (> 400 GeV). Thanks to the large mass difference, the bosons are boosted and reconstructed as a single large-R jet when the bosons decay hadronically. Such hadronic decay modes can provide a significant advantage thanks to the large branching ratio. Since we focus on the fully hadronic final state without leptons, and $W/Z/h$ are all targeted, it is possible to search for electroweakinos with a small model dependence on the SUSY parameters.

However, many backgrounds possibly originate from the quark- or gluon-initiated jets called QCD backgrounds. In most of the previous searches in ATLAS and CMS, leptonic decay of bosons is used to reject these backgrounds. Consequently, the signal acceptance is small due to the small branching ratio. On the contrary, we reject the backgrounds by developing a technique to identify bosons effectively with strong discrimination from QCD backgrounds in the fully hadronic final state. For the $W/Z \to qq$ tagging, the jet mass and substructures, such as D_2 and n_{trk}, are used for the selections, and the cut values for the selections are optimized for this analysis. The signal efficiency is approximately 50%, and the background rejection is $10 - 40$. For the $Z/h \to bb$ tagging, the jet mass and the number of b-tagged sub-jets are used for the selections. The signal efficiency is approximately 50%, and the background rejection is $10 - 1000$.

We search for electroweakinos in two decay modes simultaneously, $\tilde{\chi}_{\text{heavy}}\tilde{\chi}_{\text{heavy}} \to qqqq\tilde{\chi}_{\text{light}}\tilde{\chi}_{\text{light}}$ and $\tilde{\chi}_{\text{heavy}}\tilde{\chi}_{\text{heavy}} \to qqbb\tilde{\chi}_{\text{light}}\tilde{\chi}_{\text{light}}$. The search in the decay mode of $\tilde{\chi}_{\text{heavy}}\tilde{\chi}_{\text{heavy}} \to qqqq\tilde{\chi}_{\text{light}}\tilde{\chi}_{\text{light}}$ presented in this thesis is the first search in ATLAS and CMS experiments. Thanks to the boson tagging technique, the sensitivity of this search is significantly improved with respect to the previous searches by ATLAS and CMS experiments. Ten signal regions, defined as the combinations of the selections to search for electroweakinos, corresponding to the types of bosons in the decay processes are defined. Thus, targets in this analysis are not only simplified models but also general models targeting $\tilde{B}/\tilde{W}/\tilde{H}/\tilde{G}/\tilde{a}$, which are superpartners of the SM electroweak bosons, the Higgs boson, the graviton, and the axion, respectively.

In order to estimate major SM backgrounds, which include at most one hadronic decaying boson, the control regions are defined by inverting the $W/Z \to qq$ tagging of signal regions. These backgrounds are normalized to the data in the control regions and extrapolated from the control regions to the signal regions using the $W/Z \to qq$ tagging. Since the dominant background is $Z(\to \nu\nu)$ + jets, the background estimation method is validated using the data samples from W + jets and γ + jets, which have similar diagrams. Consequently, there is no significant deviation between the number of observed events in the data sample and the expectation, confirming the validation of this background estimation method. The other SM backgrounds, such as VVV and ttV, are estimated by the Monte Carlo simulation samples.

The numbers of the observed data in the signal regions are found to be consistent with the SM predictions, and this analysis provides model-independent upper limits at the 95% confidence level in each signal region. Furthermore, exclusion limits at the 95% confidence level are set for various theoretical models. For the ($\tilde{W}$, $\tilde{B}$)-SIM model, three models, such as C1C1-WW, C1N2-WZ, and C1N2-Wh, are considered. For the

C1C1-WW model, the lightest chargino mass between 630 GeV and 760 GeV is excluded for the lightest neutralino mass $m(\tilde{\chi}_1^0) < 80$ GeV. For the C1N2-WZ (C1N2-Wh) model, $m(\tilde{\chi}_1^\pm/\tilde{\chi}_2^0)$ between 440 GeV and 960 GeV (400 GeV and 1060 GeV) is excluded for the lightest neutralino mass $m(\tilde{\chi}_1^0) < 300$ GeV (420 GeV). The results correspond to 300-400 GeV improvement on $m(\tilde{\chi}_2^0)$ with respect to the existing best limits by ATLAS and CMS experiments. For the general models, a wino up to 1060 (900) GeV in the wino production models is excluded when the lightest SUSY particle mass is below 400 GeV and the mass difference is larger than 400 GeV. A higgsino mass up to 900 GeV in the higgsino production models is excluded when the lightest SUSY particle mass is below 240 GeV and the mass difference is larger than 450 GeV.

In this analysis, a new method of searching for electroweakinos was established. The sensitivity for heavy electroweakinos in this method is better than that of other analyses using leptons. Even if other analyses use twice the amount of data, it can not exceed the results of this analysis. In the HL-LHC ($\sqrt{s} = 14$ TeV, 3000 fb^{-1}), the sensitivity for heavy electroweakinos is expected to reach up to 1.5 TeV.

In the scenario motivated by the naturalness, 1% fine-tuning is allowed when bilinear Higgs mass parameter μ is less than 700 GeV. Whether higgsino is the LSP or the NLSP, we provide the most stringent limits on various models using the $(\tilde{H}, \tilde{B})$, $(\tilde{H}, \tilde{W})$, $(\tilde{W}, \tilde{H})$, $(\tilde{H}, \tilde{G})$, and $(\tilde{H}, \tilde{a})$ models.

Considering electroweakinos in the scenarios motivated by the dark matter, the $Z(h)$-funnel model with $m(\tilde{\chi}_1^0) \sim m(Z)/2$ ($m(h)/2$) is favored. In these models, $\tilde{B}$ is the LSP and bilinear Higgs mass parameter μ, which is nearly higgsino mass, is less than O(TeV) to explain the dark matter density. Therefore, the $(\tilde{H}, \tilde{B})$ model is a good model to explain the dark matter. This analysis set the most stringent limits on the $Z(h)$-funnel model than the other searches, such as XENON-1T and Fermi-LAT.

In order to explain the muon g-2 anomaly by SUSY, electroweakino masses are to be with the range of $O(100\text{ GeV}) - O(1\text{ TeV})$. In the light electroweakino case, for example, $\tilde{B}$, $\tilde{W}$, and $\tilde{H}$ are less than 1 TeV, there are various decay processes in this light electroweakino scenario. Then, it has not been easy to explore in the previous searches. Thanks to the small dependency on the processes this analysis targets, this analysis excludes some phase space that other analyses have not explored.

In conclusion, there is no significant excess derived from electroweakinos in the data with respect to the SM prediction in this thesis. This analysis provided the most stringent limits on the wino or higgsino pair production modes with various branching ratio and the type of the LSP. Besides, the most stringent constraints on various SUSY scenarios motivated by the dark matter, the muon g-2 anomaly, and the naturalness were set by interpreting the results.

Appendices

A Supplements of Supersymmetry framework

A.1 Operator

In the supersymmetric theory [14–19], an operator Q carries itself a half-integer spin angular momentum and transforms bosonic states to fermionic states and vice versa.

$$Q\,|\text{Boson}\rangle = |\text{Fermion}\rangle\,,\; Q\,|\text{Fermion}\rangle = \text{Boson}. \tag{A.1}$$

The fermionic (bosonic) partner of SM particles after transformations is called "superpartner," and the irreducible representations of SUSY algebra combining SM particles and the superpartners are called "supermultiplet." The Q operator and its hamiltonian conjugate ($Q^\dagger$) are defined to satisfy,

$$\begin{aligned} \{Q, Q^\dagger\} &= P^\mu, & \text{(A.2)}\\ \{Q, Q\} &= \{Q^\dagger, Q^\dagger\} = 0, & \text{(A.3)}\\ [P^\mu, Q] &= [P^\mu, Q^\dagger] = 0. & \text{(A.4)} \end{aligned}$$

where P is the four-momentum operator. Therefore, particles in the same multiplets have identical mass and quantum numbers, except for spins.

A.2 Gaugino Mass Eigenstates

Considering the assumption that electroweak symmetry breaking has a weak effect on the neutralino mass matrix such as $m_Z \ll |\mu \pm M_1|, |\mu \pm M_2|$, $\tilde{N}_{1\sim4}$ are:

$$m_{\tilde{N}_1} = M_1 + \frac{m_Z^2 s_W^2 (M_1 + \mu \sin 2\beta)}{\mu^2 - M_1^2} + \ldots, \tag{A.5}$$

$$m_{\tilde{N}_2} = M_2 - \frac{m_W^2 (M_2 + \mu \sin 2\beta)}{\mu^2 - M_2^2} + \ldots, \tag{A.6}$$

$$m_{\tilde{N}_3}, m_{\tilde{N}_4} = |\mu| + \frac{m_Z^2 (I - \sin 2\beta)(\mu + M_1 c_W^2 + M_2 s_W^2)}{2(\mu + M_1)(\mu + M_2)} + \ldots, \tag{A.7}$$

$$|\mu| + \frac{m_Z^2 (I + \sin 2\beta)(\mu - M_1 c_W^2 - M_2 s_W^2)}{2(\mu - M_1)(\mu - M_2)} + \ldots. \tag{A.8}$$

where M_1 and M_2 are taken real and positive by convention, and μ is assumed to be real with the sign $I = \pm 1$. The subscript labels of Equations A.5-A.8 are assigned if $M_1 < M_2 \ll |\mu|$ and can be rearranged depending on the parameters.

If $M_2 < |\mu|$ and $m_Z \ll |\mu \pm M_1|, |\mu \pm M_2|$ are assumed, the chargino mass eigenstates are described,

$$m_{\tilde{C}_1} = M_2 - \frac{m_W^2(M_2 + \mu \sin 2\beta)}{\mu^2 - M_2^2} + \ldots, \tag{A.9}$$

$$m_{\tilde{C}_2} = |\mu| + \frac{Im_W^2(\mu + M_2 \sin 2\beta)}{\mu^2 - M_2^2} + \ldots. \tag{A.10}$$

In many scenarios, the lightest neutralino can be a good dark matter candidate if it is LSP, as explained in Sec.2.3.4. The LSP components depend on mass parameters (M_1, M_2, and $|\mu|$), most three simple cases dominated by one component are considered. In $M_1 \ll M_2, |\mu|$ case, the lightest neutralino is dominated by Bino component and $m_{\tilde{N}_1} \sim M_1$. If $M_2 \ll M_1, |\mu|$, dominant components of the lightest neutralino and chargino are wino. In this assumption, the lightest mass eigenstates of neutralino and chargino degenerate.

A.3 Grand Unified Theory

In the Grand Unified Theory (GUT), strong, electromagnetic, and weak interactions are treated as a unification. In the SM, there is no energy scale that three couplings are the same. However, by introducing supersymmetry, there is a point at the GUT energy scale in which three couplings unify.

The quantities $\alpha_a = g_a^2/4\pi$ at one-loop order are described as,

$$\frac{d}{dt}\alpha_a^{-1} = -\frac{b_a}{2\pi}, \ (a = 1, 2, 3). \tag{A.11}$$

where α_a represents the coupling constants of the strong, weak, and electromagnetic interactions, respectively. Thus, b_a is the coefficient which is determined by the gauge bosons and the particle multiplets. In the SM and MSSM, b_a is,

$$(b_1, b_2, b_3) = \begin{cases} (41/10, -19/6, -7) & \text{(SM)}, \\ (33/5, 1, -3) & \text{(MSSM)}. \end{cases} \tag{A.12}$$

In the MSSM, the contribution of additional MSSM particles in loops leads the coefficients to be larger. Figure A.1 shows the inverse gauge couplings α_a^{-1} including the two-loop effects as a function of renormalization group scale Q. If the mass scale of the SUSY particles is O(TeV), three couplings unify at $M_U \sim 1.5 \times 10^6$ GeV.

A.4 Couplings between the Lightest Neutralino and Z/h

In the $(\tilde{H}, \tilde{B})$ model, the couplings (λ^h, λ^Z) between the lightest neutralino $(\tilde{\chi}_1^0)$ as the dark matter candidate and Z/h [41] are:

$$\lambda^Z \simeq \frac{g'}{2s_W}\left(\cos 2\beta \frac{m_Z^2 s_W^2}{\mu^2 - M_1^2} + O\left(\frac{m_Z s_W}{\mu}\right)^4\right), \tag{A.13}$$

$$\lambda^h \simeq g'\epsilon_1\left(\frac{\mu \sin 2\beta + M_1}{\mu^2 - M_1^2} m_Z s_W + O\left(\frac{m_Z s_W}{\mu}\right)^3\right), \tag{A.14}$$

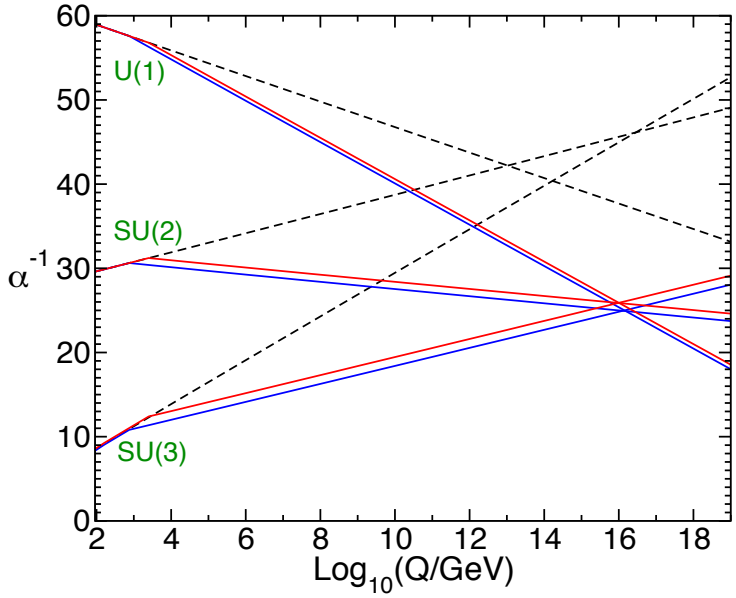

Figure A.1: Two-loop renormalization group evolution of the inverse gauge couplings α_a^{-1} [20]. Dashed lines represent the SM and Solid lines represent the MSSM. $\alpha_3(m_Z)$ is varied between 0.117 and 0.120. In the MSSM, the sparticle masses are treated as a threshold varied between 750 GeV (blue) and 2.5 TeV (red).

where g' is the $\mathrm{U}(1)_Y$ gauge coupling and satisfies that $g' = g \tan\theta_W$ (g is the $\mathrm{SU}(2)_L$ gauge coupling). The couplings depend on $\tan\beta$ and the bilinear Higgs mass parameter (μ), and the differences between the $\tilde{H}$ mass (μ) and the $\tilde{B}$ mass (M_1) are allowed to be $O(100 \sim 1000$ GeV), as shown in Figure A.2.

For the Z funnel case, higgsino mass is motivated to be nearly 480 GeV regardless of $\tan\beta$ because the dark matter-Z boson coupling ($Z - \tilde{H} - \tilde{H}$ coupling) is mild dependent on $\tan\beta$ due to independency on the mixing between $\tilde{B}$ and $\tilde{H}$. In addition, the higgsino mass parameter to explain the observed density depends on the sign of μ since the coupling has only the term with even number order of μ. For the h funnel case, higgsino mass strongly depends on $\tan\beta$ and the sign of μ since the dark matter-higgs boson coupling has terms with odd number order of μ and $\sin 2\beta$. This is because that the dark matter-h coupling ($h - \tilde{H} - \tilde{B}$ coupling) depends on the mixing between $\tilde{B}$ and $\tilde{H}$ and the magnitude is represented by $\tan\beta$.

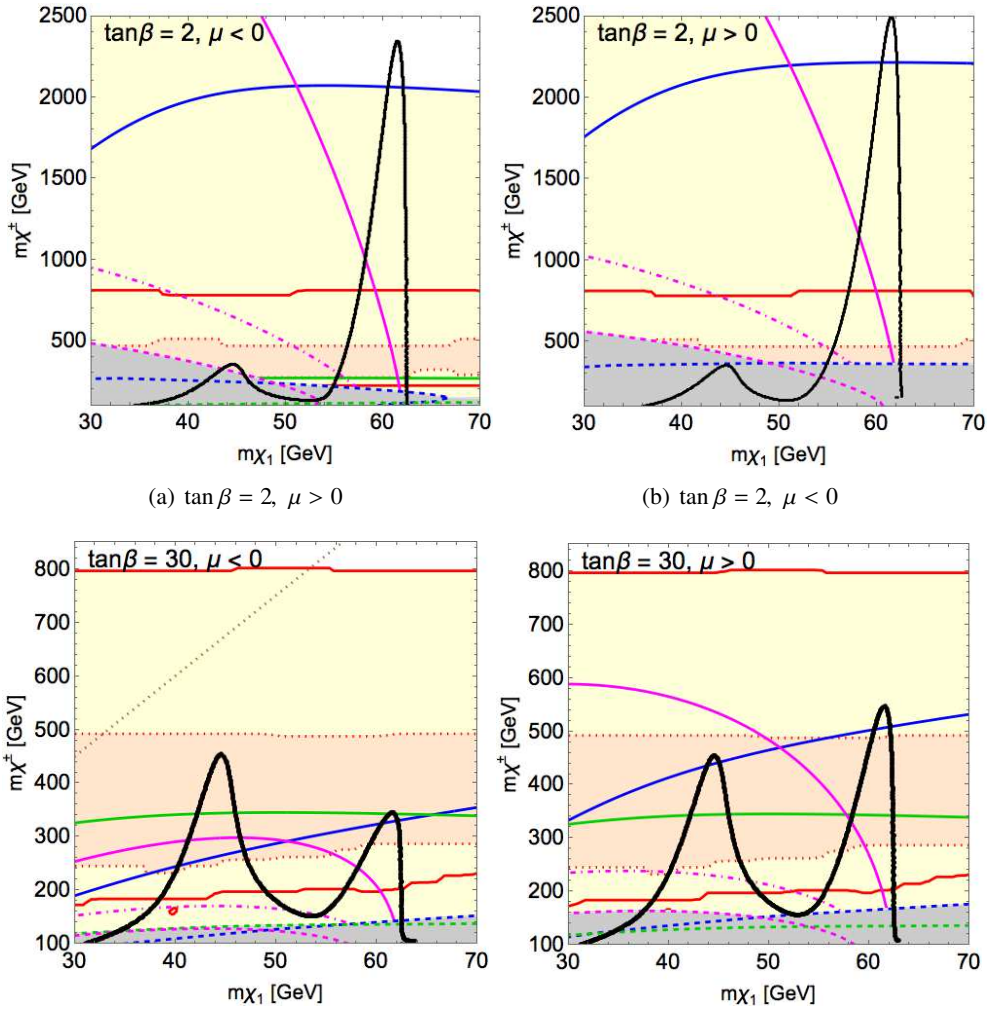

(a) $\tan\beta = 2,\ \mu > 0$ (b) $\tan\beta = 2,\ \mu < 0$

(c) $\tan\beta = 30,\ \mu > 0$ (d) $\tan\beta = 30,\ \mu < 0$

Figure A.2: The higgsino mass ($m(\tilde{\chi}_1^{\pm})$) as a function of $m(\tilde{\chi}_1^0)$ to explain the observed dark matter and the constraints and future sensitivity of the Higgs- and Z-resonant neutralino dark matter with the assumption that all SUSY multiplets except for higgsino and bino are decoupled [41]. $\tan\beta = 2$ cases are shown in the top row and $\tan\beta = 30$ cases are shown in the bottom row and for $\mu > 0$ (left) and $\mu < 0$ (right). The black lines show the observed dark matter density $\Omega_{\tilde{\chi}_1^0} h^2 \simeq 0.12$. The gray shaded region is excluded by the combination of the LUX bound on $\sigma_N^{\rm SI}$ (blue dashed) [183], the XENON100 bound on $\sigma_n^{\rm SD}$ (green dashed) [184], and the Higgs invisible decay (magenta dashed) [185, 186]. The light yellow region will be probed by some experiments in the future; the XENON-1T via SI-scattering (blue solid) [187] and SD-scattering (green solid) [188], the Higgs invisible decay at the HL-LHC (magenta dot-dashed) [189, 190] and at the ILC (magenta solid) [191], and the search for the chargino and neutralinos at the 14 TeV LHC, at 3000 fb^{-1} (red solid). In particular, the light orange region within the red dotted lines will be reached at 300 fb^{-1}.

A.5 Muon g-2 Contribution of SUSY Particles

The contributions of SUSY particles to the muon g-2 are described as the follows in Ref. [47],

$$\Delta a_\mu(\tilde{W}, \tilde{H}, \tilde{\nu}_\mu) = \frac{\alpha_2}{4\pi}\frac{m_\mu^2}{M_2\mu}\tan\beta \cdot f_C\left(\frac{M_2^2}{m_{\tilde{\nu}}^2}, \frac{\mu^2}{m_{\tilde{\nu}}^2}\right), \tag{A.15}$$

$$\Delta a_\mu(\tilde{W}, \tilde{H}, \tilde{\mu}_L) = -\frac{\alpha_2}{8\pi}\frac{m_\mu^2}{M_2\mu}\tan\beta \cdot f_N\left(\frac{M_2^2}{m_{\tilde{\mu}_L}^2}, \frac{\mu^2}{m_{\tilde{\mu}_L}^2}\right), \tag{A.16}$$

$$\Delta a_\mu(\tilde{B}, \tilde{H}, \tilde{\mu}_L) = \frac{\alpha_Y}{8\pi}\frac{m_\mu^2}{M_1\mu}\tan\beta \cdot f_N\left(\frac{M_1^2}{m_{\tilde{\mu}_L}^2}, \frac{\mu^2}{m_{\tilde{\mu}_L}^2}\right), \tag{A.17}$$

$$\Delta a_\mu(\tilde{B}, \tilde{H}, \tilde{\mu}_R) = -\frac{\alpha_Y}{4\pi}\frac{m_\mu^2}{M_1\mu}\tan\beta \cdot f_N\left(\frac{M_1^2}{m_{\tilde{\mu}_R}^2}, \frac{\mu^2}{m_{\tilde{\mu}_R}^2}\right), \tag{A.18}$$

$$\Delta a_\mu(\tilde{\mu}_L, \tilde{\mu}_R, \tilde{B}) = \frac{\alpha_Y}{4\pi}\frac{m_\mu^2 M_1\mu}{m_{\tilde{\mu}_L}^2 m_{\tilde{\mu}_R}^2}\tan\beta \cdot f_N\left(\frac{m_{\tilde{\mu}_L}^2}{M_1^2}, \frac{m_{\tilde{\mu}_R}^2}{M_1^2}\right). \tag{A.19}$$

where m_μ is the muon mass, and α_2 and α_Y represent the fine structure constants of the $\mathrm{SU(2)_L}$ and the SM $\mathrm{U(1)_Y}$ gauge symmetries. The f_C and f_N functions describe the loop, and they are defined,

$$f_C(x,y) = xy\left[\frac{5-3(x+y)+xy}{(x-1)^2(y-1)^2} - \frac{2\log x}{(x-y)(x-1)^3} + \frac{2\log y}{(x-y)(y-1)^3}\right], \tag{A.20}$$

$$f_N(x,y) = xy\left[\frac{-3+x+y+xy}{(x-1)^2(y-1)^2} + \frac{2x\log x}{(x-y)(x-1)^3} - \frac{2y\log y}{(x-y)(y-1)^3}\right]. \tag{A.21}$$

The sneutrino mass $m_{\tilde{\nu}}$ is represented using $m_{\tilde{\mu}_L}$ as $m_{\tilde{\nu}}^2 = m_{\tilde{\mu}_L}^2 + m_W^2\cos 2\beta$.

A.6 Gauge Mediated Symmetry Breaking

To understand which models satisfy the assumption of Equations 2.6 and 2.7, general cases are considered. Considering that the vacuum state is not invariant when supersymmetry is spontaneously broken in the case of SUSY, a new goldstone particle (goldstino, $\tilde{G}$) is introduced in the same way of higgs mechanism for the electroweak symmetry breaking. It has to be a massless neutral Weyl fermion with the same quantum numbers as the broken symmetry generator (the supercharge Q). The goldstiono field is described in the proportional to the following vector:

$$\tilde{G} = \begin{pmatrix} \langle D^a \rangle / \sqrt{2} \\ \langle F_i \rangle \end{pmatrix}. \tag{A.22}$$

where D^a is a bosonic auxiliary field and F_i is a fermionic auxiliary field of the supersymmetry Lagrangian, and $\langle\rangle$ represents their vacuum expectation value. In order to be non-trivial, at least one of D^a and F_i is required to have a non-zero vacuum expectation value.

In the Fayet-Iliopoulos mechanism [192], D^a has a non-zero vacuum expectation value and is the dominant source of supersymmetry breaking. However, this mechanism has difficulty in giving appropriate explanations of MSSM particles' masses. In this thesis, this mechanism is not discussed.

In the O'Raifeartaigh mechanism [193], F_i has a non-zero vacuum expectation value. In the MSSM, there is no good candidate to be a gauge singlet to have a non-zero vacuum expectation value of F-term. Thus, at least one new chiral supermultiplet is expected to add. When we consider gravity, supersymmetry is prompted to be a local symmetry, and the resulting theory is called supergravity. In this model, the spin-2 graviton [194] has the superpartner called gravitino. Gravitino ($\tilde{G}$), which is the fermion and has the spin-3/2, can be interpreted as the gauge field of local supersymmetry transformations. Gravitino mass, described as $m_{3/2}$, can be estimated as [195]:

$$m_{3/2} \sim \langle F \rangle / \Lambda_P. \tag{A.23}$$

where $\langle F \rangle$ is the vacuum expectation value of the supersymmetry-breaking F-term and Λ_P is the Planck scale.

The MSSM soft terms arising through radiative corrections do not appear at a tree level in any supersymmetry-breaking models. Supersymmetry-breaking occurs in a hidden sector, and MSSM particles remain in the visible sector. However, the hidden and visible sectors share some interactions mediating supersymmetry-breaking from the hidden to the visible sectors. In the gauge-mediated supersymmetry-breaking (GMSB) model, the mediating interactions are the ordinary electroweak and QCD gauge interactions.

In the GMSB framework [196–198], gauge interactions mediate a connection between the hidden sector and the visible sector. Gravitational communication between the source of supersymmetry-breaking and the MSSM sector remains, and the effect is smaller than the gauge interactions. The MSSM gauginos masses are contributed from the 1-loop corrections of the mediator, involving the MSSM gaugino interactions. The contribution of the squark and sfermion squared masses is the 2-loop level. In these cases, the MSSM soft terms are given by:

$$m_{\text{soft}} \approx \frac{\langle F \rangle}{M_{\text{mediator}}}. \tag{A.24}$$

Comparing Equation A.23 and Equation A.24, the gravitino mass is lighter than the rest of superpartners when the mass of the mediators is lower than the Planck scale. Thus, the gravitino is assumed to be near massless and the LSP in the general GMSB models.

Since the gauge interactions are flavor blind and the masses of the squarks and sleptons depend on the $SU(3)_C \times SU(2)_L \times U(1)_Y$ quantum numbers, flavor-changing effects are suppressed in the GMSB framework. Thus, the GMSB framework leads to a flavor-universal MSSM spectrum and is consistent with experimental results.

In the ordinary gauge mediated model, $\tilde{B}$- or stau-LSP model is favored [199] because it is assumed that singlet messengers mediate the connection between the hidden sector and visible sector, and $|\mu|$ is larger than M_1 and M_2. However, suppose doublet or triplet messengers are considered. In that case, $|\mu|$ is allowed to be small while keeping $m_{\tilde{t}} \gtrsim 1$ TeV because we can get a cancelation of the electroweak symmetry breaking in MSSM [200].

In the $(\tilde{H}, \tilde{G})$ model, M_1 and M_2 are assumed to be large and $\tilde{W}/\tilde{B}$ are decoupled. For this model, only $\tilde{\chi}_1^0 \rightarrow \tilde{G}$ decay processes with Z/h boson are considered because $\tilde{\chi}_1^0 \rightarrow \gamma + \tilde{G}$ decay mode is suppressed by large M_1 and M_2.

B Details of simulated samples

B.1 Detailed Setup of SM Background MC Simulation in the SUSY Search

In this section, the setup of SM background samples is introduced. The generator setup is summarized in Table B.1.

Table B.1: Setup of SM background samples.

Process	Matrix element	Parton shower	PDF set
W + jets, Z + jets		Sherpa 2.2.1 [139]	NNPDF 3.0 NNLO [201]
γ + jets		Sherpa 2.2.2 [139]	NNPDF 3.0 NNLO [201]
$t\bar{t}$, tW,	Powheg-Box v2 [131–134]	Pythia 8.230 [95]	NNPDF 2.3 LO [96]
$t\bar{t}+h$	Powheg-Box v2.2 [131–134]	Pythia 8.230 [95]	NNPDF 2.3 LO [96]
tWZ, tZ	MadGraph 5 _aMC@NLO 2.3.3 [137]	Pythia 8.212 [95]	NNPDF 2.3 LO [96]
$t\bar{t}+WW$	MadGraph 5 _aMC@NLO 2.2.2 [137]	Pythia 8.186 [95]	NNPDF 2.3 LO [96]
$t\bar{t}+V$	MadGraph 5 _aMC@NLO 2.3.3 [137]	Pythia 8.210 [95]	NNPDF 3.0 NNLO [201]
ttt, $tt\bar{t}\bar{t}$, $t\bar{t}+Wll$, $t\bar{t}+\gamma$, $t\bar{t}+VV$	MadGraph 5 _aMC@NLO 2.2.3-2.6.7 [137]	Pythia 8.186-240 [95]	NNPDF 2.3 LO [96]
VV	Sherpa 2.2.1/2.2.2 [139]		NNPDF 3.0 NNLO [201]
VVV	MadGraph 5 _aMC@NLO 2.6.6 [137]	Pythia 8.243 [95]	NNPDF 3.0 NNLO [201]
$V\gamma$		Sherpa 2.1.1 [139]	CT10 [202]
Vh	Powheg-Box v2.2 [131–134]	Pythia 8.186 [95] with AZNLO tune [203]	NNLO+NLO [204–210]
Multi-jet		Sherpa 2.1.1 [139]	CT10 [202]

***V*+jets** W+jets and Z+jets events with leptonically-decaying bosons are simulated using Sherpa 2.2.1 [139]. In this setup, matrix elements for up to two partons are calculated using next-to-leading-order (NLO) accuracy, and for up to four partons are calculated using leading-order (LO) accuracy by Comix [211] and OpenLoops [212–214] libraries. The default Sherpa parton shower model [215], which is based on Catani–Seymour dipole factorization and the cluster hadronization model [216], is employed. The NNPDF3.0$_{\text{NNLO}}$ PDF set [201], which parameters are tuned by the Sherpa, is used. Their cross-sections are normalized to an NLO prediction [217]. Additionally, prompt single photon samples (γ + jets) are simulated by Sherpa 2.2.2. Photons are required to satisfy a smooth-cone isolation criterion [218].

Tops $t\bar{t}$ and $t+W$ event generations are simulated by Powheg-Box [131–134] v2 at NLO with the NNPDF3.0$_{\text{NNLO}}$ PDF set. The interference for the parton shower and hadronization is simulated by Pythia 8.230 [95] using A14 set of tuned parameters [219] and the NNPDF2.3$_{\text{LO}}$ PDF set [96]. The bottom and charm hadron decays are simulated by the EvtGen 1.6.0 [220]. In this simulation, we use the h_{damp} parameter to control the matching matrix elements to the parton shower in Powheg and regulate the high-p_{T} radiation against which the $t\bar{t}$ system recoils [221], and h_{damp} is set to be 1.5 times top mass. The $t\bar{t}$ sample is normalized to the cross-section prediction of Top++ 2.0 [222–228] using the calculation at NLO in QCD, including the resummation of next-to-next-to-leading logarithmic (NNLL) soft-gluon terms. Similarly, the cross-section of $t+W$ sample is normalized to the theoretical prediction using the calculation

at NLO in QCD with NNLL soft-gluon corrections [229, 230]. However, t-channel $t + W$ samples are normalized to the theoretical prediction of the calculation at NLO in QCD with HATHOR 2.1 [231, 232]. Additionally, we employ the diagram removal scheme [146] to consider the interference between $t\bar{t}$ and $t + W$ process.

tWZ and tZ events are simulated by MADGRAPH 5 _aMC@NLO 2.3.3 [137] with the NNPDF3.0$_{\text{NNLO}}$ PDF set. The interference is simulated by PYTHIA 8.212 [95] using A14 set of tuned parameters and the NNPDF2.3$_{\text{LO}}$ PDF set. The bottom and charm hadron decays are simulated by the EVTGEN 1.2.0.

$t\bar{t} + h$ event generations are simulated with POWHEG-BOX v2.2 and and the NNPDF3.0$_{\text{NNLO}}$ PDF set. The cross-section is calculated at NLO QCD and NLO EW accuracy by MADGRAPH 5 _aMC@NLO [233]. 3/4 tops, $t\bar{t} + WW$ events are simulated by MADGRAPH 5 _aMC@NLO 2.2.2 [137] with PYTHIA 8.186 A14 set of tuned parameters and the NNPDF2.3$_{\text{LO}}$ PDF set. The bottom and charm hadron decays are simulated by the EVTGEN 1.2.0. $t\bar{t} + V$ production events are simulated by MADGRAPH 5 _aMC@NLO 2.3.3 with the NNPDF3.0$_{\text{NNLO}}$ PDF set. The interference is simulated by PYTHIA 8.210 using A14 set of tuned parameters and the NNPDF2.3$_{\text{LO}}$ PDF set. The bottom and charm hadron decays are simulated by the EVTGEN 1.2.0. The cross-sections are calculated at NLO QCD and NLO EW accuracy by MADGRAPH 5 _aMC@NLO [233]. Other top backgrounds, such as $t\bar{t}t$, $tt\bar{t}\bar{t}$, $t\bar{t} + Wll$, $t\bar{t} + \gamma$, and $t\bar{t} + VV$, are simulated by MADGRAPH 5 _aMC@NLO 2.2.3-2.6.7. The interferences are simulated by PYTHIA 8.186-8.240 using A14 set of tuned parameters and the NNPDF2.3$_{\text{LO}}$ PDF set. The bottom and charm hadron decays are simulated by the EVTGEN 1.2.0-1.7.0. Events with two tops and at least one boson are referred to as $t\bar{t} + X$ samples.

Multi-bosons Diboson processes, such as WW, WZ, ZZ, are simulated by SHERPA. Fully leptonic decaying events are simulated with SHERPA 2.2.1 ($ZZ \to \nu\nu\nu\nu$) or SHERPA 2.2.2 ($llll$, $lll\nu$, $ll\nu\nu$, and $l\nu\nu\nu$). Additionally, semi-leptonic decaying events, where one boson decays leptonically and the other decays hadronically, are simulated with SHERPA 2.2.1. Besides, gluon-initiated diboson events are simulated by SHERPA 2.2.2. In this setup, off-shell effects and Higgs boson contributions are included. Up to one additional parton is generated using matrix elements at NLO accuracy in QCD, and up to three additional parton emissions are generated at LO accuracy. Diboson associated with additional two jets events ($VVjj$) is simulated with SHERPA 2.2.2. The NNPDF3.0$_{\text{NNLO}}$ PDF set, which parameters are tuned by the SHERPA, is used.

Triboson (WWW, WWZ, WZZ, and ZZZ denoted as VVV) events are simulated with MADGRAPH 5 _aMC@NLO 2.6.6 at LO. The interference is simulated by PYTHIA 8.243 with the A14 tune and the NNPDF3.0$_{\text{NNLO}}$ PDF set is used. The cross-sections are normalized to the values calculated at LO from the generator.

$V\gamma$ events are simulated with SHERPA 2.1.1. The SHERPA default PDF and tune are used. The cross-sections are normalized to the values calculated at LO from the generator.

Higgs Events with leptonically decaying W/Z boson and hadronically decaying Higgs boson are simulated with POWHEG-BOX 2.2 interfaced with PYTHIA 8.186. The NNPDF3 PDF set and AZNLO tune [203] are used.

Multi-jets Multi-jet backgrounds are simulated with SHERPA 2.1.1 and the SHERPA default PDF and tune are used. The contribution of multi-jet backgrounds is negligible in the search for electroweakinos.

Alternative samples $t\bar{t}$ samples are used for the boson tagging efficiency measurement described in Sec.6.1.3. One of the alternative $t\bar{t}$ samples is simulated with the same settings as a nominal $t\bar{t}$ sample, except for the h_{damp}, h_{damp} is set to be 3 times top mass. The alternative $t\bar{t}$ samples are simulated with Powheg interfaced with Herwig 7.04 [135, 136] and MadGraph 5 _aMC@NLO 2.6.0 interfaced with Pythia 8.230. Additionally, $W/Z(\rightarrow qq)$+jets samples are also used for the boson tagging efficiency measurement. $W/Z(\rightarrow qq)$+jets samples are simulated with Sherpa 2.1.1 and the Sherpa default PDF and tune are used. Alternative $W/Z(\rightarrow qq)$+jets samples are simulated with Herwig++ v2.7.1.Besides, multi-jet and γ + jets samples are used for the boson tagging background rejection factor measurements. Alternative multi-jet samples are simulated with Pythia 8.186 using A14 set of tuned parameters and the NNPDF2.3$_{\text{LO}}$ PDF set. The bottom and charm hadron decays are simulated by the EvtGen 1.2.0. Besides, alternative γ + jets samples are simulated with Pythia 8.186 using the NNPDF2.3$_{\text{LO}}$ PDF set and Sherpa 2.1 using the CT10 PDF set [202].

B.2 Detailed Setup of SUSY Signal MC Simulation

All of the signal event generations are simulated with the LO matrix elements with up to two extra partons using MadGraph v2.6.2 [137]. For simulating of parton showering and hadronization, Pythia 8.230 using A14 set of tuned parameters, and the NNPDF2.3$_{\text{LO}}$ PDF set are used as the interface. The bottom and charm hadron decays are simulated by EvtGen 1.2.0. In the simulation setup, SM-like Higgs boson mass is set to 125 GeV. The signal cross-sections are calculated at NLO in the strong coupling constant. Additionally, the resummation of soft gluon emission is taken into account at NLL accuracy. In this calculation, we use the PDF4LHC15_mc PDF set [234].

In the $(\tilde{W}, \tilde{B})$-SIM samples, it is assumed that $m(\tilde{\chi}_1^{\pm}) = m(\tilde{\chi}_2^0)$. In the $(\tilde{H}, \tilde{B})$-SIM samples, it is assumed that $m(\tilde{\chi}_1^{\pm}/\tilde{\chi}_2^0) = m(\tilde{\chi}_1^0) + 1$ GeV. In the $(\tilde{H}, \tilde{G})$ samples, $m(\tilde{G})$ is asuumed to be 0.5 GeV and it is assumed that $m(\tilde{\chi}_1^{\pm}/\tilde{\chi}_2^0) = m(\tilde{\chi}_1^0) + 1$ GeV.

In this analysis, our target signatures have the mass difference $(m(\tilde{\chi}_{\text{heavy}}) - m(\tilde{\chi}_{\text{light}})) > 400$ GeV, then W/Z bosons in the models are typically fully longitudinally polarized. We use the boson tagging technique [121] to identify jets originating from hadronically decaying bosons. The performance of the boson tagging is sensitive to the boson polarization [235]. Thus, the polarization of W/Z bosons from the electroweakinos is modeled by MadSpin v2.7.3 [236, 237], and re-weighting the truth-level helicity angle distribution. In the re-weighting method, the overall cross-section is not changed.

C Wino/Higgsino Branching Fraction Calculation

For $(\tilde{W}, \tilde{H})$ and $(\tilde{H}, \tilde{W})$ models, the branching fractions with different $(M_2,\ \mu,\ \tan\beta)$ are scanned using Soft-SUSY v4.1.7 [170, 238]. The scanned parameters,

$$\begin{aligned} M_2 &= [100, 200, 300, 400, 500, 600, 700, 800, 900, 1000, 1100, 1200]\ \text{GeV}, \\ \mu &= \pm[100, 200, 300, 400, 500, 600, 700, 800, 900, 1000, 1100, 1200]\ \text{GeV}, \\ \tan\beta &= [2, 5, 10, 30]. \end{aligned}$$

Other mass parameters are all decoupled. Their values are summarized that $M_1 = 3$ TeV, $m_{\tilde{q}} = m_{\tilde{l}} = 7$ TeV, $m_{\tilde{g}} = 5$ TeV, $A_t = 2.6$ TeV and $A_t = 0$ TeV.

After the calculation of the branching fraction in each point, they are interpolated and visualized in Figure C.1-C.16.

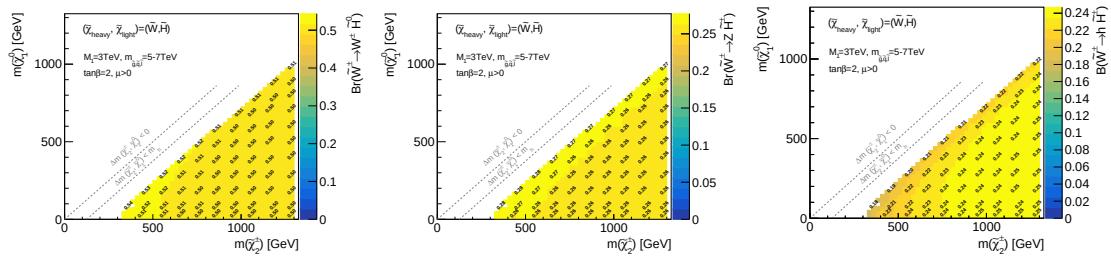

(a) $\mathcal{B}(\tilde{W}^{\pm} \to W^{\pm}\tilde{H}^0_{1,2})$ (b) $\mathcal{B}(\tilde{W}^{\pm} \to Z\tilde{H}^{\pm})$ (c) $\mathcal{B}(\tilde{W}^{\pm} \to h\tilde{H}^{\pm})$

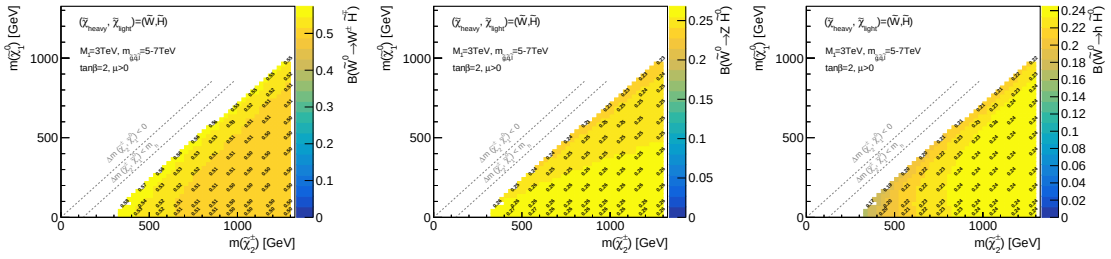

(d) $\mathcal{B}(\tilde{W}^0 \to W^{\pm}\tilde{H}^{\mp})$ (e) $\mathcal{B}(\tilde{W}^0 \to Z\tilde{H}^0_{1,2})$ (f) $\mathcal{B}(\tilde{W}^0 \to h\tilde{H}^0_{1,2})$

Figure C.1: Branching ratio of (a)(b)(c) charged and (d)(e)(f) neutral wino decaying into higgsino light state with a $W/Z/h$ $(\tan\beta = 2, \mu > 0)$. Branching into neutral higgsino is sum of the two destination states i.e. $\mathcal{B}(\ldots \to \tilde{H}^0_{1,2}) := \mathcal{B}(\ldots \to \tilde{H}^0_1) + \mathcal{B}(\ldots \to \tilde{H}^0_2)$.

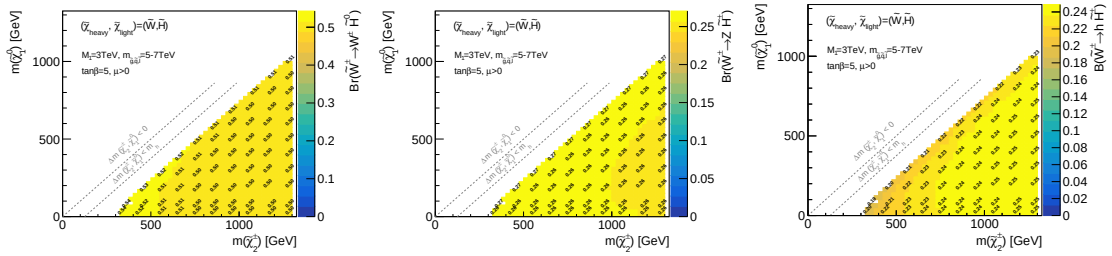

(a) $\mathcal{B}(\tilde{W}^{\pm} \to W^{\pm}\tilde{H}^{0}_{1,2})$ (b) $\mathcal{B}(\tilde{W}^{\pm} \to Z\tilde{H}^{\pm})$ (c) $\mathcal{B}(\tilde{W}^{\pm} \to h\tilde{H}^{\pm})$

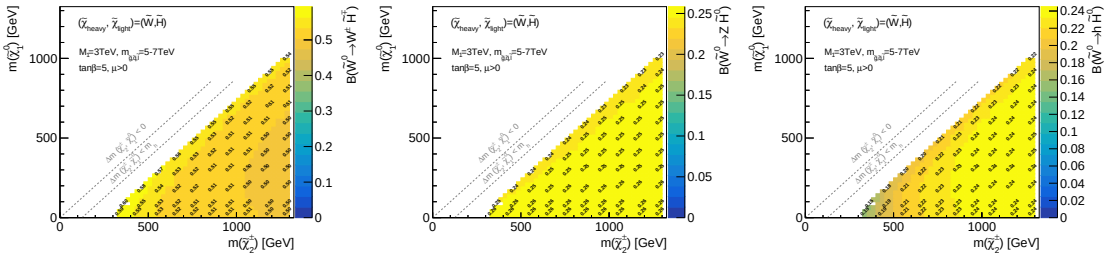

(d) $\mathcal{B}(\tilde{W}^{0} \to W^{\pm}\tilde{H}^{\mp})$ (e) $\mathcal{B}(\tilde{W}^{0} \to Z\tilde{H}^{0}_{1,2})$ (f) $\mathcal{B}(\tilde{W}^{0} \to h\tilde{H}^{0}_{1,2})$

Figure C.2: Branching ratio of (a)(b)(c) charged and (d)(e)(f) neutral wino decaying into higgsino light state with a $W/Z/h$ ($\tan\beta = 5, \mu > 0$). Branching into neutral higgsino is sum of the two destination states i.e. $\mathcal{B}(\ldots \to \tilde{H}^{0}_{1,2}) := \mathcal{B}(\ldots \to \tilde{H}^{0}_{1}) + \mathcal{B}(\ldots \to \tilde{H}^{0}_{2})$.

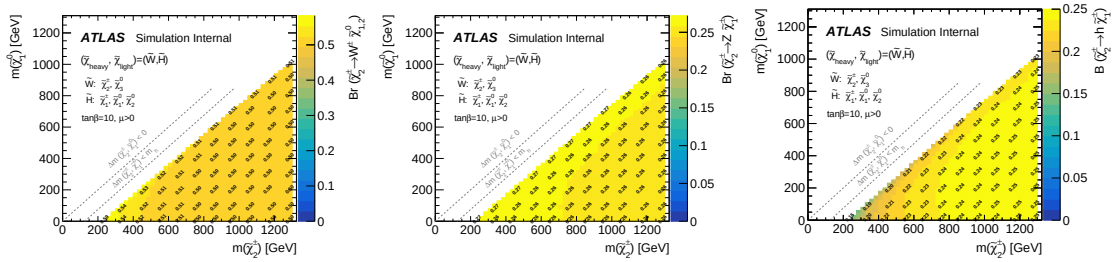

(a) $\mathcal{B}(\tilde{W}^{\pm} \to W^{\pm}\tilde{H}^{0}_{1,2})$ (b) $\mathcal{B}(\tilde{W}^{\pm} \to Z\tilde{H}^{\pm})$ (c) $\mathcal{B}(\tilde{W}^{\pm} \to h\tilde{H}^{\pm})$

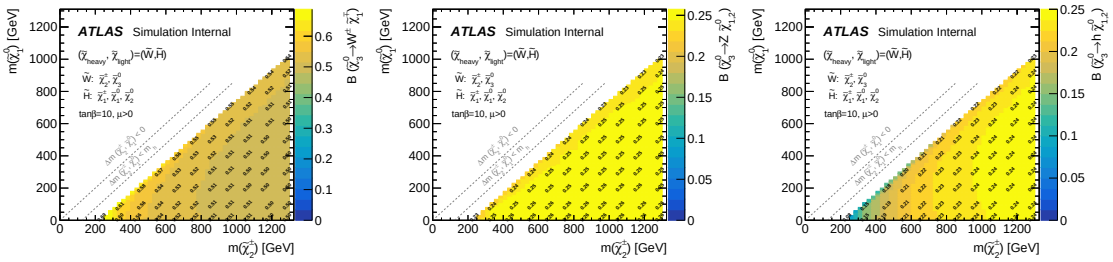

(d) $\mathcal{B}(\tilde{W}^{0} \to W^{\pm}\tilde{H}^{\mp})$ (e) $\mathcal{B}(\tilde{W}^{0} \to Z\tilde{H}^{0}_{1,2})$ (f) $\mathcal{B}(\tilde{W}^{0} \to h\tilde{H}^{0}_{1,2})$

Figure C.3: Branching ratio of (a)(b)(c) charged and (d)(e)(f) neutral wino decaying into higgsino light state with a $W/Z/h$ ($\tan\beta = 10, \mu > 0$). Branching into neutral higgsino is sum of the two destination states i.e. $\mathcal{B}(\ldots \to \tilde{H}^{0}_{1,2}) := \mathcal{B}(\ldots \to \tilde{H}^{0}_{1}) + \mathcal{B}(\ldots \to \tilde{H}^{0}_{2})$.

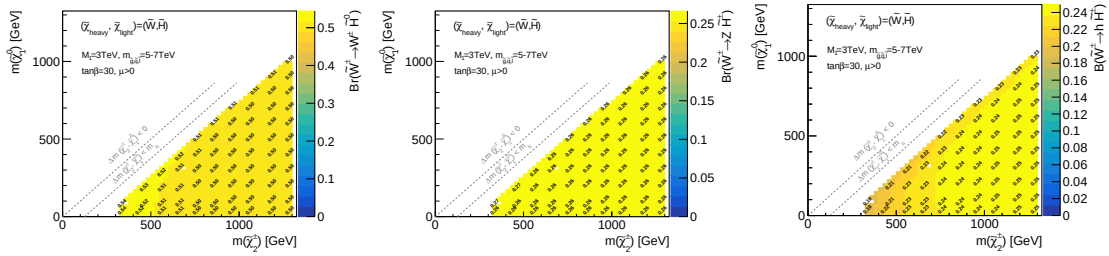

(a) $\mathcal{B}(\tilde{W}^{\pm} \to W^{\pm}\tilde{H}^{0}_{1,2})$ (b) $\mathcal{B}(\tilde{W}^{\pm} \to Z\tilde{H}^{\pm})$ (c) $\mathcal{B}(\tilde{W}^{\pm} \to h\tilde{H}^{\pm})$

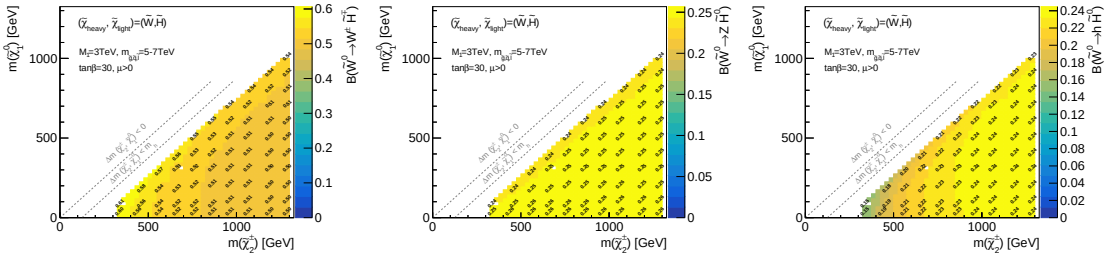

(d) $\mathcal{B}(\tilde{W}^{0} \to W^{\pm}\tilde{H}^{\mp})$ (e) $\mathcal{B}(\tilde{W}^{0} \to Z\tilde{H}^{0}_{1,2})$ (f) $\mathcal{B}(\tilde{W}^{0} \to h\tilde{H}^{0}_{1,2})$

Figure C.4: Branching ratio of (a)(b)(c) charged and (d)(e)(f) neutral wino decaying into higgsino light state with a $W/Z/h$ ($\tan\beta = 30, \mu > 0$). Branching into neutral higgsino is sum of the two destination states i.e. $\mathcal{B}(\ldots \to \tilde{H}^{0}_{1,2}) := \mathcal{B}(\ldots \to \tilde{H}^{0}_{1}) + \mathcal{B}(\ldots \to \tilde{H}^{0}_{2})$.

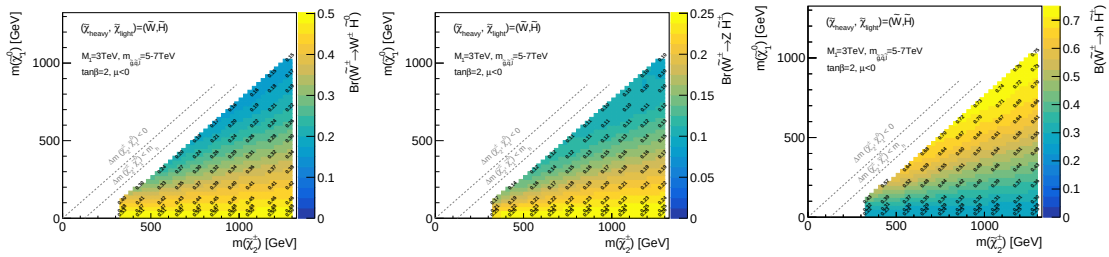

(a) $\mathcal{B}(\tilde{W}^{\pm} \to W^{\pm}\tilde{H}^{0}_{1,2})$ (b) $\mathcal{B}(\tilde{W}^{\pm} \to Z\tilde{H}^{\pm})$ (c) $\mathcal{B}(\tilde{W}^{\pm} \to h\tilde{H}^{\pm})$

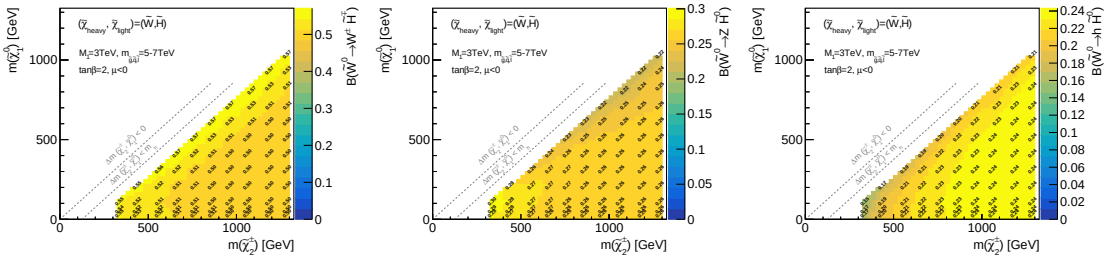

(d) $\mathcal{B}(\tilde{W}^{0} \to W^{\pm}\tilde{H}^{\mp})$ (e) $\mathcal{B}(\tilde{W}^{0} \to Z\tilde{H}^{0}_{1,2})$ (f) $\mathcal{B}(\tilde{W}^{0} \to h\tilde{H}^{0}_{1,2})$

Figure C.5: Branching ratio of (a)(b)(c) charged and (d)(e)(f) neutral wino decaying into higgsino light state with a $W/Z/h$ ($\tan\beta = 2, \mu < 0$). Branching into neutral higgsino is sum of the two destination states i.e. $\mathcal{B}(\ldots \to \tilde{H}^{0}_{1,2}) := \mathcal{B}(\ldots \to \tilde{H}^{0}_{1}) + \mathcal{B}(\ldots \to \tilde{H}^{0}_{2})$.

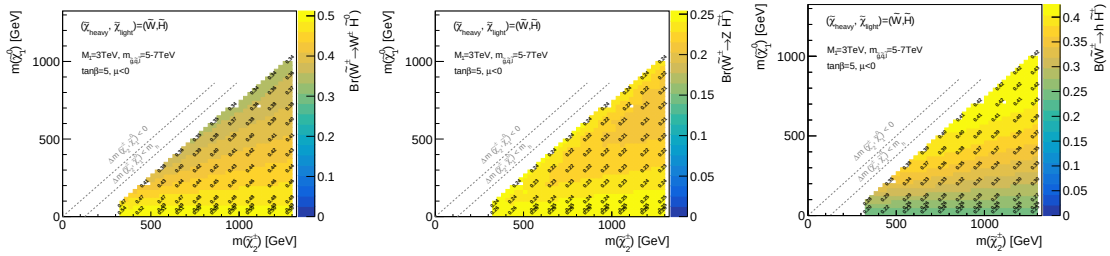

(a) $\mathcal{B}(\tilde{W}^{\pm} \to W^{\pm}\tilde{H}^{0}_{1,2})$ (b) $\mathcal{B}(\tilde{W}^{\pm} \to Z\tilde{H}^{\pm})$ (c) $\mathcal{B}(\tilde{W}^{\pm} \to h\tilde{H}^{\pm})$

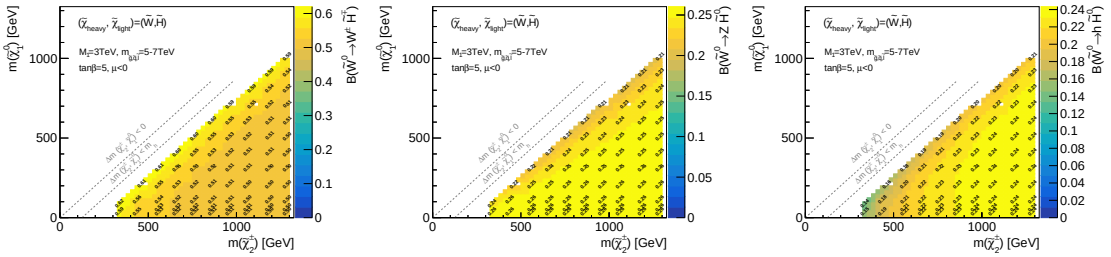

(d) $\mathcal{B}(\tilde{W}^{0} \to W^{\pm}\tilde{H}^{\mp})$ (e) $\mathcal{B}(\tilde{W}^{0} \to Z\tilde{H}^{0}_{1,2})$ (f) $\mathcal{B}(\tilde{W}^{0} \to h\tilde{H}^{0}_{1,2})$

Figure C.6: Branching ratio of (a)(b)(c) charged and (d)(e)(f) neutral wino decaying into higgsino light state with a $W/Z/h$ ($\tan\beta = 5, \mu < 0$). Branching into neutral higgsino is sum of the two destination states i.e. $\mathcal{B}(\ldots \to \tilde{H}^{0}_{1,2}) := \mathcal{B}(\ldots \to \tilde{H}^{0}_{1}) + \mathcal{B}(\ldots \to \tilde{H}^{0}_{2})$.

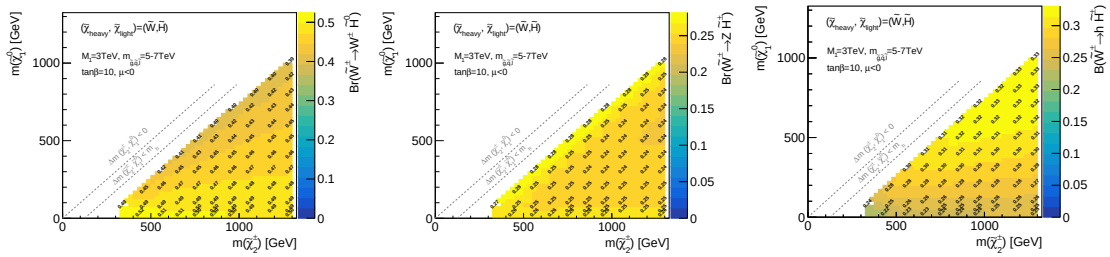

(a) $\mathcal{B}(\tilde{W}^{\pm} \to W^{\pm}\tilde{H}^{0}_{1,2})$ (b) $\mathcal{B}(\tilde{W}^{\pm} \to Z\tilde{H}^{\pm})$ (c) $\mathcal{B}(\tilde{W}^{\pm} \to h\tilde{H}^{\pm})$

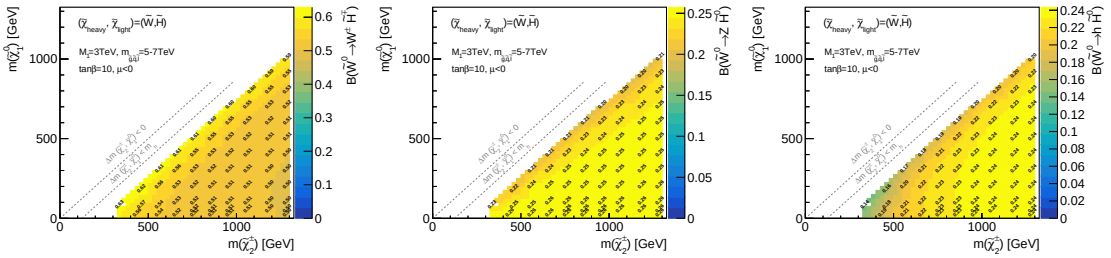

(d) $\mathcal{B}(\tilde{W}^{0} \to W^{\pm}\tilde{H}^{\mp})$ (e) $\mathcal{B}(\tilde{W}^{0} \to Z\tilde{H}^{0}_{1,2})$ (f) $\mathcal{B}(\tilde{W}^{0} \to h\tilde{H}^{0}_{1,2})$

Figure C.7: Branching ratio of (a)(b)(c) charged and (d)(e)(f) neutral wino decaying into higgsino light state with a $W/Z/h$ ($\tan\beta = 10, \mu < 0$). Branching into neutral higgsino is sum of the two destination states i.e. $\mathcal{B}(\ldots \to \tilde{H}^{0}_{1,2}) := \mathcal{B}(\ldots \to \tilde{H}^{0}_{1}) + \mathcal{B}(\ldots \to \tilde{H}^{0}_{2})$.

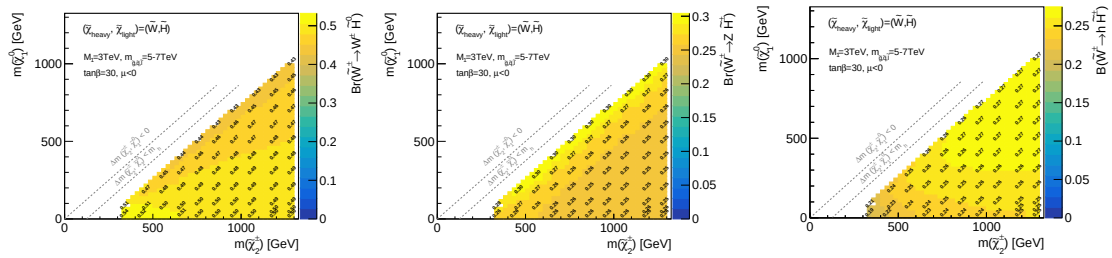

(a) $\mathcal{B}(\tilde{W}^{\pm} \to W^{\pm}\tilde{H}^{0}_{1,2})$ (b) $\mathcal{B}(\tilde{W}^{\pm} \to Z\tilde{H}^{\pm})$ (c) $\mathcal{B}(\tilde{W}^{\pm} \to h\tilde{H}^{\pm})$

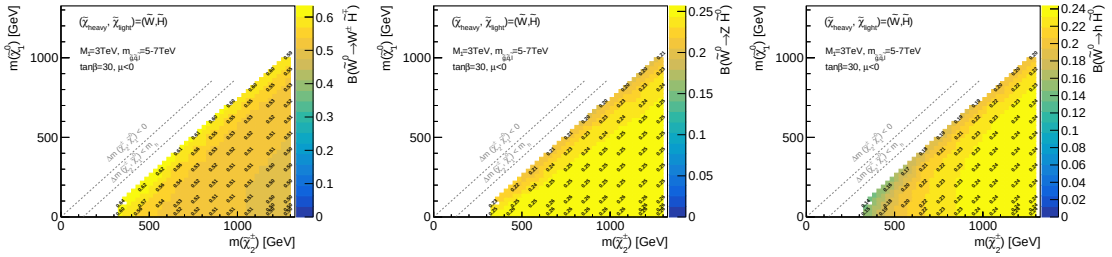

(d) $\mathcal{B}(\tilde{W}^{0} \to W^{\pm}\tilde{H}^{\mp})$ (e) $\mathcal{B}(\tilde{W}^{0} \to Z\tilde{H}^{0}_{1,2})$ (f) $\mathcal{B}(\tilde{W}^{0} \to h\tilde{H}^{0}_{1,2})$

Figure C.8: Branching ratio of (a)(b)(c) charged and (d)(e)(f) neutral wino decaying into higgsino light state with a $W/Z/h$ ($\tan\beta = 30, \mu < 0$). Branching into neutral higgsino is sum of the two destination states i.e. $\mathcal{B}(\ldots \to \tilde{H}^{0}_{1,2}) := \mathcal{B}(\ldots \to \tilde{H}^{0}_{1}) + \mathcal{B}(\ldots \to \tilde{H}^{0}_{2})$.

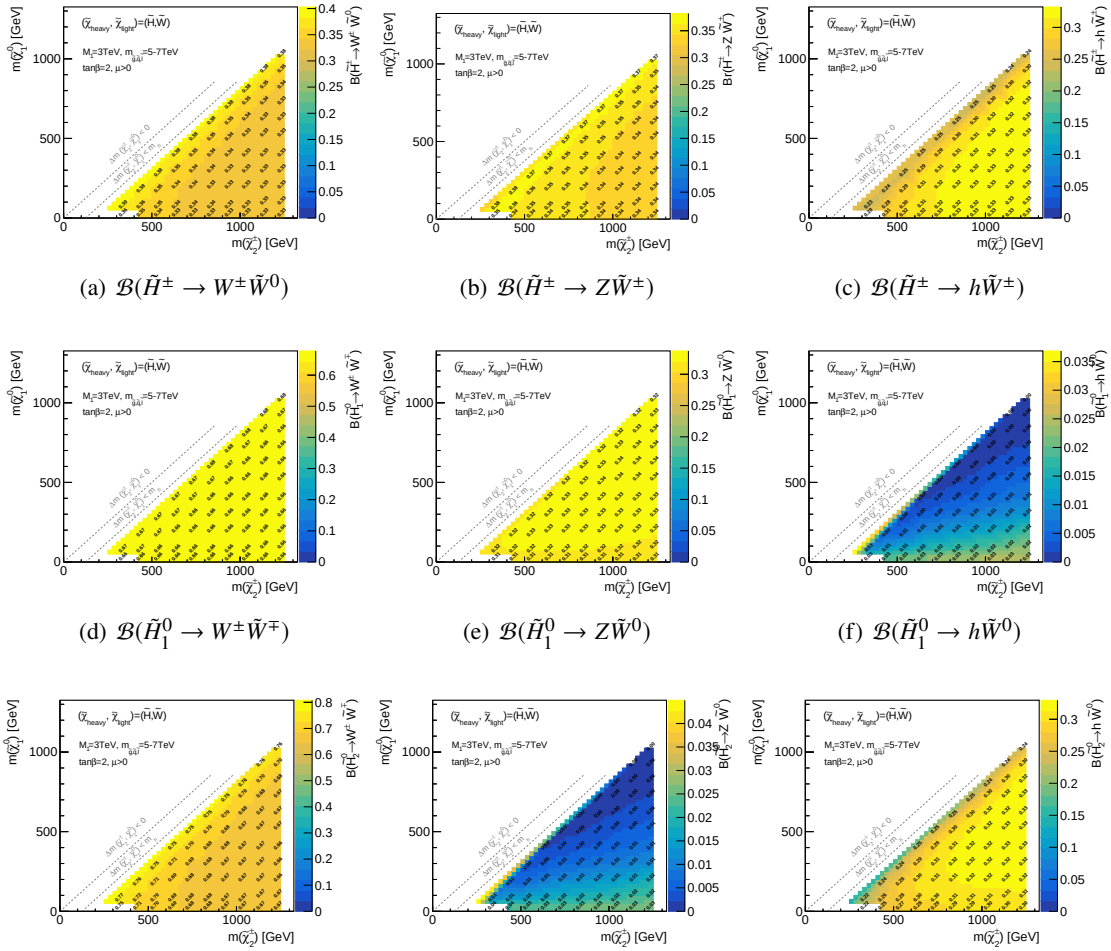

(a) $\mathcal{B}(\tilde{H}^{\pm} \to W^{\pm}\tilde{W}^{0})$ (b) $\mathcal{B}(\tilde{H}^{\pm} \to Z\tilde{W}^{\pm})$ (c) $\mathcal{B}(\tilde{H}^{\pm} \to h\tilde{W}^{\pm})$

(d) $\mathcal{B}(\tilde{H}_1^0 \to W^{\pm}\tilde{W}^{\mp})$ (e) $\mathcal{B}(\tilde{H}_1^0 \to Z\tilde{W}^{0})$ (f) $\mathcal{B}(\tilde{H}_1^0 \to h\tilde{W}^{0})$

(g) $\mathcal{B}(\tilde{H}_2^0 \to W^{\pm}\tilde{W}^{\mp})$ (h) $\mathcal{B}(\tilde{H}_2^0 \to Z\tilde{W}^{0})$ (i) $\mathcal{B}(\tilde{H}_2^0 \to h\tilde{W}^{0})$

Figure C.9: Branching ratio of (a)(b)(c) charged higgsino (d)(e)(f) light neutral higgsino and (g)(h)(i) heavy neutral higgsino ($\tilde{H}_2^0$) decaying wino light state with a into $W/Z/h$ ($\tan\beta = 2, \mu > 0$).

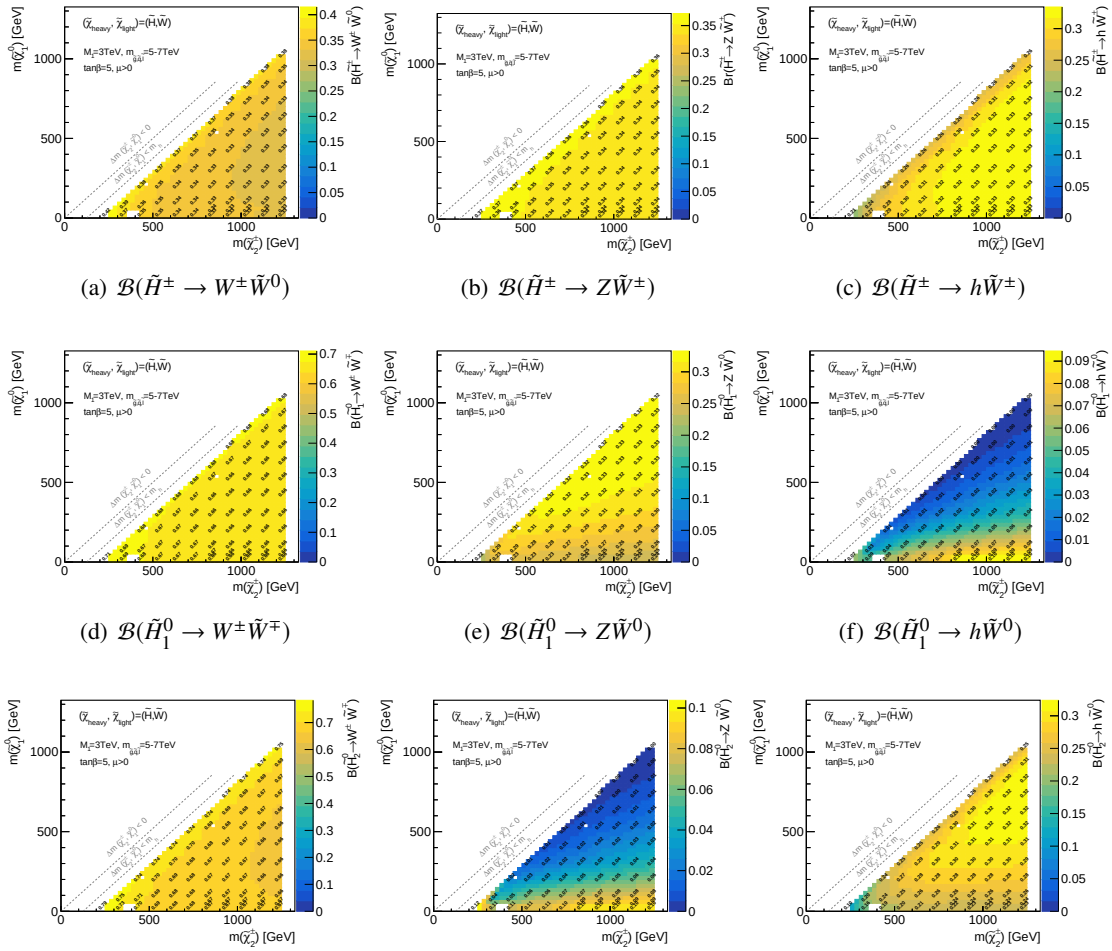

Figure C.10: Branching ratio of (a)(b)(c) charged higgsino (d)(e)(f) light neutral higgsino and (g)(h)(i) heavy neutral higgsino ($\tilde{H}_2^0$) decaying wino light state with a into $W/Z/h$ ($\tan\beta = 5, \mu > 0$).

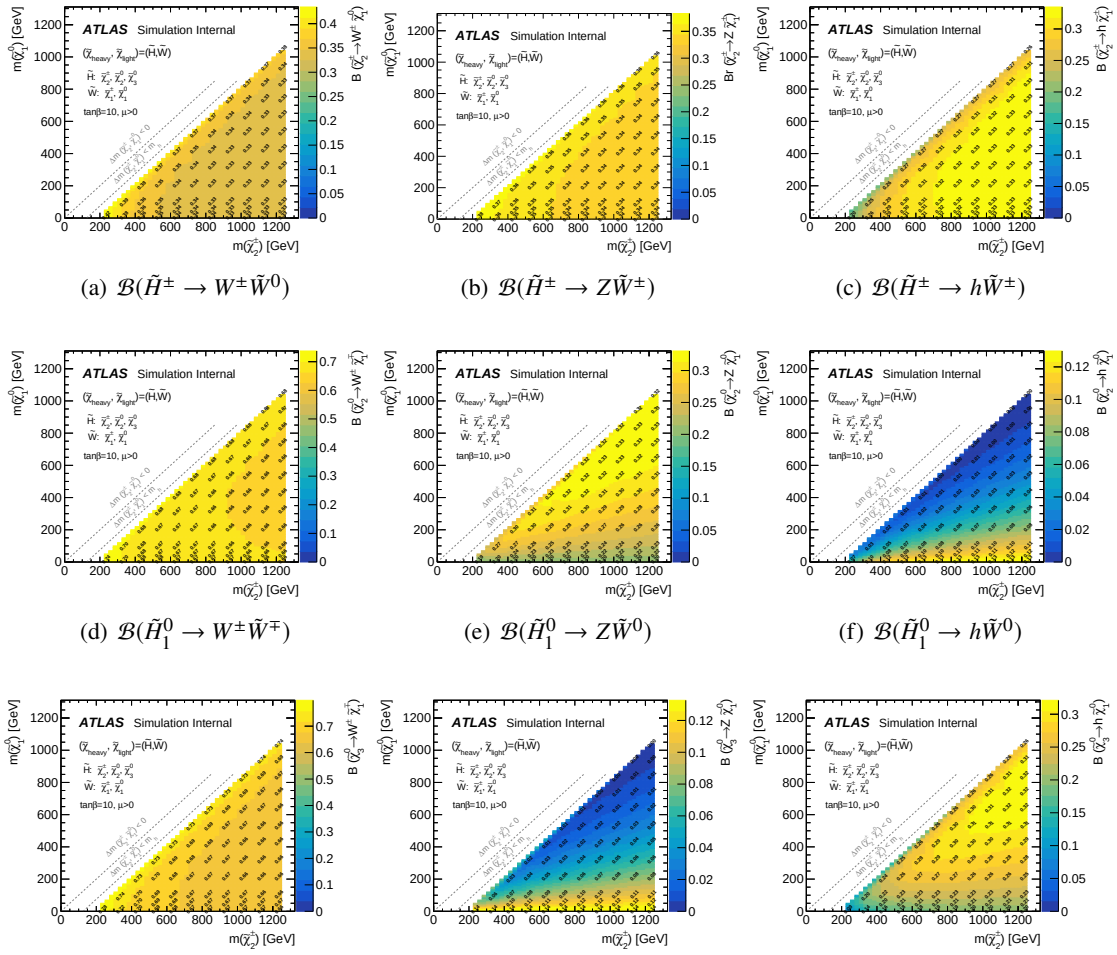

(a) $\mathcal{B}(\tilde{H}^{\pm} \to W^{\pm}\tilde{W}^0)$ (b) $\mathcal{B}(\tilde{H}^{\pm} \to Z\tilde{W}^{\pm})$ (c) $\mathcal{B}(\tilde{H}^{\pm} \to h\tilde{W}^{\pm})$

(d) $\mathcal{B}(\tilde{H}_1^0 \to W^{\pm}\tilde{W}^{\mp})$ (e) $\mathcal{B}(\tilde{H}_1^0 \to Z\tilde{W}^0)$ (f) $\mathcal{B}(\tilde{H}_1^0 \to h\tilde{W}^0)$

(g) $\mathcal{B}(\tilde{H}_2^0 \to W^{\pm}\tilde{W}^{\mp})$ (h) $\mathcal{B}(\tilde{H}_2^0 \to Z\tilde{W}^0)$ (i) $\mathcal{B}(\tilde{H}_2^0 \to h\tilde{W}^0)$

Figure C.11: Branching ratio of (a)(b)(c) charged higgsino (d)(e)(f) light neutral higgsino and (g)(h)(i) heavy neutral higgsino ($\tilde{H}_2^0$) decaying wino light state with a into $W/Z/h$ ($\tan\beta = 10, \mu > 0$).

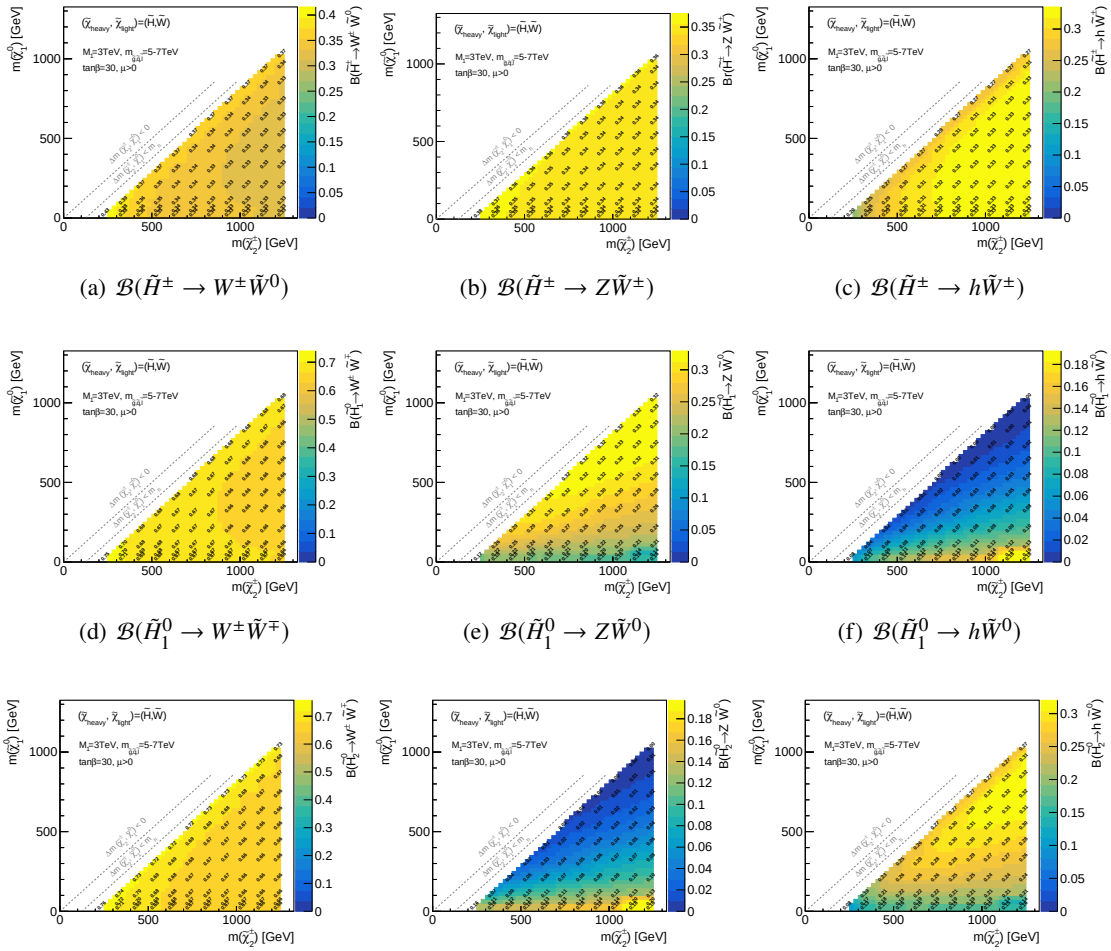

(a) $\mathcal{B}(\tilde{H}^\pm \to W^\pm \tilde{W}^0)$ (b) $\mathcal{B}(\tilde{H}^\pm \to Z \tilde{W}^\pm)$ (c) $\mathcal{B}(\tilde{H}^\pm \to h \tilde{W}^\pm)$

(d) $\mathcal{B}(\tilde{H}_1^0 \to W^\pm \tilde{W}^\mp)$ (e) $\mathcal{B}(\tilde{H}_1^0 \to Z \tilde{W}^0)$ (f) $\mathcal{B}(\tilde{H}_1^0 \to h \tilde{W}^0)$

(g) $\mathcal{B}(\tilde{H}_2^0 \to W^\pm \tilde{W}^\mp)$ (h) $\mathcal{B}(\tilde{H}_2^0 \to Z \tilde{W}^0)$ (i) $\mathcal{B}(\tilde{H}_2^0 \to h \tilde{W}^0)$

Figure C.12: Branching ratio of (a)(b)(c) charged higgsino (d)(e)(f) light neutral higgsino and (g)(h)(i) heavy neutral higgsino ($\tilde{H}_2^0$) decaying wino light state with a into $W/Z/h$ ($\tan\beta = 30, \mu > 0$).

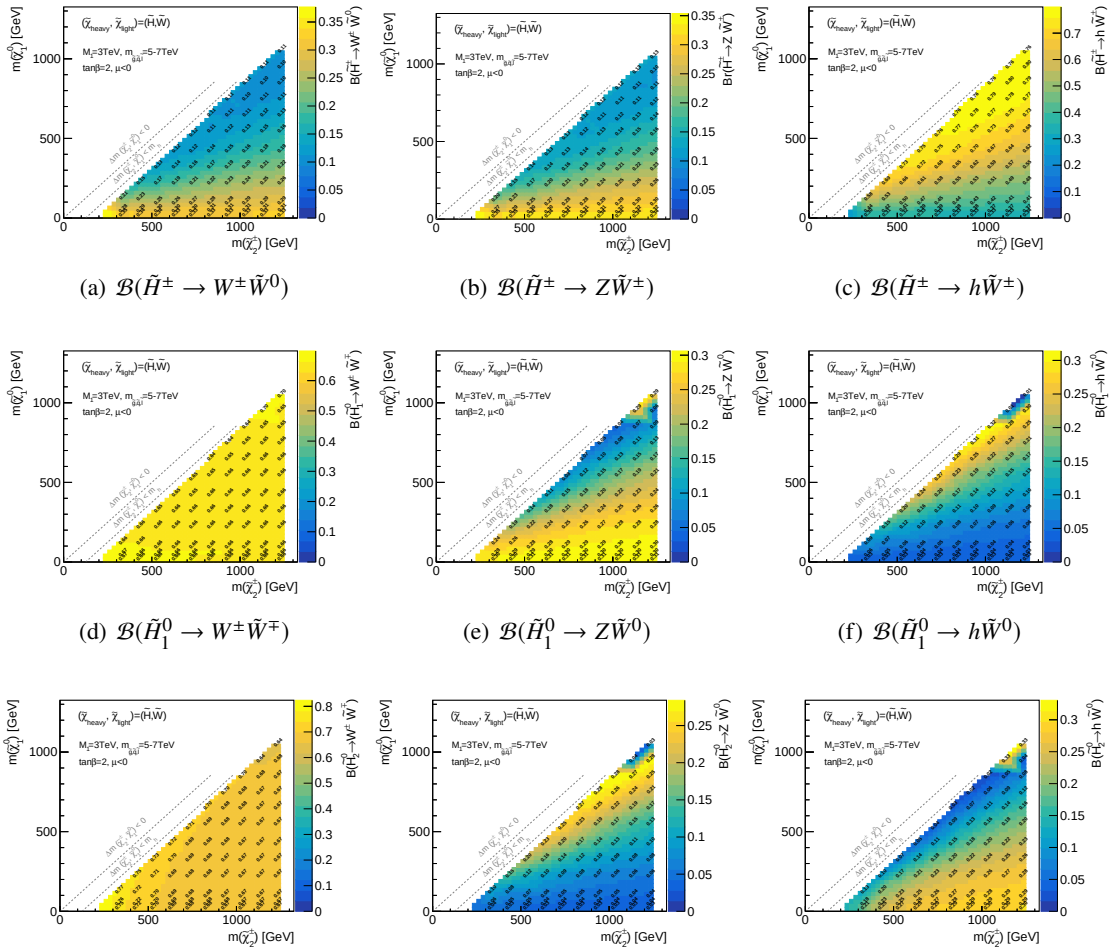

(a) $\mathcal{B}(\tilde{H}^{\pm} \to W^{\pm}\tilde{W}^{0})$ (b) $\mathcal{B}(\tilde{H}^{\pm} \to Z\tilde{W}^{\pm})$ (c) $\mathcal{B}(\tilde{H}^{\pm} \to h\tilde{W}^{\pm})$

(d) $\mathcal{B}(\tilde{H}_1^0 \to W^{\pm}\tilde{W}^{\mp})$ (e) $\mathcal{B}(\tilde{H}_1^0 \to Z\tilde{W}^{0})$ (f) $\mathcal{B}(\tilde{H}_1^0 \to h\tilde{W}^{0})$

(g) $\mathcal{B}(\tilde{H}_2^0 \to W^{\pm}\tilde{W}^{\mp})$ (h) $\mathcal{B}(\tilde{H}_2^0 \to Z\tilde{W}^{0})$ (i) $\mathcal{B}(\tilde{H}_2^0 \to h\tilde{W}^{0})$

Figure C.13: Branching ratio of (a)(b)(c) charged higgsino (d)(e)(f) light neutral higgsino and (g)(h)(i) heavy neutral higgsino ($\tilde{H}_2^0$) decaying wino light state with a into $W/Z/h$ ($\tan\beta = 2, \mu < 0$).

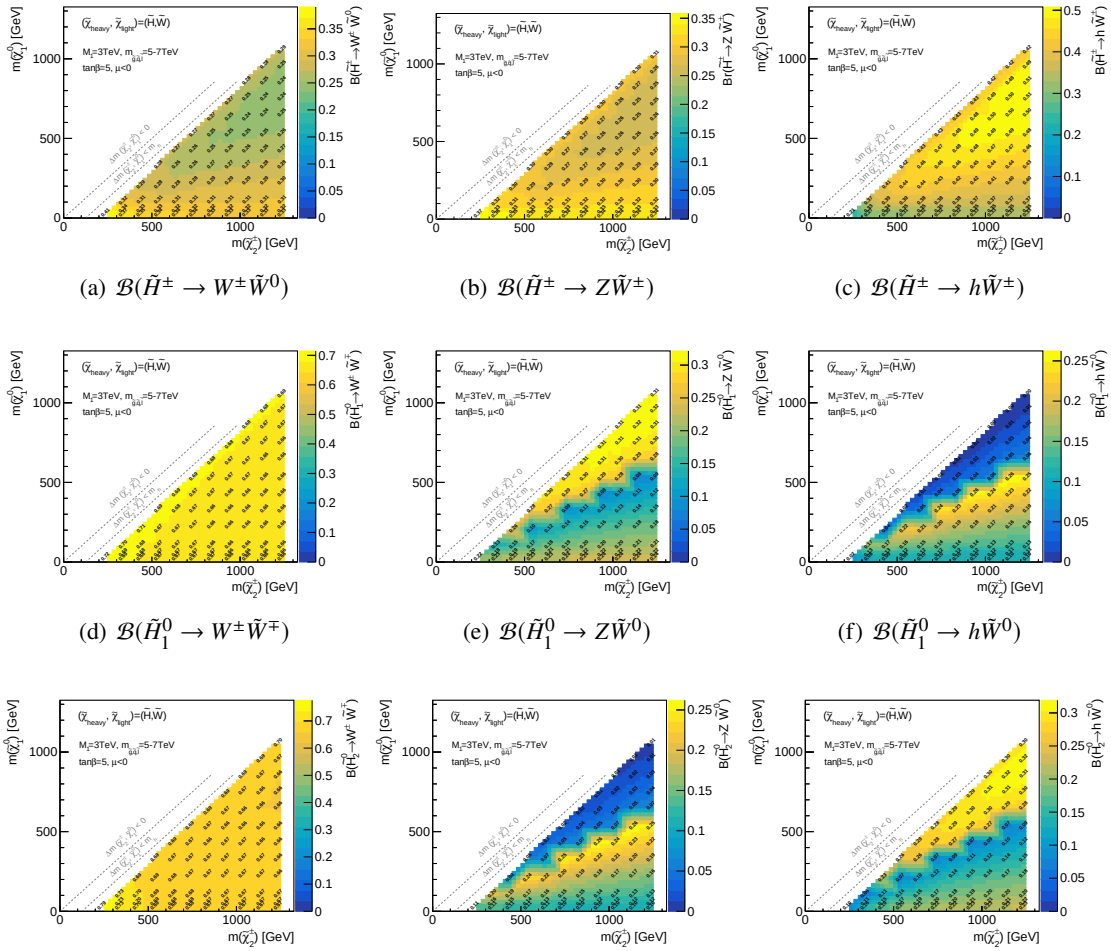

(a) $\mathcal{B}(\tilde{H}^\pm \to W^\pm\tilde{W}^0)$ (b) $\mathcal{B}(\tilde{H}^\pm \to Z\tilde{W}^\pm)$ (c) $\mathcal{B}(\tilde{H}^\pm \to h\tilde{W}^\pm)$

(d) $\mathcal{B}(\tilde{H}_1^0 \to W^\pm\tilde{W}^\mp)$ (e) $\mathcal{B}(\tilde{H}_1^0 \to Z\tilde{W}^0)$ (f) $\mathcal{B}(\tilde{H}_1^0 \to h\tilde{W}^0)$

(g) $\mathcal{B}(\tilde{H}_2^0 \to W^\pm\tilde{W}^\mp)$ (h) $\mathcal{B}(\tilde{H}_2^0 \to Z\tilde{W}^0)$ (i) $\mathcal{B}(\tilde{H}_2^0 \to h\tilde{W}^0)$

Figure C.14: Branching ratio of (a)(b)(c) charged higgsino (d)(e)(f) light neutral higgsino and (g)(h)(i) heavy neutral higgsino ($\tilde{H}_2^0$) decaying wino light state with a into $W/Z/h$ ($\tan\beta = 5, \mu < 0$).

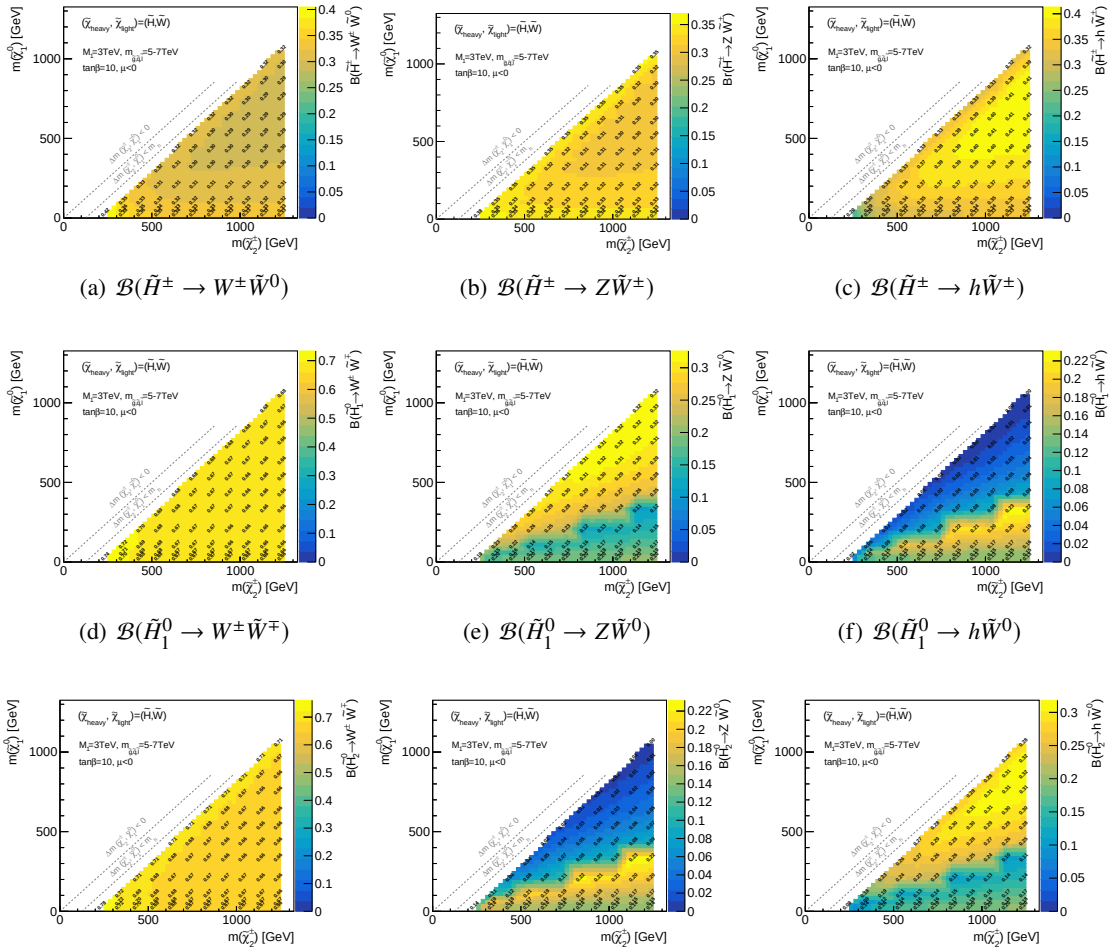

Figure C.15: Branching ratio of (a)(b)(c) charged higgsino (d)(e)(f) light neutral higgsino and (g)(h)(i) heavy neutral higgsino ($\tilde{H}_2^0$) decaying wino light state with a into $W/Z/h$ ($\tan\beta = 10, \mu < 0$).

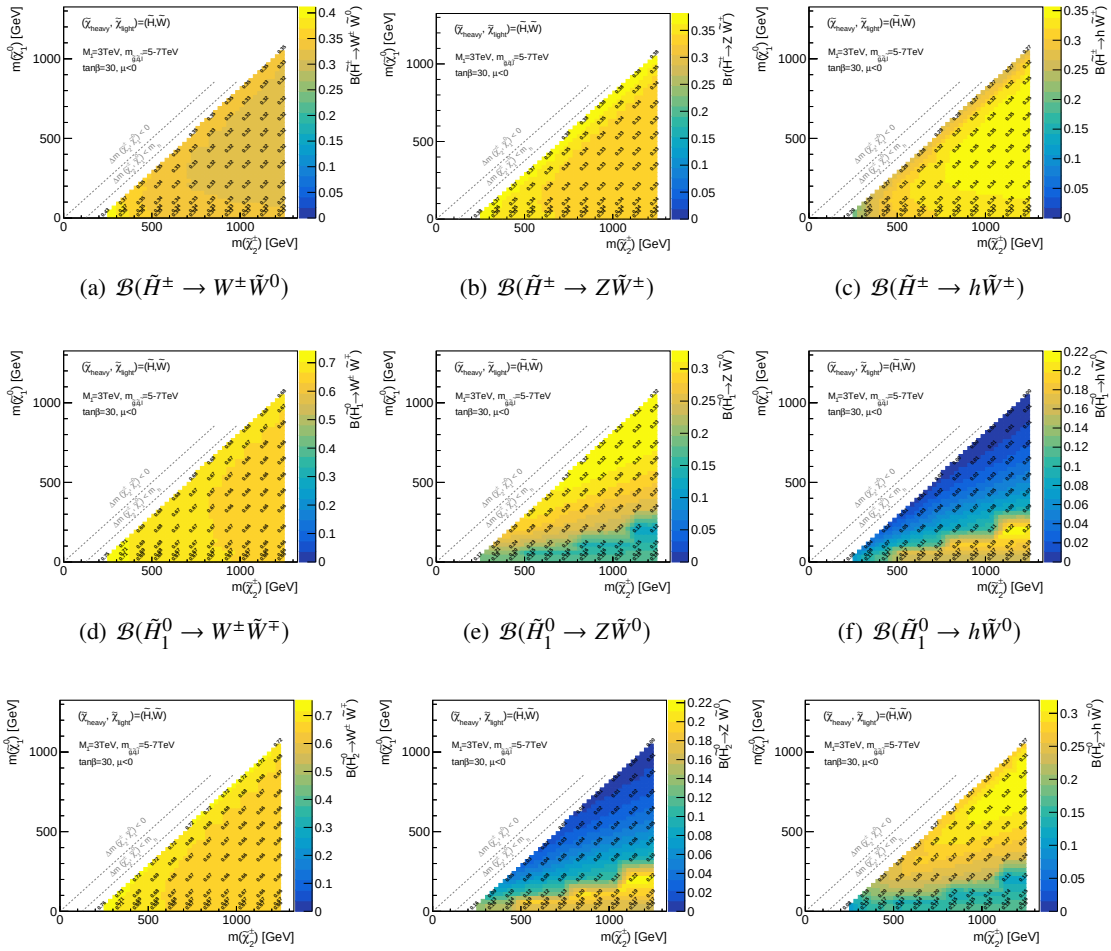

Figure C.16: Branching ratio of (a)(b)(c) charged higgsino (d)(e)(f) light neutral higgsino and (g)(h)(i) heavy neutral higgsino ($\tilde{H}_2^0$) decaying wino light state with a into $W/Z/h$ ($\tan\beta = 30, \mu < 0$).

D Supplements of Object Reconstruction

D.1 Topo-cluster Reconstruction

"Topo-clusters" are collections of calorimeter cell signals topologically connected to extract signals by particle showers separated from backgrounds by electronic noise and other sources of fluctuations, such as pile-up. In the reconstruction algorithm, we use an observable based on the calorimeter cell significance $\varsigma^{\mathrm{EM}}_{\mathrm{cell}}$ [103]:

$$\varsigma^{\mathrm{EM}}_{\mathrm{cell}} = \frac{E^{\mathrm{EM}}_{\mathrm{cell}}}{\sigma^{\mathrm{EM}}_{\mathrm{noise,cell}}}, \tag{D.1}$$

where $E^{\mathrm{EM}}_{\mathrm{cell}}$ is the measured cell energy on the electromagnetic (EM) energy scale and $\sigma^{\mathrm{EM}}_{\mathrm{noise,cell}}$ is the average (expected) noise in the cell, which is the standard deviation of the energy distribution in the data collected by signals from scintillators [239]. The EM energy scale is calibrated to reconstruct the energy deposited by electrons and photons.

A cell which satisfy $|\varsigma^{\mathrm{EM}}_{\mathrm{cell}}| > 4$ is the seed of the reconstruction. The neighboring cells with $|\varsigma^{\mathrm{EM}}_{\mathrm{cell}}| > 2$ are added to the seed cluster. If the neighboring cells have absolute energy 4σ above the noise threshold, the two clusters are merged. Besides, if a cell with $|\varsigma^{\mathrm{EM}}_{\mathrm{cell}}| > 2$ is adjacent to two different clusters, the two clusters are merged. The energies in the neighboring cells is iteratively added until finding all neighboring cells with $|\varsigma^{\mathrm{EM}}_{\mathrm{cell}}| > 2$. Finally, the neighboring cells with $|\varsigma^{\mathrm{EM}}_{\mathrm{cell}}| > 0$, i.e. all the neighboring cells, are merged to the clusters. The built clusters are called "proto-clusters." This topo-cluster algorithm largely suppresses the noise effects [103].

The proto-clusters with two or more local signal maxima ($E^{\mathrm{EM}}_{\mathrm{cell}} > 500$ MeV) are split into separate clusters. In this case, the cells are assigned to the two highest-energy clusters after the splitting procedure. The shared cells are assigned to associated clusters with a fractional weight [103],

$$\omega^{\mathrm{geo}}_{\mathrm{cell},1} = \frac{E^{\mathrm{EM}}_{\mathrm{clus},1}}{E^{\mathrm{EM}}_{\mathrm{clus},1} + rE^{\mathrm{EM}}_{\mathrm{clus},2}}, \text{ and} \tag{D.2}$$

$$\omega^{\mathrm{geo}}_{\mathrm{cell},2} = 1 - \omega^{\mathrm{geo}}_{\mathrm{cell},1}, \tag{D.3}$$

$$r = \exp(d_1 - d_2), \tag{D.4}$$

where $E^{\mathrm{EM}}_{\mathrm{clus},i}$ is the energy of the two clusters and $\omega^{\mathrm{geo}}_{\mathrm{cell},i}$ is geometrical weight calculated from the distances of the cell to the center of gravity of the cluster d_i. The energy of the topo-clusters is in the EM scale.

D.2 The Anti-k_t algorithm

To reconstruct hadronic jets from the topo-clusters, we use "anti-k_t algorithm" [104] implemented in the FastJet package [105]. In the anti-k_t algorithm, two distance variables d_{ij}, d_{iB} are used. d_{ij} represents the

distance between two clusters i and j, and d_{iB} is the distance between cluster i and the beam (B). The definitions are,

$$d_{ij} = \min(1/p_{\mathrm{T}i}^2, 1/p_{\mathrm{T}j}^2)\Delta R_{ij}^2/R^2, \text{ and} \tag{D.5}$$

$$d_{iB} = 1/p_{\mathrm{T}i}^2, \tag{D.6}$$

where $\Delta R_{ij}^2 = (y_i - y_j)^2 + (\phi_i - \phi_j)^2$, and $p_{\mathrm{T}i}$, y_i, and ϕ_i are transverse momenta, rapidity, and azimuth angle of cluster i, respectively. R is the radius parameter that approximates the cone size of jets in the $y - \phi$ plane.

D.3 Local Hadronic Cell Weighting

As described in Appendix D.1, the energy of the topo-clusters is in the EM scale. We need to calibrate the topo-cluster in the hadronic scale correctly because the response in the EM and hadronic scales are different due to non-compensating calorimeter response and calorimeter signal loss, which is caused by clustering or inactive material, and calorimeter signals for hadrons smaller than the ones for electrons and photons. This correction is called "Local hadronic cell weighting (LCW)" [103, 240].

The LCW corrects the energy of the topo-clusters with the appropriate energy scales, i.e., electromagnetic or hadronic energy scale. The noise-suppression of clustering depends on the pile-up conditions and the noise threshold for the cell energy. The correction is based on the following function:

$$\omega_{\mathrm{cell}}^{\mathrm{cal}} = P_{\mathrm{clus}}^{\mathrm{EM}} \cdot \omega_{\mathrm{cell}}^{\text{em-cal}} + (1 - P_{\mathrm{clus}}^{\mathrm{EM}}) \cdot \omega_{\mathrm{cell}}^{\text{had-cal}}, \tag{D.7}$$

where $P_{\mathrm{clus}}^{\mathrm{EM}}$ is the probability by electromagnetic energy deposit against hadronic, $\omega_{\mathrm{cell}}^{\text{em-cal}}$ and $\omega_{\mathrm{cell}}^{\text{had-cal}}$ are the signal weights to electromagnetic scale and hadronic scale, respectively.

D.4 Particle Flow Algorithm

The particle flow algorithm, where individual particles ideally represent clusters by combining track and topo-clusters, is employed to improve the hadronic measurement. The detailed algorithm is presented in Ref.[241], and the outline is introduced in this section. The flowchart of the algorithm is illustrated in Figure D.1.

Tracks, selected with stringent quality criteria, $|\eta|$, p_{T}, and ID hits, are used to categorize clusters from charged particles or neutral particles by spatial matching. In this step, each track is attempted to match a single topo-cluster. The energy and momentum of the matched cluster are re-calculated by combining the position of the cluster and the momentum of matched tracks. Since all the energy of particles does not always deposit in a single topo-cluster, we use the variable $S(E^{\mathrm{clus}})$ defined as:

$$S(E^{\mathrm{clus}}) = \frac{E^{\mathrm{clus}} - \langle E_{\mathrm{dep}} \rangle}{\sigma(E_{\mathrm{dep}})}, \text{ where } \langle E_{\mathrm{dep}} \rangle = p^{\mathrm{trk}} \left\langle E_{\mathrm{ref}}^{\mathrm{clus}}/p_{\mathrm{ref}}^{\mathrm{trk}} \right\rangle, \tag{D.8}$$

where E^{clus} and $\sigma(E_{\mathrm{dep}})$ are the energy of the topo-cluster and the spread of the expected value, p^{trk} is the momentum of the track, and $\left\langle E_{\mathrm{ref}}^{\mathrm{clus}}/p_{\mathrm{ref}}^{\mathrm{trk}} \right\rangle$ is the mean response. If $S(E^{\mathrm{clus}}) < -1$, other topo-clusters are added. Then, by subtracting the deposited energy of particles producing tracks in the calorimeter cell, the energy of the shower fluctuations remains and is removed.

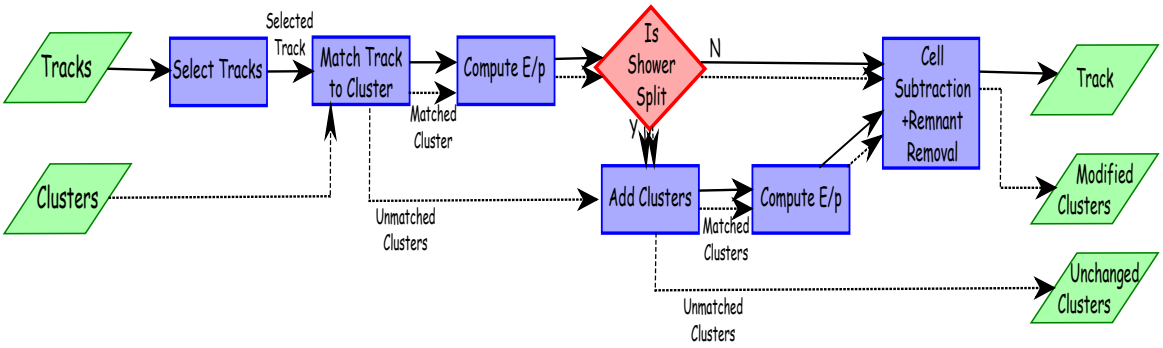

Figure D.1: A flowchart of the particle flow algorithm [241]. The energy and momentum of clusters and tracks are modified by combining them.

D.5 Jet Vertex Tagger

In the JVT algorithm, two variables, which are calculated by tracking information, are used. One is correcting jet vertex fraction (corrJVF), defined as:

$$\text{corrJVF} = \frac{\sum_m p_{\text{T},m}^{\text{track}}(\text{PV}_0)}{\sum_l p_{\text{T},l}^{\text{track}}(\text{PV}_0) + \frac{\sum_{n\geq 1}\sum_l p_{\text{T},l}^{\text{track}}(\text{PV}_n)}{k \cdot n_{\text{track}}^{\text{PU}}}}, \tag{D.9}$$

where the numerator represents the scalar sum of the p_{T} of the tracks associated with the jet originated from the hard-scatter vertex. The term in the denominator, $\sum_{n\geq 1}\sum_l p_{\text{T},l}^{\text{track}}(\text{PV}_n)$, is the ratio of the scalar sum of the p_{T} of the tracks originated from the pile-up interactions. The right term represents the correction for the number of pile-up interactions and is defined as the total number of pile-up tracks per event times the parameter ($k = 0.01$). Another discriminant variable is the ratio of the scalar sum of the p_{T} of the tracks associated with the jet originated from the hard-scatter vertex to the jet p_{T}. The definition is,

$$R_{p_{\text{T}}} = \frac{\sum_k p_{\text{T},k}^{\text{track}}(\text{PV}_0)}{p_{\text{T}}^{\text{jet}}}. \tag{D.10}$$

D.6 Track Jet *b*-tagging

Inputs for the MV2 algorithm are summarized in Table D.1. IP2D/IP3D [115] are impact parameter-based algorithms that exploit the large impact parameters of the tracks originating from the b-hadron decay. IP2D uses the signed transverse impact parameter significance for tracks, and IP3D also uses the longitudinal impact parameter significance. IP3D considers their correlation in a two-dimensional template. The probability density functions are obtained in the algorithms, and log-likelihood ratios in the b-jet, c-jet, and light-flavor jet hypotheses are calculated. Additionally, the SV1 algorithm, which is the secondary vertex tagging algorithm [242], is used to reconstruct secondary vertices. The secondary vertices are reconstructed from the track information, and the track-to-vertex association is evaluated using a χ^2 fit. To use the full b- to c-hadron decay chain, JetFitter [243], which is based on a modified Kalman filter [244], is used.

Table D.1: Input variables used by the MV2 algorithm [116].

Input	Variable	Description
Kinematics	p_{T}	Jet p_{T}
	η	Jet η
IP2D/IP3D	$\log P_b/P_{\mathrm{light}}$	Likelihood ratio between the b-jet and light flavour jet hypotheses
(two complementary impact parameter-based algorithms)	$\log P_b/P_c$	Likelihood ratio between the b-jet and c-jet hypotheses
	$\log P_c/P_{\mathrm{light}}$	Likelihood ratio between the c-jet and light flavour jet hypotheses
SV1	$m(\mathrm{SV})$	Invariant mass of tracks at the secondary vertex assuming pion mass
(secondary vertex tagging algorithm)	$f_E(\mathrm{SV})$	Energy fraction of the tracks associated with the secondary vertex
	$N_{\mathrm{TrkAtVtx}}(\mathrm{SV})$	Number of tracks used in the secondary vertex
	$N_{\mathrm{2TrkVtx}}(\mathrm{SV})$	Number of two-track vertex candidates
	$L_{xy}(\mathrm{SV})$	Transverse distance between the primary and secondary vertex
	$L_{xyz}(\mathrm{SV})$	Distance between the primary and the secondary vertex
	$S_{xyz}(\mathrm{SV})$	Distance between the primary and the secondary vertex divided by its uncertainty
	$\Delta R(\boldsymbol{p}_{\mathrm{jet}}, \boldsymbol{p}_{\mathrm{vtx}})(\mathrm{SV})$	ΔR between the jet axis and the direction of the secondary vertex relative to the primary vertex
JetFitter	$m(\mathrm{JF})$	Invariant mass of tracks from displaced vertices
	$f_E(\mathrm{JF})$	Energy fraction of the tracks associated with the displaced vertices
(topological multi-vertex algorithm)	$\Delta R(\boldsymbol{p}_{\mathrm{jet}}, \boldsymbol{p}_{\mathrm{vtx}})(\mathrm{JF})$	ΔR between the jet axis and the vectorial sum of momenta of all tracks attached to displaced vertices
	$S_{xyz}(\mathrm{JF})$	Significance of the average distance between PV and displaced vertices
	$N_{\mathrm{TrkAtVtx}}(\mathrm{JF})$	Number of tracks from multi-prong displaced vertices
	$N_{\mathrm{2TrkVtx}}(\mathrm{JF})$	Number of two-track vertex candidates (prior to decay chain fit)
	$N_{1-\mathrm{trk}\ vertices}(\mathrm{JF})$	Number of single-prong displaced vertices
	$N_{\geq\ 2-\mathrm{trk}\ vertices}(\mathrm{JF})$	Number of multi-prong displaced vertices

D.7 Electron and Photon Reconstruction

D.7.1 Reconstruction and Identification

Reconstruction The reconstruction of electrons and photons is based on similar algorithms. Detailed procedures are described in Ref.[119], only an outline is presented.

Electrons and photons are reconstructed using the information in the calorimeters and the inner detectors (ID). In the first step of the reconstruction, topo-clusters are reconstructed from the energy deposits in the electromagnetic (EM) calorimeter, not including the measured energy in the hadronic calorimeters. However, in the transition region ($1.37 < |\eta| < 1.63$), the energy measured in the presampler and scintillator between the calorimeter cryostats is also added. These clusters are seeds for the reconstruction. Only those that satisfy the requirements that the energy greater than 400 MeV and the ratio of the energy to the total cluster energy (including the energy measured in the hadronic calorimeter) are selected for the reconstruction. The selected clusters are referred to as "EM topo-clusters." In parallel, tracks are reconstructed from the ID tracks and the fixed-size clusters instead of topo-clusters. The fixed-size clusters are reconstructed by a sliding-window algorithm [245]. The size of fixed-size clusters is 3 units in $\eta \times \phi$, and the size of units is 0.025×0.025 in the $\eta - \phi$ plane and corresponds to the granularity of the second layer in the EM calorimeter. The fixed-size clusters, which have summed transverse energy greater than 2.5 GeV, are used only to create regions-of-interest. The tracks are built from the reconstructed ID tracks and the fixed clusters using a modified pattern recognition algorithm based on a Kalman filter formalism [244], the global χ^2 fit [246], and a Gaussian sum filter (GSF) algorithm [247].

Additionally, conversion vertices used for reconstructing converted photons are introduced. Both the ID tracks and tracks reconstructed only in the TRT matching the fixed-size clusters are used as input to reconstruct conversion vertices. Two types of the converted vertex are used. One is a conversion vertex associated with two opposite-charged tracks, required to be consistent with a massless particle. Another is a single-track vertex reconstructed from the TRT tracks. Additionally, we use the ID tracks and the TRT tracks matching the fixed-size clusters to reconstruct converted photons. In order to keep the converted photon purity high, the TRT tracks are required to match to electron tracks [248].

After reconstructing the EM topo-clusters, tracks, and conversion vertices, they are used to reconstruct "superclusters." The reconstruction of the supercluster candidates originating from electrons or photons is performed separately. In the first step, the EM topo-clusters are divided into "seed clusters" and "satellite clusters" with E_{T} selections track matching requirements. The satellite clusters, tracks, and converted vertices that match the seed cluster spatially are added to the seed clusters with an energy greater than thresholds. They are referred to as "superclusters."

The seed cluster candidates of electrons are required to have E_{T} greater than 1 GeV and the matched ID tracks with at least four hits. For photon candidates, it is required to have a minimum E_{T} of 1.5 GeV without requirements for track and conversion vertex matching. All EM topo-clusters not satisfying these requirements are treated as satellite clusters. In the next step, the algorithm to find satellite clusters associated with the seed clusters runs. A satellite cluster within $\Delta\eta \times \Delta\phi = 0.075 \times 0.125$ around the seed cluster barycentre is added to the seed cluster. In the reconstruction algorithm of electrons, spatial matching requirements are loosed to be $\Delta\eta \times \Delta\phi = 0.125 \times 0.300$. For photon reconstruction, a satellite cluster with the same converted vertices and tracks reconstructed from only ID hits are added to the seed cluster. In addition, a satellite cluster that has the best matched (electron) tracks associated with the same

converted vertices is also added. At this step, a satellite cluster that has already been added to seed clusters is not used.

Their energy is calculated from the corresponding calorimeter cells in the presampler and the first three LAr calorimeter layers, except in the transition region ($1.4 < |\eta| < 1.6$). In the transition region, the energy measured by the scintillator between the calorimeter cryostats is also added.

After building the electron and photon superclusters, they are corrected for their energy and position. Matching the tracks and the converted vertices to the superclusters is performed in the same way as matching the EM topo-clusters and them. At this level, a supercluster can be both candidates of electron and photon due to performing the building of the electron and photon supercluster candidates individually. To solve this problem, the logic shown in Figure D.2 is applied. The superclusters identified as "ambiguous" in the final classification are treated as photons in this thesis.

Electron Identification The discriminating variables, as shown in Table D.2, are used to distinguish promptly isolated electrons from hadronic jets, converted photons, and true electrons from heavy-flavor hadrons. The variables can be categorized into four groups, primary electron tracks, shapes of the electromagnetic shower in the calorimeter, hadronic leakage, and matching between the tracks and the clusters. These variables are used for the likelihood calculation, probability density functions (pdfs) P. The pdfs are obtained from smoothing histograms for each corresponding discriminating variables with an adaptive kernel density estimator (KDE [249]) as implemented in TVA [250]. Additionally, the pdfs for signal and background are calculated separately, and depend on $|\eta|$ and E_{T}. Thus, likelihoods are obtained individually and defined as,

$$L_{S(B)}(\boldsymbol{x}) = \prod_{i=1}^{n} P_{S(B),i}(x_i), \tag{D.11}$$

where $P_{S(B),i}(x_i)$ is the pdf of $i-$th variable for signal (background). Besides, the likelihood discriminant d_L is defined as,

$$d_L = \log(L_S(\boldsymbol{X})/L_B(\boldsymbol{X})). \tag{D.12}$$

Several working points for the electron identification are defined and called "Loose," "Medium," and "Tight." Their selections for the likelihood discriminant and other variables are different, corresponding to the efficiency. The efficiencies depend on the number of reconstructed vertices. Thus, the thresholds of likelihood discriminants are modified as linear functions of pile-up level, maintaining the rejection power of background electrons.

Photon Identification The hadronic leakage and shower shape variables are shown in Table D.2 are used to distinguish between prompt, isolated photons, and backgrounds from hadronic jets. The variables measured in the EM first layer are useful for rejecting two highly collimated photons from π^0 decays. Several working points for the photon identification are defined and referred to as "Loose," "Medium," and "Tight." Photons identified by a tight working point pass loose and medium working points. The Tight identification is optimized by TMVA (multivariate data analysis tool) and the selections depend on E_{T}. Additionally, the identification is performed separately for converted and unconverted photons.

Table D.2: Discriminating variables used for electron and photon identification. The last column indicates if the variables are used for the identification of electrons, photons, or both. For variables calculated in the first EM layer, if the cluster has more than one cell in the ϕ direction at a given η, the two cells closest in ϕ to the cluster barycentre are merged and the definitions below are given in terms of this merged cell. The sign of d_0 is conventionally chosen such that the coordinates of the perigee in the transverse plane are $(x_0, y_0) = (-d_0 \sin\phi, d_0 \cos\phi)$, where ϕ is the azimuthal angle of the track momentum at the perigee [248].

Category	Description	Name	Usage
Hadronic leakage	Ratio of E_{T} in the first layer of the hadronic calorimeter to E_{T} of the EM cluster (used over the ranges $\lvert\eta\rvert < 0.8$ and $\lvert\eta\rvert > 1.37$)	R_{had_1}	e/γ
	Ratio of E_{T} in the hadronic calorimeter to E_{T} of the EM cluster (used over the range $0.8 < \lvert\eta\rvert < 1.37$)	R_{had}	e/γ
EM third layer	Ratio of the energy in the third layer to the total energy in the EM calorimeter	f_3	e
EM second layer	Ratio of the sum of the energies of the cells contained in a 3×7 $\eta \times \phi$ rectangle (measured in cell units) to the sum of the cell energies in a 7×7 rectangle, both centred around the most energetic cell	R_η	e/γ
	Lateral shower width, $\sqrt{(\Sigma E_i \eta_i^2)/(\Sigma E_i) - ((\Sigma E_i \eta_i)/(\Sigma E_i))^2}$, where E_i is the energy and η_i is the pseudorapidity of cell i and the sum is calculated within a window of 3×5 cells	w_{η_2}	e/γ
	Ratio of the sum of the energies of the cells contained in a 3×3 $\eta \times \phi$ rectangle (measured in cell units) to the sum of the cell energies in a 3×7 rectangle, both centred around the most energetic cell	R_ϕ	e/γ
EM first layer	Total lateral shower width, $\sqrt{(\Sigma E_i (i - i_{\mathrm{max}})^2)/(\Sigma E_i)}$, where i runs over all cells in a window of $\Delta\eta \approx 0.0625$ and i_{max} is the index of the highest-energy cell	$w_{s\ \mathrm{tot}}$	e/γ
	Lateral shower width, $\sqrt{(\Sigma E_i (i - i_{\mathrm{max}})^2)/(\Sigma E_i)}$, where i runs over all cells in a window of 3 cells around the highest-energy cell	$w_{s\ 3}$	γ
	Energy fraction outside core of three central cells, within seven cells	f_{side}	γ
	Difference between the energy of the cell associated with the second maximum, and the energy reconstructed in the cell with the smallest value found between the first and second maxima	ΔE_s	γ
	Ratio of the energy difference between the maximum energy deposit and the energy deposit in a secondary maximum in the cluster to the sum of these energies	E_{ratio}	e/γ
	Ratio of the energy measured in the first layer of the electromagnetic calorimeter to the total energy of the EM cluster	f_1	e/γ
Track conditions	Number of hits in the innermost pixel layer	$n_{\mathrm{innermost}}$	e
	Number of hits in the pixel detector	n_{Pixel}	e
	Total number of hits in the pixel and SCT detectors	n_{Si}	e
	Transverse impact parameter relative to the beam-line	d_0	e
	Significance of transverse impact parameter defined as the ratio of d_0 to its uncertainty	$\lvert\lvert d_0/\sigma(d_0)\rvert\rvert$	e
	Momentum lost by the track between the perigee and the last measurement point divided by the momentum at perigee	$\delta p/p$	e
	Likelihood probability based on transition radiation in the TRT	eProbabilityHT	e
Track–cluster matching	$\Delta\eta$ between the cluster position in the first layer of the EM calorimeter and the extrapolated track	$\Delta\eta_1$	e
	$\Delta\phi$ between the cluster position in the second layer of the EM calorimeter and the momentum-rescaled track, extrapolated from the perigee, times the charge q	$\Delta\phi_{\mathrm{res}}$	e
	Ratio of the cluster energy to the measured track momentum	E/p	e

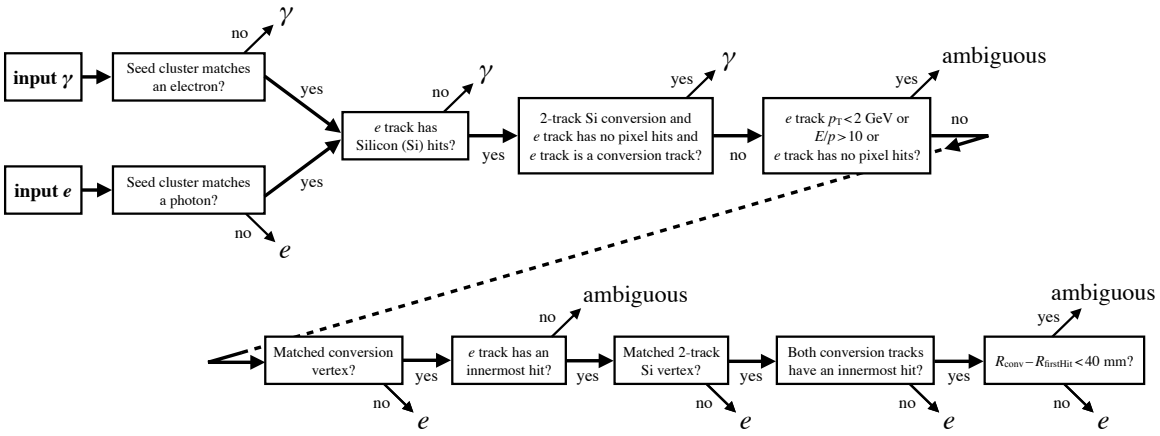

Figure D.2: A flowchart in the logic resolving particles reconstructed as both electrons and photons. An 'innermost hit' represents the nearest hit in the pixel to the beam-line along the track trajectory. E/p is defined as the ratio of the supercluster energy to the momentum of tracks. The radial position of the conversion vertex is denoted as R_{conv}. R_{firstHit} is the smallest radial position of a hit in the track or tracks that make a conversion vertex [119].

D.7.2 Isolation Criteria

In order to reject electrons from heavy hadrons and photons from bremsstrahlung and π_0, the selection called "Isolation" is applied. Two types of isolation variables to keep electrons and photons identification with high quality are used. The first one is the raw calorimeter isolation variable ($E_{\text{T,raw}}^{\text{isol}}$). $E_{\text{T,raw}}^{\text{isol}}$ is the sum of the transverse energy measured as positive-energy in topo-clusters where the center of energy (COE) of the topo-cluster is inside a cone around the electron or photon cluster COE. The second one is the fully corrected calorimeter isolation variable ($E_{\text{T}}^{\text{coneXX}}$). The definition is,

$$E_{\text{T}}^{\text{coneXX}} = E_{\text{T,raw}}^{\text{isolXX}} - E_{\text{T,core}} - E_{\text{T,leakage}}(E_{\text{T}}, \eta, \Delta R) - E_{\text{T,pile-up}}(\eta, \Delta R), \tag{D.13}$$

where XX is the cone parameter which is the distance in the $\eta - \phi$ plane, $\Delta R = \text{XX}/100$. Besides, the track isolation variables ($p_{\text{T}}^{\text{coneXX}}$) are used. $p_{\text{T}}^{\text{coneXX}}$ represents the sum of the transverse momentum measured by tracks inside a cone around the electron or photon cluster direction. Tracks associated with the electron or converted photon are excluded in the calculation. For the electron, the track isolation variables with a variable cone parameter ($p_{\text{T}}^{\text{varconeXX}}$) replace ones of a fixed cone parameter, and the definition is

$$\Delta R = \min\left(\frac{10}{p_{\text{T}}[\text{ GeV}]}, \Delta R_{\text{max}}\right), \tag{D.14}$$

where ΔR_{max} is the maximum cone parameter. The track isolation variables with a variable cone parameter are useful to reject other decay products from the heavy particles because the products are close to electrons originating from the same high-momentum heavy particles. In the calculations, we consider tracks, which have p_{T} greater than 1 GeV, $|\eta| < 2.5$ and the requirements for hits in the ID.

Electron Isolation Tracks are required that they associate with the primary vertex or satisfy $|\Delta z_0 \sin\theta| <$ 3 mm where $|z_0 \sin\theta|$ represents the shortest distance between the muon track and the primary vertex in a longitudinal projection. "Gradient" and "Tight" working points are used in this thesis, while several working points are defined in Ref.[119]. The "Gradient" working point is optimized for efficiency

depending on p_{T}, uniform in η. In the "Gradient" working point, $E_{\mathrm{T}}^{\mathrm{cone20}}$ and $p_{\mathrm{T}}^{\mathrm{varcone20}}$ calculated using tracks with $|\Delta z_0 \sin\theta| < 3$ mm are used. These cut values are optimized to keep the efficiency defined as $\epsilon = 0.1143 \times p_{\mathrm{T}} + 92.14\%$ and derived from simulated $J/\psi \to ee$ and $Z \to ee$ samples. The "Tight" isolation is required to have $E_{\mathrm{T}}^{\mathrm{cone20}} < 0.06 \times p_{\mathrm{T}}$ and $p_{\mathrm{T}}^{\mathrm{varcone20}} < 0.06 \times p_{\mathrm{T}}$. In this working point, tracks with $|\Delta z_0 \sin\theta| < 3$ mm or loose vertex association are used for the $p_{\mathrm{T}}^{\mathrm{varcone20}}$ calculation.

Photon isolation All tracks are required to satisfy $|\Delta z_0 \sin\theta| < 3$ mm. We use only "Tight" isolation working points defined in Ref.[119]. Others are not used in this thesis. Photons are required to have $E_{\mathrm{T}}^{\mathrm{cone40}} < 0.022 \times E_{\mathrm{T}} + 2.45$ GeV and $p_{\mathrm{T}}^{\mathrm{cone20}} < 0.05 \times E_{\mathrm{T}}$.

D.7.3 Efficiency Measurement

The efficiency measurement of electrons and photons is described in Ref.[119, 251, 252]. The outlines are presented in this section.

Electron efficiency measurement The efficiency measurement of isolated electrons is important in the SM measurement and searches for BSM signals. The measured efficiency includes the effects of the selection described above, such as the reconstruction, the identification, and the isolation, and so on. The total efficiency is factorized as,

$$\epsilon_{\mathrm{total}} = \epsilon_{\mathrm{reco}} \times \epsilon_{\mathrm{id}} \times \epsilon_{\mathrm{iso}} \times \epsilon_{\mathrm{trig}} = \left(\frac{N_{\mathrm{reco}}}{N_{\mathrm{all}}}\right) \times \left(\frac{N_{\mathrm{id}}}{N_{\mathrm{reco}}}\right) \times \left(\frac{N_{\mathrm{iso}}}{N_{\mathrm{id}}}\right) \times \left(\frac{N_{\mathrm{trig}}}{N_{\mathrm{iso}}}\right), \tag{D.15}$$

where N_i and ϵ_i are the number and efficiency of i, respectively. N_{all} is the number of produced electrons. The "reco," "id," "iso," and "trig" represent the variables of the reconstructed electrons at the level of the reconstruction, the identification, isolation, and trigger.

The efficiency to reconstruct electrons is extracted from the MC simulation of $J/\psi \to ee$ and $Z \to ee$ samples. Other factors are also determined from the measured efficiency using a tag-and-probe method in $J/\psi \to ee$ and $Z \to ee$ control samples of data and simulation. In the tag-and-probe method, one of the electrons is required to satisfy a strict selection for keeping high quality. Additionally, the electron is also required to fire the single electron trigger for the data-taking. The electron is referred to as a "tag" electron. Another electron is treated as a "probe" electron and used for calculating efficiency. Due to requiring no selections for "probe" electrons, no bias measurement can be performed. For correcting differences in the efficiency between data and MC samples in the measurements, the data-to-MC ratios are used as scale factors.

Photon efficiency measurement The efficiency measurement is performed using three control samples, inclusive-photon production samples, radiative photon samples ($Z \to ll\gamma$), $Z \to ee$ samples for electron extrapolation. Inclusive-photon production samples are collected by single-photon triggers and photons are required to pass "Loose" criteria. The efficiency is extracted by a matrix method using four regions where photons are required to satisfy the "Tight" identification and the track-based isolation cuts. $Z \to ll\gamma$ samples are collected by single-lepton triggers or di-lepton triggers. Additionally, the invariant mass of the di-lepton and photon system ($m_{ll\gamma}$) is required to be around the Z mass, and the invariant mass of the di-lepton system (m_{ll}) is less than the Z mass. The additional requirements are useful to reject $Z + \gamma$

samples and Z+jets samples, including mis-identified hadronic jets as photons. The efficiency is extracted from the $m_{ll\gamma}$ distributions. Finally, the efficiency of the electron extrapolation samples is based on the tag-and-probe method and extracted after the shape variables of the "probe" electrons are extrapolated by Smirov transform [253]. These measurements are performed in both data and MC samples. The observed differences are combined to obtain scale factors using a weighted average.

D.7.4 Energy Calibration

The energy calibration of electrons and photons is performed in $Z \to ee$ control samples. The energy scale is defined as a factor (α_i) to correct the energy in data samples, and the energy resolution applies to simulation samples. The mis-modeling of the energy resolution is parameterized as a constant term (c_i), and the noise term is negligible. Here, i represents different η regions. These corrections are described as,

$$E^{\text{data,corr}} = E^{\text{data}}/(1+\alpha_i), \tag{D.16}$$

$$\left(\frac{\sigma_E}{E}\right)^{\text{MC,corr}} = \left(\frac{\sigma_E}{E}\right)^{\text{MC}} \oplus c_i, \tag{D.17}$$

where $\oplus$ represents a sum in quadrature. These corrections are applied to the invariant mass of the di-electron system as follows,

$$m_{ij}^{\text{data,corr}} = m_{ij}^{\text{data}}/(1+\alpha_{ij}), \tag{D.18}$$

$$\left(\frac{\sigma_m}{m}\right)_{ij}^{\text{MC,corr}} = \left(\frac{\sigma_m}{m}\right)_{ij}^{\text{MC}} \oplus c_{ij}, \tag{D.19}$$

where i and j are the η regions of reconstructed electrons, $\alpha_{ij} = (\alpha_i + \alpha_j)/2$ and $c_{ij} = (c_i \oplus c_j)/2$. The α_i and c_i are extracted from a simultaneous fit in the m_{ee} distribution.

For the photon energy scale correction, validation in $Z \to ll\gamma$ control samples is performed. The residual energy scale factors ($\Delta\alpha$) are extracted from the $m_{ll\gamma}$ distribution.

D.8 Muon Reconstruction

D.8.1 Reconstruction

Muons can reach the outermost detectors, the muon spectrometer (MS), depositing the energy in the inner detector (ID) and the calorimeters. Muons are reconstructed from the MS and the ID information, described in Ref.[120]. The outline is introduced in this section.

Muon reconstruction starts from muon reconstruction tracks in the MS. The first step of track reconstruction in the MS is to reconstruct local track segments from hits in an individual MS station using a Hough transform. After finding track segments, they are combined with other segments in different stations to reconstruct track candidates with a loose pointing constraint that muons come from the interaction points and an assumption that a trajectory of a muon is a parabola due to the trajectory bent in the magnetic field. Finally, the muon trajectory is obtained from the global χ^2 fit, considering the effects of interactions in the detector inside the MS and misalignments between the different detector chambers. The transverse momentum (p_{T}) is calculated by re-fit with additional considerations for the energy loss in the calorimeters and back-extrapolation to the beamline.

The muon reconstructed tracks in the MS are combined with information of the ID and calorimeters. There are five reconstruction procedures and corresponding muon types. However, only two types are considered in this thesis, and they are introduced according to their priority. Other types are described in Ref.[120].

Combined muons Combined muons are obtained from a combined track fit based on the ID and MS hits considering the energy loss in the calorimeters. Their hits are re-fitted in the combined fit procedures.

Inside-out combined muons Inside-out combined muons are reconstructed using the extrapolation from the ID tracks to the MS, searching at least three aligned MS hits with a combined track fit. In this algorithm, the reconstructed MS tracks are not considered.

In order to obtain high quality of the reconstructed muons except for the SiF muons, the ID tracks used for the reconstruction are required following selections,

- Not less than one hit in the pixel detector
- Not less than five hits in the SCT detector
- Not more than two missing hits in the pixel detector and the SCT detector

For the SiF muons, at least one pixel hit and at least four hits of the pixel detector and the SCT detector in total are required at the reconstruction step. Additionally, the following selections at the reconstruction procedures of muons are applied.

- The number of MS stations where at least three hits in the MDT or CSC detectors are used to reconstruct muons is not more than two (except for $|\eta| < 0.1$).
- The number of MS stations where at least three hits in the MDT or CSC detectors is one, and muons have at most MS stations where at most two hits are used and at least three hits are missed in the trajectory ($|\eta| < 0.1$).

- The number of MS stations where at least three hits in the MDT or CSC detectors are used to reconstruct muons is at least three ($2.5 < |\eta| < 2.7$).
- q/p significance $= \frac{|q/p_{\mathrm{ID}} - q/p_{\mathrm{MS}}|}{\sqrt{\sigma^2(q/p_{\mathrm{ID}}) + \sigma^2(q/p_{\mathrm{MS}})}} < 7$ where q/p_{ID} and q/p_{MS} are the ratio of the charge q to the momentum p in the measurement of the ID and MS detectors, respectively, the corresponding uncertainties are denoted as $\sigma^2(q/p_{\mathrm{ID}})$, $\sigma^2(q/p_{\mathrm{MS}})$.

The reconstructed muons satisfying these requirements are called "medium muons."

Isolation In order to distinguish between muons from the reconstructed primary vertex and other sources, for example, pile-up interactions, cosmic rays, and hadron decays, kinematic selections called "Isolation" are applied.

Vertex association requirements to reject muons from pile-up interactions or cosmic rays are introduced. For ensuring muons originating from the reconstructed primary vertex, the shortest distance between the muon track and the primary vertex in a longitudinal projection ($|z_0 \sin\theta|$) is less than 0.5 mm, where z_0 is the longitudinal impact parameter defined as the closest point of the muon track to the beamline, measured relative to the reconstructed primary vertex position. Besides, the other selection for prompt muons is done with "d_0 significance," defined as $|d_0|/\sigma(d_0)$, where d_0 is referred to as the transverse impact parameter and represents the shortest distance between a track and the measured beamline position in the transverse plane, and $\sigma(d_0)$ is the total uncertainty of track fit. d_0 significance is required to be less than 3.

The other optional selection is employed to distinguish between muons originating from the primary vertex and ones from hadron decays. The selection consists of track-based isolation and calorimeter-based isolation. The track-based isolation uses the scalar sum of the transverse momenta of the ID tracks associated with the primary vertex in a cone with $\Delta R = \min(10\ \mathrm{GeV}/p_{\mathrm{T}}, 0.3)$ around the muon in the $\eta - \phi$ plane. The muon track itself and the ID tracks with $p_{\mathrm{T}} \leq 1$ GeV are excluded in the sum. The scalar sum of the transverse momenta of the ID tracks is denoted as $p_{\mathrm{T}}^{\mathrm{varcone30}}$. The calorimeter-based isolation uses the sum of the transverse energy of topo-clusters with $\Delta R = 0.2$ around the muon position extrapolated to the calorimeters. The energy deposit of the muon itself is not included. The sum of the transverse energy of topo-clusters is denoted as $E_{\mathrm{T}}^{\mathrm{topocone20}}$.

Two working points for isolation requirements are used. One is "Tight" and another is "TightTrackOnly." "Tight" working point requires both the track-based isolation and the calorimeter-based isolation. "TightTrackOnly" requires only the track-based isolation, which is tighter than one of the "Tight" working.

D.8.2 Muon Efficiency Measurement

The muon efficiency measurement is based on the tag-and-probe method in the samples, including di-muon pairs, such as $Z \to \mu\mu$ and $J/\psi \to \mu\mu$. In the tag-and-probe method, "tag muons" are required to be reconstructed with high quality and fire the online trigger. "Probe muons" are required to be identified with the algorithm of interest and have the charge opposite to the tag muons and $|\eta| < 2.5$.

$Z \to \mu\mu$ control samples ($p_{\mathrm{T}} > 10$ GeV) and $J/\psi \to \mu\mu$ control samples (3 GeV $\leq p_{\mathrm{T}} \leq 20$ GeV) are used. Details are described in Ref.[120]. There are disagreements of the measured efficiency between data and MC samples. In order to correct the difference, the efficiency scale factor (SF) defined as the ratio of the measured efficiency in data samples to MC samples, is used.

To extend the full MS acceptance, we use the double ratio of the data/MC in the forward region ($|\eta| > 2.5$) to near forward region ($2.2 < |\eta| < 2.5$) for the efficiency SF calculation due to the limitation of the ID coverage ($|\eta| < 2.5$). The measurement is performed in $Z \to \mu\mu$ control samples and $m_{\mu\mu}$ window cuts are required. The forward muons are required to have p_{T} greater than 10 GeV and an opposite charge to the central muons. The central muons are required to be identified with high quality and have $p_{\mathrm{T}} > 25$ GeV.

The results are shown in Figure D.3. In the overlap region of p_{T} from 10 to 20 GeV, the measured efficiencies are a good agreement between $J/\psi \to \mu\mu$ and $Z \to \mu\mu$ within uncertainties. The observed discrepancy in $|\eta| > 2.5$ is caused by the different reconstruction algorithms between the SiF muons and combined muons.

D.8.3 Momentum Calibration

The ID tracks (MS segments) are corrected by the simulated transverse momenta of reconstructed muons in the ID (MS) sub-detectors. The corrected transverse momenta, $p_{\mathrm{T}}^{\mathrm{Cor,\,Det}}$, is defined as,

$$p_{\mathrm{T}}^{\mathrm{Cor,\,Det}} = \frac{p_{\mathrm{T}}^{\mathrm{MC,\,Det}} + \sum_{n=0}^{1} s_n^{\mathrm{Det}}(\eta,\phi)\left(p_{\mathrm{T}}^{\mathrm{MC,\,Det}}\right)^n}{1 + \sum_{m=0}^{2} \Delta r_m^{\mathrm{Det}}(\eta,\phi)\left(p_{\mathrm{T}}^{\mathrm{MC,\,Det}}\right)^{m-1} g_m}, \text{ (Det denotes ID or MS),} \tag{D.20}$$

where $p_{\mathrm{T}}^{\mathrm{MC,\,Det}}$ is the transverse momentum of reconstructed muons in the simulation before the correction, g_m is normally distributed random variable for smearing, $\Delta r_m^{\mathrm{Det}}(\eta,\phi)$, $s_n^{\mathrm{Det}}(\eta,\phi)$ represent the momentum resolution smearing and the scale correction corresponding to (η,ϕ) detector region. g_m has zero mean and unit width. s_1^{Det} corrects the inaccuracy of the magnetic field, and s_0^{Det} term is the correction factor for the inaccuracy of the energy loss. We consider the energy loss only in the calorimeter and other materials inside the MS, not including one between the interaction point and the ID. The denominator represents the momentum smearing and includes the effects of energy loss, multiple scattering, and the fluctuations of hits caused by the misalignment of the MS and spatial resolution.

The correction factors are extracted using a binned maximum-likelihood fit from the invariant mass distributions in $J/\psi \to \mu\mu$ and $Z \to \mu\mu$ control samples. For the MS corrections, p_{T} imbalance variable, defined as:

$$\rho = \frac{p_{\mathrm{T}}^{\mathrm{MS}} - p_{\mathrm{T}}^{\mathrm{Cor,\,ID}}}{p_{\mathrm{T}}^{\mathrm{Cor,\,ID}}}, \tag{D.21}$$

are used to correct the energy loss in the calorimeter between the ID and the MS.

D.9 Overlap Removal

We perform the overlap removal procedure to resolve the ambiguity of duplicated objects. The procedures to find duplicated objects sharing tracks and clusters are,

1. When two electrons share the same ID track, the one with lower p_{T} is removed.
2. Electrons sharing the ID track with muons are rejected.
3. Photons within $\Delta R(\gamma, e/\mu) < 0.4$ are rejected.

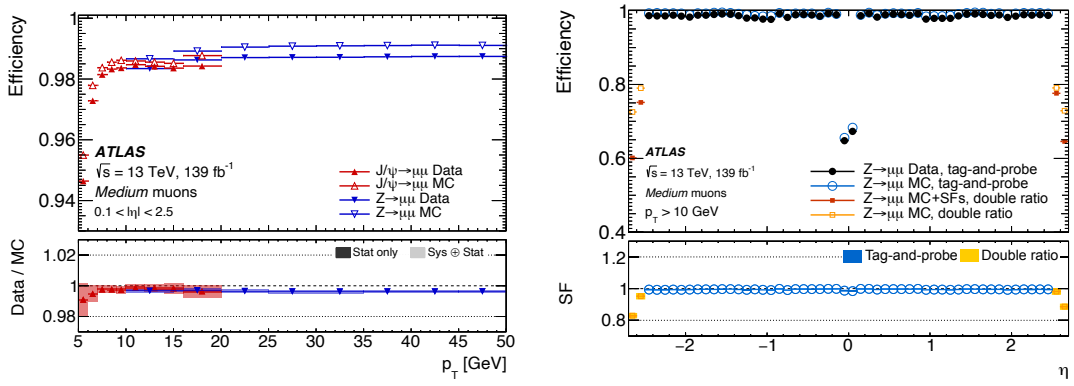

(a) Efficiency in $0.1 < |\eta| < 2.5|$

(b) Efficiency as a function of η

Figure D.3: Muon reconstruction and identification efficiencies in $0.1 < |\eta| < 2.5|$ (a) and as a function of η (b) [120].

4. Small-R jets satisfying at least one criterion are rejected:

   - $\Delta R(e, j) < 0.2$
   - $\Delta R(\mu, j) < 0.4$ and either of the following is satisfied when the number of ghost-associated tracks for the jet is ≤ 4 (≥ 4):

     a) $E_{\mathrm{T}}^{\mathrm{cone40}}(\mu) < 15$ (5) GeV.

     b) $E_{\mathrm{T}}^{\mathrm{cone40}}(\mu) < 15 + 100 \times (R - 0.7)$ GeV ($5 + (25/0.3) \times (R - 0.6)$ GeV)

     c) $R > 0.85(0.9)$

     where R represents $p_{\mathrm{T}}(\mu, \text{ID track})/\sum_j p_{\mathrm{T}}(\text{track})$.

   The above selections are applied to reject jets originating from calorimeter energy deposits from electron/photon shower or muon bremsstrahlung.

5. Photons within $\Delta R(\gamma, j) < 0.4$ (where j represents small-R jets) are removed. Electrons and muons within $\Delta R(\ell, j) < \min(0.4, 0.04 + 10 \text{ GeV}/p_{\mathrm{T}}(\ell))$ are removed.

6. Any large-R jets within $\Delta R(\ell/\gamma, J) < 1.0$ is removed.

E Jet Truth Labeling

Truth information of large-R jets is used to apply tagger efficiency SF and uncertainties. The procedures to label jets with truth information are three steps. The first step is requiring spatial matching between reconstructed jets (J) and truth jets (J_{true}), $\Delta R(J, J_{\text{true}}) < 0.75$. In the next step, we perform spatial matching between truth particles ($W/Z/h/t$) and the truth jets ($\Delta R(J_{\text{true}}, \text{particles}) < 0.75$). Finally, truth jet mass requirements corresponding to the origin of jets are applied. For jets labeled as top quarks, at least one ghost-associated b-hadron [129], $m(J_{\text{true}}) > 140$ GeV and spatially matching $\Delta R(J_{\text{true}}, t)$ are required. For jets labeled as W bosons, the jets must satisfy requirements that $\Delta R(J_{\text{true}}, W) < 0.75$, the number of ghost-associated b-hadrons is zero and 50 GeV $< m(J_{\text{true}}) <$ 100 GeV. For jets labeled as Z bosons, the jets must satisfy the ΔR-match requirement and 60 GeV $< m(J_{\text{true}}) <$ 110 GeV.

The performance of W and Z boson labeling is shown in Figure E.1. The red lines show the fraction of jets labeled as W/Z bosons, and the blue ones show the fraction of jets that only pass the requirements of ΔR-matching between truth bosons and truth jets and truth jet mass cuts. In the low p_{T} region, the daughter quarks are not collimated sufficiently inside one large-R jet, and the fraction is low. Besides, since the Z boson mass is larger than W boson, the fraction of jets labeled as Z boson is smaller due to the difference in $dR(q, q)$. For example, the fraction of W boson with $p_{\text{T}}(J_{\text{truth}}) = 400$ GeV is $\sim 85\%$ while the fraction of Z boson is $\sim 77\%$. These jets labeled as W/Z bosons are referred to as "signal jets."

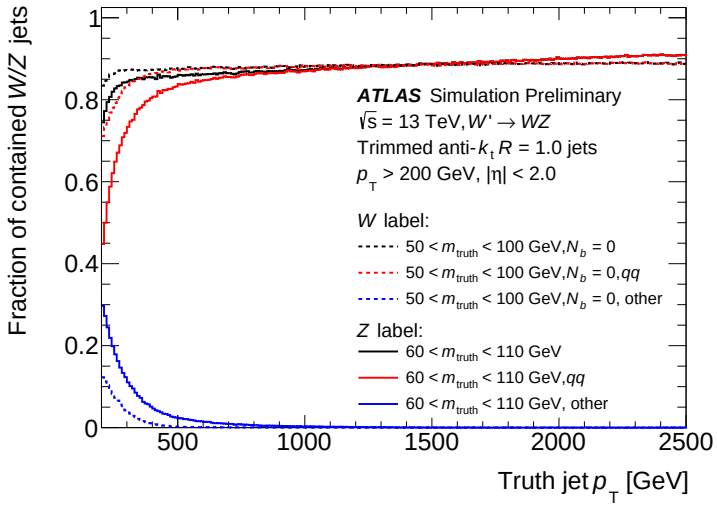

Figure E.1: Fraction of jets as a function of truth jet p_{T} matched to W (dashed lines) or Z bosons (solid lines) that pass the corresponding label criteria in a p_{T} flattened HVT W' samples. The black lines represent the fractions after ΔR-matching between truth bosons and truth jets, truth mass cuts, and ghost-associated b-hadron [129] requirements. The red lines show the fractions required to satisfy ΔR-matching between truth jets and truth particles from hadronically decaying bosons, and the blue ones are not satisfied [121].

F Pre-/Post-fit Jet Mass Distribution in W bosons Enriched Regions

In order to measure the signal efficiency in W bosons enriched region, the fits of the jet mass distributions are performed. Figure 6.7 shows the jet mass distributions with 250 GeV $< p_{\mathrm{T}} <$ 300 GeV before/after fitting. Figure F.1, Figure F.2, and Figure F.3 show the pre-/post-fit jet mass distributions with different p_{T} bins.

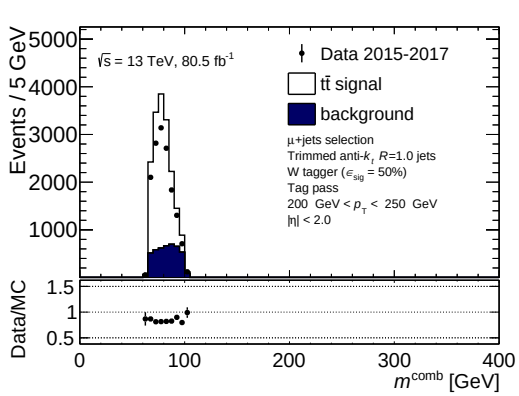

(a) m^{comb} in W-tag pass region before fitting

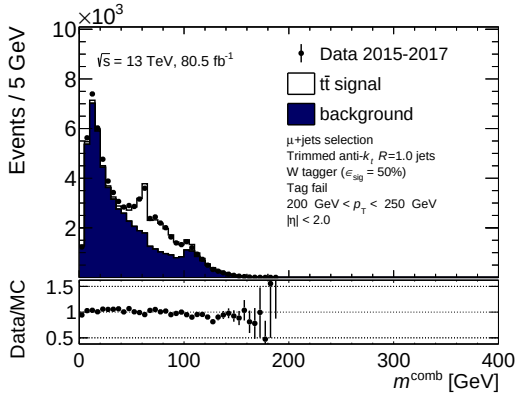

(b) m^{comb} in W-tag fail region before fitting

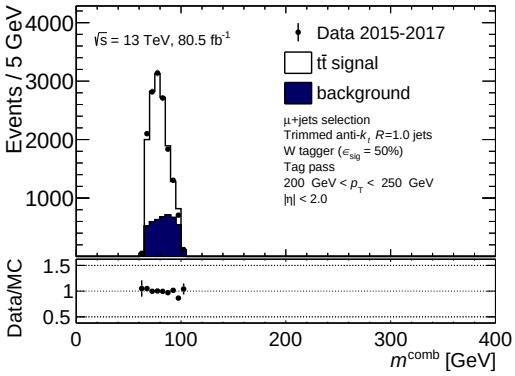

(c) m^{comb} in W-tag pass region after fitting

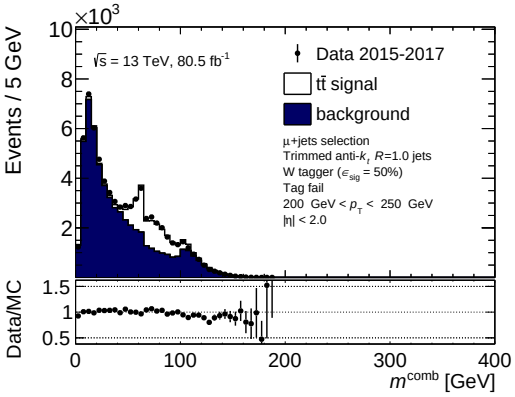

(d) m^{comb} in W-tag fail region after fitting

Figure F.1: (a)(b) Pre-fit or (c)(d) post-fit distribution of m^{comb} in the (200 GeV $< p_{\mathrm{T}} <$ 250 GeV) bin. The regions passing ((a)(c)) or failing ((b)(d)) are shown.

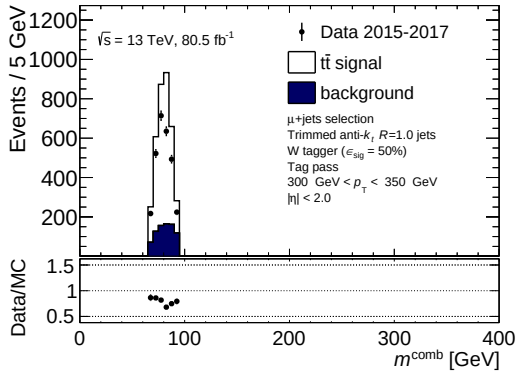

(a) m^{comb} in W-tag pass region before fitting

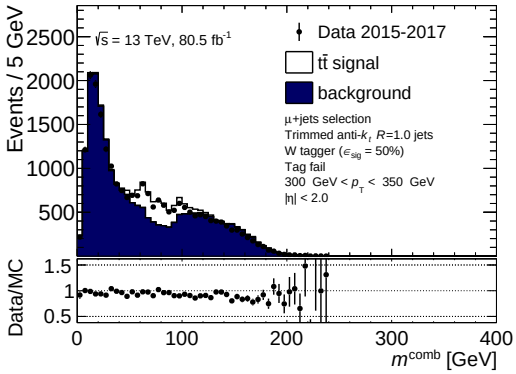

(b) m^{comb} in W-tag fail region before fitting

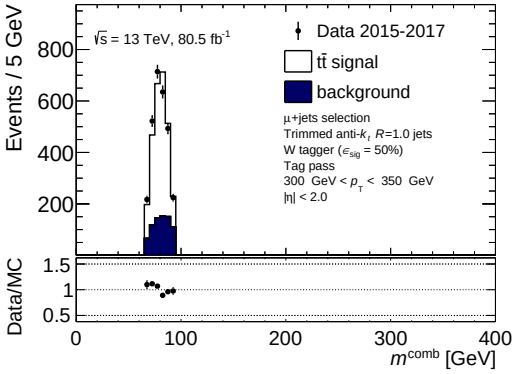

(c) m^{comb} in W-tag pass region after fitting

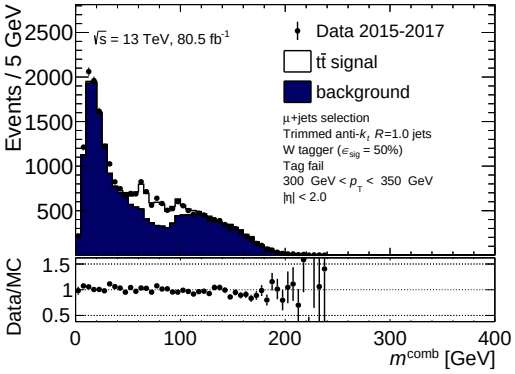

(d) m^{comb} in W-tag fail region after fitting

Figure F.2: (a)(b) Pre-fit or (c)(d) post-fit distribution of m^{comb} in the (300 GeV $< p_{\text{T}} <$ 350 GeV) bin. The regions passing ((a)(c)) or failing ((b)(d)) are shown.

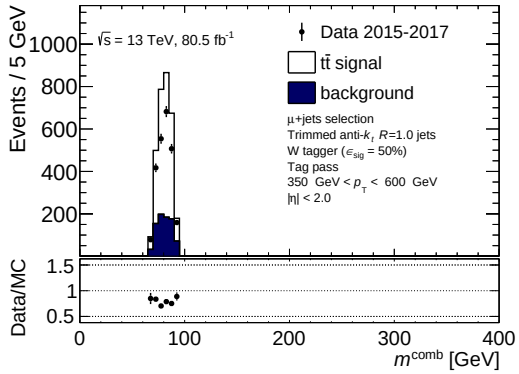

(a) m^{comb} in W-tag pass region before fitting

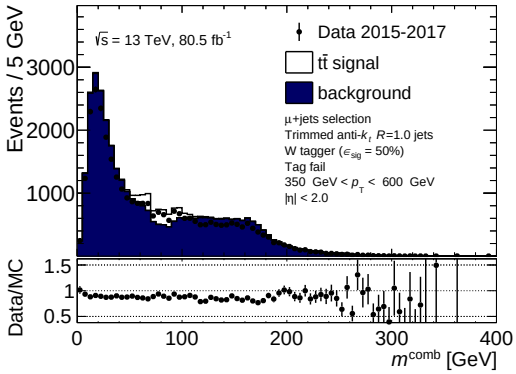

(b) m^{comb} in W-tag fail region before fitting

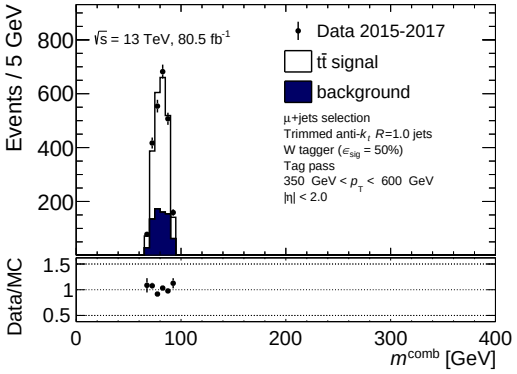

(c) m^{comb} in W-tag pass region after fitting

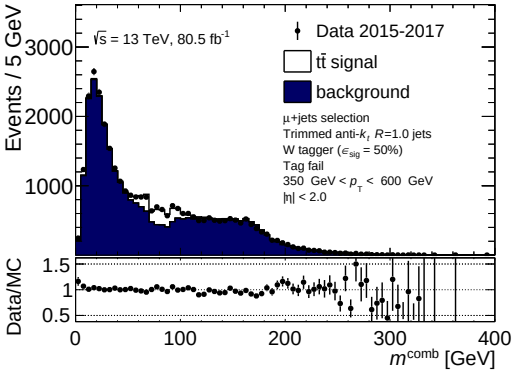

(d) m^{comb} in W-tag fail region after fitting

Figure F.3: (a)(b) Pre-fit or (c)(d) post-fit distribution of m^{comb} in the (350 GeV $< p_{\text{T}} <$ 600 GeV) bin. The regions passing ((a)(c)) or failing ((b)(d)) are shown.

G Comparison of Jet Substructure Variables between Different $t\bar{t}$ MC in the SF Measurement Region

In this section, comparisons of the jet substructure variables with different MC generators are shown. As shown in Figure 6.9, parton shower variation samples have the slightly different tendencies in D_2 and n_{trk} distributions. However, the differences become smaller in the high p_{T} region. Figure G.1, Figure G.2, and Figure G.3 show the jet substructure distributions of jets originating from W bosons. Additionally, the distributions of all jets are shown in Figure G.4-G.7.

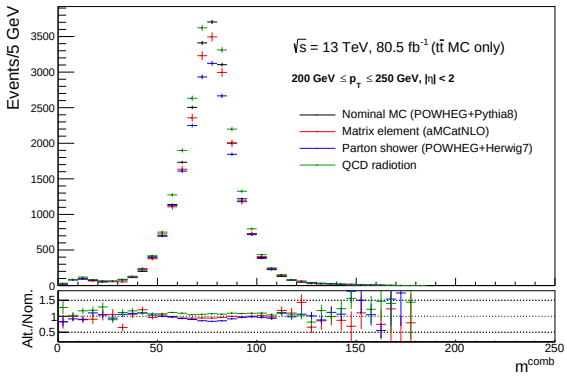

(a) m^{comb}

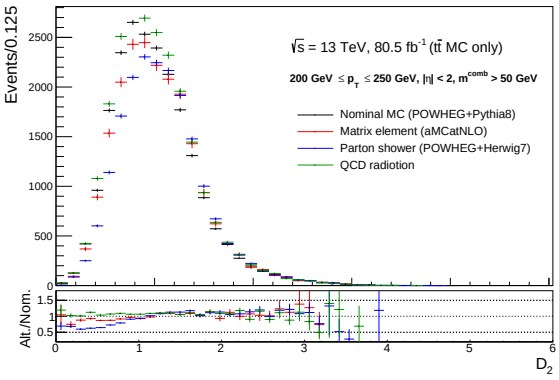

(b) D_2

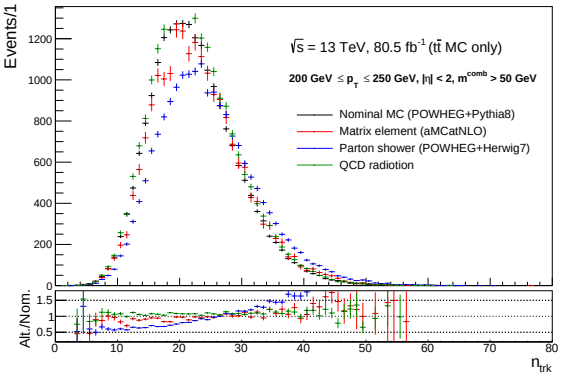

(c) n_{trk}

Figure G.1: Distributions of m^{comb} (a), D_2 (b) and n_{trk} (c) in $t\bar{t}$ MC samples (200 GeV $< p_{\mathrm{T}} <$ 250 GeV). Nominal MC represents the black line. Alternative MCs for the variation of matrix elements (red), parton shower (blue), and QCD radiation (green) are shown.

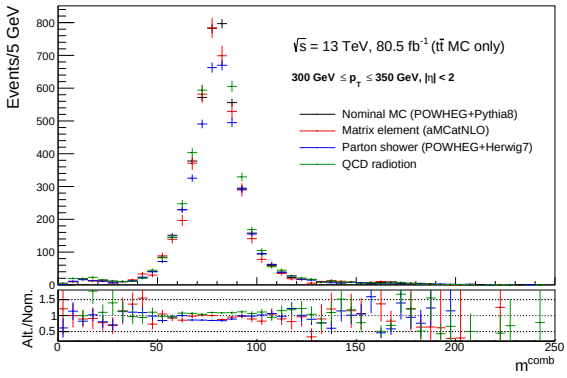

(a) m^{comb}

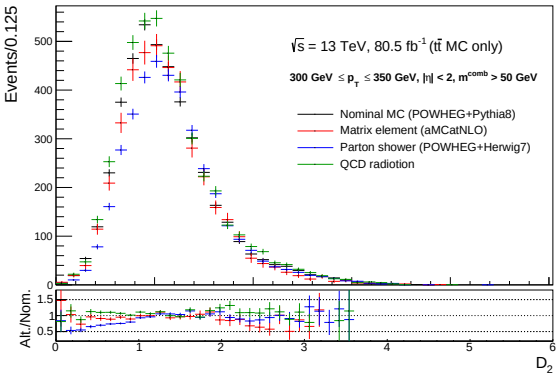

(b) D_2

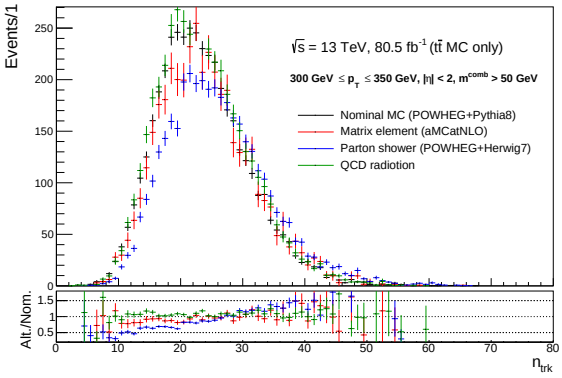

(c) n_{trk}

Figure G.2: Distributions of m^{comb} (a), D_2 (b) and n_{trk} (c) in $t\bar{t}$ MC samples (300 GeV $< p_{\text{T}} <$ 350 GeV). Nominal MC represents the black line. Alternative MCs for the variation of matrix elements (red), parton shower (blue), and QCD radiation (green) are shown.

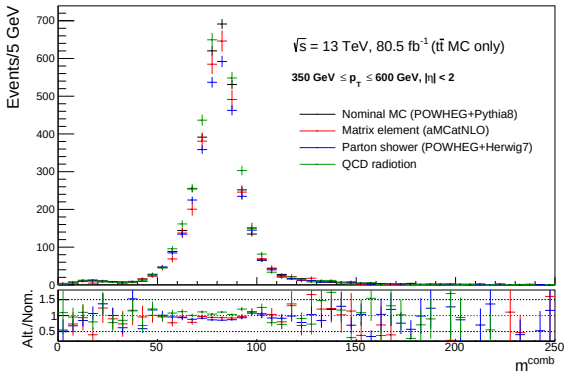

(a) m^{comb}

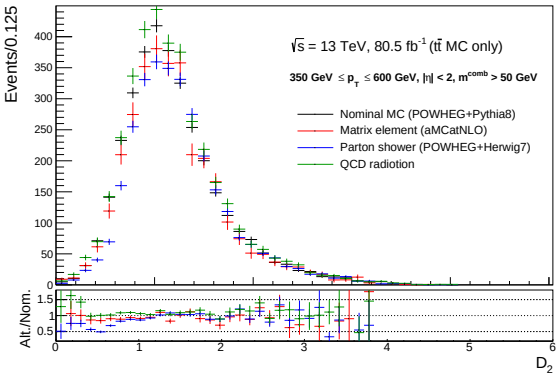

(b) D_2

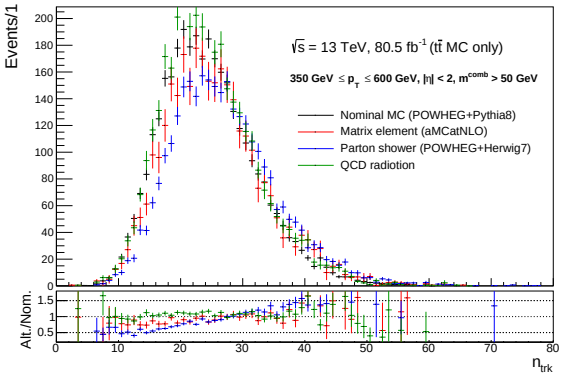

(c) n_{trk}

Figure G.3: Distributions of m^{comb} (a), D_2 (b) and n_{trk} (c) in $t\bar{t}$ MC samples (350 GeV $< p_{\text{T}} <$ 600 GeV). Nominal MC represents the black line. Alternative MCs for the variation of matrix elements (red), parton shower (blue), and QCD radiation (green) are shown.

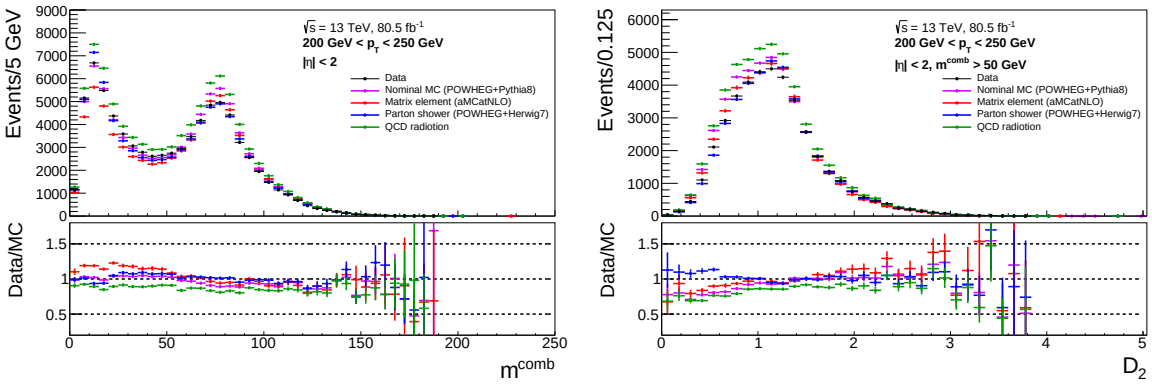

(a) m^{comb}

(b) D_2

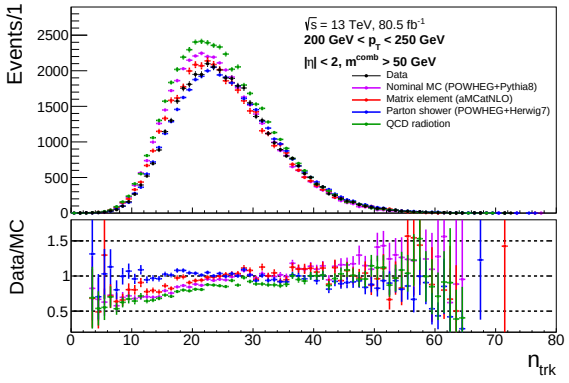

(c) n_{trk}

Figure G.4: Distributions of m^{comb} (a), D_2 (b), and n_{trk} (c) in data and MC samples with 200 GeV $<$ jetp_{T} $<$ 250 GeV. The black line represents data samples. Except for the black line, each color line represents MC expected distributions with different $t\bar{t}$ MC samples (other samples are common). The violet line represents a nominal MC sample, alternative MCs for the variation of matrix elements (red), parton shower (blue), and QCD radiation (green) are shown.

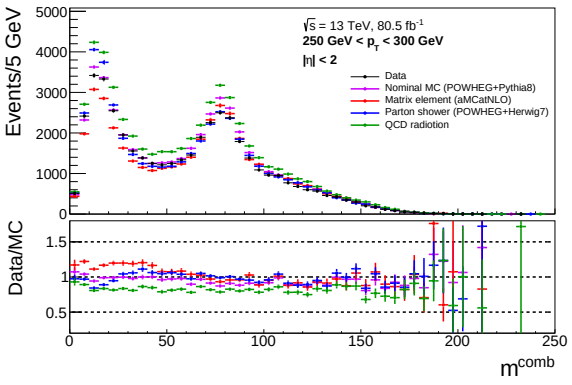

(a) m^{comb}

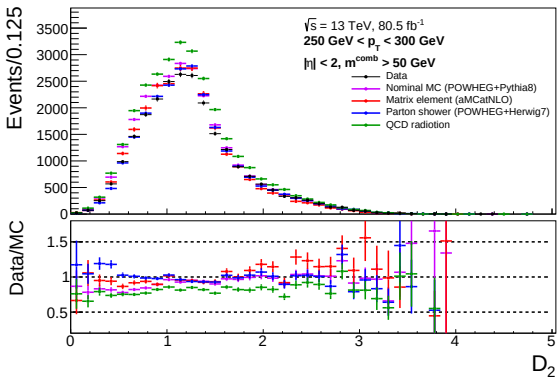

(b) D_2

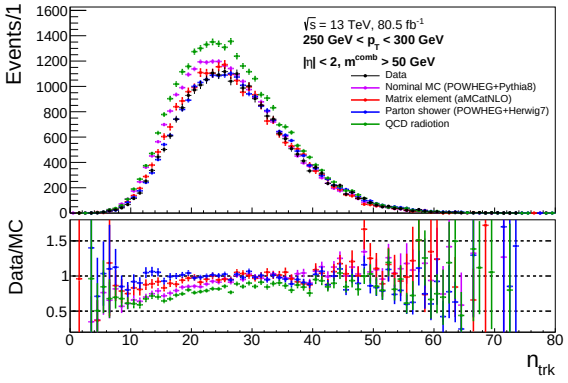

(c) n_{trk}

Figure G.5: Distributions of m^{comb} (a), D_2 (b), and n_{trk} (c) in data and MC samples with 250 GeV $<$ jetp_{T} $<$ 300 GeV. The black line represents data samples. Except for the black line, each color line represents MC expected distributions with different $t\bar{t}$ MC samples (other samples are common). The violet line represents a nominal MC sample, alternative MCs for the variation of matrix elements (red), parton shower (blue), and QCD radiation (green) are shown.

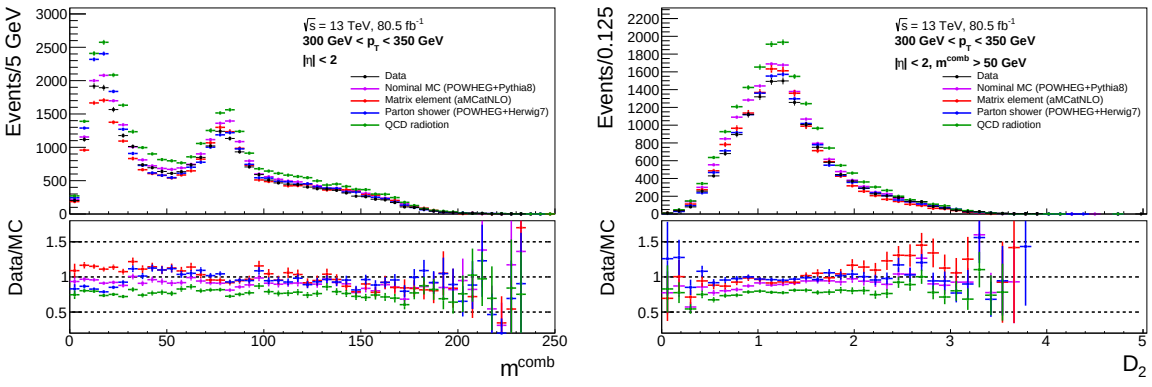

(a) m^{comb}

(b) D_2

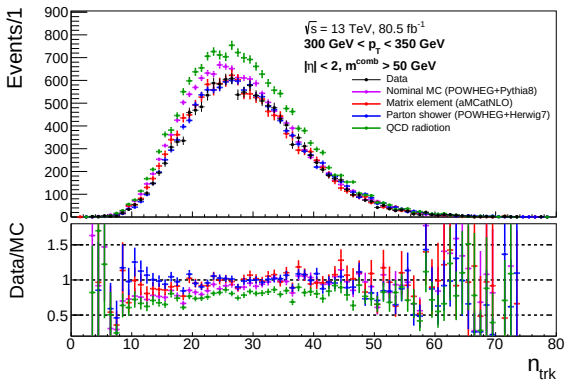

(c) n_{trk}

Figure G.6: Distributions of m^{comb} (a), D_2 (b), and n_{trk} (c) in data and MC samples with 300 GeV $<$ jetp_{T} $<$ 350 GeV. The black line represents data samples. Except for the black line, each color line represents MC expected distributions with different $t\bar{t}$ MC samples (other samples are common). The violet line represents nominal MC sample, alternative MCs for the variation of matrix elements (red), parton shower (blue), and QCD radiation (green) are shown.

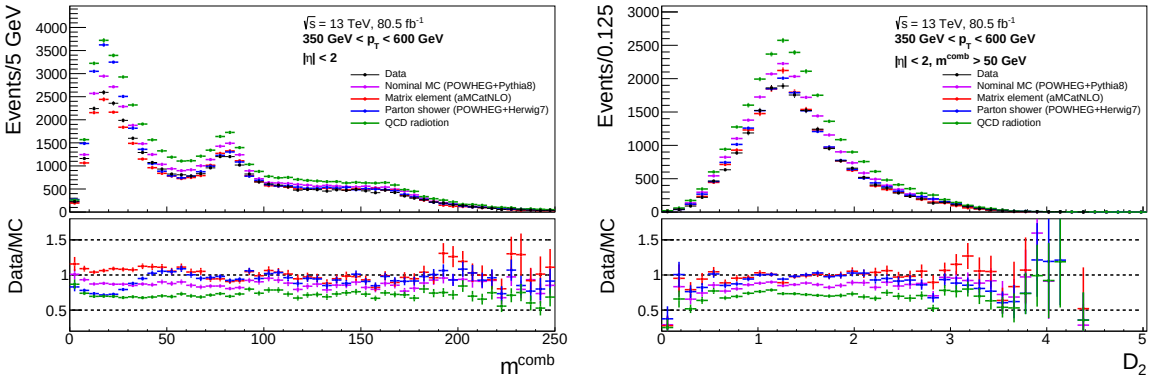

(a) m^{comb}

(b) D_2

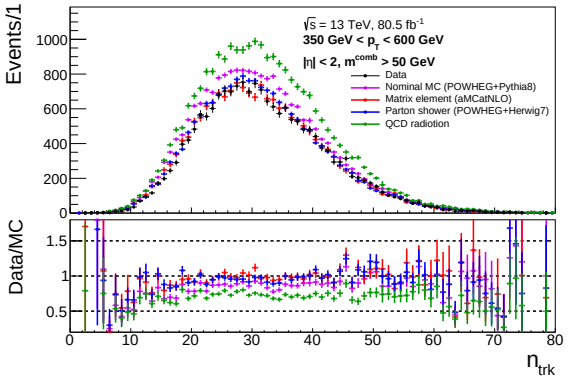

(c) n_{trk}

Figure G.7: Distributions of m^{comb} (a), D_2 (b), and n_{trk} (c) in data and MC samples with 350 GeV $<$ jetp_{T} $<$ 600 GeV. The black line represents data samples. Except for the black line, each color line represents MC expected distributions with different $t\bar{t}$ MC samples (other samples are common). The violet line represents a nominal MC sample, alternative MCs for the variation of matrix elements (red), parton shower (blue), and QCD radiation (green) are shown.

H Event Cleaning

In this section, event cleaning selections are introduced. They are applied to reduce the effects from the data-specific detector responses, mis-measurement of $E_{\mathrm{T}}^{\mathrm{miss}}$, and the double-counting b-quarks.

H.1 Event Cleaning Based on Detector Responses

In order to reject fake jets caused by noise in the LAr calorimeters, some variables based on the signal pulse shape and energy in the LAr calorimeters are used. These variables are estimated as the deviation from the expected signal shape in simulation samples and evaluated as the fraction of the energy in LAr and the hadronic endcap calorimeters to the jet. Additionally, the measured energy in the electromagnetic calorimeter and the scalar sum of track p_{T} associated with the jets are used. Moreover, an additional variable defined as the difference between the calorimeter time measured by the trigger and the energy-squared weighted average of the time in the cells is used.

H.2 Dead Tile Module Jets Veto

In the period of the data taking, some tile calorimeter modules (summarized in Table H.1) are not operating. The events containing jets oriented to the dead tile modules are vetoed because the jets are not reconstructed correctly, and $E_{\mathrm{T}}^{\mathrm{miss}}$ is mis-measured. Since the condition of the dead tile modules is not reflected on the simulation, the weird peaks are seen in the $\phi(E_{\mathrm{T}}^{\mathrm{miss}})$ distribution of data samples before cleaning as shown in Figure H.1, After rejecting the events containing jets oriented to the dead tile modules, the peaks are removed. The efficiency of cleaning is about 95%-98% in data and simulation.

H.3 Non-collision Background Veto

It is known that beam-induced particles knock the detector materials directly and create jet-like signatures [255], mainly caused by the beam-induced muons [256]. These events are recorded accidentally and called "Non-collision background." These events are observed in only data samples, and additional cleaning is needed.

As shown in Figure H.2(a), data excess is seen in $\min \Delta\phi(j, E_{\mathrm{T}}^{\mathrm{miss}}) > 2.9$. This is caused by the mis-measured fake jets in the calorimeters. Track-based $E_{\mathrm{T}}^{\mathrm{miss}}$ (denoted as $E_{T,\mathrm{track}}^{\mathrm{miss}}$) is used to suppress these backgrounds. The distribution of $E_{T,\mathrm{track}}^{\mathrm{miss}}$ and azimuthal angle between the measured directions of $E_{\mathrm{T}}^{\mathrm{miss}}$ and $E_{T,\mathrm{track}}^{\mathrm{miss}}$ with $\min \Delta\phi(j, E_{\mathrm{T}}^{\mathrm{miss}}) > 2.9$ is shown in Figure H.3. Small $E_{T,\mathrm{track}}^{\mathrm{miss}}$ events remain in data samples, while $E_{\mathrm{T}}^{\mathrm{miss}} > 200$ GeV cuts are applied, and large $\Delta\phi(E_{T,\mathrm{track}}^{\mathrm{miss}}, E_{\mathrm{T}}^{\mathrm{miss}})$ events also remain caused by the mis-measurement of $E_{\mathrm{T}}^{\mathrm{miss}}$. To reject these events, additional cleaning cuts are defined as,

Table H.1: Location of dead tile modules in the Run2 (Ref [254]). Modules partly dead or are accounted for by the simulation/reconstruction are not listed.

Year	RunNumber	Module name	η region	ϕ region
2015	266904–284484	LBA10	$0. < \eta < 0.9$	$0.8 < \phi < 1.0$
		EBC21	$-1.6 < \eta < -0.9$	$1.9 < \phi < 2.1$
2016	302053–311481	LBA52	$0. < \eta < 0.9$	$-1.33 < \phi < -1.13$
	306988–311481	LBC5	$-0.9 < \eta < 0.$	$0.34 < \phi < 0.54$
2017	325713–340453	LBC63	$-0.9 < \eta < 0.$	$-0.25 < \phi < -0.05$
		EBA3	$0.8 < \eta < 1.7$	$0.14 < \phi < 0.34$
2018	350310–352514	LBA29, 30	$0. < \eta < 0.9$	$2.7 < \phi < -3.0$
	355261–364292	LBA32	$0. < \eta < 0.9$	$\lvert\phi\rvert > 3.0$

- $E^{\text{miss}}_{T,\text{track}} > 75$ GeV
- $\Delta\phi(E^{\text{miss}}_{T,\text{track}}, E^{\text{miss}}_{\text{T}}) > 2.0$

After applying these cuts, there is no data excess in the distribution of $\min \Delta\phi(j, E^{\text{miss}}_{\text{T}})$ as shown in Figure H.2(b).

H.3.1 Track Jets Cleaning

In this thesis, the b-tagged track jets are used to identify $Z/h \to bb$ signals and reject background events, including top quarks. When two track jets are in the vicinity, one can be included by the other where the b-tagging performance and the MC modeling can be unstable. To avoid such topology with overlapping track jets, following cleaning selection is applied on events:

$$\Delta R(\text{jet}_i, \text{jet}_j) < \min(R(\text{jet}_i), R(\text{jet}_j)) \,, \tag{H.1}$$

where i running on the track jets considered for the b-tagging algorithm (in this analysis, $p_{\text{T}} > 20$ GeV and $n_{\text{trk}} \geq 2$) and j running on the jets with a $p_{\text{T}} > 5$ GeV and $n_{\text{trk}} \geq 2$. The efficiency of the selection is larger than $\sim 90\%$.

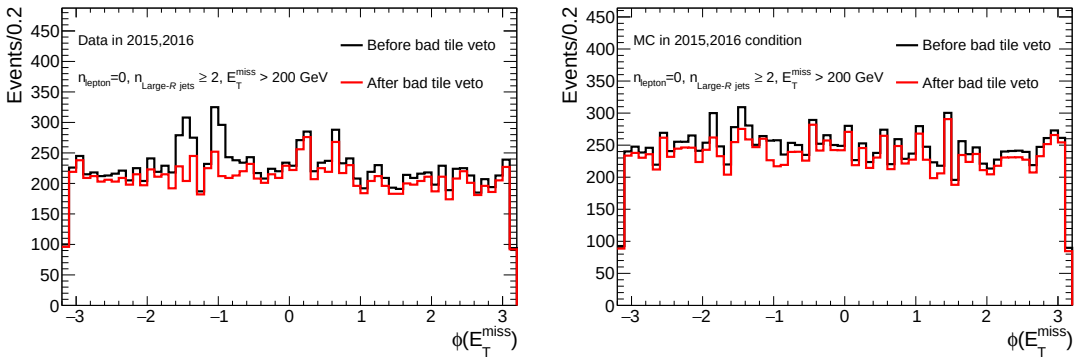

(a) Data in 2015,2016

(b) MC samples in 2015,2016 condition

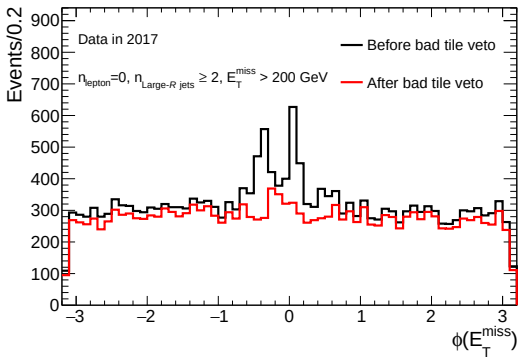

(c) Data in 2017

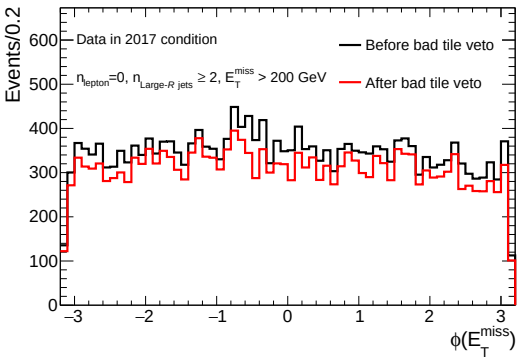

(d) MC samplesin 2017 condition

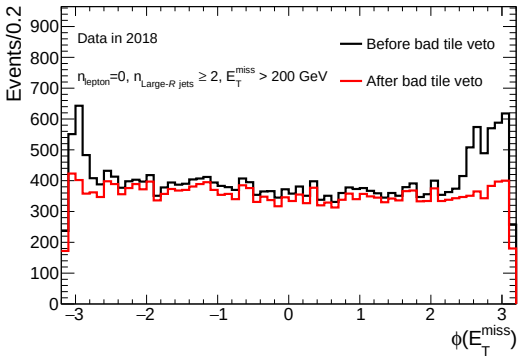

(e) Data in 2018

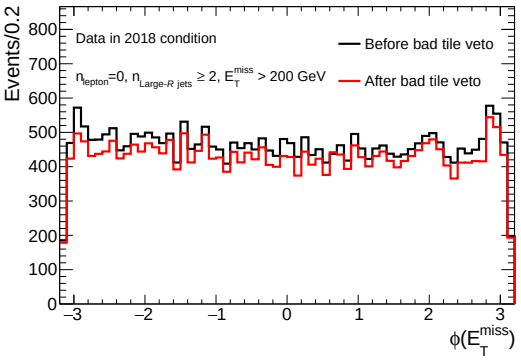

(f) MC samples in 2018 condition

Figure H.1: $\phi(E_{\mathrm{T}}^{\mathrm{miss}})$ distribution in each period. There are peaks in the data samples by the mis-measured $E_{\mathrm{T}}^{\mathrm{miss}}$ generated from the jet into the dead tile regions. However, the distribution is flat in simulation samples because the conditions of dead tile modules are not reflected.

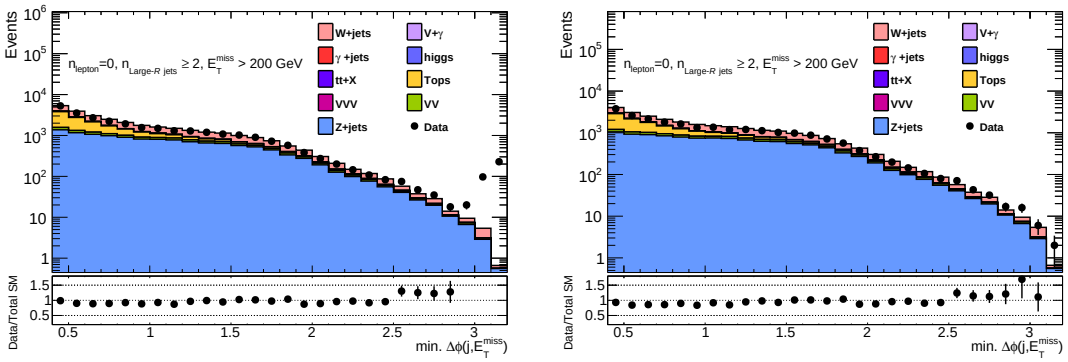

(a) Before applying non collision veto

(b) After applying non collision veto

Figure H.2: $\min \Delta\phi(j, E_{\mathrm{T}}^{\mathrm{miss}})$ distribution applying $n_{\mathrm{lepton}} = 0, n_{\mathrm{Large-}R\ \mathrm{jets}} \geq 2$ and $E_{\mathrm{T}}^{\mathrm{miss}} > 200$ GeV , these variables are defined in Section 7.3. Non-collision veto works to reject the weird peak correctly.

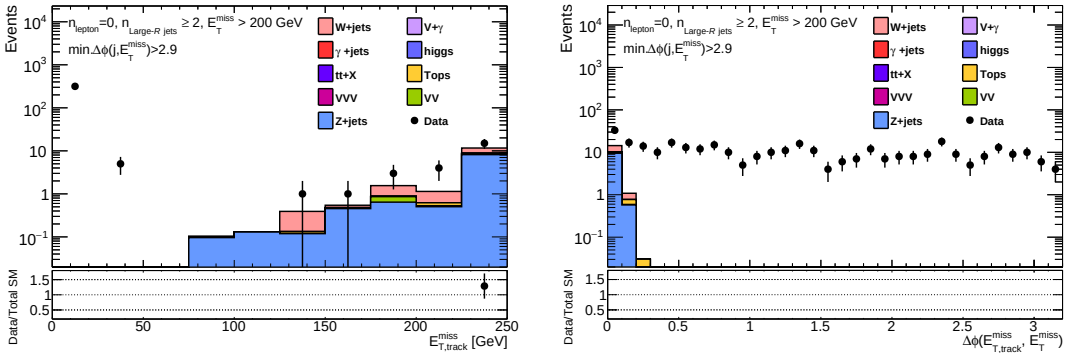

(a) $E_{T,\mathrm{track}}^{\mathrm{miss}}$

(b) Azimuthal angle between $E_{\mathrm{T}}^{\mathrm{miss}}$ and $E_{T,\mathrm{track}}^{\mathrm{miss}}$

Figure H.3: $E_{T,\mathrm{track}}^{\mathrm{miss}}$(a) and $\Delta\phi(E_{T,\mathrm{track}}^{\mathrm{miss}}, E_{\mathrm{T}}^{\mathrm{miss}})$ (b) distribution of the events with $\min \Delta\phi(j, E_{\mathrm{T}}^{\mathrm{miss}}) > 2.9$. Events with $E_{T,\mathrm{track}}^{\mathrm{miss}} < 75$ GeV in data are remained, while $E_{\mathrm{T}}^{\mathrm{miss}} > 200$ GeV cuts are applied. They are mis-measured $E_{\mathrm{T}}^{\mathrm{miss}}$ events and will be rejected. Large $\Delta\phi(E_{T,\mathrm{track}}^{\mathrm{miss}}, E_{\mathrm{T}}^{\mathrm{miss}})$ events are still remained, and they will be rejected.

I Kinematic distributions with Preselection

In this section, the kinematic distributions of each preselection are shown in Figure I.1-I.12. There is no significant slope of each kinematic distribution.

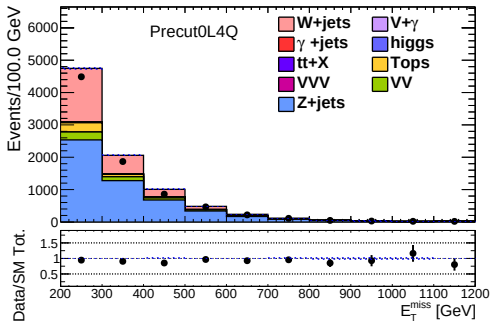

(a) $E_{\mathrm{T}}^{\mathrm{miss}}$

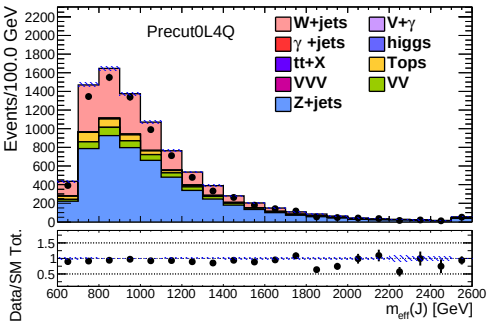

(b) $m_{\mathrm{eff}}(J)$

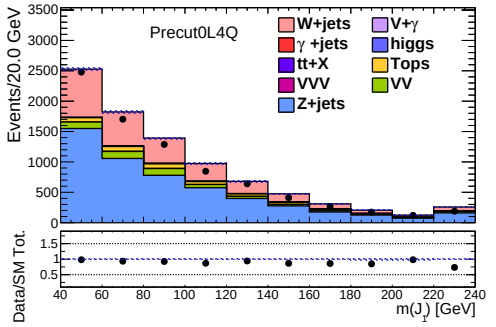

(c) leading large-R jet mass

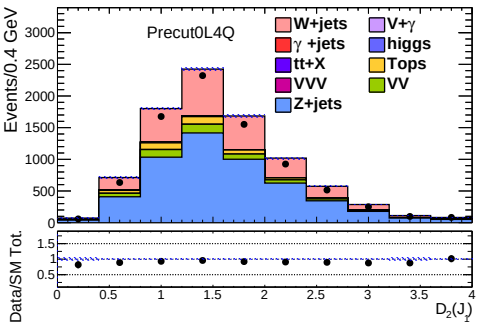

(d) leading large-R jet D_2

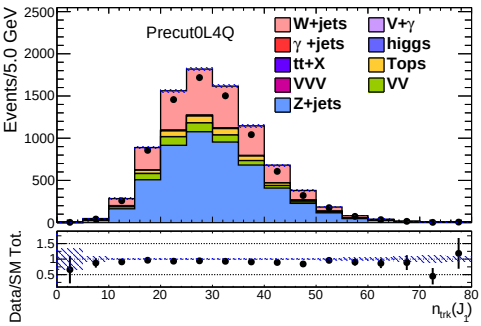

(e) leading large-R jet n_{trk}

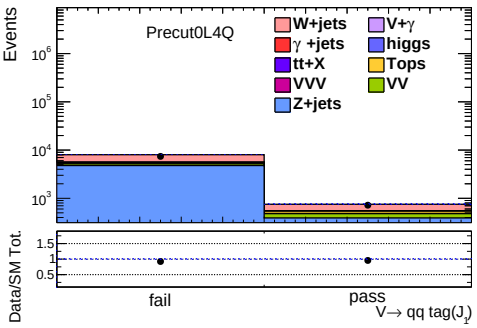

(f) boson tagging result of leading large-R jet

Figure I.1: Kinematic distributions of $E_{\mathrm{T}}^{\mathrm{miss}}$ (a), $m_{\mathrm{eff}}(J)$ (b), and leading large-R jet mass (c), D_2 (d), n_{trk} (e), and boson tagging result (f) with Precut0L4Q selections.

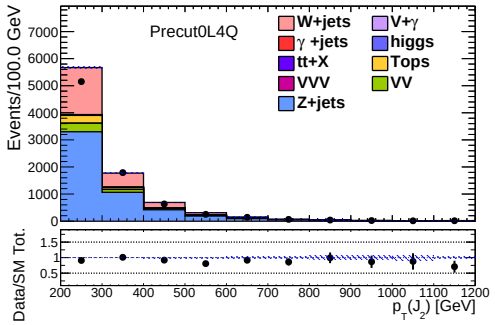

(a) sub-leading large-R jet p_{T}

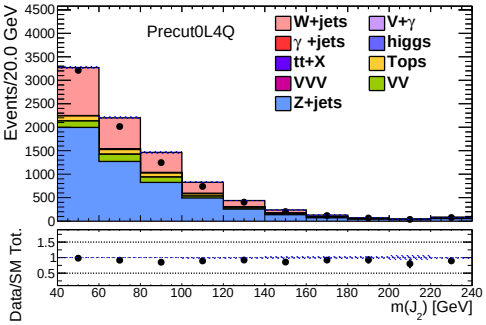

(b) sub-leading large-R jet mass

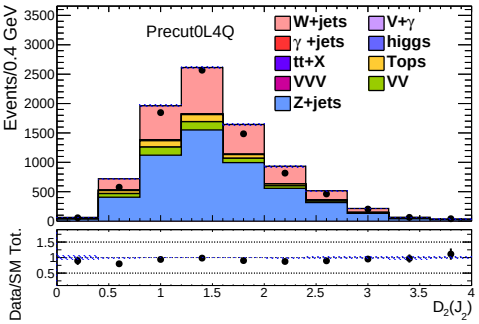

(c) sub-leading large-R jet D_2

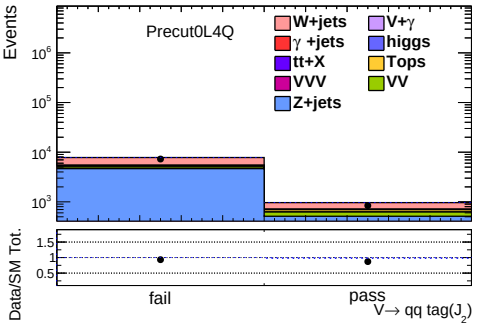

(d) boson tagging result of sub-leading large-R jet

Figure I.2: Kinematic distributions of sub-leading large-R jet p_{T} (a), mass (b), D_2 (c), and boson tagging result (d) with Precut0L4Q selections.

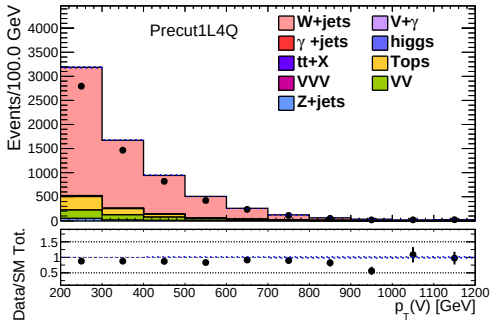

(a) $p_{\mathrm{T}}(V)$

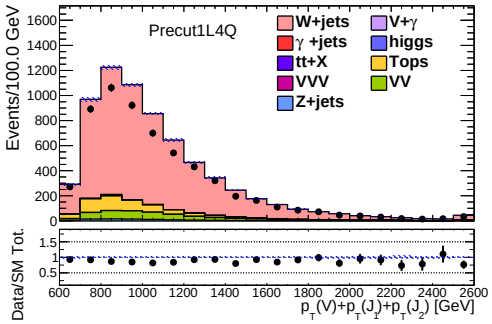

(b) $p_{\mathrm{T}}(V) + p_{\mathrm{T}}(J_1) + p_{\mathrm{T}}(J_2)$

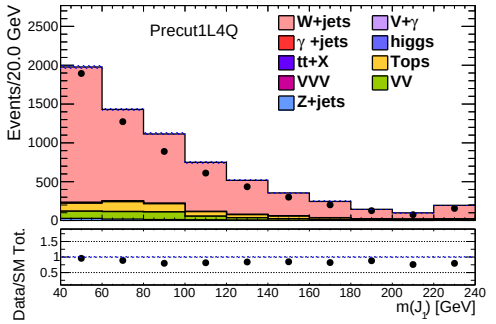

(c) leading large-R jet mass

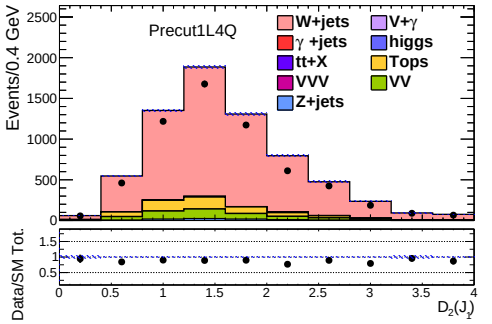

(d) leading large-R jet D_2

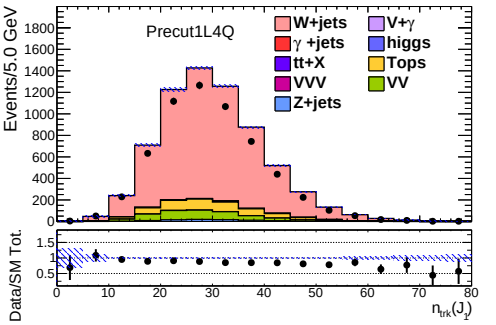

(e) leading large-R jet n_{trk}

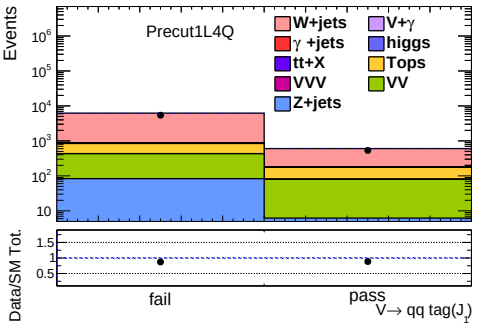

(f) boson tagging result of leading large-R jet

Figure I.3: Kinematic distributions of $p_{\mathrm{T}}(V)$ (a), $p_{\mathrm{T}}(V) + p_{\mathrm{T}}(J_1) + p_{\mathrm{T}}(J_2)$ (b), and leading large-R jet mass (c), D_2 (d), n_{trk} (e), and boson tagging result (f) with Precut1L4Q selections. In the 1L region, V represents the reconstructed W boson from leading lepton and $E_{\mathrm{T}}^{\mathrm{miss}}$.

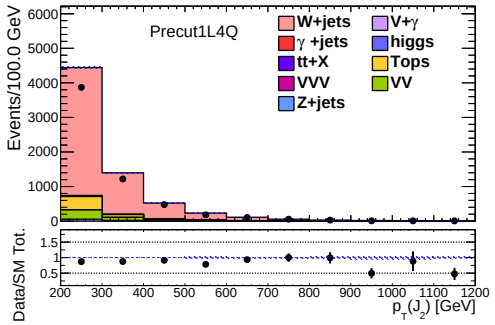

(a) sub-leading large-R jet p_{T}

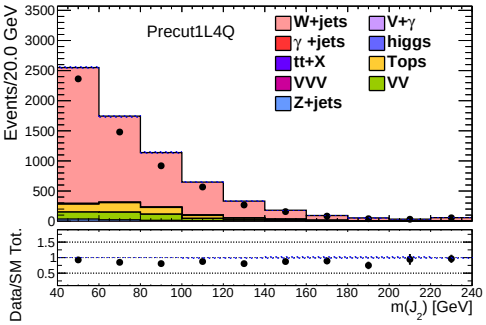

(b) sub-leading large-R jet mass

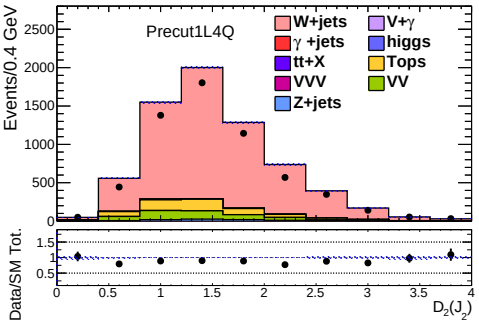

(c) sub-leading large-R jet D_2

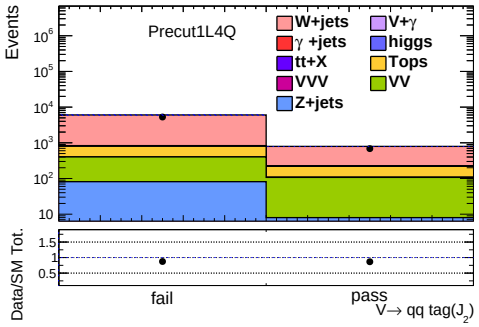

(d) boson tagging result of sub-leading large-R jet

Figure I.4: Kinematic distributions of sub-leading large-R jet p_{T} (a), mass (b), D_2 (c), and boson tagging result (d) with Precut1L4Q selections.

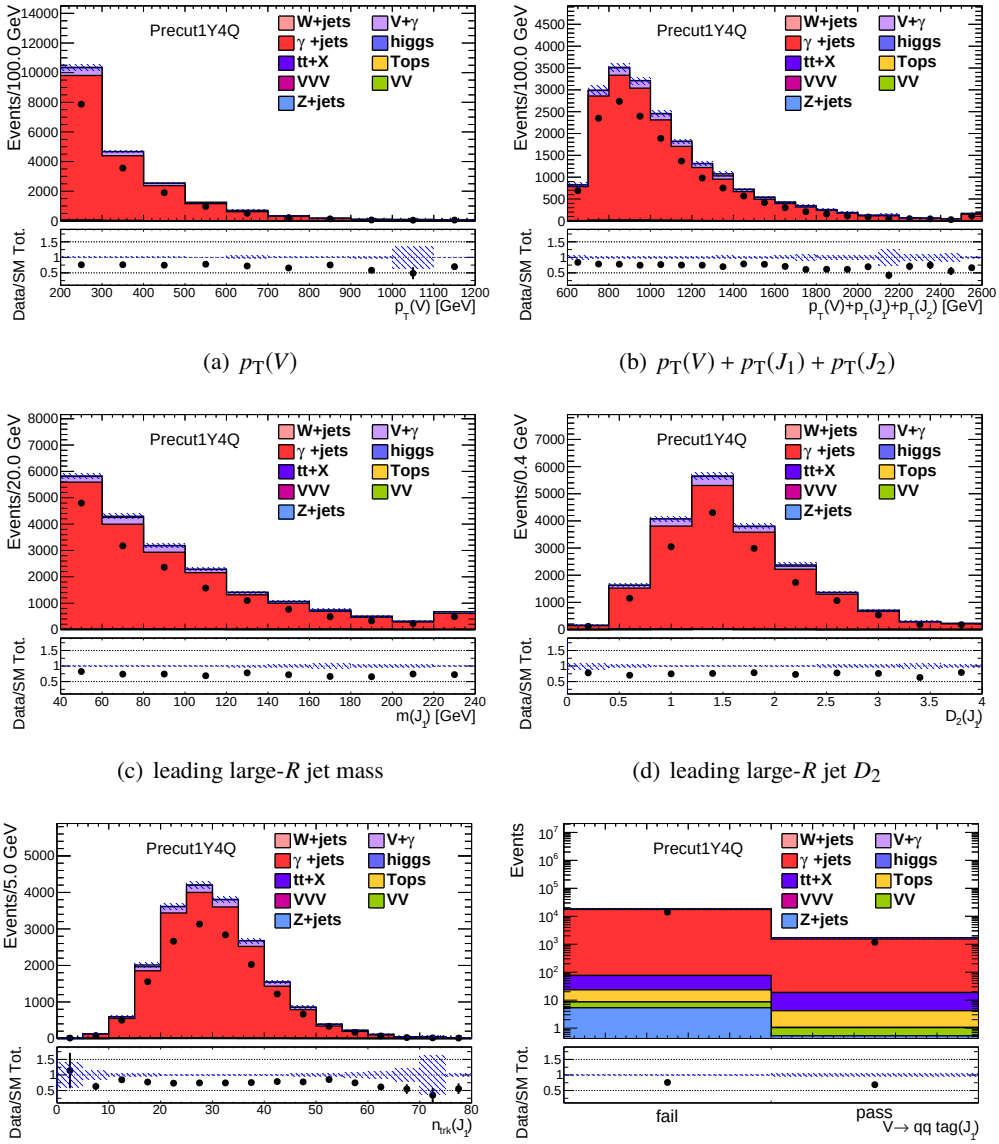

(a) $p_{\mathrm{T}}(V)$

(b) $p_{\mathrm{T}}(V) + p_{\mathrm{T}}(J_1) + p_{\mathrm{T}}(J_2)$

(c) leading large-R jet mass

(d) leading large-R jet D_2

(e) leading large-R jet n_{trk}

(f) boson tagging result of leading large-R jet

Figure I.5: Kinematic distributions of $p_{\mathrm{T}}(V)$ (a), $p_{\mathrm{T}}(V) + p_{\mathrm{T}}(J_1) + p_{\mathrm{T}}(J_2)$ (b), and leading large-R jet mass (c), D_2 (d), n_{trk} (e), and boson tagging result (f) with Precut1Y4Q selections. In the 1Y region, V represents the reconstructed photon.

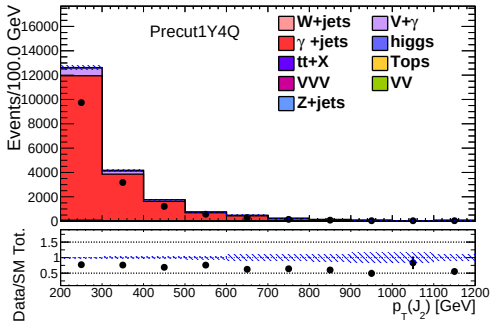

(a) sub-leading large-R jet p_{T}

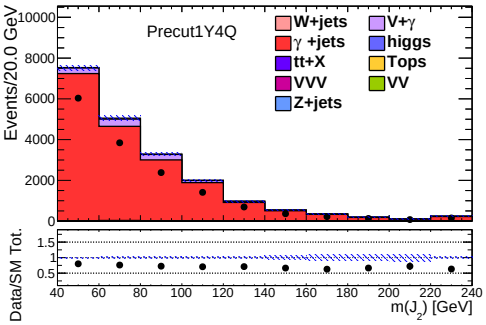

(b) sub-leading large-R jet mass

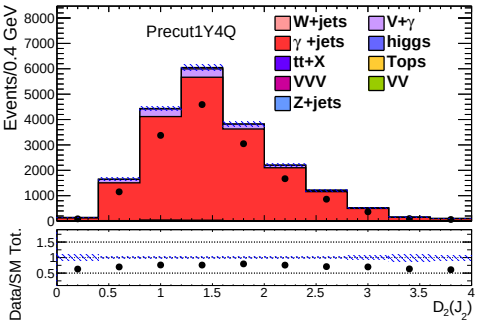

(c) sub-leading large-R jet D_2

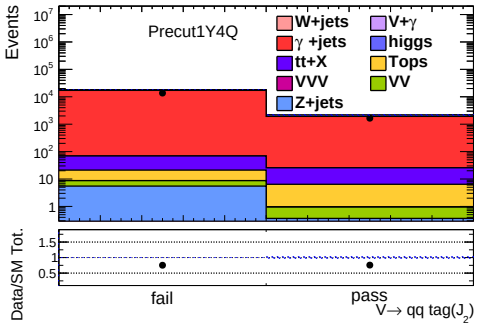

(d) boson tagging result of sub-leading large-R jet

Figure I.6: Kinematic distributions of sub-leading large-R jet p_{T} (a), mass (b), D_2 (c), and boson tagging result (d) with Precut1Y4Q selections.

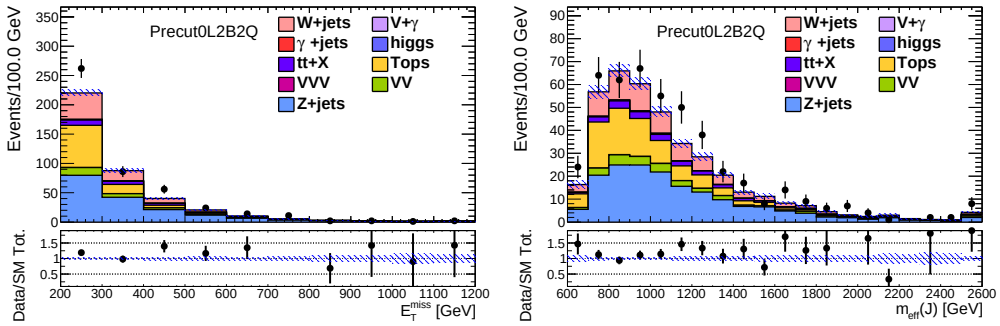

(a) $E_{\mathrm{T}}^{\mathrm{miss}}$ (b) $m_{\mathrm{eff}}(J)$

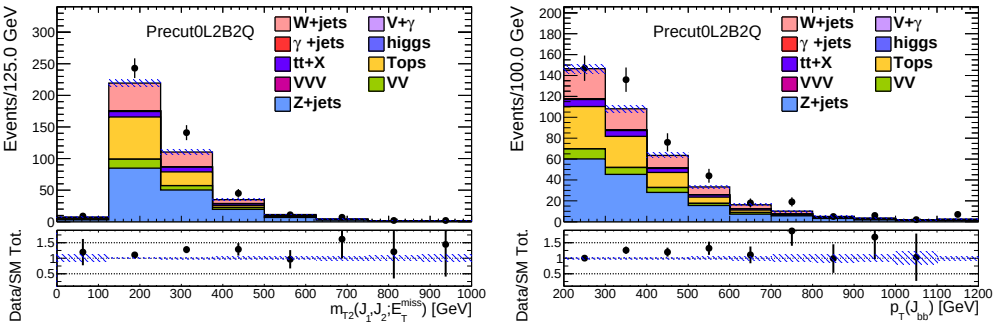

(c) $m_{\mathrm{T2}}(J_1, J_2; E_{\mathrm{T}}^{\mathrm{miss}})$ (d) J_{bb} p_{T}

Figure I.7: Kinematic distributions of $E_{\mathrm{T}}^{\mathrm{miss}}$ (a), $m_{\mathrm{eff}}(J)$ (b), $m_{\mathrm{T2}}(J_1, J_2; E_{\mathrm{T}}^{\mathrm{miss}})$ (b), $2b$-tagged large-R jet p_{T} (d) with Precut0L2B2Q selections.

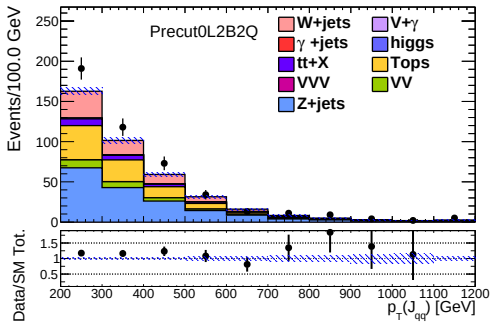

(a) J_{qq} p_{T}

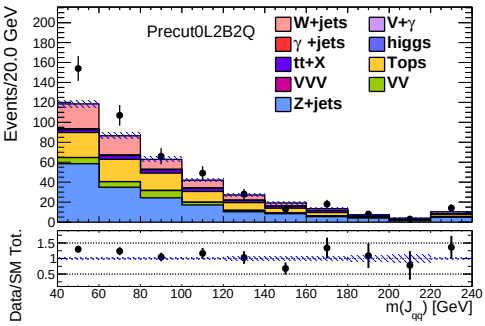

(b) J_{qq} mass

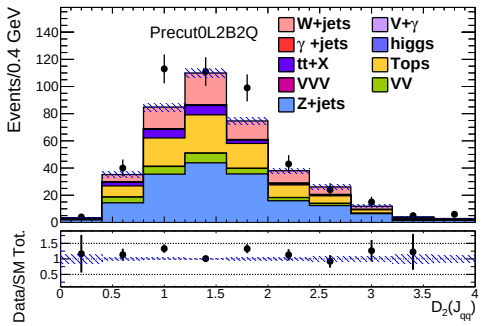

(c) J_{qq} D_2

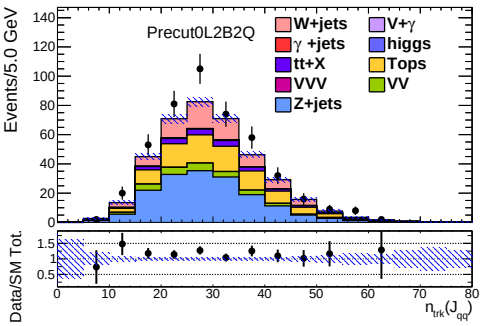

(d) J_{qq} n_{trk}

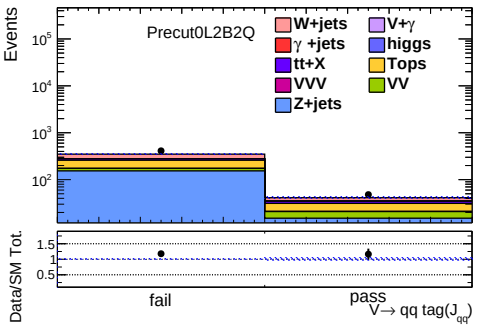

(e) boson tagging result of J_{qq}

Figure I.8: Kinematic distributions of J_{qq} p_{T} (a), mass (b), D_2 (c), n_{trk} (d) and boson tagging result (e) with Precut0L2B2Q selections.

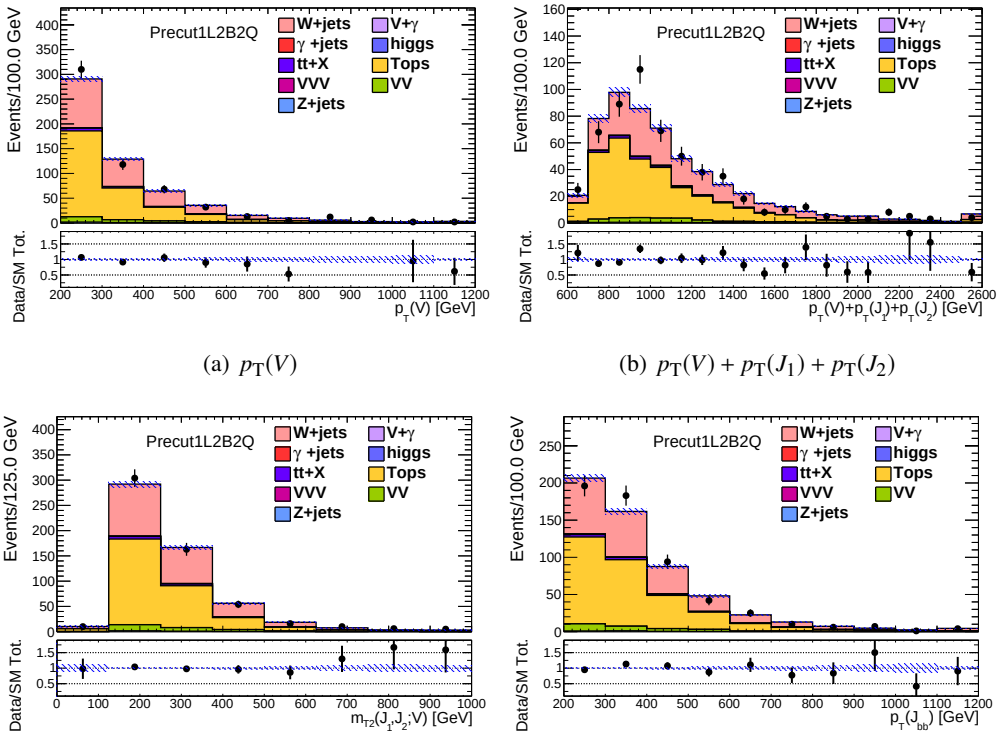

(a) $p_{\mathrm{T}}(V)$ (b) $p_{\mathrm{T}}(V) + p_{\mathrm{T}}(J_1) + p_{\mathrm{T}}(J_2)$

(c) $m_{\mathrm{T2}}(J_1, J_2; V)$ (d) J_{bb} p_{T}

Figure I.9: Kinematic distributions of $E_{\mathrm{T}}^{\mathrm{miss}}$ (a), $m_{\mathrm{eff}}(J)$ (b), $m_{\mathrm{T2}}(J_1, J_2; E_{\mathrm{T}}^{\mathrm{miss}})$ (c), $2b$-tagged large-R jet p_{T} (d) with Precut1L2B2Q selections. In the 1L region, V represents the reconstructed W boson from leading lepton and $E_{\mathrm{T}}^{\mathrm{miss}}$.

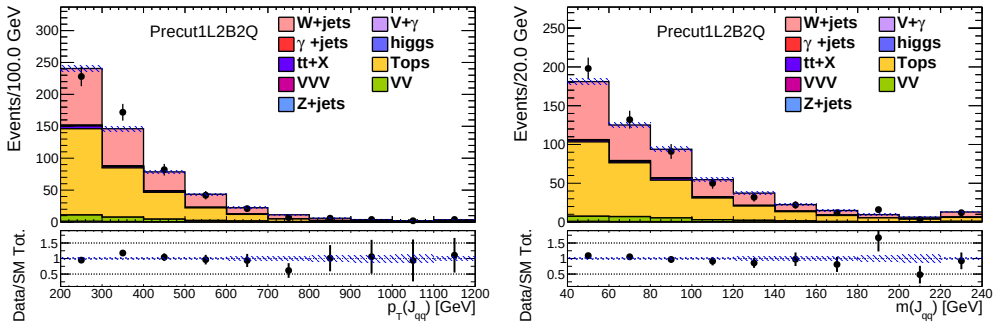

(a) J_{qq} p_{T}

(b) J_{qq} mass

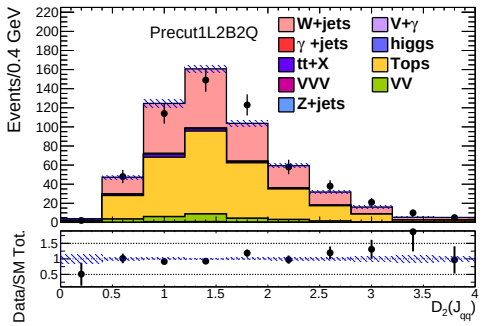

(c) J_{qq} D_2

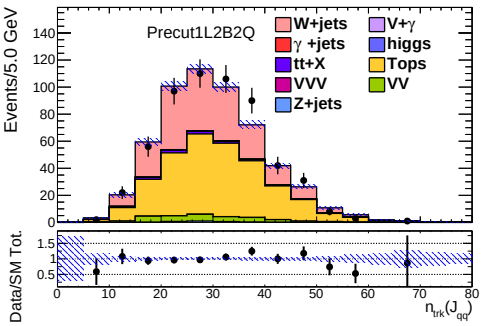

(d) J_{qq} n_{trk}

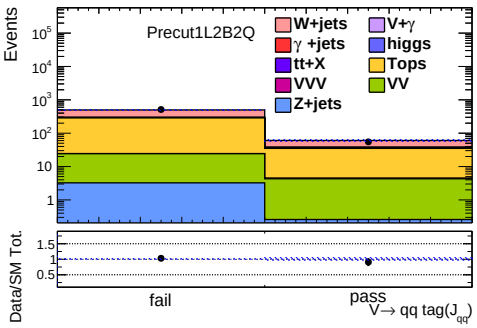

(e) boson tagging result of J_{qq}

Figure I.10: Kinematic distributions of J_{qq} p_{T} (a), mass (b), D_2 (c), n_{trk} (d) and boson tagging result (e) with Precut1L2B2Q selections. In the 1L region, V represents the reconstructed W boson from leading lepton and $E_{\mathrm{T}}^{\mathrm{miss}}$.

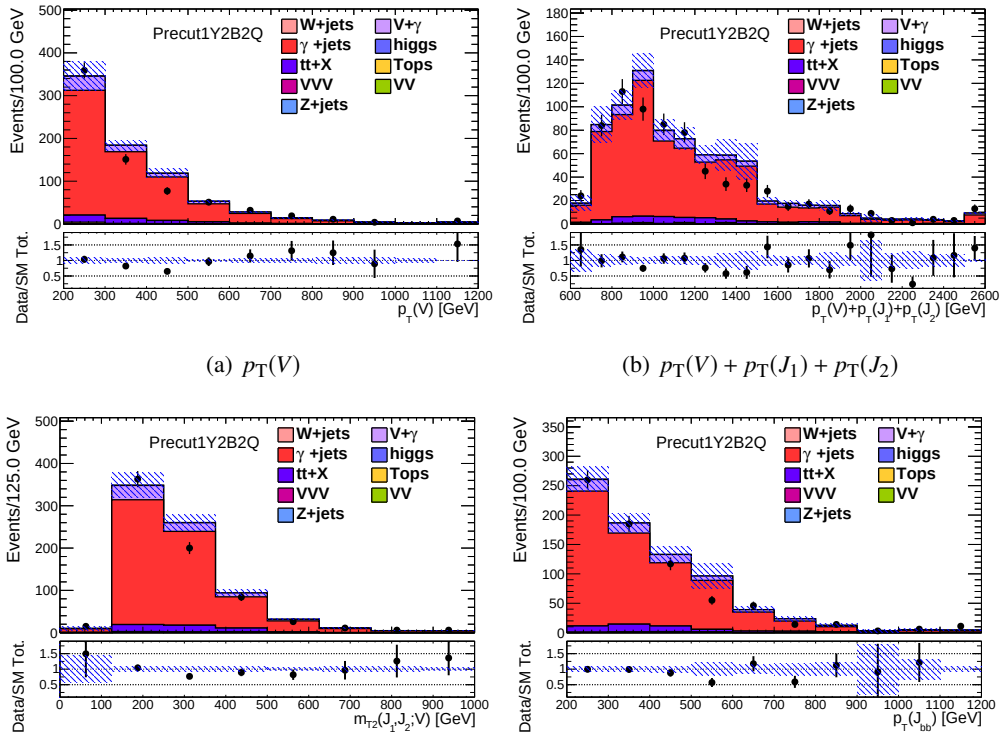

(a) $p_{\mathrm{T}}(V)$

(b) $p_{\mathrm{T}}(V) + p_{\mathrm{T}}(J_1) + p_{\mathrm{T}}(J_2)$

(c) $m_{\mathrm{T2}}(J_1, J_2; V)$

(d) J_{bb} p_{T}

Figure I.11: Kinematic distributions of $E_{\mathrm{T}}^{\mathrm{miss}}$ (a), $m_{\mathrm{eff}}(J)$ (b), $m_{\mathrm{T2}}(J_1, J_2; E_{\mathrm{T}}^{\mathrm{miss}})$ (c), $2b$-tagged large-R jet p_{T} (d) with Precut1Y2B2Q selections. In the 1Y region, V represents the reconstructed photon.

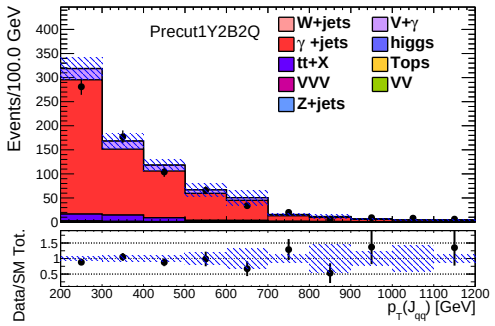

(a) J_{qq} p_{T}

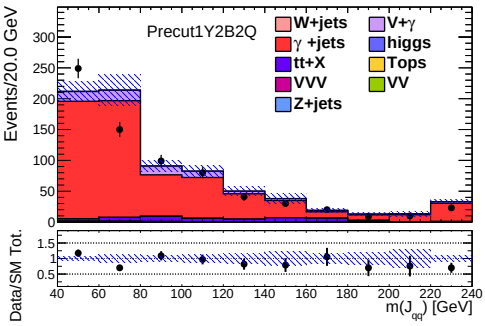

(b) J_{qq} mass

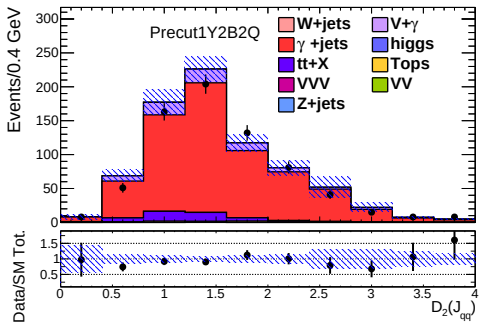

(c) J_{qq} D_2

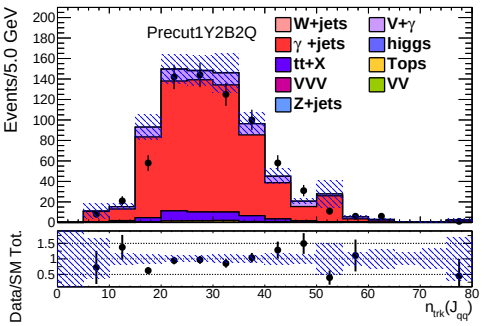

(d) J_{qq} n_{trk}

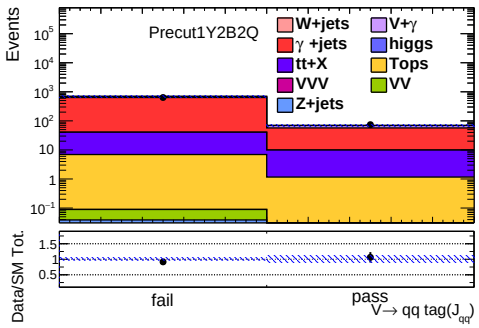

(e) boson tagging result of J_{qq}

Figure I.12: Kinematic distributions of J_{qq} p_{T} (a), mass (b), D_2 (c), n_{trk} (d) and boson tagging result (e) with Precut1Y2B2Q selections. In the 1Y region, V represents the reconstructed photon.

J Multi-jet Backgrounds in SRs/CRs/VRs

Multi-jet backgrounds are supposed to be negligible due to $E_{\mathrm{T}}^{\mathrm{miss}} > 200$ GeV in the SRs, an isolated lepton with $p_{\mathrm{T}} > 30$ GeV, $E_{\mathrm{T}}^{\mathrm{miss}} > 50$ GeV, $p_{\mathrm{T}}(W) > 200$ GeV in the 1L category and an isolated photon with $p_{\mathrm{T}} > 200$ GeV in the 1Y category. In similar phase spaces of the previous studies [257–259], multi-jet backgrounds are negligible. However, multi-jet backgrounds are still part of the "reducible backgrounds," the contribution should be taken into account by the reducible background estimation in the first order. Additionally, the jet composition of multi-jet samples is not similar to other samples, such as V + jets or $t\bar{t}$. Therefore, the goal in this section is that multi-jet backgrounds are confirmed to be negligible in each region using a data-driven method, i.e., the impact of jet composition differences between multi-jet and other backgrounds is small.

J.1 0-lepton Category

Multi-jet backgrounds remain in the 0L category due to "fake $E_{\mathrm{T}}^{\mathrm{miss}}$" caused by mis-measured jets typically. However, $\min \Delta\phi(j, E_{\mathrm{T}}^{\mathrm{miss}}) > 1.0$ is required by Precut0L, and the selection suppresses multi-jet backgrounds. The blue line in Figure J.1(a) represents the $\min \Delta\phi(j, E_{\mathrm{T}}^{\mathrm{miss}})$ distribution of multi-jet backgrounds with no $E_{\mathrm{T}}^{\mathrm{miss}}$ cut and failing leading and sub-leading large-R jets for boson tagging requirements.

As shown in Figure J.1, $\min \Delta\phi(j, E_{\mathrm{T}}^{\mathrm{miss}})$ and the result of boson tagging is not correlated. Thus, an ABCD method exploiting the invariant nature of $\min \Delta\phi(j, E_{\mathrm{T}}^{\mathrm{miss}})$ shape regardless of the result of boson tagging is used for the multi-jet backgrounds estimation. The definition of each region is summarized in Table J.1. With high $E_{\mathrm{T}}^{\mathrm{miss}}$ cut, multi-jet backgrounds are strongly suppressed, and MC statistics are limited in high $\min \Delta\phi(j, E_{\mathrm{T}}^{\mathrm{miss}})$ region ($\min \Delta\phi(j, E_{\mathrm{T}}^{\mathrm{miss}}) > 1.0$). In order to avoid limited statistics, multi-jet backgrounds are estimated from an exponential function fitted to the post-subtraction data, defined as the data subtracted non-multi-jet backgrounds of MC samples. For example, multi-jet yield in region-B is calculated from the fitted exponential function in region-A. The MC statistics are limited in region-C and region-D since at least one large-R jet is required to satisfy boson tagging requirements. Therefore, multi-jet yields in region-D are calculated as the estimated yields in region-B times the ratio of the failed region to pass region, i.e. $n(\text{region-B}) \times n(\text{region-C})/n(\text{region-A})$.

In order to calculate the upper yields of multi-jet backgrounds, the yields in region-B are estimated with an exponential function, such as e^{ax+b}. Figure J.3 shows the $\min \Delta\phi(j, E_{\mathrm{T}}^{\mathrm{miss}})$ distribution of multi-jet candidates in region-(A+B) with $E_{\mathrm{T}}^{\mathrm{miss}} > 200$ GeV. Black points represent (Data - non-multi-jet MC), and red histogram represents multi-jet MC samples. The blue line is a fitted function. The results of the ABCD method and the yields estimated from MC samples directly are shown in Table J.2. After applying $E_{\mathrm{T}}^{\mathrm{miss}} > 300$ GeV, multi-jet backgrounds are negligible. In the CRs and SRs, the contribution of multi-jet backgrounds is smaller since additional selections, such as boson tagging and $m_{\mathrm{eff}}(J)$, are applied.

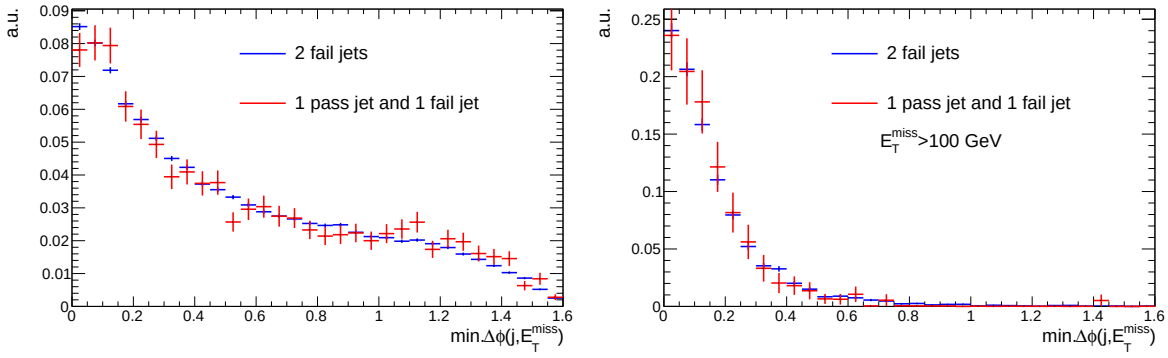

(a) no $E_{\mathrm{T}}^{\mathrm{miss}}$ cut

(b) $E_{\mathrm{T}}^{\mathrm{miss}} > 100$ GeV

Figure J.1: $\min \Delta\phi(j, E_{\mathrm{T}}^{\mathrm{miss}})$ distributions of multi-jet background MC samples. (a) is not applied any $E_{\mathrm{T}}^{\mathrm{miss}}$ cut and (b) is selected with $E_{\mathrm{T}}^{\mathrm{miss}} > 100$ GeV. The blue line represents the events with failing leading and sub-leading large-R jets of boson tagging requirements, and the red line represents the events that contain one passing large-R jet and one failing large-R jet. Each distribution is normalized to unity.

Table J.1: Definition of each region with an ABCD method in 0-lepton region. Multi-thresholds of $E_{\mathrm{T}}^{\mathrm{miss}}$ are used to confirm the $\min \Delta\phi(j, E_{\mathrm{T}}^{\mathrm{miss}})$ distribution with sufficient statistics and calculate upper yields in the SRs. $\sigma(E_{\mathrm{T}}^{\mathrm{miss}})$ is used to suppress the other background contributions. $\sigma(E_{\mathrm{T}}^{\mathrm{miss}})$ cut is only applied to the ABCD method, it is not applied to the search for electroweakinos.

	Region-A	Region-B	Region-C	Region-D(target)
Trigger: $E_{\mathrm{T}}^{\mathrm{miss}}$ OR single-jet				
$E_{\mathrm{T}}^{\mathrm{miss}}$ trigger	See Table **??**			
Single-jet trigger	prescaled and unprescaled triggers			
	Jet p_{T} threshold is larger than 15 GeV			
Cleaning cuts (Section 7.2)				
Bad-tile veto	yes			
Non-collision veto	yes			
Selection				
n_{lepton}	$= 0$			
$n_{\mathrm{Large-}R\ \mathrm{jets}}$	≥ 2			
$E_{\mathrm{T}}^{\mathrm{miss}}$ [GeV]	$> 100, > 150, > 200, > 300$			
$m_{\mathrm{eff}}(J)$ [GeV]	> 1000			
$\sigma(E_{\mathrm{T}}^{\mathrm{miss}})$	< 10			
"ABCD" variables				
$n_{W\mathrm{or}Z\to qq}$	$= 0$	$= 0$	$= 1$	$= 1$
$n(\mathrm{Fail\ jets}) = 2 - n_{W\mathrm{or}Z\to qq}$	$= 2$	$= 2$	$= 1$	$= 1$
$\min \Delta\phi(j, E_{\mathrm{T}}^{\mathrm{miss}})$	< 1.0	> 1.0	< 1.0	> 1.0

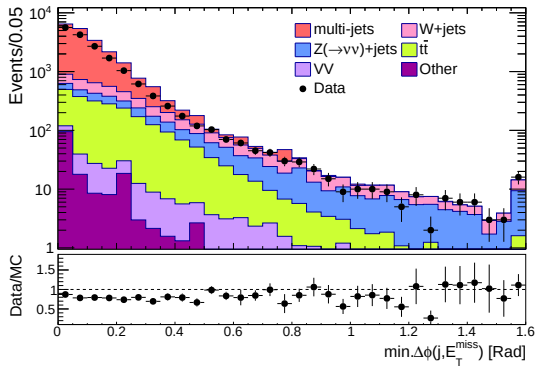

(a) $E_{\mathrm{T}}^{\mathrm{miss}} > 200$ GeV in region-(A+B)

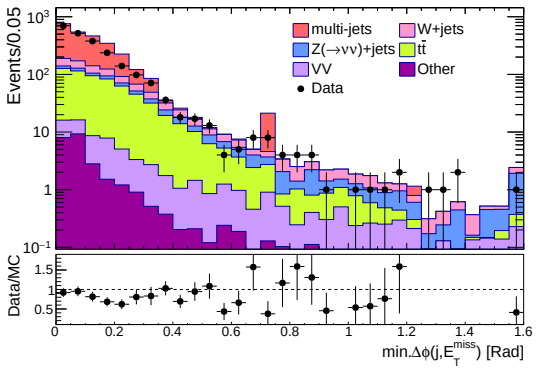

(b) $E_{\mathrm{T}}^{\mathrm{miss}} > 200$ GeV in region-(C+D)

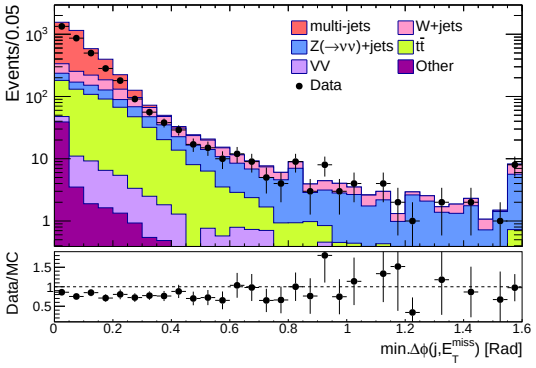

(c) $E_{\mathrm{T}}^{\mathrm{miss}} > 300$ GeV in region-(A+B)

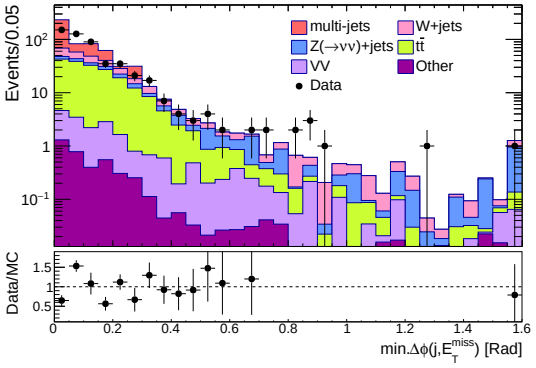

(d) $E_{\mathrm{T}}^{\mathrm{miss}} > 300$ GeV in region-(C+D)

Figure J.2: $\min \Delta\phi(j, E_{\mathrm{T}}^{\mathrm{miss}})$ distributions in each region of the ABCD method. $\min \Delta\phi(j, E_{\mathrm{T}}^{\mathrm{miss}})$ distributions with $E_{\mathrm{T}}^{\mathrm{miss}} > 200$ GeV, in the region where 2 fail leading large-R jets of $W/Z \to qq$ tagging (a) or one of leading large-R jets pass (b). $\min \Delta\phi(j, E_{\mathrm{T}}^{\mathrm{miss}})$ distributions with $E_{\mathrm{T}}^{\mathrm{miss}} > 300$ GeV is shown in (c) and (d).

Table J.2: Upper limits of the yield from the ABCD method and MC prediction directly with different $E_{\mathrm{T}}^{\mathrm{miss}}$ threshold. "-" represents no MC entry.

$E_{\mathrm{T}}^{\mathrm{miss}}$ [GeV]	ABCD estimation	MC prediction	Non multi-jet BG
> 100	121 ± 5	118 ± 39	58.5 ± 3.6
> 150	1.66 ± 0.15	3.11 ± 2.30	23.0 ± 1.4
> 200	$(4.87 \pm 0.94) \times 10^{-2}$	0.27 ± 1.05	12.2 ± 1.0
> 300	$(9.05 \pm 4.57) \times 10^{-5}$	-	3.54 ± 0.44
$E_{\mathrm{T}}^{\mathrm{miss}}$ [GeV] + b-tag	ABCD estimation	MC prediction	Non multi-jet BG
$> 300, n^{\mathrm{trk}}_{b-\text{jet (inside J)}} \leq 1$ (4Q)	$(2.95 \pm 1.77) \times 10^{-5}$	-	3.37 ± 0.44
$> 200, n(J_b b) = 1$ (2B2Q)	$(5.51 \pm 2.66) \times 10^{-3}$	-	0.43 ± 0.20

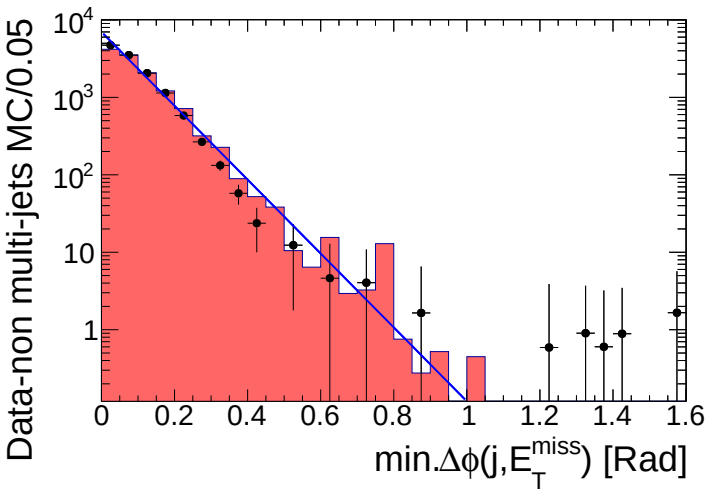

Figure J.3: min $\Delta\phi(j, E_{\mathrm{T}}^{\mathrm{miss}})$ distribution of multi-jet candidates in the region-(A+B) with $E_{\mathrm{T}}^{\mathrm{miss}} > 200$ GeV. The black points represent (Data - non multi-jet MC), and red histogram represents multi-jet MC samples. The blue line is a fitted function.

J.2 1L Category

Multi-jet events with mis-identified leptons may remain in the 1L category. Mis-identified leptons are referred to as "fake leptons," and they are estimated by the fake-factor method [260, 261]. In the fake factor method, the ratio is defined as the number of leptons with loose selections to ones with tight selections. The loose selected leptons are referred to as "anti-signal" leptons. They are defined as the ones, which fail the isolation selection and pass all the other signal lepton selections described in Table 5.2. The tightly selected leptons are the signal leptons. Thus, the fake factor (FF) is defined as,

$$\mathrm{FF} = \frac{N_{\text{signal}}}{N_{\text{anti-signal}}}. \tag{J.1}$$

For estimating the fake factor, a kinematically loosely selected region is usually defined in a data-driven method. However, such a region cannot be defined due to tight lepton identification criteria and large p_{T} (> 30 GeV). Therefore, the fake factor is evaluated from multi-jet MC samples directly.

The fake factors of electrons and muons are shown in Figure J.4. The systematic uncertainty derived from the fake component variation is the largest source of uncertainty on the fake factor, and it is represented as the red box in Figure J.4. These values are estimated as the variations with the fraction of fake events shifted up and down by a factor of two, originating from b-hadron decays, c-hadron decays, light-flavor hadron decays, punch-through pions (for μ), and photon conversion (for e).

In the ID region (= the 1L category), multi-jet events are estimated using the fake factor from the corresponding anti-ID region. Multi-jet backgrounds in the anti-ID region are evaluated from the data after subtracting the contribution of non-multi-jet backgrounds and normalized to be consistent with the data. A flat 20% uncertainty of the normalization factor is assigned to account for the typical level of uncertainty of the subtracted backgrounds.

The estimated yields in the 1L category with different selections are summarized in Table J.3. The contributions of multi-jet backgrounds typically account for 3%-5% of the total background in 1-electron regions and less than 1% in 1-muon regions. Therefore, the contribution of multi-jet background is negligible in 1-lepton regions.

J.3 1Y category

Multi-jet events containing "fake photons" remain in the 1Y category. The contribution of multi-jet backgrounds is estimated using an ABCD method. Region-D is the target region, and the definitions are,

- **A:** pass loose identification criteria, fail tight identification criteria, and fail isolation criteria
- **B:** pass loose identification criteria, fail tight identification criteria, and pass isolation criteria
- **C:** pass tight identification criteria, and fail isolation criteria
- **D:** pass tight identification criteria, and pass isolation criteria

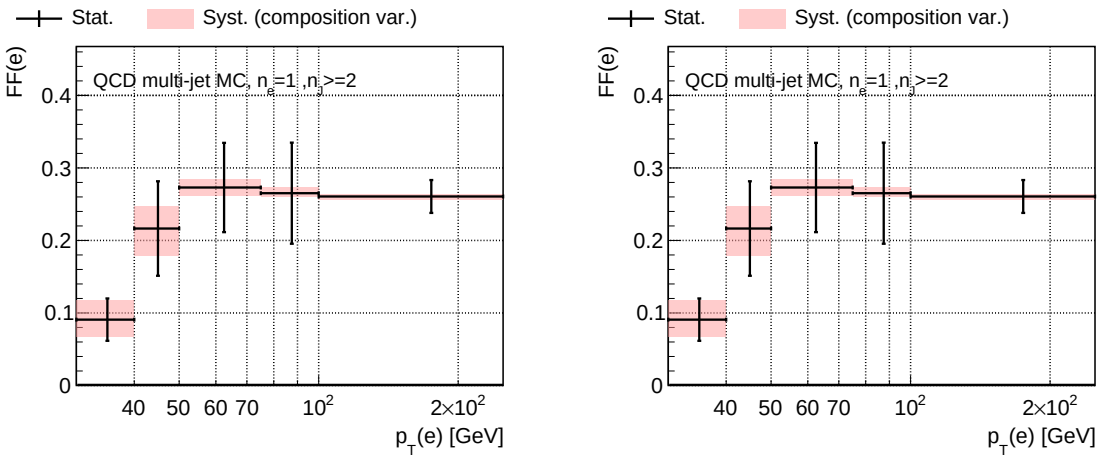

(a) Electron (b) Muon

Figure J.4: Fake factors for electrons (a) and muons (b) calculated using multi-jet MC samples. The error bars and the red boxes represent the statistical and systematic uncertainty, respectively. The systematic uncertainty is based on the fake composition modeling.

Table J.3: Multi-jet events in the 1-lepton regions estimated using the fake-factor method. Track jet cleaning is not applied to each selected region.

Region	Multi-jet	W + jets	$t\bar{t}$	Others	Total BG (= Data)	Multi-jet fraction (%)
Electron channel						
Precut1L4Q	83.7 ± 18	2520 ± 504	154 ± 31	180 ± 36	2938	2.85 ± 0.6
CR1L4Q	6.28 ± 2.0	175 ± 35	16.5 ± 3.5	38.6 ± 8.1	236	2.66 ± 0.83
VR1L4Q	0.591 ± 0.4	4.18 ± 0.96	0.581 ± 0.21	1.65 ± 0.53	7	8.44 ± 5.7
Precut1L2B2Q	8.37 ± 2.4	114 ± 23	106 ± 22	16.0 ± 3.4	280	2.99 ± 0.85
CR1L2B2Q	2.09 ± 0.93	25.3 ± 5.3	14.1 ± 3.0	4.47 ± 1.1	46	4.54 ± 2.0
VR1L2B2Q	0.249 ± 0.27	1.53 ± 0.44	0.952 ± 0.33	0.275 ± 0.12	3	8.30 ± 8.8
Muon channel						
Precut1L4Q	10.6 ± 2.3	2324 ± 465	138 ± 28	165 ± 33	2638	0.402 ± 0.089
CR1L4Q	0.541 ± 0.26	149 ± 30	12.6 ± 2.7	32.6 ± 6.8	195	0.278 ± 0.13
VR1L4Q	−0.02 ± 0.01	6.37 ± 1.5	1.16 ± 0.4	2.50 ± 0.83	7	−0.3 ± 0.2
Precut1L2B2Q	1.43 ± 0.46	105 ± 21	105 ± 21	14.3 ± 3.1	239	0.597 ± 0.19
CR1L2B2Q	0.247 ± 0.17	25.5 ± 5.4	14.5 ± 3.1	3.81 ± 0.96	55	0.45 ± 0.3
VR1L2B2Q	−0.003 ± 0.001	1.49 ± 0.57	0.773 ± 0.29	0.738 ± 0.33	3	−0.09 ± 0.04

where loose identification criteria are the “LoosePrime4a” working point and it is identical to LoosePrime4 in Ref.[119].

We perform the closure test using multi-jet MC samples in a loose 1-photon region. The ID efficiency and the isolation efficiency with a function of photon p_{T} are shown in Figure J.5. In $p_{\mathrm{T}} < 350$ GeV, good closure is observed. However, we can see that there is a discrepancy at $p_{\mathrm{T}} > 350$ GeV. The discrepancy causes underestimation, and a flat 50% closure uncertainty is assigned for this discrepancy.

The yield of multi-jet events in region-D is calculated as n(region-C) × n(region-B)/n(region-A). Data events subtracted from the non-multi-jet MC samples are used as the multi-jet events. The normalization factor is applied to agree with the observed data in region-D. Like the estimation in the 1-lepton region,

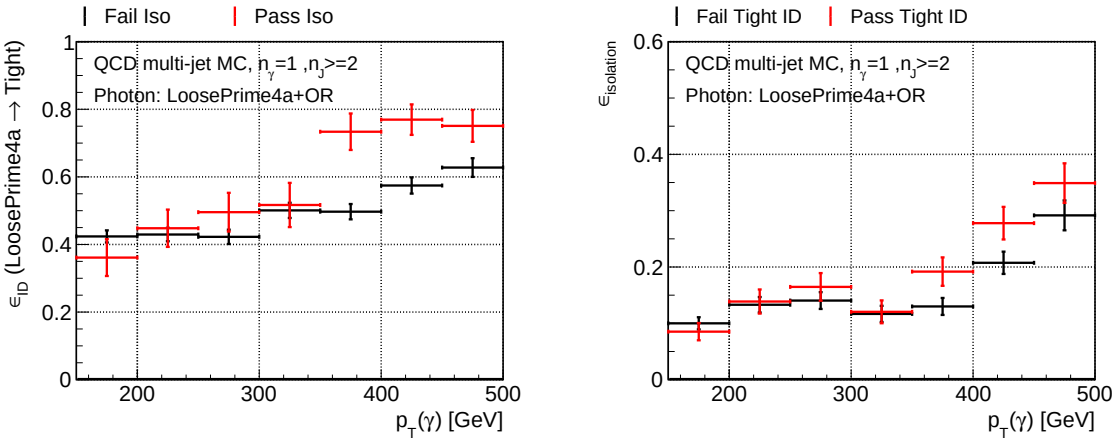

(a) ϵ(ID) (b) ϵ(Iso)

Figure J.5: Efficiency of the tight photon ID selection (a) and the isolation for photons passing the loose ID (b), overlap removal, calculated using the multi-jet MC.

a flat 20% uncertainty on the normalization factor is added. The results are summarized in Table J.4. The contributions of multi-jet backgrounds typically account for 2%-5% of the total background, and the contribution is enough to be negligible as an independent background component in the fit.

Table J.4: Multi-jet events in the 1-photon regions estimated using the ABCD method in terms of the ID and isolation selection. Track jet cleaning is not applied to each selected region. The statistical uncertainty in the A, B, and C region data events, and the subtraction uncertainty are taken into account, and they are represented as the errors.

Region	QCD	γ+jets	$V(\rightarrow qq)+\gamma$	Others	Total BG (=Data)	QCD fraction [%]
Precut1Y4Q	335 ± 175	13380 ± 2679	804 ± 161	74.4 ± 30	14593	2.29 ± 1.2
CR1Y4Q	22.1 ± 13	819 ± 166	146 ± 29	3.09 ± 0.79	990	2.23 ± 1.3
VR1Y4Q	0.644 ± 0.92	25.0 ± 6.5	4.38 ± 1.0	0.023 ± 0.01	30	2.15 ± 3.1
Precut1Y2B2Q	20.6 ± 13	589 ± 122	64.8 ± 13	2.15 ± 0.63	677	3.04 ± 1.9
CR1Y2B2Q	8.01 ± 5.2	123 ± 26	14.8 ± 3.0	0.218 ± 0.14	146	5.48 ± 3.5
VR1Y2B2Q	−0.1 ± 0.1	9.75 ± 3.1	2.36 ± 0.61	0.009 ± 0.009	12	−0.9 ± 0.9

K Jet Compositions in CRs/VRs/SRs

In this section, the jet origins of SM background MC samples in each region are shown in Figure K.1-K.11. The x-axes represent the origins of J_{bb} in the 2B2Q category, J_{pass} in the CR-4Q bins and J_1 in SR-4Q/VR1L-4Q/VR1Y-4Q bins. The y-axes represent the origins of J_{qq} in the 2B2Q category, J_{fail} in the CR-4Q bins and J_2 in SR-4Q/VR1L-4Q/VR1Y-4Q bins.

For reducible backgrounds, dominant sources of the failing jets are quark- or gluon-initiated jets in CRs. The difference between background samples is small. Thus, the reducible backgrounds can be treated as one component.

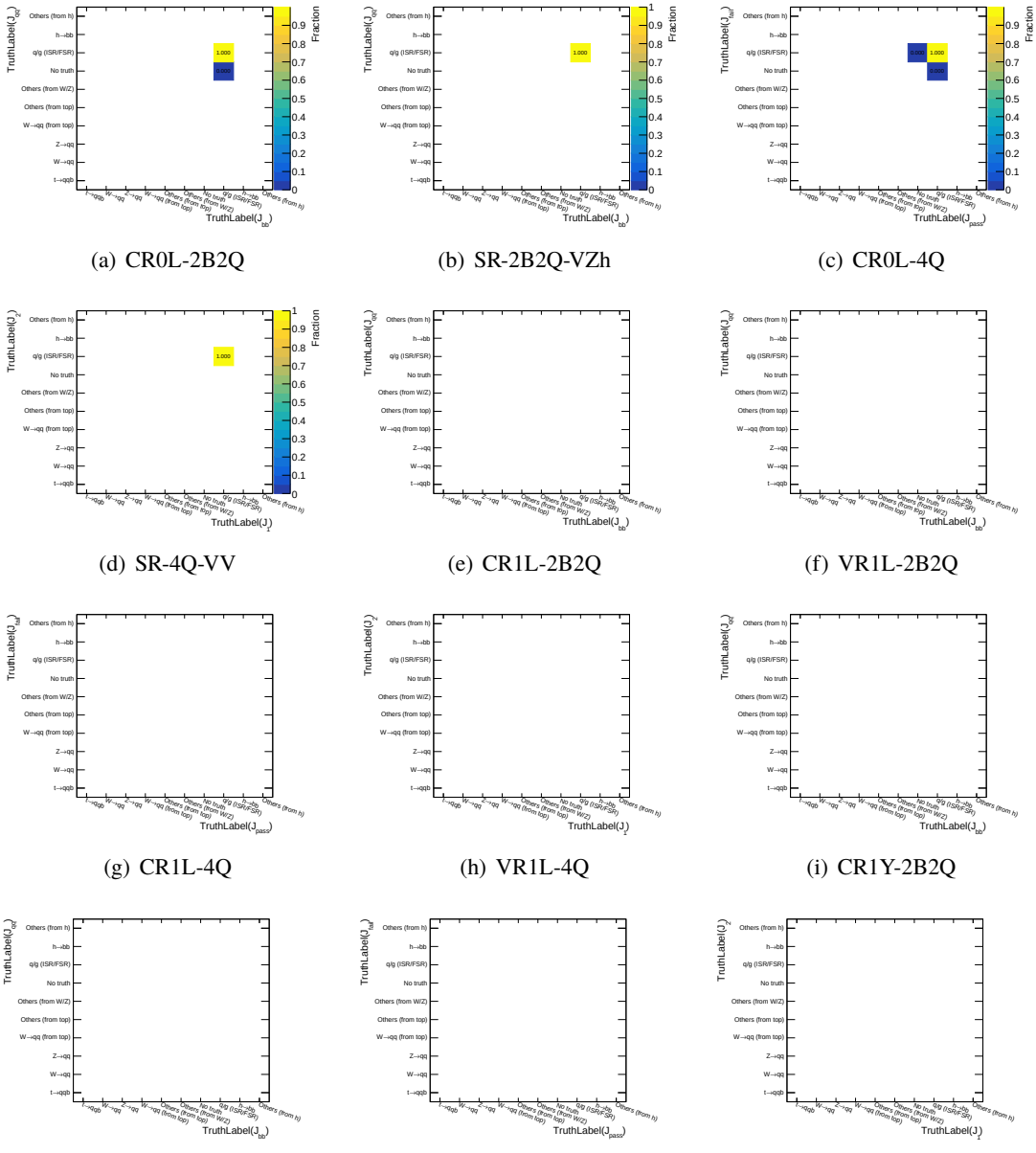

(a) CR0L-2B2Q (b) SR-2B2Q-VZh (c) CR0L-4Q

(d) SR-4Q-VV (e) CR1L-2B2Q (f) VR1L-2B2Q

(g) CR1L-4Q (h) VR1L-4Q (i) CR1Y-2B2Q

(j) VR1Y-2B2Q (k) CR1Y-4Q (l) VR1Y-4Q

Figure K.1: Jet compositions of $Z(\rightarrow \nu\nu)$ + jets events.

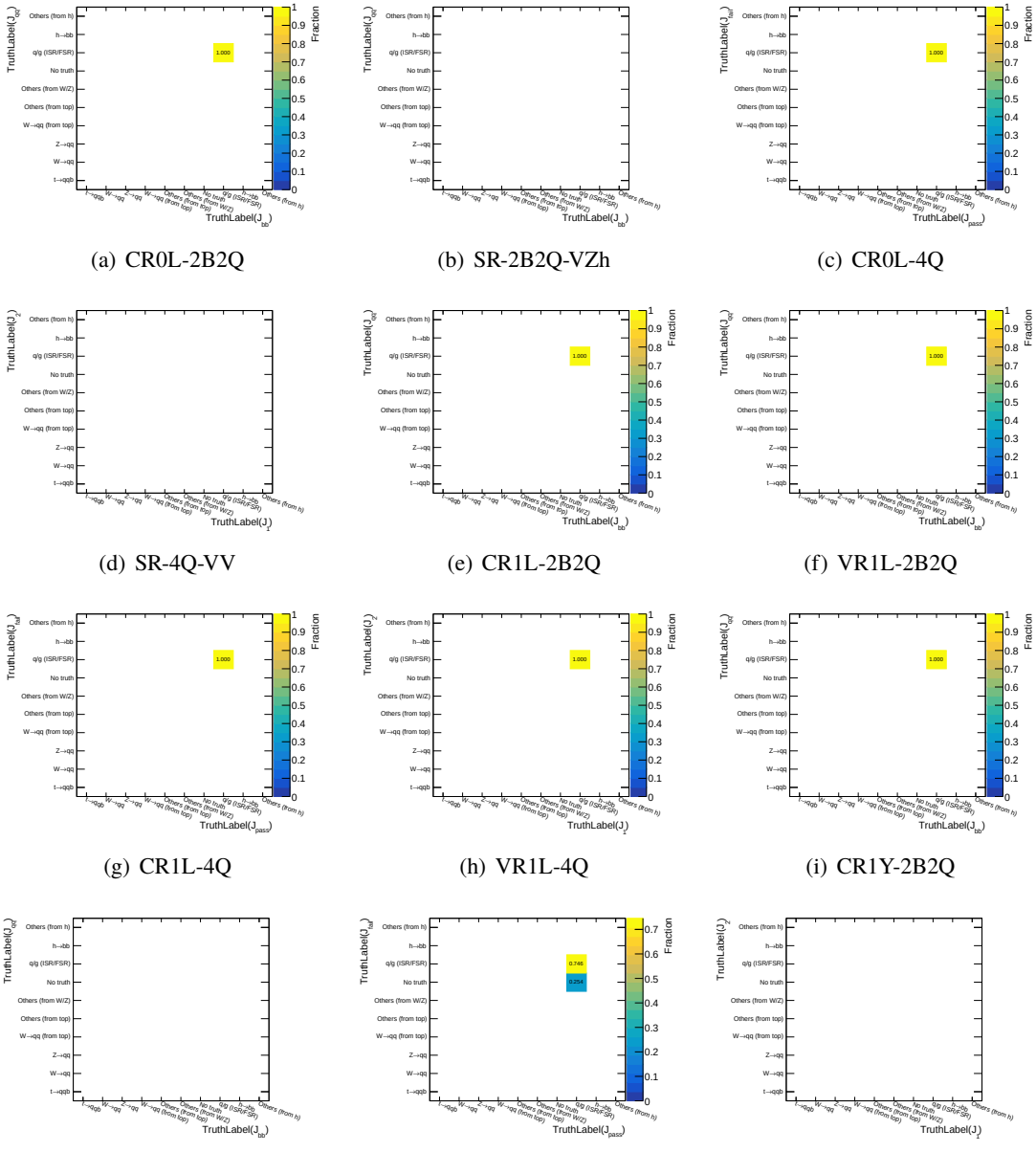

(a) CR0L-2B2Q (b) SR-2B2Q-VZh (c) CR0L-4Q

(d) SR-4Q-VV (e) CR1L-2B2Q (f) VR1L-2B2Q

(g) CR1L-4Q (h) VR1L-4Q (i) CR1Y-2B2Q

(j) VR1Y-2B2Q (k) CR1Y-4Q (l) VR1Y-4Q

Figure K.2: Jet compositions of $Z(\rightarrow ll)$+jets events.

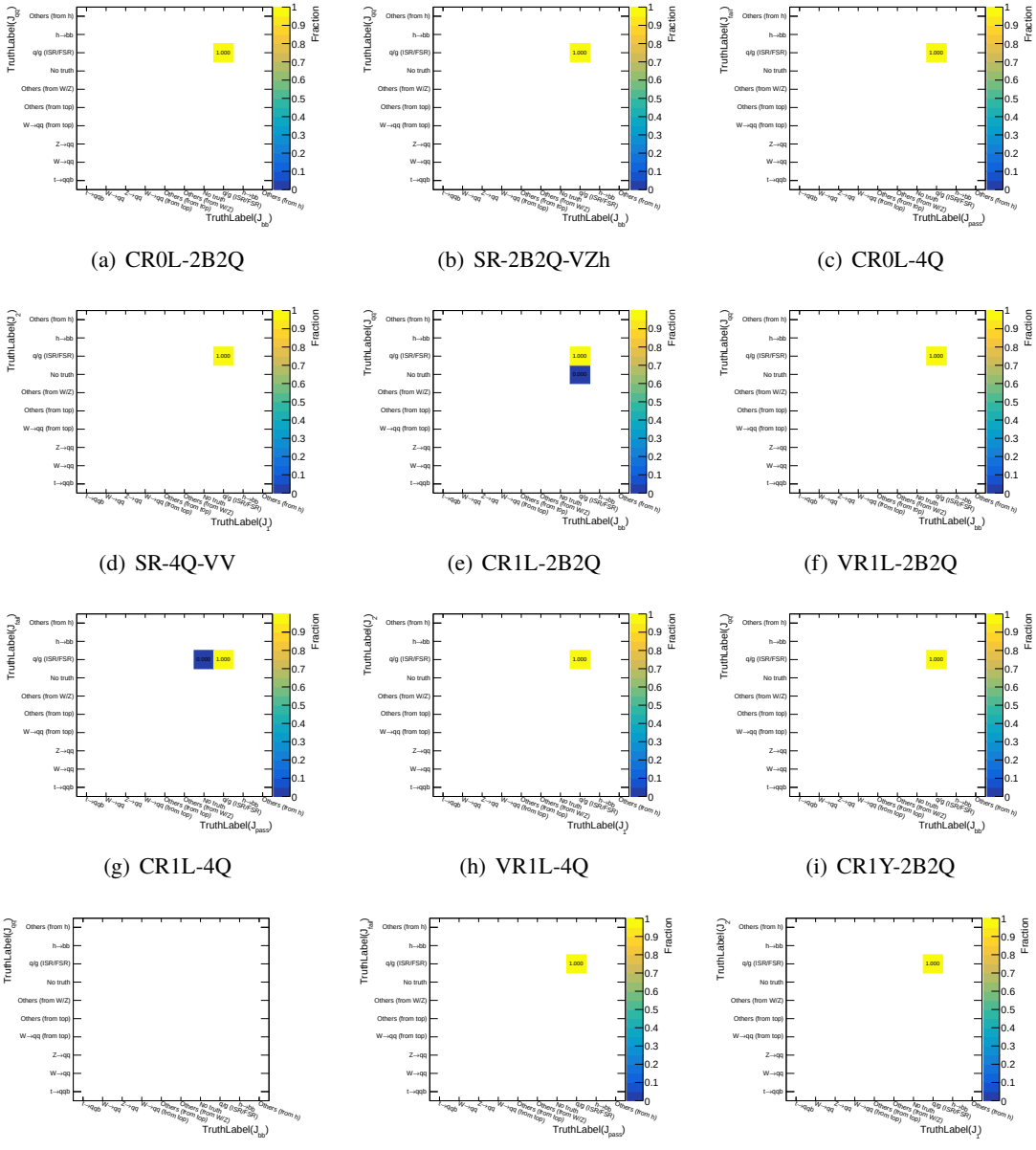

(a) CR0L-2B2Q (b) SR-2B2Q-VZh (c) CR0L-4Q

(d) SR-4Q-VV (e) CR1L-2B2Q (f) VR1L-2B2Q

(g) CR1L-4Q (h) VR1L-4Q (i) CR1Y-2B2Q

(j) VR1Y-2B2Q (k) CR1Y-4Q (l) VR1Y-4Q

Figure K.3: Jet compositions of W + jets events.

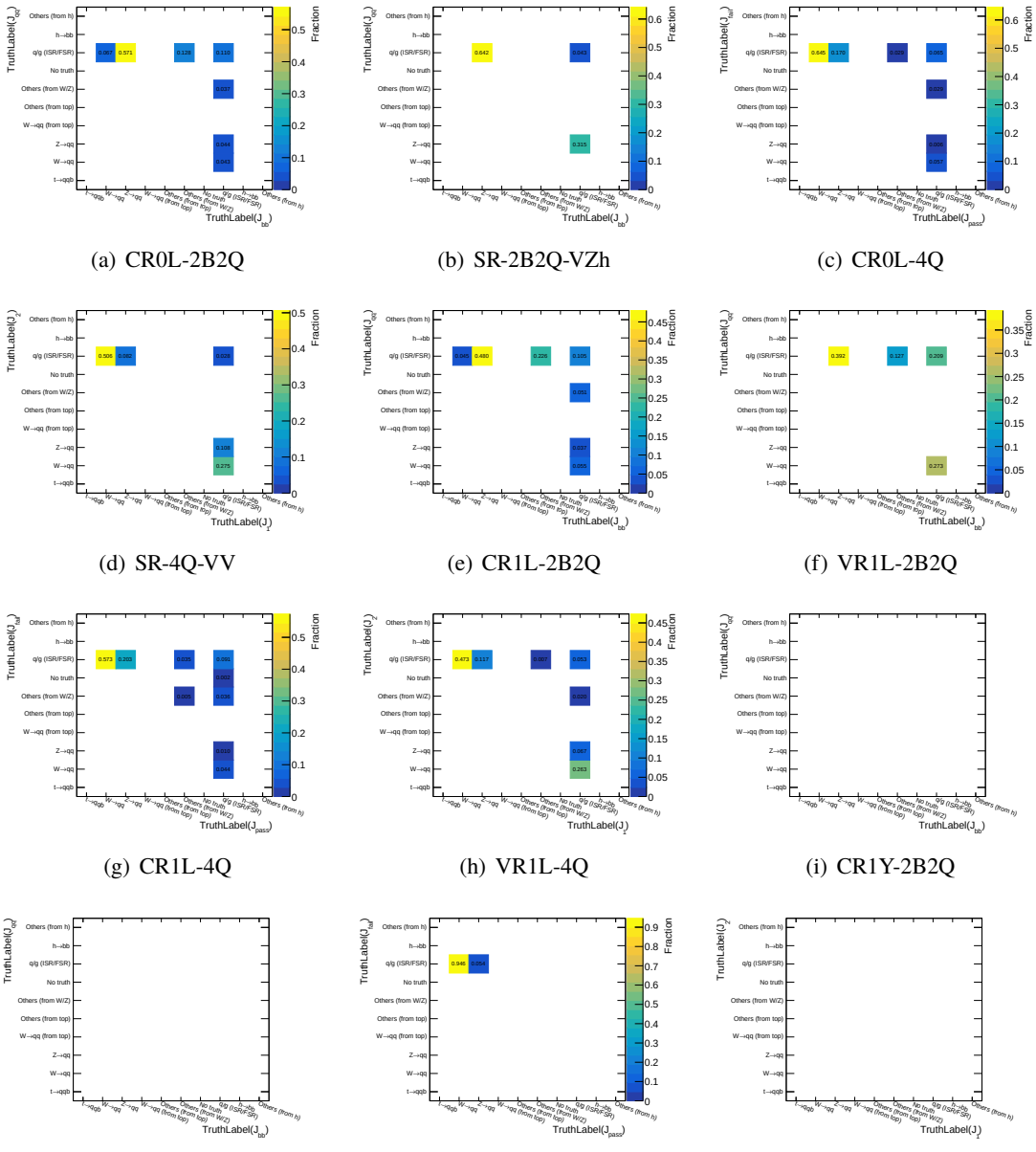

(a) CR0L-2B2Q (b) SR-2B2Q-VZh (c) CR0L-4Q

(d) SR-4Q-VV (e) CR1L-2B2Q (f) VR1L-2B2Q

(g) CR1L-4Q (h) VR1L-4Q (i) CR1Y-2B2Q

(j) VR1Y-2B2Q (k) CR1Y-4Q (l) VR1Y-4Q

Figure K.4: Jet compositions of diboson events.

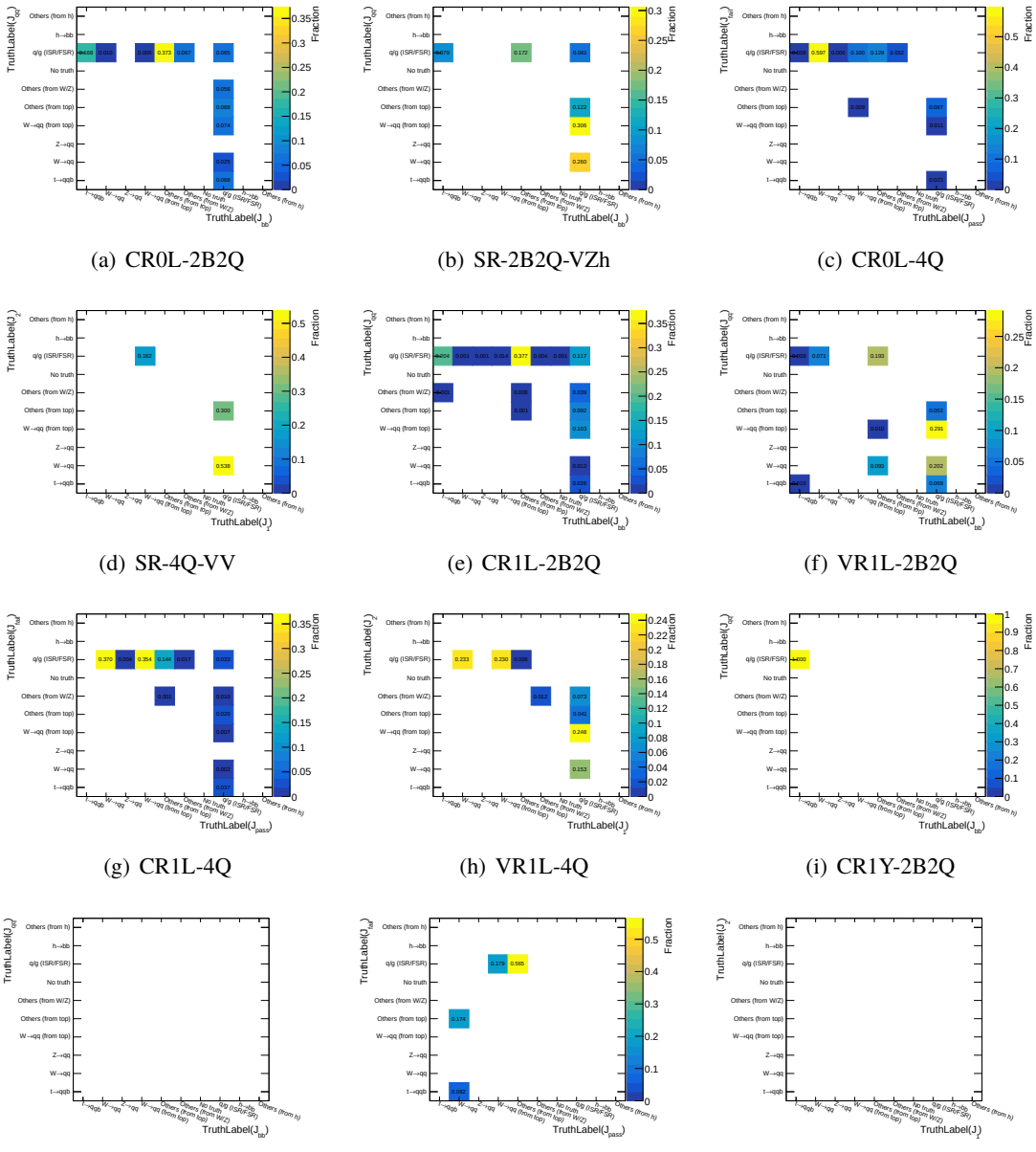

(a) CR0L-2B2Q (b) SR-2B2Q-VZh (c) CR0L-4Q

(d) SR-4Q-VV (e) CR1L-2B2Q (f) VR1L-2B2Q

(g) CR1L-4Q (h) VR1L-4Q (i) CR1Y-2B2Q

(j) VR1Y-2B2Q (k) CR1Y-4Q (l) VR1Y-4Q

Figure K.5: Jet compositions of $t + X$ events.

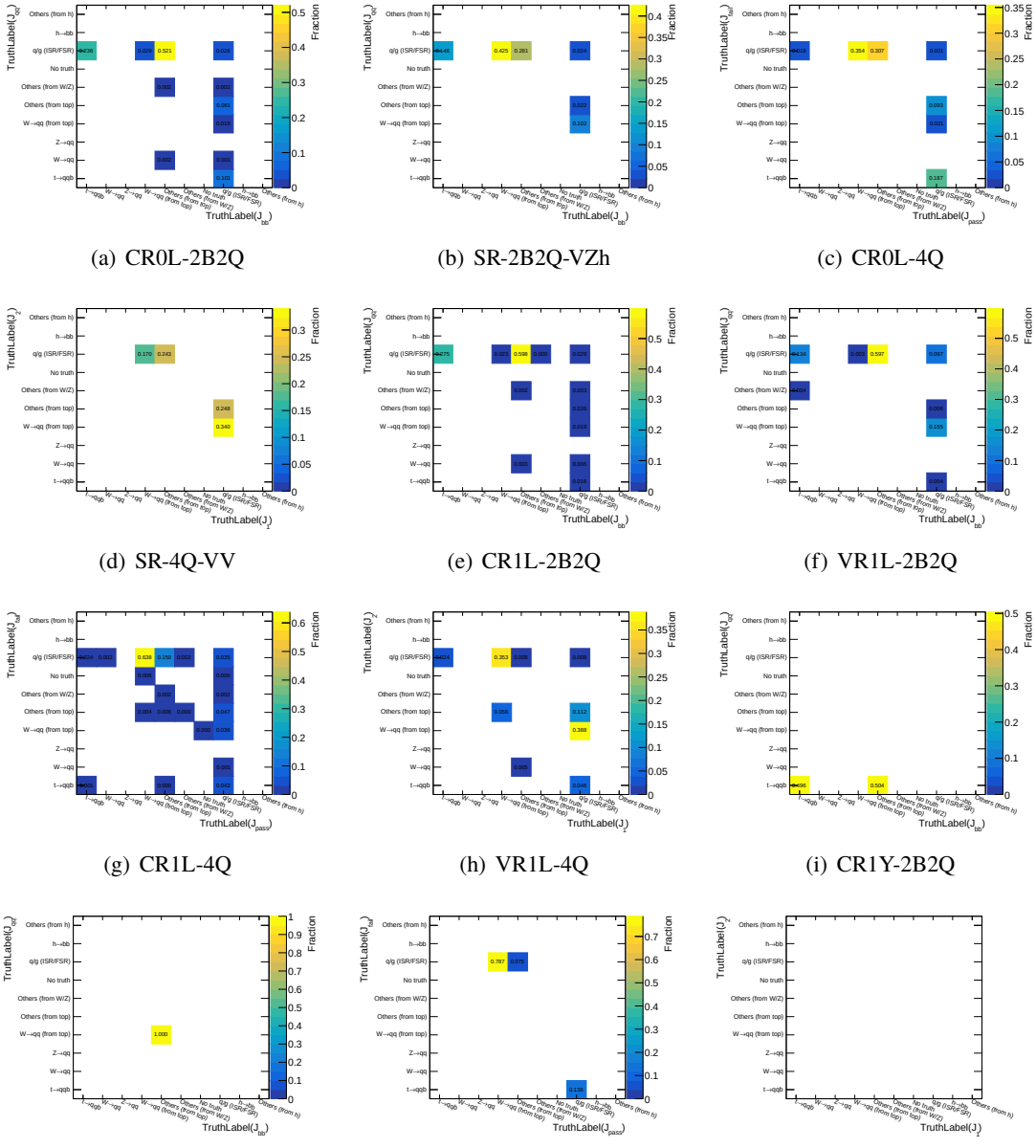

(a) CR0L-2B2Q (b) SR-2B2Q-VZh (c) CR0L-4Q

(d) SR-4Q-VV (e) CR1L-2B2Q (f) VR1L-2B2Q

(g) CR1L-4Q (h) VR1L-4Q (i) CR1Y-2B2Q

(j) VR1Y-2B2Q (k) CR1Y-4Q (l) VR1Y-4Q

Figure K.6: Jet compositions of $t\bar{t}$ events.

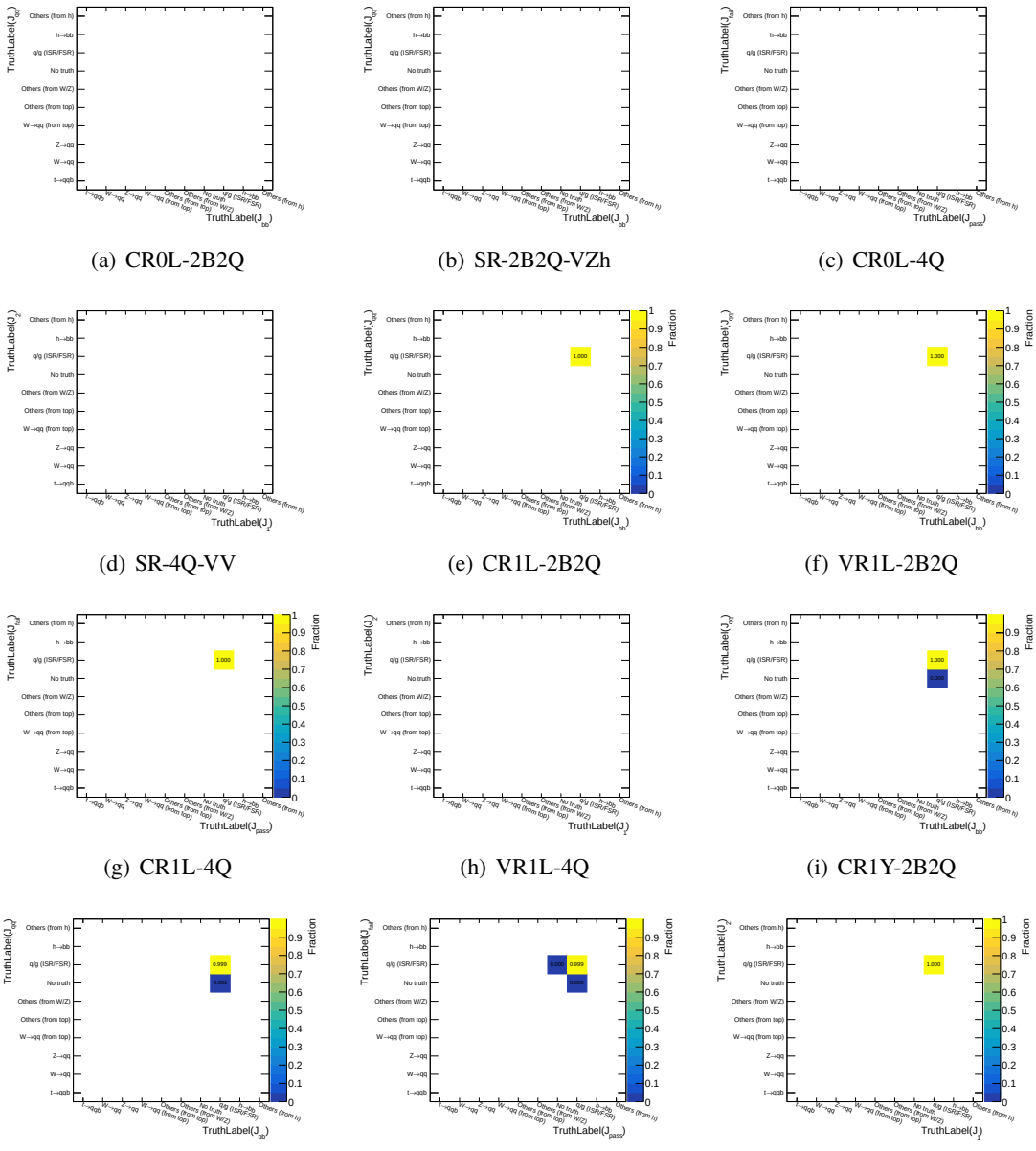

(a) CR0L-2B2Q (b) SR-2B2Q-VZh (c) CR0L-4Q

(d) SR-4Q-VV (e) CR1L-2B2Q (f) VR1L-2B2Q

(g) CR1L-4Q (h) VR1L-4Q (i) CR1Y-2B2Q

(j) VR1Y-2B2Q (k) CR1Y-4Q (l) VR1Y-4Q

Figure K.7: Jet compositions of γ + jets events.

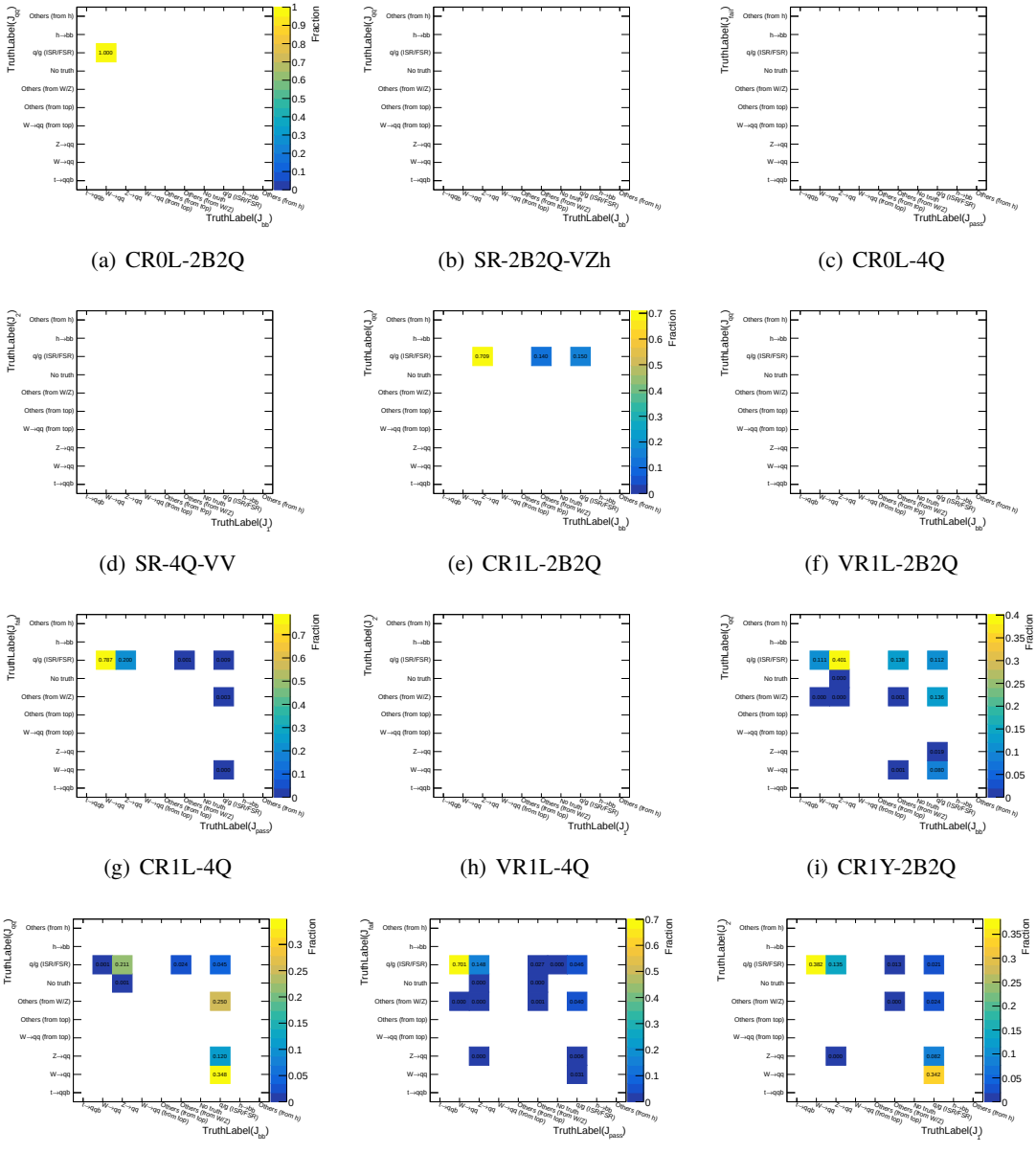

(a) CR0L-2B2Q (b) SR-2B2Q-VZh (c) CR0L-4Q

(d) SR-4Q-VV (e) CR1L-2B2Q (f) VR1L-2B2Q

(g) CR1L-4Q (h) VR1L-4Q (i) CR1Y-2B2Q

(j) VR1Y-2B2Q (k) CR1Y-4Q (l) VR1Y-4Q

Figure K.8: Jet compositions of $V\gamma$ events.

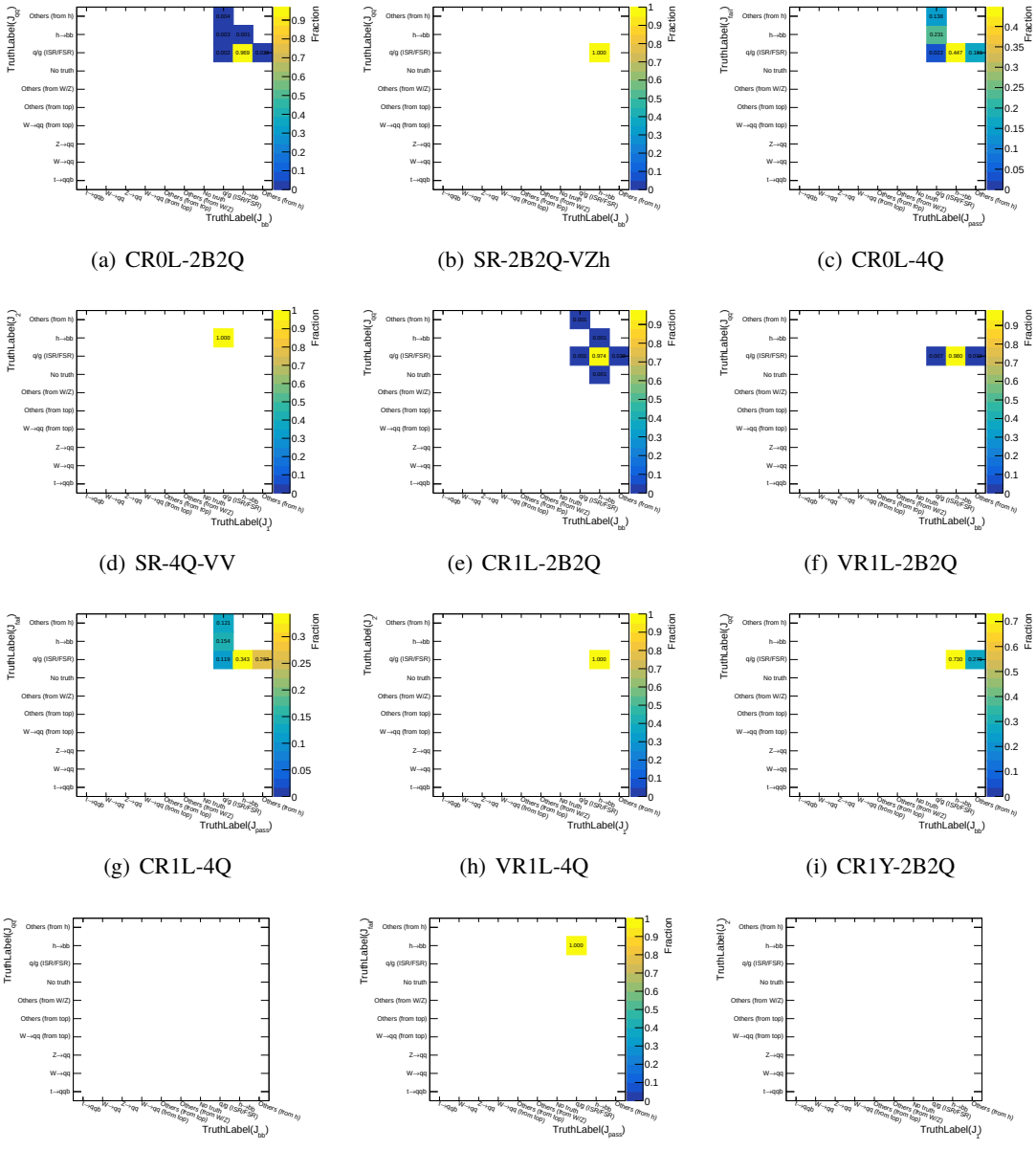

(a) CR0L-2B2Q (b) SR-2B2Q-VZh (c) CR0L-4Q

(d) SR-4Q-VV (e) CR1L-2B2Q (f) VR1L-2B2Q

(g) CR1L-4Q (h) VR1L-4Q (i) CR1Y-2B2Q

(j) VR1Y-2B2Q (k) CR1Y-4Q (l) VR1Y-4Q

Figure K.9: Jet compositions of higgs events.

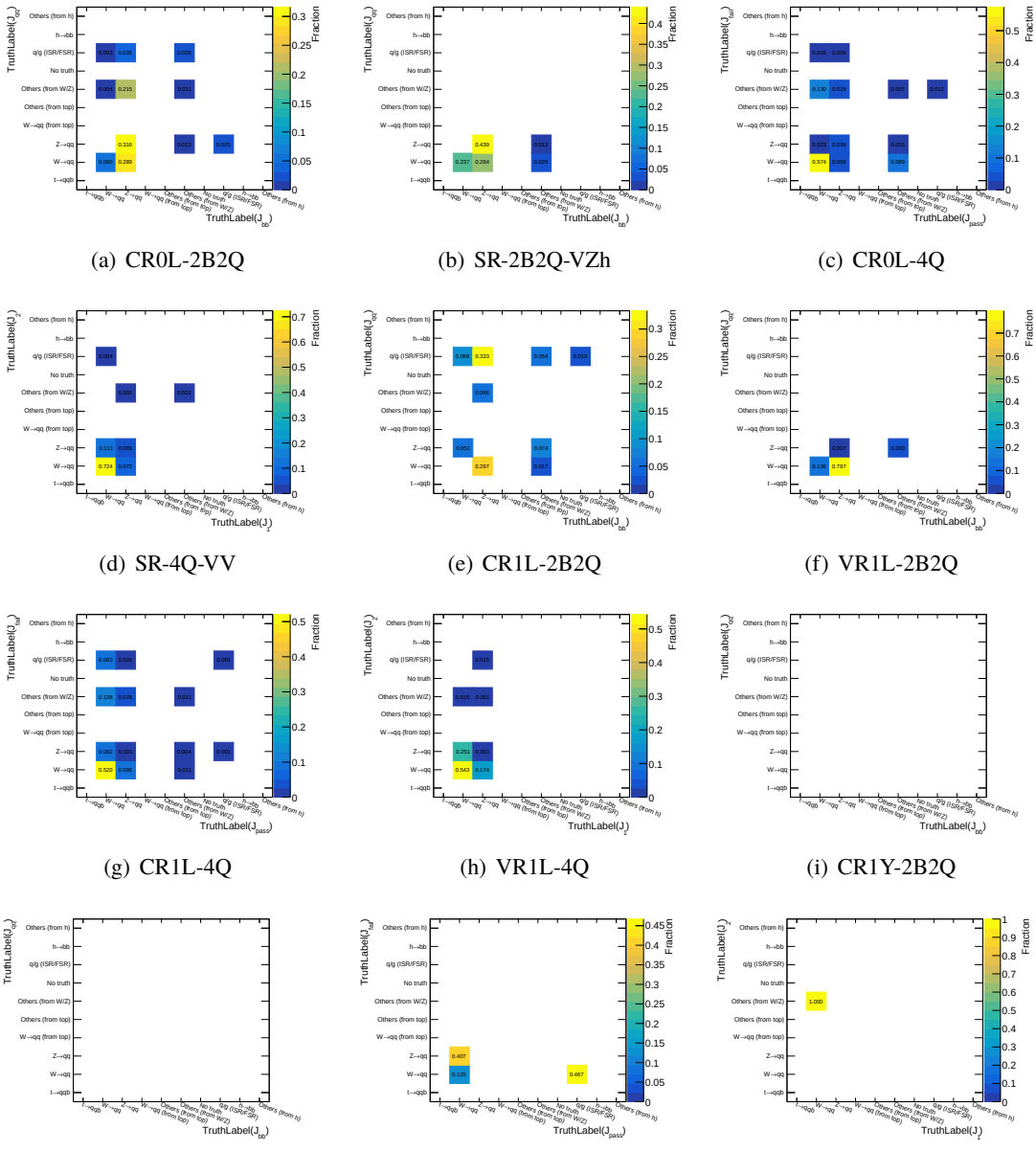

(a) CR0L-2B2Q (b) SR-2B2Q-VZh (c) CR0L-4Q

(d) SR-4Q-VV (e) CR1L-2B2Q (f) VR1L-2B2Q

(g) CR1L-4Q (h) VR1L-4Q (i) CR1Y-2B2Q

(j) VR1Y-2B2Q (k) CR1Y-4Q (l) VR1Y-4Q

Figure K.10: Jet compositions of triboson events.

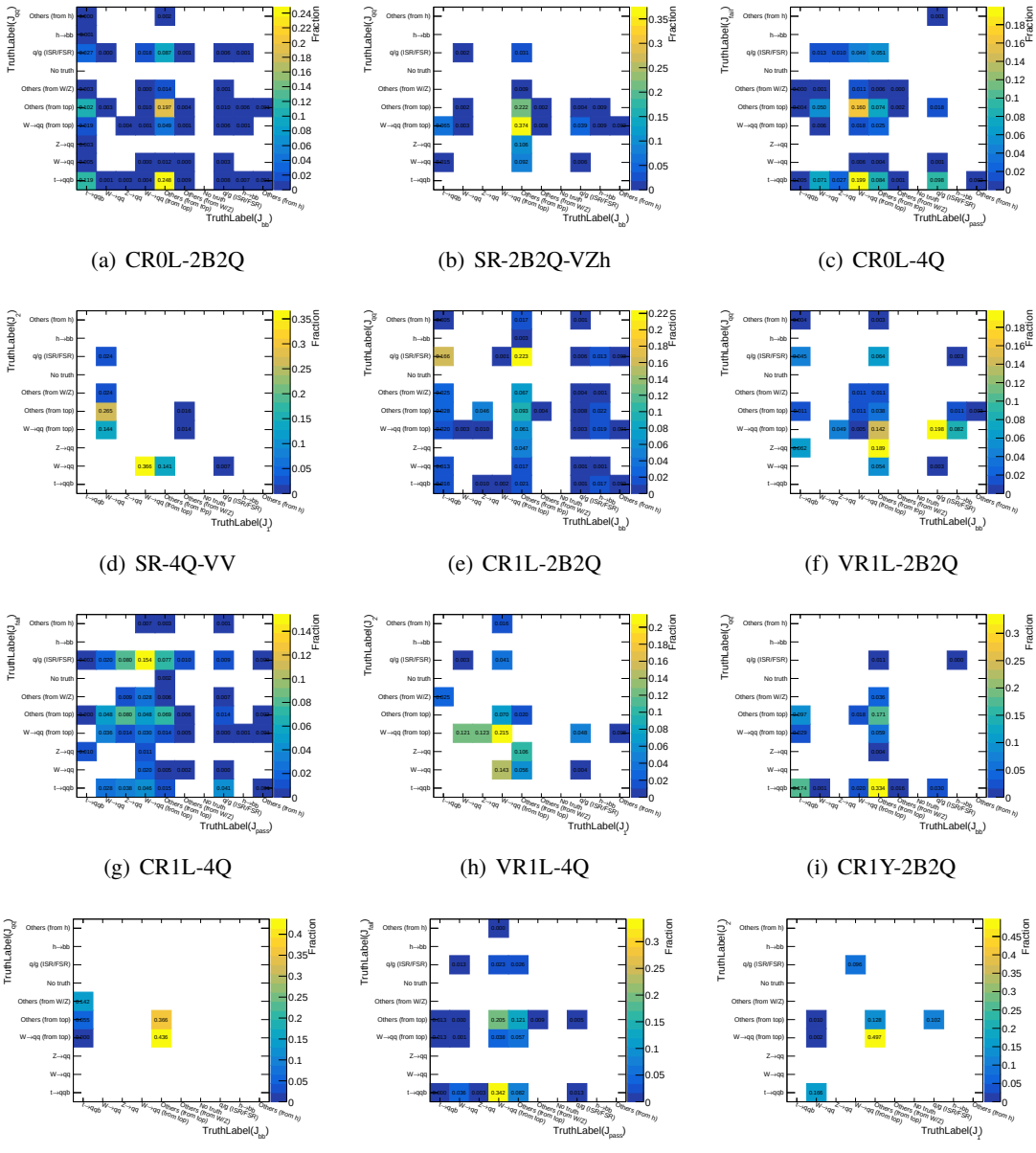

(a) CR0L-2B2Q (b) SR-2B2Q-VZh (c) CR0L-4Q

(d) SR-4Q-VV (e) CR1L-2B2Q (f) VR1L-2B2Q

(g) CR1L-4Q (h) VR1L-4Q (i) CR1Y-2B2Q

(j) VR1Y-2B2Q (k) CR1Y-4Q (l) VR1Y-4Q

Figure K.11: Jet compositions of $t\bar{t} + X$ events.

L Signal Contamination in 1L/1Y-CRs/VRs

Signal contaminations in CR0L-4Q and CR0L-2B2Q are shown in Figure L.1, L.2. Signal contaminations in CRs/VRs of the 1L/1Y categories are shown in Figure L.3-L.10.

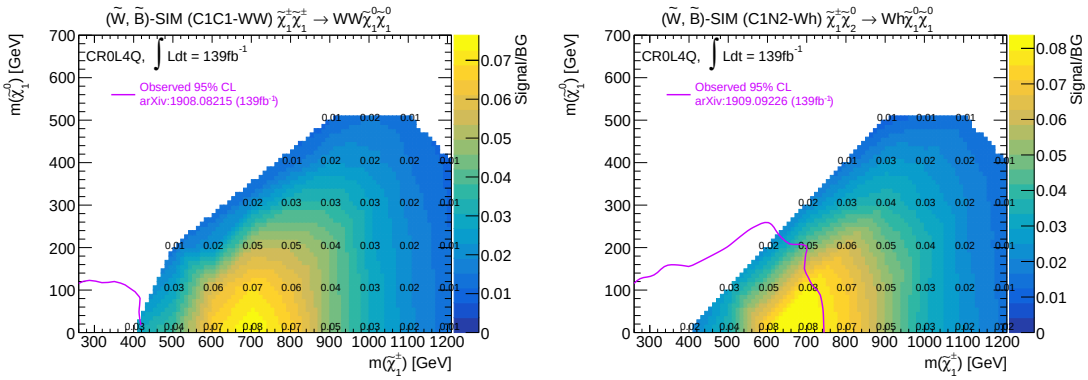

(a) $\tilde{\chi}_1^+\tilde{\chi}_1^- \rightarrow WW\tilde{\chi}_1^0\tilde{\chi}_1^0$ of $(\tilde{W},\tilde{B})$-SIM

(b) $\tilde{\chi}_1^{\pm}\tilde{\chi}_2^0 \rightarrow Wh\tilde{\chi}_1^0\tilde{\chi}_1^0$ of $(\tilde{W},\tilde{B})$-SIM

Figure L.1: Signal contamination of C1C1-WW and C1N2-Wh signals relative to the total BG in CR0L-4Q. Previous searches exclude regions surrounded by lines.

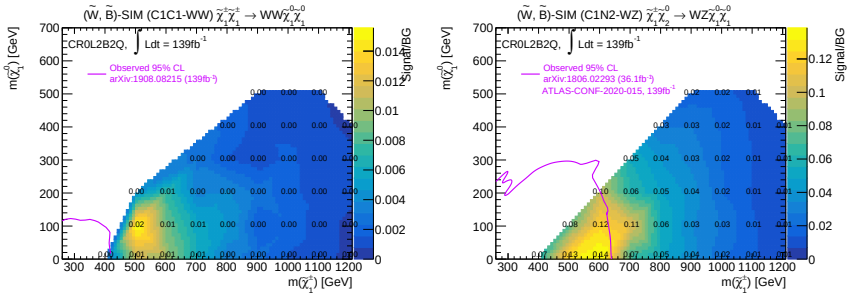

(a) $\tilde{\chi}_1^+\tilde{\chi}_1^- \rightarrow WW\tilde{\chi}_1^0\tilde{\chi}_1^0$ of $(\tilde{W},\tilde{B})$-SIM

(b) $\tilde{\chi}_1^{\pm}\tilde{\chi}_2^0 \rightarrow WZ\tilde{\chi}_1^0\tilde{\chi}_1^0$ of $(\tilde{W},\tilde{B})$-SIM

Figure L.2: Signal contamination of C1C1-WW and C1N2-WZ signals relative to the total BG in CR0L-2B2Q. Previous searches exclude regions surrounded by lines.

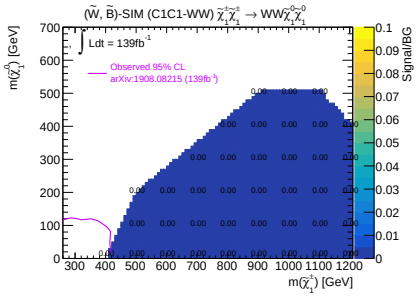

(a) $\tilde{\chi}_1^+\tilde{\chi}_1^- \rightarrow WW\tilde{\chi}_1^0\tilde{\chi}_1^0$ of $(\tilde{W},\tilde{B})$-SIM

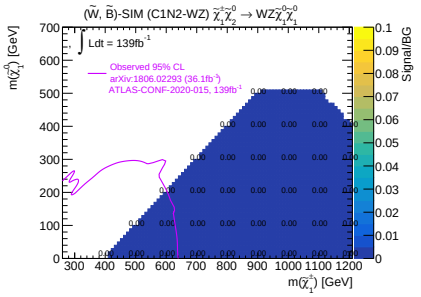

(b) $\tilde{\chi}_1^\pm\tilde{\chi}_2^0 \rightarrow WZ\tilde{\chi}_1^0\tilde{\chi}_1^0$ of $(\tilde{W},\tilde{B})$-SIM

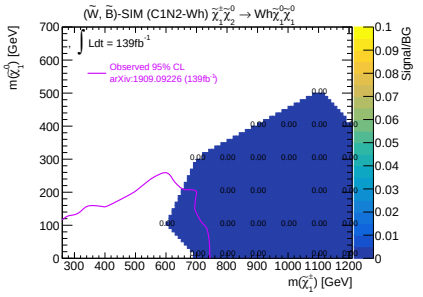

(c) $\tilde{\chi}_1^\pm\tilde{\chi}_2^0 \rightarrow Wh\tilde{\chi}_1^0\tilde{\chi}_1^0$ of $(\tilde{W},\tilde{B})$-SIM

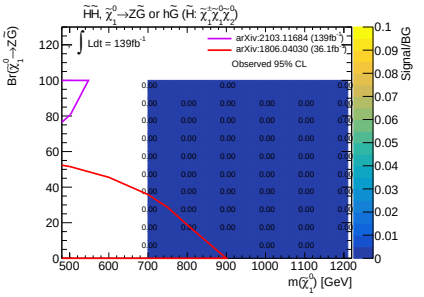

(d) $(\tilde{H},\tilde{G})$

Figure L.3: Signal contamination relative to the total BG in CR1L4Q. Previous searches exclude regions surrounded by lines.

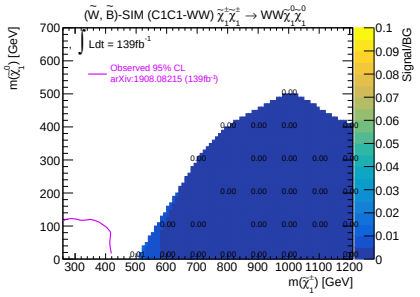

(a) $\tilde{\chi}_1^+\tilde{\chi}_1^- \rightarrow WW\tilde{\chi}_1^0\tilde{\chi}_1^0$ of $(\tilde{W},\tilde{B})$-SIM

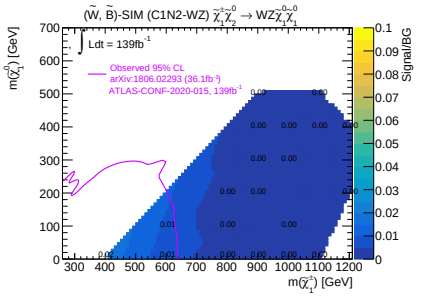

(b) $\tilde{\chi}_1^\pm\tilde{\chi}_2^0 \rightarrow WZ\tilde{\chi}_1^0\tilde{\chi}_1^0$ of $(\tilde{W},\tilde{B})$-SIM

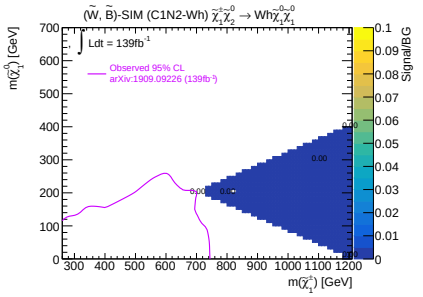

(c) $\tilde{\chi}_1^\pm\tilde{\chi}_2^0 \rightarrow Wh\tilde{\chi}_1^0\tilde{\chi}_1^0$ of $(\tilde{W},\tilde{B})$-SIM

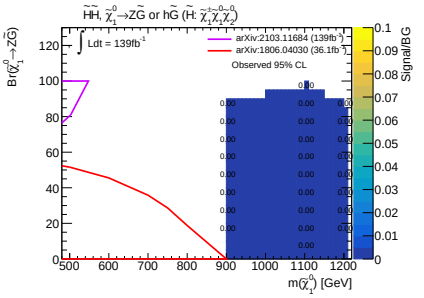

(d) $(\tilde{H},\tilde{G})$

Figure L.4: Signal contamination relative to the total BG in VR1L4Q. Previous searches exclude regions surrounded by lines.

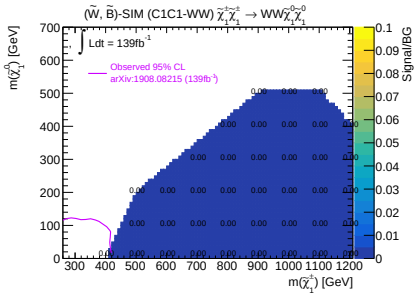

(a) $\tilde{\chi}_1^+\tilde{\chi}_1^- \to WW\tilde{\chi}_1^0\tilde{\chi}_1^0$ of $(\tilde{W},\tilde{B})$-SIM

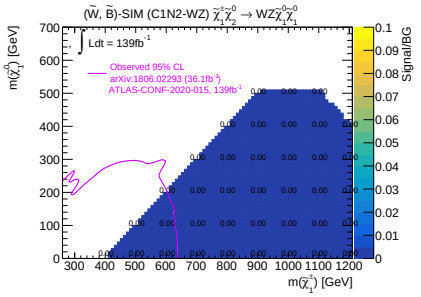

(b) $\tilde{\chi}_1^\pm\tilde{\chi}_2^0 \to WZ\tilde{\chi}_1^0\tilde{\chi}_1^0$ of $(\tilde{W},\tilde{B})$-SIM

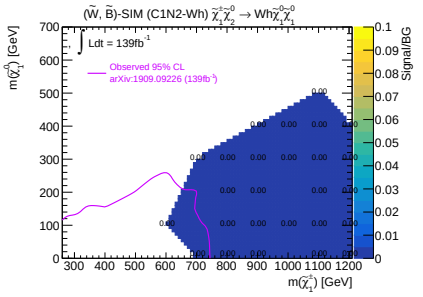

(c) $\tilde{\chi}_1^\pm\tilde{\chi}_2^0 \to Wh\tilde{\chi}_1^0\tilde{\chi}_1^0$ of $(\tilde{W},\tilde{B})$-SIM

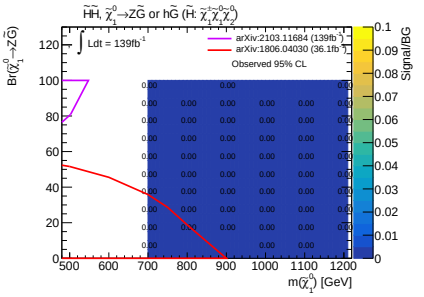

(d) $(\tilde{H},\tilde{G})$

Figure L.5: Signal contamination relative to the total BG in CR1Y4Q. Previous searches exclude regions surrounded by lines.

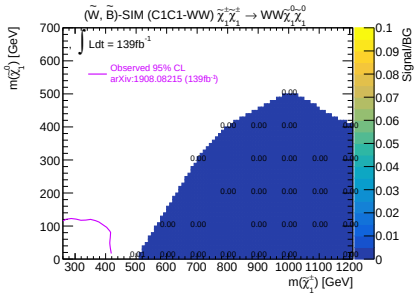

(a) $\tilde{\chi}_1^+\tilde{\chi}_1^- \to WW\tilde{\chi}_1^0\tilde{\chi}_1^0$ of $(\tilde{W},\tilde{B})$-SIM

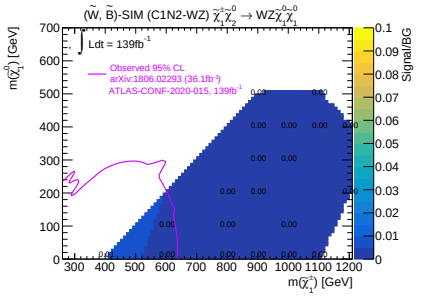

(b) $\tilde{\chi}_1^\pm\tilde{\chi}_2^0 \to WZ\tilde{\chi}_1^0\tilde{\chi}_1^0$ of $(\tilde{W},\tilde{B})$-SIM

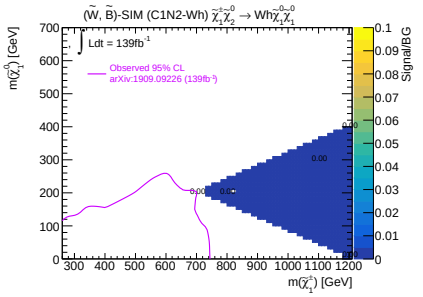

(c) $\tilde{\chi}_1^\pm\tilde{\chi}_2^0 \to Wh\tilde{\chi}_1^0\tilde{\chi}_1^0$ of $(\tilde{W},\tilde{B})$-SIM

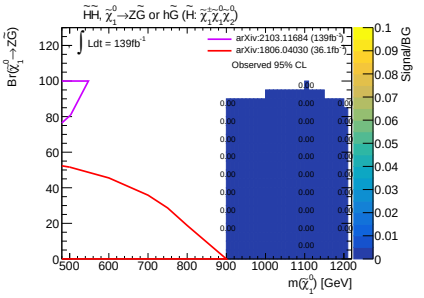

(d) $(\tilde{H},\tilde{G})$

Figure L.6: Signal contamination relative to the total BG in VR1Y4Q. Previous searches exclude regions surrounded by lines.

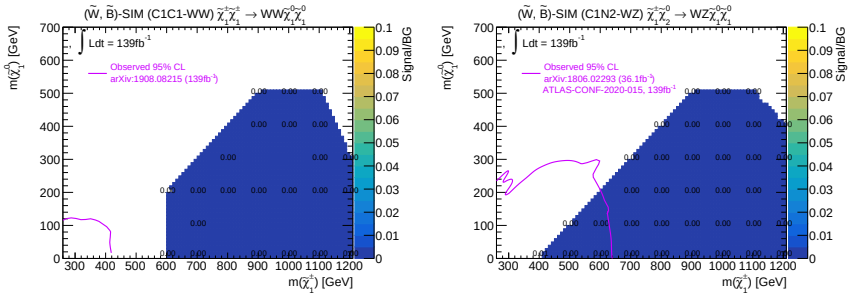

(a) $\tilde{\chi}_1^+\tilde{\chi}_1^- \rightarrow WW\tilde{\chi}_1^0\tilde{\chi}_1^0$ of $(\tilde{W},\tilde{B})$-SIM

(b) $\tilde{\chi}_1^\pm\tilde{\chi}_2^0 \rightarrow WZ\tilde{\chi}_1^0\tilde{\chi}_1^0$ of $(\tilde{W},\tilde{B})$-SIM

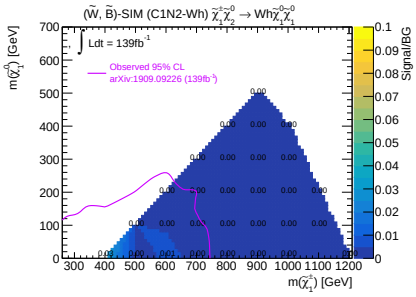

(c) $\tilde{\chi}_1^\pm\tilde{\chi}_2^0 \rightarrow Wh\tilde{\chi}_1^0\tilde{\chi}_1^0$ of $(\tilde{W},\tilde{B})$-SIM

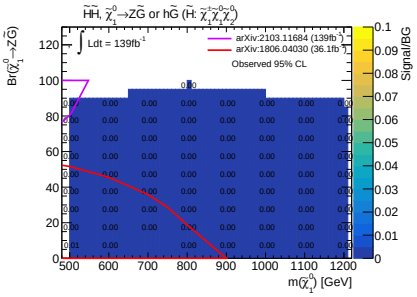

(d) $(\tilde{H},\tilde{G})$

Figure L.7: Signal contamination relative to the total BG in CR1L2B2Q. Previous searches exclude regions surrounded by lines.

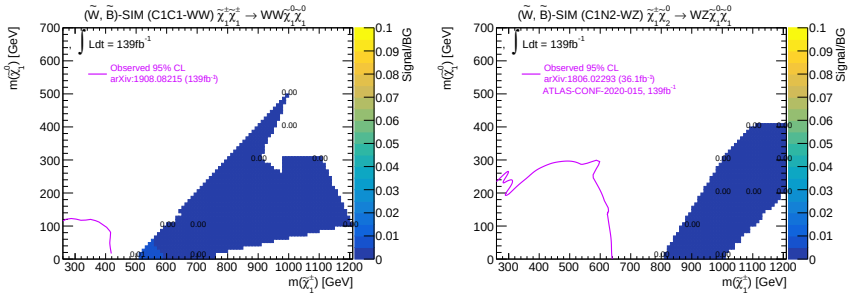

(a) $\tilde{\chi}_1^+\tilde{\chi}_1^- \rightarrow WW\tilde{\chi}_1^0\tilde{\chi}_1^0$ of $(\tilde{W},\tilde{B})$-SIM

(b) $\tilde{\chi}_1^\pm\tilde{\chi}_2^0 \rightarrow WZ\tilde{\chi}_1^0\tilde{\chi}_1^0$ of $(\tilde{W},\tilde{B})$-SIM

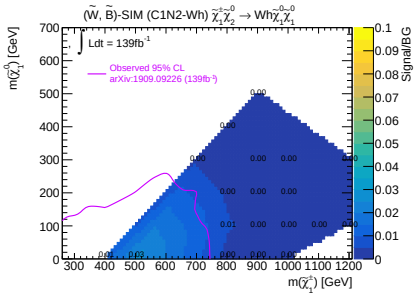

(c) $\tilde{\chi}_1^\pm\tilde{\chi}_2^0 \rightarrow Wh\tilde{\chi}_1^0\tilde{\chi}_1^0$ of $(\tilde{W},\tilde{B})$-SIM

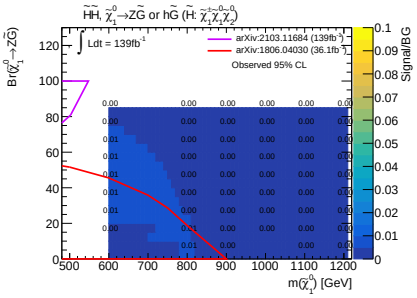

(d) $(\tilde{H},\tilde{G})$

Figure L.8: Signal contamination relative to the total BG in VR1L2B2Q. Previous searches exclude regions surrounded by lines.

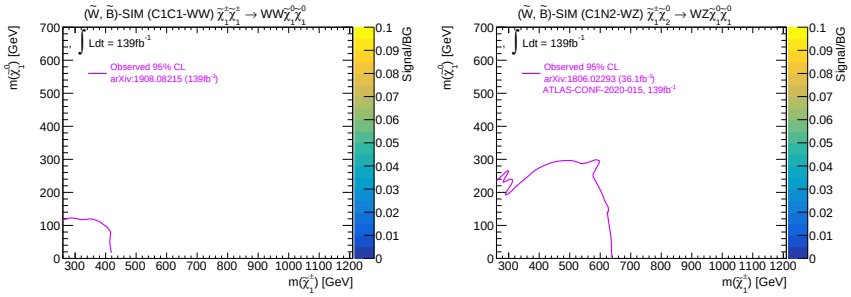

(a) $\tilde{\chi}_1^+\tilde{\chi}_1^- \to WW\tilde{\chi}_1^0\tilde{\chi}_1^0$ of $(\tilde{W},\tilde{B})$-SIM

(b) $\tilde{\chi}_1^\pm\tilde{\chi}_2^0 \to WZ\tilde{\chi}_1^0\tilde{\chi}_1^0$ of $(\tilde{W},\tilde{B})$-SIM

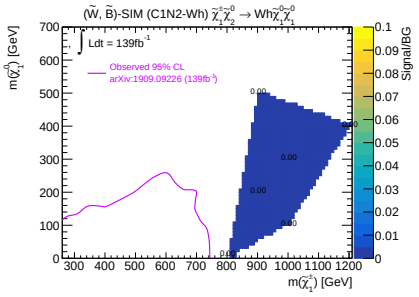

(c) $\tilde{\chi}_1^\pm\tilde{\chi}_2^0 \to Wh\tilde{\chi}_1^0\tilde{\chi}_1^0$ of $(\tilde{W},\tilde{B})$-SIM

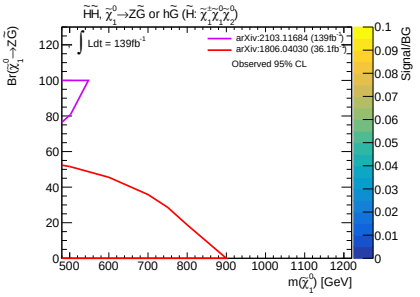

(d) $(\tilde{H},\tilde{G})$

Figure L.9: Signal contamination relative to the total BG in CR1Y2B2Q. Previous searches exclude regions surrounded by lines.

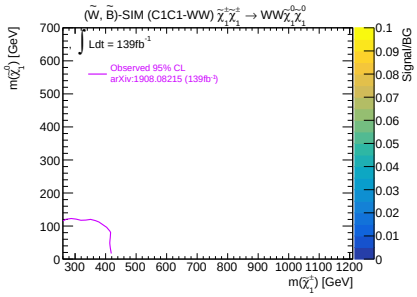

(a) $\tilde{\chi}_1^+\tilde{\chi}_1^- \to WW\tilde{\chi}_1^0\tilde{\chi}_1^0$ of $(\tilde{W},\tilde{B})$-SIM

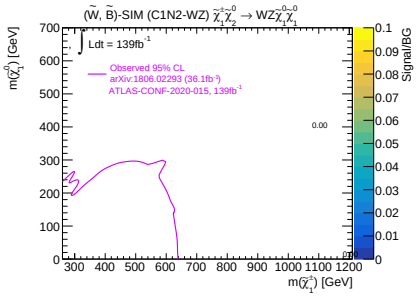

(b) $\tilde{\chi}_1^\pm\tilde{\chi}_2^0 \to WZ\tilde{\chi}_1^0\tilde{\chi}_1^0$ of $(\tilde{W},\tilde{B})$-SIM

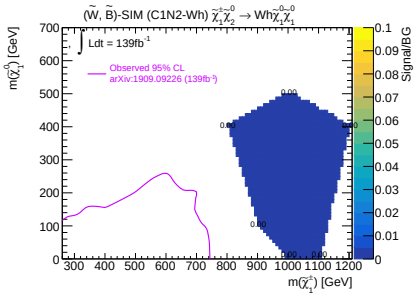

(c) $\tilde{\chi}_1^\pm\tilde{\chi}_2^0 \to Wh\tilde{\chi}_1^0\tilde{\chi}_1^0$ of $(\tilde{W},\tilde{B})$-SIM

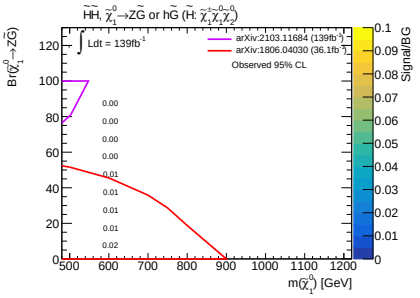

(d) $(\tilde{H},\tilde{G})$

Figure L.10: Signal contamination relative to the total BG in VR1Y2B2Q. Previous searches exclude regions surrounded by lines.

M Kinematic Distributions in CRs

Kinematic distributions in CRs are shown in Figure M.1-M.12. Black arrows represent the selection values. In CR-4Q bins, jet substructure variables with boson tagging requirements (pass or fail) are shown. D_2 distributions of $J_{\text{un-tagged}}$ have 2 components. Since D_2 and m^{comb} are correlated, the two peaks in the D_2 distributions represent the results of $V \to qq$ mass requirements. The peak in the lower D_2 value corresponds to jets that fail mass requirements of $V \to qq$ tagging, and the peak in the higher value corresponds to jets that pass mass requirements.

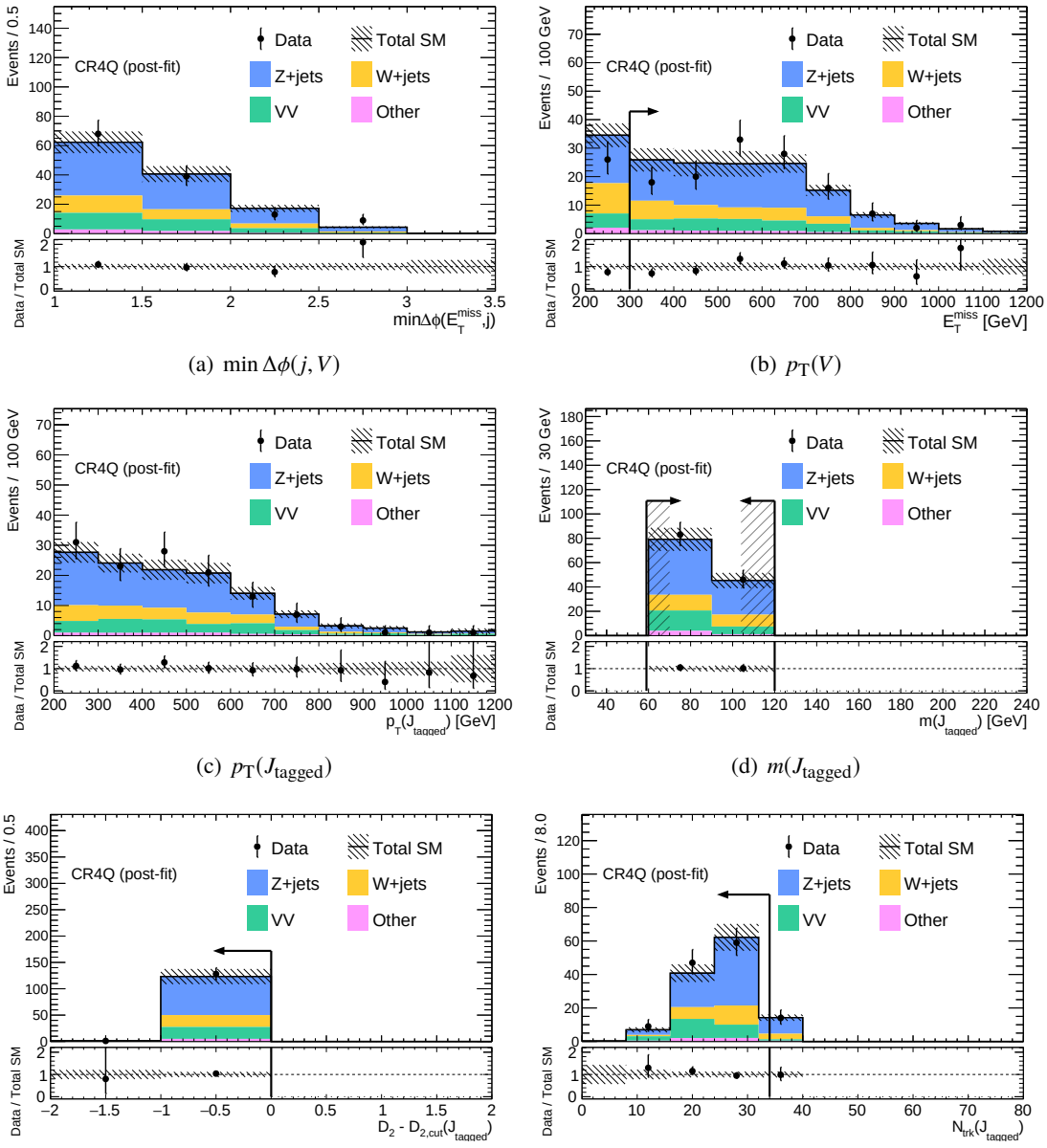

(a) $\min \Delta\phi(j, V)$ (b) $p_{\mathrm{T}}(V)$

(c) $p_{\mathrm{T}}(J_{\mathrm{tagged}})$ (d) $m(J_{\mathrm{tagged}})$

(e) $D_2(J_{\mathrm{tagged}}) - D_2(\mathrm{cut})$ (f) $n_{\mathrm{trk}}(J_{\mathrm{tagged}})$

Figure M.1: Distributions of $\min \Delta\phi(j, V)$ (a), $p_{\mathrm{T}}(V)$ (=$E_{\mathrm{T}}^{\mathrm{miss}}$) (b), and p_{T} (c), mass (d), D_2 (e), n_{trk} (f) of J_{tagged} in CR0L-4Q.

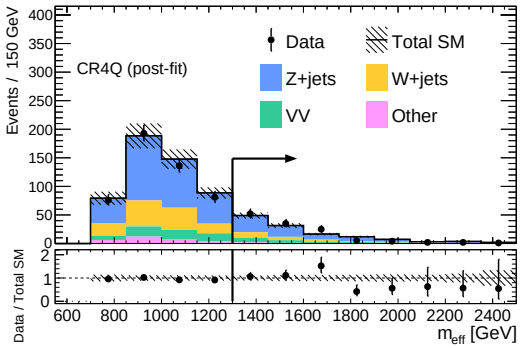

(a) $p_{\mathrm{T}}(V) + p_{\mathrm{T}}(J_1) + p_{\mathrm{T}}(J_2)$

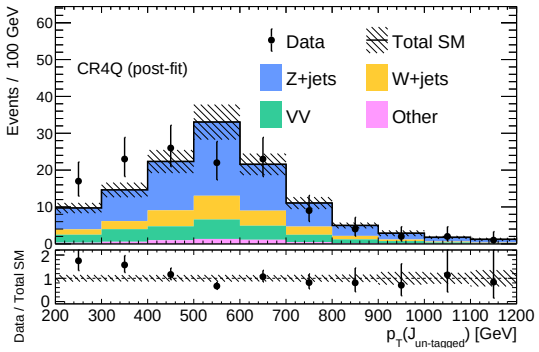

(b) $p_{\mathrm{T}}(J_{\text{un-tagged}})$

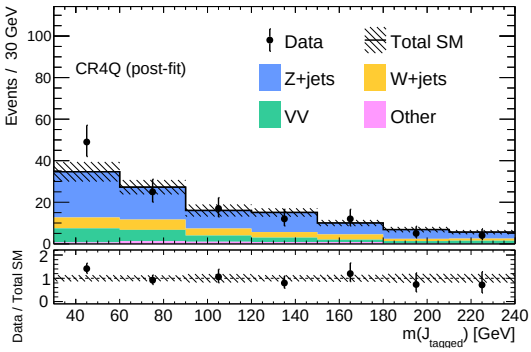

(c) $m(J_{\text{un-tagged}})$

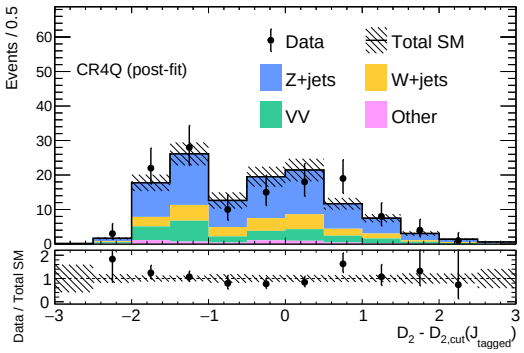

(d) $D_2(J_{\text{un-tagged}}) - D_2(\text{cut})$

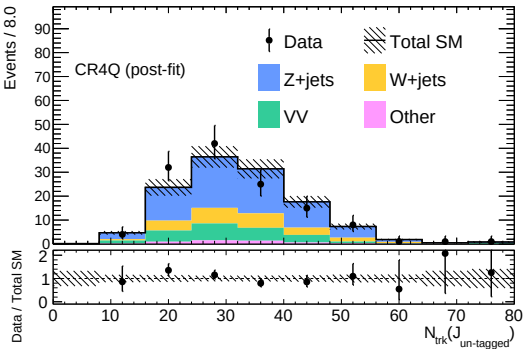

(e) $n_{\mathrm{trk}}(J_{\text{un-tagged}})$

Figure M.2: Distributions of $\min \Delta\phi(j, V)$ (a), $p_{\mathrm{T}}(V)$ (=$E_{\mathrm{T}}^{\mathrm{miss}}$) (b), and p_{T} (c), mass (d), D_2 (e), n_{trk} (f) of $J_{\text{un-tagged}}$ in CR0L-4Q.

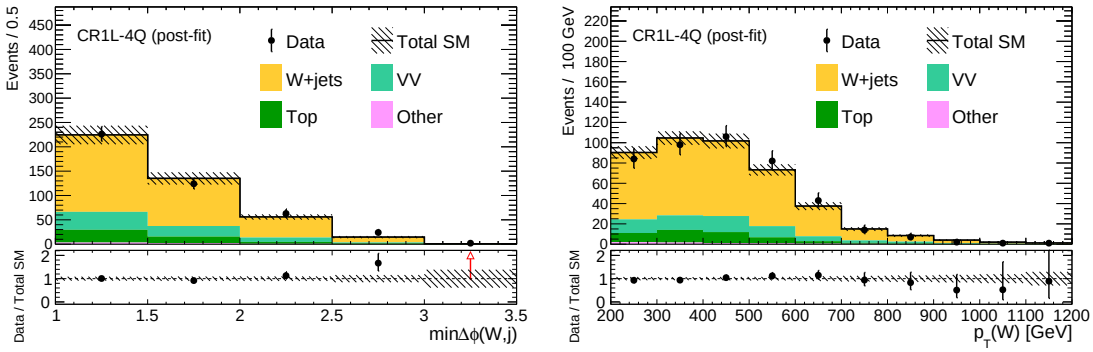

(a) $\min \Delta\phi(j, V)$

(b) $p_{\mathrm{T}}(V)$

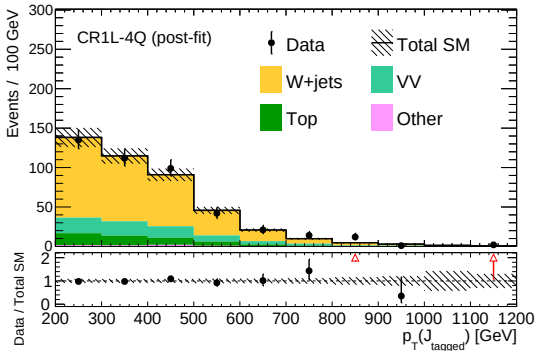

(c) $p_{\mathrm{T}}(J_{\mathrm{tagged}})$

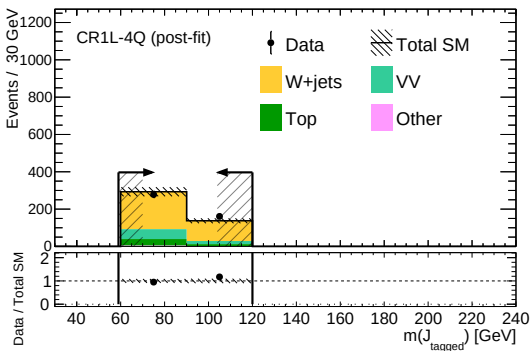

(d) $m(J_{\mathrm{tagged}})$

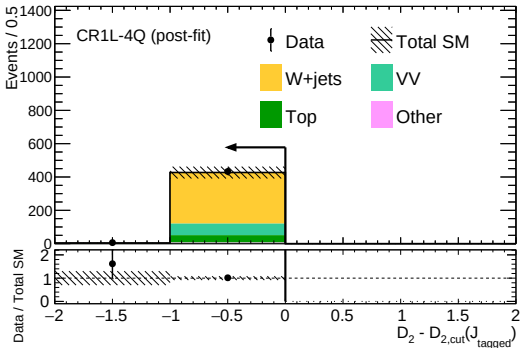

(e) $D_2(J_{\mathrm{tagged}}) - D_2(\mathrm{cut})$

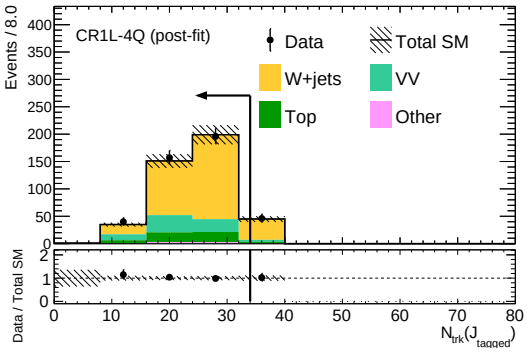

(f) $n_{\mathrm{trk}}(J_{\mathrm{tagged}})$

Figure M.3: Distributions of $\min \Delta\phi(j, V)$ (a), $p_{\mathrm{T}}(V)$ (=$E_{\mathrm{T}}^{\mathrm{miss}}$) (b), and p_{T} (c), mass (d), D_2 (e), n_{trk} (f) of J_{tagged} in CR1L-4Q.

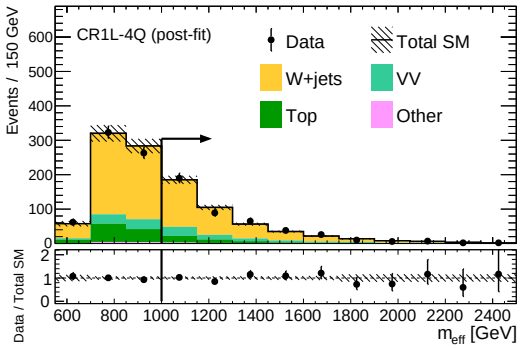

(a) $p_{\mathrm{T}}(V) + p_{\mathrm{T}}(J_1) + p_{\mathrm{T}}(J_2)$

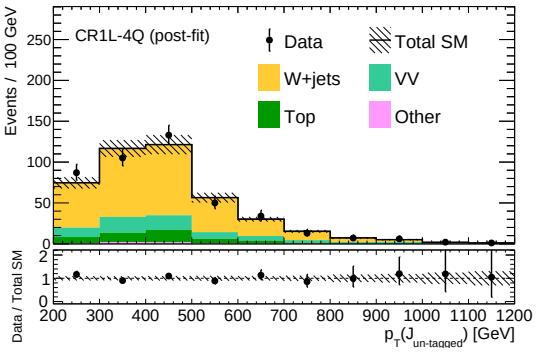

(b) $p_{\mathrm{T}}(J_{\text{un-tagged}})$

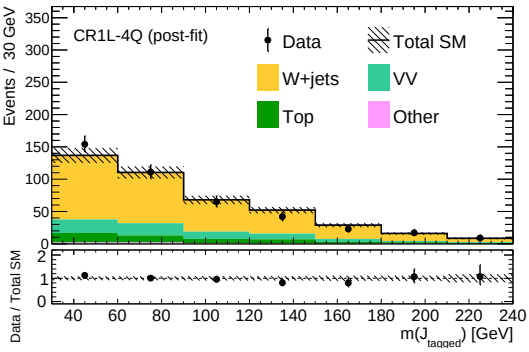

(c) $m(J_{\text{un-tagged}})$

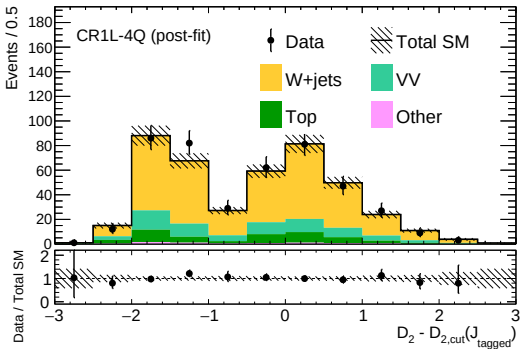

(d) $D_2(J_{\text{un-tagged}}) - D_2(\text{cut})$

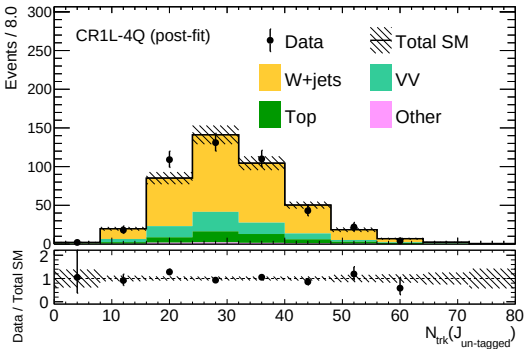

(e) $n_{\mathrm{trk}}(J_{\text{un-tagged}})$

Figure M.4: Distributions of $\min \Delta\phi(j, V)$ (a), $p_{\mathrm{T}}(V)$ (=$E_{\mathrm{T}}^{\mathrm{miss}}$) (b), and p_{T} (c), mass (d), D_2 (e), n_{trk} (f) of $J_{\text{un-tagged}}$ in CR1L-4Q.

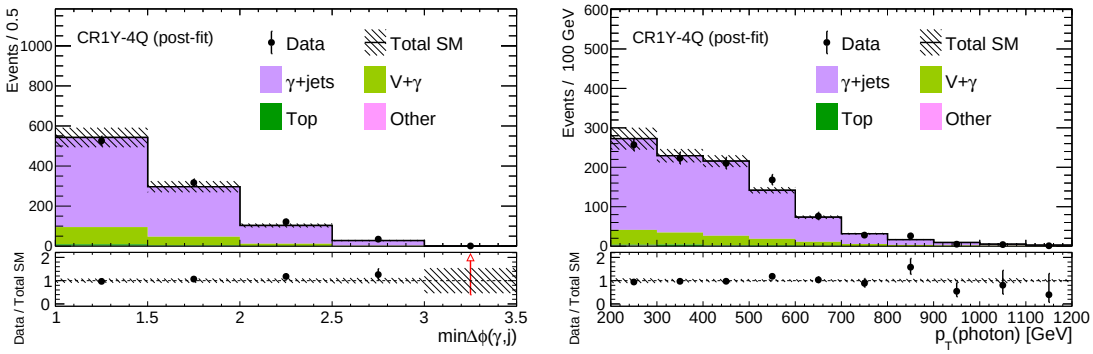

(a) $\min \Delta\phi(j, V)$

(b) $p_{\mathrm{T}}(V)$

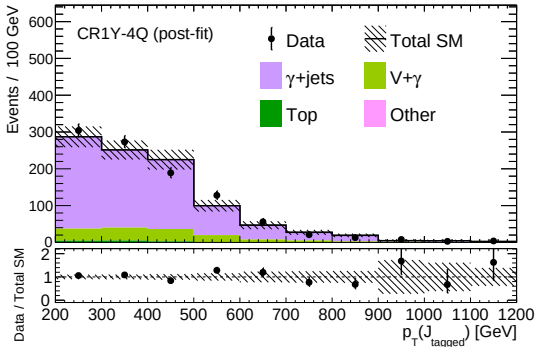

(c) $p_{\mathrm{T}}(J_{\mathrm{tagged}})$

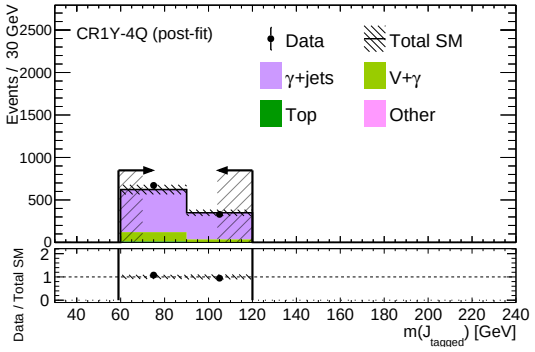

(d) $m(J_{\mathrm{tagged}})$

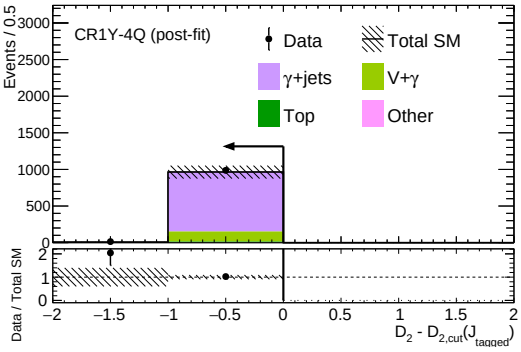

(e) $D_2(J_{\mathrm{tagged}}) - D_2(\mathrm{cut})$

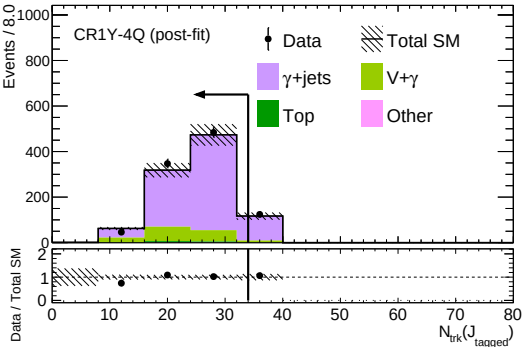

(f) $n_{\mathrm{trk}}(J_{\mathrm{tagged}})$

Figure M.5: Distributions of $\min \Delta\phi(j, V)$ (a), $p_{\mathrm{T}}(V)$ (=$E_{\mathrm{T}}^{\mathrm{miss}}$) (b), and p_{T} (c), mass (d), D_2 (e), n_{trk} (f) of J_{tagged} in CR1Y-4Q.

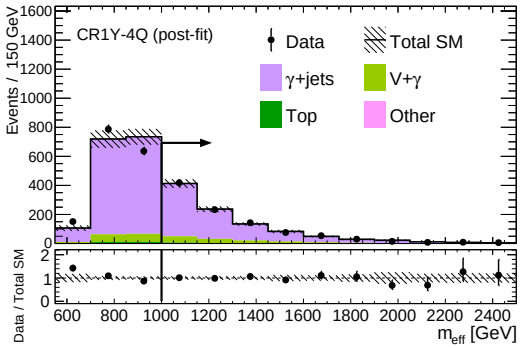

(a) $p_{\mathrm{T}}(V) + p_{\mathrm{T}}(J_1) + p_{\mathrm{T}}(J_2)$

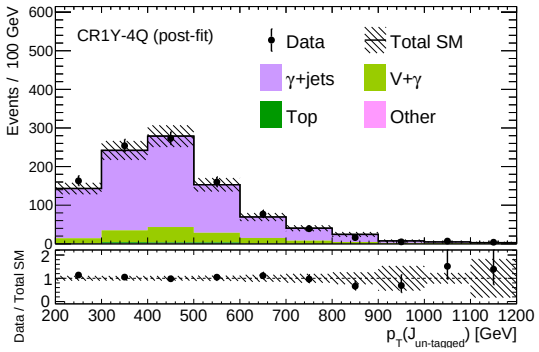

(b) $p_{\mathrm{T}}(J_{\text{un-tagged}})$

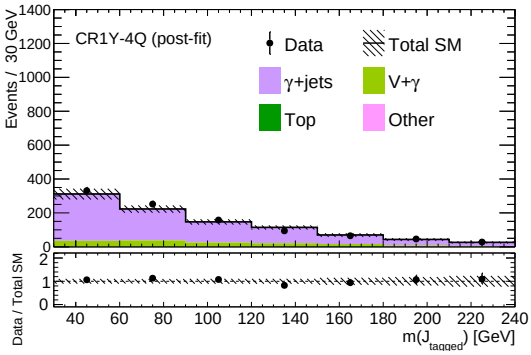

(c) $m(J_{\text{un-tagged}})$

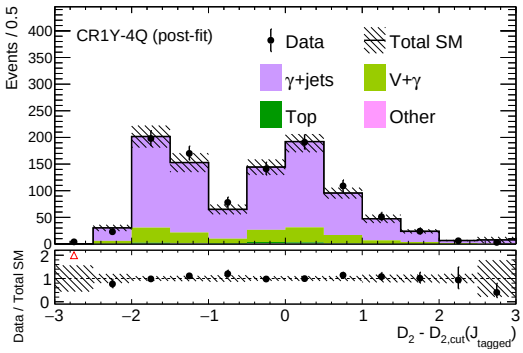

(d) $D_2(J_{\text{un-tagged}}) - D_2(\text{cut})$

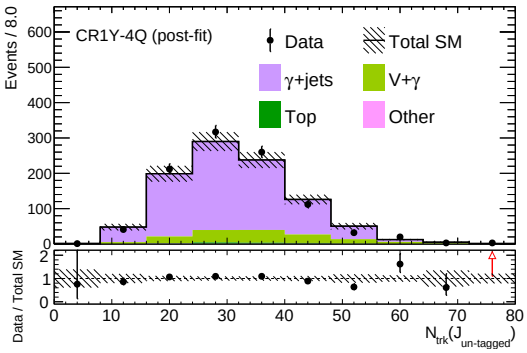

(e) $n_{\mathrm{trk}}(J_{\text{un-tagged}})$

Figure M.6: Distributions of $\min \Delta\phi(j, V)$ (a), $p_{\mathrm{T}}(V)$ (=$E_{\mathrm{T}}^{\mathrm{miss}}$) (b), and p_{T} (c), mass (d), D_2 (e), n_{trk} (f) of $J_{\text{un-tagged}}$ in CR1Y-4Q.

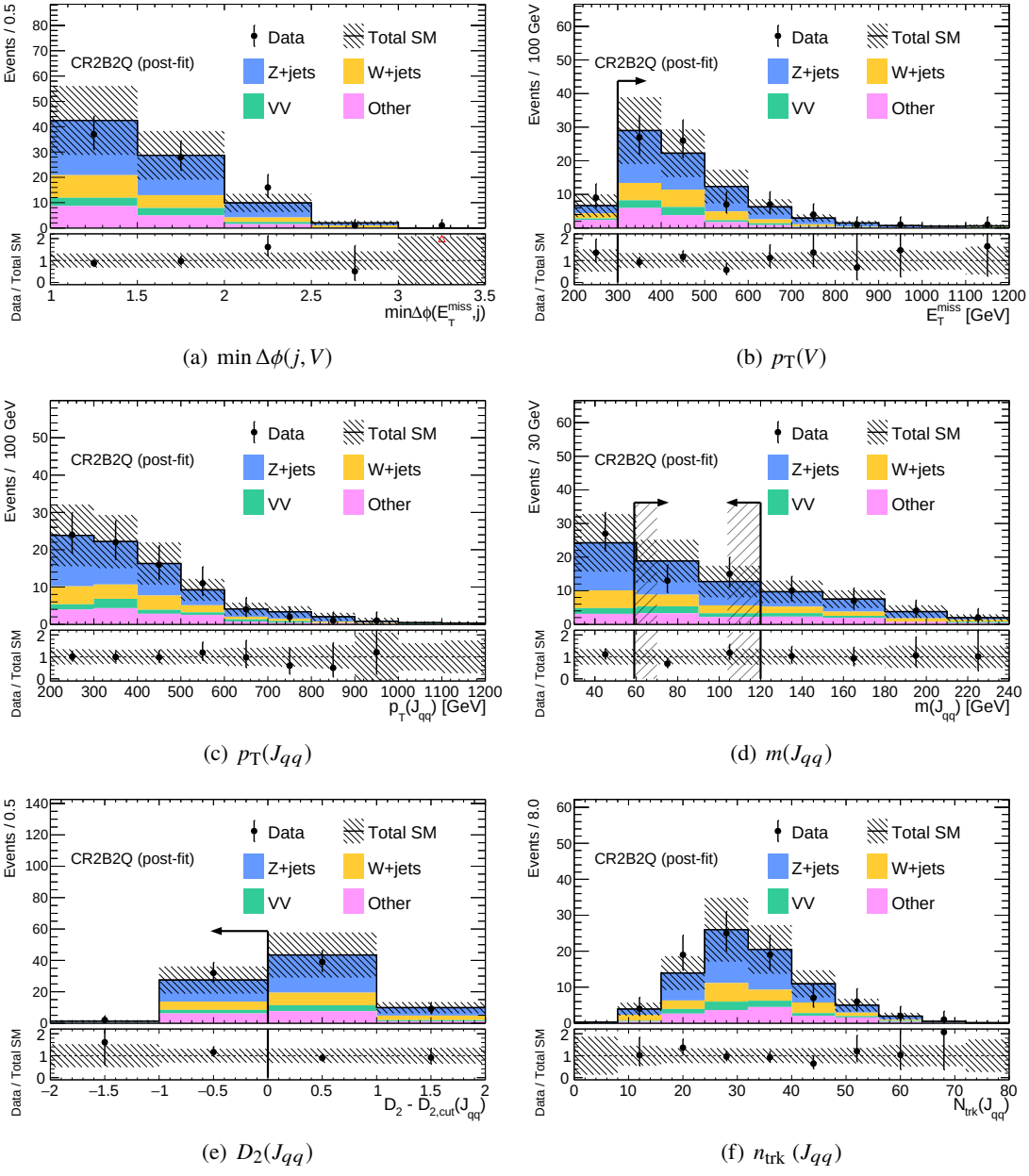

(a) $\min \Delta\phi(j, V)$ (b) $p_{\mathrm{T}}(V)$

(c) $p_{\mathrm{T}}(J_{qq})$ (d) $m(J_{qq})$

(e) $D_2(J_{qq})$ (f) n_{trk} (J_{qq})

Figure M.7: Distributions of $\min \Delta\phi(j, V)$ (a), $p_{\mathrm{T}}(V)$ (b), and p_{T} (c), mass (d), D_2 (e), n_{trk} (f) of J_{qq} in CR0L-2B2Q.

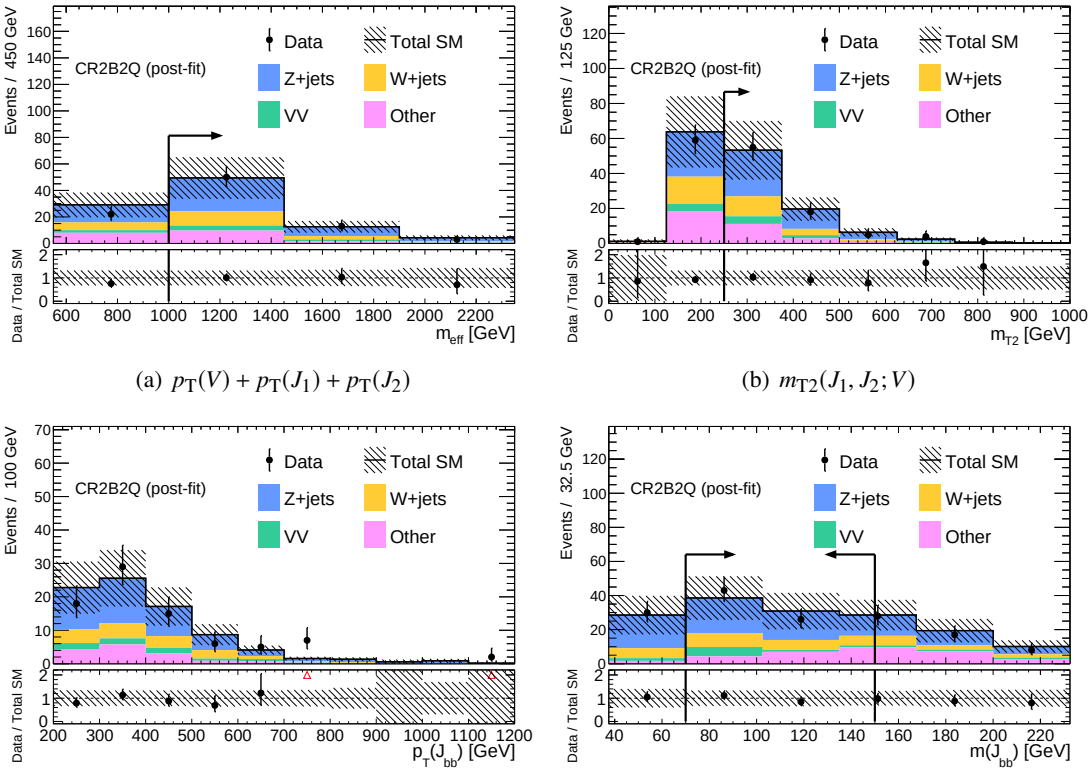

(a) $p_{\mathrm{T}}(V) + p_{\mathrm{T}}(J_1) + p_{\mathrm{T}}(J_2)$

(b) $m_{\mathrm{T2}}(J_1, J_2; V)$

(c) $p_{\mathrm{T}}(J_{bb})$

(d) mass (J_{bb})

Figure M.8: Distributions of $p_{\mathrm{T}}(V)+p_{\mathrm{T}}(J_1)+p_{\mathrm{T}}(J_2)$ (a), $m_{\mathrm{T2}}(J_1, J_2; V)$ (b) and p_{T} (c), mass (d) of J_{bb} in CR0L-2B2Q.

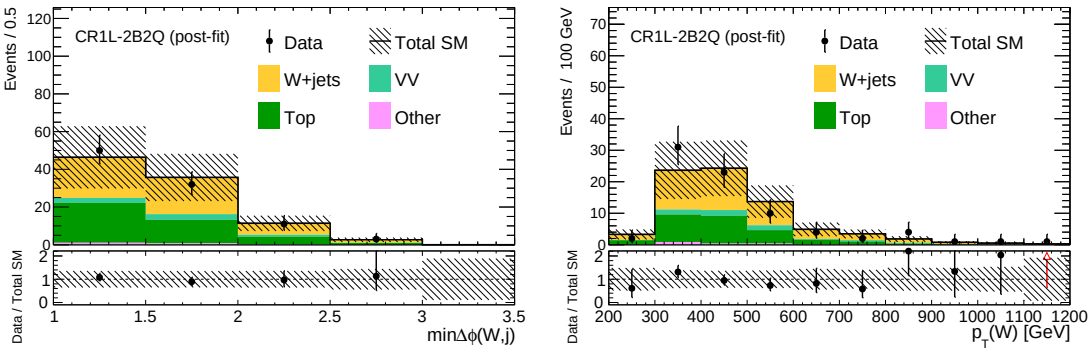

(a) $\min \Delta\phi(j, V)$

(b) $p_{\mathrm{T}}(V)$

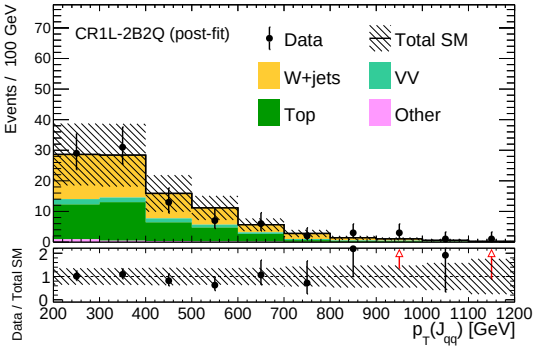

(c) $p_{\mathrm{T}}(J_{qq})$

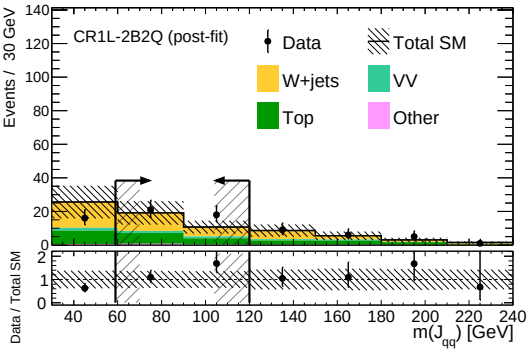

(d) $m(J_{qq})$

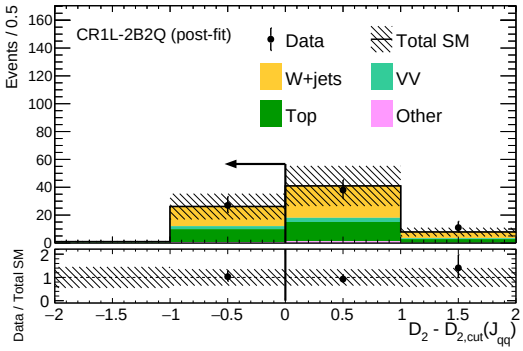

(e) $D_2(J_{qq})$

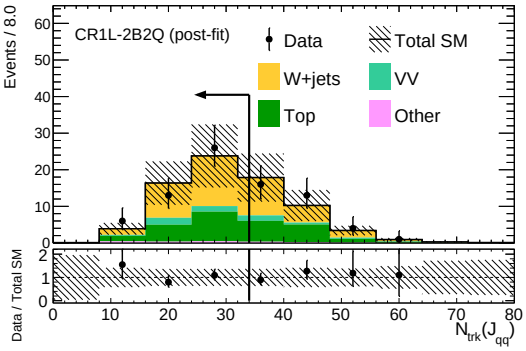

(f) n_{trk} (J_{qq})

Figure M.9: Distributions of $\min \Delta\phi(j, V)$ (a), $p_{\mathrm{T}}(V)$ (b), and p_{T} (c), mass (d), D_2 (e), n_{trk} (f) of J_{qq} in CR1L-2B2Q.

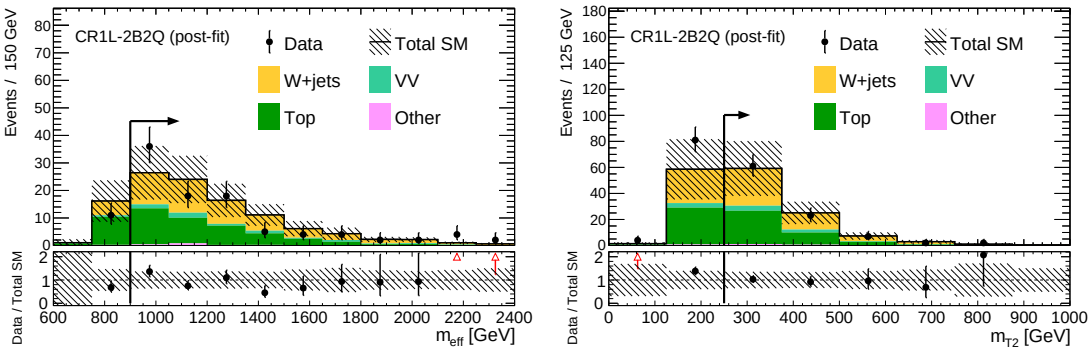

(a) $p_{\mathrm{T}}(V) + p_{\mathrm{T}}(J_1) + p_{\mathrm{T}}(J_2)$

(b) $m_{\mathrm{T2}}(J_1, J_2; V)$

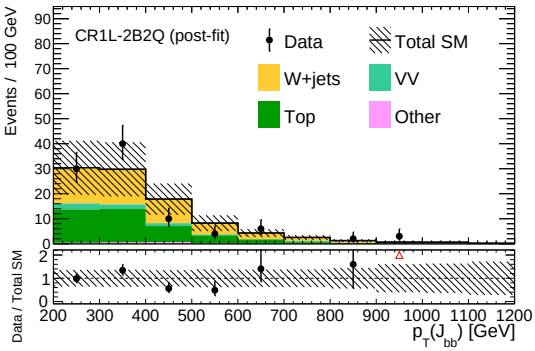

(c) $p_{\mathrm{T}}(J_{bb})$

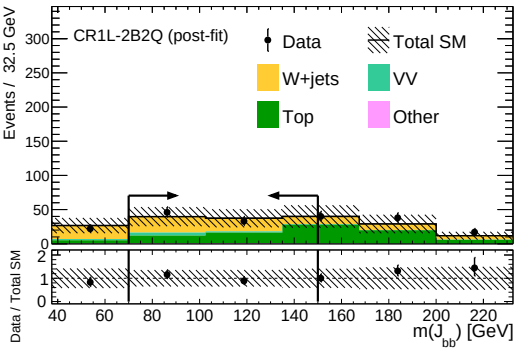

(d) mass (J_{bb})

Figure M.10: Distributions of $p_{\mathrm{T}}(V) + p_{\mathrm{T}}(J_1) + p_{\mathrm{T}}(J_2)$ (a), $m_{\mathrm{T2}}(J_1, J_2; V)$ (b) and p_{T} (c), mass (d) of J_{bb} in CR1L-2B2Q.

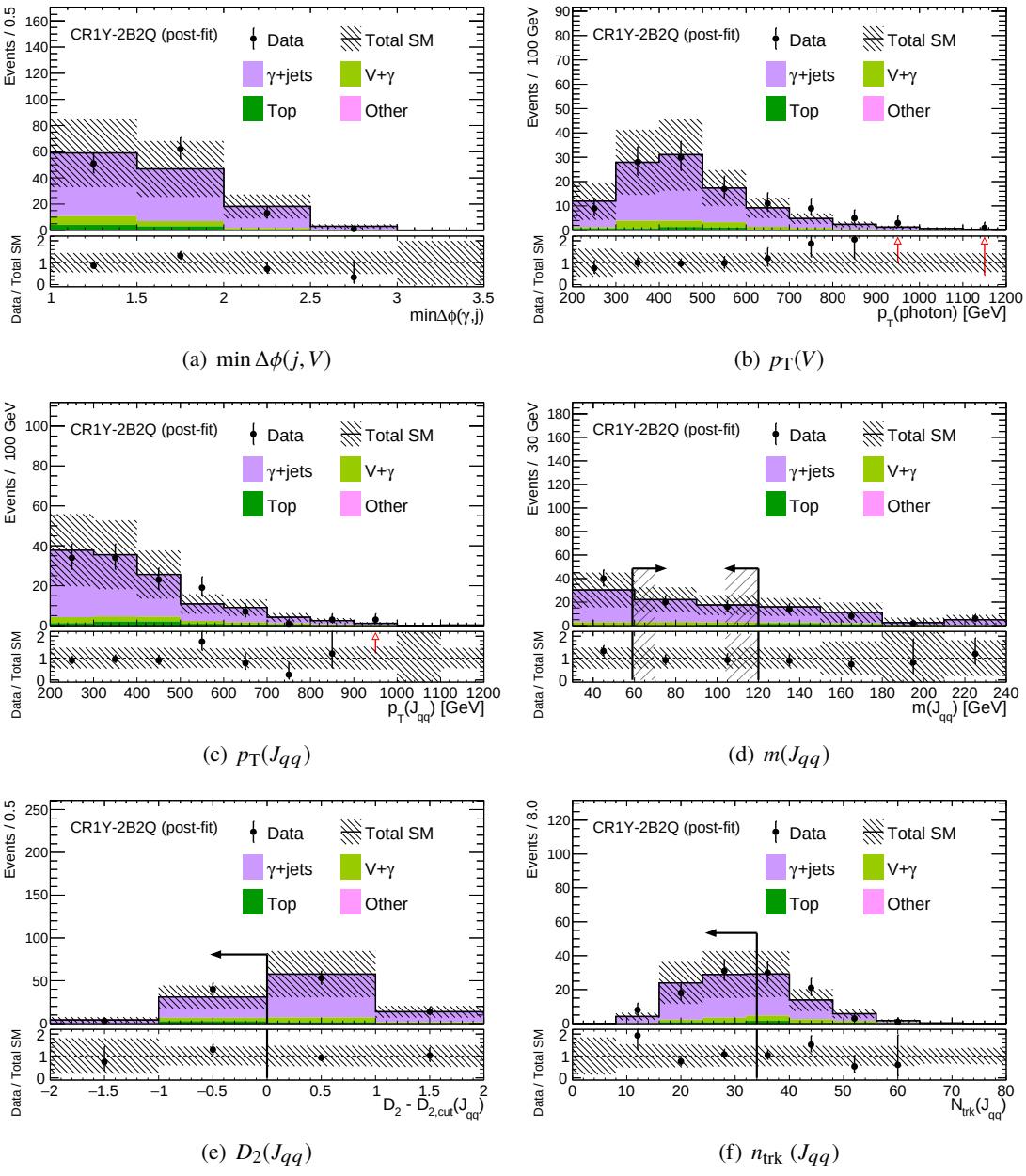

(a) $\min \Delta\phi(j, V)$ (b) $p_{\mathrm{T}}(V)$

(c) $p_{\mathrm{T}}(J_{qq})$ (d) $m(J_{qq})$

(e) $D_2(J_{qq})$ (f) n_{trk} (J_{qq})

Figure M.11: Distributions of $\min \Delta\phi(j, V)$ (a), $p_{\mathrm{T}}(V)$ (b), and p_{T} (c), mass (d), D_2 (e), n_{trk} (f) of J_{qq} in CR1Y-2B2Q.

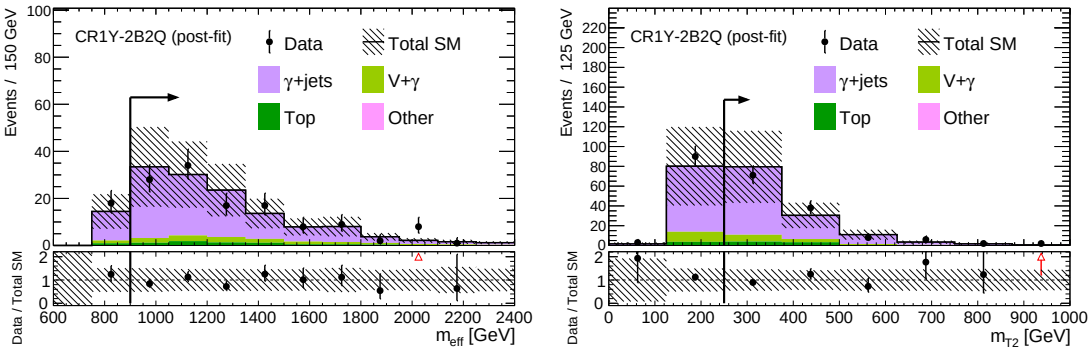

(a) $p_{\mathrm{T}}(V) + p_{\mathrm{T}}(J_1) + p_{\mathrm{T}}(J_2)$

(b) $m_{\mathrm{T2}}(J_1, J_2; V)$

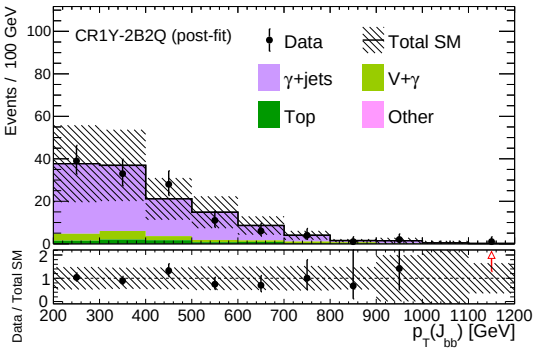

(c) $p_{\mathrm{T}}(J_{bb})$

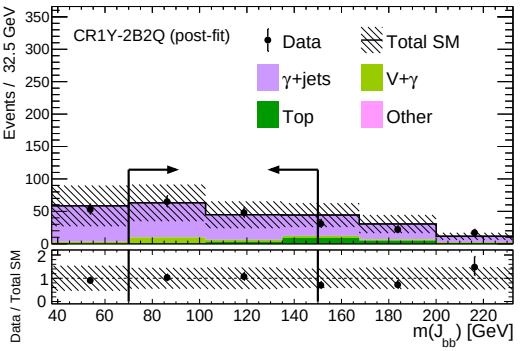

(d) mass (J_{bb})

Figure M.12: Distributions of $p_{\mathrm{T}}(V) + p_{\mathrm{T}}(J_1) + p_{\mathrm{T}}(J_2)$ (a), $m_{\mathrm{T2}}(J_1, J_2; V)$ (b) and p_{T} (c), mass (d) of J_{bb} in CR1Y-2B2Q.

N Jet Variables of the Data Sample in CRs and MC Sample in SRs/VRs

The data-to-data distributions of $J^{\text{fail V-tag}}$ variables in CR0L-4Q, CR1L-4Q, and CR1Y-4Q are shown in Figure N.1. CR0L-4Q selections are loosened so that they are consistent with the same as selections of CR1L-4Q and CR1Y-4Q, i.e., $p_{\mathrm{T}}(V) + p_{\mathrm{T}}(J_1) + p_{\mathrm{T}}(J_2)$ ($p_{\mathrm{T}}(V)$) cut is loosened from 1300(300) GeV to 1000 (200) GeV. Reasonable agreements of jet variables between the three regions are also found in the data and MC distributions are shown in Section 8.3.4. Figure N.2 shows a similar data-to-data comparison for the 2B2Q category. Like the 4Q category, reasonable consistencies within the limited data statistics are seen.

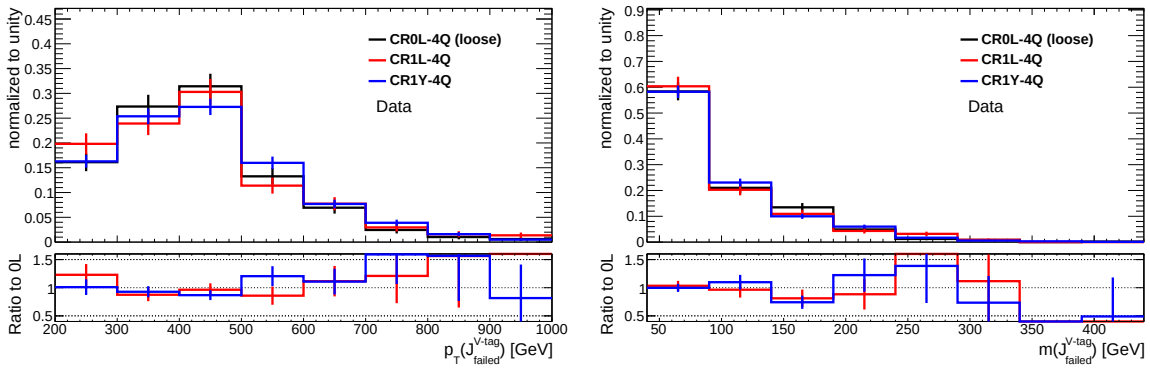

(a) p_{T}

(b) mass

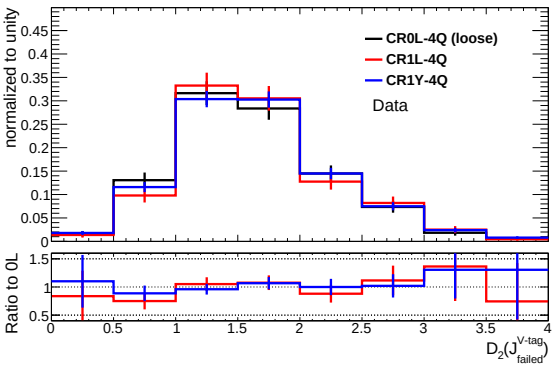

(c) D_2

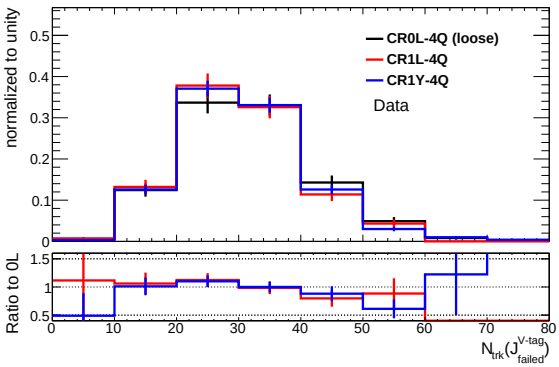

(d) n_{trk}

Figure N.1: Data-to-data comparison of et substructure variables of the failed jet for boson tagging requirements in CR0L-4Q, CR1L-4Q, and CR1Y-4Q. CR0L-4Q selections are loosened to $p_{\mathrm{T}}(V) + p_{\mathrm{T}}(J_1) + p_{\mathrm{T}}(J_2) > 1000$ GeV, $p_{\mathrm{T}}(V) > 200$ GeV, respectively, to align with CR1L-4Q and CR1Y-4Q.

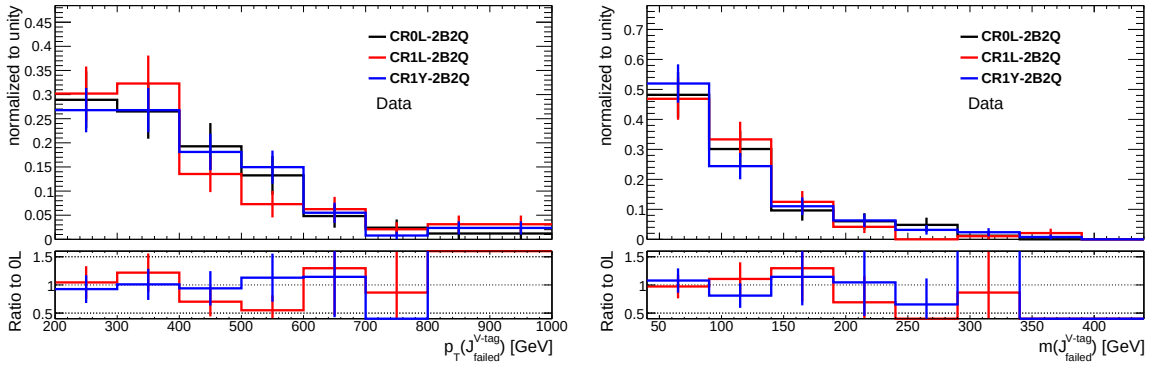

(a) p_{T}

(b) mass

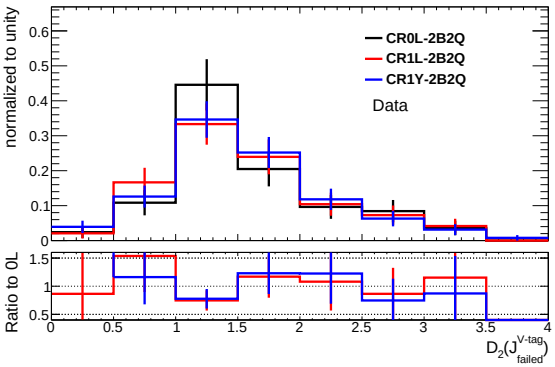

(c) D_2

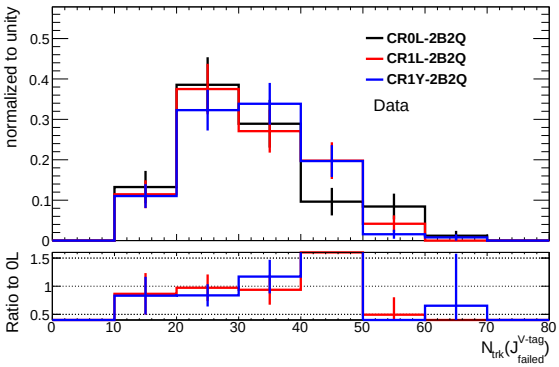

(d) n_{trk}

Figure N.2: Data-to-data comparison of jet substructure variables of the failed jet for boson tagging requirements in CR0L-2B2Q, CR1L-2B2Q, and CR1Y-2B2Q.

The MC-to-MC distributions of J_{qq} variables in SR-4Q-VV/VR1L-4Q/VR1Y-4Q are shown in Figure N.3, N.4. Additionally, the same distributions in SR-2B2Q-VZh/VR1L-2B2Q/VR1Y-2B2Q are shown in Figure N.5. The p_{T} distributions are shown in Figure 8.16. To maintain MC statistics, we apply loose kinematic cuts, $p_{\mathrm{T}}(V) + p_{\mathrm{T}}(J_1) + p_{\mathrm{T}}(J_2) > 800$ GeV and $p_{\mathrm{T}}(V) > 200$ GeV for 4Q regions and $p_{\mathrm{T}}(V) + p_{\mathrm{T}}(J_1) + p_{\mathrm{T}}(J_2) > 800$ GeV for 2B2Q regions. There is no significant difference.

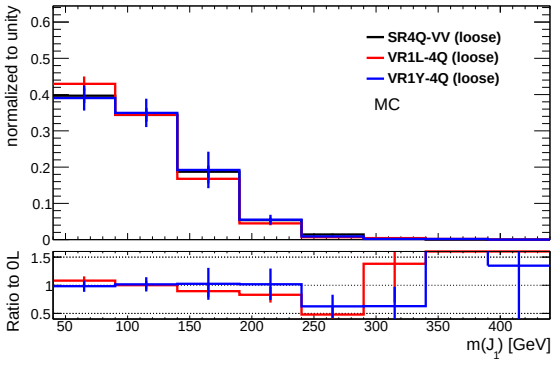

(a) mass

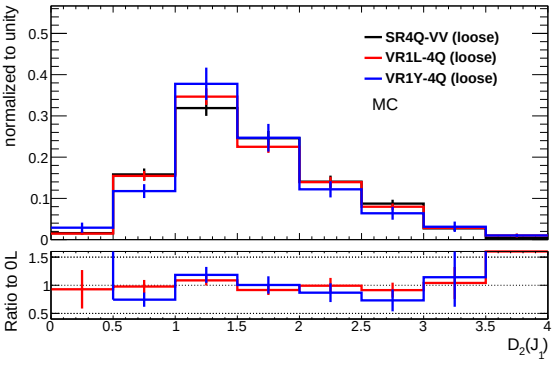

(b) D_2

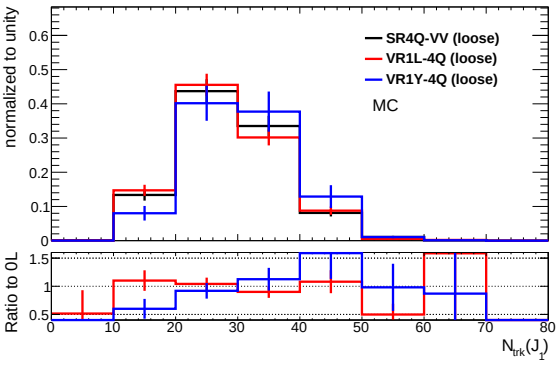

(c) n_{trk}

Figure N.3: MC-to-MC comparison of the jet distributions of the leading jet in SR-4Q-VV, VR1L-4Q, and VR1Y-4Q. Kinematic selections are loosened to $p_{\text{T}}(V) + p_{\text{T}}(J_1) + p_{\text{T}}(J_2) > 800$ GeV, $p_{\text{T}}(V) > 200$ GeV in all regions to maintain MC statistics. The distributions of jet substructure variables (p_{T}, D_2 and n_{trk}) are shown as N-1 plots, for example, mass distribution is required only D_2 and n_{trk} cuts, without mass cuts.

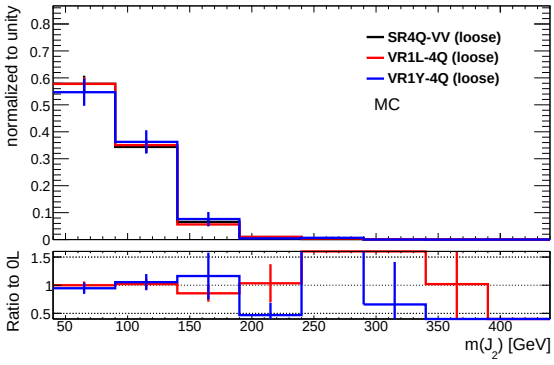

(a) mass

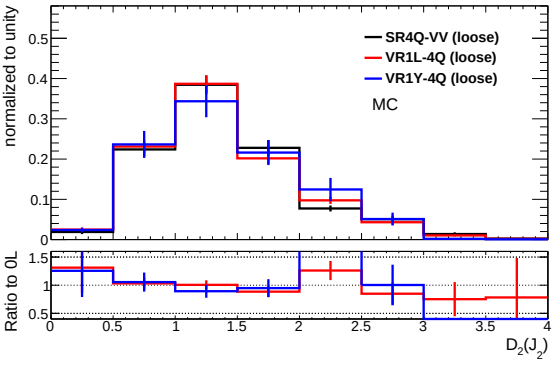

(b) D_2

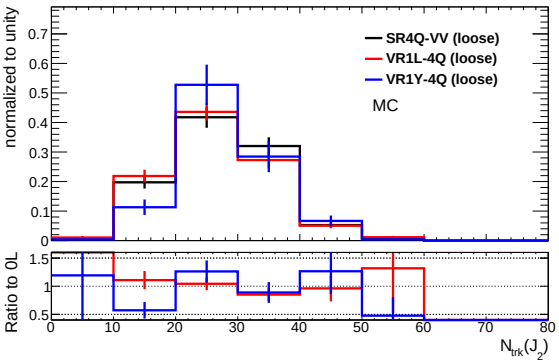

(c) n_{trk}

Figure N.4: MC-to-MC comparison of the jet distributions of the sub-leading jet in SR-4Q-VV, VR1L-4Q and VR1Y-4Q. Kinematic selections are loosened to $p_{\text{T}}(V) + p_{\text{T}}(J_1) + p_{\text{T}}(J_2) > 800$ GeV, $p_{\text{T}}(V) > 200$ GeV in all regions to maintain MC statistics. The distributions of jet substructure variables (p_{T}, D_2 and n_{trk}) are shown as N-1 plots.

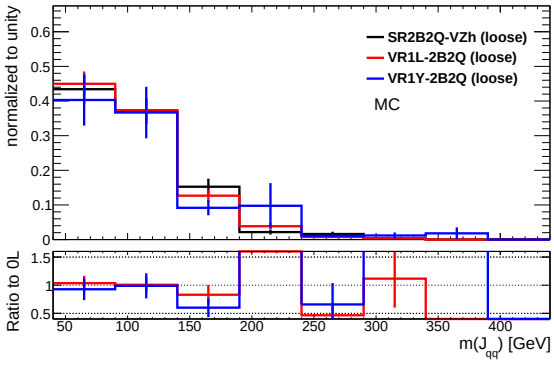

(a) mass

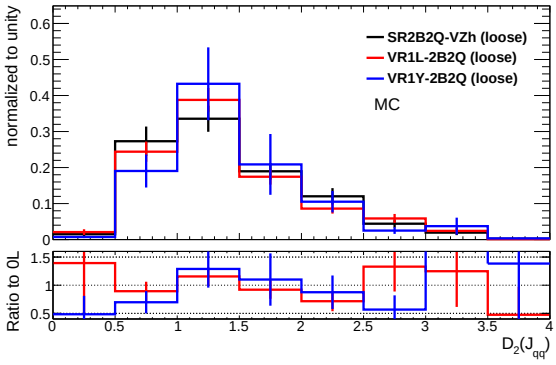

(b) D_2

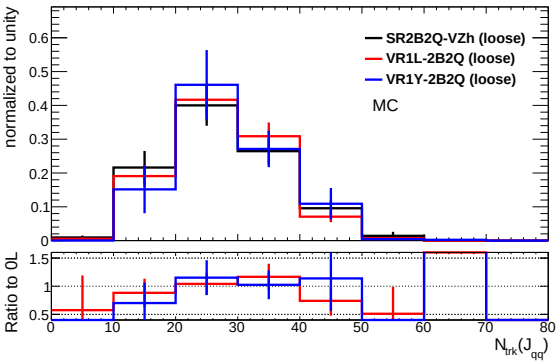

(c) n_{trk}

Figure N.5: MC-to-MC comparison of the jet distributions of J_{qq} in SR-2B2Q-VZh, VR1L-2B2Q and VR1Y-2B2Q. Kinematic selections are loosened to $p_{\text{T}}(V) + p_{\text{T}}(J_1) + p_{\text{T}}(J_2) > 800$ GeV in all regions to maintain MC statistics. The distributions of jet substructure variables (p_{T}, D_2 and n_{trk}) are shown as N-1 plots.

O Comparisons of the Physics Processes of the ISR/FSR Large-R Jet Distribution

Comparisons of the physics processes of the ISR/FSR large-R jet distribution in the 0L-2B2Q, 1L-4Q, 1L-2B2Q, and 1Y-2B2Q regions. Only the main backgrounds of these regions are shown.

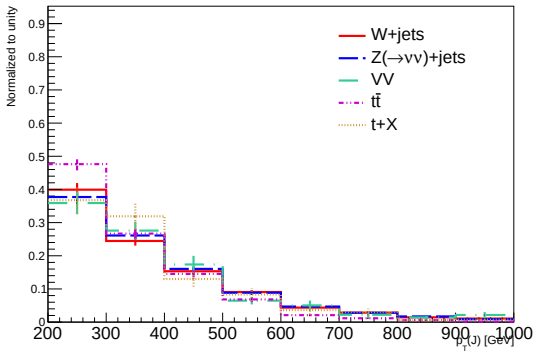

(a) p_{T}

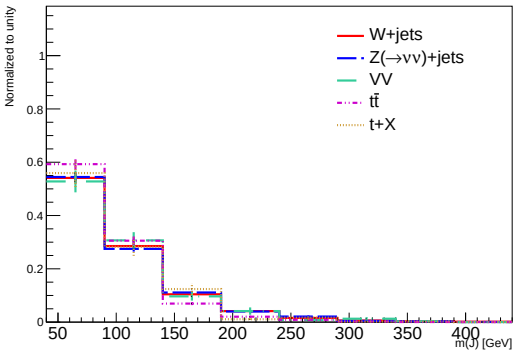

(b) Mass

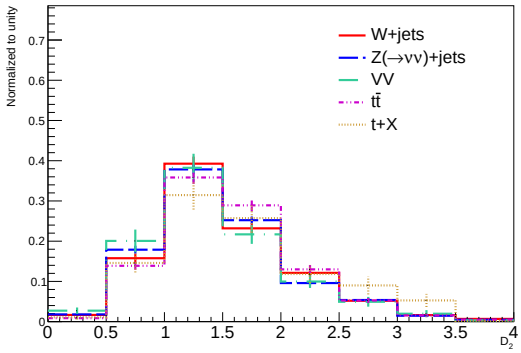

(c) D_2

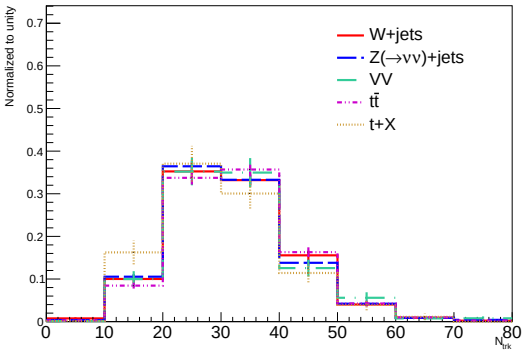

(d) n_{trk}

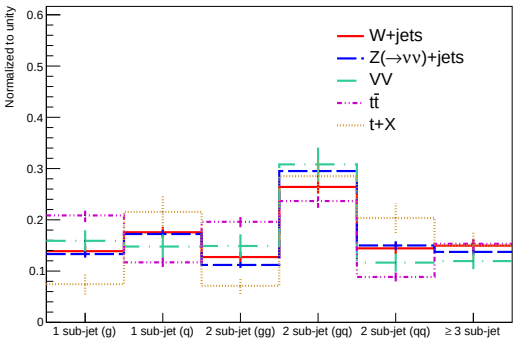

(e) `TruthPartonLabel` of the sub-jets

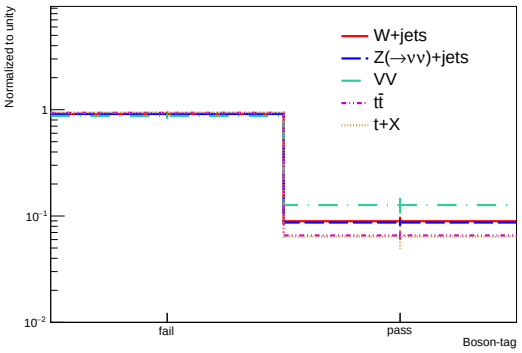

(f) Passes W/Z-tag?

Figure O.1: The kinematic distributions of large-R jets which originate from quarkis or gluons with Precut0L2B2Q in various physics processes. The same descriptions as Figure 8.21 are applied.

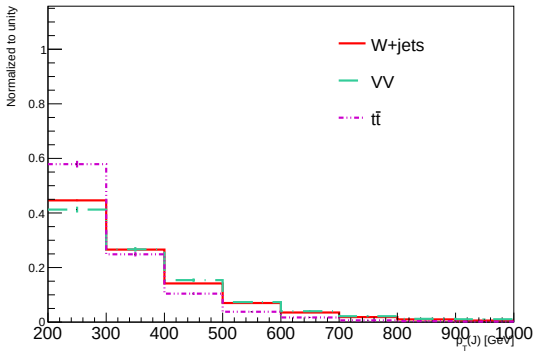

(a) p_{T}

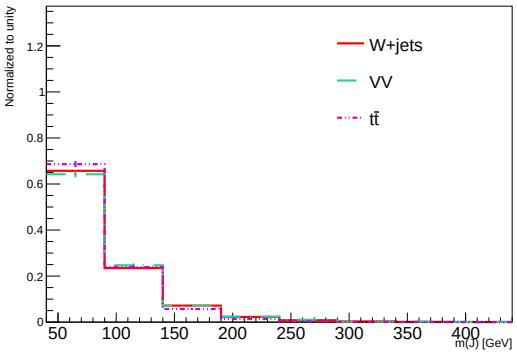

(b) Mass

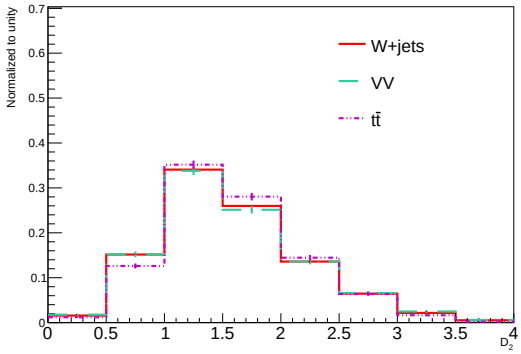

(c) D_2

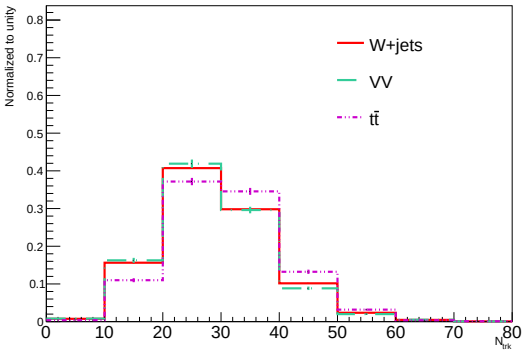

(d) n_{trk}

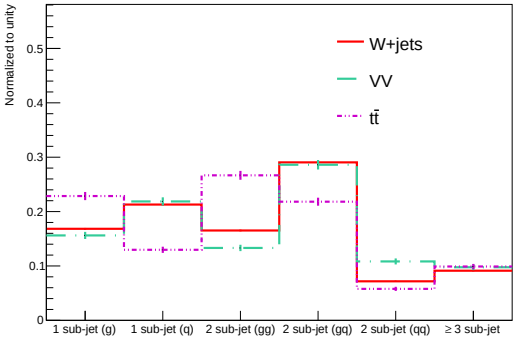

(e) `TruthPartonLabel` of the sub-jets

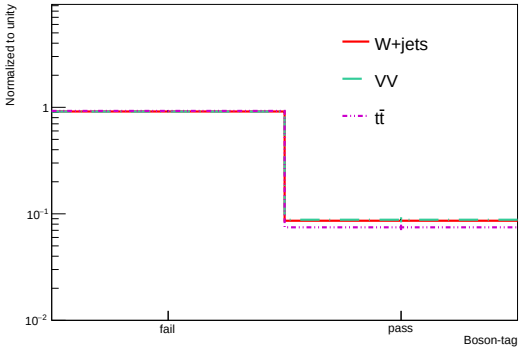

(f) Passes W/Z-tag?

Figure O.2: The kinematic distributions of large-R jets which originate from quarkis or gluons with Precut1L4Q in various physics processes. The same descriptions as Figure 8.21 are applied.

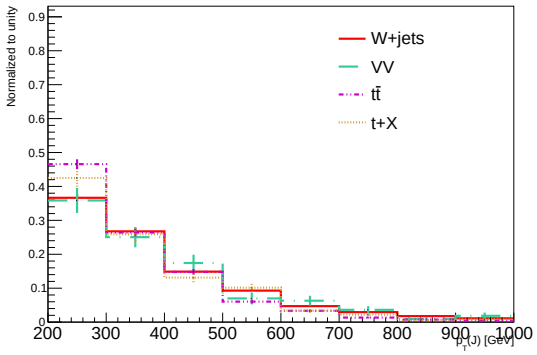

(a) p_{T}

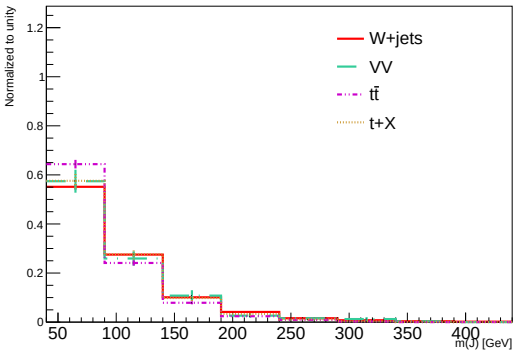

(b) Mass

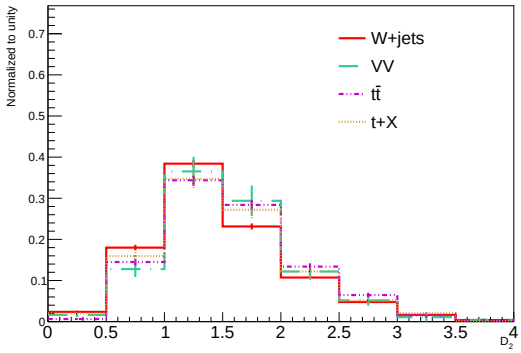

(c) D_2

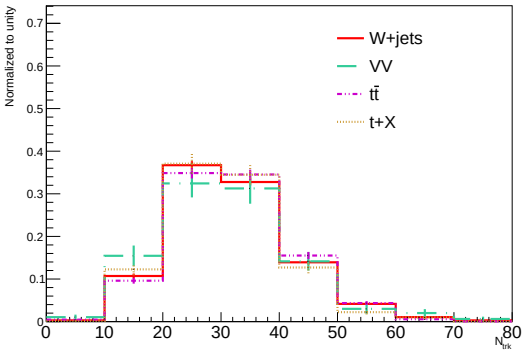

(d) n_{trk}

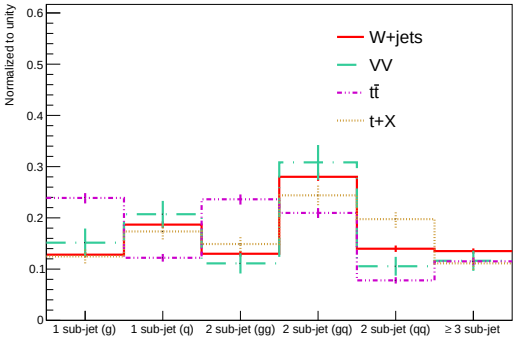

(e) `TruthPartonLabel` of the sub-jets

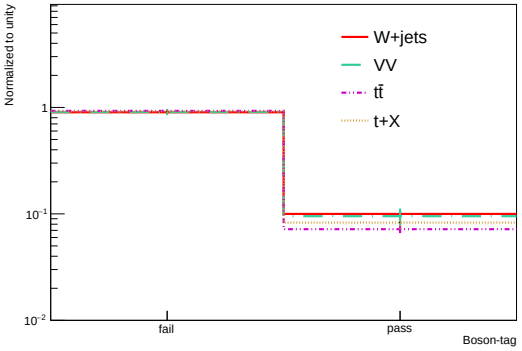

(f) Passes W/Z-tag?

Figure O.3: The kinematic distributions of large-R jets which originate from quarkis or gluons with Precut1L2B2Q in various physics processes. The same descriptions as Figure 8.21 are applied.

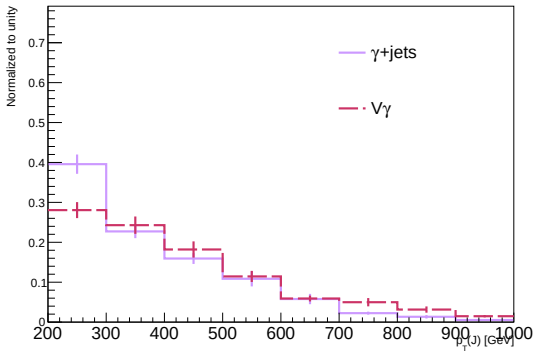

(a) p_{T}

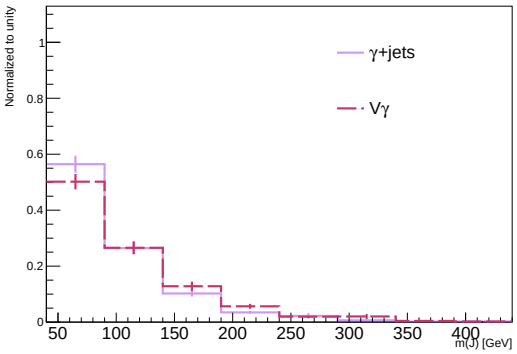

(b) Mass

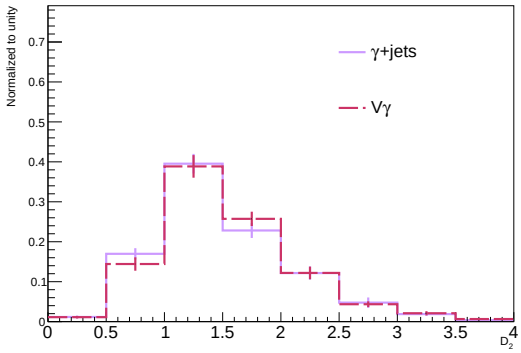

(c) D_2

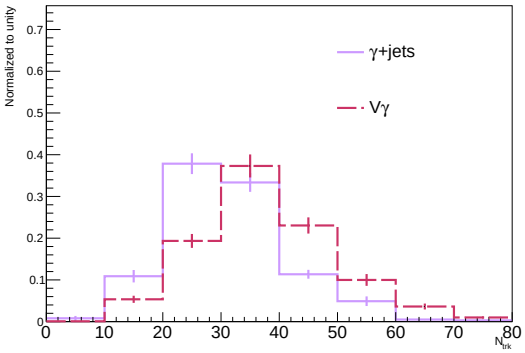

(d) n_{trk}

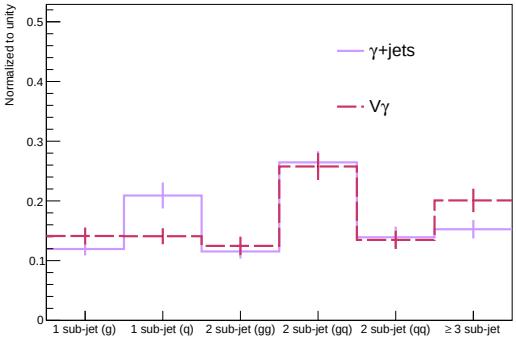

(e) `TruthPartonLabel` of the sub-jets

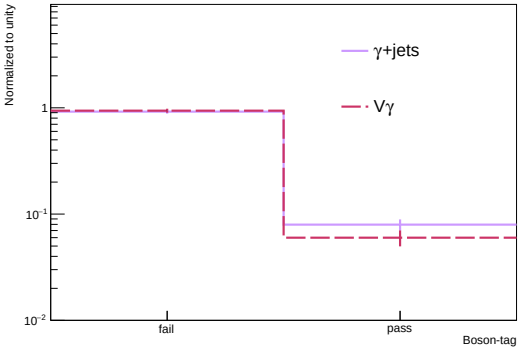

(f) Passes W/Z-tag?

Figure O.4: The kinematic distributions of large-R jets which originate from quarkis or gluons with Precut1Y2B2Q in various physics processes. The same descriptions as Figure 8.21 are applied.

P Minor Experimaental Uncertainties

The experimental uncertainties originate from the mis-modeling of the experimental circumstances in the MC sample. "Scale factors" are often used, evaluated as the difference between the data and the MC. In this section, the experimental uncertainties for the reconstruction and beam effects are presented. Large-R jet uncertainties are described in Sec.9.1.

P.1 Small-R Jets

In this thesis, small-R jets are used to calculate $E_{\mathrm{T}}^{\mathrm{miss}}$ and $\min \Delta\phi(j, E_{\mathrm{T}}^{\mathrm{miss}})$. The uncertainties on the jet energy scale (JES) and the jet energy resolution (JER) are considered. Additional uncertainty from the pile-up rejection (Jet Vertex Tagger) is also taken into account.

Jet Energy Scale (JES) The energy of small-R jets is corrected in the multi-steps as explained in Section 5.3.2.2. In-situ techniques measure the final jet energy correction, and the uncertainties are derived. The in-situ techniques for the jet energy correction are described in Ref [113], the outline is introduced. As described in Section 5.3.2.2, three control samples are used depending on the jet p_{T} to be calibrated, and the p_{T} balance of each jet relative to a reference object is measured using the data and MC samples. Z + jets samples are used for the energy calibration of the jets with 17 GeV $< p_{\mathrm{T}}^{j} <$ 1000 GeV and $|\eta| < 0.8$. In Z + jets events, the reference object is a Z boson reconstructed by the opposite sign lepton pair. γ+jets sample is used to calibrate jets, which have 25 GeV $< p_{\mathrm{T}}^{j} <$ 1200 GeV and $|\eta| < 0.8$, and photon is the reference object. Additionally, multi-jets events are used to calibrate high p_{T} jets to extend the p_{T} range $\sim$ 2.4 TeV. In the multi-jets events, calibrated jets with the in-situ method using Z/γ+ jets are used as reference objects. Since these methods are used to calibrate the central jets ($|\eta| < 0.8$), we need additional study for applying the calibration to the forward jets ($0.8 < |\eta| < 4.5$). We use di-jets topology (use only two jets, unlike multi-jets topology) and measure the ratio of the two jets using data and MC samples. Systematic uncertainties are evaluated as differences between data and MC samples after applying the correction of η inter-calibration. The results of the two methods are shown in Figure P.1. In the central region, the scale factors for jet p_{T} in data are about 3%. As shown in Figure P.1(b), some spikes caused by the detector transition regions are seen in the forward region.

The uncertainties in the jet energy scale calibration are account for:

- Uncertainties from the modeling of the physics process
- Uncertainties of the reference objects
- Uncertainties from the measurement, such as pile-up effects, flavor dependence, selection cuts, and topology dependence

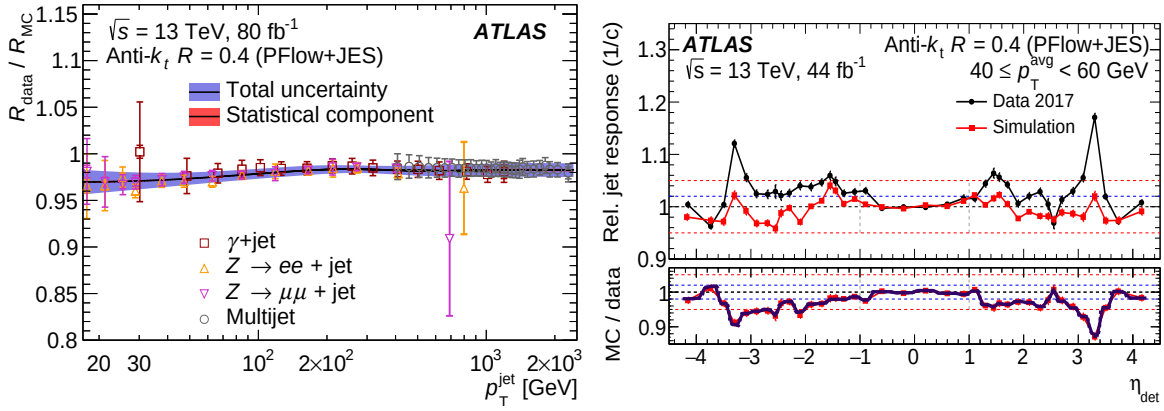

(a) In-situ method for the central jets

(b) η intercalibration

Figure P.1: (a) Ratio of small-R jets response of data to that in MC samples as a function of the jet p_{T} in the measurement using Z + jets, γ+jets, and multi-jets events. The response is defined as $R = \left\langle p_{\mathrm{T}}^{j}/p_{\mathrm{T}}^{\mathrm{reference}} \right\rangle$, where the bracket represents the average. The black curve shows the corrected value, and total (statistical) uncertainty is shown in the blue (red) area. The statistical uncertainty is too small to be visible in most regions. (b) Relative response pf jets (40 GeV $< p_{\mathrm{T}} <$ 60 GeV) in data (black circles) and MC samples (red squares) as a function of η in the detector. This figure shows the result of only 2017. The lower panel shows the ratio of the simulation to data. The dashed lines provide reference points for the viewer [113].

They are summarized in Table P.1 and the uncertainties are shown in Figure P.2. The spikes at $|\eta| \sim 2.5$ are caused by the uncertainty of the non-closure in the η inter-calibration. This uncertainty is derived from the modeling of the LAr pulse shape. We resolve the correlations between them and redefine them as uncorrelated components. These uncertainties are taken into account independently and used in statistical analysis.

Jet Energy Resolution (JER) As described in Section 5.3.2.2, the uncertainties on the jet energy resolution are evaluated as the difference of p_{T} scalar balance between data and MC samples using di-jet control samples. In the measurement, we consider systematic uncertainties of the jet energy scale, physics modeling, event selections, pile-up rejection, and non-closure uncertainty evaluated as the difference between the resolutions of the data and MC samples. Additionally, in order to consider the contribution of electric noise, we measure the fluctuations in the energy deposits by pile-up effects using data samples collected by random unbiased triggers. It is called the random cone method. The difference between the energy deposits in the calorimeter summed inside $R = 0.4$ circles are measured, and the estimated pile-up noise is determined by the central 68% confidence interval of the distribution. The uncertainties are shown in Figure P.3

Jet Vertex Tagger (JVT) As described in Section 5.3.2, Jet Vertex Tagger (JVT) is used to suppress pile-up effects. The performance is measured using $Z \rightarrow \mu\mu$ +jets control samples, and the measurement method is described in Ref. [111]. The difference between the data and the MC samples is assigned as a simulation-to-data scale factor. A systematic uncertainty is evaluated as the difference between two JVT working points.

Table P.1: Sources of uncertainty in the jet energy scale [113].

Component	Description
	η intercalibration
Systematic mis-modelling	Envelope of the generator, pileup, and event topology variations
Statistical component	Statistical uncertainty (single component)
Non-closure	Three components describing non-closure at high energy and at $\eta \sim \pm 2.4$
Non-closure, 2018 only	Single component describing non-closure at $\eta \sim \pm 1.5$ due to Tile calibration
	Z + jet
Electron scale	Uncertainty in the electron energy scale
Electron resolution	Uncertainty in the electron energy resolution
Muon scale	Uncertainty in the muon momentum scale
Muon resolution (ID)	Uncertainty in muon momentum resolution in the ID
Muon resolution (MS)	Uncertainty in muon momentum resolution in the MS
MC generator	Difference between MC event generators
JVT cut	Jet vertex tagger uncertainty
$\Delta\phi$ cut	Variation of $\Delta\phi$ between the jet and Z boson
Subleading jet veto	Radiation suppression through second-jet veto
Showering & topology	Modelling energy flow and distribution in and around a jet
Statistical	Statistical uncertainty in 28 discrete p_{T} terms
	γ + jet
Photon scale	Uncertainty in the photon energy scale
Photon resolution	Uncertainty in the photon energy resolution
MC generator	Difference between MC event generators
JVT cut	Jet vertex tagger uncertainty
$\Delta\phi$ cut	Variation of $\Delta\phi$ between the jet and photon
Subleading jet veto	Radiation suppression through second-jet veto
Showering & topology	Modelling energy flow and distribution in and around a jet
Photon purity	Purity of sample used for γ + jet balance
Statistical	Statistical uncertainty in 16 discrete p_{T} terms
	Multijet balance
$\Delta\phi$ (lead, recoil system)	Angle between leading jet and recoil system
$\Delta\phi$ (lead, any sublead)	Angle between leading jet and closest subleading jet
MC generator	Difference between MC event generators
$p_{\mathrm{T}}^{\mathrm{asym}}$ selection	Second jet's p_{T} contribution to the recoil system
Jet p_{T}	Jet p_{T} threshold
Statistical	Statistical uncertainty in 28 discrete p_{T} terms
	Pileup
μ offset	Uncertainty in the μ modelling in MC simulation
N_{PV} offset	Uncertainty in the number of primary vertex modelling in MC simulation
ρ topology	Uncertainty in the per-event p_{T} density modelling in MC simulation
p_{T} dependence	Uncertainty in the residual p_{T} dependence
	Jet flavour
Flavour composition	Uncertainty in the proportional sample composition of quarks and gluons
Flavour response	Uncertainty in the response of gluon-initiated jets
b-jets	Uncertainty in the response of b-quark-initiated jets
Punch-through	Uncertainty in GSC punch-through correction
Single-particle response	High-p_{T} jet uncertainty from single-particle and test-beam measurements
AFII non-closure	Difference in the absolute JES calibration for simulations in AFII

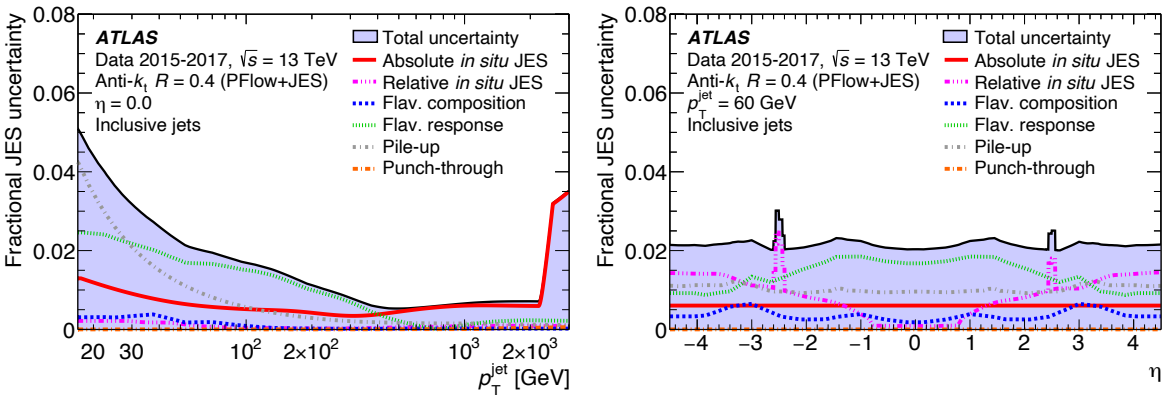

(a) $p_{\mathrm{T}}^{\mathrm{jet}}$ at $\eta = 0$ (b) η at $p_{\mathrm{T}}^{\mathrm{jet}} = 60$ GeV

Figure P.2: Total uncertainty is shown as a filled region with a function of jet p_{T} (a) and η (b). Each component is summarized in Table P.1. Flavor uncertainties are assumed to be a dijet flavor composition. "Relative *in situ* JES" are uncertainties from η inter-calibration, and "Absolute *in situ* JES" includes all uncertainties of in-situ measurement in the central region except for pile-up, flavor, punch-through. Total uncertainties are determined as the quadruple sum of each component [113].

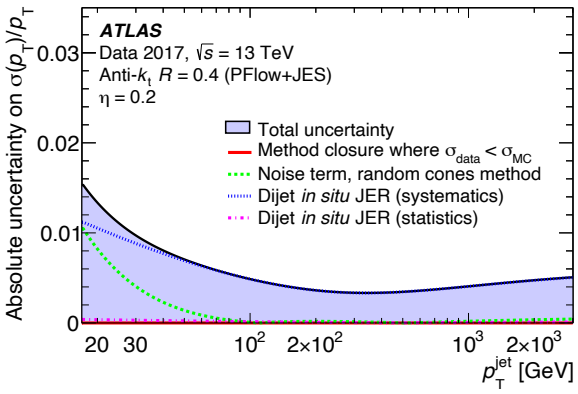

Figure P.3: Absolute uncertainty on the relative jet energy resolution as a function of jet p_{T}. Uncertainties from the two in situ measurements using dijet events and random triggered events for the noise measurement [113].

P.2 Track Jet b-tagging

b-tagging efficiencies for light-, c- and b-quark are measured using di-jet and $t\bar{t}$ events. Measurements are described in Ref. [116–118, 251] The uncertainty from the physics modeling is estimated as the generator differences. As shown in Figure 6.18, b-tagging uncertainty affects the performance of $Z/h \to bb$ tagging. However, the uncertainty on $Z/h \to bb$ tagging is small.

P.3 Electron and Photon

Uncertainties relevant to electrons and photons are three parts. One of them is derived from the calibration of the energy scale and resolution. The second one is the uncertainty from the efficiency of the reconstruction, identification, and isolation. The last one is the trigger uncertainty. They are studied in Ref.[119, 138, 252]. The outline is introduced in this section. However, these uncertainties have a small impact on this analysis.

As presented in Section D.7.4, the energy scale and resolution measurement of electrons is performed in $Z \to ee$ events. The correction factor for the energy scale and resolution is extracted from the di-electron invariant mass distribution. Major uncertainties in the energy scale measurement are derived from the detector response and mis-modeling of pile-up between data and MC samples. Dominant uncertainty of the energy resolution also comes from pile-up noise.

The electron reconstruction efficiency and isolation measurement are performed using the tag-and-probe method [251, 262] in $J/\psi \to ee$ and $Z \to ee$ events. The dominant systematic sources in the electron identification measurement are derived from the background subtraction at low E_{T}. Single electron trigger efficiency measurement is also performed in $Z \to ee$ events. The uncertainties come from a background subtraction method, a difference between data and MC samples, and a statistical uncertainty [138].

As presented in Section D.7.4, the energy scale and resolution measurement of photons is performed in the same way with electrons using $Z \to ee$ and $Z \to ll\gamma$ events are used for the validation. Major uncertainties are also derived from the detector response and mis-modeling of pile-up between data and MC samples.

We use selected events by single photon trigger to measure the photon identification and isolation, such as $Z \to ll\gamma$ events and $Z \to ee$ events with a method that transforms the electron shower shapes to resemble the photon shower shapes. In $Z \to ll\gamma$ events, we consider systematic uncertainties derived from a closure test to validate the measurement using signal and background samples, generator difference, the shower shape correction, and the efficiency differences in the different $m_{ll\gamma}$ binning. In inclusive-photon production events collected by a single photon trigger, uncertainty sources from a closure test in the measurement, mis-modeling in the MC-based correction, and the background estimation are considered. The uncertainty sources are derived from the difference in the efficiency measurement between the data and MC samples, the modeling of identification variables of MC simulation, and the background subtraction method in a study to resemble photon shower shapes using the extrapolation method for electrons.

To measure the single photon trigger efficiency, we perform two methods. One is the bootstrap method using photons triggered by a lower level or unbiased trigger, and the other uses radiative $Z \to ll\gamma$ decays. In the bootstrap method, we treat a discrepancy between the efficiency measured in data and MC samples of different physics processes, which are $h \to \gamma\gamma$ and prompt photon as a systematic uncertainty. In the $Z \to ee\gamma$ events, we use the tag-and-probe method where the two leptons are tagged, and the photon is the

probe. We estimate the difference in the measured trigger efficiency with changing event selections as the systematic uncertainty.

P.4 Muon

Uncertainties relevant to muons are similar to electrons. We consider the momentum scale and resolution uncertainties, the reconstruction/identification/isolation uncertainties, and the muon trigger uncertainty. These studies are described in Ref.[120, 130, 263], the outline is introduced in this section. Like electrons and photons, the uncertainties of muons are minor in this thesis.

As described in Section D.8.3, the momentum scale and resolution measurements are performed in $Z \to \mu\mu$ and $J/\psi \to \mu\mu$ events. The momentum scale and resolution are also extracted from the di-muon invariant mass distribution. The dominant sources of uncertainty are derived from event selections related to $Z \to \mu\mu$ candidates, background estimation, the determination of scale parameters by fitting the $J/\psi \to \mu\mu$ and $Z \to \mu\mu$ events separately. Additionally, the uncertainty from the alignment of the muon detectors has a contribution. It is estimated using special runs with the toroidal magnetic field turned off.

The reconstruction/isolation and trigger efficiency measurement of muons is performed in $Z \to \mu\mu$ events using the tag-and-probe method. In the reconstruction/identification efficiency measurement, the main contributions to the systematic uncertainties are differences of the muon kinematic distributions of the data and MC samples, selections of muons as the probe, background estimation derived from mis-modeling, and cross-section uncertainty of $Z \to \mu\mu$. In the isolation efficiency measurement, we consider additional uncertainty sources, such as muon candidate selections as the probe and $m_{\mu\mu}$ cuts and jet modeling, which are used to require isolation for muons. $Z \to \mu\mu$ events are used for muons that have $p_{\mathrm{T}} > 10$ GeV. Thus, for low p_{T} muons, a similar study using $J/\psi \to \mu\mu$ events is conducted.

For trigger efficiency measurement, we use the tag-and-probe method in $Z \to \mu\mu$ events. However, due to the limitation of data statistics in the high p_{T} region, we use $t\bar{t}$ and W + jets events. In the high p_{T} region, $E_{\mathrm{T}}^{\mathrm{miss}}$, and muon identifications largely contribute to the systematic uncertainty.

P.5 $E_{\mathrm{T}}^{\mathrm{miss}}$

The uncertainties for the scale and resolution of $E_{\mathrm{T}}^{\mathrm{miss}}$ are considered. $E_{\mathrm{T}}^{\mathrm{miss}}$ performance is measured in $Z(\to \ell\ell)$ + jets events, described in Ref.[264]. Jet energy scale and η inter-calibration uncertainties have large contributions to the systematic uncertainty. Additionally, uncertainties from the energy scale of electrons, the momentum scale of muons, the modeling of the underlying event, and the tracking performance are included.

P.6 Pile-up Modeling

We use the correction of MC samples to match the profile of the average number of interactions per bunch crossing. However, the number of hard scattering vertices of MC simulation is not consistent with data perfectly. Thus, we add more correction for the number of hard scattering vertices based on the analysis in Ref.[265] and consider systematic uncertainties.

P.7 Luminosity

An uncertainty of 1.7% is considered on the integrated luminosity for 2015 $\sim$ 2018 combined datasets based on Ref.[92].

Q Statistical Analysis

We use the HistFitter [266] framework to perform the statistical analysis. The outline is introduced in this section.

We use the profile likelihood method to search for new phenomena in this analysis. As described in Sec.8, the reducible backgrounds are estimated using MC samples normalized to the data in control regions. The normalization factors are determined in a fitting with systematic uncertainties described in Sec.9. In this section, the outline of the profile likelihood method is described. Additionally, we introduce the method of hypothesis tests for background estimation and signal model tests.

Q.1 Profile Likelihood

Generally, if we use a set of free parameters $\boldsymbol{\theta}$ that perform background estimation in N independent regions $E = (E_0(\boldsymbol{\theta}), ..., E_N(\boldsymbol{\theta}))$, the likelihood can be written as

$$L(x;\boldsymbol{\theta}) = \prod_{j=1}^{N} \frac{(E_j(\boldsymbol{\theta}))^{x_j}}{x_j!} e^{-E_j(\boldsymbol{\theta})}, \tag{Q.1}$$

where $\boldsymbol{x} = (x_1, ..., x_N)$ is observed events. It is a simple product of the Poisson distribution. In a maximum likelihood method, we find a set of $\boldsymbol{\theta}$ values that plausibly explains the measurement under the condition of maximizing the likelihood. The set values of $\boldsymbol{\theta}$ are denoted as $\hat{\boldsymbol{\theta}}$. We perform the maximum likelihood approach to fit MC samples to the observed data for estimating the background or signal yields.

In this analysis, reducible backgrounds are normalized by fitting to the data in control regions, i.e. the normalization factor of reducible backgrounds (denoted as μ_B) is a parameter $\boldsymbol{\theta}$ calculated using the maximum likelihood method. Additionally, the signal strength is a parameter $\boldsymbol{\theta}$ and the most interesting parameter in this analysis. It is denoted as μ_S. μ_S and μ_B are treated as free parameters in the likelihood formula.

Other parameters included in $\boldsymbol{\theta}$ are derived from systematic uncertainties described in Sec.9. They are called "nuisance parameters." From the measurement in the control regions, a Bayesian probability ($\rho(\theta|\tilde{\theta})$) can be obtained. $\tilde{\theta}$ is the central value of the measurement in the control regions and $\rho(\theta|\tilde{\theta})$ reflects the degree of our belief in what the true value of θ is. From the Bayes' theorem, $\rho(\theta|\tilde{\theta})$ is approximated as follows,

$$\rho(\theta|\tilde{\theta}) = p(\tilde{\theta}|\theta) \times \pi(\theta), \tag{Q.2}$$

where $p(\tilde{\theta}|\theta)$ is a "frequentist" probability and $\pi(\theta)$ is a Bayesian prior density. $\pi(\theta)$ can be re-formulated to flat before choosing the distribution of $p(\tilde{\theta}|\theta)$ [267]. Thus, the distribution of $\rho(\theta|\tilde{\theta})$ can be used as the distribution of $p(\tilde{\theta}|\theta)$ directly. In this analysis, we consider the probability functions of systematic

uncertainties as a Gaussian distribution and statistical uncertainty as a Gamma distribution. The Gaussian probability density function is described as,

$$\rho(\theta|\tilde{\theta}) = p(\tilde{\theta}|\theta) = \frac{1}{\sqrt{2\pi}\sigma}\exp\left(-\frac{(\theta-\tilde{\theta})^2}{2\sigma^2}\right), \tag{Q.3}$$

where σ is the uncertainty in the measurement. For the Gamma probability density function,

$$\rho(\theta|N) = p(N|\theta) = \frac{\theta^N}{N!}\exp(-\theta), \tag{Q.4}$$

where $\tilde{\theta} = N$ and N is the number of observed events. The combined form with all nuisance parameters ($p(\boldsymbol{\theta})$) is described as,

$$p(\boldsymbol{\theta}) = \prod_i p(\theta_i|\tilde{\theta}_i), \tag{Q.5}$$

and works as a constraint term in the likelihood function.

Using μ_S, μ_B, and $p(\boldsymbol{\theta})$, the likelihood function is written as,

$$L(x;(\mu_S,\mu_B,\boldsymbol{\theta})) = \prod_j^N \frac{(E_j(\mu_S,\mu_B,\boldsymbol{\theta}))^{x_j}}{x_j!}e^{-E_j(\mu_S,\mu_B,\boldsymbol{\theta})}, \tag{Q.6}$$

where the expected number of events in j-th region is $E_j = \mu_S s_j(\boldsymbol{\theta}) + b_j(\mu_B,\boldsymbol{\theta})$, s_j and b_j are the expected number of events of signals and backgrounds. b_j includes the term of irreducible backgrounds which are not related to μ_B.

We use the profile likelihood ratio method [154] to calculate the significance and upper limit on a cross-section. In this method, we obtain a set of parameters to maximize the likelihood function with fixed signal strength. The obtained parameters are denoted as $\hat{\hat{\boldsymbol{\theta}}}$. For a fixed μ_S value, a profile likelihood ratio is defined as,

$$\lambda(\mu_S) = \frac{L(\mu_S,\hat{\hat{\mu}}_B,\hat{\hat{\boldsymbol{\theta}}})}{L(\hat{\mu}_S,\hat{\mu}_B,\hat{\boldsymbol{\theta}})}. \tag{Q.7}$$

The numerator is the conditional maximum likelihood estimator of $\boldsymbol{\theta}$ and a function of μ_S. The denominator is called the unconditional maximum likelihood function.

Q.2 Hypothesis Tests

From the definition of $\lambda(\mu_S)$ described in Eq.Q.7, if $\lambda(\mu_S)$ is nearly 1, then there is a good agreement between data and the assumption of certain μ_S value. The μ_S is converted to be a statistic,

$$q_{\mu_S} = -2\ln\lambda(\mu_S), \tag{Q.8}$$

where q_{μ_S} is treated as the basis of a statistical test and referred to as "test statistics." We use the p-value to quantify the level of disagreement between data and the hypothesis, and the definition of the p-value is,

$$p_{\mu_S} = \int_{q_{\mu_S,\mathrm{obs}}}^{\infty} f(q_{\mu_S}|\mu_S)\, dq_{\mu_S}, \tag{Q.9}$$

where $q_{\mu_S,\mathrm{obs}}$ is the statistic value q_{μ_S} of the observed data, $f(q_{\mu_S}|\mu)$ is the probability density function of q_{μ_S} with the assumption of the fixed signal strength μ_S. Figure 10.5 illustrates the relation between the p-value and $f(q_{\mu_S}|\mu_S)$ distribution, and the significance Z.

To perform the hypothesis tests, we need obtain a $f(q_{\mu_S}|\mu)$ function for each μ_S test. The $f(q_{\mu_S}|\mu_S)$ function can be obtained by the pseudo experiments called "toy experiments" or an analytic approximation approach. The data of pseudo experiments are generated with fixed nuisance parameters to the maximum likelihood estimation and the test statistic function is sampled using the data. The alternative method is using an analytic approximation of $f(q_{\mu_S}|\mu)$. Wald's theorem [268] provides the statistic q_{μ_S} as a function of $\hat{\mu_S}$ and the error. The asymptotic formula uses "Asimov dataset" [154] generated under the condition where the derivatives of the log-likelihood to nuisance parameters are zero.

We set upper limits on cross-sections and other parameters of signals. Generally, we consider a μ_S value where the median p-value is equal to 0.05 as an upper limit because it is equivalent to be the median upper limit on μ_S at the 95% confidence level. For setting upper limits or excluding signal models, we use a statistic called CLs. The definition of CLs is,

$$\mathrm{CL_s} = \frac{\mathrm{CL_{splusb}}}{\mathrm{CL_b}} = \frac{p_{\mu_S}}{p_b}, \tag{Q.10}$$

where p_{μ_S}, p_b are the p-value of signal-and-background hypothesis and background-only hypothesis [155]. When the CLs value is less than 0.05, the signal model is excluded with the 95% confidence level.

We perform three hypothesis tests. One is "background-only fit" based on the background-only hypothesis with $\mu_S = 0$. In this analysis, we consider no contribution of any BSM signals and estimate the deviation between the data and MC samples. The second is "model-independent fit." In the model-independent fit, the CLs calculation is performed with a various number of the signal event. In this calculation, the signal model is assumed to be a generic BSM signal, not just SUSY models. A number of signal events satisfying that $\mathrm{CL_s} = 0.05$ is obtained and we set an upper limit on a visible cross-section for each signal region. The last one is "model-dependent fit." In this test, signal models are assumed, and the μ_S value is fixed to be 1. CLs values are obtained for each signal model and mass point. We set the exclusion limit on the SUSY mass parameter plane for each signal model.

R Kinematic Distributions in VRs/SRs after Fit

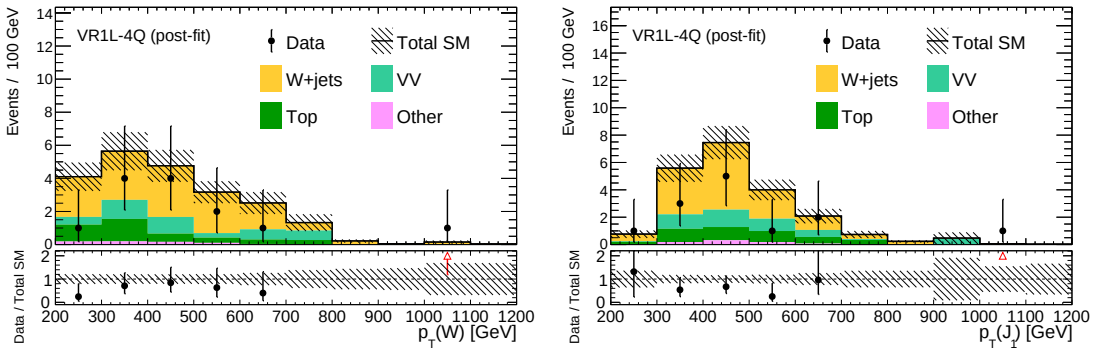

(a) $p_{\mathrm{T}}(V)$ (b) $p_{\mathrm{T}}(J_1)$

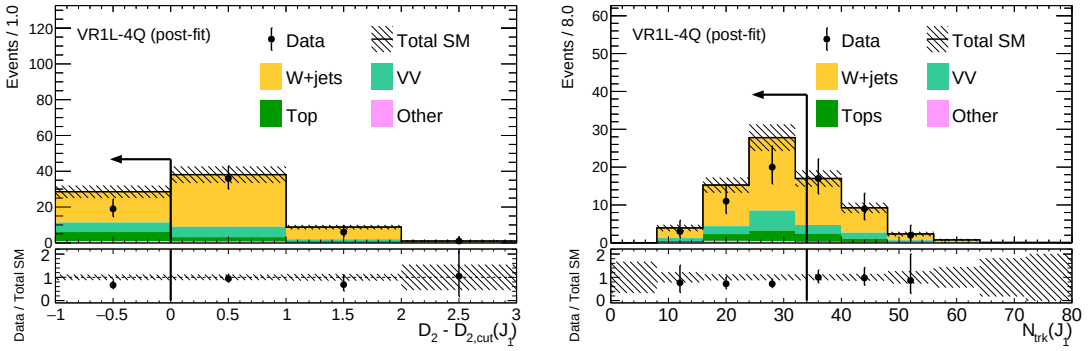

(c) $D_2(J_1)$ (d) n_{trk} (J_1)

Figure R.1: Distributions of $p_{\mathrm{T}}(V)$ (a), and leading large-R jet p_{T} (b), D_2 (c), n_{trk} (d) in VR1L-4Q. "Tops" includes $t\bar{t}$, $t+X$, and $t\bar{t}+X$. "Other" includes Z + jets, VVV, Vh, γ + jets, and $V\gamma$.In the D_2 and n_{trk} plots, kinematic cuts except for $W/Z \to qq$ tagging cuts and mass cuts for the targeting jets are applied.

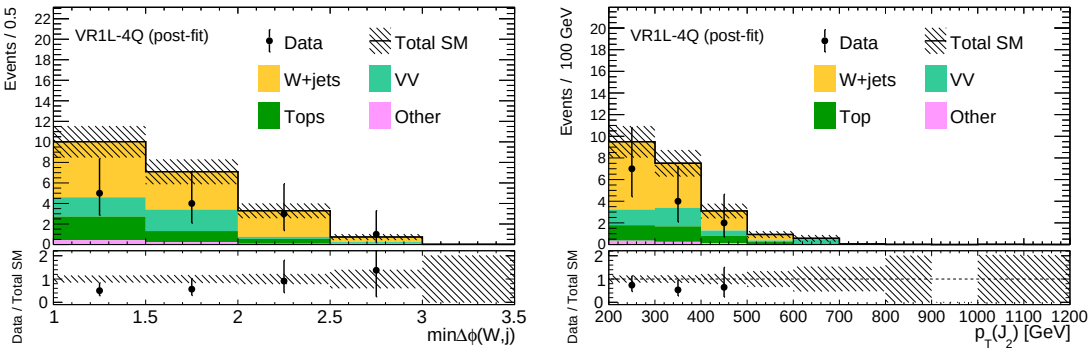

(a) $\min \Delta\phi(j, V)$

(b) $p_{\mathrm{T}}(J_2)$

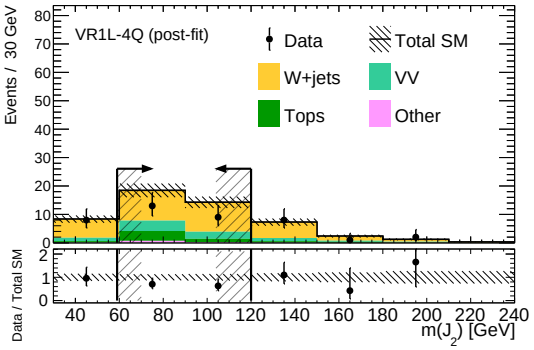

(c) $m(J_2)$

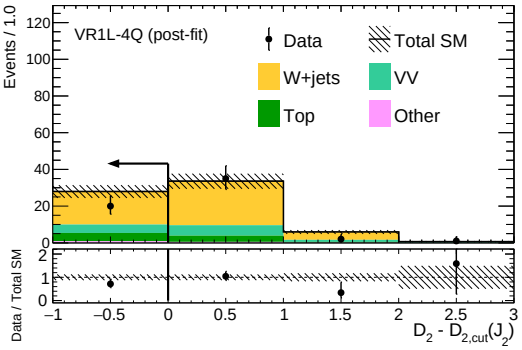

(d) $D_2(J_2)$

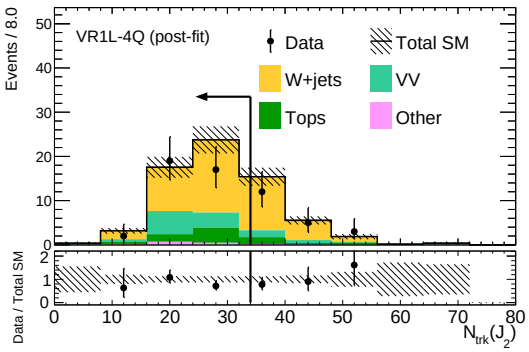

(e) n_{trk} (J_2)

Figure R.2: Distributions of $\min \Delta\phi(j, V)$ (a), and sub-leading large-R jet p_{T} (b), mass (c), D_2 (d), n_{trk} (e) in VR1L-4Q. "Tops" includes $t\bar{t}$, $t + X$, and $t\bar{t} + X$. "Other" includes Z + jets, VVV, Vh, γ + jets, and $V\gamma$.In the D_2 and n_{trk} plots, kinematic cuts except for $W/Z \to qq$ tagging cuts and mass cuts for the targeting jets are applied.

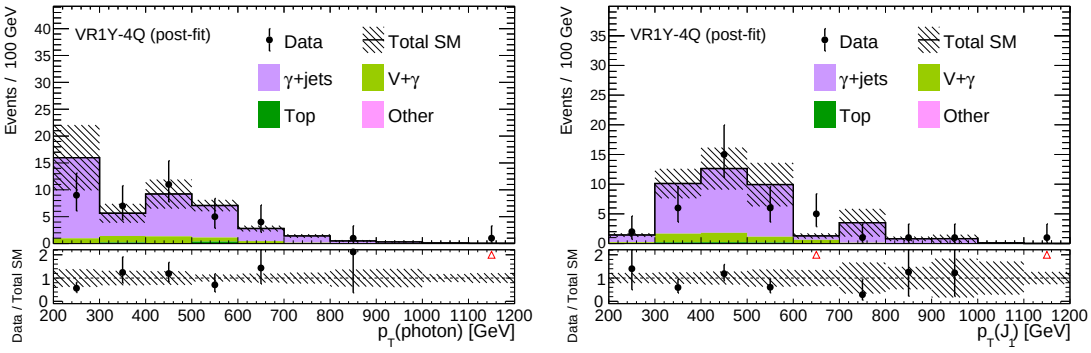

(a) $p_{\mathrm{T}}(V)$ (b) $p_{\mathrm{T}}(J_1)$

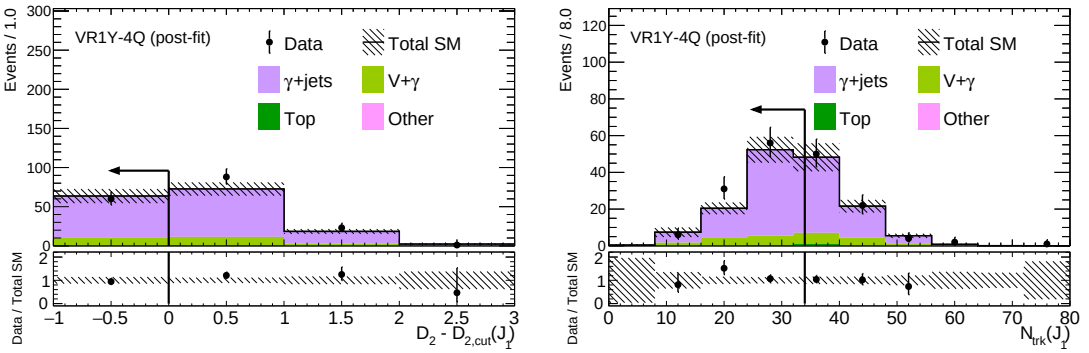

(c) $D_2(J_1)$ (d) n_{trk} (J_1)

Figure R.3: Distributions of $p_{\mathrm{T}}(V)$ (a), and leading large-R jet p_{T} (b), D_2 (c), n_{trk} (d) in VR1Y-4Q. "Tops" includes $t\bar{t}$, $t + X$, and $t\bar{t} + X$. "Other" includes Z + jets, VVV, Vh, W + jets, and VV.In the D_2 and n_{trk} plots, kinematic cuts except for $W/Z \to qq$ tagging cuts and mass cuts for the targeting jets are applied.

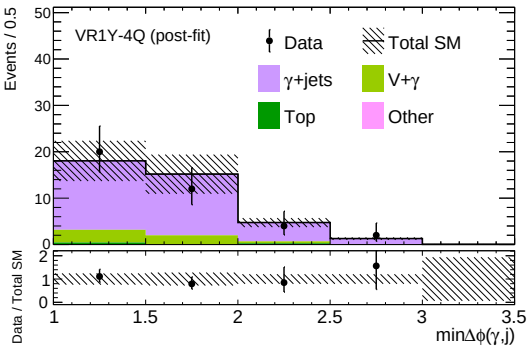

(a) $\min \Delta\phi(j, V)$

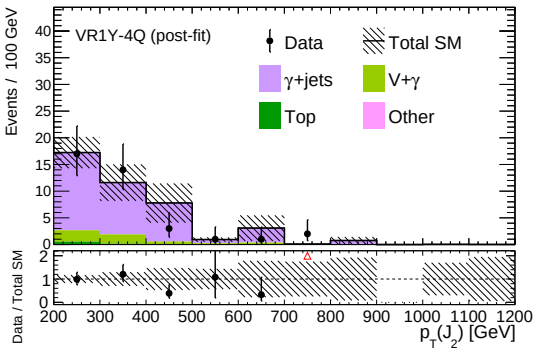

(b) $p_{\mathrm{T}}(J_2)$

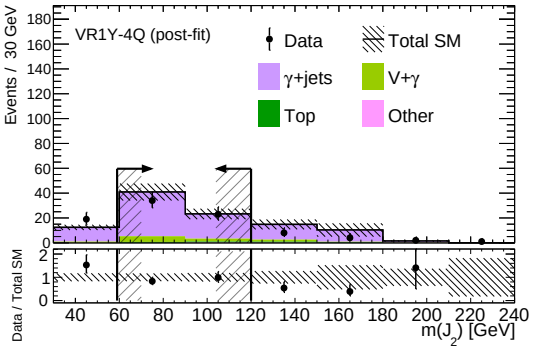

(c) $m(J_2)$

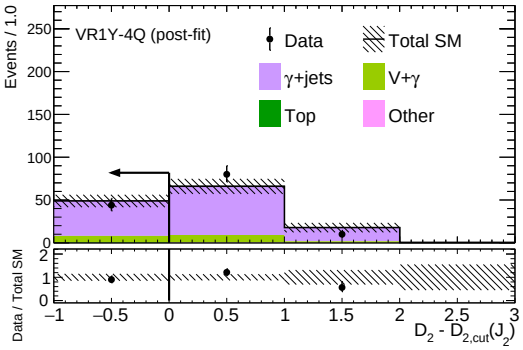

(d) $D_2(J_2)$

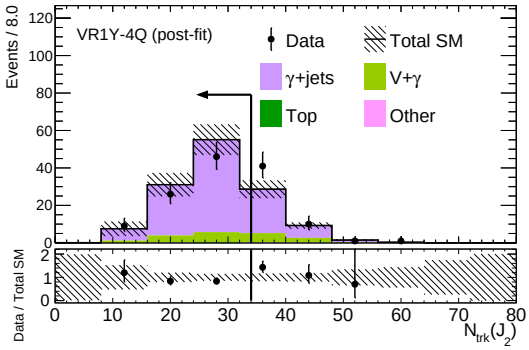

(e) n_{trk} (J_2)

Figure R.4: Distributions of $\min \Delta\phi(j, V)$ (a), and sub-leading large-R jet p_{T} (b), mass (c), D_2 (d), n_{trk} (e) in VR1Y-4Q. "Tops" includes $t\bar{t}$, $t + X$, and $t\bar{t} + X$. "Other" includes Z + jets, VVV, Vh, W + jets, and VV.In the D_2 and n_{trk} plots, kinematic cuts except for $W/Z \to qq$ tagging cuts and mass cuts for the targeting jets are applied.

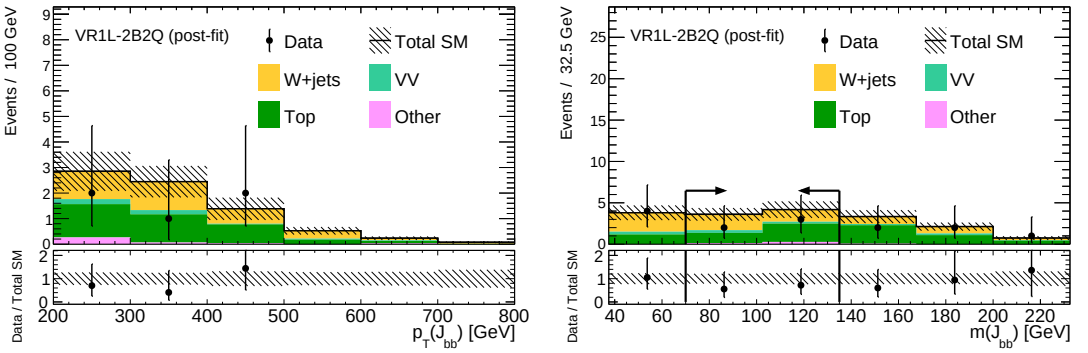

(a) $p_{\mathrm{T}}(J_{bb})$

(b) $m(J_{bb})$

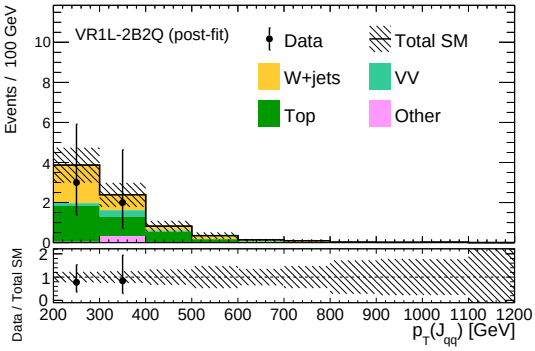

(c) $p_{\mathrm{T}}(J_{qq})$

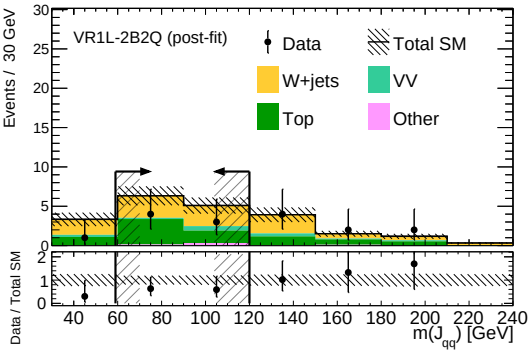

(d) $m(J_{qq})$

Figure R.5: Distributions of p_{T} (J_{bb}) (a), $m(J_{bb})$ (b), p_{T} (J_{qq}) (c), and $m(J_{qq})$ (d) in VR1L-2B2Q. "Tops" includes $t\bar{t}$, $t + X$, and $t\bar{t} + X$. "Other" includes Z + jets, VVV, Vh, γ + jets, and $V\gamma$.

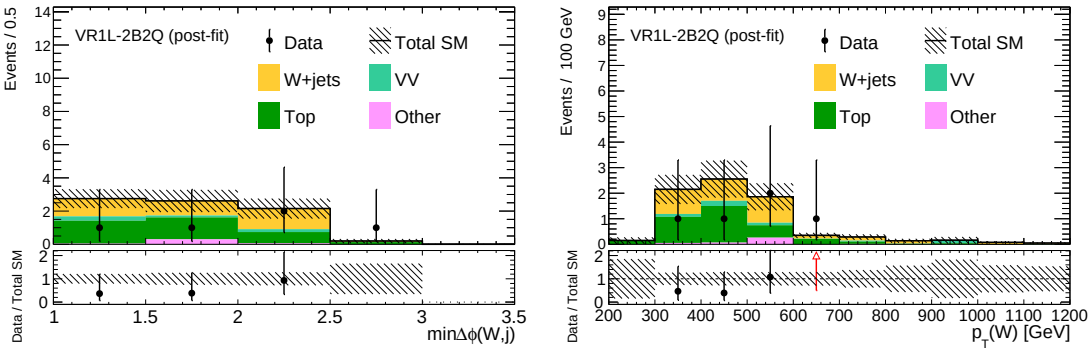

(a) $\min \Delta\phi(j, V)$ (b) $p_{\mathrm{T}}(V)$

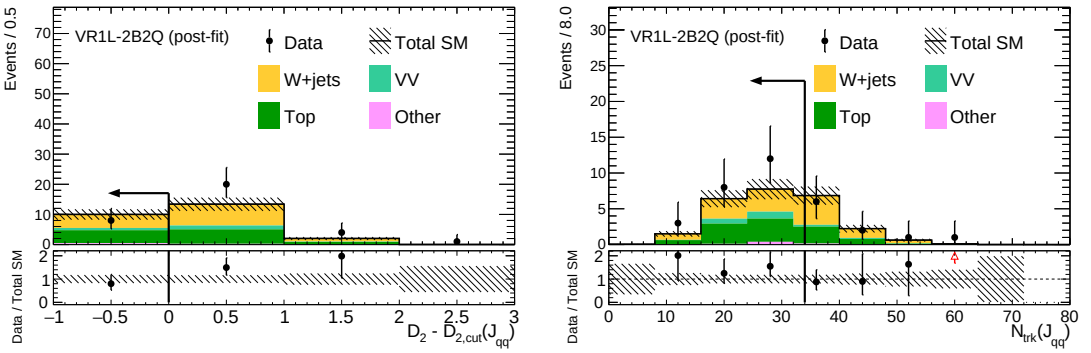

(c) $D_2(J_{qq})$ (d) n_{trk} (J_{qq})

Figure R.6: Distributions of $\min \Delta\phi(j, V)$ (a), $p_{\mathrm{T}}(V)$ (b), and D_2 (c), n_{trk} (d) of J_{qq} in VR1L-2B2Q. "Tops" includes $t\bar{t}$, $t + X$, and $t\bar{t} + X$. "Other" includes Z + jets, VVV, Vh, γ + jets, and $V\gamma$.In the D_2 and n_{trk} plots, kinematic cuts except for $W/Z \to qq$ tagging cuts and mass cuts for the targeting jets are applied.

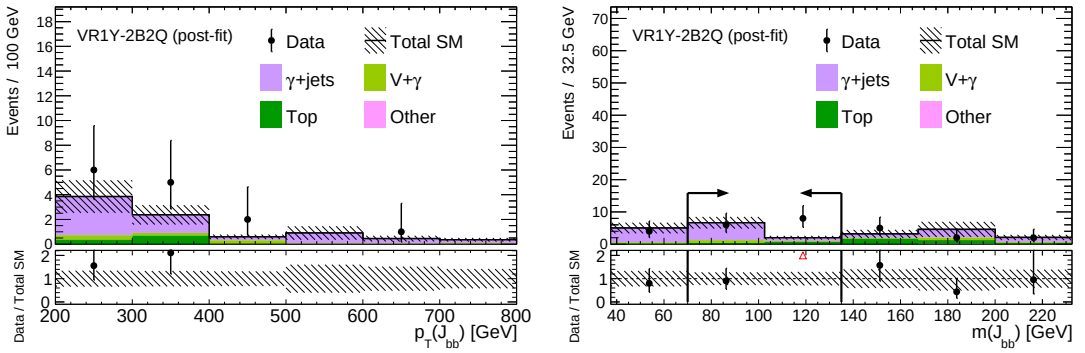

(a) $p_{\mathrm{T}}(J_{bb})$

(b) mass (J_{bb})

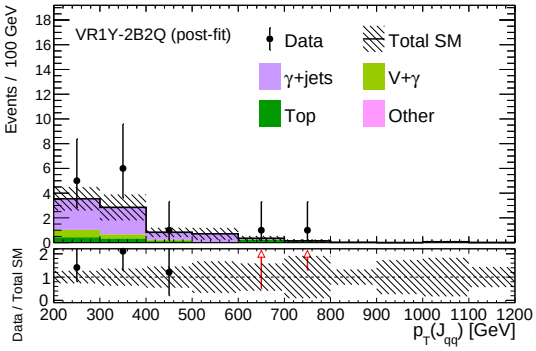

(c) $p_{\mathrm{T}}(J_{qq})$

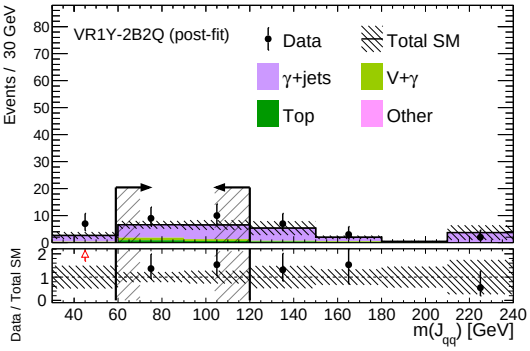

(d) $m(J_{qq})$

Figure R.7: Distributions of p_{T} (J_{bb}) (a), $m(J_{bb})$ (b), p_{T} (J_{qq}) (c), and $m(J_{qq})$ (d) in VR1Y-2B2Q. "Tops" includes $t\bar{t}$, $t + X$, and $t\bar{t} + X$. "Other" includes Z + jets, VVV, Vh, W + jets, and VV.

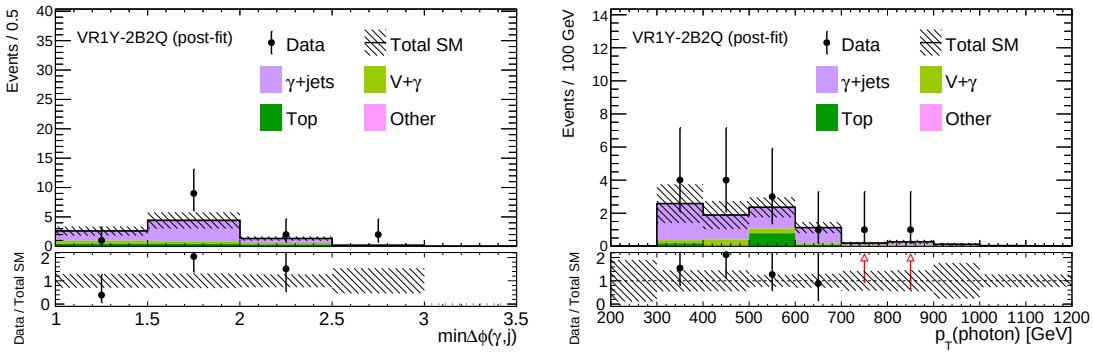

(a) $\min \Delta\phi(j, V)$ (b) $p_{\mathrm{T}}(V)$

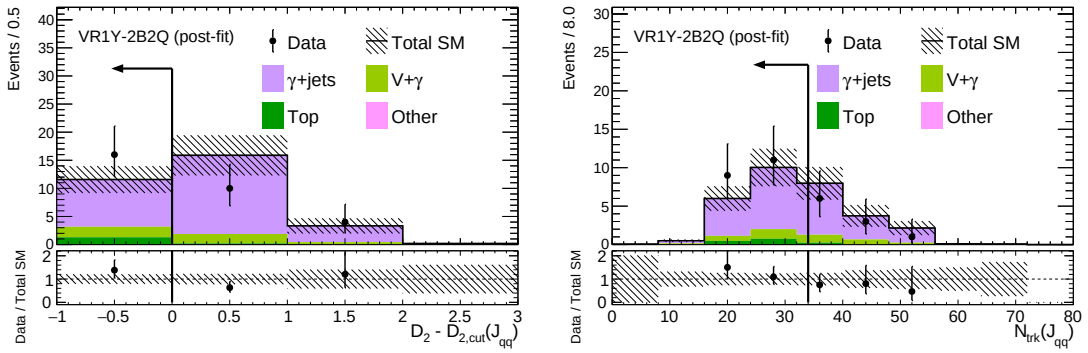

(c) $D_2(J_{qq})$ (d) n_{trk} (J_{qq})

Figure R.8: Distributions of min $\Delta\phi(j, V)$ (a), $p_{\mathrm{T}}(V)$ (b), and D_2 (c), n_{trk} (d) of J_{qq} in VR1Y-2B2Q. "Tops" includes $t\bar{t}$, $t + X$, and $t\bar{t} + X$. "Other" includes Z + jets, VVV, Vh, W + jets, and VV.In the D_2 and n_{trk} plots, kinematic cuts except for $W/Z \to qq$ tagging cuts and mass cuts for the targeting jets are applied.

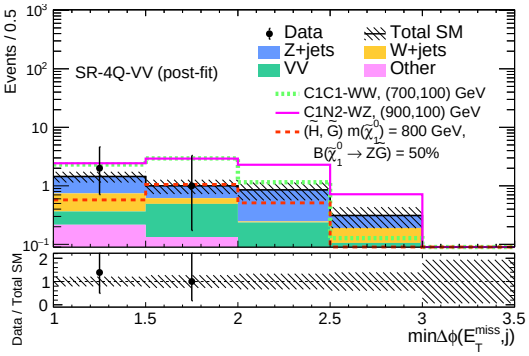

(a) $\min \Delta\phi(j, E_{\mathrm{T}}^{\mathrm{miss}})$

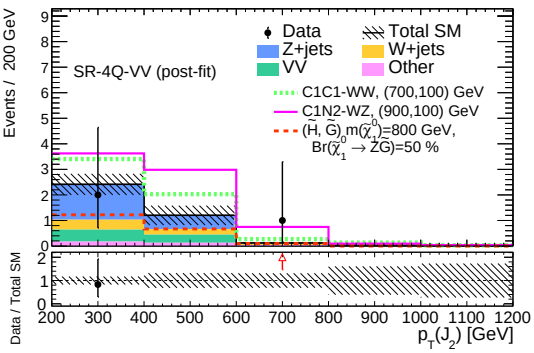

(b) $p_{\mathrm{T}}(J_2)$

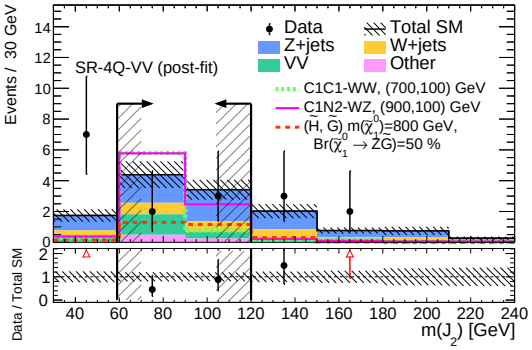

(c) $m(J_2)$

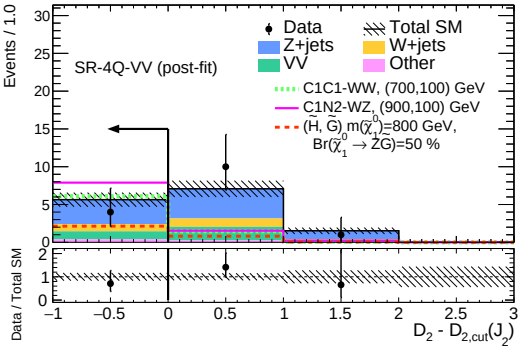

(d) $D_2(J_2)$

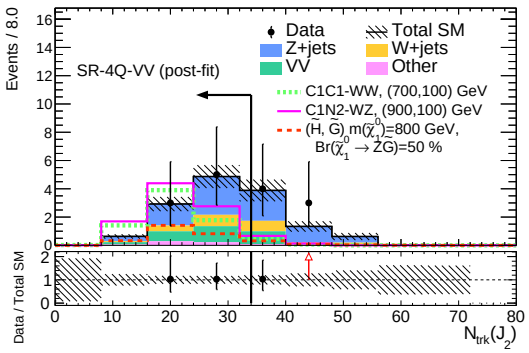

(e) n_{trk} (J_2)

Figure R.9: Distributions of $\min \Delta\phi(j, E_{\mathrm{T}}^{\mathrm{miss}})$ (a), and sub-leading large-R jet p_{T} (b), mass (c), D_2 (d), n_{trk} (e) in SR-4Q-VV. "Other" includes VVV, $t\bar{t}$, $t + X$, $t\bar{t} + X$, Vh, γ + jets, and $V\gamma$.In the D_2 and n_{trk} plots, kinematic cuts except for $W/Z \to qq$ tagging cuts and mass cuts for the targeting jets are applied.

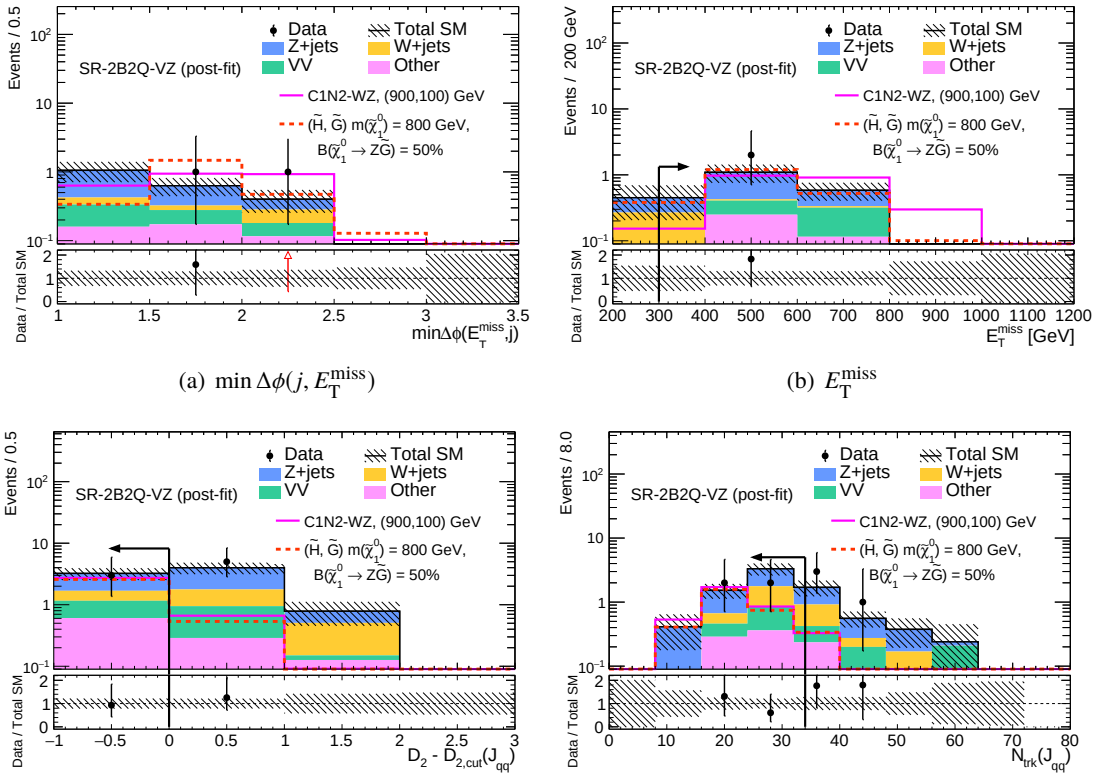

(a) $\min \Delta\phi(j, E_{\mathrm{T}}^{\mathrm{miss}})$

(b) $E_{\mathrm{T}}^{\mathrm{miss}}$

(c) $D_2(J_{qq})$

(d) n_{trk} (J_{qq})

Figure R.10: Distributions of $\min \Delta\phi(j, V)$ (a), $p_{\mathrm{T}}(V)$ (b), and D_2 (c), n_{trk} (d) of J_{qq} in SR-2B2Q-VZ. "Other" includes VVV, $t\bar{t}$, $t + X$, $t\bar{t} + X$, Vh, γ + jets, and $V\gamma$.In the D_2 and n_{trk} plots, kinematic cuts except for $W/Z \to qq$ tagging cuts and mass cuts for the targeting jets are applied.

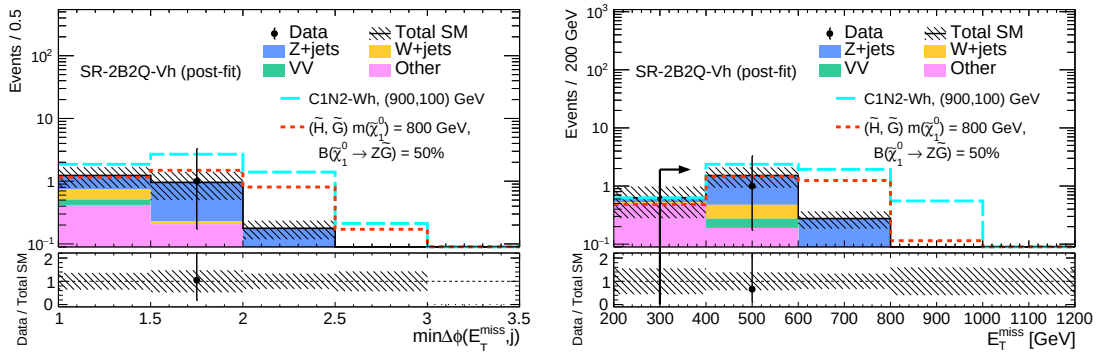

(a) $\min \Delta\phi(j, E_{\mathrm{T}}^{\mathrm{miss}})$ (b) $E_{\mathrm{T}}^{\mathrm{miss}}$

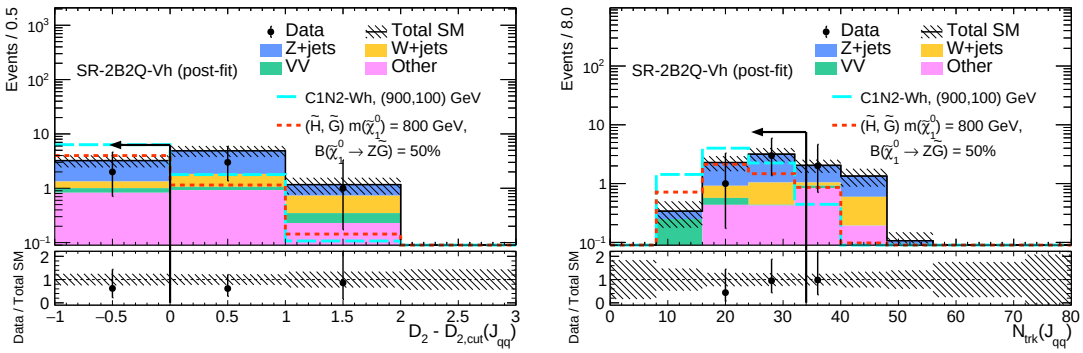

(c) $D_2(J_{qq})$ (d) n_{trk} (J_{qq})

Figure R.11: Distributions of $\min \Delta\phi(j, V)$ (a), $p_{\mathrm{T}}(V)$ (b), and p_{T} (c), mass (d), D_2 (c), n_{trk} (d) of J_{qq} in SR-2B2Q-Vh. "Other" includes VVV, $t\bar{t}$, $t + X$, $t\bar{t} + X$, Vh, $\gamma +$ jets, and $V\gamma$.In the D_2 and n_{trk} plots, kinematic cuts except for $W/Z \to qq$ tagging cuts and mass cuts for the targeting jets are applied.

S Auxiliary Materials for Specific SUSY models

S.1 Acceptance

Acceptance is the ratio of the weighted events with the SR selections to the weighted total generated events, including $W/Z/h$ decays. Generator-level particle information is used to apply the selections. The efficiencies of the reconstruction/identification of leptons, b-tagging, D_2 and n_{trk} selection of the boson tagging are assumed to be 100% in the calculation of the acceptance. Each process, except for $(\tilde{H}, \tilde{G})$, is calculated using the simplified signal samples directly.

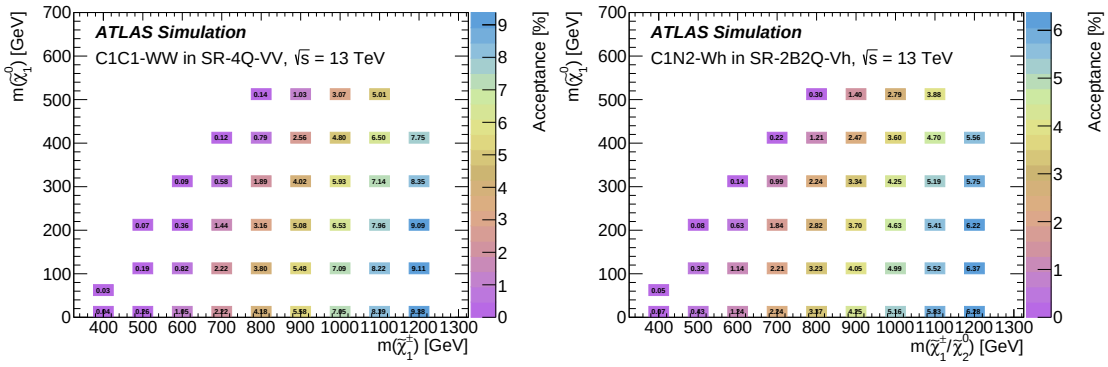

(a) C1C1-WW in SR-4Q-VV (b) C1N2-Wh in SR-2B2Q-Vh

Figure S.1: Acceptance of the C1C1-WW in SR-4Q-VV and C1N2-Wh in SR-2B2Q-Vh [49].

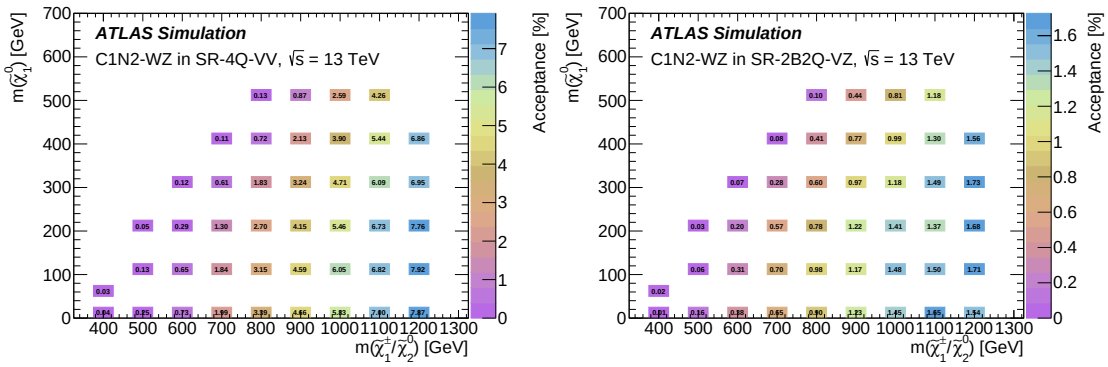

(a) C1N2-WZ in SR-4Q-VV (b) C1N2-WZ in SR-2B2Q-VZ

Figure S.2: Acceptance of the C1N2-WZ in SR-4Q-VV (a) and SR-2B2Q-VZ (b) [49].

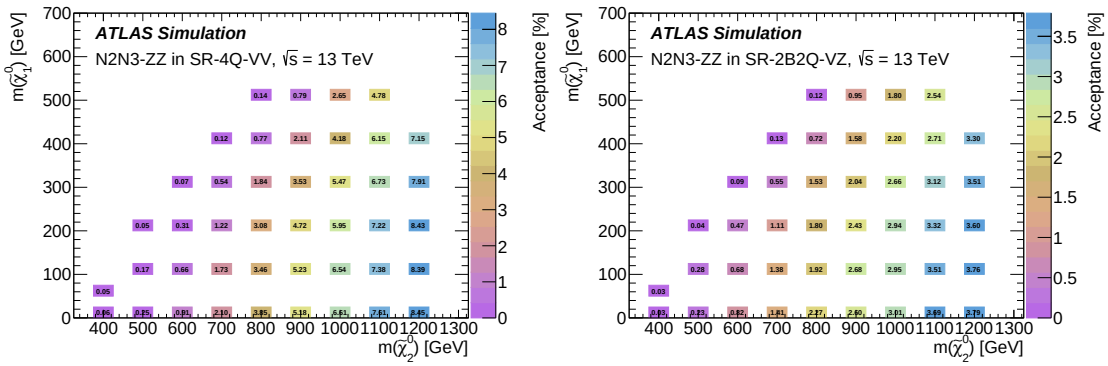

(a) N2N3-ZZ in SR-4Q-VV (b) N2N3-ZZ in SR-2B2Q-VZ

Figure S.3: Acceptance of the N2N3-ZZ in SR-4Q-VV (a) and SR-2B2Q-VZ (b) [49].

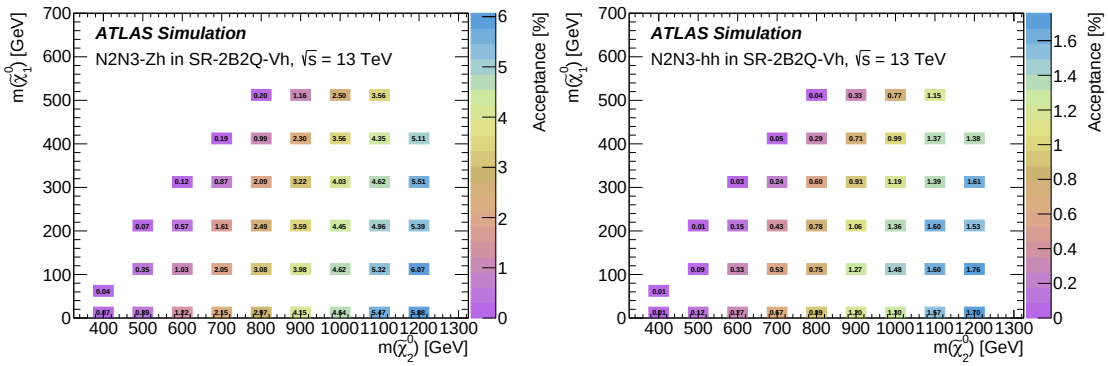

(a) N2N3-Zh in SR-2B2Q-Vh (b) N2N3-hh in SR-2B2Q-Vh

Figure S.4: Acceptance of the N2N3-Zh (a) and N2N3-hh in SR-2B2Q-Vh [49].

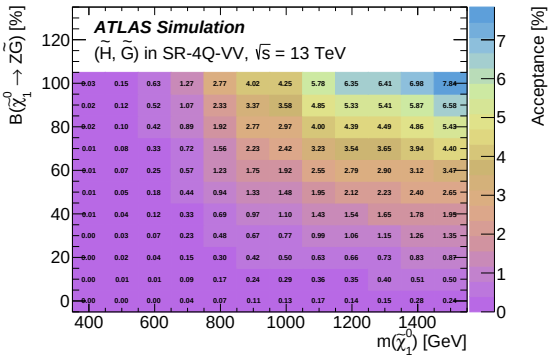

Figure S.5: Acceptance of the $(\tilde{H}, \tilde{G})$ model in SR-4Q-VV [49].

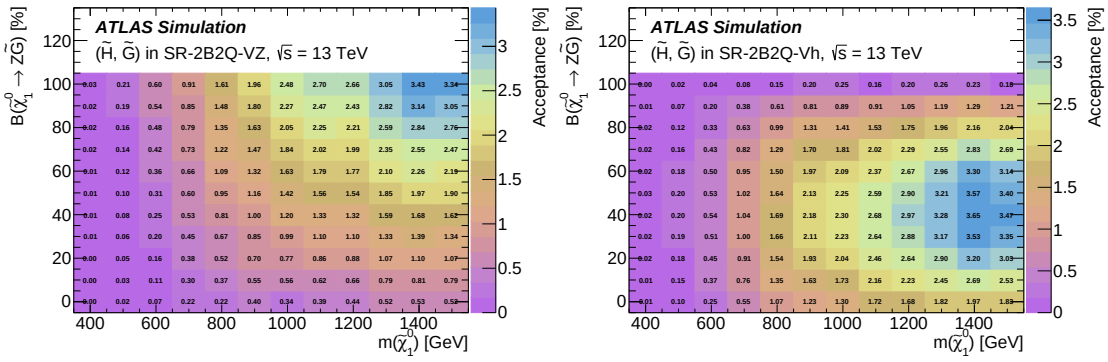

(a) $(\tilde{H}, \tilde{G})$ in SR-2B2Q-VZ

(b) $(\tilde{H}, \tilde{G})$ in SR-2B2Q-Vh

Figure S.6: Acceptance of the $(\tilde{H}, \tilde{G})$ model in SR-2B2Q-VZ (a) and SR-2B2Q-Vh (b) [49].

S.2 Efficiency

Efficiency is defined as the ratio of weighted events with SR selections using generator-level information and ones using detector simulation and object reconstruction. The efficiencies of the reconstruction/identification of leptons, b-tagging, D_2 and n_{trk} selection of the boson tagging are taken into account. The efficiency can be larger than 100%, due to the definition. For example, in the detector simulation, $Z \to qq$ events at generator-level can be categorized to 2B2Q regions with mis-2b-tagged jets.

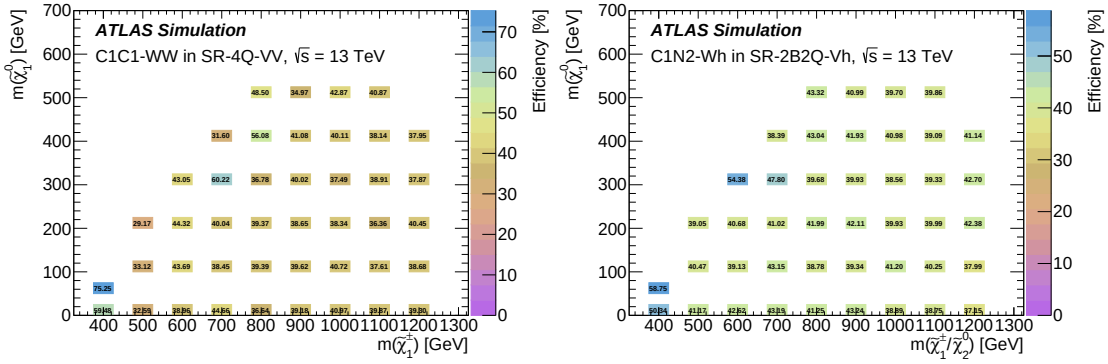

(a) C1C1-WW in SR-4Q-VV (b) C1N2-Wh in SR-2B2Q-Vh

Figure S.7: Efficiency of the C1C1-WW in SR-4Q-VV and C1N2-Wh in SR-2B2Q-Vh [49].

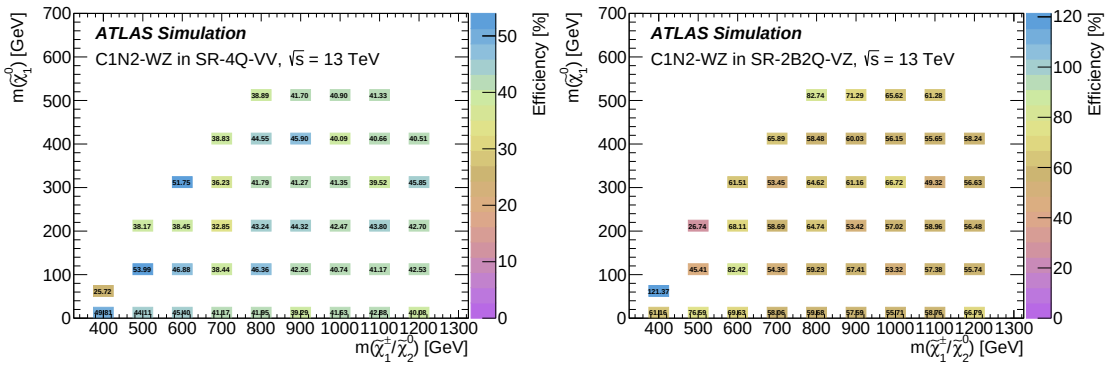

(a) C1N2-WZ in SR-4Q-VV (b) C1N2-WZ in SR-2B2Q-VZ

Figure S.8: Efficiency of the C1N2-WZ in SR-4Q-VV (a) and SR-2B2Q-VZ (b) [49]. Due to mis-2b-tagged jets, the efficiencies in some mass points are slightly larger, and the efficiency of (400 GeV , 50 GeV) of C1N2-WZ in SR-2B2Q-VZ is larger than 100%. This is caused by low MC statistical.

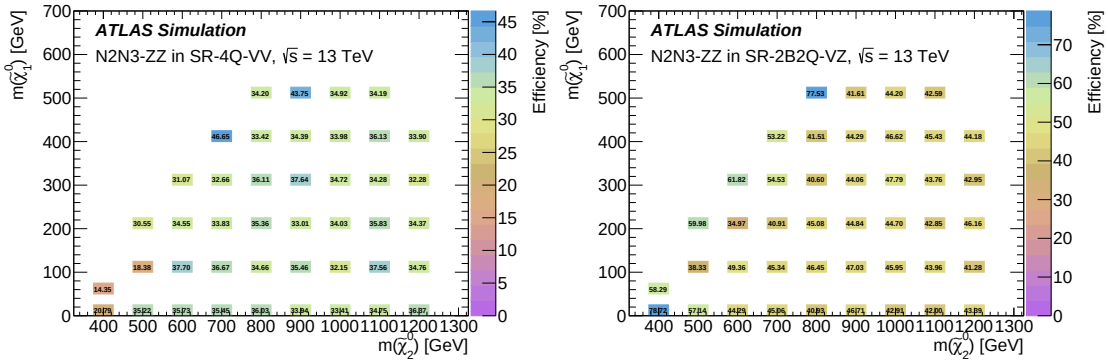

(a) N2N3-ZZ in SR-4Q-VV (b) N2N3-ZZ in SR-2B2Q-VZ

Figure S.9: Efficiency of the N2N3-ZZ in SR-4Q-VV (a) and SR-2B2Q-VZ (b) [49].

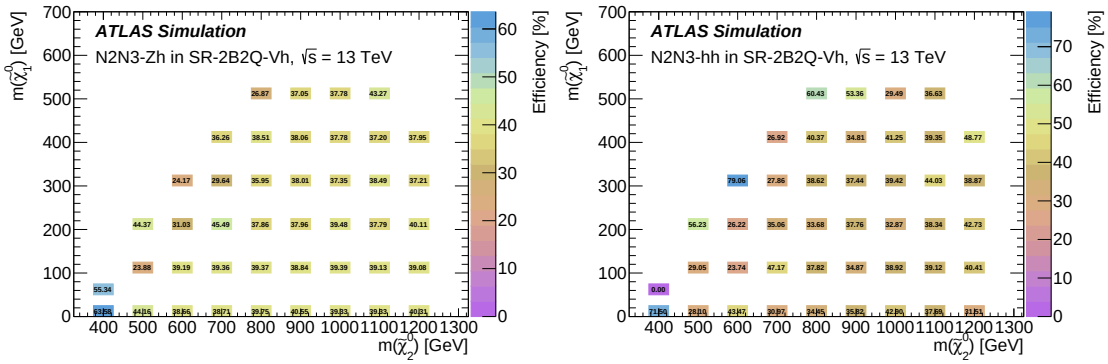

(a) N2N3-Zh in SR-2B2Q-Vh (b) N2N3-hh in SR-2B2Q-Vh

Figure S.10: Efficiency of the N2N3-Zh (a) and N2N3-hh in SR-2B2Q-Vh [49]. Efficiency below 0.005% is rounded to 0.00 in the entry.

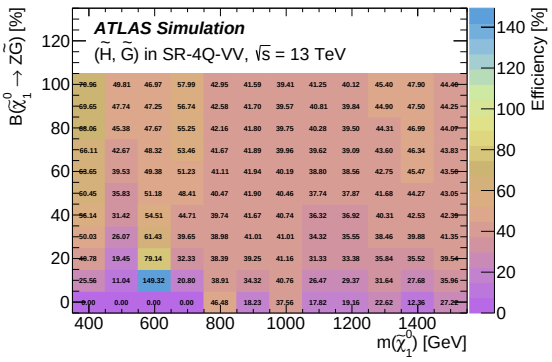

Figure S.11: Efficiency of the $(\tilde{H}, \tilde{G})$ model in SR-4Q-VV [49]. Efficiency below 0.005% is rounded to 0.00 in the entry. Due to the difference of large-R jets between generator-level and detector simulation originating from $h \to VV^* \to qqqq$, the efficiencies in some mass points are slightly larger, and the efficiency of (400 GeV , 50 GeV) of C1N2-WZ in SR-2B2Q-VZ is larger than 100%. This is caused by low MC statistical.

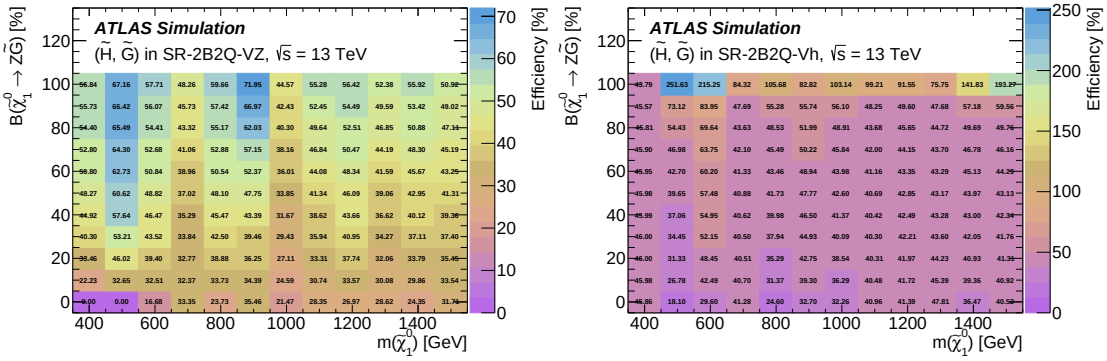

(a) $(\tilde{H}, \tilde{G})$ in SR-2B2Q-VZ

(b) $(\tilde{H}, \tilde{G})$ in SR-2B2Q-Vh

Figure S.12: Efficiency of the $(\tilde{H}, \tilde{G})$ model in SR-2B2Q-VZ (a) and SR-2B2Q-Vh (b) [49]. Efficiency below 0.005% is rounded to 0.00 in the entry. Due to mis-2b-tagged jets, the efficiencies in some mass points are slightly larger, and the efficiency of (400 GeV , 50 GeV) of C1N2-WZ in SR-2B2Q-VZ is larger than 100%. This is caused by low MC statistical.

S.3 Cross-section Upper Limits of Benchmark models

In this section, upper limits on cross-sections of the benchmark models at 95% CL are summarized. The MC expected upper limits are discussed in Appendix S.3.1, and the observed upper limits are discussed in Appendix S.3.2.

S.3.1 Expected Cross-section Upper Limits

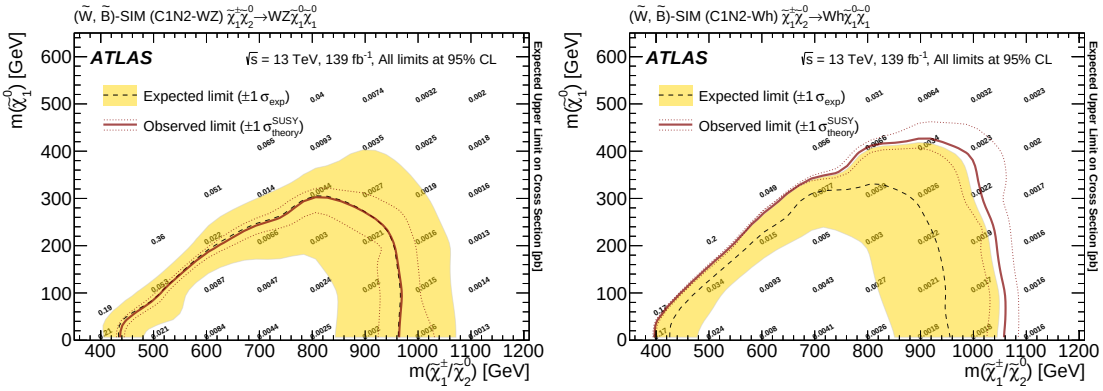

(a) $\tilde{\chi}_1^{\pm}\ \tilde{\chi}_2^0 \to WZ\tilde{\chi}_1^0\ \tilde{\chi}_1^0$ (b) $\tilde{\chi}_1^{\pm}\ \tilde{\chi}_2^0 \to Wh\tilde{\chi}_1^0\ \tilde{\chi}_1^0$

Figure S.13: The black numbers represent the expected cross-section upper limits of the C1N2-WZ (a) and C1N2-Wh (b) [49]. The black dashed (brown solid) lines represent the expected (observed) exclusion limits.

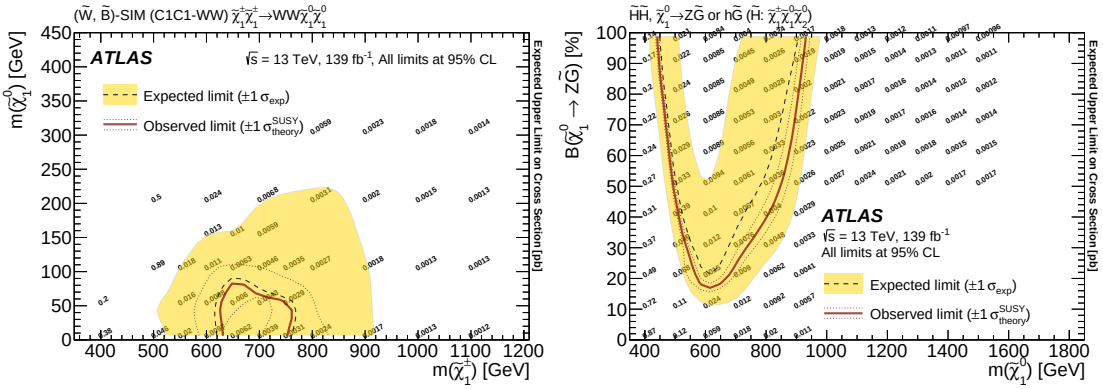

(a) $\tilde{\chi}_1^{\pm}\ \tilde{\chi}_1^{\pm} \to WW\tilde{\chi}_1^0\ \tilde{\chi}_1^0$ (b) $(\tilde{H}, \tilde{G})$

Figure S.14: The black numbers represent the expected cross-section upper limit of the C1C1-WW (a) and $(\tilde{H}, \tilde{G})$ (b) [49]. The black dashed (brown solid) lines represent the expected (observed) exclusion limits.

S.3.2 Observed Cross-section Upper Limits

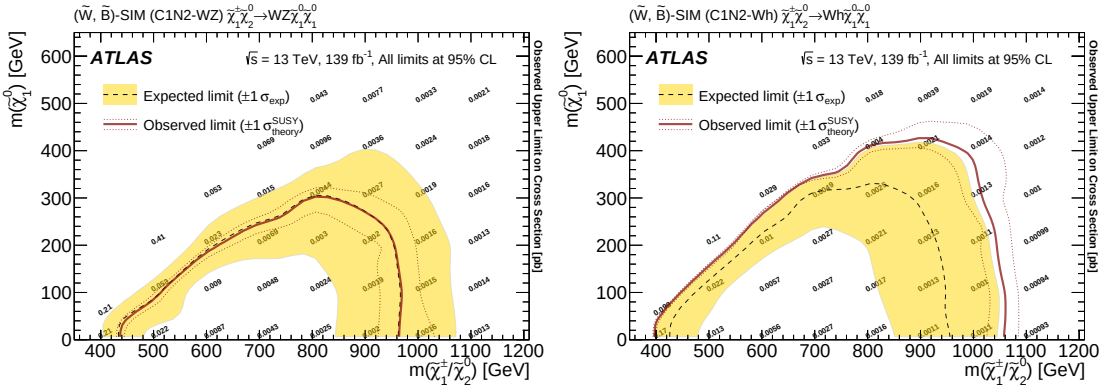

(a) $\tilde{\chi}_1^{\pm}\ \tilde{\chi}_2^0 \to WZ\tilde{\chi}_1^0\ \tilde{\chi}_1^0$ (b) $\tilde{\chi}_1^{\pm}\ \tilde{\chi}_2^0 \to Wh\tilde{\chi}_1^0\ \tilde{\chi}_1^0$

Figure S.15: The black numbers represent the observed cross-section upper limits of the C1N2-WZ (a) and C1N2-Wh (b) [49]. The black dashed (brown solid) lines represent the expected (observed) exclusion limits.

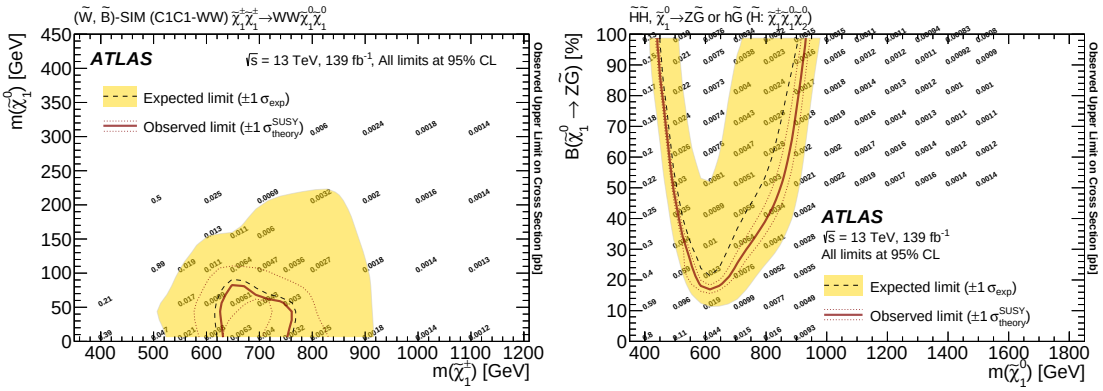

(a) $\tilde{\chi}_1^{\pm}\ \tilde{\chi}_1^{\pm} \to WW\tilde{\chi}_1^0\ \tilde{\chi}_1^0$ (b) $(\tilde{H}, \tilde{G})$

Figure S.16: The black numbers represent the observed cross-section upper limit of the C1C1-WW (a) and $(\tilde{H}, \tilde{G})$ (b) [49]. The black dashed (brown solid) lines represent the expected (observed) exclusion limits.

S.4 $(\tilde{W}, \tilde{B})$

In this section, the expected and observed upper limits on the cross-section with exclusion limits in the $(\tilde{W}, \tilde{B})$ model assuming various branching ratios are shown. The summary plot is shown in Figure 10.12.

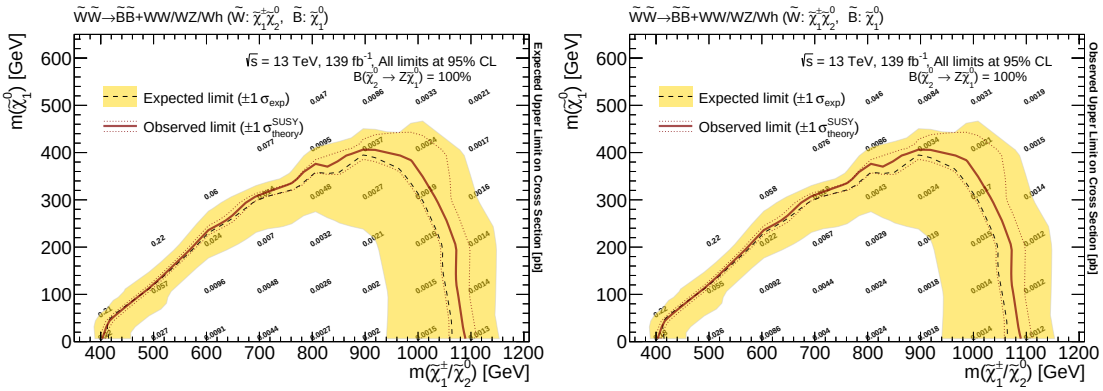

(a) The expected upper limits on the cross-section (b) The observed upper limits on the cross-section

Figure S.17: Expected (a) and observed (b) upper limits on the cross-section with exclusion limits of the $(\tilde{W}, \tilde{B})$ model assuming $\mathcal{B}(\tilde{\chi}_2^0 \to Z\tilde{\chi}_1^0) = 100\%$

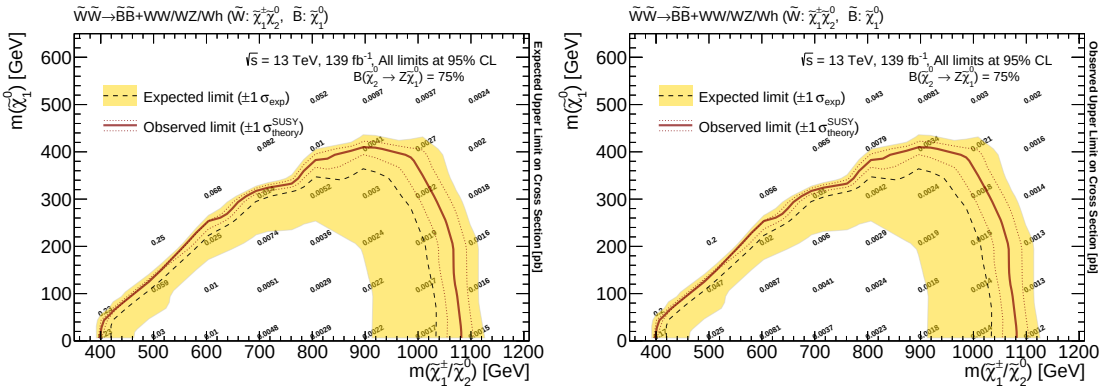

(a) The expected upper limits on the cross-section (b) The observed upper limits on the cross-section

Figure S.18: Expected (a) and observed (b) upper limits on the cross-section with exclusion limits of the $(\tilde{W}, \tilde{B})$ model assuming $\mathcal{B}(\tilde{\chi}_2^0 \to Z\tilde{\chi}_1^0) = 75\%$

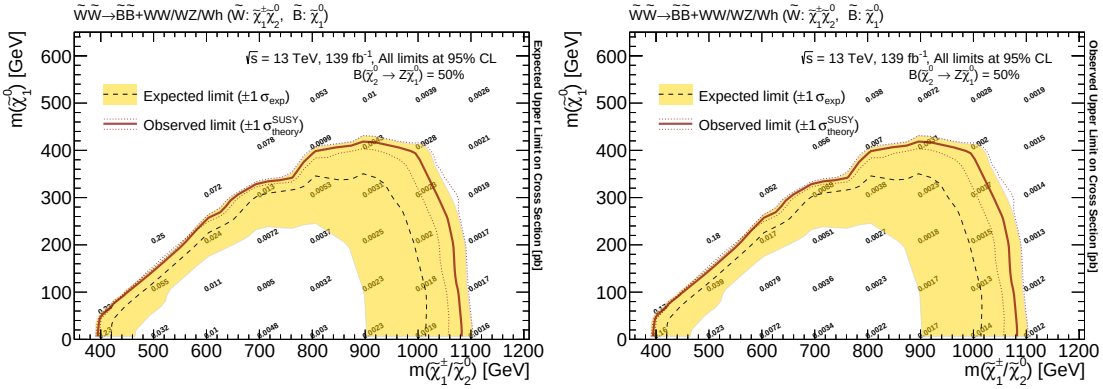

(a) The expected upper limits on the cross-section (b) The observed upper limits on the cross-section

Figure S.19: Expected (a) and observed (b) upper limits on the cross-section with exclusion limits of the $(\tilde{W}, \tilde{B})$ model assuming $\mathcal{B}(\tilde{\chi}_2^0 \to Z\tilde{\chi}_1^0) = 50\%$

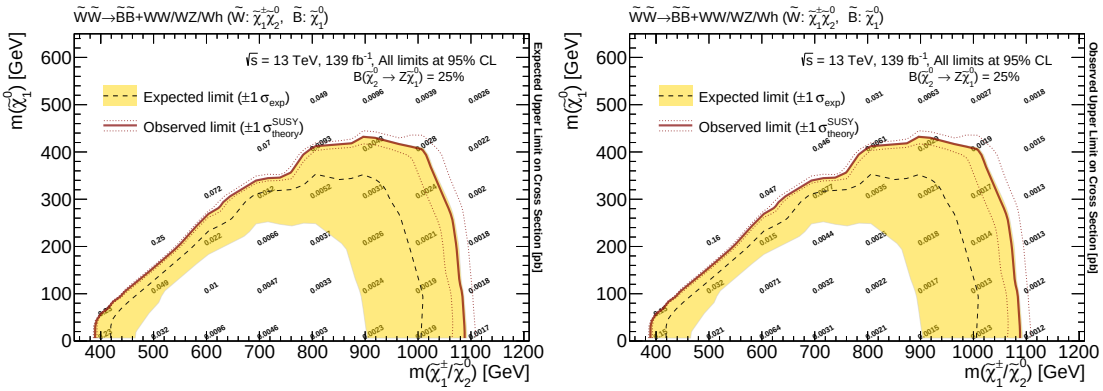

(a) The expected upper limits on the cross-section (b) The observed upper limits on the cross-section

Figure S.20: Expected (a) and observed (b) upper limits on the cross-section with exclusion limits of the $(\tilde{W}, \tilde{B})$ model assuming $\mathcal{B}(\tilde{\chi}_2^0 \to Z\tilde{\chi}_1^0) = 25\%$

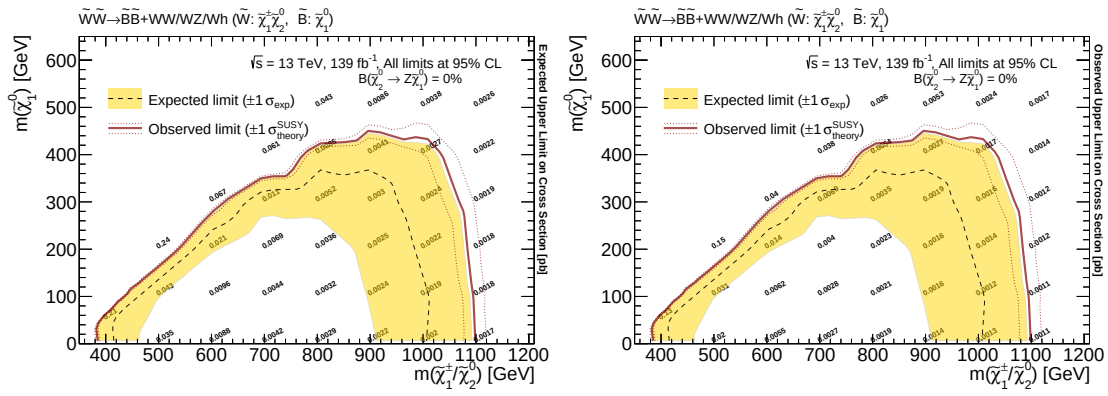

(a) The expected upper limits on the cross-section

(b) The observed upper limits on the cross-section

Figure S.21: Expected (a) and observed (b) upper limits on the cross-section with exclusion limits of the $(\tilde{W}, \tilde{B})$ model assuming $\mathcal{B}(\tilde{\chi}_2^0 \to Z\tilde{\chi}_1^0) = 0\%$

S.5 $(\tilde{H}, \tilde{B})$

In this section, the expected and observed upper limits on the cross-section with exclusion limits in the $(\tilde{H}, \tilde{B})$ model assuming various branching ratios are shown. The summary plot is shown in Figure 10.12.

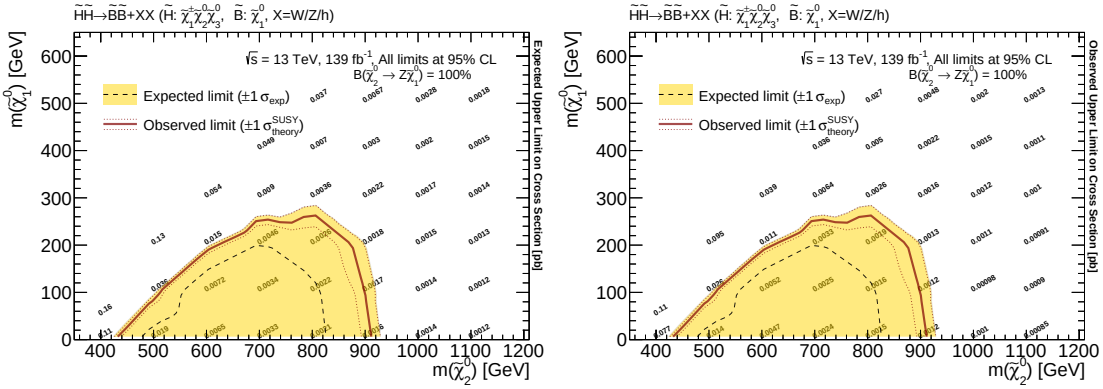

(a) The expected upper limits on the cross-section (b) The observed upper limits on the cross-section

Figure S.22: Expected (a) and observed (b) upper limits on the cross-section with exclusion limits of the $(\tilde{H}, \tilde{B})$ model assuming $\mathcal{B}(\tilde{\chi}_2^0 \to Z\tilde{\chi}_1^0) = 100\%$

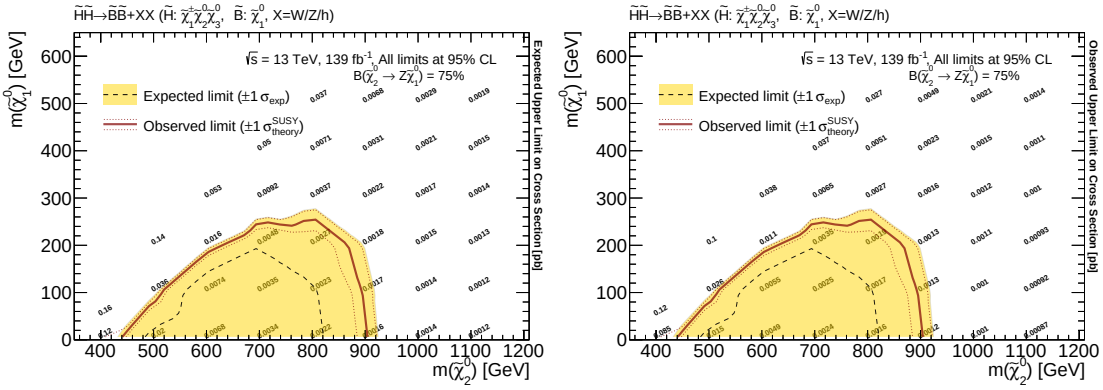

(a) The expected upper limits on the cross-section (b) The observed upper limits on the cross-section

Figure S.23: Expected (a) and observed (b) upper limits on the cross-section with exclusion limits of the $(\tilde{H}, \tilde{B})$ model assuming $\mathcal{B}(\tilde{\chi}_2^0 \to Z\tilde{\chi}_1^0) = 75\%$

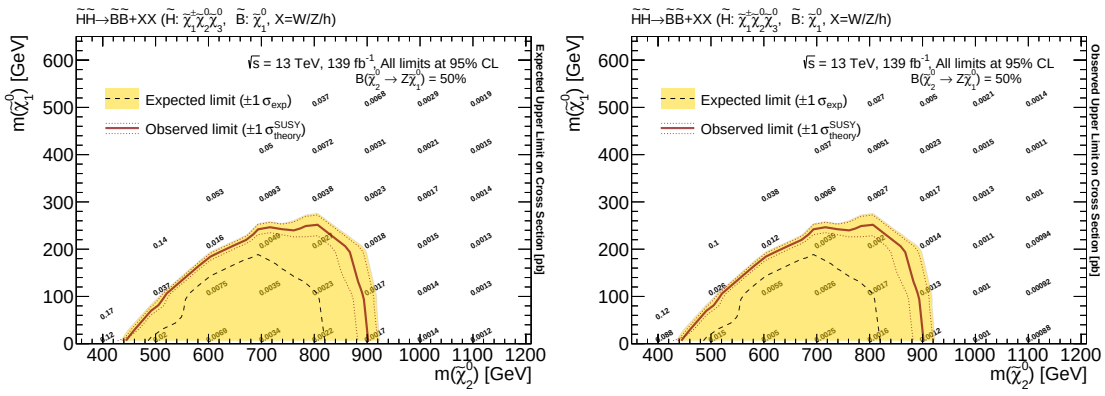

(a) The expected upper limits on the cross-section

(b) The observed upper limits on the cross-section

Figure S.24: Expected (a) and observed (b) upper limits on the cross-section with exclusion limits of the $(\tilde{H}, \tilde{B})$ model assuming $\mathcal{B}(\tilde{\chi}_2^0 \to Z\tilde{\chi}_1^0) = 50\%$

S.6 $(\tilde{W}, \tilde{H})$

In this section, the expected and observed upper limits on the cross-section with exclusion limits in the $(\tilde{W}, \tilde{H})$ model assuming various $\tan\beta$ and sign(μ) are shown. The summary plot is shown in Figure 10.13.

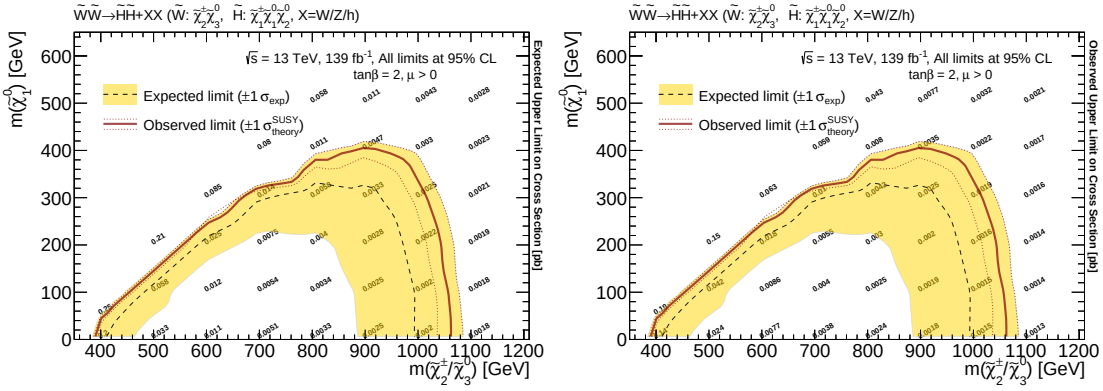

(a) The expected upper limits on the cross-section (b) The observed upper limits on the cross-section

Figure S.25: Expected (a) and observed (b) upper limits on the cross-section with exclusion limits of the $(\tilde{W}, \tilde{H})$ model assuming $\tan\beta = 2, \mu > 0$.

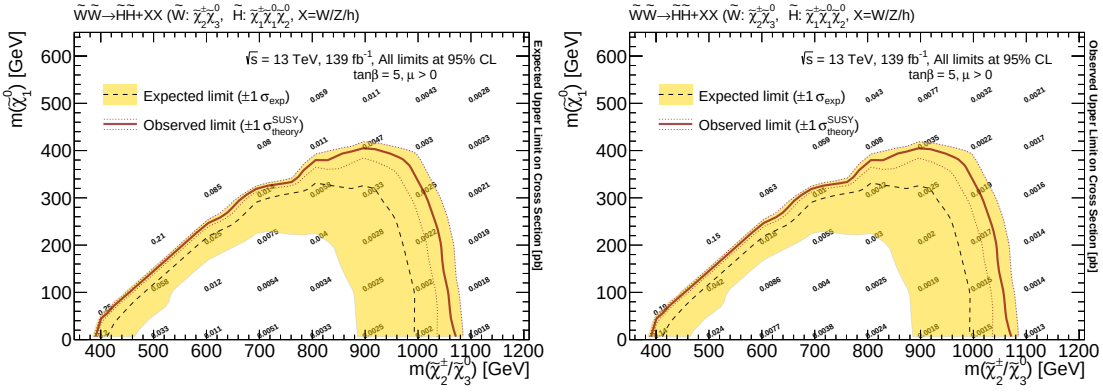

(a) The expected upper limits on the cross-section (b) The observed upper limits on the cross-section

Figure S.26: Expected (a) and observed (b) upper limits on the cross-section with exclusion limits of the $(\tilde{W}, \tilde{H})$ model assuming $\tan\beta = 5, \mu > 0$.

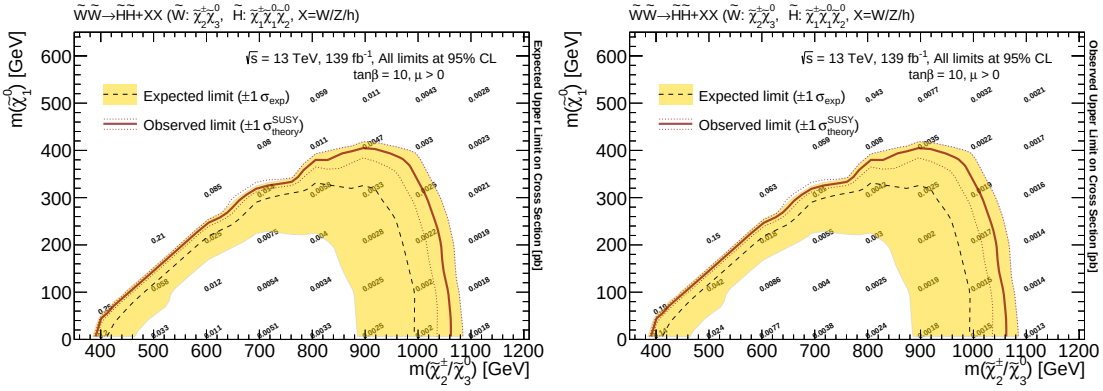

(a) The expected upper limits on the cross-section (b) The observed upper limits on the cross-section

Figure S.27: Expected (a) and observed (b) upper limits on the cross-section with exclusion limits of the $(\tilde{W}, \tilde{H})$ model assuming $\tan\beta = 10, \mu > 0$.

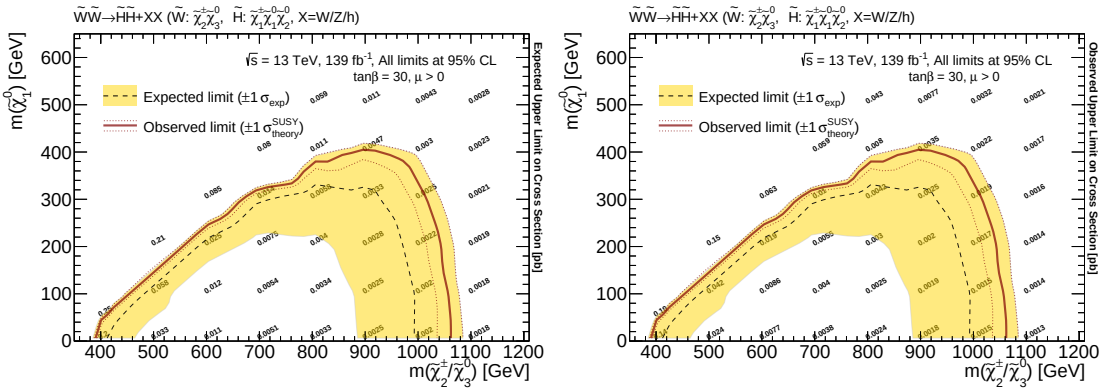

(a) The expected upper limits on the cross-section (b) The observed upper limits on the cross-section

Figure S.28: Expected (a) and observed (b) upper limits on the cross-section with exclusion limits of the $(\tilde{W}, \tilde{H})$ model assuming $\tan\beta = 30, \mu > 0$.

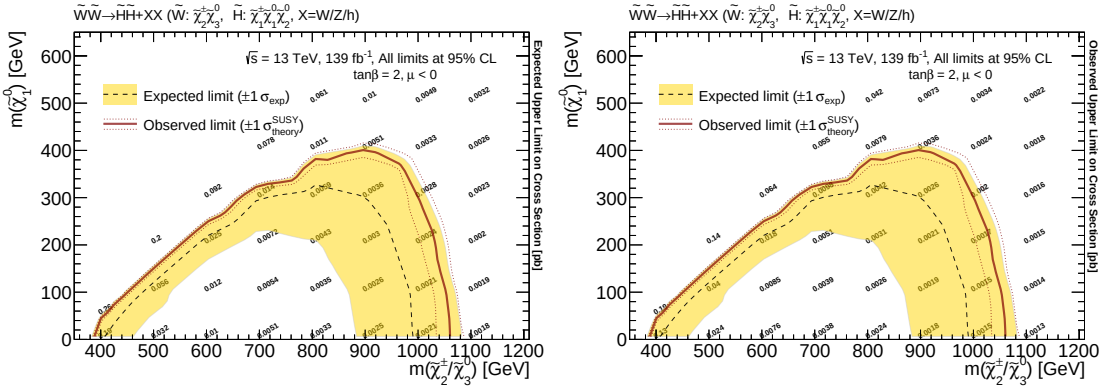

(a) The expected upper limits on the cross-section (b) The observed upper limits on the cross-section

Figure S.29: Expected (a) and observed (b) upper limits on the cross-section with exclusion limits of the $(\tilde{W}, \tilde{H})$ model assuming $\tan\beta = 2, \mu < 0$.

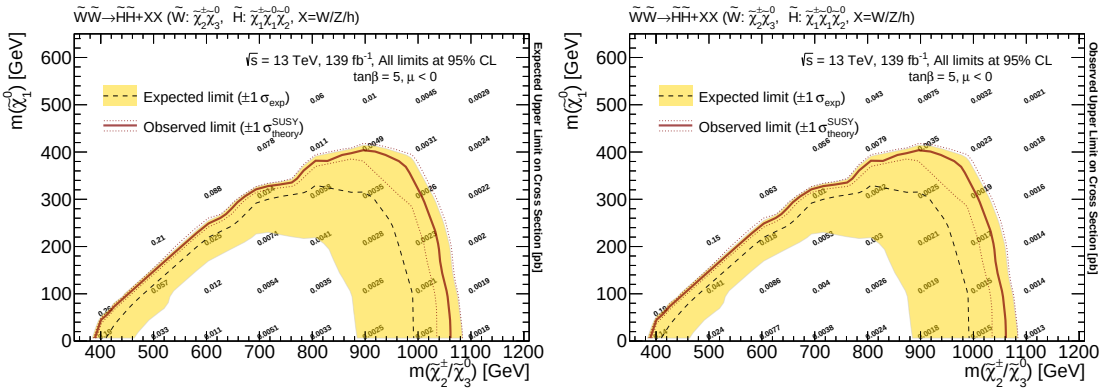

(a) The expected upper limits on the cross-section (b) The observed upper limits on the cross-section

Figure S.30: Expected (a) and observed (b) upper limits on the cross-section with exclusion limits of the $(\tilde{W}, \tilde{H})$ model assuming $\tan\beta = 5, \mu < 0$.

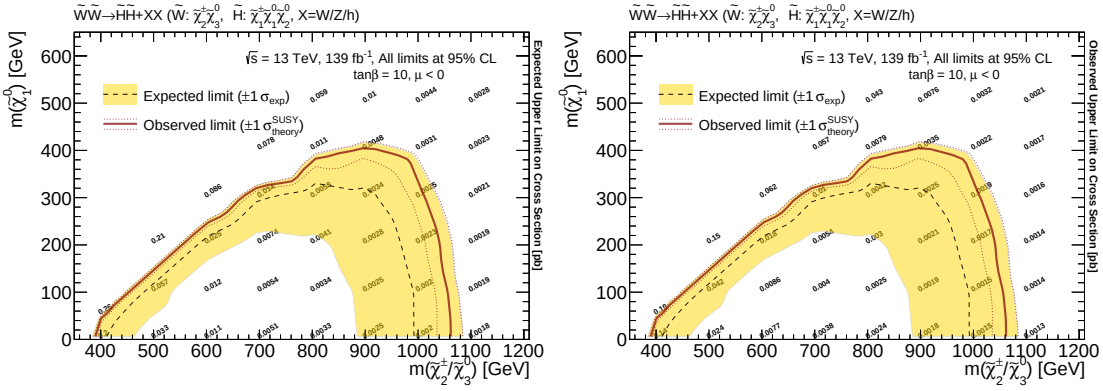

(a) The expected upper limits on the cross-section (b) The observed upper limits on the cross-section

Figure S.31: Expected (a) and observed (b) upper limits on the cross-section with exclusion limits of the $(\tilde{W}, \tilde{H})$ model assuming $\tan\beta = 10, \mu < 0$.

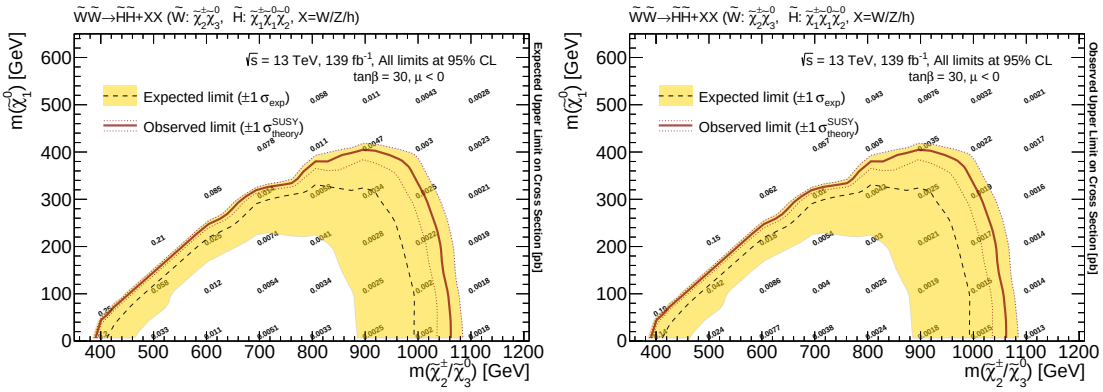

(a) The expected upper limits on the cross-section (b) The observed upper limits on the cross-section

Figure S.32: Expected (a) and observed (b) upper limits on the cross-section with exclusion limits of the $(\tilde{W}, \tilde{H})$ model assuming $\tan\beta = 30, \mu < 0$.

S.7 $(\tilde{H}, \tilde{W})$

In this section, the expected and observed upper limits on the cross-section with exclusion limits in the $(\tilde{H}, \tilde{W})$ model assuming various $\tan\beta$ and sign(μ) are shown. The summary plot is shown in Figure 10.13.

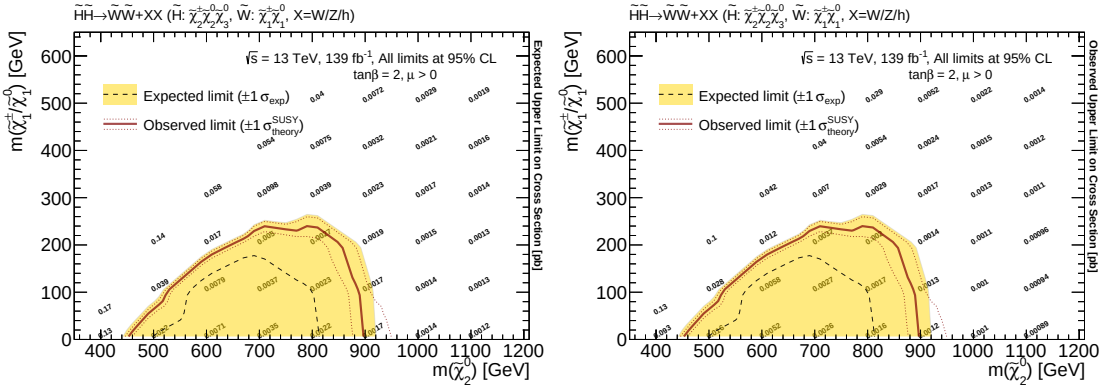

(a) The expected upper limits on the cross-section (b) The observed upper limits on the cross-section

Figure S.33: Expected (a) and observed (b) upper limits on the cross-section with exclusion limits of the $(\tilde{H}, \tilde{W})$ model assuming $\tan\beta = 2, \mu > 0$.

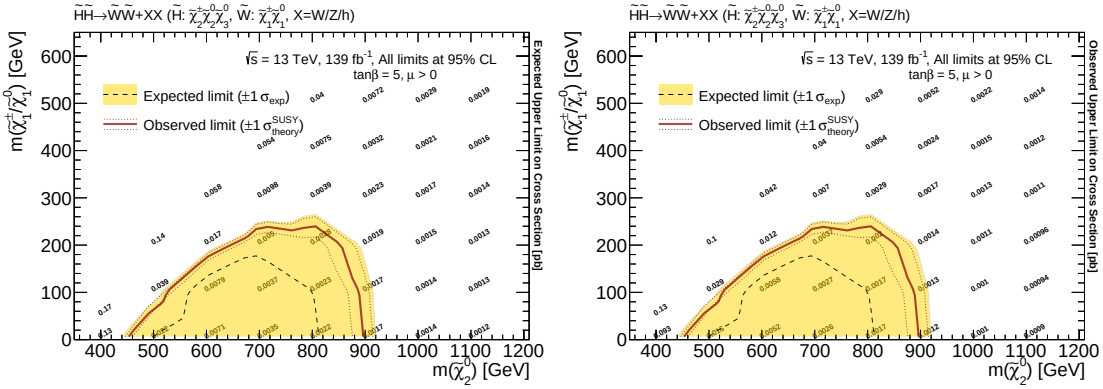

(a) The expected upper limits on the cross-section (b) The observed upper limits on the cross-section

Figure S.34: Expected (a) and observed (b) upper limits on the cross-section with exclusion limits of the $(\tilde{H}, \tilde{W})$ model assuming $\tan\beta = 5, \mu > 0$.

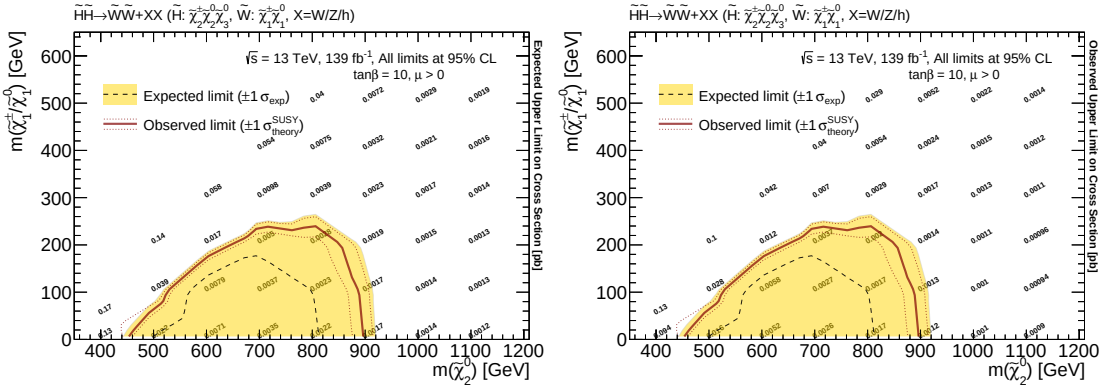

(a) The expected upper limits on the cross-section (b) The observed upper limits on the cross-section

Figure S.35: Expected (a) and observed (b) upper limits on the cross-section with exclusion limits of the $(\tilde{H}, \tilde{W})$ model assuming $\tan\beta = 10, \mu > 0$.

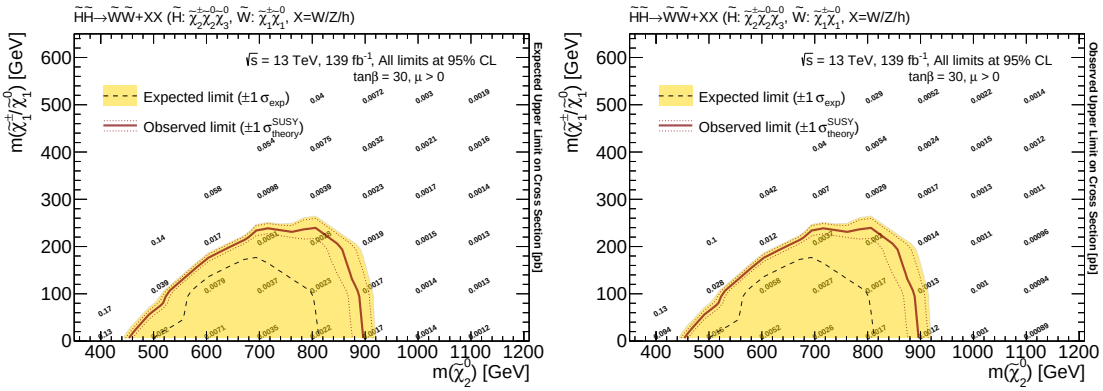

(a) The expected upper limits on the cross-section (b) The observed upper limits on the cross-section

Figure S.36: Expected (a) and observed (b) upper limits on the cross-section with exclusion limits of the $(\tilde{H}, \tilde{W})$ model assuming $\tan\beta = 30, \mu > 0$.

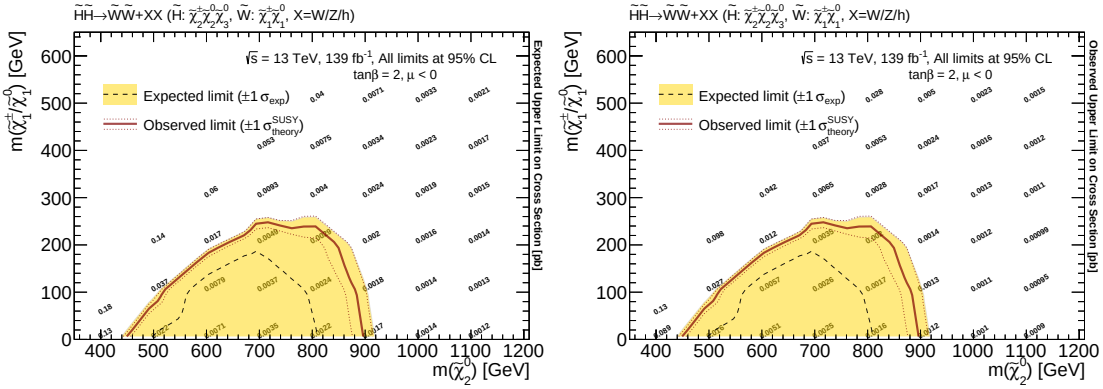

(a) The expected upper limits on the cross-section (b) The observed upper limits on the cross-section

Figure S.37: Expected (a) and observed (b) upper limits on the cross-section with exclusion limits of the $(\tilde{H}, \tilde{W})$ model assuming $\tan\beta = 2, \mu < 0$.

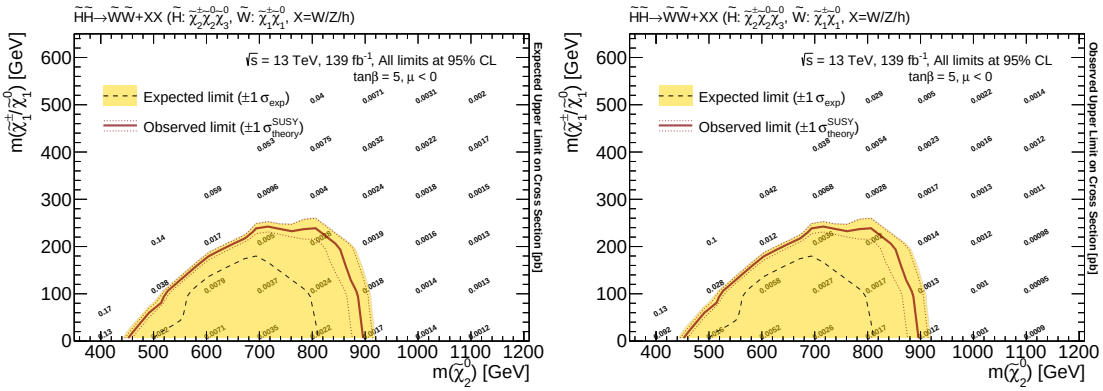

(a) The expected upper limits on the cross-section (b) The observed upper limits on the cross-section

Figure S.38: Expected (a) and observed (b) upper limits on the cross-section with exclusion limits of the $(\tilde{H}, \tilde{W})$ model assuming $\tan\beta = 5, \mu < 0$.

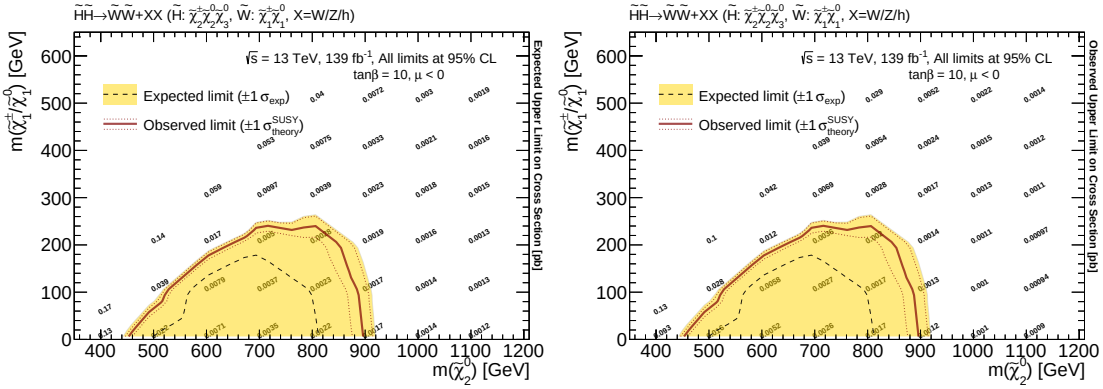

(a) The expected upper limits on the cross-section (b) The observed upper limits on the cross-section

Figure S.39: Expected (a) and observed (b) upper limits on the cross-section with exclusion limits of the $(\tilde{H}, \tilde{W})$ model assuming $\tan\beta = 10, \mu < 0$.

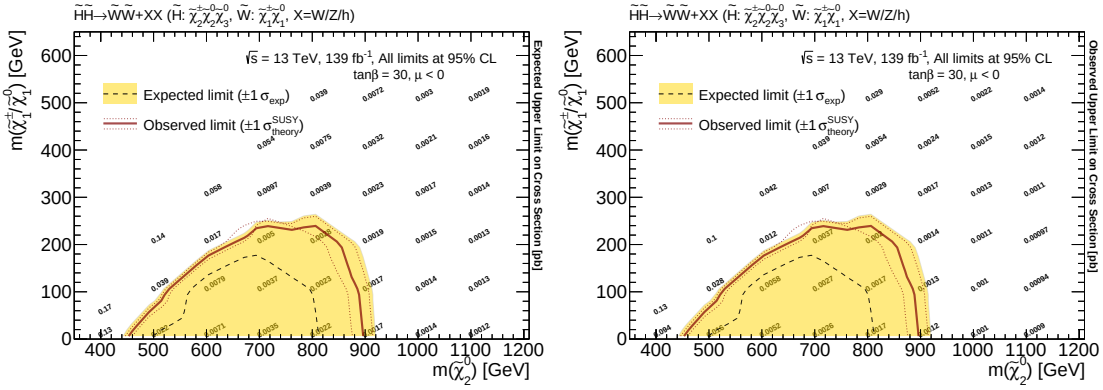

(a) The expected upper limits on the cross-section (b) The observed upper limits on the cross-section

Figure S.40: Expected (a) and observed (b) upper limits on the cross-section with exclusion limits of the $(\tilde{H}, \tilde{W})$ model assuming $\tan\beta = 30, \mu < 0$.

S.8 $(\tilde{H}, \tilde{a})$

In this section, the expected and observed upper limits on the cross-section with exclusion limits in the $(\tilde{H}, \tilde{a})$ model assuming various branching ratios are shown. The summary plot is shown in Figure 10.15.

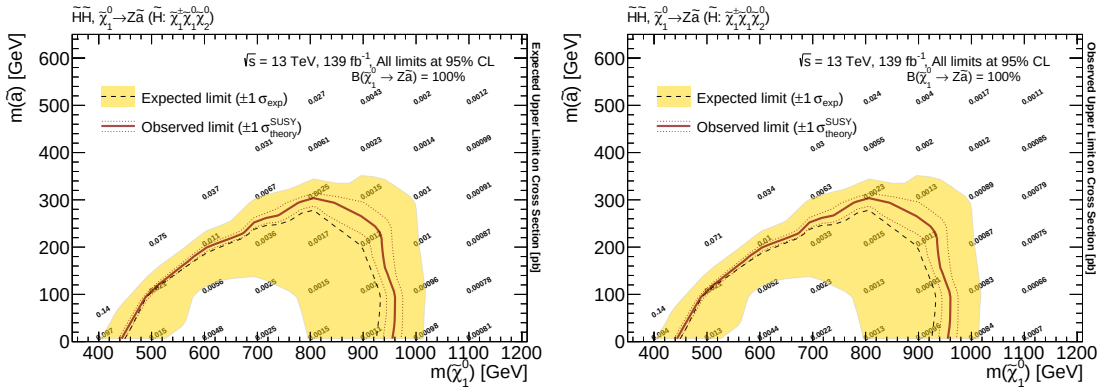

(a) The expected upper limits on the cross-section (b) The observed upper limits on the cross-section

Figure S.41: Expected (a) and observed (b) upper limits on the cross-section with exclusion limits of the $(\tilde{H}, \tilde{a})$ model assuming $\mathcal{B}(\tilde{\chi}_1^0 \to Z\tilde{a}) = 100\%$

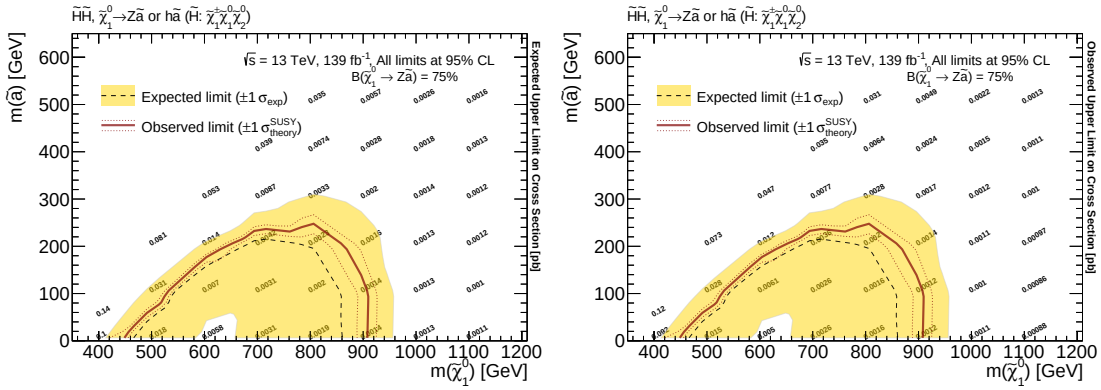

(a) The expected upper limits on the cross-section (b) The observed upper limits on the cross-section

Figure S.42: Expected (a) and observed (b) upper limits on the cross-section with exclusion limits of the $(\tilde{H}, \tilde{a})$ model assuming $\mathcal{B}(\tilde{\chi}_1^0 \to Z\tilde{a}) = 75\%$

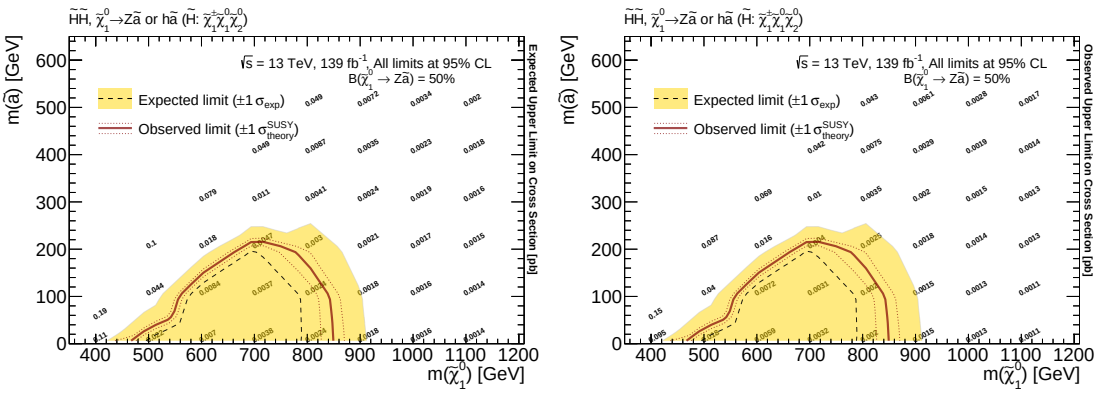

(a) The expected upper limits on the cross-section

(b) The observed upper limits on the cross-section

Figure S.43: Expected (a) and observed (b) upper limits on the cross-section with exclusion limits of the $(\tilde{H}, \tilde{a})$ model assuming $\mathcal{B}(\tilde{\chi}_1^0 \to Z\tilde{a}) = 50\%$

T Event Display

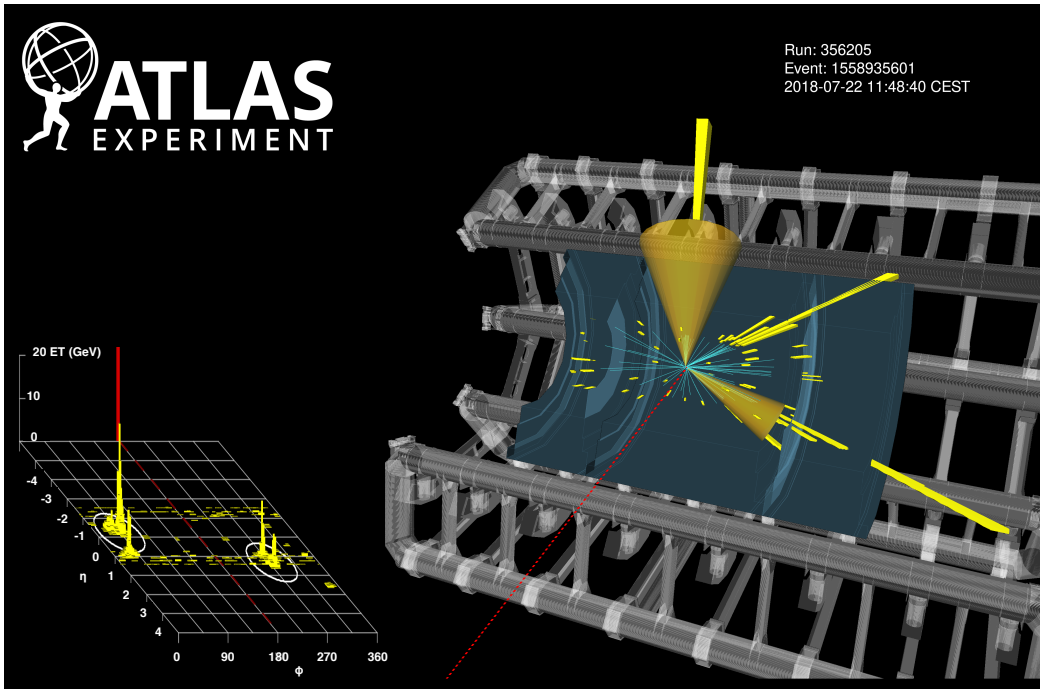

Figure T.1: Event displays of a data event recorded in July of 2018 which is categorized into SR-4Q-VV [49]. In the right display, the reconstructed objects are illustrated in the detector. The light blue lines represent the inner-detector tracks ($p_{\mathrm{T}} > 1.5$ GeV). The yellow bars indicate the energy deposit in the calorimeter clusters. The profile of calorimeter energy deposit projected on the $\eta - \phi$ plane in the left display. The orange cones on the right or white circles on the left represent large-R jets and the red lines indicate missing tranverse momentum. The two large-R jets have kinematic properties ($p_{\mathrm{T}}, m, \eta, \phi$) of (436.65 GeV , 69.75 GeV , -0.24, 0.75) and (325.63 GeV , 83.23 GeV , 1.34, -1.54), with a clear two-prong substructure seen in the energy deposit. The missing tranverse momentum has a magnitude of $E_{\mathrm{T}}^{\mathrm{miss}} = 569.5$ GeV and $\phi = -3.03$.

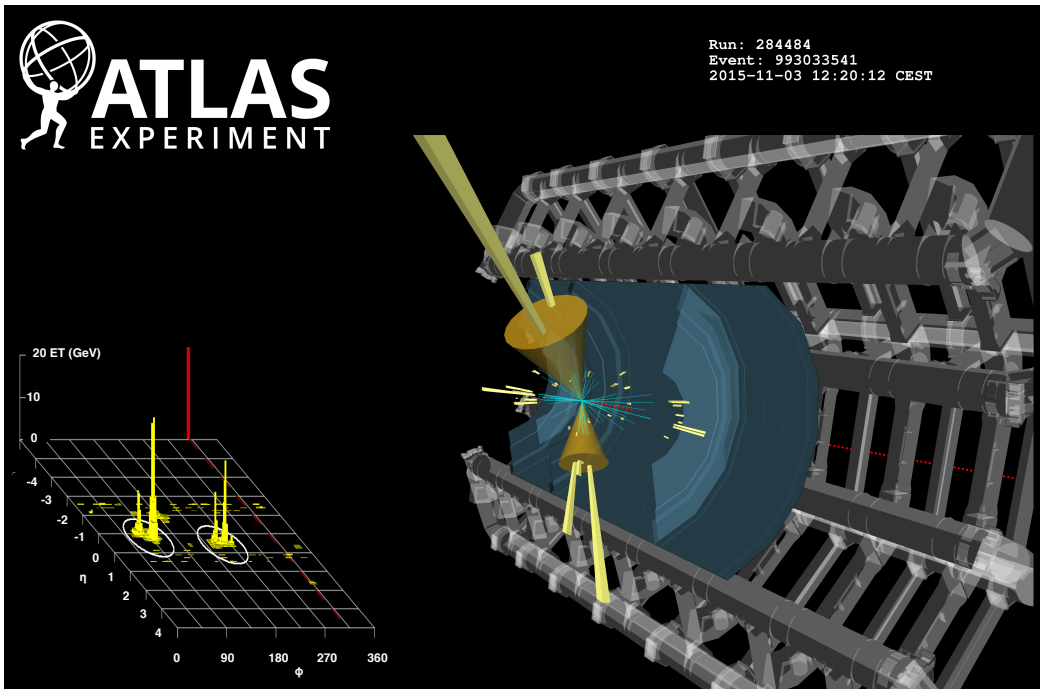

Figure T.2: Event displays of a data event recorded in November of 2015 which is categorized into SR-2B2Q-VZ [49]. In the right display, the reconstructed objects are illustrated in the detector. The light blue lines represent the inner-detector tracks ($p_{\mathrm{T}} > 1.5$ GeV). The yellow bars indicate the energy deposit in the calorimeter clusters. The profile of calorimeter energy deposit projected on the $\eta - \phi$ plane in the left display. The orange cones on the right or white circles on the left represent large-R jets and the red lines indicate missing tranverse momentum. The two large-R jets have kinematic properties ($p_{\mathrm{T}}, m, \eta, \phi$) of (313.21 GeV , 70.50 GeV , 0.58, -2.61) and (454.71 GeV , 85.98 GeV , 0.23, 1.49) respectively, where the former also contains two b-tagged VR track jets in it. A clear two-prong substructure seen in the energy deposit in both large-R jets. The missing tranverse momentum has a magnitude of $E_{\mathrm{T}}^{\mathrm{miss}} = 499.5$ GeV and $\phi = -0.87$.

Bibliography

[1] ATLAS Collaboration, *Observation of a new particle in the search for the Standard Model Higgs boson with the ATLAS detector at the LHC*, Phys. Lett. B **716** (2012) 1, arXiv: 1207.7214 [hep-ex] (cit. on pp. 23, 26).

[2] CMS Collaboration, *Observation of a new boson at a mass of 125 GeV with the CMS experiment at the LHC*, Phys. Lett. B **716** (2012) 30, arXiv: 1207.7235 [hep-ex] (cit. on pp. 23, 26).

[3] ATLAS Collaboration, *The ATLAS Experiment at the CERN Large Hadron Collider*, JINST **3** (2008) S08003 (cit. on p. 23).

[4] CMS Collaboration, *The CMS experiment at the CERN LHC*, JINST **3** (2008) S08004 (cit. on pp. 23, 47).

[5] A. Collaboration, *Additional plots of the ATLAS Higgs physics group*, URL: https://atlas.web.cern.ch/Atlas/GROUPS/PHYSICS/CombinedSummaryPlots/HIGGS/ (cit. on p. 23).

[6] V. C. Rubin and W. K. F. Jr., *Rotation of the Andromeda Nebula from a Spectroscopic Survey of Emission Regions*, Astrophys.J. **159** (1970) 379 (cit. on pp. 23, 35).

[7] N. T. V. C. Rubin and W. K. F. Jr., *Rotational properties of 21 SC galaxies with a large range of luminosities and radii, from NGC 4605 /R = 4kpc/ to UGC 2885 /R = 122 kpc/*, Astrophys.J. **238** (1980) 471 (cit. on pp. 23, 35).

[8] C. L. Bennett et al., *Nine-Year Wilkinson Microwave Anisotropy Probe (WMAP) Observations: Final Maps and Results*, The Astrophysical Journal Supplement Series **208** (2012), ISSN: 0067-0049, arXiv: 1212.5225 (cit. on pp. 23, 35, 183).

[9] Planck Collaboration, *Astrophysics Special feature Planck 2015 results*, Astronomy & Astrophysics **594** (2016), arXiv: 1502.01589 (cit. on pp. 23, 35, 183).

[10] A. J. Larkoski, I. Moult, and D. Neill, *Power Counting to Better Jet Observables*, JHEP **12** (2014) 009, arXiv: 1409.6298 [hep-ph] (cit. on pp. 25, 77).

[11] M. E. Peskin and D. V. Schroeder, *An Introduction to quantum field theory*, Addison-Wesley, 1995, ISBN: 978-0-201-50397-5 (cit. on p. 26).

[12] F. Englert and R. Brout, *Broken Symmetry and the Mass of Gauge Vector Mesons*, Phys. Rev. Lett. **13** (9 1964) 321 (cit. on p. 26).

[13] P. Higgs, *Broken symmetries, massless particles and gauge fields*, Physics Letters **12** (1964) 132 (cit. on p. 26).

[14] Y. A. Gol'fand and E. P. Likhtman, *Extension of the Algebra of Poincare Group Generators and Violation of p Invariance*, JETP Lett. **13** (1971) 323, [Pisma Zh.Eksp.Teor.Fiz.13:452-455,1971] (cit. on pp. 27, 191).

[15] D. V. Volkov and V. P. Akulov, *Is the Neutrino a Goldstone Particle?* Phys. Lett. B **46** (1973) 109 (cit. on pp. 27, 191).

[16] J. Wess and B. Zumino, *Supergauge Transformations in Four-Dimensions*, Nucl. Phys. B **70** (1974) 39 (cit. on pp. 27, 191).

[17] J. Wess and B. Zumino, *Supergauge Invariant Extension of Quantum Electrodynamics*, Nucl. Phys. B **78** (1974) 1 (cit. on pp. 27, 191).

[18] S. Ferrara and B. Zumino, *Supergauge Invariant Yang-Mills Theories*, Nucl. Phys. B **79** (1974) 413 (cit. on pp. 27, 191).

[19] A. Salam and J. A. Strathdee, *Supersymmetry and Nonabelian Gauges*, Phys. Lett. B **51** (1974) 353 (cit. on pp. 27, 191).

[20] S. P. Martin, *A Supersymmetry Primer*, Adv. Ser. Direct. High Energy Phys. **18** (1998) 1, arXiv: hep-ph/9709356 (cit. on pp. 28, 29, 31, 32, 193).

[21] G. Branco, P. Ferreira, L. Lavoura, M. Rebelo, M. Sher, et al., *Theory and phenomenology of two-Higgs-doublet models*, Phys. Rept. **516** (2012) 1, arXiv: 1106.0034 [hep-ph] (cit. on p. 28).

[22] S. Dimopoulos and D. W. Sutter, *The Supersymmetric flavor problem*, Nucl. Phys. **B452** (1995) 496, arXiv: 9504415 [hep-ph] (cit. on p. 29).

[23] L. J. Hall, D. Pinner, and J. T. Ruderman, *A natural SUSY Higgs near 125 GeV*, Journal of High Energy Physics **2012** (2012) 131, ISSN: 11266708, arXiv: 1112.2703 (cit. on pp. 31, 33).

[24] M. Papucci, J. T. Ruderman, and A. Weiler, *Natural SUSY endures*, Journal of High Energy Physics **2012** (2012), ISSN: 1029-8479, URL: http://dx.doi.org/10.1007/JHEP09(2012)035 (cit. on pp. 31–33).

[25] A. Djouadi, J.-L. Kneur, and G. Moultaka, *SuSpect: A Fortran code for the Supersymmetric and Higgs particle spectrum in the MSSM*, Computer Physics Communications **176** (2007) 426 455, ISSN: 0010-4655, URL: http://dx.doi.org/10.1016/j.cpc.2006.11.009 (cit. on p. 33).

[26] S. Heinemeyer, W. Hollik, and G. Weiglein, *FeynHiggs: A Program for the calculation of the masses of the neutral CP even Higgs bosons in the MSSM*, Comput.Phys.Commun. **124** (2000) 76, arXiv: hep-ph/9812320 (cit. on p. 33).

[27] S. Heinemeyer, W. Hollik, and G. Weiglein, *The Masses of the neutral CP-even Higgs bosons in the MSSM: Accurate analysis at the two loop level*, Eur. Phys. J. C **9** (1999) 343, arXiv: hep-ph/9812472 (cit. on p. 33).

[28] G. Degrassi, S. Heinemeyer, W. Hollik, P. Slavich, and G. Weiglein, *Towards high precision predictions for the MSSM Higgs sector*, Eur. Phys. J. C **28** (2003) 133, arXiv: hep-ph/0212020 (cit. on p. 33).

[29] T. A. Collaboration, *SUSY March 2021 Summary Plot Update*, ATL-PHYS-PUB-2021-007, 2021 (cit. on pp. 32, 34, 43, 45).

[30] C. Collaboration, *CMS Supersymmetry Physics Results*, URL: https://twiki.cern.ch/twiki/bin/view/CMSPublic/PhysicsResultsSUS (cit. on p. 32).

[31] J. Alwall, M.-P. Le, M. Lisanti, and J. G. Wacker, *Searching for directly decaying gluinos at the Tevatron*, Phys. Lett. B **666** (2008) 34, arXiv: 0803.0019 [hep-ph] (cit. on pp. 32, 38).

[32] J. Alwall, P. Schuster, and N. Toro, *Simplified models for a first characterization of new physics at the LHC*, Phys. Rev. D **79** (2009) 075020, arXiv: 0810.3921 [hep-ph] (cit. on pp. 32, 38).

[33] D. Alves et al., *Simplified models for LHC new physics searches*, J. Phys. G **39** (2012) 105005, arXiv: 1105.2838 [hep-ph] (cit. on pp. 32, 38).

[34] J. A. Casas, J. M. Moreno, S. Robles, K. Rolbiecki, and B. Zaldívar, *What is a natural SUSY scenario?* Journal of High Energy Physics **2015** (2015), ISSN: 1029-8479, URL: http://dx.doi.org/10.1007/JHEP06(2015)070 (cit. on p. 32).

[35] R. Barbieri and D. Pappadopulo, *S-particles at their naturalness limits*, Journal of High Energy Physics **2009** (2009) 061–061, ISSN: 1029-8479, URL: http://dx.doi.org/10.1088/1126-6708/2009/10/061 (cit. on p. 32).

[36] H. Baer, V. Barger, and P. Huang, *Hidden SUSY at the LHC: the light higgsino-world scenario and the role of a lepton collider*, Journal of High Energy Physics **2011** (2011), ISSN: 1029-8479, URL: http://dx.doi.org/10.1007/JHEP11(2011)031 (cit. on p. 32).

[37] H. Baer, V. Barger, P. Huang, A. Mustafayev, and X. Tata, *Radiative Natural Supersymmetry with a 125 GeV Higgs Boson*, Physical Review Letters **109** (2012), ISSN: 1079-7114, URL: http://dx.doi.org/10.1103/PhysRevLett.109.161802 (cit. on p. 32).

[38] A. Djouadi et al., *The Minimal supersymmetric standard model: Group summary report*, 1998, arXiv: hep-ph/9901246 (cit. on p. 35).

[39] ATLAS Collaboration, *Summary of the ATLAS experiment's sensitivity to supersymmetry after LHC Run 1 — interpreted in the phenomenological MSSM*, JHEP **10** (2015) 134, arXiv: 1508.06608 [hep-ex] (cit. on p. 36).

[40] T. L.S. W. Group, L. the ALEPH DELPHI, and O. experiments, *note LEPSUSYWG/01-03.1*, URL: http://lepsusy.web.cern.ch/lepsusy (cit. on pp. 36, 177, 179, 183).

[41] K. Hamaguchi and K. Ishikawa, *Prospects for Higgs- and Z-resonant Neutralino Dark Matter*, Phys. Rev. **D93** (2016) 055009, arXiv: 1510.05378 [hep-ph] (cit. on pp. 35, 43, 177, 178, 192, 194).

[42] A. Keshavarzi, D. Nomura, and T. Teubner, *g-2 of charged leptons, α(MZ2), and the hyperfine splitting of muonium*, Physical Review D **101** (2020), ISSN: 2470-0029, URL: http://dx.doi.org/10.1103/PhysRevD.101.014029 (cit. on p. 36).

[43] M. Davier, A. Hoecker, B. Malaescu, and Z. Zhang, *A new evaluation of the hadronic vacuum polarisation contributions to the muon anomalous magnetic moment and to $\alpha(m_Z^2)$*, The European Physical Journal C **80** (2020), ISSN: 1434-6052, URL: http://dx.doi.org/10.1140/epjc/s10052-020-7792-2 (cit. on p. 36).

[44] T. Albahri et al., *Measurement of the anomalous precession frequency of the muon in the Fermilab Muon g-2 Experiment*, Physical Review D **103** (2021), ISSN: 2470-0029, URL: http://dx.doi.org/10.1103/PhysRevD.103.072002 (cit. on p. 36).

[45] B. Abi et al., *Measurement of the Positive Muon Anomalous Magnetic Moment to 0.46 ppm*, Physical Review Letters **126** (2021), ISSN: 1079-7114, URL: http://dx.doi.org/10.1103/PhysRevLett.126.141801 (cit. on pp. 36, 181, 182).

[46] S. Iwamoto, T. T. Yanagida, and N. Yokozaki, *Wino-Higgsino dark matter in the MSSM from the $g-2$ anomaly*, 2021, arXiv: 2104.03223 [hep-ph] (cit. on pp. 37, 181).

[47] M. Endo, K. Hamaguchi, S. Iwamoto, and T. Yoshinaga, *Muon $g-2$ vs LHC in supersymmetric models*, Journal of High Energy Physics **2014** (2014), ISSN: 1029-8479, URL: http://dx.doi.org/10.1007/JHEP01(2014)123 (cit. on pp. 36, 195).

[48] L. S.C.S. W. Group, *SUSYCrossSections*, URL: https://twiki.cern.ch/twiki/bin/view/LHCPhysics/SUSYCrossSections (cit. on p. 38).

[49] A. Collaboration, *Search for charginos and neutralinos in final states with two boosted hadronically decaying bosons and missing transverse momentum in pp collisions at $\sqrt{s}$ = 13 TeV with the ATLAS detector*, 2021, arXiv: 2108.07586 [hep-ex] (cit. on pp. 39, 40, 45, 46, 83, 97, 110, 149, 152, 153, 158–160, 165, 166, 168–171, 178, 323–330, 346, 347).

[50] C. Collaboration, *Search for chargino-neutralino production in events with Higgs and W bosons using 137 fb^{-1} of proton-proton collisions at $\sqrt{s}$ = 13 TeV*, 2021, arXiv: 2107.12553 [hep-ex] (cit. on p. 42).

[51] CMS Collaboration, *Search for supersymmetry in final states with two oppositely charged same-flavor leptons and missing transverse momentum in proton–proton collisions at $\sqrt{s}$ = 13 TeV*, (2020), arXiv: 2012.08600 [hep-ex] (cit. on p. 42).

[52] A. Collaboration, *Search for chargino–neutralino pair production in final states with three leptons and missing transverse momentum in $\sqrt{s}$ = 13 TeV pp collisions with the ATLAS detector*, 2021, arXiv: 2106.01676 [hep-ex] (cit. on pp. 42, 44).

[53] ATLAS Collaboration, *Searches for electroweak production of supersymmetric particles with compressed mass spectra in $\sqrt{s}$ = 13 TeV pp collisions with the ATLAS detector*, Phys. Rev. D **101** (2020) 052005, arXiv: 1911.12606 [hep-ex] (cit. on pp. 42, 178, 183, 187).

[54] ATLAS Collaboration, *Search for long-lived charginos based on a disappearing-track signature using 136 fb^{-1} of pp collisions at $\sqrt{s}$ = 13 TeV with the ATLAS detector*, ATLAS-CONF-2021-015, 2021, URL: https://cds.cern.ch/record/2759676 (cit. on p. 42).

[55] ATLAS Collaboration, *Search for long-lived charginos based on a disappearing-track signature in pp collisions at $\sqrt{s}$ = 13 TeV with the ATLAS detector*, JHEP **06** (2018) 022, arXiv: 1712.02118 [hep-ex] (cit. on pp. 42, 178, 179, 181, 183, 187).

[56] ATLAS Collaboration, *Search for direct pair production of higgsinos by reinterpretation of the disappearing track analysis with 36.1 fb^{-1} of $\sqrt{s}$ = 13 TeV data collected with the ATLAS experiment*, ATL-PHYS-PUB-2017-019, 2017, URL: https://cds.cern.ch/record/2297480 (cit. on p. 42).

[57] CMS Collaboration, *Search for disappearing tracks in proton–proton collisions at $\sqrt{s}$ = 13 TeV*, Phys. Lett. B **806** (2020) 135502, arXiv: 2004.05153 [hep-ex] (cit. on p. 42).

[58] ATLAS Collaboration, *SUSY Summary Plots June 2021*, ATL-PHYS-PUB-2021-019, 2021, URL: http://cdsweb.cern.ch/record/2771785 (cit. on pp. 44, 182).

[59] E. Aprile et al., *Conceptual design and simulation of a water Cherenkov muon veto for the XENON1T experiment*, Journal of Instrumentation **9** (2014) P11006–P11006, ISSN: 1748-0221, URL: http://dx.doi.org/10.1088/1748-0221/9/11/P11006 (cit. on p. 42).

[60] E. Aprile et al., *Dark Matter Search Results from a One Ton-Year Exposure of XENON1T*, Physical Review Letters **121** (2018), ISSN: 1079-7114, URL: http://dx.doi.org/10.1103/PhysRevLett.121.111302 (cit. on pp. 42, 178, 183, 187).

[61] E. Aprile et al., *Constraining the Spin-Dependent WIMP-Nucleon Cross Sections with XENON1T*, Physical Review Letters **122** (2019), ISSN: 1079-7114, URL: http://dx.doi.org/10.1103/PhysRevLett.122.141301 (cit. on pp. 42, 178, 183, 187).

[62] C. Amole et al., *Dark matter search results from the complete exposure of the PICO-60 C_3F_8 bubble chamber*, Physical Review D **100** (2019), ISSN: 2470-0029, URL: http://dx.doi.org/10.1103/PhysRevD.100.022001 (cit. on p. 42).

[63] M. Ackermann et al., *Searching for Dark Matter Annihilation from Milky Way Dwarf Spheroidal Galaxies with Six Years of Fermi Large Area Telescope Data*, Physical Review Letters **115** (2015), ISSN: 1079-7114, URL: http://dx.doi.org/10.1103/PhysRevLett.115.231301 (cit. on pp. 42, 177).

[64] A. Cuoco, J. Heisig, M. Korsmeier, and M. Krämer, *Constraining heavy dark matter with cosmic-ray antiprotons*, Journal of Cosmology and Astroparticle Physics **2018** (2018) 004–004, ISSN: 1475-7516, URL: http://dx.doi.org/10.1088/1475-7516/2018/04/004 (cit. on pp. 42, 177, 178, 183).

[65] L. Hall, J. Lykken, and S. Weinberg, *Supergravity as the messenger of supersymmetry breaking*, Phys. Rev. D **27** (10 1983) 2359, URL: https://link.aps.org/doi/10.1103/PhysRevD.27.2359 (cit. on p. 43).

[66] G. F. Giudice, M. A. Luty, H. Murayama, and R. Rattazzi, *Gaugino mass without singlets*, JHEP **12** (1998) 027, arXiv: hep-ph/9810442 (cit. on p. 43).

[67] L. Randall and R. Sundrum, *Out of this world supersymmetry breaking*, Nucl. Phys. B **557** (1999) 79, arXiv: hep-th/9810155 (cit. on p. 43).

[68] J. S. Kim, S. Pokorski, K. Rolbiecki, and K. Sakurai, *Gravitino vs. neutralino LSP at the LHC*, Journal of High Energy Physics **2019** (2019), ISSN: 1029-8479, URL: http://dx.doi.org/10.1007/JHEP09(2019)082 (cit. on p. 44).

[69] CMS Collaboration, *Combined search for electroweak production of charginos and neutralinos in proton–proton collisions at* $\sqrt{s} = 13$ *TeV*, JHEP **03** (2018) 160, arXiv: 1801.03957 [hep-ex] (cit. on p. 44).

[70] T. Moroi, H. Murayama, and M. Yamaguchi, *Cosmological constraints on the light stable gravitino*, Physics Letters B **303** (1993) 289, ISSN: 0370-2693, URL: https://www.sciencedirect.com/science/article/pii/037026939391434O (cit. on p. 44).

[71] T. Asaka, K. Hamaguchi, and K. Suzuki, *Cosmological gravitino problem in gauge-mediated supersymmetry breaking models*, Physics Letters B **490** (2000) 136–146, ISSN: 0370-2693, URL: http://dx.doi.org/10.1016/S0370-2693(00)00959-X (cit. on p. 44).

[72] M. Bolz, A. Brandenburg, and W. Buchmüller, *Thermal production of gravitinos*, Nuclear Physics B **606** (2001) 518, ISSN: 0550-3213, URL: https://www.sciencedirect.com/science/article/pii/S0550321301001328 (cit. on p. 44).

[73] L. Roszkowski, R. R. d. Austri, and K.-Y. Choi, *Gravitino dark matter in the CMSSM and implications for leptogenesis and the LHC*, Journal of High Energy Physics **2005** (2005) 080–080, ISSN: 1029-8479, URL: http://dx.doi.org/10.1088/1126-6708/2005/08/080 (cit. on p. 44).

[74] D. G. Cerdeño, K.-Y. Choi, K. Jedamzik, L. Roszkowski, and R. R. d. Austri, *Gravitino dark matter in the constrained minimal supersymmetric standard model with improved constraints from big bang nucleosynthesis*, Journal of Cosmology and Astroparticle Physics **2006** (2006) 005–005, ISSN: 1475-7516, URL: http://dx.doi.org/10.1088/1475-7516/2006/06/005 (cit. on p. 44).

[75] J. Pradler and F. D. Steffen, *Thermal gravitino production and collider tests of leptogenesis*, Physical Review D **75** (2007), ISSN: 1550-2368, URL: http://dx.doi.org/10.1103/PhysRevD.75.023509 (cit. on p. 44).

[76] J. Pradler and F. D. Steffen, *Constraints on the reheating temperature in gravitino dark matter scenarios*, Physics Letters B **648** (2007) 224–235, ISSN: 0370-2693, URL: http://dx.doi.org/10.1016/j.physletb.2007.02.072 (cit. on p. 44).

[77] J. M. P. et al., *Revised experimental upper limit on the electric dipole moment of the neutron*, () (cit. on p. 45).

[78] K. J. E. Chun E J and N. H. P, *AXINO MASS*, Phys.Lett.B **287** (1-3 1992) 123, URL: https://doi.org/10.1016/0370-2693(92)91886-E (cit. on p. 45).

[79] C. J and L. A, *Axino Mass in Supergravity Models*, Phys.Lett.B **357** (1-2 1995) 43, URL: https://doi.org/10.1016/0370-2693(95)00881-K (cit. on p. 45).

[80] T. Goto and M. Yamaguchi, *Is axino dark matter possible in supergravity?* Physics Letters B **276** (1992) 103, ISSN: 0370-2693, URL: https://www.sciencedirect.com/science/article/pii/037026939290547H (cit. on p. 45).

[81] K. J. Bae, E. J. Chun, and S. H. Im, *Cosmology of the DFSZ axino*, Journal of Cosmology and Astroparticle Physics **2012** (2012) 013, URL: https://iopscience.iop.org/article/10.1088/1475-7516/2012/03/013 (cit. on p. 46).

[82] L. Covi and J. E. Kim, *Axinos as dark matter particles*, New Journal of Physics **11** (2009) 105003, URL: https://iopscience.iop.org/article/10.1088/1367-2630/11/10/105003 (cit. on p. 46).

[83] A. Brandenburg and F. D. Steffen, *Axino dark matter from thermal production*, Journal of Cosmology and Astroparticle Physics **2004** (2004) 008–008, ISSN: 1475-7516, URL: http://dx.doi.org/10.1088/1475-7516/2004/08/008 (cit. on p. 46).

[84] *LHC Design Report. 3. The LHC injector chain*, (2004), ed. by M. Benedikt, P. Collier, V. Mertens, J. Poole, and K. Schindl (cit. on p. 47).

[85] G. Aad et al., *The ATLAS Experiment at the CERN Large Hadron Collider*, JINST **3** (2008) S08003 (cit. on pp. 47, 48, 50–53, 55).

[86] J. Alves A.Augusto et al., *The LHCb Detector at the LHC*, JINST **3** (2008) S08005 (cit. on p. 47).

[87] K. Aamodt et al., *The ALICE experiment at the CERN LHC*, JINST **3** (2008) S08002 (cit. on p. 47).

[88] E. Mobs, *The CERN accelerator complex - August 2018*, OPEN-PHO-ACCEL-2018-005 (2018), URL: https://cds.cern.ch/record/2636343 (cit. on p. 48).

[89] B. Abbott et al., *Production and integration of the ATLAS Insertable B-Layer*, JINST **13** (2018) T05008, arXiv: 1803.00844 [physics.ins-det] (cit. on p. 49).

[90] () (cit. on p. 56).

[91] ATLAS Collaboration, *Standard Model Summary Plots March 2021*, (2021), URL: http://cdsweb.cern.ch/record/2758261/files/ATL-PHYS-PUB-2021-005.pdf (cit. on p. 57).

[92] ATLAS Collaboration, *Luminosity determination in pp collisions at $\sqrt{s} = 13$ TeV using the ATLAS detector at the LHC*, ATLAS-CONF-2019-021, 2019, URL: https://cds.cern.ch/record/2677054 (cit. on pp. 58, 308).

[93] G. Avoni et al., *The new LUCID-2 detector for luminosity measurement and monitoring in ATLAS*, JINST **13** (2018) P07017 (cit. on p. 58).

[94] ATLAS Collaboration, *ATLAS data quality operations and performance for 2015–2018 data-taking*, JINST **15** (2020) P04003, arXiv: 1911.04632 [physics.ins-det] (cit. on p. 59).

[95] T. S. et al., *An Introduction to PYTHIA 8.2*, Comput. Phys. Commun. **191** (2015) 159, arXiv: 1410.3012 [hep-ph] (cit. on pp. 58, 84, 91, 197, 198).

[96] R. D. Ball et al., *Parton distributions with LHC data*, Nucl. Phys. **B867** (2013) 244, arXiv: 1207.1303 [hep-ph] (cit. on pp. 58, 148, 197).

[97] ATLAS Collaboration, *The Pythia 8 A3 tune description of ATLAS minimum bias and inelastic measurements incorporating the Donnachie–Landshoff diffractive model*, ATL-PHYS-PUB-2016-017, 2016, URL: https://cds.cern.ch/record/2206965 (cit. on p. 58).

[98] ATLAS Collaboration, *The ATLAS Simulation Infrastructure*, Eur. Phys. J. C **70** (2010) 823, arXiv: 1005.4568 [physics.ins-det] (cit. on p. 58).

[99] S. Agostinelli et al., *GEANT4: A Simulation toolkit*, Nucl.Instrum.Meth. **A506** (2003) 250 (cit. on p. 58).

[100] P. Skands, *QCD for Collider Physics*, 2012, arXiv: 1104.2863 [hep-ph] (cit. on p. 60).

[101] ATLAS Collaboration, *Performance of the ATLAS track reconstruction algorithms in dense environments in LHC Run 2*, Eur. Phys. J. C **77** (2017) 673, arXiv: 1704.07983 [hep-ex] (cit. on p. 64).

[102] ATLAS Collaboration, *Vertex Reconstruction Performance of the ATLAS Detector at* $\sqrt{s} = 13$ *TeV*, ATL-PHYS-PUB-2015-026, 2015, URL: https://cds.cern.ch/record/2037717 (cit. on p. 64).

[103] ATLAS Collaboration, *Topological cell clustering in the ATLAS calorimeters and its performance in LHC Run 1*, Eur. Phys. J. C **77** (2017) 490, arXiv: 1603.02934 [hep-ex] (cit. on pp. 65, 213, 214).

[104] M. Cacciari, G. P. Salam, and G. Soyez, *The anti-k_t jet clustering algorithm*, JHEP **04** (2008) 063, arXiv: 0802.1189 [hep-ph] (cit. on pp. 65, 66, 213).

[105] M. Cacciari, G. P. Salam, and G. Soyez, *FastJet User Manual*, Eur. Phys. J. C **72** (2012) 1896, arXiv: 1111.6097 [hep-ph] (cit. on pp. 65, 213).

[106] D. Krohn, J. Thaler, and L.-T. Wang, *Jet trimming*, JHEP **02** (2010) 084, arXiv: 0912.1342 [hep-ph] (cit. on p. 65).

[107] ATLAS Collaboration, *Studies of the impact and mitigation of pile-up on large radius and groomed jets in ATLAS at* $\sqrt{s} = 7$ *TeV*, ATLAS-CONF-2012-066, 2012, URL: https://cds.cern.ch/record/1459531 (cit. on p. 67).

[108] ATLAS Collaboration, *Jet mass reconstruction with the ATLAS Detector in early Run 2 data*, ATLAS-CONF-2016-035, 2016, URL: https://cds.cern.ch/record/2200211 (cit. on p. 68).

[109] ATLAS Collaboration, *In situ calibration of large-radius jet energy and mass in* 13 *TeV proton–proton collisions with the ATLAS detector*, Eur. Phys. J. C **79** (2019) 135, arXiv: 1807.09477 [hep-ex] (cit. on pp. 68–71, 143, 145).

[110] A. Collaboration, *Jet ETMiss Public Results*, URL: https://twiki.cern.ch/twiki/bin/view/AtlasPublic/JetEtmissPublicResults (cit. on pp. 71, 144).

[111] ATLAS Collaboration, *Performance of pile-up mitigation techniques for jets in pp collisions at* $\sqrt{s} = 8$ *TeV using the ATLAS detector*, Eur. Phys. J. C **76** (2016) 581, arXiv: 1510.03823 [hep-ex] (cit. on pp. 72, 303).

[112] ATLAS Collaboration, *Forward jet vertex tagging using the particle flow algorithm*, ATL-PHYS-PUB-2019-026, 2019, URL: https://cds.cern.ch/record/2683100 (cit. on p. 72).

[113] ATLAS Collaboration, *Jet energy scale and resolution measured in proton–proton collisions at $\sqrt{s}$ = 13 TeV with the ATLAS detector*, (2020), arXiv: 2007.02645 [hep-ex] (cit. on pp. 72, 302–305).

[114] D. Krohn, J. Thaler, and L.-T. Wang, *Jets with variable R*, Journal of High Energy Physics **2009** (2009) 059–059, ISSN: 1029-8479, URL: http://dx.doi.org/10.1088/1126-6708/2009/06/059 (cit. on p. 72).

[115] ATLAS Collaboration, *Optimisation and performance studies of the ATLAS b-tagging algorithms for the 2017-18 LHC run*, ATL-PHYS-PUB-2017-013, 2017, URL: https://cds.cern.ch/record/2273281 (cit. on pp. 73, 215).

[116] ATLAS Collaboration, *ATLAS b-jet identification performance and efficiency measurement with $t\bar{t}$ events in pp collisions at $\sqrt{s}$ = 13 TeV*, (2019), arXiv: 1907.05120 [hep-ex] (cit. on pp. 73, 216, 306).

[117] ATLAS Collaboration, *Measurement of b-tagging efficiency of c-jets in $t\bar{t}$ events using a likelihood approach with the ATLAS detector*, ATLAS-CONF-2018-001, 2018, URL: https://cds.cern.ch/record/2306649 (cit. on pp. 73, 306).

[118] ATLAS Collaboration, *Calibration of light-flavour b-jet mistagging rates using ATLAS proton–proton collision data at $\sqrt{s}$ = 13 TeV*, ATLAS-CONF-2018-006, 2018, URL: https://cds.cern.ch/record/2314418 (cit. on pp. 73, 306).

[119] ATLAS Collaboration, *Electron and photon performance measurements with the ATLAS detector using the 2015-2017 LHC proton–proton collision data*, JINST **14** (2019) P12006, arXiv: 1908.00005 [hep-ex] (cit. on pp. 73–75, 217, 220, 221, 260, 306).

[120] A. Collaboration, *Muon reconstruction and identification efficiency in ATLAS using the full Run 2 pp collision data set at $\sqrt{s}$ = 13 TeV*, 2020, arXiv: 2012.00578 [hep-ex] (cit. on pp. 74, 75, 223, 224, 226, 307).

[121] ATLAS Collaboration, *Boosted hadronic vector boson and top quark tagging with ATLAS using Run 2 data*, ATL-PHYS-PUB-2020-017, 2020, URL: http://cdsweb.cern.ch/record/2724149/files/ATL-PHYS-PUB-2020-017.pdf (cit. on pp. 77, 199, 227).

[122] ATLAS Collaboration, *Variable Radius, Exclusive-k_T, and Center-of-Mass Subjet Reconstruction for Higgs($\rightarrow b\bar{b}$) Tagging in ATLAS*, ATL-PHYS-PUB-2017-010, 2017, URL: https://cds.cern.ch/record/2268678 (cit. on pp. 77, 95).

[123] A. J. Larkoski, G. P. Salam, and J. Thaler, *Energy Correlation Functions for Jet Substructure*, JHEP **06** (2013) 108, arXiv: 1305.0007 [hep-ph] (cit. on p. 77).

[124] A. J. Larkoski, I. Moult, and D. Neill, *Analytic Boosted Boson Discrimination*, 2016, arXiv: 1507.03018 [hep-ph] (cit. on p. 77).

[125] J. M. Butterworth, B. E. Cox, and J. R. Forshaw, *WWscattering at the CERN LHC*, Physical Review D **65** (2002), ISSN: 1089-4918, URL: http://dx.doi.org/10.1103/PhysRevD.65.096014 (cit. on p. 77).

[126] J. Thaler and K. Van Tilburg, *Identifying boosted objects with N-subjettiness*, Journal of High Energy Physics **2011** (2011), ISSN: 1029-8479, URL: http://dx.doi.org/10.1007/JHEP03(2011)015 (cit. on p. 77).

[127] J. Thaler and K. Van Tilburg, *Maximizing boosted top identification by minimizing N-subjettiness*, Journal of High Energy Physics **2012** (2012), ISSN: 1029-8479, URL: http://dx.doi.org/10.1007/JHEP02(2012)093 (cit. on p. 77).

[128] ATLAS Collaboration, *Identification of boosted, hadronically decaying W bosons and comparisons with ATLAS data taken at $\sqrt{s}$ = 8 TeV*, Eur. Phys. J. C **76** (2016) 154, arXiv: 1510.05821 [hep-ex] (cit. on p. 77).

[129] M. Cacciari, G. P. Salam, and G. Soyez, *The Catchment Area of Jets*, JHEP **04** (2008), eprint: 0802.1188, URL: https://iopscience.iop.org/article/10.1088/1126-6708/2008/04/005 (cit. on pp. 78, 227).

[130] () (cit. on pp. 81, 122, 307).

[131] S. Frixione, P. Nason, and G. Ridolfi, *A positive-weight next-to-leading-order Monte Carlo for heavy flavour hadron production*, JHEP **09** (2007) 126, arXiv: 0707.3088 [hep-ph] (cit. on pp. 84, 197).

[132] P. Nason, *A New method for combining NLO QCD with shower Monte Carlo algorithms*, JHEP **11** (2004) 040, arXiv: 0409146 [hep-ph] (cit. on pp. 84, 197).

[133] S. Frixione, P. Nason, and C. Oleari, *Matching NLO QCD computations with Parton Shower simulations: the POWHEG method*, JHEP **11** (2007) 070, arXiv: 0709.2092 [hep-ph] (cit. on pp. 84, 197).

[134] S. Alioli, P. Nason, C. Oleari, and E. Re, *A general framework for implementing NLO calculations in shower Monte Carlo programs: the POWHEG BOX*, JHEP **06** (2010) 043, arXiv: 1002.2581 [hep-ph] (cit. on pp. 84, 197).

[135] J. B. et al., *Herwig 7.0 / Herwig++3.0 release note*, Eur. Phys. J. C **76** (2016) 196, arXiv: 1512.01178 [hep-ph] (cit. on pp. 84, 199).

[136] M. Bähr et al., *Herwig++ physics and manual*, The European Physical Journal C **58** (2008) 639–707, ISSN: 1434-6052, URL: http://dx.doi.org/10.1140/epjc/s10052-008-0798-9 (cit. on pp. 84, 199).

[137] J. Alwall et al., *The automated computation of tree-level and next-to-leading order differential cross sections, and their matching to parton shower simulations*, JHEP **07** (2014) 079, arXiv: 1405.0301 [hep-ph] (cit. on pp. 84, 197–199).

[138] ATLAS Collaboration, *Performance of electron and photon triggers in ATLAS during LHC Run 2*, (2019), arXiv: 1909.00761 [hep-ex] (cit. on pp. 91, 122, 306).

[139] E. Bothmann et al., *Event Generation with Sherpa 2.2*, SciPost Phys. **7** (2019) 034, arXiv: 1905.09127 [hep-ph] (cit. on pp. 91, 197).

[140] ATLAS and CMS Collaborations, *Combination of the W boson polarization measurements in top quark decays using ATLAS and CMS data at $\sqrt{s}$ = 8 TeV*, JHEP **08** (2020) 051, arXiv: 2005.03799 [hep-ex] (cit. on p. 95).

[141] ATLAS Collaboration, *Performance of the ATLAS trigger system in 2015*, Eur. Phys. J. C **77** (2017) 317, arXiv: 1611.09661 [hep-ex] (cit. on p. 99).

[142] ATLAS Collaboration, *Performance of the missing transverse momentum triggers for the ATLAS detector during Run-2 data taking*, JHEP **08** (2020) 080, arXiv: 2005.09554 [hep-ex] (cit. on p. 100).

[143] G. Aad et al., *Measurement of the associated production of a Higgs boson decaying into b-quarks with a vector boson at high transverse momentum in pp collisions at s=13 TeV with the ATLAS detector*, Physics Letters B **816** (2021) 136204, ISSN: 0370-2693, URL: http://dx.doi.org/10.1016/j.physletb.2021.136204 (cit. on p. 107).

[144] URL: https://root.cern.ch/doc/v606/namespaceRooStats_1_1NumberCountingUtils.html#acc62261fa2a9671cf80a70285133ff40 (cit. on p. 108).

[145] ATLAS Collaboration, *Measurement of the cross section for isolated-photon plus jet production in pp collisions at $\sqrt{s}$ = 13 TeV using the ATLAS detector*, Phys. Lett. B **780** (2018) 578, arXiv: 1801.00112 [hep-ex] (cit. on p. 122).

[146] S. Frixione, E. Laenen, P. Motylinski, B. R. Webber, and C. D. White, *Single-top hadroproduction in association with a W boson*, JHEP **07** (2008) 029, arXiv: 0805.3067 [hep-ph] (cit. on pp. 136, 198).

[147] ATLAS Collaboration, *Evidence for the production of three massive vector bosons with the ATLAS detector*, (2019), arXiv: 1903.10415 [hep-ex] (cit. on p. 140).

[148] CMS Collaboration, *Observation of the production of three massive gauge bosons at $\sqrt{s}$ = 13 TeV*, (2020), arXiv: 2006.11191 [hep-ex] (cit. on p. 140).

[149] ATLAS Collaboration, *Jet Mass Resolutions in ATLAS using Run 2 Monte Carlo Simulation*, ATL-PHYS-PUB-2018-015, 2018, URL: https://cds.cern.ch/record/2631339 (cit. on p. 144).

[150] A. Martin, W. Stirling, R. Thorne, and G. Watt, *Parton distributions for the LHC*, Eur.Phys.J. **C63** (2009) 189, arXiv: 0901.0002 [hep-ph] (cit. on p. 148).

[151] L. A. Harland-Lang, A. D. Martin, P. Motylinski, and R. S. Thorne, *Parton distributions in the LHC era: MMHT 2014 PDFs*, Eur. Phys. J. **C75** (2015) 204, arXiv: 1412.3989 [hep-ph] (cit. on p. 148).

[152] S. Dulat et al., *New parton distribution functions from a global analysis of quantum chromodynamics*, Phys. Rev. **D93** (2016) 033006, arXiv: 1506.07443 [hep-ph] (cit. on p. 148).

[153] J. Butterworth et al., *PDF4LHC recommendations for LHC Run II*, J. Phys. **G43** (2016) 023001, arXiv: 1510.03865 [hep-ph] (cit. on p. 149).

[154] G. Cowan, K. Cranmer, E. Gross, and O. Vitells, *Asymptotic formulae for likelihood-based tests of new physics*, Eur. Phys. J. C **71** (2011) 1554, [Erratum: Eur. Phys. J. C 73 (2013) 2501], arXiv: 1007.1727 [physics.data-an] (cit. on pp. 158, 310, 311).

[155] T. Junk, *Confidence level computation for combining searches with small statistics*, Nuclear Instruments and Methods in Physics Research Section A: Accelerators, Spectrometers, Detectors and Associated Equipment **434** (1999) 435–443, ISSN: 0168-9002, URL: http://dx.doi.org/10.1016/S0168-9002(99)00498-2 (cit. on pp. 157, 311).

[156] X.-G. G. R.Foot H.Lew, *See-saw neutrino masses induced by a triplet of leptons* (cit. on p. 157).

[157] ATLAS Collaboration, *Search for electroweak production of charginos and sleptons decaying into final states with two leptons and missing transverse momentum in $\sqrt{s}$ = 13 TeV pp collisions using the ATLAS detector*, (2019), arXiv: 1908.08215 [hep-ex] (cit. on pp. 164, 165, 181).

[158] ATLAS Collaboration, *Search for chargino–neutralino production using recursive jigsaw reconstruction in final states with two or three charged leptons in proton–proton collisions at $\sqrt{s}$ = 13 TeV with the ATLAS detector*, Phys. Rev. D **98** (2018) 092012, arXiv: 1806.02293 [hep-ex] (cit. on pp. 164, 166).

[159] ATLAS Collaboration, *Search for chargino-neutralino pair production in final states with three leptons and missing transverse momentum in $\sqrt{s}$ = 13 TeV pp collisions with the ATLAS detector*, ATLAS-CONF-2020-015, 2020, URL: https://cds.cern.ch/record/2719521 (cit. on pp. 164, 166).

[160] ATLAS Collaboration, *Search for direct production of electroweakinos in final states with one lepton, missing transverse momentum and a Higgs boson decaying into two b-jets in pp collisions at $\sqrt{s}$ = 13 TeV with the ATLAS detector*, Eur. Phys. J. C **80** (2020) 691, arXiv: 1909.09226 [hep-ex] (cit. on pp. 164, 166).

[161] ATLAS Collaboration, *Search for supersymmetry in events with four or more leptons in* 139 fb^{-1} *$\sqrt{s}$ = 13 TeV pp collisions with the ATLAS detector*, ATLAS-CONF-2020-040, 2020, URL: https://cds.cern.ch/record/2727861 (cit. on p. 170).

[162] ATLAS Collaboration, *Search for pair production of higgsinos in final states with at least three b-tagged jets in $\sqrt{s}$ = 13 TeV pp collisions using the ATLAS detector*, Phys. Rev. D **98** (2018) 092002, arXiv: 1806.04030 [hep-ex] (cit. on p. 170).

[163] G. Barenboim, E. J. Chun, S. Jung, and W. I. Park, *Implications of an axino LSP for naturalness*, Phys. Rev. D **90** (3 2014) 035020, URL: https://link.aps.org/doi/10.1103/PhysRevD.90.035020 (cit. on p. 171).

[164] URL: https://project-hl-lhc-industry.web.cern.ch/content/project-schedule (cit. on p. 172).

[165] ATLAS Collaboration, *Search for Supersymmetry at the high luminosity LHC with the ATLAS Detector*, ATL-PHYS-PUB-2014-010, 2014, URL: https://cds.cern.ch/record/1735031 (cit. on pp. 172, 173).

[166] ATLAS Collaboration, *Prospect for a search for direct pair production of a chargino and a neutralino decaying via aW boson and the lightest Higgs boson in final states with one lepton, two b-jets and missing transverse momentum at the high luminosity LHC with the ATLAS Detector*, ATL-PHYS-PUB-2015-032, 2015, URL: https://cds.cern.ch/record/2038565 (cit. on p. 174).

[167] J. Liu, N. McGinnis, C. E. M. Wagner, and X.-P. Wang, *Searching for the Higgsino-Bino sector at the LHC*, Journal of High Energy Physics **2020** (2020), ISSN: 1029-8479, URL: http://dx.doi.org/10.1007/JHEP09(2020)073 (cit. on p. 174).

[168] H. Baer et al., *Same-Sign Diboson Signature from Supersymmetry Models with Light Higgsinos at the LHC*, Physical Review Letters **110** (2013), ISSN: 1079-7114, URL: http://dx.doi.org/10.1103/PhysRevLett.110.151801 (cit. on p. 173).

[169] G. Barenboim, E. J. Chun, S. Jung, and W. I. Park, *Implications of an axino LSP for naturalness*, Physical Review D **90** (2014), ISSN: 1550-2368, URL: http://dx.doi.org/10.1103/PhysRevD.90.035020 (cit. on p. 173).

[170] B. Allanach, *SOFTSUSY: A program for calculating supersymmetric spectra*, Computer Physics Communications **143** (2002) 305–331, ISSN: 0010-4655, URL: http://dx.doi.org/10.1016/S0010-4655(01)00460-X (cit. on pp. 177, 182, 200).

[171] W. Porod and F. Staub, *SPheno 3.1: extensions including flavour, CP-phases and models beyond the MSSM*, Computer Physics Communications **183** (2012) 2458–2469, ISSN: 0010-4655, URL: http://dx.doi.org/10.1016/j.cpc.2012.05.021 (cit. on pp. 177, 182).

[172] H. Bahl et al., *Precision calculations in the MSSM Higgs-boson sector with FeynHiggs 2.14*, 2019, arXiv: 1811.09073 [hep-ph] (cit. on pp. 177, 182).

[173] P. Athron et al., *GM2Calc: precise MSSM prediction for* $(g-2)$ *of the muon*, The European Physical Journal C **76** (2016), ISSN: 1434-6052, URL: http://dx.doi.org/10.1140/epjc/s10052-015-3870-2 (cit. on pp. 177, 182).

[174] G. Bélanger, F. Boudjema, A. Goudelis, A. Pukhov, and B. Zaldívar, *micrOMEGAs5.0 : Freeze-in*, Computer Physics Communications **231** (2018) 173–186, ISSN: 0010-4655, URL: http://dx.doi.org/10.1016/j.cpc.2018.04.027 (cit. on pp. 177, 182).

[175] M. Ackermann et al., *Dark matter constraints from observations of 25 Milky Way satellite galaxies with the Fermi Large Area Telescope*, Physical Review D **89** (2014), ISSN: 1550-2368, URL: http://dx.doi.org/10.1103/PhysRevD.89.042001 (cit. on pp. 178, 183).

[176] CMS Collaboration, *Search for new physics in events with two soft oppositely charged leptons and missing transverse momentum in proton–proton collisions at* $\sqrt{s} = 13$ *TeV*, Phys. Lett. B **782** (2018) 440, arXiv: 1801.01846 [hep-ex] (cit. on pp. 178, 183, 187).

[177] M. Misiak et al., *Estimate of* $B(B^- \to X_s\gamma)$ *at* $O(\alpha_s^2)$, Physical Review Letters **98** (2007), ISSN: 1079-7114, URL: http://dx.doi.org/10.1103/PhysRevLett.98.022002 (cit. on pp. 179, 184).

[178] Y. Amhis et al., *Averages of b-hadron, c-hadron, and* τ*-lepton properties as of 2018*, The European Physical Journal C **81** (2021), ISSN: 1434-6052, URL: http://dx.doi.org/10.1140/epjc/s10052-020-8156-7 (cit. on pp. 179, 184).

[179] R. Aaij et al., *Measurement of the* $B_s^0 \to \mu^+\mu^-$ *Branching Fraction and Effective Lifetime and Search for* $B^0 \to \mu^+\mu^-$ *Decays*, Physical Review Letters **118** (2017), ISSN: 1079-7114, URL: http://dx.doi.org/10.1103/PhysRevLett.118.191801 (cit. on pp. 179, 184).

[180] CMS Collaboration, *Measurement of properties of* $B_s^0 \to \mu^+\mu^-$ *decays and search for* $B^0 \to \mu^+\mu^-$ *with the CMS experiment*, JHEP **04** (2020) 188, arXiv: 1910.12127 [hep-ex] (cit. on pp. 179, 184).

[181] J. L. Rosner, S. Stone, and R. S. V. de Water, *Leptonic Decays of Charged Pseudoscalar Mesons - 2015*, 2016, arXiv: 1509.02220 [hep-ph] (cit. on pp. 179, 184).

[182] J. Charles et al., *CP violation and the CKM matrix: assessing the impact of the asymmetric B factories*, The European Physical Journal C **41** (2005) 1–131, ISSN: 1434-6052, URL: http://dx.doi.org/10.1140/epjc/s2005-02169-1 (cit. on pp. 179, 184).

[183] D. Akerib et al., *First Results from the LUX Dark Matter Experiment at the Sanford Underground Research Facility*, Physical Review Letters **112** (2014), ISSN: 1079-7114, URL: http://dx.doi.org/10.1103/PhysRevLett.112.091303 (cit. on p. 194).

[184] E. Aprile et al., *Limits on Spin-Dependent WIMP-Nucleon Cross Sections from 225 Live Days of XENON100 Data*, Physical Review Letters **111** (2013), ISSN: 1079-7114, URL: http://dx.doi.org/10.1103/PhysRevLett.111.021301 (cit. on p. 194).

[185] P. P. Giardino, K. Kannike, I. Masina, M. Raidal, and A. Strumia, *The universal Higgs fit*, Journal of High Energy Physics **2014** (2014), ISSN: 1029-8479, URL: http://dx.doi.org/10.1007/JHEP05(2014)046 (cit. on p. 194).

[186] G. Bélanger, B. Dumont, U. Ellwanger, J. F. Gunion, and S. Kraml, *Global fit to Higgs signal strengths and couplings and implications for extended Higgs sectors*, Physical Review D **88** (2013), ISSN: 1550-2368, URL: http://dx.doi.org/10.1103/PhysRevD.88.075008 (cit. on p. 194).

[187] E. Aprile and X. collaboration, *The XENON1T Dark Matter Search Experiment*, 2012, arXiv: 1206.6288 [astro-ph.IM] (cit. on p. 194).

[188] M. Garny, A. Ibarra, M. Pato, and S. Vogl, *On the spin-dependent sensitivity of XENON100*, Physical Review D **87** (2013), ISSN: 1550-2368, URL: http://dx.doi.org/10.1103/PhysRevD.87.056002 (cit. on p. 194).

[189] H. Okawa, J. Kunkle, and E. Lipeles, *Prospects on the search for invisible Higgs decays in the ZH channel at the LHC and HL-LHC: A Snowmass White Paper*, 2014, arXiv: 1309.7925 [hep-ex] (cit. on p. 194).

[190] S. Dawson et al., *Higgs Working Group Report of the Snowmass 2013 Community Planning Study*, 2014, arXiv: 1310.8361 [hep-ex] (cit. on p. 194).

[191] D. M. Asner et al., *ILC Higgs White Paper*, 2018, arXiv: 1310.0763 [hep-ph] (cit. on p. 194).

[192] P. Fayet and J. Iliopoulos, *Spontaneously Broken Supergauge Symmetries and Goldstone Spinors*, Phys. Lett. B **51** (1974) 461 (cit. on p. 195).

[193] L. O'Raifeartaigh, *Spontaneous Symmetry Breaking for Chiral Scalar Superfields*, Nucl. Phys. B **96** (1975) 331 (cit. on p. 196).

[194] S. Weinberg, *Photons and Gravitons in Perturbation Theory: Derivation of Maxwell's and Einstein's Equations*, Phys. Rev. **138** (4B 1965) B988, URL: https://link.aps.org/doi/10.1103/PhysRev.138.B988 (cit. on p. 196).

[195] S. Deser and B. Zumino, *Broken Supersymmetry and Supergravity*, Phys. Rev. Lett. **38** (1977) 1433 (cit. on p. 196).

[196] M. Dine and W. Fischler, *A Phenomenological Model of Particle Physics Based on Supersymmetry*, Phys. Lett. B **110** (1982) 227 (cit. on p. 196).

[197] L. Alvarez-Gaume, M. Claudson, and M. B. Wise, *Low-Energy Supersymmetry*, Nucl. Phys. B **207** (1982) 96 (cit. on p. 196).

[198] C. R. Nappi and B. A. Ovrut, *Supersymmetric Extension of the SU(3) x SU(2) x U(1) Model*, Phys. Lett. B **113** (1982) 175 (cit. on p. 196).

[199] P. Meade, N. Seiberg, and D. Shih, *General Gauge Mediation*, Prog. Theor. Phys. Suppl. **177** (2009) 143, arXiv: 0801.3278 [hep-ph] (cit. on p. 196).

[200] C. Cheung, A. L. Fitzpatrick, and D. Shih, *(Extra)ordinary gauge mediation*, JHEP **07** (2008) 054, arXiv: 0710.3585 [hep-ph] (cit. on p. 196).

[201] R. D. Ball et al., *Parton distributions for the LHC Run II*, JHEP **04** (2015) 040, arXiv: 1410.8849 [hep-ph] (cit. on p. 197).

[202] H.-L. Lai et al., *New parton distributions for collider physics*, Phys. Rev. D **82** (2010) 074024, arXiv: 1007.2241 [hep-ph] (cit. on pp. 197, 199).

[203] G. Aad et al., *Measurement of the Z/γ^* boson transverse momentum distribution in pp collisions at $\sqrt{s} = 7$ TeV with the ATLAS detector*, JHEP **09** (2014) 145, arXiv: 1406.3660 [hep-ex] (cit. on pp. 197, 198).

[204] M. Ciccolini, S. Dittmaier, and M. Kramer, *Electroweak radiative corrections to associated WH and ZH production at hadron colliders*, Phys.Rev. **D68** (2003) 073003, arXiv: hep-ph/0306234 [hep-ph] (cit. on p. 197).

[205] O. Brein, A. Djouadi, and R. Harlander, *NNLO QCD corrections to the Higgs-strahlung processes at hadron colliders*, Phys.Lett. **B579** (2004) 149, arXiv: hep-ph/0307206 [hep-ph] (cit. on p. 197).

[206] O. Brein, R. Harlander, M. Wiesemann, and T. Zirke, *Top-Quark Mediated Effects in Hadronic Higgs-Strahlung*, Eur. Phys. J. **C72** (2012) 1868, arXiv: 1111.0761 [hep-ph] (cit. on p. 197).

[207] L. Altenkamp, S. Dittmaier, R. V. Harlander, H. Rzehak, and T. J. E. Zirke, *Gluon-induced Higgs-strahlung at next-to-leading order QCD*, JHEP **02** (2013) 078, arXiv: 1211.5015 [hep-ph] (cit. on p. 197).

[208] A. Denner, S. Dittmaier, S. Kallweit, and A. Mück, *HAWK 2.0: A Monte Carlo program for Higgs production in vector-boson fusion and Higgs strahlung at hadron colliders*, Comput. Phys. Commun. **195** (2015) 161, arXiv: 1412.5390 [hep-ph] (cit. on p. 197).

[209] O. Brein, R. V. Harlander, and T. J. E. Zirke, *vh@nnlo - Higgs Strahlung at hadron colliders*, Comput. Phys. Commun. **184** (2013) 998, arXiv: 1210.5347 [hep-ph] (cit. on p. 197).

[210] R. V. Harlander, A. Kulesza, V. Theeuwes, and T. Zirke, *Soft gluon resummation for gluon-induced Higgs Strahlung*, JHEP **11** (2014) 082, arXiv: 1410.0217 [hep-ph] (cit. on p. 197).

[211] T. Gleisberg and S. Höche, *Comix, a new matrix element generator*, JHEP **12** (2008) 039, arXiv: 0808.3674 [hep-ph] (cit. on p. 197).

[212] F. Buccioni et al., *OpenLoops 2*, The European Physical Journal C **79** (2019), ISSN: 1434-6052, URL: http://dx.doi.org/10.1140/epjc/s10052-019-7306-2 (cit. on p. 197).

[213] F. Cascioli, P. Maierhöfer, and S. Pozzorini, *Scattering Amplitudes with Open Loops*, Phys. Rev. Lett. **108** (2012) 111601, arXiv: 1111.5206 [hep-ph] (cit. on p. 197).

[214] A. Denner, S. Dittmaier, and L. Hofer, *Collier: A fortran-based complex one-loop library in extended regularizations*, Comput. Phys. Commun. **212** (2017) 220, arXiv: 1604.06792 [hep-ph] (cit. on p. 197).

[215] S. Schumann and F. Krauss, *A parton shower algorithm based on Catani-Seymour dipole factorisation*, JHEP **03** (2008) 038, arXiv: 0709.1027 [hep-ph] (cit. on p. 197).

[216] J.-C. Winter, F. Krauss, and G. Soff, *A modified cluster-hadronization model*, Eur. Phys. J. C **36** (2004) 381, arXiv: hep-ph/0311085 (cit. on p. 197).

[217] C. Anastasiou, L. J. Dixon, K. Melnikov, and F. Petriello, *High precision QCD at hadron colliders: Electroweak gauge boson rapidity distributions at NNLO*, Phys. Rev. D **69** (2004) 094008, arXiv: hep-ph/0312266 (cit. on p. 197).

[218] S. Frixione, *Isolated photons in perturbative QCD*, Phys. Lett. B **429** (1998) 369, arXiv: hep-ph/9801442 (cit. on p. 197).

[219] *ATLAS Run 1 Pythia8 tunes*, tech. rep. ATL-PHYS-PUB-2014-021, CERN, 2014, URL: https://cds.cern.ch/record/1966419 (cit. on p. 197).

[220] D. Lange, *The EvtGen particle decay simulation package*, Nucl. Instrum. Meth. A **462** (2001) 152 (cit. on p. 197).

[221] *Studies on top-quark Monte Carlo Modelling for Top 2016*, tech. rep. ATL-PHYS-PUB-2016-020, CERN, 2016, URL: https://cds.cern.ch/record/2216168 (cit. on p. 197).

[222] M. Beneke, P. Falgari, S. Klein, and C. Schwinn, *Hadronic top-quark pair production with NNLL threshold resummation*, Nucl. Phys. B **855** (2012) 695, arXiv: 1109.1536 [hep-ph] (cit. on p. 197).

[223] M. Cacciari, M. Czakon, M. Mangano, A. Mitov, and P. Nason, *Top-pair production at hadron colliders with next-to-next-to-leading logarithmic soft-gluon resummation*, Phys. Lett. B **710** (2012) 612, arXiv: 1111.5869 [hep-ph] (cit. on p. 197).

[224] P. Bärnreuther, M. Czakon, and A. Mitov, *Percent-Level-Precision Physics at the Tevatron: Next-to-Next-to-Leading Order QCD Corrections to $q\bar{q} \to t\bar{t} + X$*, Phys. Rev. Lett. **109** (2012) 132001, arXiv: 1204.5201 [hep-ph] (cit. on p. 197).

[225] M. Czakon and A. Mitov, *NNLO corrections to top-pair production at hadron colliders: the all-fermionic scattering channels*, JHEP **12** (2012) 054, arXiv: 1207.0236 [hep-ph] (cit. on p. 197).

[226] M. Czakon and A. Mitov, *NNLO corrections to top pair production at hadron colliders: the quark-gluon reaction*, JHEP **01** (2013) 080, arXiv: 1210.6832 [hep-ph] (cit. on p. 197).

[227] M. Czakon, P. Fiedler, and A. Mitov, *Total Top-Quark Pair-Production Cross Section at Hadron Colliders Through $\alpha(\frac{4}{S})$*, Phys. Rev. Lett. **110** (2013) 252004, arXiv: 1303.6254 [hep-ph] (cit. on p. 197).

[228] M. Czakon and A. Mitov, *Top++: A program for the calculation of the top-pair cross-section at hadron colliders*, Comput. Phys. Commun. **185** (2014) 2930, arXiv: 1112.5675 [hep-ph] (cit. on p. 197).

[229] N. Kidonakis, *Two-loop soft anomalous dimensions for single top quark associated production with a W- or H-*, Phys.Rev. **D82** (2010) 054018, arXiv: 1005.4451 [hep-ph] (cit. on p. 198).

[230] N. Kidonakis, "Top Quark Production," *Proceedings, Helmholtz International Summer School on Physics of Heavy Quarks and Hadrons (HQ 2013): JINR, Dubna, Russia, July 15-28, 2013*, 2014 139, arXiv: 1311.0283 [hep-ph] (cit. on p. 198).

[231] M. Aliev, H. Lacker, U. Langenfeld, S. Moch, P. Uwer, et al., *HATHOR: Hadronic Top and Heavy quarks cross section calculator*, Comput.Phys.Commun. **182** (2011) 1034, arXiv: 1007.1327 [hep-ph] (cit. on p. 198).

[232] P. Kant et al., *HatHor for single top-quark production: Updated predictions and uncertainty estimates for single top-quark production in hadronic collisions*, Comput. Phys. Commun. **191** (2015) 74, arXiv: 1406.4403 [hep-ph] (cit. on p. 198).

[233] D. de Florian et al., *Handbook of LHC Higgs Cross Sections: 4. Deciphering the Nature of the Higgs Sector*, (2016), arXiv: 1610.07922 [hep-ph] (cit. on p. 198).

[234] J. Butterworth et al., *PDF4LHC recommendations for LHC Run II*, J. Phys. **G43** (2016) 023001, arXiv: 1510.03865 [hep-ph] (cit. on p. 199).

[235] ATLAS Collaboration, *Performance of top-quark and W-boson tagging with ATLAS in Run 2 of the LHC*, Eur. Phys. J. C **79** (2019) 375, arXiv: 1808.07858 [hep-ex] (cit. on p. 199).

[236] P. Artoisenet, R. Frederix, O. Mattelaer, and R. Rietkerk, *Automatic spin-entangled decays of heavy resonances in Monte Carlo simulations*, JHEP **03** (2013) 015, arXiv: 1212.3460 [hep-ph] (cit. on p. 199).

[237] S. Frixione, E. Laenen, P. Motylinski, and B. R. Webber, *Angular correlations of lepton pairs from vector boson and top quark decays in Monte Carlo simulations*, JHEP **04** (2007) 081, arXiv: hep-ph/0702198 (cit. on p. 199).

[238] B. Allanach and T. Cridge, *The calculation of sparticle and Higgs decays in the minimal and next-to-minimal supersymmetric standard models: SOFTSUSY4.0*, Computer Physics Communications **220** (2017) 417–502, ISSN: 0010-4655, URL: http://dx.doi.org/10.1016/j.cpc.2017.07.021 (cit. on p. 200).

[239] T Martin, *Development and online operation of minimum bias triggers in ATLAS*, **5** (2010) C12051, URL: https://doi.org/10.1088/1748-0221/5/12/c12051 (cit. on p. 213).

[240] T. B. et al., *Local Hadronic Calibration*, ATL-LARG-PUB-2009-001-2, 2008, URL: https://cds.cern.ch/record/1112035/ (cit. on p. 214).

[241] ATLAS Collaboration, *Jet reconstruction and performance using particle flow with the ATLAS Detector*, Eur. Phys. J. C **77** (2017) 466, arXiv: 1703.10485 [hep-ex] (cit. on pp. 214, 215).

[242] ATLAS Collaboration, *Secondary vertex finding for jet flavour identification with the ATLAS detector*, ATL-PHYS-PUB-2017-011, 2017, URL: https://cds.cern.ch/record/2270366 (cit. on p. 215).

[243] ATLAS Collaboration, *Topological b-hadron decay reconstruction and identification of b-jets with the JetFitter package in the ATLAS experiment at the LHC*, ATL-PHYS-PUB-2018-025, 2018, URL: https://cds.cern.ch/record/2645405 (cit. on p. 215).

[244] R. Frühwirth, *Application of Kalman filtering to track and vertex fitting*, Nuclear Instruments and Methods in Physics Research Section A: Accelerators, Spectrometers, Detectors and Associated Equipment **262** (1987) 444 , ISSN: 0168-9002, URL: http://www.sciencedirect.com/science/article/pii/0168900287908874 (cit. on pp. 215, 217).

[245] W. Lampl et al., *Calorimeter Clustering Algorithms: Description and Performance*, ATL-LARG-PUB-2008-002, 2008, URL: https://cds.cern.ch/record/1099735 (cit. on p. 217).

[246] T. G. Cornelissen et al., *The global χ2track fitter in ATLAS*, Journal of Physics: Conference Series **119** (2008) 032013, URL: https://doi.org/10.1088/1742-6596/119/3/032013 (cit. on p. 217).

[247] *Improved electron reconstruction in ATLAS using the Gaussian Sum Filter-based model for bremsstrahlung*, tech. rep. ATLAS-CONF-2012-047, CERN, 2012, URL: https://cds.cern.ch/record/1449796 (cit. on p. 217).

[248] ATLAS Collaboration, *Particle Identification Performance of the ATLAS Transition Radiation Tracker*, ATLAS-CONF-2011-128, 2011, URL: https://cds.cern.ch/record/1383793 (cit. on pp. 217, 219).

[249] D. W. Scott, *Multivariate Density Estimation, Theory, Practice, and Visualization*, Wiley-Interscience, 1992 (cit. on p. 218).

[250] A. Hoecker et al., *TMVA - Toolkit for Multivariate Data Analysis*, 2007, arXiv: 0703039 [physics.data-an] (cit. on p. 218).

[251] ATLAS Collaboration, *Electron reconstruction and identification in the ATLAS experiment using the 2015 and 2016 LHC proton–proton collision data at* $\sqrt{s} = 13$ *TeV*, Eur. Phys. J. C **79** (2019) 639, arXiv: 1902.04655 [hep-ex] (cit. on pp. 221, 306).

[252] ATLAS Collaboration, *Measurement of the photon identification efficiencies with the ATLAS detector using LHC Run 2 data collected in 2015 and 2016*, Eur. Phys. J. C **79** (2019) 205, arXiv: 1810.05087 [hep-ex] (cit. on pp. 221, 306).

[253] L. Devroye, *Non-Uniform Random Variate Generation*, Springer-Verlag, 1986 (cit. on p. 222).

[254] ATLAS Collaboration, *Internal note of the Run2 data quality summary.*, ATL-COM-DAPR-2019-001, 2019, URL: https://cds.cern.ch/record/2663169/ (cit. on p. 239).

[255] ATLAS Collaboration, *Non-collision backgrounds as measured by the ATLAS detector during the 2010 proton–proton run*, ATLAS-CONF-2011-137, 2011, URL: https://cds.cern.ch/record/1383840 (cit. on p. 238).

[256] *Characterisation and mitigation of beam-induced backgrounds observed in the ATLAS detector during the 2011 proton-proton run*, Journal of Instrumentation **8** (2013) P07004, URL: https://doi.org/10.1088%2F1748-0221%2F8%2F07%2Fp07004 (cit. on p. 238).

[257] ATLAS Collaboration, *Search for squarks and gluinos in final states with jets and missing transverse momentum using 139 fb^{-1} of $\sqrt{s}$ =13 TeV pp collision data with the ATLAS detector*, JHEP **2102** () 143. 64 p, arXiv: 2010.14293 [hep-ex] (cit. on p. 255).

[258] ATLAS Collaboration, *Search for a scalar partner of the top quark in the all-hadronic $t\bar{t}$ plus missing transverse momentum final state at $\sqrt{s}$=13 TeV with the ATLAS detector*, Eur. Phys. J. C **80** () 737. 44 p, arXiv: 2004.14060 [hep-ex] (cit. on p. 255).

[259] ATLAS Collaboration, *Search for new phenomena in final states with b-jets and missing transverse momentum in $\sqrt{s}$ = 13 TeV pp collisions with the ATLAS detector*, JHEP **2105** () 093. 51 p, arXiv: 2101.12527 [hep-ex] (cit. on p. 255).

[260] ATLAS Collaboration, *Measurement of the WW cross section in $\sqrt{s}$ = 7 TeV pp collisions with the ATLAS detector and limits on anomalous gauge couplings*, Phys. Lett. B **712** (2012) 289, arXiv: 1203.6232 [hep-ex] (cit. on p. 259).

[261] ATLAS Collaboration, *Prospects for Higgs boson searches using the $H \to WW^{(*)} \to \ell\nu\ell\nu$ decay mode with the ATLAS detector at* 10 *TeV*, ATL-PHYS-PUB-2010-005, 2010, URL: https://cds.cern.ch/record/1270568 (cit. on p. 259).

[262] ATLAS Collaboration, *Electron efficiency measurements with the ATLAS detector using 2012 LHC proton–proton collision data*, Eur. Phys. J. C **77** (2017) 195, arXiv: 1612.01456 [hep-ex] (cit. on p. 306).

[263] ATLAS Collaboration, *Muon reconstruction performance of the ATLAS detector in proton–proton collision data at $\sqrt{s}$ = 13 TeV*, Eur. Phys. J. C **76** (2016) 292, arXiv: 1603.05598 [hep-ex] (cit. on p. 307).

[264] ATLAS Collaboration, *E_T^{miss} performance in the ATLAS detector using 2015–2016 LHC pp collisions*, ATLAS-CONF-2018-023, 2018, URL: https://cds.cern.ch/record/2625233 (cit. on p. 307).

[265] ATLAS Collaboration, *Measurement of the Inelastic Proton–Proton Cross Section at $\sqrt{s}$ = 13 TeV with the ATLAS Detector at the LHC*, Phys. Rev. Lett. **117** (2016) 182002, arXiv: 1606.02625 [hep-ex] (cit. on p. 307).

[266] M. Baak et al., *HistFitter software framework for statistical data analysis*, Eur. Phys. J. C **75** (2015) 153, arXiv: 1410.1280 [hep-ex] (cit. on p. 309).

[267] The ATLAS and CMS Collaborations, *Procedure for the LHC Higgs boson search combination in Summer 2011*, ATL-PHYS-PUB-2011-11/CMS NOTE-2011/005 (2011) (cit. on p. 309).

[268] A. Wald, *Tests of Statistical Hypotheses Concerning Several Parameters When the Number of Observations is Large*, vol. Vol.54 No.3, 1943 426, URL: https://www.jstor.org/stable/1990256 (cit. on p. 311).